J. M. Arias M. Lozano (Eds.)

An Advanced Course in Modern Nuclear Physics

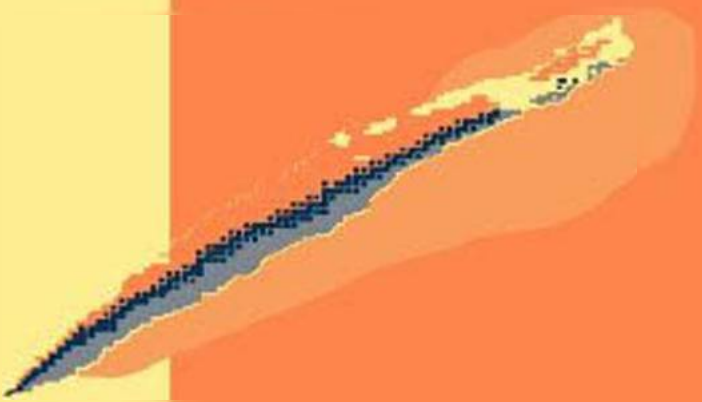

Springer

The theory of the nucleon-nucleon interaction

Robert Vinh Mau

Laboratoire de Physique Théorique des Particules Elémentaires,
Université Pierre et Marie Curie, 4, Place Jussieu F-75252 Paris Cedex 05, France

Abstract. Various approaches to the theory of the nucleon-nucleon interaction are reviewed with a special attention to the comparison of theoretical predictions with the rich body of existing experimental data.

1 Introduction

> *"In the past quarter century physicists have devoted a huge amount of experimentation and mental labour to this problem (the NN interaction) - probably more man hours than have been given to any other scientific question in the history of mankind"*
>
> H.A. Bethe (1953)

With the advent of Quantum Chromodynamics (QCD) which is believed to be the underlying theory of strong interactions, one is entitled to demand that hadron physics be described in terms of the degrees of freedom of the fundamental constituents in QCD. The trouble is that QCD has a running coupling constant $\alpha(q^2)$. For large momentum transfers q, as in the region of deep inelastic scattering of leptons by hadrons, $\alpha(q^2)$ is small. One can use there perturbation theory to make theoretical predictions which turn out to be in good agreement with experiment. But for processes of interest in nuclear forces or in low energy hadron physics, the length scale is typically 1 fm, corresponding to small momentum transfer q. The running coupling constant $\alpha(q^2)$ is then large and perturbation theory is no longer operative. In this strong-coupling regime, non perturbative methods are indispensable, but so far, apart from calculations on lattices, not much success has been achieved in this respect. Thus, one is led to modelling non perturbative QCD. For example, in bag models, non perturbative effects are simulated by the pressure on the bag, in string models they are described by the tension, in non relativistic potential models they are described by confining potentials. All these models make explicit use of the quark degrees of freedom.

J.M. Arias and M. Lozano (Eds.): LNP 581, pp. 1–38, 2001.
© Springer-Verlag Berlin Heidelberg 2001

On the other hand, a rich body of experimental data, most of them with very high accuracy, have been accumulated over the last three decades in the nucleon nucleon scattering. Most of these data can be analyzed quantitatively in the framework of theoretical models based on the degrees of freedom of hadrons themselves (nucleons, mesons, isobars, etc...). At present, it is fair to say that models built explicitly with quark degrees of freedom have not achieved the same success. Therefore, bridging these models based on hadrons with QCD seems to be one of the challenges for the physics of strong interactions. In this search, one can envisage another alternative. Since the fundamental constituents in QCD, quarks and gluons, are confined, it might be more appropriate to eliminate their degrees of freedom not directly observable and incorporate their effects into an effective theory framed in terms of observable hadronic degrees of freedom but including as many relevant properties of QCD as possible. This alternative is given support by the important conjecture of Witten [1] that, in the large N_c limit (N_c being the number of colors), QCD is equivalent to a theory of weakly coupled MESONS (and glueballs). BARYONS emerge in the theory as SOLITONS. To implement these ideas, one is led to construct effective Lagrangians from meson fields (π, ρ, ω, ϵ, etc..). These effective Lagrangians are required to fulfill the principal symmetries of QCD (like chiral symmetry for example). The free parameters, if there are any, can be determined in fitting the experimental observables in the physics of mesons. The soliton type solutions are then looked for, and used to predict static properties of baryons. The baryon-baryon interaction can also be deduced from the soliton-soliton interaction. The Skyrme model [12] proposed long ago is a prototype of this class of effective Lagrangians.

If the results of this approach turn out to be satisfactory, it can be regarded as a theoretically sound approximation scheme to non perturbative QCD at low energies. Moreover, the connection of the conventional models based on hadron degrees of freedom with QCD through this approximation scheme appears then quite naturally.

In this series of lectures, the main features and results of the nucleon-nucleon interaction in the framework of conventional hadronic degrees of freedom are recalled in Section 2, and recent tests of the NN potential models are described. In Section 3, results obtained with the explicit use of quark degrees of freedom are reviewed, and finally an introduction to Skyrme solitons and recent developments on effective Lagrangians for low energy hadron physics with the application to the NN forces are presented in Section 4.

2 Conventional low energy hadron physics

The case of the nucleon-nucleon forces is an enlightening example to illustrate the role of hadronic degrees of freedom in nuclear physics or more generally in low energy hadron physics. The two nucleon system is still relatively simple but rich enough to be regarded as a test case for theoretical models. Furthermore, the considerable wealth of experimental data provide extremely severe constraints.

2.1 Meson degrees of freedom

The One Pion Exchange Potential (OPEP)

The first main step towards the understanding of the forces between two nucleons was made by H. Yukawa in 1935. He proposed that these forces are induced by the exchange of a π meson (Fig. 1) leading to a nuclear potential, the One Pion Exchange Potential (OPEP) of the form

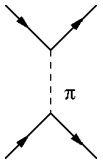

Fig. 1. The OPEP

$$V_{OPEP} = \frac{g^2}{4\pi}\left(\frac{m_\pi}{m}\right)^2 \frac{\boldsymbol{\tau}_1 \cdot \boldsymbol{\tau}_2}{12}\left[\boldsymbol{\sigma}_1 \cdot \boldsymbol{\sigma}_2 + (1 + \frac{3}{m_\pi r} + \frac{3}{(m_\pi r)^2})S_{12}\right]\frac{e^{-m_\pi r}}{r}$$

The pion mass m_π being 140 MeV, the OPEP has a range larger than $\frac{1}{m_\pi} \sim 2$ fm and provides the long range part of the nucleon-nucleon interaction.

The 4th order Two Pion Exchange Potential (TPEP)

After the experimental discovery of the pion confirming Yukawa's ideas, a great theoretical activity was devoted to the theory of mesons (Mesodynamics). At that time (early 50's), the analogy of this new field theory with Quantum Electrodynamics (QED) was hardly avoidable. Thus, methods and techniques used in QED, including perturbation theories, were transposed to it. This led to the calculation of 4th order diagrams of the Two Pion Exchange Potential (TPEP) represented in Fig. 2. The range of this TPEP is of shorter range than the OPEP, of the order of $\frac{1}{2m_\pi} \sim 1$ fm. We shall see later that these 4th order diagrams are only part of the TPEP, which contains other important contributions. In spite of efforts of prominent theorists, it is realized soon that the results of such calculations are hampered by ambiguities arising from the use of perturbation theories.

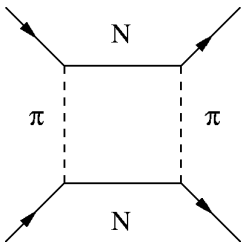

Fig. 2. The TPEP (4th order)

The One Boson Exchange Potential (OBEP)

In the early 60's, a new impetus to the theory of nucleon-nucleon forces was given by the experimental discovery of the ρ meson, and soon after, of the ω meson with the following characteristics :

$$\begin{aligned} \rho \text{ meson} &: J^{PG} = 1^{-+},\ I = 1,\ m_\rho = 769 \text{ MeV} \\ &\quad \text{decays into } 2\pi,\ \Gamma_\rho = 150 \text{ MeV} \\ \omega \text{ meson} &: J^{PG} = 1^{--},\ I = 0,\ m_\omega = 783 \text{ MeV} \\ &\quad \text{decays into } 3\pi,\ \Gamma_\omega = 10 \text{ MeV} \end{aligned}$$

It was then natural to generalize the initial theory of Yukawa with the idea that the pion exchange is responsible for the long range part of the NN forces and heavier mesons like the ρ and ω mesons are reponsible for the short range part. The OPEP becomes the OBEP (One Boson Exchange Potential) which now includes besides the exchange of the pion that of the ρ-meson and ω-meson. These can be easily calculated and their dominant contributions to the NN potential are

$$V_{\rho exch.} = \frac{g_\rho^2}{4\pi}\left(\frac{m_\rho}{m}\right)^2 \boldsymbol{\tau}_1\boldsymbol{\tau}_2(1+\frac{f_\rho}{g_\rho})^2\left[\boldsymbol{\sigma}_1\boldsymbol{\sigma}_2 - \frac{1}{12}(1+\frac{3}{m_\rho r}+\frac{3}{(m_\rho r)^2})S_{12}\right]\frac{e^{-m_\rho r}}{r}$$

$$V_{\omega exch.} = \frac{g_\omega^2}{4\pi}\left(1+\frac{m_\omega^2}{2m^2}+\frac{f_\omega m_\omega^2}{2g_\omega m^2}\right)\frac{e^{-m_\omega r}}{r} - \\ -\frac{g_\omega^2}{4\pi}\frac{m_\omega^2}{m^2}(3+\frac{f_\omega}{g_\omega})\left(\frac{1}{m_\omega r}+\frac{1}{(m_\omega r)^2}\right)\frac{e^{-m_\omega r}}{r}\boldsymbol{LS}$$

Thus, when the nucleon-nucleon potential is written in its general form

$$V_{NN} = V_C^+ + V_{SS}^+(r)\boldsymbol{\sigma}_1\boldsymbol{\sigma}_2 + V_T^+(r)S_{12} + V_{LS}^+(r)\boldsymbol{LS} \\ + \boldsymbol{\tau}_1\boldsymbol{\tau}_2[V_C^-(r) + V_{SS}^-(r)\boldsymbol{\sigma}_1\boldsymbol{\sigma}_2 + V_T^-(r)S_{12} + V_{LS}^- + V_{LS}^-(r)\boldsymbol{LS}$$

the π and ρ mesons contribute to the spin-spin component V_{SS}^- and the tensor component V_T^-, and the ω meson contributes to the central component V_C^+ and the spin-orbit component V_{LS}^+. Moreover, the ω meson contribution to V_C^+ is repulsive. This leads to purely *repulsive* forces in the central component V_C^+ which is the dominant part of the NN forces (Fig. 3). In contrast, for this component, phenomenology requires short range repulsion, responsible for nuclear matter saturation but medium range attraction, responsible for the binding of nucleons in nuclei.

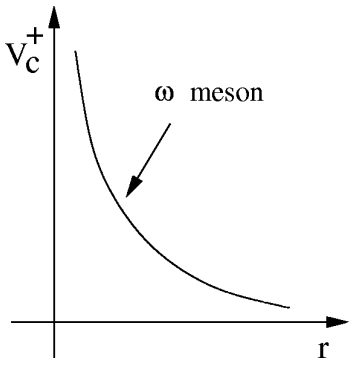

Fig. 3. The ω meson contribution to V_C^+

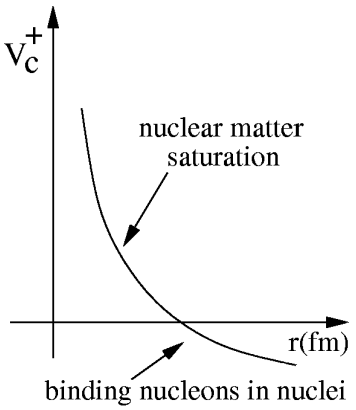

Fig. 4. The phenomenological shape for V_C^+

At this point, the first conclusion to be drawn is : in the OBE models with only the exchange of *observed* low mass mesons (π, ρ, ω), one cannot get the *intermediate range attraction* which is indispensable for the existence of nuclei[1]. The most obvious way of overcoming this serious difficulty is to introduce the exchange of a fictitious low mass ($\sim$ 500 MeV) scalar isoscalar meson ($J^{PG} = 0^{++}$, $I = 0$) which provides the missing medium range attraction. Such a low mass scalar meson is not observed experimentally. This makes the OBE models much less appealing in spite of their simplicity.

2.2 Isobar degrees of freedom

It is well known from π-nucleon scattering studies that formation of πN resonances (Δ_{33}, m_Δ= 1232 MeV ; P_{11}, m_{N^*}= 1440 MeV) is very important (Fig. 5). These resonances can be also formed in nuclei.

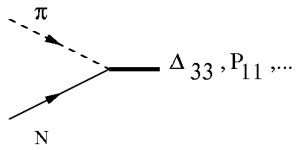

Fig. 5.

It is therefore expected that in the two pion exchange (TPE) processes, one or two nucleons can be easily excited to one or two such resonances in the intermediate state, and diagrams such as those of Fig. 6 should be added to the 4th order terms of Fig. 2.

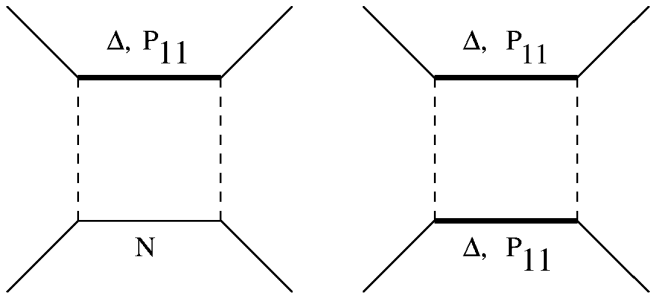

Fig. 6.

Such diagrams were studied long ago in reference [3], and it is found that their contributions give rise to attraction in the NN potential with a range of the order of $\frac{1}{2m_\pi} \sim 1$ fm. This corresponds precisely to the attraction which is missing in the (π, ρ, ω) exchange potential. The arguments presented above show the important role of the TPE contributions to the NN interaction besides the well established OPE contribution. Now, the exchanged pions in the TPE can be uncorrelated (Fig. 7b) or strongly correlated (Fig. 7c), since the $\pi\pi$ interaction is known to be very strong in the P wave giving rise to the ρ resonance and strong

[1] We will see later that this feature occurs also in other models like the quark or Skyrme models.

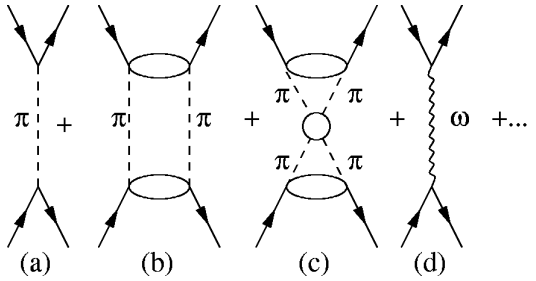

Fig. 7.

enough in the S wave to give rise to a broad resonance around 1 GeV (the ϵ meson). Great care should be, therefore, taken in the calculation of the TPE contributions.

All the previous discussion shows that a realistic description of the long range (LR) and medium range (MR) NN forces must include the isobar degrees of freedom as well as the meson degrees of freedom. This is summarized in Fig. 7 where the blobs in both Figures 7b and 7c represent the πN interaction (containing all the isobars) and the central blob of Fig. 7c represents the $\pi\pi$ interaction (containing the P wave ρ meson and the S wave ϵ meson). It is claimed sometimes that the short range (SR) part of the NN interaction can be described by the exchange of heavier mesons. However, in this part subhadronic (quarks, gluons, etc...) degrees of freedom can play, in principle, a significant role. This question will be discussed in Section 3.

2.3 The NN potentials from hadronic degrees of freedom

At present, potential models that are the most frequently used in the literature are the Bonn, the Nijmegen and the Paris potentials. They are all derived from *hadronic* degrees of fredom.

The BONN Potential

This potential is originally [4] a One Boson Exchange (OBE) type potential. It includes essentially the exchange of the π, ρ, ω mesons and a fictitious "σ" meson. Recently the Bonn group realizes the importance of the two-pion exchange (TPE) contribution and in the newest version [5] of the Bonn potential this contribution, calculated in the non-covariant perturbation theory, is added to the original OBE potential. This procedure, however, leads to double counting and other problems related to the use of the non-covariant perturbation theory. The $\pi - \rho$ exchange contribution is also calculated with the same method and included. Smooth form factors are used to cut-off the potential at short distances.

The NIJMEGEN Potential

This potential[6] is constructed from the exchange of the π, η, η', ρ, ω, ϕ, δ, S^*, ε Regge trajectories and also from the exchange of the Pomeron, f, f' and A_2 trajectories. At the Reggeon vertices exponential form factors are used. This leads to a OBE type potential for the π, $\eta, \ldots,$ ε exchange and a gaussian potential for the Pomeron-type exchange. The values of the free parameters are searched to fit to the NN phase shifts.

The PARIS potential

This potential [7]-[10] is representative of the philosophy elaborated above. This means :

a) the (LR + MR) parts (internucleon distances $r > 0.8$ fm) are given by the OPE, the TPE and the ω meson exchange, as part of the three pion exchange. The TPE as represented in Figs. 7b and 7c is calculated carefully via dispersion relations and unitarity from the πN amplitudes and the dominant S and P waves of the $\pi\pi$ interaction. The inputs of the calculation are, thus, the πN phase shifts $\delta_\ell^{\pi N}$ and the $\pi\pi$ phase shifts $\delta_0^{\pi\pi}$ and $\delta_1^{\pi\pi}$. The values of $\delta_\ell^{\pi N}$ are taken from phase shift analyses, and $\delta_0^{\pi\pi}$ and $\delta_1^{\pi\pi}$ directly from experiments. This includes automatically all the πN *isobars* and the $\pi\pi$ *resonances* in the S wave (the ε meson) and in the P wave (the ρ meson) as well as the πN and $\pi\pi$ non resonant backgrounds. It is sometimes argued that dispersion relations can only yield an empirical "black box" TPE contribution to the NN interaction, whereas a calculation in the non-covariant perturbation theory provides a more "microscopic" description. This statement is incorrect since one could have derived the πN and $\pi\pi$ phase shift from a "microscopic" model, and inserted them into the dispersion relations. We do not proceed in this way because we have more faith in the πN phase shift analyses, based on very accurate data, than in any presently available "microscopic" model which, in any case, should reproduce those phases. Thus, in the Paris potential the uncorrelated and correlated two pion exchange is completely fixed *with no free parameters*. The effective coupling constant of the ω to the nucleons is taken to be $g_\omega/4\pi = 11.75$. The details of these rather complicate calculations can be found in reference [7].

b) as mentioned above, the presently available theoretical results on the (SR) forces are still uncertain. On the other hand, there exists a rich body of experimental data. For $T_{LAB} < 350$ MeV, several thousand data points have been accumulated [11]. For these reasons, a phenomenological viewpoint was deliberately taken for the description of the (SR) part ($r < 0.8$ fm).

It was proposed [8] as a first step, to describe the core with a very simple phenomenological model : namely, the $LR + MR$ $(\pi + 2\pi + \omega)$ exchange potential is cut off rather sharply at an internucleon distance $r \sim 0.8$ fm and the SR ($r < 0.8$ fm) is described simply by a constant soft core. This introduces a minimum number (five) of adjustable parameters corresponding to the five components (central, spin-spin, tensor, spin-orbit, and quadratic spin-orbit) of the potential for each isospin state. On the other hand, it was found that the central

component of the theoretical $LR + MR$ potential has a weak but significant energy dependence and this energy dependence is, in a very good approximation, linear. One then expects also an energy dependent core for the central potential, the energy dependence is taken to be again linear. This introduces one additional parameter, the slope of the energy dependence. The proposed SR part is then determined by fitting to all the known phase shifts ($J < 6$) up to 330 MeV and the deuteron parameters. Although the number of free parameters is small (six in total for each isospin state) the quality of the fit is very good [8]. The χ^2/data are as good as those given by the best phenomenological potentials, which contain many more free parameters :

$$\chi^2/\text{data} = \left\{ \begin{array}{l} 2.5 \text{ for } pp \text{ scattering} \\ 3.7 \text{ for } np \text{ scattering} \end{array} \right\} \text{ with the Paris potential}$$

$$\chi^2/\text{data} = 2.4 \text{ for } pp + np \text{ scattering with the Reid soft core potential [12]}$$

The previous model with a sharp cutoff procedure (rather than smooth form factors often used in other works) was purposely chosen in its simplest form to demonstrate that, once the $(LR + MR)$ forces are accurately determined, the (SR) forces can be described by a model with few parameters that does not perturb the theoretical inputs of the $(LR + MR)$ part. This procedure has the advantage of a clear-cut separation between the theoretical $LR + MR$ and phenomenological SR parts. The latter contains all the free parameters. In a subsequent paper [9], an analytical expression for the complete potential was developed in terms of a parametrization as a discrete sum of Yukawa terms. This has the advantage of being simple in both configuration and momentum spaces. This parametrization is a purely mathematical representation and made convenient enough to facilitate its use in many-body calculations. The determination of the core parameters is now performed by fitting not only the phase shifts but also the scattering data themselves. Use was made of the world set of data consisting of 913 data points for pp scattering ($3 \leq T_{LAB} \leq 330$ MeV) and 2239 data points for np scattering ($13 \leq T_{LAB} \leq 350$ MeV). This set includes measurements on cross sections, polarization, Wolfenstein parameters and spin correlations. Examples of the fit can be found in reference [10]. The fit yields a total χ^2/data shown in Table 1. In this table, these values are compared, for reference with those of phase shift analysis [13]. The total χ^2/ data for the same set of data was also calculated in reference [10] for the Reid soft core potential [12]. The values are also shown in Table 1.

It is worth noticing that the χ^2/ data for the Reid soft core potential obtained previously in fitting the phase shifts, has deteriorated quite significantly.

Table 1.

	χ^2/data for pp scattering	χ^2/data for np scattering
Paris	1.99	2.17
P.S.A. [13]	1.33	1.80
R.S.C.	4.76	9.99

This is an illustration of a situation where a potential can fit very well the phase shifts without being in agreement with data. A phase shift representation is useful and gives a good idea of the overall properties of the NN interaction but for an accurate quantitative test of theoretical models, it is more decisive to compare theoretical predictions and experimental data directly rather than through phase shifts. The deuteron parameters are also predicted in nice agreement with experiment.

2.4 Recent tests of NN potential models

During the last two years, several very high precision experiments have been completed. They consist of new measurements of the analyzing power for np scattering at very low energies (10-25 MeV) [14]-[15], measurements of cross sections and polarization for np scattering at higher energies and various spin observables for pp scattering [16]-[18].

The np data at low energies are very important because of their high degree of accuracy (10^{-3}) and also because for such low energies (10-20 MeV) the S waves are accurately known from the effective range formula, and the P and higher waves are only sensitive to the $(LR + MR)$ forces. Thus, these low energy analyzing power data provide severe tests on the $(LR + MR)$ part of the NN interaction, that part which is supposed to possess the soundest theoretical grounds in the potential models.

The data for the analyzing power $A_y(\theta)$ at 10.03 MeV, 16.9 MeV and 25 MeV are displayed in figures 8-10. Predictions from the Bonn, Nijmegen and Paris potentials are also shown for comparison.

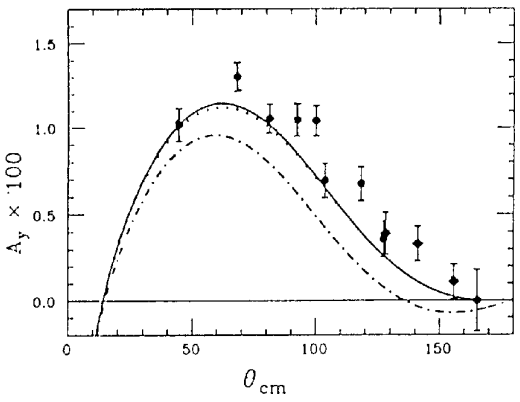

Fig. 8. Analyzing power A_y in np scattering at 10.03 MeV [14]. The solid, dotted, and dot-dashed curves are results using the Paris, Nijmegen, and Bonn potentials, respectively.

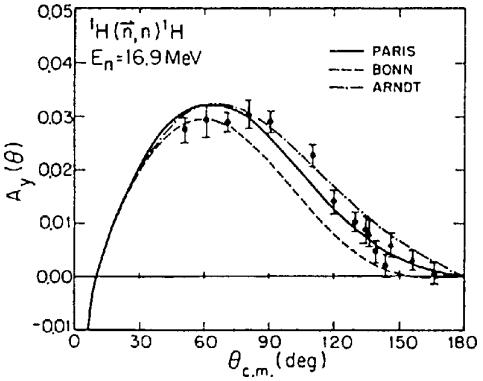

Fig. 9. $A_y(\theta)$ in np scattering at 16.9 MeV [15].The curves are predictions calculated from the Paris potential (solid curve), Bonn potential (dashed curve), and from Arndt's recent 0-1.3 GeV NN phase shift analysis (dashed-dotted curve).

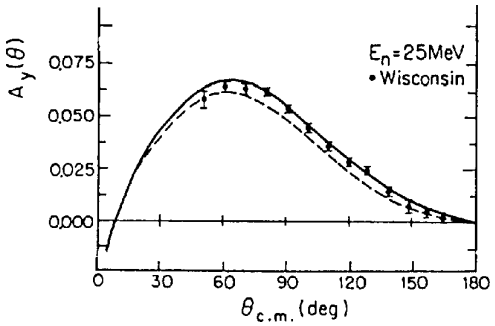

Fig. 10. $A_y(\theta)$ in np scattering at 25 MeV [14]. The solid and dashed curves are results using the Paris and the Bonn potentials, respectively.

It is concluded in reference [14] that "fair agreement is obtained with the Paris and Nijmegen potentials but clear disagreement with the new Bonn potential", and in reference [15] that "the experimental data in this energy range are better described by the Paris potential than by the new Bonn potential". It is also stated in reference [14] that "increasing the ω meson exchange contribution in the Bonn potential improves the agreement with the present results while retaining the overall description of the NN observables". This statement seems rather odd, given the very large coupling of the ω already needed in that potential.

Examples of very recent pp spin observables and np cross sections and polarization at higher energies are shown in figures 11-14 and compared with the Paris potential predictions (not a new fit).

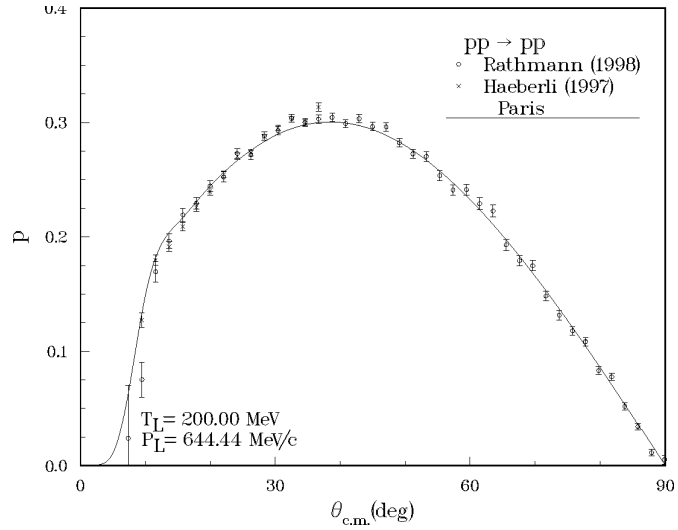

Fig. 11. Polarization in *pp* scattering at 200 MeV. The data are from references [16].

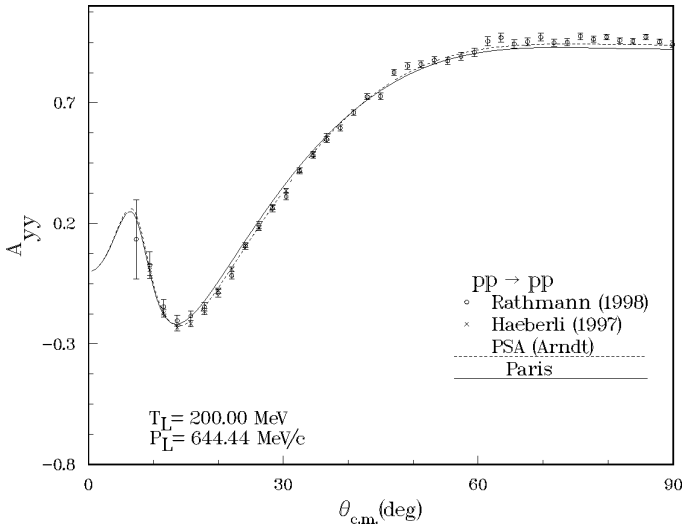

Fig. 12. Spin correlation parameter $A_{yy}(\theta)$ in *pp* scattering at 20 MeV. The data are from the same references as in Fig. 11.

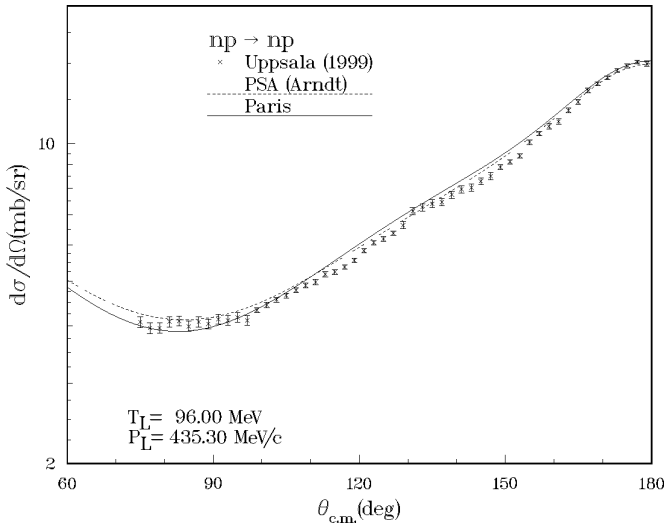

Fig. 13. Differential cross section for *np* scattering at 96 MeV. The data are from references [17].

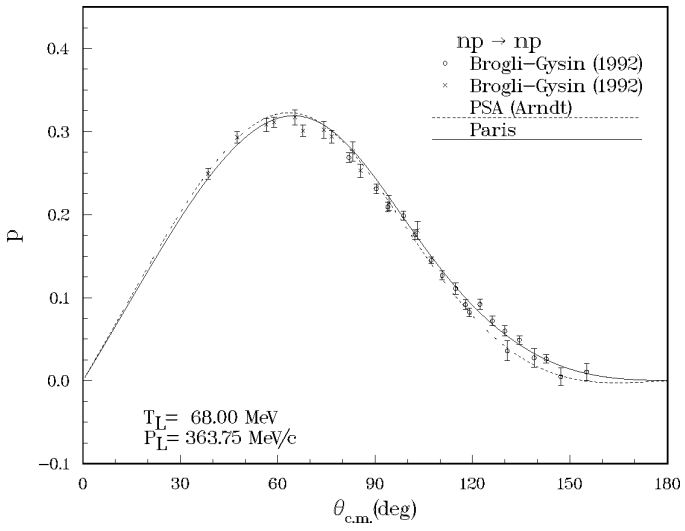

Fig. 14. Polarization in *np* scattering at 68 MeV. The data are from ref. [18].

To conclude this Section, one can say that NN potentials based on *hadronic* degrees of freedom, when they are properly constructed, continue to pass with success the different new and more severe experimental tests . This is remarkable as some of the models, like the Paris potential, are more than 20 years old, and have never been altered since. So far there is no need for it. Yet the predictions are still in good agreement with the more and more accurate experimental data. The present χ^2/data is 1.83 for the world set of 1832 *pp* data points and 3.39 for 3577 *np* data points.

3 Quark degrees of freedom

As was mentioned before, nuclear physics or more generally low energy hadron physics corresponds to the non perturbative phase of QCD. Therefore, a description of low energy hadron processes in terms of quark degrees of freedom must take into account in one way or another these non perturbative effects. Models for these are represented by bag models, string models or nonrelativistic quark models with confining potentials. Single hadron spectroscopy, meson and baryon mass spectra, as well as static properties of baryon have been analyzed in the framework of these models with somewhat equal success. However, at present, easily tractable methods for the quantitative calculation of the two baryon interaction do not exist for the bag or the string models. For the potential models, the non relativistic calculations for a single hadron have been extended to the system of two baryons by using methods that are well known is nuclear physics like those of the cluster model [19]-[22].

3.1 The quark cluster model (QCM) and the NN interaction

The Hamiltonian considered for the quark system is

$$H = \sum_i \frac{p_i^2}{2m_i} - K(CM) + \sum_{i<j} V_{ij} \tag{1}$$

K(CM) is the kinetic energy for the total c.m. motion. The two body interaction V_{ij} consists of the confinement term $V_{ij}^{conf.}$ which is supposed to account for the non perturbative effects of QCD and $V_{ij}^{res.}$ the residual interaction.

$$V_{ij} = V_{ij}^{conf.} + V_{ij}^{res.} \tag{2}$$

Usually the confinement potential is taken to be linear or quadratic

$$V_{ij}^{conf.} = -(\lambda_i \lambda_j) a_n r_{ij}^n \quad (n = 1 \text{ or } 2) \tag{3}$$

and the residual interaction to be given by the one gluon exchange potential

$$V_{ij}^{res.} = V_{ij}^{OGE} = \lambda_i \lambda_j \left[\frac{\alpha_s}{4 r_{ij}} - \frac{\pi \alpha_s}{4 m_i^2} (1 + \frac{2}{3} \boldsymbol{\sigma}_i \boldsymbol{\sigma}_j) \right] \delta(r_{ij}) \tag{4}$$

with the neglect of the tensor and spin orbit components. λ_i are the color matrices.

In the quark cluster model, the wave function for a 6-quark system is assumed to be of the form

$$\Psi_\beta(1,2,3,\dots 6) = \mathbf{A}[\{\phi_a(123)\phi_b(456)\}_\beta \chi_\beta(R_a - R_b] \tag{5}$$

where
$\phi_{a,b}$: wave function of nucleon a or b (cluster of 3 quarks)
χ_β : relative wave function
$R_a - R_b = R_{ab}$: relative coordinate between the 2 clusters
$\mathbf{A}$: antisymmetrization operator with respect to the quarks
β : coupling of a and b into a well defined flavor and spin state β

When the internal wavefunctions of the two clusters ϕ_a and ϕ_b are known, the Schrödinger equation gives

$$\sum_\beta \int \{\phi_a^*(\boldsymbol{\xi}_a)\phi_b^*(\boldsymbol{\xi}_b)\}_\alpha [H - E]\Psi_\beta(\boldsymbol{\xi}_a, \boldsymbol{\xi}_b, \boldsymbol{R}_{ab}), d\boldsymbol{\xi}_a \; d\boldsymbol{\xi}_b = 0 \tag{6}$$

where the internal coordinates of the clusters a and b are now introduced explicitly :

$$\begin{array}{lll} & \boldsymbol{\xi}_a = (\boldsymbol{\xi}_1, \boldsymbol{\xi}_2) & \boldsymbol{\xi}_b = (\boldsymbol{\xi}_3, \boldsymbol{\xi}_4) \\ \text{with} & \boldsymbol{\xi}_1 = \boldsymbol{r}_1 - \boldsymbol{r}_2, & \boldsymbol{\xi}_2 = \frac{\boldsymbol{r}_1 + \boldsymbol{r}_2}{2} - \boldsymbol{r}_3 \\ & \boldsymbol{\xi}_3 = \boldsymbol{r}_4 - \boldsymbol{r}_5, & \boldsymbol{\xi}_4 = \frac{\boldsymbol{r}_4 + \boldsymbol{r}_5}{2} - \boldsymbol{r}_6 \\ \text{and} & \boldsymbol{R}_a = \frac{1}{3}(\boldsymbol{r}_1 + \boldsymbol{r}_2 + \boldsymbol{r}_3), & \boldsymbol{R}_b = \frac{1}{3}(\boldsymbol{r}_4 + \boldsymbol{r}_5 + \boldsymbol{r}_6) \end{array} \tag{7}$$

Straightforward manipulations in this equation lead to the coupled channel equation, the Resonating Group Method (RGM) equation :

$$\sum_\beta \int d\boldsymbol{R}' [H_{\alpha\beta}(\boldsymbol{R}, \boldsymbol{R}') - E N_{\alpha\beta}(\boldsymbol{R}, \boldsymbol{R}')]\chi_\beta(\boldsymbol{R}') = 0 \tag{8}$$

where

$$\begin{aligned} H(\boldsymbol{R}, \boldsymbol{R}') &= \int \phi_a^+(\boldsymbol{\xi}_a)\phi_b^+(\boldsymbol{\xi}_b)\delta(\boldsymbol{R} - \boldsymbol{R}_{ab})H(1 - \mathbf{A})\phi_a(\boldsymbol{\xi}_a)\phi_b(\boldsymbol{\xi}_b)\times \\ &\quad \times \delta(\boldsymbol{R}' - \boldsymbol{R}_{ab}) d\boldsymbol{\xi}_a d\boldsymbol{\xi}_b d\boldsymbol{R}_{ab} \\ &= H^d(\boldsymbol{R}')\delta(\boldsymbol{R}' - \boldsymbol{R}) - H^{ex}(\boldsymbol{R}, \boldsymbol{R}') \end{aligned} \tag{9}$$

$$\begin{aligned} N(\boldsymbol{R}, \boldsymbol{R}') &= \int \phi_a^+(\boldsymbol{\xi}_a)\phi_b^+(\boldsymbol{\xi}_b)\delta(\boldsymbol{R} - \boldsymbol{R}_{ab})(1 - \mathbf{A})\phi_a(\boldsymbol{\xi}_a)\phi_b(\boldsymbol{\xi}_b)\times \\ &\quad \times \delta(\boldsymbol{R}' - \boldsymbol{R}_{ab}) d\boldsymbol{\xi}_a d\boldsymbol{\xi}_b d\boldsymbol{R}_{ab} \\ &= N^d(\boldsymbol{R}')\delta(\boldsymbol{R}' - \boldsymbol{R}) - N^{ex}(\boldsymbol{R}, \boldsymbol{R}') \end{aligned} \tag{10}$$

$$\mathbf{A} = 1 - \sum_{i=1}^{3}\sum_{j=4}^{6} P_{ij} = 1 - \mathbf{A}' \tag{11}$$

Introducing the following renormalized wave function

$$\chi_\beta(\boldsymbol{R}) = \int N_\beta^{1/2}(\boldsymbol{R}, \boldsymbol{R}')\chi_\beta(\boldsymbol{R}')d\boldsymbol{R}' \tag{12}$$

and the corresponding renormalized hamiltonian kernel

$$H_{\alpha\beta}(\boldsymbol{R},\boldsymbol{R}') = \int N_{\alpha}^{-1/2}(\boldsymbol{R},\boldsymbol{R}'')H_{\alpha}(\boldsymbol{R}'',\boldsymbol{R}''')N_{\beta}^{1/2}(\boldsymbol{R}''',\boldsymbol{R}')d\boldsymbol{R}''d\boldsymbol{R}''' \qquad (13)$$

one obtains an ordinary Schrödinger type equation.

Once this latter equation is solved, one can also define an equivalent local potential (ELP) in terms of $\chi(\boldsymbol{R})$ through the equation

$$-\frac{\nabla_R^2}{2\mu}\chi(\boldsymbol{R}) + V(R)\chi(\boldsymbol{R}) = E_{\chi}(\boldsymbol{R}) \qquad (14)$$

The low partial wave phase shifts ($^1S_0$ and $^3S_1$) were calculated [19],[20] from the RGM equation and the results shown in Fig. 15. The phase shifts have negative values indicating the *repulsive* character of the forces.

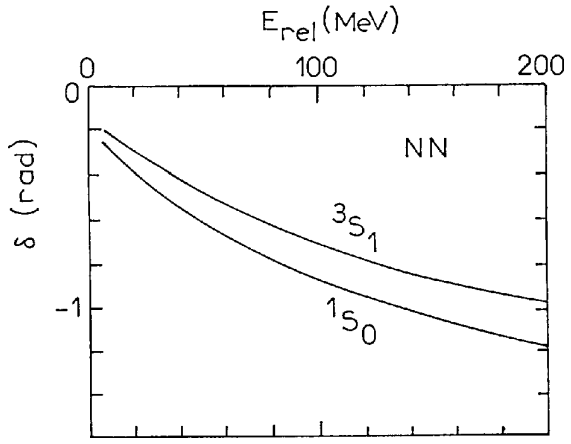

Fig. 15. The results correspond to the set of parameters : $m_q = 313$ MeV, b = 0.6 fm, $a_2 = 62.5$ MeV/fm^2, $\alpha_s = 1.517$.

An equivalent local potential (ELP) was also derived [19], showing the following properties.

i) the central potential V_c^+ is *repulsive* for all distances confirming the results obtained with the phase shifts. The lack of attraction in the medium range suggests that these calculations should be taken seriously only for short distances.
ii) a linear energy dependence for the $^1S_0$ and $^3S_1$ potentials very much like the one existing in the Paris potential for short ranges.

So far, the nucleon is considered as a 3 valence quark system interacting weakly via the residual interaction given by the OGE potential. Configurations

with the excitation of quark-antiquark pairs for baryons, as shown in Fig. 16 are considered in reference [23].

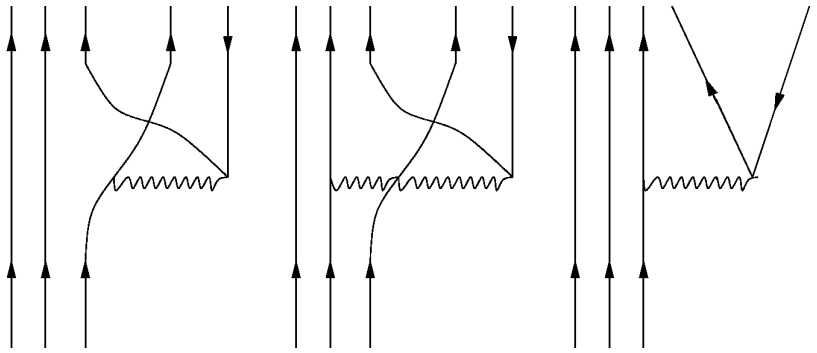

Fig. 16. The excitation of a $(q\bar{q})$ pair in the 3 valence quark configuration of baryons.

The baryon wave function is now given by

$$\phi = \phi_0(3q) + \sum_\alpha C_\alpha \phi_\alpha[(3q)(q\bar{q})] \tag{15}$$

The additional components are given in terms of two cluster wave functions

$$\phi_\alpha[(3q)(q\bar{q})] \propto \mathbf{A}\{\phi_{\alpha_1}(3q)\phi_{\alpha_2}(q\bar{q})]\}_\alpha \chi_\alpha \tag{16}$$

where the notations are similar to eq. (5) and self explanatory.

Some attraction to the NN potential was found through these $q\bar{q}$ excitations. However, the effects due to the excitation of one $q\bar{q}$ pair are small. Larger effects can be obtained if one introduces the excitation of two $q\bar{q}$ pairs i.e. additionnal components $\phi_\beta[(3q)(q\bar{q})^2]$, but, the model becomes then quite involved. On the other hand, while it is reasonable to assume that the SR forces can be described in terms of the quark degrees of freedom, it is uneconomical to extend such a description to all distances since, as shown before, the meson exchanges and isobar excitations provide an accurate account of the $(LR + MR)$ forces.

A more realistic approach seems to be a hybrid one where the SR forces derived from quark degrees of freedom are combined with the $(LR + MR)$ forces derived from hadronic degrees of freedom.

3.2 The hybrid (quark + meson exchanges) model

This kind of models were considered first in references [19], [21] in order to amend the results given by the quark cluster models. In reference [19], a phenomenological potential with intermediate range attractive forces is added in the equations of the quark cluster model whereas in reference [21] the additionnal potential is given by coupling the quarks to the pion and a σ-meson.

In the following, the more complete works of references [24], [25] will be described. In these works, it is assumed that the quark and gluon exchange interaction is dominant only in the region where the two clusters overlap while the hadronic degrees of freedom are effective at long and intermediate distances. This approximation has the good feature that it does not need any ambiguous coupling of quarks to mesons. Thus, the ELP of reference [19] is cut off sharply at a distance R_c and replaced, outside R_c, by the $(\pi + 2\pi + \omega)$ exchange potential. The TPEP is given by the Paris potential. The model is materialized by the following potential.

$$V(r) = V_{quark}(r)f(r) + V_{meson}(r)[1 - f(r)]$$

where V_{quark} = ELP of reference [19]

$$V_{meson} = (\pi + 2\pi + \omega) \text{ exchange potential}$$

The cut off function is chosen of the form $f(r) = \frac{1}{1+(r/R_c)^\alpha}$, the same as that used in reference [8]. The sharpness of $f(r)$ is realized by choosing $\alpha = 10$. R_c is the only free parameter, and in reference [24] adjusted to fit the deuteron binding energy which yields $R_c = 0.626$ fm. Different phase shifts are then calculated. The agreement with experimental data and the predictions of the Paris potential is very good except for the $^1D_2$, $^3P_1$ and $^3P_2$ phase shifts. However, as seen before, a fit to the phase shifts is not a good enough test of the model. One should make a direct comparison of the predictions with the data of observables. This was done in reference [25]. There the parameter R_c is adjusted to reproduce the $^1S_0$ phase shift at low energy. This yields $R_c = 0.83$ fm. Interestingly enough, this value is very close to that used in the Paris potential to delimit the phenomenological and theoretical parts. The predictions of the model are then compared with the existing world data set for pp scattering. The agreement with experiment is not good, leading to a total χ^2 divided by the number of data points, χ^2/ data=140, for the 1553 pp data points in the range $25 < T_L < 333$ MeV, and χ^2/ data=20, for 2268 np data points in the range $25 < T_L < 325$ MeV. For comparison let us recall that the Paris potential gives χ^2/ data=1.99 and 2.17, respectively, for the same set of data. Some typical examples of the results are displayed in figures 17-20. In these figures are also shown the results obtained with the model of reference [26]. The results of reference [25] could seem surprising in view of conclusions which can be found in the literature. However, most of the calculations on which these conclusions are based concern only the NN S-wave phase shifts, apart form the works of reference [24] and [26] where other higher partial waves are also computed. Furthermore, in these calculations, phenomenological LR+MR forces, often unrealistic, are added to the QCM contribution and adjusted to get a good fit to the phase shifts. For example, in reference [26] the good fit to the phase shifts, in particular for the $^3P_2$ state, is obtained at the expense of introducing a phenomenological potential with a strong attraction (which amounts to as much as 150-190 MeV at 1 fm). This work of reference [25] shows, to say the least, that conclusions on the

ability of the QCM to describe the SR nucleon-nucleon forces clearly differ, depending on whether one adopts the viewpoint of supplementing the QCM with adjustable LR+MR forces or one chooses to associate the QCM with realistic and well founded LR+MR forces.

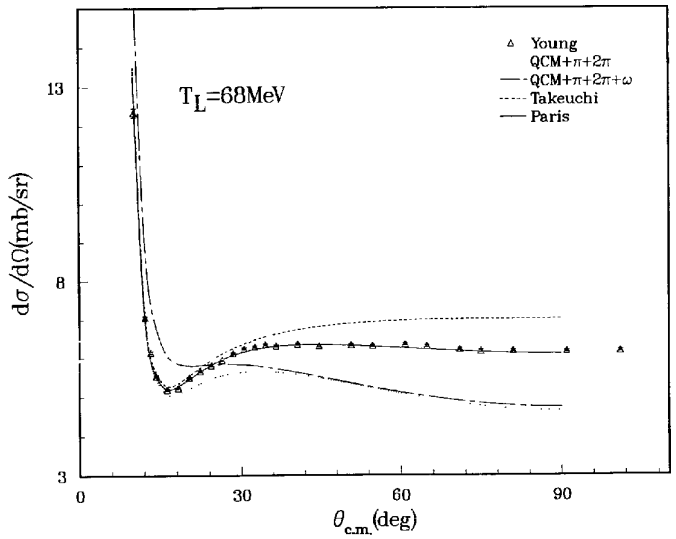

Fig. 17. Differential cross setion for *pp* scattering at 68 MeV. The data are from reference [27]. The curves are predictions of reference [25] (dotted and dash-dotted), reference [26] (dashed) and the Paris potential (solid).

4 Topological solitons and effective lagrangians for non perturbative QCD and the NN forces

In the quark cluster model presented above, non perturbative effects of QCD are simulated by the confining potentials and quark degrees of freedom are considered explicitly. As mentioned above it might be more appropriate since the fundamental constituents in QCD are confined, to eliminate their degrees of freedom not directly observable and incorporate their effects into an effective theory framed in terms of observable hadronic degrees of freedom but including as many relevant properties of QCD as possible. This alternative is given support by the important result of Witten [1]that, in the large N_c limit, N_c being the number of colors, QCD is equivalent to a theory of weakly coupled MESONS (and glueballs). BARYONS emerge in the theory as SOLITONS. The Skyrme model [2] proposed almost thirty years ago, falls precisely in this class of effective theories.

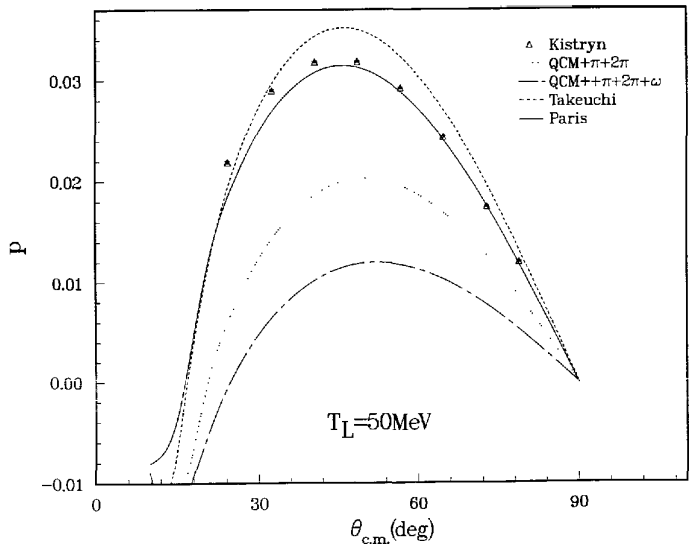

Fig. 18. Polarization for pp scattering at 50 MeV. The data are from reference [28]. The curves are the same as in fig. 17.

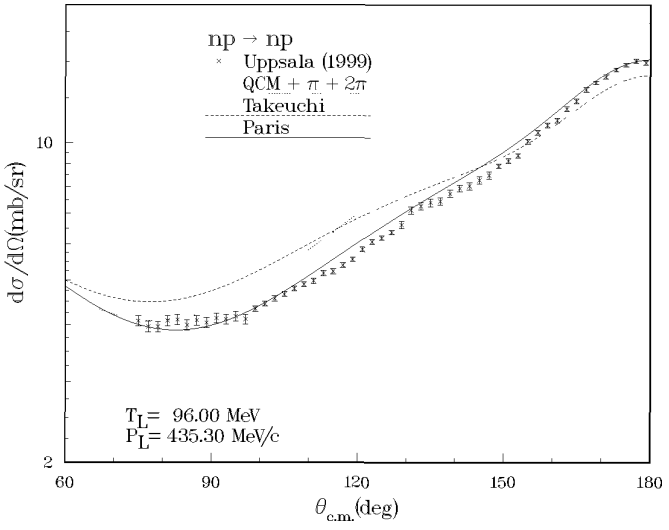

Fig. 19. Differential cross section for np scattering at 96 MeV. The data are from reference [17].

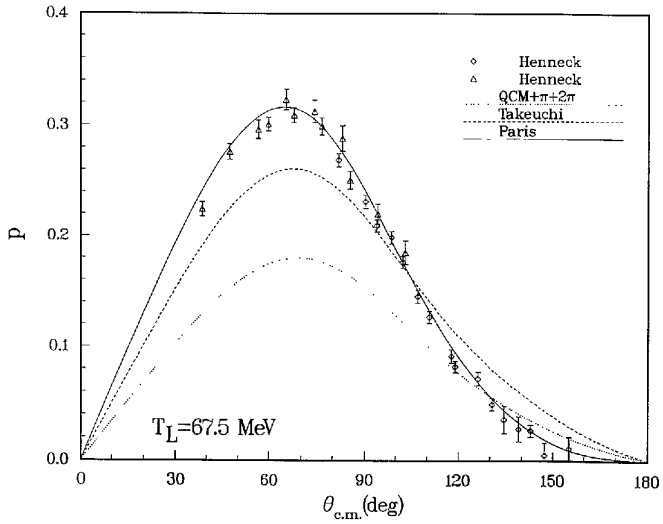

Fig. 20. Polarization for np scattering at 67.5 MeV. The data are from reference [29]. The curves are the same as in fig. 17.

4.1 The physics of Skyrme solitons

An important property of QCD is its chiral symmetry, and this invariance must be preserved in the corresponding effective field theories.

The σ model

The simplest chirally invariant effective field theory is the σ model [30]. Its version without fermions belongs to the class of effective field theories contemplated above. This version of the σ model can be formulated in the following way. Consider a 2 x 2 matrix field :

$$U(x) = \frac{1}{f_\pi}\begin{pmatrix} \sigma + i\pi_3 & i\pi_1 + \pi_2 \\ i\pi_1 - \pi_2 & \sigma - i\pi_3 \end{pmatrix} = \frac{1}{f_\pi}[\sigma(x) + i\boldsymbol{\tau}\cdot\boldsymbol{\pi}(x)]$$

where σ is a scalar and isoscalar field and π is the pion field. The Lagrangian density can then be written as

$$\mathcal{L}_2(x) = \frac{f_\pi^2}{4} Tr[\partial_\mu U(x)\partial^\mu U^+(x)] \tag{17}$$

In the non-linear realization of the σ model, the σ field is eliminated from the model via the chirally invariant constraint,

$$\sigma^2 + \boldsymbol{\pi}^2 = f_\pi^2, \tag{18}$$

implying that U is unitary. Defining

$$\sigma = f_\pi \cos\theta(r) \text{ and } \boldsymbol{\pi} = f_\pi \hat{\pi} \sin\theta(r), \tag{19}$$

we can write

$$U = e^{i\boldsymbol{\tau}\cdot\hat{\pi}\ \theta(r)}. \tag{20}$$

In eqs. 17-19, f_π is the pion decay constant. The trouble with the non-linear σ model is that it leads to energetically unstable solutions. By dimensional arguments, one can see that the energy scales like R, where R is the size of the system, and it vanishes when the system shrinks to zero size.

The Skyrme Model

To remedy this shortcoming, Skyrme [2] proposed the addition of higher-order terms in the derivative $\partial_\mu U$ to the Lagrangian density $\mathcal{L}_2(x)$. He chose to add to $\mathcal{L}_2(x)$ a term of the form

$$\mathcal{L}_4(x) = \frac{1}{32e^2} Tr[(\partial_\mu U)U^+, (\partial_\nu U)U^+] \tag{21}$$

The resulting Lagrangian density

$$\mathcal{L}(x) = \mathcal{L}_2(x) + \mathcal{L}_4(x) \tag{22}$$

yields a complicate non-linear Euler-Lagrange equation which is difficult to solve. However, if one makes the ansatz that the pion field is directed radially in configuration space, i.e. $\hat{\pi} = \hat{r}$, $\hat{r}$ being a unit vector in coordinate space, the U field is of the "hedgehog" form

$$U = e^{i\boldsymbol{\tau}\cdot\hat{r}\ \theta(|\boldsymbol{r}|)} \tag{23}$$

In this case, the Lagrangian is

$$\begin{aligned} L &= \int d^3x \mathcal{L}(x) \\ &= \frac{\pi}{2}\frac{F_\pi}{e}\int_0^\infty d\tilde{r}\left\{\tilde{r}^2(\dot{\theta}^2 + \tfrac{2\sin^2\theta}{\tilde{r}^2}) + 4\sin^2\theta(\tfrac{\sin^2\theta}{\tilde{r}^2} + 2\dot{\theta}^2)\right\} \end{aligned} \tag{24}$$

with the choice of length scale $\tilde{r} = eF_\pi \boldsymbol{r}$, $\dot{\theta} = d\theta/d\tilde{r}$ and $F_\pi = 2f_\pi$. Minimizing L with respect θ, one gets the following Euler-Lagrange equation

$$\ddot{\theta}\left(\frac{\tilde{r}^2}{4} + 2\sin^2\theta\right) + \tilde{r}\ \frac{\dot{\theta}}{2} - \frac{\sin 2\theta}{4} + \dot{\theta}^2 \sin 2\theta - \frac{\sin^2\theta \sin 2\theta}{\tilde{r}^2} = 0 \tag{25}$$

Soliton solutions can be found [2] with the boundary conditions

$$\theta(\infty) = 0 \text{ and } \theta(0) = n\pi, \quad n = \text{ integer} \tag{26}$$

This solution is now energetically stable since the contribution of the term $\mathcal{L}_4(x)$ of eq. (22) to the energy is proportional to $1/R$ so that the total energy can be minimized with respect to R to give a finite value. It can also be shown [2] that the solutions characterized by these boundary conditions are topological solitons whose winding number is n.

The Baryonic Current

Besides the usual Noether currents, such as V_μ and A_μ, associated with various symmetries fullfilled by the Lagrangian $\mathcal{L}(x)$, Skyrme showed that one can construct an "anomalous" current

$$B_\mu = \frac{1}{24\pi^2}\varepsilon_{\mu\alpha\beta\gamma}Tr[(U^+\partial_\alpha U)(U^+\partial_\beta U)(U^+\partial_\gamma U) \tag{27}$$

which is automatically conserved. A new quantum number can be therefore associated to B_μ since this current does not correspond to any initial symmetry of the Lagrangian. With the hedgehog solution, the time component of B_μ is

$$B_0 = \frac{1}{4\pi^2 r^2}(\cos 2\theta - 1)\frac{d\theta}{dr} \tag{28}$$

Integrating this density over all space and taking into account the boundary conditions (26) one gets

$$B = \int d^3x B_0(r) = n$$

where n is the winding number characterizing the soliton solution U. At this point Skyrme identified n with the baryon number, or equivalently B_μ with the baryonic current. BARYONS therefore emerge from the model as TOPOLOGICAL SOLITONS.

Quantization

So far, the Lagrangian as well as the Euler-Lagrange equation are classical. U is a classical field and therefore carries no definite spin and isospin values. A simple quantization method starting from the classical solution $U_0 = e^{i\boldsymbol{\tau}\cdot\hat{r}\ \theta}$ was proposed by Adkins, Nappi and Witten [31]. These authors introduce collective coordinate through the unitary transformation

$$A = a_4 + \boldsymbol{\tau}\cdot\boldsymbol{a} \tag{29}$$

where the a_μ' s are independent of $\boldsymbol{r}$ but can depend on time t. The a_μ also satisfy the constraint

$$\sum_{\mu=1}^{4} a_\mu^2 = 1 \tag{30}$$

since A is unitary. Under this transformation, U_0 becomes $U = A(t)U_0A^+(t)$. Substituting U into the Lagrangian yields

$$L = \int d^3(x)\mathcal{L}(U = A^+U_0A) \tag{31}$$

$$= -M + \lambda\, Tr\left(\frac{\partial A}{\partial t}\ \frac{\partial A^+}{\partial t}\right) \tag{32}$$

$$= -M + 2\lambda\sum_{m=1}^{4}(\dot{a}_\mu)^2, \quad \dot{a}_\mu = \frac{da_\mu}{dt} \tag{33}$$

where M is given by eq. (24) and

$$\lambda = \frac{2\pi}{3F_\pi e^3} \int_0^\infty d\tilde{r}\ \tilde{r}^2 \sin^2\theta \left[1 + 4\left((\frac{d\theta}{d\tilde{r}})^2 + \frac{\sin^2\theta}{\tilde{r}^2}\right)\right]. \tag{34}$$

From the Lagrangian one gets the Hamiltonian

$$H = \Pi_\mu \dot{a}_\mu - L, \tag{35}$$

where the Π_μ's are the conjugate momenta

$$\Pi_\mu = \frac{\partial L}{\partial \dot{a}_\mu} = 4\lambda \dot{a}_\mu \tag{36}$$

Substitution of (33) and (36) into eq. (35) yields

$$H = M + \frac{1}{8\lambda} \sum_{\mu=1}^{4} \Pi_\mu^2 \tag{37}$$

With the usual canonical quantization procedure

$$\Pi_\mu = -i\ \frac{\partial}{\partial a_\mu} \tag{38}$$

the Hamiltonian takes the form

$$H = M + \frac{1}{8\lambda} \sum_{\mu=1}^{4} \left(-\frac{\partial^2}{\partial a_\mu^2}\right) \tag{39}$$

with the constraint $\sum_\mu a_\mu^2 = 1$.

Because of this constraint the term $\sum_\mu \frac{\partial^2}{\partial a_\mu^2}$ is to be interpreted as the Laplacian on a 3-dimensional sphere. The eigenfunctions of H are polynomials in a_μ.

Under a rotation about the z-axis in configuration space by a small angle δ, it is easy to show that

$$e^{i\boldsymbol{\tau}\cdot\boldsymbol{\tau}} \to e^{i\frac{\delta}{2}\tau_z} e^{i\boldsymbol{\tau}\cdot\boldsymbol{\tau}} e^{i\frac{\delta}{2}\tau_z} \tag{40}$$

Hence, under this rotation the field configuration A $e^{i\boldsymbol{\tau}\cdot\hat{r}\ \theta(r)} A^+$ transforms into a new one with

$$A \to A e^{i\frac{\delta}{2}\tau_z} \tag{41}$$

or

$$(a_4 + i\boldsymbol{\tau}\cdot\boldsymbol{a}) \to (a_4 + i\boldsymbol{\tau}\cdot\boldsymbol{a})(1 + i\frac{\delta}{2}\tau_z) \tag{42}$$

This gives after some algebra

$$\left.\begin{aligned} a_4 &\to a_4 - \tfrac{\delta}{2} a_z \\ a_z &\to a_z + \tfrac{\delta}{2} a_4 \\ a_x &\to a_x - \tfrac{\delta}{2} a_y \\ a_y &\to a_y + \tfrac{\delta}{2} a_x \end{aligned}\right\} \tag{43}$$

Identifying this transformation with the initial rotation written in terms of the spin operators, i.e. $a_\mu \to (1 + i\delta J_z)a_\mu$ one finds

$$J_z = \frac{i}{2}\left[-a_4\frac{\partial}{\partial a_z} + a_z\frac{\partial}{\partial a_4} - a_x\frac{\partial}{\partial a_y} + a_y\frac{\partial}{\partial a_x}\right] \tag{44}$$

Under a rotation about the z-axis of isospin space by a small angle δ

$$A \to e^{-i\frac{\delta}{2}\tau_z}A \tag{45}$$

and the same calculation as before leads to

$$I_z = \frac{i}{2}\left[a_4\frac{\partial}{\partial a_z} - a_z\frac{\partial}{\partial a_4} - a_x\frac{\partial}{\partial a_y} + a_y\frac{\partial}{\partial a_x}\right] \tag{46}$$

It is now easy to verify that the spin-isospin wave functions for various baryons are :

$$\begin{array}{ll} |p\uparrow\rangle = \frac{1}{\pi}(a_x + ia_y) & |p\downarrow\rangle = \frac{-i}{\pi}(a_4 + ia_z) \\ |n\uparrow\rangle = \frac{i}{\pi}(a_4 + ia_z) & |n\downarrow\rangle = \frac{-i}{\pi}(a_x + ia_y) \\ |\Delta^+; S_z = \frac{1}{2}\rangle = -\frac{\sqrt{2}}{\pi}(a_x - ia_y)[1 - 3(a_4^2 + a_z^2)] & \\ |\Delta^{++}; S_z = \frac{3}{2}\rangle = \frac{\sqrt{2}}{\pi}(a_x - ia_y)^3 & \\ \text{etc}\ldots & \end{array} \tag{47}$$

The calculation of observables is then reduced to the evaluation of appropriate matrix elements of operators (constructed from the field configuration) with these spin-isospin wave functions.

For example, the proton mass is

$$\langle p\uparrow|H|p\uparrow\rangle = \frac{1}{\pi^2}\int d^4a\delta\left(\sum a_\mu^2 - 1\right)(a_x - ia_y)H(a_x + ia_y) \tag{48}$$

$$= M + \frac{3}{8\lambda} \tag{49}$$

the delta mass is

$$\langle\Delta^{++}, s_z = \frac{3}{2}|H|\ \Delta^{++}, s_z = \frac{3}{2}\rangle = M + \frac{15}{8\lambda} \tag{50}$$

where the expression (39) for $H(U = AU_0A^+)$ has been used.

Results for the Static Properties of Baryons

The previous procedure has been applied in reference [31] to the calculation of baryon masses (nucleon and delta resonance), charge radii, magnetic moments and coupling constants. These authors adjust F_π and e to fit the nucleon and Δ masses. This gives $F_\pi = 129$ MeV and $e = 5.45$. The other quantities are predicted. They are, except for axial vector coupling constant g_A, in qualitative agreement with experiment (within 30%)).

The Baryon-Baryon Interaction

Another field of application where the model can be confronted by experiment is the baryon-baryon interaction and especially the low energy nucleon-nucleon interaction.

With the hedgehog form (23) and the Lagrangian density (22) it is not difficult to derive the static interaction between two solitons, if one makes the approximation that the field configuration, when the solitons are at a distance $\boldsymbol{R}$ apart, is a simple product of the form

$$U(\boldsymbol{r}) = U_0(\boldsymbol{r} + \frac{\boldsymbol{R}}{2})U_0(\boldsymbol{r} - \frac{\boldsymbol{R}}{2}) \tag{51}$$

where $U_0(\boldsymbol{r}) = e^{i\boldsymbol{\tau}\ \hat{r}\ \theta(|\boldsymbol{r}|)}$ is the classical solution. However, this field configuration is again spin and isospin degenerate. One has to map out the spin and isospin content of the two-soliton interaction, if one wants to identify the baryon-baryon interaction of interest. The projection of the soliton-soliton interaction into different baryon-baryon channels can be achieved by rotating the soliton through collective coordinates. Because of the symmetry between space and isospin in the hedgehog solutions, the rotation can be performed either in configuration space [32] or in isospin space [33]-[34]. In the following, I shall describe the methods using isospin rotations. The two solitons are rotated independently in $SU(2)$ space

$$\begin{aligned} U_0(\boldsymbol{r} + \tfrac{\boldsymbol{R}}{2}) &\to AU_0(\boldsymbol{r} + \tfrac{\boldsymbol{R}}{2})A^+ \\ U_0(\boldsymbol{r} - \tfrac{\boldsymbol{R}}{2}) &\to BU_0(\boldsymbol{r} - \tfrac{\boldsymbol{R}}{2})B^+ \end{aligned} \tag{52}$$

where A and B are unitary matrices

$$A = a_4 + i\ \boldsymbol{\tau}\cdot\boldsymbol{a} \qquad B = b_4 + i\ \boldsymbol{\tau}\cdot\boldsymbol{b} \tag{53}$$

the components a_μ and b_μ lie on the surfaces of four-spheres,

$$\sum_{\mu=1}^{4} a_\mu^2 = \sum_{\mu=1}^{4} b_\mu^2 = 1 \tag{54}$$

The Soliton-Soliton Interaction . Under the rotation (52) the field configuration (51) for the two solitons becomes

$$U(\boldsymbol{r}) = AU_0(\boldsymbol{r} + \frac{\boldsymbol{R}}{2})A^+BU_0(\boldsymbol{r} - \frac{\boldsymbol{R}}{2})B^+ \tag{55}$$

It is clear that only the relative rotation of the two solitons is relevant and the energy in the field of eq. (55) is the same as in

$$U(\boldsymbol{r}) = U_0(\boldsymbol{r} + \frac{\boldsymbol{R}}{2})CU_0(\boldsymbol{r} - \frac{\boldsymbol{R}}{2})C^+ \tag{56}$$

where $C = A^+B = c_4 + i\boldsymbol{\tau}\boldsymbol{c}$ and

$$c_4 = a_4b_4 + \boldsymbol{a}\cdot\boldsymbol{b}, \qquad \boldsymbol{c} = a_4\boldsymbol{b} - b_4\boldsymbol{a} + \boldsymbol{a}\wedge\boldsymbol{b} \tag{57}$$

When eq. (56) for U is substituted into the energy density and when this density is integrated over all space $\boldsymbol{r}$, the total energy can be expressed as the sum of two parts. The first comes from terms in which the derivatives all act upon the same soliton $U_0(\boldsymbol{r}+\boldsymbol{R}/2)$ or $U_0(\boldsymbol{r}-\boldsymbol{R}/2)$. This term is independent of C and of R and is simply twice the static baryon mass. The second part, which will be denoted by $v(\boldsymbol{R}, C)$ involves only mixed derivatives. It is a function of both R and the variables c_μ and is identified as the baryon-baryon potential.

By a choice of length scale $\tilde{r} = eF_\pi \boldsymbol{r}$, $\tilde{R} = eF_\pi \boldsymbol{R}$ the two parameters in the theory are made into simple scales of length and of energy and one finds that

$$v(\tilde{R}, C) = v_2(\tilde{R}, C) + v_4(\tilde{R}, C) \tag{58}$$

where

$$v_2(\tilde{R}, C) = \frac{F_\pi}{8e} \int d^3\tilde{r}\ \rho_2(\tilde{R}, \tilde{r}, C) \tag{59}$$

$$v_4(\tilde{R}, C) = \frac{F_\pi}{8e} \int d^3\tilde{r}\ \rho_4(\tilde{R}, \tilde{r}, C) \tag{60}$$

and

$$\begin{aligned} \rho_2 = Tr[&-X_i C Y_i C^+ + C^+ X_i C (Y_j Y_j Y_i + Y_i Y_j Y_j - 2 Y_j Y_i Y_j) \\ &+ C Y_i C^+ (X_j X_j X_i + X_i X_j X_j - 2 X_j X_i X_j) \\ &+ C Y_i Y_i C^+ X_j X_j + C Y_i Y_j C^+ X_j X_i \\ &- 2 C Y_i Y_j C^+ X_i X_j] \end{aligned} \tag{61}$$

$$\begin{aligned} \rho_4 = \tfrac{1}{2} Tr[&X_i C Y_j C^+ (X_j C Y_i C^+ - X_i C Y_j C^+) \\ &+ C Y_i C^+ X_j (C Y_j C^+ X_i - C Y_i C^+ X_j)] \end{aligned} \tag{62}$$

with

$$\begin{aligned} X_i &= U_0^+(\boldsymbol{r}+\boldsymbol{R}/2)\partial_i U_0^+(\boldsymbol{r}+\boldsymbol{R}/2) \\ Y_i &= \partial_i U_0(\boldsymbol{r}-\boldsymbol{R}/2) U_0^+(\boldsymbol{r}-\boldsymbol{R}/2) \end{aligned} \tag{63}$$

∂_i is the partial derivative with respect to $\tilde{r}$.

For calculational purpose it is convenient not to immediately impose the constraint $\sum_\mu c_\mu^2 = 1$. Before this constraint is imposed v_2 and ρ_2 are quadratic forms and v_4 and ρ_4 quartic forms in the variables c_μ.

The first term of eq. (61) which is quadratic in X_i and Y_j is the contribution of the quadratic term $\mathcal{L}_2(x)$ in the Lagrangian (22); all the remaining terms in eqs. (61) and (62), which are quartic in X_i and Y_j, are from the quartic piece $\mathcal{L}_4$ of the Lagrangian.

$$\langle v(\tilde{R}, C)\rangle = \int\int dadb\ \phi^*(a,b) v(\tilde{R}, C) \phi(a,b) \tag{64}$$

where the integrals are over the surface of the unit four-sphere. The c_μ are related to a_μ and b_μ by eq. (57) and a_μ act upon the soliton centered at $\tilde{r} = \tilde{R}/2$. These functions of a_μ and b_μ act like spin and isospin operators, but can also transform one baryon state into another and in particular they mix the nucleon and the delta states. The baryon number $B = 2$ wave functions $\phi(a,b)$ are constructed from single nucleon and delta states and these are given in eqs. (47).

For example

$$\langle p\uparrow p\uparrow|V|p\uparrow p\uparrow\rangle = \int d^4a\delta(\sum a_\mu^2 - 1)d^4b\delta(\sum b_\mu^2 - 1)(a_x^2+a_y^2)(b_x^2+b_y^2)v(\tilde{R},C)$$

It can be shown from eqs. (59)-(60) that the general form of $v(\tilde{R},C)$ is

$$v_2(\tilde{R},C) = \alpha_1(c_4^2+\boldsymbol{c}^2) + \alpha_2 c_4^2 + \alpha_3\frac{(\boldsymbol{c}\cdot\tilde{R})^2}{\tilde{R}^2} \tag{65}$$

and

$$\begin{aligned} v_4(\tilde{R},C) = (\boldsymbol{c}^2+c_4^2)(\beta_1(\boldsymbol{c}^2+c_4^2) + \beta_2 c_4^2 + \beta_3\tfrac{(\boldsymbol{c}\cdot\tilde{R})^2}{\tilde{R}^2} \\ + \beta_4 c_4^4 + \beta_5 c_4^2\tfrac{(\boldsymbol{c}\cdot\tilde{R})^2}{\tilde{R}^2} + \beta_6\tfrac{(\boldsymbol{c}\cdot\tilde{R})^4}{\tilde{R}^4} \end{aligned} \tag{66}$$

where the α's and β's are functions of $|\tilde{R}|$ only. They can be calculated by letting the vector $\tilde{R}$ lie in the z-direction; then for example $\alpha_1(|\tilde{R}|)$ is the right-hand side of eqs. (59), (61) with $C = i\tau x$, $\beta_1+\beta_2+\beta_4$ is the right-hand side of eqs. (60), (62) with $C = 1$. Six choices of the matrix C can yield enough independent linear equations to determine the α's and β's.

Imposing the constraint $c_4^2 + \boldsymbol{c}^2 = 1$ yields

$$\begin{aligned} v(\tilde{R},C) = (\alpha_1+\beta_1) + (\alpha_2+\beta_2)c_4^2 + (\alpha_3+\beta_3)\tfrac{(\boldsymbol{c}\cdot\tilde{R})^2}{\tilde{R}^2} \\ + \beta_4 c_4^4 + \beta_5 c_4^2\tfrac{(\boldsymbol{c}\cdot\tilde{R})^2}{\tilde{R}^2} + \beta_6\tfrac{(\boldsymbol{c}\cdot\tilde{R})^4}{\tilde{R}^4} \end{aligned} \tag{67}$$

The Static Nucleon-Nucleon Potential . Let us now consider the contribution of $v(\tilde{R},C)$ to the static nucleon-nucleon potential. This potential, in both isospin states, is the sum of central, spin-spin and tensor parts, and can be written as

$$\begin{aligned} V(\tilde{R}) = V_c^+(|\tilde{R}|) + \boldsymbol{\tau}_1\cdot\boldsymbol{\tau}_2 V_c^-(|\tilde{R}|) + \boldsymbol{\sigma}_1\cdot\boldsymbol{\sigma}_2[V_{SS}^+(|\tilde{R}|) + \boldsymbol{\tau}_1\cdot\boldsymbol{\tau}_2 V_{SS}^-(|\tilde{R}|)] \\ + \left(\tfrac{3\boldsymbol{\sigma}_1\tilde{R}\boldsymbol{\sigma}_2\tilde{R}}{\tilde{R}^2} - \boldsymbol{\sigma}_1\cdot\boldsymbol{\sigma}_2\right)[V_T^+(|\tilde{R}|) + \boldsymbol{\tau}_1\cdot\boldsymbol{\tau}_2 V_T^-(|\tilde{R}|)] \end{aligned} \tag{68}$$

These conventional potentials can be related to the functions $\alpha_i(\tilde{R})$ and $\beta_i(\tilde{R})$ by taking six matrix elements of $V(\tilde{R},C)$. Eq. (64) is used for calculating the latter with the wave functions of eq. (47) in a_μ for the first soliton and in b_μ for the second. For example,

$$\begin{aligned} \langle p\uparrow p\uparrow|V|p\uparrow p\uparrow\rangle &= \textstyle\int d^4a\delta(\sum a_\mu^2 - 1)d^4b\delta(\sum b_\mu^2 - 1) \\ &\qquad (a_x^2+a_y^2)(b_x^2+b_y^2)v(\tilde{R},C) \\ &= (\alpha_1+\beta_1) + \tfrac{5}{18}(\alpha_2+\beta_2+\alpha_3+\beta_3) + \\ &+ \tfrac{7}{48}(\beta_4 + \tfrac{1}{3}\beta_5 + \beta_6) \end{aligned} \tag{69}$$

where $|p\uparrow p\uparrow\rangle$ is the state of two protons both with spin oriented along the z-axis (the direction of $\tilde{R}$). This matrix element can be equated to

$$V_C^+ + V_C^- + V_{SS}^+ + V_{SS}^- + 2(V_T^+ + V_T^-) \tag{70}$$

By solving six such algebraic equations one finds that, independent of the functional forms of the α's and β's

$$C_C^- = V_{SS}^+ + V_T^+ = 0$$

and

$$\begin{aligned} V_C^+ &= \alpha_1 + \beta_1 + \frac{1}{4}(\alpha_2 + \beta_2 + \alpha_3 + \beta_3) + \frac{1}{8}(\alpha_4 + \beta_6) + \frac{1}{24}\beta_5 \\ V_{SS}^- &= \frac{1}{36}(\alpha_2 + \beta_2) - \frac{1}{108}(\alpha_3 + \beta_3) + \frac{1}{48}\beta_4 + \frac{1}{432}\beta_5 - \frac{1}{144}\beta_6 \\ V_T^- &= \frac{1}{54}(\alpha_3 + \beta_3) + \frac{1}{432}\beta_5 + \frac{1}{72}\beta_6 \end{aligned} \tag{71}$$

One also finds the following identities in the functions α's and β's

$$\begin{aligned} 8\beta_3 + \beta_5 + 6\beta_6 &= 0 \\ 8\beta_2 + \beta_5 + 6\beta_4 &= 0 \end{aligned} \tag{72}$$

These are in fact the combinations which occur in V_{SS}^- and V_T^- so that the quartic terms in C in $v(\tilde{R}, C)$ contribute only to the central potential V_C^+. The quadratic term in the Lagrangian (22) contributes only to V_{SS}^- and V_T^-.

The previous method can be applied to the calculation of the nucleon-delta potential as well as the transition potential [33].

Numerical Results. At large R the nucleon-nucleon potential is known to be dominated by the one pion-exchange tensor potential which, for massless pions, is

$$V_T^- = (4m^2)^{-1}(g^2/4\pi)R^{-3} \tag{73}$$

where g is the conventional pion-nucleon coupling constant and m is the nucleon mass. It is found that at large R the tensor potential calculated here does indeed dominate and is of the form

$$V_T^- = (F_\pi/e)25.6/\tilde{R}^3 = (F_\pi^2 e^4)^{-1}25.6/R^3 \tag{74}$$

Identifying the long-range Skyrme-model potential with the conventional one pion-exchange yield the result

$$g/2m = 18/F_\pi e^2, \tag{75}$$

which is the same as that of reference [31] but by a very different method. The numerical results are shown in Fig. 21.

It can be seen that at intermediate range, i.e. for 1fm $\leq R \leq$ 2 fm the calculated V_T^- and V_{SS}^- deviate from the one-pion-exchange contribution by about the same amount as that due to the ρ meson exchange. These components of the potential are therefore in agreement with the NN phenomenology. As for the V_c^+ component, there is no attraction in the intermediate range. This deficiency is the same as that encountered above in the OBE models without the "σ" meson and in the quark cluster model.

4.2 Beyond the Skyrme model

The Skyrme model is a prototype of effective meson theories in which baryons emerge as topological solitons. Considering the results discussed in the previous sections, the question arises whether baryon physics can be deduced from meson

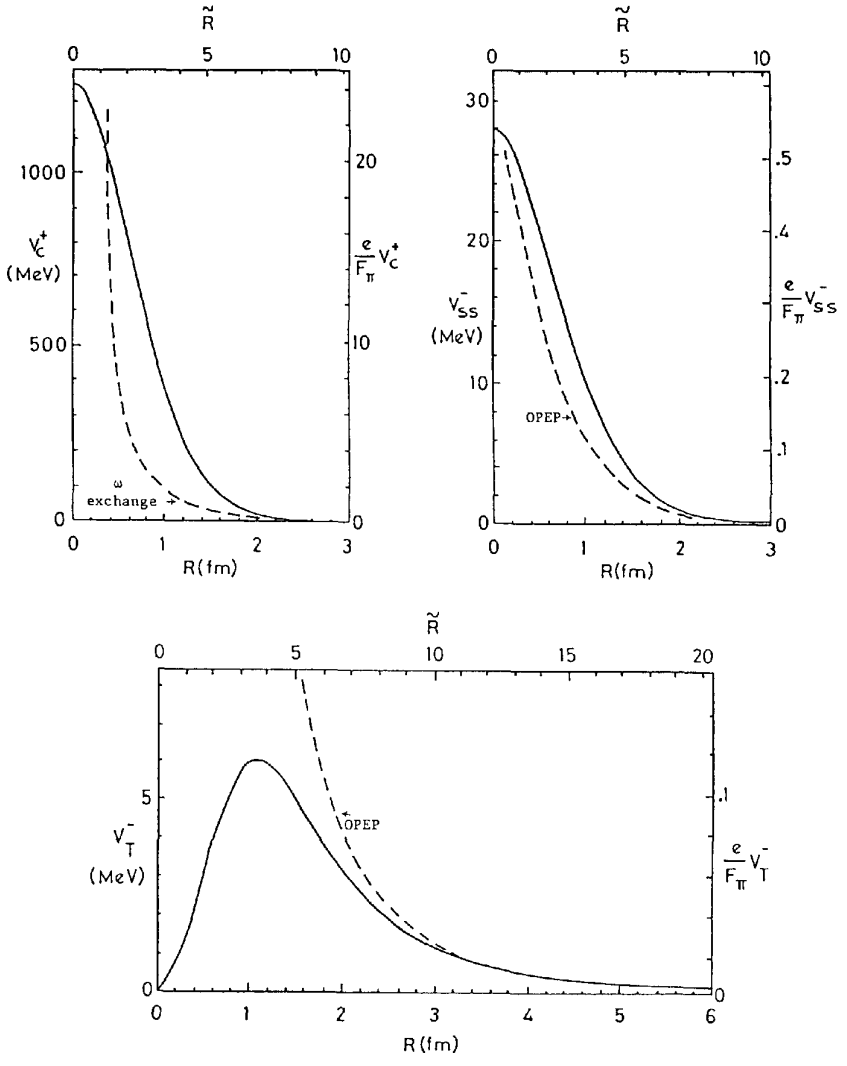

Fig. 21. The potentials V_C^+, V_{SS}^-, and V_T^- as a function of R.

physics via solitons [35]. For such a program, a fundamental dynamical theory for meson physics is, however, still missing. On the other hand, the Skyrme model which can be considered as the first two terms of an expansion of a chiral effective Lagrangian in powers of the derivatives of the pion field, is probably too crude. The next improvement one can think of, is to include higher order terms in the derivative expansion. Attempts in this direction have been made in references [36]-[38].

A more realistic improvement consists of constructing an effective Lagrangian implementing the known phenomenological features of meson physics at energies below about 1 GeV. In particular, one must incorporate the observed low mass mesons which, on the other hand, are known to couple into baryons. References [39] follow this viewpoint and an effective Lagrangian is constructed from the non linear σ model along with the low lying mesons, namely, isovector mesons (the ρ and its chiral partner A_1), a chiral singlet vector meson (the ω), and a chiral singlet scalar meson (the ε, which is responsible for the enhancement at around 1 GeV of the $\pi\pi$ S wave).

The effective Lagrangian density considered is of the form

$$\mathcal{L}(x) = \mathcal{L}_{\pi\rho A_1}(x) + \mathcal{L}_{\omega}(x) + \mathcal{L}_{\varepsilon}(x) \tag{76}$$

where

$$\begin{aligned}\mathcal{L}_{\pi\rho A_1}(x) = &-\frac{1}{8}Tr(X_{\mu\nu}^2 + Y_{\mu\nu}^2) + \frac{1}{4}m_\rho^2 Tr(X_\mu^2 + Y_\mu^2) + f\ Tr(D_\mu U(D^\mu U)^+) \\ &+ \frac{\Delta m^2}{8}Tr[(X_\mu U - UY_\mu)(U^+X^\mu - Y^\mu U^+)]\end{aligned} \tag{77}$$

$$\begin{aligned}\mathcal{L}_{\omega}(x) = &-\tfrac{1}{4}(\partial_\mu\omega_\nu - \partial_\nu\omega_\mu)^2 + \tfrac{1}{2}m_\omega^2\omega_\mu^2 + \beta_\omega\omega_\mu B^\mu \\ &- \tfrac{i\beta_\omega g}{8\pi^2}\varepsilon^{\mu\nu\alpha\beta}\partial_\mu\omega_\nu Tr[X_\alpha L_\beta - Y_\alpha R_\beta + ig(UY_\alpha U^+X_\beta - Y_\alpha X_\beta)]\end{aligned} \tag{78}$$

$$\mathcal{L}_{\varepsilon}(x) = \frac{1}{2}(\partial_\mu\varepsilon)^2 - \frac{1}{2}m_\varepsilon^2 - \delta_\varepsilon\varepsilon Tr(\partial_\mu U\partial^\mu U^+) \tag{79}$$

and

$$\begin{aligned} U &= e^{2i\boldsymbol{\tau}\cdot\boldsymbol{\phi}/F_\pi} \\ B_\mu(x) &= \frac{\varepsilon_{\mu\nu\alpha\beta}}{24\pi^2}Tr[(U^+\partial^\nu U)(U^+\partial^\alpha U)(U^+\partial^\beta U)] \\ D_\mu U &= \partial_\mu U + ig(X_\mu U - UY_\mu) \\ X_{\mu\nu} &= \partial_\mu X_\nu - \partial_\nu X_\mu + ig[X_\mu, X_\nu] \\ Y_{\mu\nu} &= \partial_\mu Y_\nu - \partial_\nu Y_\mu + ig[Y_\mu, Y_\nu] \\ L_\alpha &= \partial_\alpha U U^+ \quad R_\alpha = \partial_\alpha U^+ U \end{aligned} \tag{80}$$

$\boldsymbol{\phi}(x)$ and $\omega_\mu(x)$ are the pion and omega meson fields, $X_\mu = \boldsymbol{X}_\mu\boldsymbol{\tau}$, $Y_\mu = \boldsymbol{Y}_\mu\boldsymbol{\tau}$, and $\boldsymbol{X}_\mu(x)$, $\boldsymbol{Y}_\mu(x)$, are the left handed and right handed isovector fields. These left and right handed fields are more convenient to handle in chiral invariant theories than the vector and axial vector fields.

This Lagrangian takes full account of the Wess-Zumino anomalies. It is worthnoting that in the approximation where the "kinetic" terms of the ε, X_μ, Y_μ and ω_μ fields are neglected in comparison with their masses, these fields can be eliminated from the Lagrangian through the field equations. In this case $\mathcal{L}_{\pi\rho A_1}$

yields the Skyrme model with the parameter $e^2 = 2g^2[1-((m_\rho^2+\Delta m^2)/m_A^2)^2]^2$, $\mathcal{L}_\varepsilon$ the symmetric quartic term in $\partial_\mu U$ and $\mathcal{L}_\omega$ a sixth order term. The fact that, in this low energy approximation, the first terms in the derivative expansion are recovered, gives confidence in the model. The parameters of the model are determined from meson physics as shown below.

The Meson Sector

The different meson observables are obtained by expanding the U field into powers of the pion field ϕ.
By considering the quadratic contributions to $\mathcal{L}$ of the meson fields and expressing the physical ρ and A_1 meson fields in terms of X_μ, Y_μ, and normalizing the pion field as usual, one deduces the relations

$$\begin{aligned} m_A^2 &= m_\rho^2 + \Delta m^2 + 8g^2 f \\ f &= \frac{F_\pi^2 m_A^2}{16(m_\rho^2+\Delta m^2)} \end{aligned} \tag{81}$$

The A_1 mass is then given by

$$m_A = (m_\rho^2+\Delta m^2)/[m_\rho^2+\Delta m^2-\frac{1}{2}g^2F_\pi^2]^{1/2} \tag{82}$$

The ρ and A_1 fields are the combinations

$$\boldsymbol{\rho}_\mu = \frac{1}{\sqrt{2}}(\boldsymbol{X}_\mu + \boldsymbol{Y}_\mu) \tag{83}$$

$$\boldsymbol{A}_\mu = \frac{1}{\sqrt{2}}(\boldsymbol{X}_\mu + \boldsymbol{Y}_\mu) + \frac{gF_\pi}{m_\rho^2+\Delta m^2}\partial_\mu \boldsymbol{\phi} \tag{84}$$

The cubic terms in the fields give the $\rho\pi\pi$ and $A_1\rho\pi$ couplings

$$\mathcal{L}_{\rho\to 2\pi} = \sqrt{2}g\varepsilon^{ijk}[(1-\frac{\Delta m^2}{m_\rho^2+\Delta m^2})\rho_i^\mu \partial_\mu\phi_j\phi_k + \frac{g^2F_\pi^2}{2(m_\rho^2+\Delta m^2)^2}\partial^\nu\rho_i^\mu\partial_\nu\phi_j\partial_\mu\phi_k] \tag{85}$$

$$\begin{aligned} \mathcal{L}_{A_1\to\rho\pi} = \frac{g^2F_\pi\varepsilon^{ijk}}{m_\rho^2+\Delta m^2}\{&[m_A^2 + \frac{2\Delta m^2(m_\rho^2+\Delta m^2)}{g^2F_\pi^2}]\rho_{i\mu}A_j^\mu\phi_k \\ &+ [\rho_{i\mu}(\partial_\mu A_j^\nu - \partial_\nu A_j^\mu) - (\partial_\mu\rho_{i\nu} - \partial_\nu\rho_{j\mu})A_j^\mu]\partial^\nu\phi_k\} \end{aligned} \tag{86}$$

from which the widths $\Gamma_{\rho\to\pi\pi}$ and $\Gamma_{A_1\to\rho\pi}$ can be easily obtained [39]. The cubic terms also give the $\omega\rho\pi$ coupling

$$\mathcal{L}_{\omega\to\rho\pi} = \frac{\beta_\omega g}{\sqrt{2}\pi^2F_\pi}\varepsilon^{\mu\nu\alpha\beta}\partial_\mu\omega_\nu\rho_\alpha^i\partial_\beta\phi_i \tag{87}$$

which contributes virtually to the $\Gamma_{\omega\to 3\pi}$ width.
The quartic terms give rise to the direct three body decays $\omega\to 3\pi$ and $A_1\to 3\pi$. For example

$$\mathcal{L}_{\omega\to 3\pi} = \frac{2\beta_\omega}{3\pi^2F_\pi^3}\varepsilon^{\mu\nu\alpha\beta}\omega_\mu(\partial_\nu\boldsymbol{\phi}\times\partial_\alpha\boldsymbol{\phi})\partial_\beta\boldsymbol{\phi} \tag{88}$$

The quartic terms also contribute to $\pi\pi$ scattering.
Electromagnetic and axial vector currents can be constructed from the Lagrangian (76). They are

$$J^3_\mu = i\ Tr\{\tau^3[f(D_\mu UU^+ + D_\mu U^+U) + \frac{1}{4}([X^\nu, X_{\mu\nu}] + [Y^\nu, Y_{\mu\nu}]) + \\ + \frac{\beta_\omega}{16\pi^2}\varepsilon_{\mu\nu\alpha\beta}\partial^\nu\omega^\alpha(L^\beta - R^\beta + ig(U^+X^\beta U - UY^\beta U^+ + Y^\beta - X^\beta)]\} \tag{89}$$

for the isovector part.

$$J^{I=0}_\mu = \frac{1}{2}B_\mu - \frac{ig}{16\pi^2}\varepsilon_{\mu\nu\alpha\beta}Tr\{\partial^\nu[X^\alpha L^\beta + Y^\alpha R^\beta + ig(UY^\alpha U^+X^\beta - Y^\alpha X^\beta)]\} \tag{90}$$

for the isoscalar part, and

$$\boldsymbol{J}^A_\mu = i\ Tr\{\boldsymbol{\tau}[f(D_\mu UU^+ - D_\mu U^+U) + \frac{1}{4}([X^\nu, X_{\mu\nu}] + [Y^\nu, Y_{\mu\nu}]) \\ + \frac{\beta_\omega}{16\pi^2}\varepsilon_{\mu\nu\alpha\beta}\partial^\nu\omega^\alpha(L^\beta + R^\beta - ig(U^+X^\beta U + UY^\beta U^+ + Y^\beta + X^\beta)]\} \tag{91}$$

for the axial current.

From these currents, the electromagnetic decays of various mesons can be easily calculated [39]. Except for $\pi\pi$ scattering, the ε meson term $\mathcal{L}_\varepsilon$ of eq.(76) has no effects on the previous meson observables. Among the parameters involved in those processes, the pion decay constant F_π, the ρ and ω masses are well known, $F_\pi = 186$ MeV, $m_\rho = 769$ MeV and $m_\omega = 782.6$ MeV. The parameter f is given by eq. (81). The others i.e. g, β_ω and Δm^2 are obtained by fitting to the $\rho \to \pi\gamma$, $\omega \to \pi\gamma$ and $\rho \to \pi\pi$ widths. By using these values all the other meson observables can be predicted and listed in Table 2.

As can be seen, the predictions are in good agreement with experiment. The A_1 meson mass is one of these predictions and is found to be very sensitive to the values of the parameters g and Δm^2. Within the uncertainties for g and Δm^2, eq. (82) yields a rather weak relation $m_A > 976$ MeV while the mean values of Δm^2 and g make the A_1 meson mass almost infinite. It is shown in reference [39] that making the A_1 meson mass infinite is equivalent to impose a chiral covariant relationship between the left and right handed fields X_μ and Y_μ. This relation can be used to eliminate the A_1 field. It is also shown that under this constraint, the $\mathcal{L}_{\pi\rho A_1}$ part of the Lagrangian given by eq. (61) is identical with that obtained in the so called hidden local symmetry approach of reference [40] if one takes $g^2 = m_\rho^2/F_\pi^2$, which is the KSFR relation, and $\Delta m^2 = -m_\rho^2/2$. Precisely these relations are well satisfied by the values of g and Δm^2 given in Table 2. It is also worthnoticing that if $\Delta m^2 = 0$, it would not be possible to get the width $\Gamma_{\rho\to\pi\pi}$ with the values of g given by the electromagnetic decays $\Gamma_{\omega\to\pi\gamma}$.

The Baryon Sector

Unlike the previous meson obsevables, the static properties of baryons get contributions from the ε meson.

Table 2. Meson observables - The $\Gamma_{\rho\to\pi\gamma}$, $\Gamma_{\omega\to\pi\gamma}$ and $\Gamma_{\rho\to\pi\pi}$ widths were used as inputs to determine the parameters g, β_ω and Δm^2 respectively. The other results are predictions. The uncertainties on the theoretical values arise from the quoted uncertainties g, β_ω and Δm^2.

Observables	Calculated	Experiment
$\Gamma_{\rho\to\pi\gamma}$	input $\to g = 3.9 \pm 0.3$	(70 ± 10) keV
$\Gamma_{\omega\to\pi\gamma}$	input $\to \beta_\omega = 9.3 \pm 0.3$	(850 ± 70) keV
$\Gamma_{\rho\to\pi\pi}$	input $\to \frac{\Delta m^2}{m_\rho^2} = -0.48 \pm 0.09$	(153 ± 2) keV
$\Gamma_{\rho\to e^+ + e^-}$	(5.7 ± 0.8) keV	(6.9 ± 0.3) keV
$\Gamma_{\omega\to e^+ + e^-}$	(0.5 ± 0.03) keV	(0.66 ± 0.04) keV
$\Gamma_{\omega\to 3\pi}$	(12 ± 4) MeV	8.9 MeV
$\Gamma_{A_1\to\pi\rho}$	(150 ± 70) MeV	$\Gamma_A^{tot} = (462 \pm 56 \pm 30)$ MeV
m_A	> 976 MeV	$(1194 \pm 14 \pm 10)$ MeV
$\Gamma_{\tau^-\to\pi^-\nu}$	$2.5\ 10^{-10}$ MeV	$(2.0 \pm 0.2)10^{-10}$ MeV
$\Gamma_{\tau^-\to\rho^-\nu}$	$(5.1 \pm 1.0)10^{-10}$ MeV	$(4.4 \pm 0.4)10^{-10}$ MeV

As usual, the hedgehog ansatz is assumed for the static field $U = e^{i\boldsymbol{\tau}\cdot\hat{r}\ \theta(r)}$ and for the space components of the field X and Y

$$\begin{aligned} X_i &= \alpha(r)(\hat{r}x(\boldsymbol{\tau}\times\hat{r}))\cdot\boldsymbol{i} + \beta(r)(\boldsymbol{\tau}\cdot\hat{r})(\hat{r}\cdot\boldsymbol{i}) + \gamma(r)(\boldsymbol{\tau}\times\hat{r})\cdot\boldsymbol{i} \\ Y_i &= -\alpha(r)(\hat{r}x(\boldsymbol{\tau}\times\hat{r}))\cdot\boldsymbol{i} - \beta(r)(\boldsymbol{\tau}\cdot\hat{r})(\hat{r}\cdot\boldsymbol{i}) + \gamma(r)(\boldsymbol{\tau}\times\hat{r})\cdot\boldsymbol{i} \end{aligned} \tag{92}$$

The time components of the fields X and Y are zero in the static limit as are the space components of the ω field.
The energy of the system is then

$$\begin{aligned} E = 4\pi \int_0^\infty dr r^2 \{ & -\tfrac{1}{2}(\omega_0'^2 + m_\omega^2) + (\beta_\omega/2\pi^2)\omega_0\theta'(\sin^2\theta)/r^2 + \\ & + \tfrac{1}{2}(\varepsilon'^2 + m_\varepsilon^2\varepsilon^2) - 2\delta_\varepsilon\varepsilon[\theta'^2 + 2(\sin^2\theta)/r^2] + \\ & + m_\rho^2(2\alpha^2 + \beta^2 + 3\gamma^2) + 4[\gamma/r - g(\alpha^2+\gamma^2)]^2 + 2(\gamma' + \gamma/r - 2g\alpha\beta)^2 \\ & + 4f[(\sin\theta)/r + 2g(\alpha\cos\theta - \gamma\sin\theta)]^2 \\ & - (\beta_\omega/2\pi^2)g\omega_0'[(\gamma/r)\sin 2\theta + 2(\alpha/r)\sin^2\theta + g(\alpha^2-\gamma^2)\sin 2\theta - 4g\alpha\gamma\sin^2\theta] \\ & + \Delta m^2[2(\alpha\cos\theta - \gamma\sin\theta)^2 + \beta^2]\} \end{aligned} \tag{93}$$

Stationary values of E with respect to the variables θ, ε, ω_0, α, β, γ give the classical Euler Lagrange equations for these variables. Their expression can be found in references [39].

Soliton solutions exist with the boundary conditions imposed on the chiral angle $\theta(0) = \pi$ and $\theta(\infty) = 0$. The boundary condition for the other fields follow from the stationary action principle. The classical soliton mass M can be readily obtained by inserting these solutions into eq. (93). In the literature, most of the calculations deal only with this quantity. However, the interesting physical quantities which can be directly compared with experiments are rather

the baryon static properties such as the baryon masses, radii, magnetic moments etc... To calculate them we have to quantize the classical solutions. This is done in the same way as described previously by introducing rotational dynamics through a unitary transformation $A(t)$ on the fields U, X_μ and Y_μ. This rotation induces non trivial field configurations for the space components of the ω field

$$\omega_i(r) = \ell(r)\varepsilon_{ij\ell}\kappa_j\hat{r}_\ell \tag{94}$$

and for the time components X_0, Y_0 of the gauge fields

$$\begin{aligned} A^+X_0A &= a(r)[\hat{r}\times(\boldsymbol{\tau}\times\hat{r})]\cdot\kappa + b(r)(\boldsymbol{\tau}\cdot\hat{r})(\hat{r}\cdot\boldsymbol{\kappa}) + c(r)(\boldsymbol{\tau}\times\hat{r})\cdot\boldsymbol{\kappa} \\ A^+Y_0A &= a(r)[\hat{r}\times(\boldsymbol{\tau}\times\hat{r})]\cdot\kappa + b(r)(\boldsymbol{\tau}\cdot\hat{r})(\hat{r}\cdot\boldsymbol{\kappa}) - c(r)(\boldsymbol{\tau}\times\hat{r})\cdot\boldsymbol{\kappa} \end{aligned} \tag{95}$$

with

$$\boldsymbol{\kappa} = -(i/2)Tr[A^+(dA/dt)\boldsymbol{\tau}] \tag{96}$$

The effective Lagrangian is now

$$L = -M + \Lambda\, Tr[(dA/dt)(dA^+/dt)] \tag{97}$$

with

$$\begin{aligned} \Lambda = {} & \tfrac{2\pi}{3}\int_0^\infty dr\; r^2\{-\ell'^2 - \tfrac{2}{r}\ell\ell' - \tfrac{3}{r^2}\ell^2 - m_\omega^2\ell^2 - \tfrac{2\beta_\omega}{\pi^2 r}\theta'\ell\sin^2\theta - \\ & - \tfrac{2\beta_\omega}{\pi^2r^2}\{r\theta' b\ell + (\ell r)'[a\cos\theta - c\sin\theta - 2r(1+ga)(\alpha\sin\theta+\gamma\cos\theta) - \\ & - 2gcr(\alpha\cos\theta - \gamma\sin\theta)]\sin\theta\} - 16\delta_\varepsilon\varepsilon\sin^2\theta + \\ & + 16f[\sin\theta + g(a\sin\theta + c\cos\theta)]^2 + 2[(a-b)/r + 2\gamma(1+gb)]^2 + \\ & + 2[c/r - 2\alpha(1+gb)]^2 + 2\{(a-b)/r + 2[gc\alpha - \gamma(1+ga)]\}^2 + \\ & + +2\{c/r - 2[gc\gamma + \alpha(1+g\alpha)]\}^2 + 2[a' + 2gc\beta]^2 + 2[c' - 2\beta(1+ga)]^2 + \\ & + b'^2 + m_\rho^2[2(a^2+c^2) + b^2] + 2\Delta m^2(a\sin\theta + c\cos\theta)^2\} \end{aligned} \tag{98}$$

Stationary values of L or effectively of Λ with respect to the variables ℓ, a, b and c give another set of Euler Lagrange equations the expressions of which can be found again in references [39].

The soliton moment of inertia Λ is obtained by inserting the solutions of these equations into eq. (98). The nucleon and delta masses are given in terms of the soliton mass M and moment of inertia by $M_N = M + 3/8\Lambda$ and $M_\Delta = M + 15/8\Lambda$.

The static electromagnetic properties of nucleons such as magnetic moments and mean square radii as well as the axial coupling constant g_A are also calculated [39].

Numerical results

Taking strictly the values $F_\pi = 186$ MeV, $m_\rho = 769$ MeV, $m_\omega = 782.6$ MeV, $g = 3.9$, $\beta_\omega = 9.3$, $\Delta m^2 = -0.48 m_\rho 2$ as determined in the meson sector and omitting first the ε meson, one obtains the results listed in column 1 of Table 3.

In order to examine the effects of the uncertainties in the parameters g, β_ω and Δm^2, these parameters were varied within the errors quoted in Table 2.

Table 3. Static properties of baryons - The different columns correspond to the different sets of the parameter values. The corresponding predictions for the A_1 meson are also shown.

	1	2	3	Exp
F_π (MeV)	186	186	186	186
g	3.9	3.78	4.1	
β_ω	9.3	9.3	9.3	
$\Delta m^2/m_\rho^2$	-0.482	-0.462	-	
δ_ε	0	0	51	
M (MeV)	1449	1428	929	
M_N (MeV)	1519	1502	991	939
$(M_\Delta - M_N$ (MeV)	279	295	249	293
$\mu_p(e/2M_N)$	2.46	2.36	2.18	2.79
$\mu_n(e/2M_N)$	-2.03	-1.94	-1.59	-1.91
$\lvert\mu_p/\mu_n\rvert$	1.21	1.22	1.37	1.46
$\langle r^2\rangle_{I=0}^{1/2}$ (fm)	0.62	0.60	0.66	0.72
$\langle r^2\rangle_{M\ I=0}^{1/2}$ (fm)	1.04	1.00	0.76	0.81
g_A	1.03	0.96	0.41	1.23
m_A (MeV)	1473	1194	-	1194

The results shown in column 2 illustrate such a variation which was chosen to give the A_1 mass the value of 1194 MeV as recently measured [41]. It can be seen from columns 1 and 2 that, apart form the soliton mass and to a lesser extent the isoscalar magnetic radius, the static baryon properties are quite well reproduced. The Δ-nucleon mass difference, in particular, is predicted in very good agreement with experiment. It was shown [37] that the inclusion of the ε meson has the desirable feature of lowering the soliton mass. This feature is confirmed in a later work [42] where an improved model with the ε meson but treated in the large mass limit of the heavy meson fields. The results are shown in column 3 of Table 3. The major success of this model is that it gives good values for the nucleon and delta masses without any modification of the values of F_π, g and β_ω as given by the meson observables. However the other static properties of the nucleon and especially the axial vector coupling constant g_A are less satisfactory. In any case, comparison of the values of Table 3 with those of reference [31] shows a quite significant improvement over the original Skyrme model.

The derivation of the NN interaction from these more realistic effective Lagrangians was made in reference [43] where it is shown that the lack of the intermediate range attraction in the central potential V_c^+ can be circumvented. From this viewpoint, the role of the ε meson is very important. It has the nice

property of lowering the baryon masses and of providing the intermediate range attraction for the NN interaction.

The effective Lagrangian given by eqs. (76)-(79) is terminated at the quadratic level in the derivatives of the fields. Even though it is obtained with very little freedom it is quite general. Particular cases of this Lagrangian can be found in the literature. Some works are restricted to the study of meson physics [44]-[48], others are more interested in properties of baryons[37],[38],[49]-[51]. None of these works, however, deals simultaneously with the meson and the baryon sectors. It is interesting to note that the model of Bando and collaborators[40] where the vector mesons are introduced as dynamical gauge bosons of hidden local symmetries is also a particular case of the Lagrangian (76) although the two models start from different theoretical points of view.

5 Conclusions

i) As time elapses, there is more and more evidence, thanks to new high precision exprimental data, that the description of the long-range and medium-range NN interaction in terms of *hadronic* (nucleons, mesons, isobars) degrees of freedom is *quantitatively* very successful.

ii) From the attempts at a description in terms of quark degrees of freedom, it appears that the repulsion at short range seems compatible with our empirical knowledge. However, this description fails to produce the intermediate-range attraction indispensable for the binding of nucleons in nuclei.

iii) Conceptually the hybrid models (quark exchange for short range and meson exchange for long and medium ranges) seem promising, as they implement the composite nature of the nucleon as well as the notion of quark confinement. It is a great pity that the predictions of these models in the framework of the QCM fail to agree with the NN scattering experimental data.

iv) Like the quark model, the original Skyrme model also fails to provide a medium range attraction for the NN potential but extensions of the Skyrme model to incorporate mesons other than pions (ρ, ω, ε, $A_1, \ldots$) can cure this shortcoming.

v) The relevance of models with topological solitons is to provide satisfactory approximation schemes "bridging" conventionnal hadron physics and non perturbative QCD.

References

1. E. Witten: Nucl. Phys. **B160**, 57 (1979)
2. T.H.R. Skyrme: Proc. Roy. Soc. **A260**, 127 (1961). Nucl. Phys. **31**, 556
3. W.N. Cottingham and R. Vinh Mau: Phys. Rev. **130**, 735 (1963)
4. K. Holinde: Phys. Rep. **68**, n°3 (1981)
5. R. Machleidt, K. Holinde, and Ch. Elster: Phys. Rep. **149**,1 (1987)
6. M.M. Nagels, T.A. Rijken and J.J. de Swart: Phys. Rev. **D17**, 768 (1978)

7. W.N. Cottingham, M. Lacombe, B. Loiseau, J-M. Richard, R. Vinh Mau: Phys. Rev. **D8**, 800 (1973); R. Vinh Mau, in *Mesons in Nuclei*, edited by M. Rho and D. Wilkinson (North Holland, Amsterdam, 1979)
8. M. Lacombe et al.: Phys. Rev. **D12**, 1495 (1975)
9. M. Lacombe et al.: Phys. Rev. **C21**, 861 (1980)
10. M. Lacombe et al.: Phys. Rev. **C23**, 2405 (1981)
11. J. Bystricky and F. Lehar: Physics Data **11** (Karlsruhe, 1978) 1
12. R.V. Reid: Ann. Phys. (N.Y.), **50**, 411 (1968)
13. R.A. Arndt and L.D. Roper: Phys. Rev. **C15**, 1002 (1977)
14. J. Sromicki et al.: Phys. Rev. Lett. **57**, 2359 (1986); D. Holslin, J. Mc Aninch, P.A. Quin and W. Haeberli: Phys. Rev. Lett. **61**, 1561 (1988).
15. W. Tornow et al.: Phys. Rev. **C37**, 2326 (1988)
16. F. Rathmann et al.: Phys. Rev. **C58**, 658 (1998) ; W. Haeberlin et al.: Phys. Rev. **C55**, 597 (1997)
17. J. Rahm et al.: Phys. Rev. **C** (to be published)
18. C. Brogli-Gysin et al.: Nucl. Phys. **A541**, 137 (1992)
19. M. Oka and K. Yazaki: Phys. Lett. **B90**, 41C (1980); Prog. Theor. Phys. **66**, 556, 572 (1981), Nucl. Phys. **A402**, 477 (1983)
20. A. Faessler, F. Fernandez, G. Lübeck and K. Shimizu: Phys. Lett. **B112**, 201 (1982), Nucl. Phys. **A402**, 555 (1983)
21. A. Faessler and F. Fernandez: Phys. Lett. **B124**, 145 (1983)
22. Y. Suzuki and K.T. Hecht: Phys. Rev. **C27**, 299 (1983), **C28**, 1458 (1983), **C29**, 1586 (1984)
23. Y. Fujiwara and K.T. Hecht: Nucl. Phys. **A444**, 541 (1985), Phys. Lett. **171B**, 17 (1986), Nucl. Phys. **A451**, 625 (1986), **A456**, 669 (1986)
24. Y. Yamauchi, R. Yamamoto and M. Wakamatsu: Nucl. Phys. **A443**, 628 (1985)
25. R. Vinh Mau, C. Semay, B. Loiseau and M. Lacombe: Phys. Rev. Lett. **67**, 1392 (1991)
26. S. Takeuchi et al.: Nucl. Phys. **A504**, 77 (1989)
27. D. E. Young et al.: Phys. Rev. **119**, 313 (1960)
28. S. Kistryn et al.: Few Body Syst. Suppl. **2**,534 (1987)
29. R. Henneck et al.: AIP Conf. Proc. **176**, 1108 (1988)
30. M. Gell-Mann and M. Lévy: Il Nuovo Cimento, **16**, 705 (1960)
31. G.S.A. Adkins, C.R. Nappi and E. Witten: Nucl. Phys. **B228**, 552 (1983)
32. A. Jackson, A.D. Jackson and V. Pasquier: Nucl. Phys. **A432**, 567 (1985)
33. R. Vinh Mau, M. Lacombe, B. Loiseau, W.N. Cottingham and P. Lisboa: Phys. Lett. **B150**, 259 (1985)
34. H. Yabu and K. Ando: Prog. of theor. Phys. **74**, 750 (1985)
35. E. Witten: in Solitons in Nuclear and Elementary Particle Physics, edited by A. Chodos and E. Hadjimichael and C. Tze (World Scientific, Singapore, 1984) p. 306
36. J.F. Donoghue, E. Golowich and B.R. Holstein: Phys. Rev. Lett. **53**, 747 (1984)
37. M. Lacombe, B. Loiseau, R. Vinh Mau and W.N. Cottingham: Phys. Lett. **B161**, 31 (1985) and **B169**, 121 (1986)
38. M. Mashaal, T.N. Pham and T.N. Truong: Phys. Rev. Lett. **56**, 436 (1986), Phys. Rev. **D34**, 3484 (1986)
39. M. Lacombe, B. Loiseau, R. Vinh Mau and W.N. Cottingham: Phys. Rev. Lett. **57**, 170 (1986); Phys. Rev. **D38**,1491 (1988)
40. M. Bando *et al.*: Phys. Rev. Lett. **54**, 1215 (1985)
41. W.B. Schmidke et al.: Phys. Rev. Lett. **57**, 527 (1986)
42. M. Lacombe, B. Loiseau, R. Vinh Mau and W.N. Cottingham: Phys. Rev. **D40**, 3012 (1989)

43. D. Kalafatis and R. Vinh Mau: Phys. Rev. **D46**, 3903 (1992)
44. O. Kaymakcalan, S. Rajeev and J. Schechter: Phys. Rev. **D30**, 594 (1984); H. Gomm, O. Kaymakcalan and J. Schechter: Phys. Rev. **D30**, 2345 (1984); O. Kaymakcalan and J. Schechter: Phys. Rev. **D31**, 1109 (1985)
45. Y. Brihaye, N. K. Patt and P. Rossi: Nucl. Phys. **B254**,71 (1985) ; Phys. Lett. **B164**, 111 (1985)
46. T. Fujiwara et al.: Prog. Theor. Phys. **73**, 926 (1985)
47. I. J. R. Aitchison and C. M. Fraser: in Workshop on Nuclear Chromodynamics, edited by S. Brodsky and E. Moniz: World Scientific, p. 421 (1986)
48. B.R. Holstein: Phys. Rev. **D33**, 3316 (1986)
49. U.G. Meissner and I. Zahed: Phys. Rev. Lett. **56**, 1035 (1986); Z. Phys. **A327**, 5 (1987) ; U. G. Meissner et al.: Phys. Rev. Lett. **57**, 1676 (1986)
50. J. Kunz, D. Masak and T. Reitz: Phys. Lett. **B195**, 459 (1987)
51. M. Chemtob: Nucl. Phys. **A466**, 509 (1987)

The atomic nucleus observed with electromagnetic probes

Thomas William Donnelly

Center for Theoretical Physics, Laboratory for Nuclear Science and
Department of Physics, Massachusetts Institute of Technology,
Cambridge, Massachusetts 02139-4307 U.S.A.

Abstract. The basic formalism used when investigating nuclear structure via electron scattering is summarized. Two of the major themes that run through contemporary studies are emphasized: exploration of the extended sets of response functions that become accessible when one or more particles are detected in coincidence with the scattered electron and/or when polarization degrees of freedom are active. In contrast to previous decades when the focus was largely restricted to studies of unpolarized inclusive electron scattering, these have come into the mainstream of the field since modern experimental facilities are now able to address both themes.

1 Introduction

In these lectures my goal has been to introduce some of the basic formalism required in modern studies of the atomic nucleus via electron scattering — clearly this is a large subject and only introductory concepts could be covered in the allotted space. Accordingly I have made the choice of focusing on parity-conserving electron scattering, even though very interesting progress is being made in studies of parity-violation using electron scattering. And, while most of the ideas are applicable for low, intermediate and high energies (and consequently are relevant for nuclear structure studies, as well as for studies of hadronic substructure at high energies), I have chosen to emphasize the former in these lectures, since the summer school at which the lectures were given was oriented more towards issues of nuclear structure than to those of particle physics.

Two aspects of electron scattering from nuclei are receiving considerable attention in the physics community, both from theorists and from experimentalists: coincidence reactions in which one or more particles are detected together with the scattered electron and studies in which polarization degrees of freedom are active. The former has provided one of the main motivations for the new generation of high duty factor accelerators, while the latter has been spurred on by technical developments in polarized electron beams, polarized nuclear targets and capabilities for analyzing the polarization of particles in the final state. The now-being-realized feasibility of exploiting these two aspects is revolutionizing the field. In these lectures I have tried to provide an overview of the classes of electromagnetic response that become accessible when polarizations and/or coincidence reactions can be exploited, and have highlighted a few of the new types of insight that may be gained with the present generation of accelerators and

J.M. Arias and M. Lozano (Eds.): LNP 581, pp. 39–69, 2001.
© Springer-Verlag Berlin Heidelberg 2001

detectors. Indeed, many new results are being reported in recent publications and the reader is encouraged to scan the current literature to obtain a broader picture of activity in the field than can be presented in the limited space available here.

We begin the developments at the fundamental starting point for descriptions of electron scattering from nuclei [1,2] with the basic diagram required in the one-proton-exchange or first Born approximation , shown in Fig. 1. Here an electron with 4-momentum[1] $K = (\epsilon,\mathbf{k})$ and spin projection λ is scattered through an angle θ_e to 4-momentum $K' = (\epsilon',\mathbf{k}')$. The virtual photon exchanged in the process carries 4-momentum transfer $Q = (\omega,\mathbf{q})$ and, in interacting with the nucleus, causes it to proceed from state $|i\rangle$ with total 4-momentum P_i to state $|f\rangle$ with total 4-momentum P_f. Conservation of 4-momentum tells us that $Q = K - K' = P_f - P_i$. Furthermore, we have $Q^2 = \omega^2 - q^2 < 0$ for electron scattering, corresponding to the exchange of spacelike virtual photons. The real-photon point involved in photoexcitation or gamma-decay corresponds to the limit $Q^2 \to 0$.

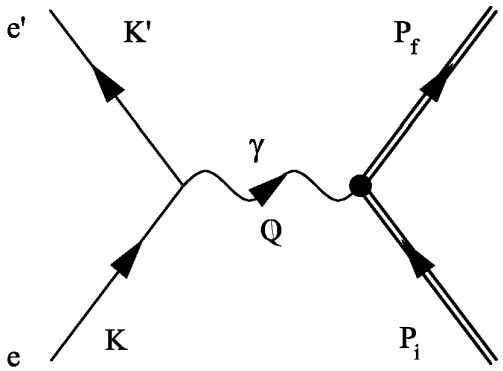

Fig. 1. Electron scattering in the one-photon-exchange approximation.

The cross section for the process shown in Fig. 1 follows by applying the Feynman rules [3] and involves the square of the absolute value of the invariant matrix element, $\mathcal{M}_{fi}$, which is in turn made up as a product of three factors — the electron current j^μ, the photon propagator $g_{\mu\mu'}/Q^2$ and the nuclear current matrix element, $J^{\mu'}_{fi}$:

$$d\sigma \sim |\mathcal{M}_{fi}|^2 \sim \left| j_\mu \frac{1}{Q^2} J^\mu_{fi} \right|^2 = \frac{1}{Q^4} j^*_\mu j_\nu \cdot J^{\mu *}_{fi} J^\nu_{fi}. \tag{1}$$

[1] Four-vectors are generally indicated with capital letters, K; 3-vectors are generally indicated with boldface lower-case letters, $\mathbf{k}$, and their magnitudes with non-boldface lower-case letters, $k = |\mathbf{k}|$. The conventions used here are otherwise those of Bjorken and Drell [3] so that, for example, $K^2 = K_\mu K^\mu = \epsilon^2 - k^2 = m_e^2$. As usual $\not{K} \equiv K_\mu \gamma^\mu$.

Of course, we must perform the appropriate average-over-initial and sum-over-final states (indicated $\overline{\sum}$) to obtain the cross section pertaining to the actual experimental conditions (*e.g.*, electron polarized or not, target polarized or not, inclusive or exclusive scattering, *etc.*). This yields the leptonic and hadronic tensors

$$\eta_{\mu\nu} \equiv \overline{\sum}_{\text{leptons}} j^*_\mu j_\nu \tag{2}$$

$$W^{\mu\nu} \equiv \overline{\sum}_{\text{hadrons}} J^{\mu *}_{fi} J^\nu_{fi} \tag{3}$$

whose contraction is involved in forming the cross section: $d\sigma \sim \eta_{\mu\nu} W^{\mu\nu}/Q^4$. Furthermore, it proves useful to decompose both leptonic and hadronic tensors into pieces symmetric (s) or antisymmetric (a) under the interchange $\mu \leftrightarrow \nu$:

$$W^{\mu\nu} = W^{\mu\nu}_s + W^{\mu\nu}_a \tag{4}$$

$$\eta_{\mu\nu} = \eta^s_{\mu\nu} + \eta^a_{\mu\nu} \ . \tag{5}$$

Clearly, in contracting with the leptonic tensor no cross-terms are allowed. Furthermore, we shall make use of the fact that both the leptonic and nuclear electromagnetic currents are conserved: $Q_\mu W^{\mu\nu}_s = Q_\mu W^{\mu\nu}_a = Q^\mu \eta^s_{\mu\nu} = Q^\mu \eta^a_{\mu\nu} = 0$. Let us now turn to a discussion of the leptonic tensor.

2 Leptonic tensor

Substituting for the electron current

$$j_\mu(K', \lambda'; K, \lambda) \sim \bar{u}(K', \lambda')\gamma_\mu u(K, \lambda) \tag{6}$$

in (2), we have

$$\eta_{\mu\nu} = \overline{\sum} [\bar{u}(K, \lambda)\gamma_\mu u(K', \lambda')][\bar{u}(K', \lambda')\gamma_\nu u(K, \lambda)], \tag{7}$$

where properties [3] of the spinors u and gamma matrices γ have been used to obtain the complex conjugate of the electron current as the first group of three factors in (7). We can guarantee that electrons and not positrons occur by inserting projection operators $\left(\not{K}' + m_e\right)/2m_e$ and $\left(\not{K} + m_e\right)/2m_e$ in the appropriate places:

$$\eta_{\mu\nu} = \frac{1}{4m_e^2} \overline{\sum} \bar{u}(K, \lambda)\gamma_\mu(\not{K}' + m_e)u(K', \lambda')\bar{u}(K', \lambda')\gamma_\nu(\not{K} + m_e)u(K, \lambda). \tag{8}$$

Let us first consider unpolarized electron scattering, in which case $\overline{\sum}$ corresponds to an unrestricted sum over all four components in the spinors divided by two for the initial-state spin average. This is in fact simply a trace which can be evaluated using standard techniques [3]:

$$\begin{aligned} 2m_e^2 \eta^{\text{unpol}}_{\mu\nu} &= \frac{1}{4} \text{Tr} \left\{ \gamma_\mu(\not{K}' + m_e)\gamma_\nu(\not{K} + m_e) \right\} \\ &= K_\mu K'_\nu + K'_\mu K_\nu - g_{\mu\nu} \left(K \cdot K' - m_e^2 \right) \\ &\equiv \chi^{\text{unpol}}_{\mu\nu}. \end{aligned} \tag{9}$$

Note that this tensor is symmetric under the interchange $\mu \leftrightarrow \nu$ and manifestly satisfies the current conservation condition , $Q^\mu \chi^{\rm unpol}_{\mu\nu} = 0$. Choosing the 3-axis to be along $\mathbf{q}$ this implies that $\chi^{\rm unpol}_{3\mu} = \chi^{\rm unpol}_{\mu 3} = (\omega/q)\chi^{\rm unpol}_{0\mu} = (\omega/q)\chi^{\rm unpol}_{\mu 0}$.

Various classes of response will arise when particular combinations of the Lorentz indices μ and ν are selected. For example, familiar unpolarized single-arm electron scattering (see also Sec. 3) involves the combinations

$$\begin{aligned} 2\left(\chi^{\rm unpol}_{00} - (\omega/q)\chi^{\rm unpol}_{03} + (\omega/q)^2\chi^{\rm unpol}_{33}\right) &\equiv v_0 V_L \\ \chi^{\rm unpol}_{11} + \chi^{\rm unpol}_{22} &\equiv v_0 V_T, \end{aligned} \tag{10}$$

where here the labels L and T refer to projections of the current matrix elements longitudinal and transverse to the virtual photon direction, respectively. In the extreme relativistic limit (ERL), where the electron's mass may be neglected with respect to its energy, one obtains the familiar expressions, $V_L \to v_L$ and $V_T \to v_T$, involving the longitudinal and transverse electron kinematic factors

$$\begin{aligned} v_L &= \rho^2 \\ v_T &= \frac{1}{2}\rho + \tan^2\frac{\theta_e}{2}\,, \end{aligned} \tag{11}$$

where $\rho \equiv -Q^2/q^2 = 1 - (\omega/q)^2 \to 0 \le \rho \le 1$ and $v_0 \equiv (\epsilon + \epsilon')^2 - q^2$.

With polarized electrons things are somewhat more complicated. Let us assume that the scattered electron's polarization is not measured, but that the incident electron beam is prepared with its spin pointing in some direction characterized by the 4-vector S^μ which must satisfy [3] $S^2 = -1$ and $S \cdot K = 0$. The more general situation with both incident and scattered electrons polarized is discussed in [4]. We may then insert into (8) just after the factor γ_ν the spin projection operator $(1 + \gamma_5 \not{S})/2$ and once again now have a sum over all four spinor components and hence a trace:

$$\begin{aligned} 2m_e^2\eta_{\mu\nu} &= \frac{1}{8}\,{\rm Tr}\,\left\{\gamma_\mu\left(\not{K}' + m_e\right)\gamma_\nu\left(1 + \gamma_5\not{S}\right)\left(\not{K} + m_e\right)\right\} \\ &\equiv \frac{1}{2}\left[\chi^{\rm unpol}_{\mu\nu} + \chi^{\rm pol}_{\mu\nu}\right], \end{aligned} \tag{12}$$

where $\chi^{\rm unpol}_{\mu\nu}$ is the leptonic tensor in (9) and, upon evaluation of the trace [4], the new piece which contains all reference to the electron spin is given by

$$\chi^{\rm pol}_{\mu\nu} = i\epsilon_{\mu\nu\alpha\beta}\, m_e S^\alpha Q^\beta. \tag{13}$$

Note that this tensor is antisymmetric under the interchange $\mu \leftrightarrow \nu$ and separately satisfies the current conservation condition, $Q^\mu \chi^{\rm pol}_{\mu\nu} = 0$.

Now let us specify the spin direction of the incident electron by writing for the 3-vector $\mathbf{s}$ the following:

$$\mathbf{s} = hs\left(\cos\zeta\,\mathbf{u}_L + \sin\zeta\,\mathbf{u}_\perp\right), \tag{14}$$

where $\mathbf{u}_L$ is a unit vector pointing along $\mathbf{k}$ and $\mathbf{u}_\perp$ is a unit vector in the plane perpendicular to $\mathbf{k}$:

$$\mathbf{u}_\perp = \cos\eta\,\mathbf{u}_S + \sin\eta\,\mathbf{u}_N. \tag{15}$$

The three orthogonal unit vectors ($L \leftrightarrow$ longitudinal, $S \leftrightarrow$ sideways, $N \leftrightarrow$ normal) are indicated in Fig. 2. The factor $h = \pm 1$ is added only for convenience in flipping the spin; alternatively the angles (ζ, η) can be chosen to have $\mathbf{s}$ point

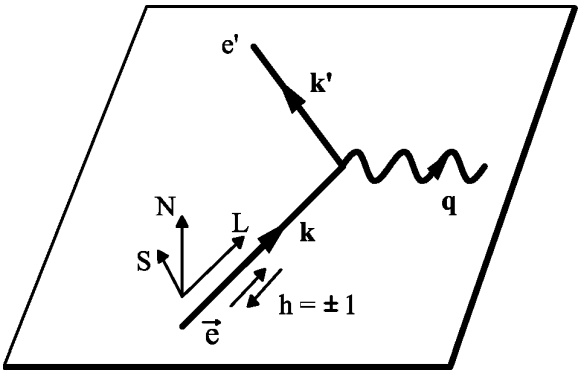

Fig. 2. Coordinate system for electron spin: $\mathbf{u}_L$ along $\mathbf{k}$, $\mathbf{u}_N$ normal to the electron scattering plane ($\mathbf{u}_N \sim \mathbf{k} \times \mathbf{k}'$) and $\mathbf{u}_S = \mathbf{u}_N \times \mathbf{u}_L$ in the "sideways" direction.

in two opposing directions. The conditions $S^2 = -1$ and $S \cdot K = 0$ imply that

$$s \;\; = |\mathbf{s}| = \frac{1}{\sqrt{1 - \beta^2 \cos^2\zeta}} = \frac{\gamma}{\sqrt{\cos^2\zeta + \gamma^2 \sin^2\zeta}} \tag{16}$$

$$S^0 = h\beta s \cos\zeta, \tag{17}$$

where $\beta = k/\epsilon = \sqrt{1 - (m_e/\epsilon)^2}$ and $\gamma = 1/\sqrt{1-\beta^2} = \epsilon/m_e$ are the familiar relativistic factors. It is convenient to define

$$\tan\mu \equiv \gamma \tan\zeta \tag{18}$$

and the spin 4-vector multiplied by m_e (as this is what occurs in (13)) is then

$$m_e S^\mu = h\epsilon\left(\beta\cos\mu,\ \cos\mu\ \mathbf{u}_L + \frac{1}{\gamma}\cdot\sin\mu\ \mathbf{u}_\perp\right). \tag{19}$$

If the angle μ is small, then the electron is longitudinally polarized; if near 90°, then it is transversely polarized. One must remember that $\gamma = \epsilon/m_e$ is very large in all practical studies in nuclear or particle physics and hence μ near 0°

or 90° implies that ζ is extremely near 0° or 90°, respectively. For the latter the scale of how close to the limits "extremely near" really is depends on the actual value of $1/\gamma$. In the case of purely longitudinal polarized electrons we have

$$\text{longitudinal polarization:} \qquad m_e S^\mu = h\epsilon(\beta, \mathbf{u}_L), \tag{20}$$

while in the case of purely transversely polarized electrons we have

$$\text{transverse polarization:} \qquad m_e S^\mu = \frac{1}{\gamma} \cdot h\epsilon(0, \mathbf{u}_\perp). \tag{21}$$

Thus we see that transverse polarization effects are suppressed relative to longitudinal polarization effects by a factor $1/\gamma$. Henceforth in treating situations where only the incident electron beam is polarized, we shall restrict our attention to purely longitudinally polarized electrons and shall take the extreme relativistic limit (ERL) where $\beta \to 1$, $\gamma \to \infty$:

$$K^\mu \longrightarrow \epsilon(1, \mathbf{u}_L) \tag{22}$$

$$(m_e S^\mu)_L \longrightarrow h\epsilon(1, \mathbf{u}_L) = hK^\mu; \tag{23}$$

that is, $h = \pm 1$ becomes the electron helicity. The leptonic tensors under these ERL conditions become

$$\chi^{\rm unpol}_{\mu\nu} \to K_\mu K'_\nu + K'_\mu K_\nu - g_{\mu\nu} K \cdot K' \tag{24}$$

$$\eta^{\rm pol}_{\mu\nu} \to -ih\epsilon_{\mu\nu\alpha\beta} K^\alpha K'^\beta, \tag{25}$$

and we see that they are in general comparable in magnitude, both being characterized by the product of the electron energies, $\epsilon\epsilon'$.

With these developments, we are in a position to proceed with discussions of parity-conserving electron scattering with or without a polarized beam. One important consequence of the arguments summarized in this section is that only *longitudinally polarized electrons* are relevant for most studies in nuclear or particle physics. In electron storage/stretcher rings this observation has important design implications if one wishes to use polarized electrons with internal targets, since then some provision must be made to counter the $g - 2$ precession of the electron's spin and restore it to a longitudinal direction at the target.

3 Unpolarized single-arm scattering

Turning now to the hadronic tensor , let us begin by repeating the familiar arguments [1,2,4–6]) which pertain in the case of single-arm parity-conserving electron scattering from unpolarized targets, $A(e, e')$ and $A(\vec{e}, e')$. The nuclear vertex involved is shown in Fig. 3. Here the virtual photon from the electron scattering (Fig. 1) brings in 4-momentum Q and causes the nucleus to go from state $|i\rangle$ to state $|f\rangle$. These hadronic states have 4-momenta P_i and P_f, respectively, as shown in the figure. Thus, we must build the hadronic tensors from

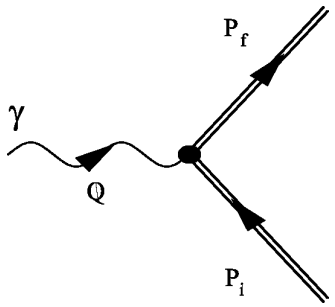

Fig. 3. Hadronic vertex for inclusive scattering.

Q, P_i and P_f. In fact, we can use momentum conservation to eliminate one, say $P_f = P_i + Q$ leaving two independent 4-momenta: $\{Q, P_i\}$. The possible Lorentz scalars in the problem are Q^2, P_i^2 and $Q \cdot P_i$. Since we presumably know what the target is and since $P_i^2 = M_i^2$, we are left with two independent scalars to vary: $\{Q^2, Q \cdot P_i\}$. Moreover, since $Q^2 = \omega^2 - q^2$ and $Q \cdot P_i = \omega M_i$ in the laboratory system, we can regard our hadronic tensors to be functions of $\{Q^2, Q \cdot P_i\}$ or $\{q, \omega\}$.

Now we wish to write $W_s^{\mu\nu}$ and $W_a^{\mu\nu}$ in terms of the two independent 4-vectors Q^μ and P_i^μ. Alternatively, instead of P_i it turns out to be useful to employ the 4-vector

$$V_i^\mu \equiv \frac{1}{M_i} \left\{ P_i^\mu - \left(\frac{Q \cdot P_i}{Q^2} \right) Q^\mu \right\}, \tag{26}$$

which is especially convenient because $Q \cdot V_i = 0$, by construction. To begin with, $W^{\mu\nu}$ must be a second-rank Lorentz tensor and so we can write the following general expansions:

$$W_s^{\mu\nu} = X_1 g^{\mu\nu} + X_2 Q^\mu Q^\nu + X_3 V_i^\mu V_i^\nu + X_4 \left(Q^\mu V_i^\nu + V_i^\mu Q^\nu \right) \tag{27}$$

$$W_a^{\mu\nu} = iY_1 \left(Q^\mu V_i^\nu - V_i^\mu Q^\nu \right) + iY_2 \epsilon^{\mu\nu\alpha\beta} Q_\alpha V_{i\beta}, \tag{28}$$

where the scalar response functions depend on the scalars discussed above: $X_\ell = X_\ell \left(Q^2, Q \cdot P_i \right)$, $\ell = 1, \ldots, 4$ and $Y_\ell = Y_\ell \left(Q^2, Q \cdot P_i \right)$, $\ell = 1, 2$.

Next we note that, in the absence of parity-violating effects from the weak interaction, the hadronic electromagnetic current matrix elements are polar vectors and so the tensors here must have specific properties under spatial inversion. In particular, the ϵ-terms in (28) have the wrong behavior and so Y_2 must vanish. Finally, we must make use of the current conservation conditions. These lead us to the following expressions (recall that $Q \cdot V_i = 0$)

$$Q_\mu W_s^{\mu\nu} = 0 = (X_1 + X_2 Q^2) Q^\nu + (X_4 Q^2) V_i^\nu \tag{29}$$

$$Q_\mu W_a^{\mu\nu} = 0 = (Y_1 Q^2) V_i^\nu \tag{30}$$

and so $X_1 + X_2 Q^2 = 0$, $X_4 = 0$ and $Y_1 = 0$, using the linear independence of Q^ν and V_i^ν. Defining $W_1 \equiv -X_1$ and $W_2 \equiv X_3$, to use more common nomenclature, we have then rederived the familiar results

$$W_s^{\mu\nu} = -W_1 \left(g^{\mu\nu} - \frac{Q^\mu Q^\nu}{Q^2} \right) + W_2 V_i^\mu V_i^\nu \tag{31}$$

$$W_a^{\mu\nu} = 0. \tag{32}$$

Contracting these hadronic tensors with the leptonic tensors obtained above (see Sec. 2, (24) and (25)), we obtain for unpolarized electron scattering

$$\chi_{\mu\nu}^{\text{unpol}} W_s^{\mu\nu} \sim W_2 + 2W_1 \tan^2 \frac{\theta_e}{2}, \tag{33}$$

where of course only the symmetric responses enter. This familiar form for inclusive unpolarized electron scattering [6] contains only two independent response functions W_1 and W_2 which may be separated at fixed q and ω (or, equivalently, fixed Q^2 and $Q \cdot P_i$) by varying the electron scattering angle to make a Rosenbluth decomposition.

On the other hand, for polarized parity-conserving electron scattering

$$\chi_{\mu\nu}^{\text{pol}} W_a^{\mu\nu} = 0, \tag{34}$$

where now only the antisymmetric responses enter. Thus, if only parity-conserving interactions are considered and if only inclusive scattering with no hadronic polarizations is discussed, then no differences will be seen when the electron's helicity is flipped from $+1$ to -1; however, this statement does not obtain for the case of parity-violating electron scattering , providing a very special opportunity to study such effects (see, *e.g.*, [7]).

In passing, let us go a little further with the unpolarized parity-conserving scattering problem. When we contract the unpolarized leptonic tensor developed in the preceding section with the general hadronic tensor for inclusive electron scattering from unpolarized nuclei we obtain a sum involving projections of the current matrix elements. It is convenient to choose these to be transverse (T) or longitudinal (L) with respect to the direction $\mathbf{q}$. Note that "L" used here is not the same as "L" used in Sec. 2 in discussing the electron's polarization; the correct choice is usually clear from the context. Thus we obtain a structure of the form $v_L W^L + v_T W^T$ (see (10)) and can write the inclusive cross section in the laboratory system as

$$\left(\frac{d\sigma}{d\Omega_e d\omega} \right)^{\text{unpol}} = \frac{1}{M_i} \sigma_{\text{Mott}} \left\{ v_L W^L + v_T W^T \right\} \tag{35}$$

$$= \frac{\rho}{2M_i \mathcal{E}} \sigma_{\text{Mott}} \left\{ 2\rho \mathcal{E} W^L + W^T \right\}, \tag{36}$$

using the ERL and hence (11). Here the Mott cross section is given by

$$\sigma_{\text{Mott}} = \left\{ \frac{\alpha \cos \frac{\theta_e}{2}}{2\epsilon \sin^2 \frac{\theta_e}{2}} \right\}^2 \tag{37}$$

and we have introduced the quantity

$$\mathcal{E} \equiv \left[1 + \frac{2}{\rho} \tan^2 \frac{\theta_e}{2}\right]^{-1}, \tag{38}$$

which is referred to as the photon's longitudinal polarization and represents the "virtualness" of the exchanged photon: $\mathcal{E} \to 1(0)$ when $\theta_e \to 0°(180°)$. W^L and W^T are related to W_1 and W_2 by

$$\begin{aligned} W^L &= \left(W_2 - \rho W_1\right)/\rho^2 \\ W^T &= 2W_1. \end{aligned} \tag{39}$$

If discrete states are involved, then a single-differential cross section can be obtained (see [1,2,4]):

$$\left(\frac{d\sigma}{d\Omega_e}\right)^{\text{unpol}} = 4\pi\sigma_{\text{Mott}} f_{\text{rec}}^{-1} \left\{v_L F_L^2(q) + v_T F_T^2(q)\right\} \tag{40}$$

$$= 4\pi\sigma_{\text{Mott}} f_{\text{rec}}^{-1} F^2(q, \theta_e), \tag{41}$$

where the recoil factor is given by $f_{\text{rec}} = 1 + \frac{2\epsilon}{M_i} \sin^2 \frac{\theta_e}{2}$ and where the form factors F_L^2 and F_T^2 result from integrating the responses W^L and W^T over an energy-conserving δ-function (*i.e.*, the form factors are only functions of q, where ω is fixed by the excitation energy and the momentum transfer). For given angular momentum and parity quantum numbers only a finite set of multipole form factors occur:

$$\begin{aligned} F_L^2(q) &= \sum_{J \geq 0} F_{CJ}^2(q) \\ F_T^2(q) &= \sum_{J \geq 1} \left\{F_{EJ}^2(q) + F_{MJ}^2(q)\right\}, \end{aligned} \tag{42}$$

where the sums are restricted to $|J_f - J_i| \leq J \leq J_f + J_i$ (in addition to $J \geq 0$ for Coulomb multipoles and $J \geq 1$ for transverse electric and magnetic multipoles), where natural parity multipoles CJ/EJ are present only when $(-1)^J = \pi \equiv \pi_f \pi_i$ (non-natural parity multipoles MJ only when $(-1)^J = -\pi$), and where no electric multipoles are present at all for elastic scattering ($f = i$).

To make this completely clear, let us take a specific example — for more detailed discussions see [1,2,4]. Consider a nucleus with ground-state spin-parity $3/2^+$ (for instance, ^{39}K) and assume that the electron scattering kinematics are chosen to select out a specific excited state having spin-parity $7/2^-$. For such a transition the parity changes ($\Delta\pi$ = yes) and the multipolarities allowed are $\Delta J = 2$, 3, 4 and 5, that is we have M2, C3, E3, M4, C5 and E5:

$$\begin{aligned} F_L^2(q) &= F_{C3}^2(q) + F_{C5}^2(q) \\ F_T^2(q) &= F_{M2}^2(q) + F_{E3}^2(q) + F_{M4}^2(q) + F_{E5}^2(q), \end{aligned} \tag{43}$$

namely, only two observables $F^2_{L,T}(q)$, but six independent form factors. Clearly by fixing q (and hence ω) and varying θ_e, it is possible to make a Rosenbluth decomposition and separately determine $F^2_L(q)$ and $F^2_T(q)$. However, in general more terms than one occur in the sums here or in (42) and so the individual multipole form factors cannot be extracted without polarization information: this constitutes the focus of the next section.

4 Single-arm scattering with nuclear polarizations

As discussed in [4], when polarized targets are involved or when final-state nuclear polarizations are determined, a much richer variety of polarization observables becomes accessible. In general these contain interferences between the various form factors and consequently a complete decomposition into the underlying electromagnetic matrix elements can in principle be achieved (up to a simple phase ambiguity in the arbitrary spin case — see [4]). For such cases the helicity asymmetry is generally nonzero *even for strictly parity-conserving interactions*. Moreover, for situations where no hadronic polarizations are specified but where coincidence reactions are considered there can also be nonzero helicity asymmetries *again, even for strictly parity-conserving interactions* — an example is the so-called "5^{th} response" discussed in Sec. 5.4. As a consequence when the typically extremely small helicity asymmetries that arise from parity-violating interactions are to be studied, it is necessary to have no parity-conserving helicity-asymmetry "noise" as the latter is generally much larger than the parity-violating effects of interest. In this regard, the inclusive scattering of *longitudinally polarized* electrons from *unpolarized* targets plays a very special role [7].

This brings us to the next stage in the developments presented here. Let us begin by considering what happens when the target is polarized but initially where the *electron is unpolarized*. The kinematics for this class of reactions, $\overrightarrow{A}(e,e')$, are illustrated in Fig. 4. In addition to the electron variables, which are treated exactly as above, we now have to specify an axis along which the target polarization is given; two angles, θ^* and ϕ^*, characterize this axis of quantization. The target polarization is then given in terms of the magnetic substate population probabilities or equivalently [4] the Fano tensors $\{f^{(i)}_J\}$ referred to this axis. The angles (θ^*,ϕ^*) are assumed to be at our disposal to vary as we wish. The cross section for electron unpolarized but target polarized will be denoted $\Sigma(\theta^*,\phi^*)$ and may be expressed as a generalization of (40):

$$\begin{aligned}\Sigma(\theta^*,\phi^*) = 4\pi\sigma_{\text{Mott}} f_{\text{rec}}^{-1} \big\{ & v_L W^L(\theta^*) + v_T W^T(\theta^*) \\ & + v_{TL}\cos\phi^* W^{TL}(\theta^*) + v_{TT}\cos 2\phi^* W^{TT}(\theta^*) \big\}\,, \end{aligned} \tag{44}$$

where the new electron kinematical factors (to be compared with v_L and v_T in (11)) are

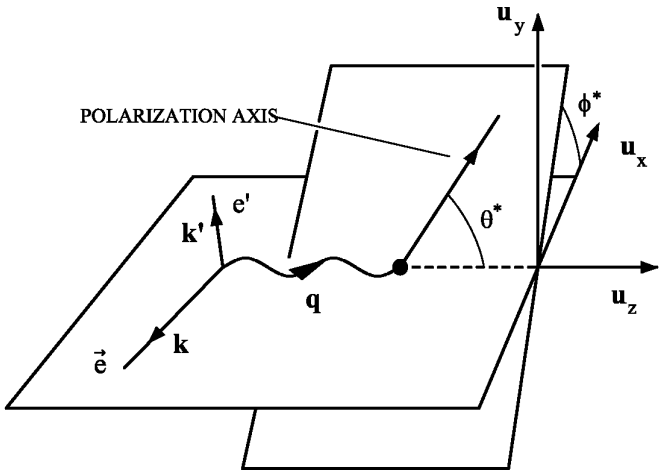

Fig. 4. Kinematics for electron scattering from polarized targets. Here $\mathbf{u}_z$ is along $\mathbf{q}$, $\mathbf{u}_y$ is normal to the electron scattering plane and $\mathbf{u}_x = \mathbf{u}_y \times \mathbf{u}_z$ lies in the scattering plane. The target polarization direction is then specified by the angles (θ^*, ϕ^*) in this coordinate system.

$$
\begin{aligned}
v_{TL} &= -\frac{1}{\sqrt{2}}\rho\sqrt{\rho + \tan^2\frac{\theta_e}{2}} \\
v_{TT} &= -\frac{1}{2}\rho.
\end{aligned}
\tag{45}
$$

The dependence on ϕ^* is explicit in (44) and so, using this together with the θ_e-dependence (in the v's), it is possible to isolate four classes of responses. The resulting W's are functions of q and ω (as above), as well as of the polar angle θ^*. This last dependence can also be made explicit (see [4] for details):

$$
\begin{aligned}
W^L(\theta^*) &= F_L^2 + \sum_{\substack{I\geq 2 \\ \text{even}}} f_I^{(i)} P_I(\cos\theta^*) W_I^L \\
W^T(\theta^*) &= F_T^2 + \sum_{\substack{I\geq 2 \\ \text{even}}} f_I^{(i)} P_I(\cos\theta^*) W_I^T \\
W^{TL}(\theta^*) &= \sum_{\substack{I\geq 2 \\ \text{even}}} f_I^{(i)} P_I^1(\cos\theta^*) W_I^{TL} \\
W^{TT}(\theta^*) &= \sum_{\substack{I\geq 2 \\ \text{even}}} f_I^{(i)} P_I^2(\cos\theta^*) W_I^{TT}.
\end{aligned}
\tag{46}
$$

Thus, in addition to the unpolarized form factors F_L^2 and F_T^2, there are four classes of new observables W_I^K, $K = L, T, TL$ and TT. These are characterized

by tensor rank I, where $2 \leq I \leq 2J_i$ (the tensors with $I = 0$ are just the unpolarized form factors). Only even-rank tensors occur in the sums. The new polarization observables W_I^K, $K = L, T \ldots$, with $I > 0$, contain the nuclear electromagnetic current matrix elements, just as the unpolarized responses F_L^2 and F_T^2 do, however, in new *interfering* combinations: there are now CJ/EJ', CJ/MJ' and EJ/MJ' interferences. This additional information provides us with a kind of "multipole meter." It is beyond the scope of the present lectures to derive complete expressions for (46) and, furthermore, these details are given in [4].

There are immediate consequences of the statements made above. For $J_i = 0$, the only tensors have $I = 0$; for $J_i = \frac{1}{2}$, tensors with $I = 0$ and $I = 1$ can be formed, but only the former are allowed since the rank must be even. Thus, with targets having $J_i = 0$ or $J_i = \frac{1}{2}$, only the unpolarized cross section is recovered.

With $J_i \geq 1$, however, the situation is more interesting for now rank-2 information becomes accessible. For instance, for elastic scattering from a spin-1 target such as $^2\vec{H}$ there are three basic form factors, $C0$, $M1$ and $C2$ (see [4]). The unpolarized cross section involves the longitudinal and transverse form factors

$$\begin{aligned} F_L^2 &= F_{C0}^2 + F_{C2}^2 \\ F_T^2 &= F_{M1}^2, \end{aligned} \tag{47}$$

but the $C0$ and $C2$ contributions are summed incoherently and no relative phase information is available. The additional reduced response functions which become accessible with polarized targets are [4]

$$\begin{aligned} W_2^L &= -2\sqrt{3}\, F_{C2} \left(F_{C0} + \frac{1}{2\sqrt{2}} F_{C2} \right) \\ W_2^T &= -\frac{1}{2}\sqrt{\frac{3}{2}} F_{M1}^2 \\ W_2^{TL} &= \frac{3}{\sqrt{2}} F_{M1} F_{C2} \\ W_2^{TT} &= \frac{1}{4}\sqrt{\frac{3}{2}} F_{M1}^2. \end{aligned} \tag{48}$$

Clearly with this polarization information it is possible to separate the individual multipole form factors. In particular, the first of these, W_2^L, forms the interesting part of the tensor polarization t_{20}. Having this together with F_L^2 permits the extraction of the individual F_{C0} and F_{C2} multipoles. In passing, a special circumstance should be mentioned: for elastic scattering and light nuclei it is possible to obtain the same information with polarized targets or by measurement of the final-state recoil polarization — both techniques have been used for deuterium.

Now let us turn to the situation where *both the target and the electron beam are polarized*, $\overrightarrow{A}(\overrightarrow{e}, e')$. The complete differential cross section may be written

$$\left(\frac{d\sigma}{d\Omega_e}\right)^h = \Sigma(\theta^*, \phi^*) + h\Delta(\theta^*, \phi^*), \tag{49}$$

and so we may isolate Σ and Δ by forming the helicity sum and difference:

$$\Sigma(\theta^*, \phi^*) = \frac{1}{2}\left[\frac{d\sigma^{+1}}{d\Omega_e} + \frac{d\sigma^{-1}}{d\Omega_e}\right] \tag{50}$$

$$\Delta(\theta^*, \phi^*) = \frac{1}{2}\left[\frac{d\sigma^{+1}}{d\Omega_e} - \frac{d\sigma^{-1}}{d\Omega_e}\right]. \tag{51}$$

$\Sigma(\theta^*, \phi^*)$ is discussed above; in addition, with polarized electrons we can now study $\Delta(\theta^*, \phi^*)$ which may be written (cf. (44))

$$\Delta(\theta^*, \phi^*) = 4\pi\sigma_{\rm Mott} f_{\rm rec}^{-1}\left\{v_{T'}W^{T'}(\theta^*) + v_{TL'}\cos\phi^* W^{TL'}(\theta^*)\right\}, \tag{52}$$

and contains two more electron kinematical factors (compare v_L, v_T in (11) and v_{TL}, v_{TT} in (45)):

$$\begin{aligned} v_{T'} &= \sqrt{\rho + \tan^2\frac{\theta_e}{2}}\,\tan\frac{\theta_e}{2} \\ v_{TL'} &= -\frac{1}{\sqrt{2}}\rho\tan\frac{\theta_e}{2}. \end{aligned} \tag{53}$$

Again using the explicit ϕ^*-dependence in (52) it is possible to isolate, in this case, two responses $W^{T'}$ and $W^{TL'}$ which can be written in forms similar to those in (46):

$$\begin{aligned} W^{T'}(\theta^*) &= \sum_{\substack{I\geq 1 \\ \rm odd}} f_I^{(i)} P_I(\cos\theta^*) W_I^{T'} \\ W^{TL'}(\theta^*) &= \sum_{\substack{I\geq 1 \\ \rm odd}} f_I^{(i)} P_I^1(\cos\theta^*) W_I^{TL'}. \end{aligned} \tag{54}$$

These sums appear to be similar to the ones encountered above in (46), but now, importantly, they involve only odd-rank tensors with $1 \leq I \leq 2J_i$. The consequences are immediate: even for $J_i = \frac{1}{2}$ now there are new observables having $I = 1$ (vector polarizations).

Let us pursue this spin-1/2 case a little further. From (44), (46), (52) and (54) we have

$$\Sigma(\theta^*, \phi^*) = \left(\frac{d\sigma}{d\Omega_e}\right)^{\rm unpol} = 4\pi\sigma_{\rm Mott} f_{\rm rec}^{-1}\left\{v_L F_L^2 + v_T F_T^2\right\} \tag{55}$$

$$\begin{aligned} \Delta(\theta^*, \phi^*) &= 4\pi\sigma_{\rm Mott} f_{\rm rec}^{-1} f_1^{(i)} \\ &\quad \times \left\{\cos\theta^* v_{T'} W_1^{T'} + \sin\theta^*\cos\phi^* v_{TL'} W_1^{TL'}\right\}, \end{aligned} \tag{56}$$

where Σ has no (θ^*, ϕ^*)-dependence and where we have evaluated the Legendre polynomials to make this dependence explicit for Δ in (56). Clearly to emphasize the T' contributions the polarization axis should be chosen along $\mathbf{q}$, whereas to emphasize the TL' contributions it should be chosen perpendicular to $\mathbf{q}$ and in the electron scattering plane (*i.e.*, with $\phi^* = 0°$ or $180°$).

First, consider elastic scattering in which F_{C0} and F_{M1} form factors occur (equivalently, up to some subtleties involving relativistic factors [8,9] we can use G_E and G_M for the nucleon). The unpolarized cross section in (55) involves $F_L^2 = F_{C0}^2$ and $F_T^2 = F_{M1}^2$ which can in principle be separated by making a Rosenbluth decomposition . In practice, however, one contribution may be dominant and it may be very difficult to extract the smaller from the larger. For example, at low-to-intermediate values of q, $|G_{E_n}| \ll |G_{M_n}|$ and the separation is very poorly defined. Now suppose that polarized electron/polarized target information is added via the response in (56):

$$\begin{aligned} W_1^{T'} &= -\sqrt{2}\, F_{M1}^2 \\ W_1^{TL'} &= -2\sqrt{2}\, F_{C0} F_{M1}. \end{aligned} \tag{57}$$

The former just involves F_T^2 again, whereas the latter is the one of interest for the present purposes: it involves the *interference* between the two form factors and, when one is small in magnitude and the other large, it provides a much more sensitive way to extract one from the other, in contrast to measuring their squares. The specific measurements of relevance here are $\overrightarrow{p}(\overrightarrow{e}, e)p$ (to extract G_{E_p} from G_{M_p}; even this is interesting for some values of momentum transfer) and ${}^2\overrightarrow{H}(\overrightarrow{e}, e')$ or ${}^3\overrightarrow{H}e(\overrightarrow{e}, e')$ in the region where the process corresponds best to quasi-free scattering from a nucleon. In these last cases the hope is to be able to extract both G_{E_n} and G_{M_n}. All approaches of this type are being actively pursued experimentally.

As another example, consider inelastic scattering for the transition $\frac{1}{2}^{\pm} \to \frac{3}{2}^{\pm}$ in which F_{M1}, F_{C2} and F_{E2} form factors occur. Again using polarized electron scattering from a polarized target, the four accessible responses here are [4]

$$\begin{aligned} F_L^2 &= F_{C2}^2 \\ F_T^2 &= F_{M1}^2 + F_{E2}^2 \\ W_1^{T'} &= \frac{1}{\sqrt{2}} \left(F_{M1}^2 - F_{E2}^2 - 2\sqrt{3}\, F_{M1} F_{E2} \right) \\ W_1^{TL'} &= -\sqrt{2}\, F_{C2} \left(F_{M1} + \sqrt{3}\, F_{E2} \right). \end{aligned} \tag{58}$$

A specific situation is the $N \to \Delta$ transition, say in $\overrightarrow{p}(\overrightarrow{e}, e')\Delta$. To the extent that channels other than the $\frac{3}{2}^+$ final state can be neglected, we have the above responses. For this transition the $M1$ contribution is dominant and the $C2/E2$ pieces, which reflect the baryon deformations, are small. The polarization responses, in contrast to the unpolarized responses, involve interferences and especially the $W_1^{TL'}$ contribution is interesting, since it can only be nonzero when $F_{C2} \neq 0$.

One nuclear structure example may help to illustrate even more of the potential of studying inclusive electron scattering from polarized targets. Consider the case of scattering from polarized ^{7}Li whose ground state has spin-parity $3/2^-$ and hence rank-0, -1, -2 and -3 polarization observables enter. At 4.63 MeV lithium has a $7/2^-$ state and thus the inelastic transition to this state has C2, E2, M3, C4, E4 and M5 multipoles. The behavior expected for these multipoles reflects rather varied physics, as may be argued in the following way. Starting with one-body electromagnetic operators and a valence model space restricted to the 1p shell (these are reasonable beginning assumptions), only matrix elements of the form $< 1p_{j'}|\mathcal{O}_J^{(1)}|1p_j >$ can occur. Here $\mathcal{O}_J$ is one of the multipole operators of multipolarity J and the label "(1)" indicates that only one-body currents are being considered. Since j and j' are $1/2$ or $3/2$, under these assumptions the allowed multipolarities are $J = 0$, 1, 2 and 3, but not 4 or 5. On the other hand if the model space is extended to include the 2s-1d shell, then matrix elements of the form $< 1d_{j'}|\mathcal{O}_J^{(1)}|1d_j >$ may occur and lead to all multipolarities $J = 0 - 5$. Alternatively, with two-body meson-exchange currents (indicated "(2)") even within the 1p shell high multipolarities may occur via matrix elements of the sort $< [1p_{j'}]^2_{K'}|\mathcal{O}_J^{(2)}|[1p_{j'}]^2_K >$ with $K, K' = 0 - 3$. Additionally, the MEC are known to be dominantly transverse in nature and hence expected to affect primarily the E2, M3, E4 and M5 form factors, whereas the extension to configurations in the larger 1p/2s-1d model space can affect the C2 and C4 Coulomb form factors as well. By using polarizations to separate all six multipole form factors in this way one has the opportunity to learn about several interesting and elusive aspects of nuclear structure. Clearly this example is one of a large class of new opportunities that could be exploited.

5 Two-arm coincidence reactions

5.1 Hadronic tensor/no nuclear polarizations

Next let us repeat the arguments that lead to the general form for the reactions $A(e, e'x)$ and $A(\overrightarrow{e}, e'x)$ — see also [5,12] where multi-particle coincidence reactions are also discussed. For two-arm coincidence reactions a particle with 4-momentum P_x is detected in coincidence with the scattered electron, called "exclusive-1" scattering . Referring to Fig. 5, let us again assume that the total final nuclear state has 4-momentum P_f, so that all but the particle in coincidence (*i.e.*, the unobserved particles) have 4-momentum P_0. Momentum conservation allows us to eliminate these two ($P_f = P_i + Q$ and $P_0 = P_f - P_x$), so that we are left with three independent 4-momenta from which to build the hadronic tensor: $\{Q, P_i, P_x\}$.

The possible Lorentz scalars in the problem are Q^2, P_i^2, P_x^2, $Q \cdot P_i$, $P_x \cdot P_i$ and $Q \cdot P_x$. Again, we know the target mass, M_i and the mass of the detected particle, M_x, and so, since $P_i^2 = M_i^2$ and $P_x^2 = M_x^2$ are fixed, we are left with four independent scalars to vary: $\{Q^2, Q \cdot P_i, P_x \cdot P_i, Q \cdot P_x\}$. It is useful to express the kinematical dependence in the response functions in terms of laboratory system

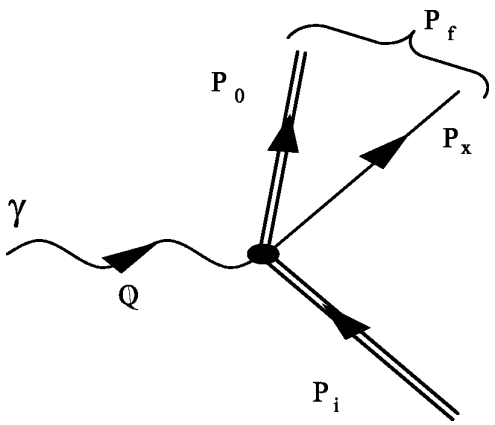

Fig. 5. Hadronic vertex for exclusive-1 electron scattering, $(e, e'x)$

variables. We shall use the coordinate system in Fig. 6 to describe exclusive-1 electron scattering in which the detected particle has 3-momentum $p_x = |\mathbf{p}_x|$ and is detected at angles (θ_x, ϕ_x) with respect to the chosen basis. The four scalar variables may be re-expressed in this laboratory system:

$$\begin{aligned} Q^2 &= \omega^2 - q^2 \\ Q \cdot P_i &= \omega M_i \\ P_x \cdot P_i &= E_x M_i \\ Q \cdot P_x &= \omega E_x - q p_x \cos\theta_x, \end{aligned} \tag{59}$$

where $E_x = \sqrt{p_x^2 + M_x^2}$ is the total energy of the detected particle. Note that the azimuthal angle ϕ_x, does not occur here; that is, the internal functional dependence involves θ_x, but not ϕ_x. Thus, the hadronic tensors for two-arm coincidence reactions can be regarded to be functions of the scalar variables $\{Q^2,\ Q \cdot P_i,\ P_x \cdot P_i,\ Q \cdot P_x\}$ or of the laboratory quantities $\{q,\ \omega,\ E_x,\ \theta_x\}$.

Now, as in the case of inclusive scattering, we wish to write $W_s^{\mu\nu}$ and $W_a^{\mu\nu}$ in terms of the independent 4-momenta in the problem. Instead of $\{Q^\mu,\ P_i^\mu,\ P_x^\mu\}$ we use the equivalent set $\{Q^\mu,\ V_i^\mu,\ V_x^\mu\}$, where [5]

$$V_i^\mu \equiv \frac{1}{M_i}\left\{P_i^\mu - \left(\frac{Q \cdot P_i}{Q^2}\right) Q^\mu\right\} \tag{60}$$

$$V_x^\mu \equiv P_x^\mu - \left(\frac{Q \cdot P_x}{Q^2}\right) Q^\mu, \tag{61}$$

and these have the convenient properties, $Q \cdot V_i = Q \cdot V_x = 0$. Since $W^{\mu\nu}$ must be a second-rank Lorentz tensor, we have the following expansions:

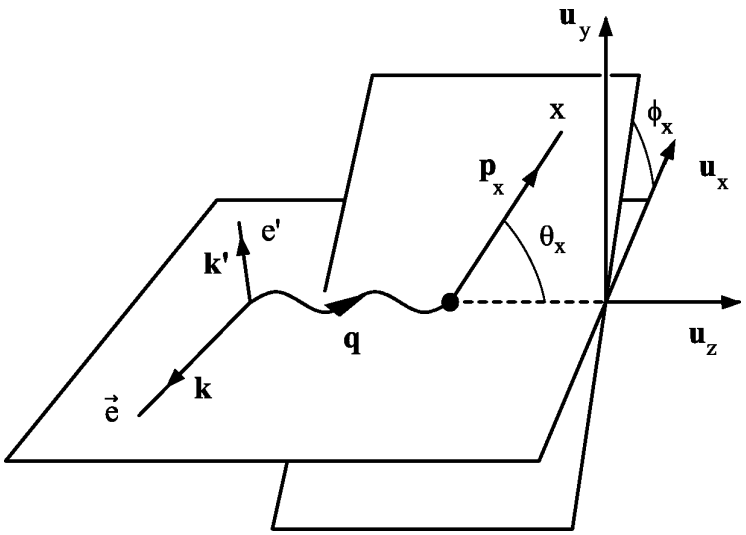

Fig. 6. Two-arm (exclusive-1) coincidence reactions, $A(e,e'x)$ and $A(\vec{e},e'x)$. The direction in which particle x is detected is specified by the angles (θ_x,ϕ_x).

$$\begin{aligned} W_s^{\mu\nu} &= X_1 g^{\mu\nu} + X_2 Q^\mu Q^\nu + X_3 V_i^\mu V_i^\nu + X_4 V_x^\mu V_x^\nu \\ &\quad + X_5(Q^\mu V_i^\nu + V_i^\mu Q^\nu) + X_6(Q^\mu V_x^\nu + V_x^\mu Q^\nu) \\ &\quad + X_7(V_i^\mu V_1^\nu + V_1^\mu V_i^\nu) \qquad (62) \\ W_a^{\mu\nu} &= iY_1(Q^\mu V_i^\nu - V_i^\mu Q^\nu) + iY_2(Q^\mu V_x^\nu - V_x^\mu Q^\nu) \\ &\quad + iY_3(V_i^\mu V_x^\nu - V_x^\mu V_i^\nu), \qquad (63) \end{aligned}$$

where we have not written any ϵ-terms (cf. (28)) using the parity properties of the electromagnetic tensor ($\sim VV$). The scalar response functions depend on the scalars discussed above: $X_\ell = X_\ell(Q^2,\ Q\cdot P_i,\ P_x\cdot P_i,\ Q\cdot P_x),\ \ell = 1,\ldots,7$ and $Y_\ell = Y_\ell(Q^2,\ Q\cdot P_i,\ P_x\cdot P_i,\ Q\cdot P_x),\ \ell = 1,\ldots,3$.

Finally, we use the current conservation conditions to obtain the constraints

$$Q_\mu W_s^{\mu\nu} = 0 = (X_1 + X_2 Q^2)Q^\nu + (X_5 Q^2)V_i^\nu + (X_6 Q^2)V_x^\nu \qquad (64)$$

$$Q_\mu W_a^{\mu\nu} = 0 = (Q^2 Y_1)V_i^\nu + (Q^2 Y_2)V_x^\nu, \qquad (65)$$

and so $X_1 + X_2 Q^2 = 0,\ X_5 = 0,\ X_6 = 0$, and $Y_1 = 0,\ Y_2 = 0$ using the linear independence of $Q^\nu,\ P_i^\nu$ and P_x^ν. For the symmetric hadronic tensor we obtain

$$\begin{aligned} W_s^{\mu\nu} &= X_1\left(g^{\mu\nu} - \tfrac{Q^\mu Q^\nu}{Q^2}\right) + X_3 V_i^\mu V_i^\nu \\ &\quad + X_4 V_x^\mu V_x^\nu + X_7(V_i^\mu V_x^\nu + V_x^\mu V_i^\nu), \qquad (66) \end{aligned}$$

in which there are four independent response functions, to be compared with inclusive scattering (31) in which only two appeared. For the antisymmetric tensor we obtain

$$W_a^{\mu\nu} = iY_3(V_i^\mu V_x^\nu - V_x^\mu V_i^\nu), \tag{67}$$

in which a fifth response function appears (see Sec. 5.4), in contrast to inclusive scattering (32) where the antisymmetric tensor vanishes.

When these hadronic tensors are contracted with the previous results given in (24,25) for the electron scattering leptonic tensor we obtain

$$\eta_{\mu\nu} W^{\mu\nu} = \eta^s_{\mu\nu} W_s^{\mu\nu} + \eta^a_{\mu\nu} W_a^{\mu\nu}, \tag{68}$$

where for the symmetric contributions to exclusive-1 scattering we have

$$\eta^s_{\mu\nu} W_s^{\mu\nu} \sim v_L \; W^L_{(x)} + v_T \; W^T_{(x)} + v_{TL} \; W^{TL}_{(x)} \cos\phi_x \; + v_{TT} \; W^{TT}_{(x)} \cos 2\phi_x, \tag{69}$$

where the notation "(x)" is used to indicate that *one* particle $x = p$, n, α, π, γ, $K, \ldots$ is detected in coincidence with the scattered electron (we assume the ERL here for simplicity). For simplicity we shall sometimes omit this subscript when the context is clear. Now, in addition to longitudinal (L) and transverse (T) pieces (cf. (35)), we also have a transverse-transverse interference (TT) and a transverse-longitudinal interference (TL). Of course, the four response functions here are linear combinations of X_1, X_3, X_4 and X_7, and depend on the four scalar quantities discussed above. For the antisymmetric contribution we have

$$\eta^a_{\mu\nu} W_a^{\mu\nu} \sim h v_{TL'} \; W^{TL'}_{(x)} \sin\phi_x, \tag{70}$$

which is directly proportional to Y_3.

To obtain the inclusive cross section from these results we must integrate over the angle dependence (θ_x, ϕ_x) and sum over all open channels. Indeed, as is apparent from (69,70), integrating over the explicit ϕ_x-dependence immediately causes the TT, TL, and TL' contributions to vanish, leaving only the L and T pieces as expected (see (35)). It should be stressed that, while similar notation is used for the response functions in the various situations (unpolarized inclusive scattering, polarized inclusive scattering, unpolarized two-arm coincidence, polarized two-arm coincidence, *etc.*), the actual responses are different, but related. Clearly for the more controlled situations with polarizations specified the responses depend on more dynamical variables and specific spin projections are accessible, in contrast to unpolarized scattering where only spin averages are involved. And when particles are detected in coincidence with the scattered electron (exclusive-1, exclusive-2, *etc.*), increasingly more specific channels are being selected. For instance, under appropriate conditions in $(e, e'p)$ only a proton may be ejected from a nucleus, and not a neutron (this would be $(e, e'n)$), whereas the inclusive cross section at high energy loss will arise from the sum over (at least) these two channels. Indeed, each level of exclusivity, when integrated over one final-state particle and summed over all channels involving that particle, will lead to the next level down, exclusive-n $\rightarrow$ exclusive-(n-1).

5.2 General form of the cross section for exclusive-1 scattering

Let us now proceed to the general form of the two-arm coincidence cross section, allowing for the possibility of target polarizations (Fig. 7). For clarity here we shall limit our discussion to the general kinematics of $\overrightarrow{A}(\overrightarrow{e},e'N)B$, with N = p or n, although clearly the same ideas may be used for coincidences with particles other than nucleons. The hadronic variables are the following: $P_A^\mu \equiv (M_A, \mathbf{0})$, $P_B^\mu \equiv (E_B, \mathbf{p_B})$, $P_N^\mu \equiv (E_N, \mathbf{p_N})$ are the 4-momenta of the target, residual nucleus and emitted nucleon, respectively. We have the relationships $E_B = \sqrt{p_B^2 + M_B^2}$ and $E_N = \sqrt{p_N^2 + m_N^2}$, where m_N is the nucleon mass, M_B is the rest-mass of the residual nucleus (and includes any internal excitation energy in that system), $p_B \equiv |\mathbf{p_B}|$ and $p_N \equiv |\mathbf{p_N}|$. In the next section we deal with these kinematical variables in more detail. The general cross section for exclusive-1 electron scattering in the laboratory system (see the preceding section) can be written as

$$\frac{d\sigma}{d\Omega_e d\omega d\Omega_N dE_N} = \frac{2\alpha^2}{Q^4}\left(\frac{\epsilon'}{\epsilon}\right)\frac{p_N m_N M_B}{(2\pi)^3 E_B}\,\eta_{\mu\nu}W^{\mu\nu}\delta(E_N + E_B - M_A - \omega). \quad (71)$$

Here $\eta_{\mu\nu}$ is the familiar leptonic tensor in the ERL discussed in Sec. 2, whereas $W^{\mu\nu}$ is the hadronic tensor containing all of the nuclear structure and dynamics information, treated above. The latter is given in terms of the nuclear electromagnetic transition currents in momentum space by (see (3))

$$W^{\mu\nu} = \overline{\sum_{i,f}}\langle f|\hat{J}^\mu|i\rangle^*\langle f|\hat{J}^\nu|i\rangle, \quad (72)$$

where $|i\rangle$ represents the nuclear target state and $|f\rangle$ the final state characterized by the emitted nucleon and the residual nucleus. As usual, conservation of the

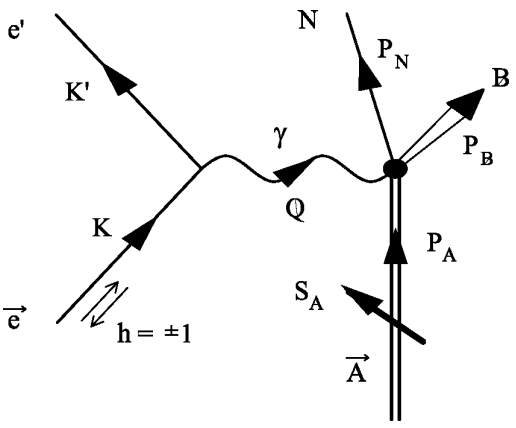

Fig. 7. Feynman diagram for the exclusive-2 electromagnetic $\overrightarrow{A}(\overrightarrow{e},e'N)B$ electron scattering process in the one-photon-exchange approximation.

nuclear electromagnetic current implies that only three of the components of the 4-current J^μ are independent quantities. Integrating the delta function of energy over E_N, we obtain

$$\frac{d\sigma}{d\Omega_e d\omega d\Omega_N} = \frac{2\alpha^2}{Q^4}\left(\frac{\epsilon'}{\epsilon}\right)\frac{p_N m_N M_B}{(2\pi)^3 M_A} f_{\rm rec}^{-1}\eta_{\mu\nu}W^{\mu\nu}, \tag{73}$$

where now p_N is specified by solving the energy balance equation

$$\sqrt{p_N^2+m_N^2}+\sqrt{p_N^2-2p_N q\cos\theta_N+q^2+M_B^2}=M_A+\omega \tag{74}$$

with θ_N being the angle between $\mathbf{p}_N$ and $\mathbf{q}$ (see Fig. 8). The general expression for the contraction of the electron and hadronic tensors can be written

$$2\eta_{\mu\nu}W^{\mu\nu} = v_0\overline{\sum_{i,f}}[R_{fi}+hR'_{fi}]. \tag{75}$$

Using the general properties of the leptonic tensor, as discussed above, it may be shown that these total responses have the following decompositions:

$$R_{fi} = v_L W_{fi}^L + v_T W_{fi}^T + v_{TL}W_{fi}^{TL} + v_{TT}W_{fi}^{TT} \tag{76}$$

$$R'_{fi} = v_{T'}W_{fi}^{T'} + v_{TL'}W_{fi}^{TL'}, \tag{77}$$

where the W's are discussed in the last section (cf. also (69,70)). The differential cross section in (73) may now be written

$$\begin{aligned}\frac{d\sigma^h}{d\omega d\Omega_e d\Omega_N} &= \frac{p_N m_N M_B}{(2\pi)^3 M_A}\sigma_{\rm Mott} f_{\rm rec}^{-1}\left\{R_{fi}+hR'_{fi}\right\}\\ &\equiv \Sigma_{fi}+h\Delta_{fi},\end{aligned} \tag{78}$$

containing the helicity-sum (electron unpolarized) cross section

$$\Sigma_{fi} = \frac{1}{2}\left[\frac{d\sigma^+}{d\omega d\Omega_e d\Omega_N}+\frac{d\sigma^-}{d\omega d\Omega_e d\Omega_N}\right] \tag{79}$$

and the helicity-difference (electron polarized) cross section

$$\Delta_{fi} = \frac{1}{2}\left[\frac{d\sigma^+}{d\omega d\Omega_e d\Omega_N}-\frac{d\sigma^-}{d\omega d\Omega_e d\Omega_N}\right]. \tag{80}$$

In particular, later we shall briefly discuss the situation where only the initial electron and target nucleus are possibly polarized, with no polarization in the final state (indicated by fi). Furthermore, the only final-state information (aside from knowing that q and ω have been transferred to the nucleus and hence that only certain final states are accessible) is contained in the fact that a nucleon is presumed to be detected at specific angles (θ_N, ϕ_N) and has energy E_N (see Fig. 8). Under these conditions it is possible to show [12] that the dependences on

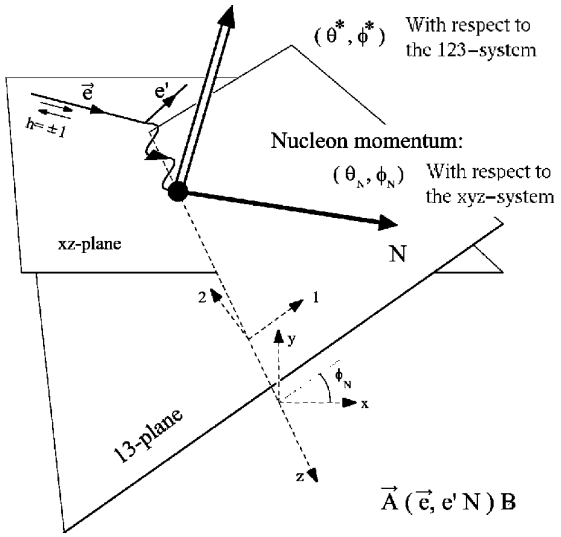

Fig. 8. Kinematics for two-arm (exclusive-1) coincidence reactions with polarized targets. $\mathbf{u}_z$ is along $\mathbf{q}$, $\mathbf{u}_y$ is normal to the electron scattering plane and $\mathbf{u}_x = \mathbf{u}_y \times \mathbf{u}_z$ lies in the scattering plane. The target polarization direction is specified by the angles (θ^*, ϕ^*) in this coordinate system. The unit vectors $\mathbf{u}_1$, $\mathbf{u}_2$, $\mathbf{u}_3$ are constructed by rotating the previous ones $(\mathbf{u}_x, \mathbf{u}_y, \mathbf{u}_z)$ by an angle ϕ_N: $\mathbf{u}_3 \equiv \mathbf{u}_z$, $\mathbf{u}_1$ lies in the nucleonic plane and $\mathbf{u}_2$ is perpendicular to it.

the azimuthal angles ϕ_N and ϕ^* (the azimuthal angle of the target polarization axis of quantization) are the following:

$$\begin{aligned} \Sigma_{fi} \sim\ & v_L W^L_{fi}(\Delta\phi) + v_T W^T_{fi}(\Delta\phi) \\ & + v_{TL}\left(\cos\phi_N W^{TL}_{fi}(\Delta\phi) + \sin\phi_N \tilde{W}^{TL}_{fi}(\Delta\phi)\right) \\ & + v_{TT}\left(\cos 2\phi_N W^{TT}_{fi}(\Delta\phi) + \sin 2\phi_N \tilde{W}^{TT}_{fi}(\Delta\phi)\right) \end{aligned} \tag{81}$$

and

$$\begin{aligned} \Delta_{fi} \sim\ & v_{T'} \tilde{W}^{T'}_{fi}(\Delta\phi) \\ & + v_{TL'}\left(\sin\phi_N W^{TL'}_{fi}(\Delta\phi) + \cos\phi_N \tilde{W}^{TL'}_{fi}(\Delta\phi)\right), \end{aligned} \tag{82}$$

where each response depends on q, ω, p_N (or E_N) and θ_N as well as on the target polarization angles θ^* and $\Delta\phi$. It should be noted that these results have been expressed in terms of $\Delta\phi \equiv \phi^* - \phi_N$, where the direction of the target polarization is referred to the nucleon plane rather than to the electron plane.

5.3 Kinematics of exclusive-1 electron scattering

Having set up the basic form for the exclusive-1 cross section, let us next consider the kinematics in more detail. We shall simply use energy-momentum conservation to inter-relate the various energies and momenta; no assumption is made about the reaction mechanism. We have seen above that the cross section depends on a set of kinematic variables. First, explicit dependences on the electron scattering angle θ_e (through the generalized Rosenbluth factors v_K in (11,45, 53)) and an azimuthal angle ϕ_N (see (69); in the present discussions we shall suppress the target polarization dependences, although they are straightforward to incorporate — see (81)) have been isolated and will no longer be discussed.

More complicated are the dependences on the set of "dynamical" (in contrast to "geometrical") variables $\{q, \omega, E_N, \theta_N\}$ or equivalently $\{Q^2, Q\cdot P_A, P_N\cdot P_A, Q\cdot P_N\}$ (compare (59)), since these dependences involve detailed aspects of the nuclear dynamics . However, while these sets of dynamical variables are, of course, completely usable and indeed natural from an experimental point of view, as we shall see in the following it turns out that alternative sets of four quantities are more convenient when studying the specifics of the cross section. Let us begin with the set $\{q, \omega, E_N, \theta_N\}$ and make a sequence of changes of variable. First, let us define $\mathbf{p} \equiv -\mathbf{p}_B = \mathbf{p}_N - \mathbf{q} = -\mathbf{p}_m$, where $\mathbf{p}_m$ is the so-called missing momentum, and then the daughter energy becomes $E_B = \sqrt{M_B^2 + p^2}$. Clearly $p = |\mathbf{p}|$ characterizes the split in momentum flow between the detected nucleon and the unobserved daughter nucleus. We need some corresponding energy variable to characterize the split in energy; several possibilities come to mind. One choice is to introduce the energy

$$\mathcal{E} \equiv E_B - E_B^0 \geq 0, \tag{83}$$

to represent the excitation of the residual nucleus, where as before $E_B = \sqrt{M_B^2 + p^2}$ and now also $E_B^0 = \sqrt{{M_B^0}^2 + p^2}$. Here M_B includes the internal excitation energy of the B system, while M_B^0 is its rest mass when it is in its ground state. By construction $\mathcal{E}$ is greater than or equal to zero — and equal to zero when the daughter nucleus is left in its ground state. As we shall see below, we could now use $\mathcal{E}$ and p in place of E_N and θ_N.

Another energy in the problem is the separation energy (or "Q-value"), given by $E_s \equiv m_N + M_B^0 - M_A$, the minimum energy needed to separate the nucleus A into a nucleon and the residual nucleus B in its ground state. If the recoil kinetic energy corresponding to the (in general excited) residual nucleus is denoted $T_{\rm rec} = E_B - M_B$ and likewise $T_{\rm rec}^0 = E_B^0 - M_B^0$ for the residual nucleus in its ground state, then what is sometimes called the missing energy (note that there are other definitions for this quantity) is given by

$$\begin{aligned} E_m &= m_N + M_B - M_A \\ &= E_s + \mathcal{E} + (T_{\rm rec}^0 - T_{\rm rec}) \\ &\cong E_s + [1 - \frac{p^2}{2M_B^0 M_B}]^{-1}\mathcal{E}, \end{aligned} \tag{84}$$

where the last approximation pertains when $p^2 \ll 2M_B^0 M_B$ (which is usually the case). Overall energy conservation yields a value for E_N for given ω:

$$E_N = M_A + \omega - E_B. \tag{85}$$

Since $E_B = E_B^0 + \mathcal{E}$, we have an equation for $\mathcal{E}$ in terms of q, ω, p and the angle θ (between $\mathbf{p}$ and $\mathbf{q}$):

$$\mathcal{E} = M_A + \omega - \sqrt{m_N^2 + p^2 + q^2 + 2pq\cos\theta} - \sqrt{{M_B^0}^2 + p^2}, \tag{86}$$

which just a re-writing of (74). Thus there are clear relationships between the sets $\{E_N, \theta_N\}$ and $\{p, \theta\}$ and hence $\{\mathcal{E}, p\}$. Instead of the first set, we shall now use the last set as a pair of dynamical variables.

Now let us see what kinematic flexibility we have in probing this cross section, as indeed we have not yet required that the kinematic relationships discussed above should be satisfied. When we do so, we find that only selected regions are accessible. Noting that (86) yields a curve of $\mathcal{E}$ versus p in the $(\mathcal{E}, p)$-plane for each choice of θ, let us see what constraint the requirement that $-1 \leq \cos\theta \leq +1$ imposes on the kinematics. First, consider "ω small" (to be specified completely below) and plot the trajectory when $\cos\theta = -1$. A curve rising from negative $\mathcal{E}$ to intersect $\mathcal{E} = 0$ at $p = p_{\min} > 0$ which peaks at some value of p and then falls to intersect $\mathcal{E} = 0$ again, this time at $p = p_{\max} > p_{\min}$, is generally obtained. All physically allowable values of $\mathcal{E}$ and p must lie below this curve and, of course, above $\mathcal{E} = 0$. To obtain the other extreme, $\cos\theta = +1$, one can simply replace p by $-p$ in (86); the physically allowable values of $\mathcal{E}$ and p must lie above this curve. For "ω small", no physically allowable values at all occur near the latter curve and the physical region is completely defined by the $\cos\theta = -1$ curve and $\mathcal{E} = 0$. Following past work we shall call the minimum value of momentum $p_{\min} \equiv -y$ and the maximum value $p_{\max} \equiv +Y$. The formal definition of "ω small" then becomes "$y < 0$". We can set $\mathcal{E} = 0$ in (86) and solve for y and Y, yielding

$$y(q,\omega) = \tfrac{1}{W^2}\Big\{(M_A+\omega)\sqrt{\Lambda^2 - {M_B^0}^2 W^2} - q\Lambda\Big\} \tag{87}$$

$$Y(q,\omega) = \tfrac{1}{W^2}\Big\{(M_A+\omega)\sqrt{\Lambda^2 - {M_B^0}^2 W^2} + q\Lambda\Big\} \tag{88}$$

with

$$\begin{aligned} W &= \sqrt{(M_A+\omega)^2 - q^2} \\ \Lambda &= \tfrac{1}{2}\big(W^2 + {M_B^0}^2 - m_N^2\big). \end{aligned} \tag{89}$$

A useful relationship is the following:

$$\omega = \sqrt{(q+y)^2 + m_N^2} + \sqrt{y^2 + {M_B^0}^2} - M_A. \tag{90}$$

In particular, assuming that the quasielastic peak occurs when $y = 0$, one has

$$\omega_{\mathrm{QE}} \equiv \big\{\sqrt{q^2 + m_N^2} - m_N\big\} + E_s = |Q^2|/2m_N + E_s. \tag{91}$$

Furthermore, the equation for the upper boundary of the allowed region (*i.e.*, corresponding to $\cos\theta = -1$) is given by

$$\mathcal{E}_M = \sqrt{m_N^2 + (q+y)^2} - \sqrt{m_N^2 + (q-p)^2} + \sqrt{M_B^{0\,2} + y^2} - \sqrt{M_B^{0\,2} + p^2}. \quad (92)$$

When the momentum transfer become very large this goes to the *finite* asymptotic limit

$$\mathcal{E}_M \to \mathcal{E}_M^\infty = y + p - \left[\sqrt{M_B^{0\,2} + p^2} - \sqrt{M_B^{0\,2} + y^2}\right]. \quad (93)$$

Henceforth, instead of the sets $\{q, \omega, E_N, \theta_N\}$ or $\{Q^2, Q \cdot P_A, P_N \cdot P_A, Q \cdot P_N\}$ we shall use the set $\{q, y, \mathcal{E}, p\}$ to characterize the general two-arm coincidence cross section.

In Fig. 9 are shown families of curves of $\mathcal{E}_M$ versus p for specific values of q and $y < 0$. The physical regions lie below these curves for chosen kinematics. Clearly, by comparing these kinematic constraints with the generic cross section it is possible to see what features of the dynamics are or are not accessible in the $y < 0$ region. Note that even when $q \to \infty$ only a limited part of the dynamics is accessible. Also note that inclusive scattering corresponds to integrating over the entire accessible region for q and y (or equivalently ω) fixed, and summing over all allowed particle species (protons, neutrons, ...).

These developments can be extended rather easily to the "ω large" region, which becomes equivalent to $y > 0$. Again the curves of $\mathcal{E}$ versus p when $\cos\theta = \pm 1$ define boundaries. The $\cos\theta = -1$ curve (namely, $\mathcal{E} = \mathcal{E}_M$ above) is much as

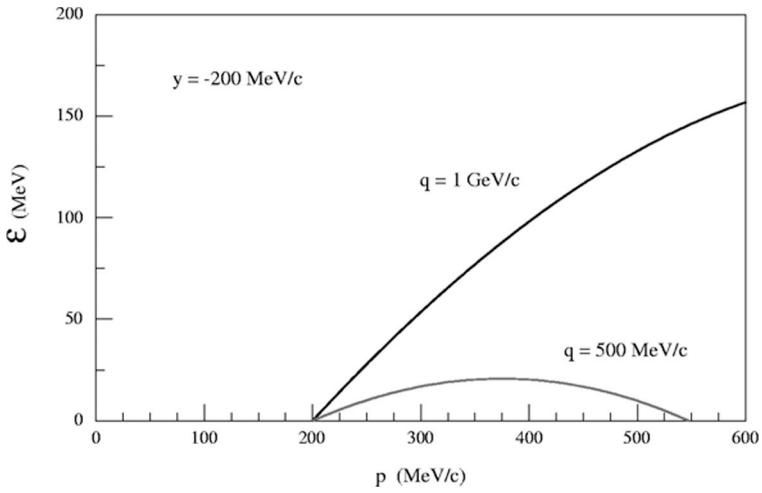

Fig. 9. Plots of $\mathcal{E}_M$ (see (92)) for various values of q and $y < 0$ for the reaction ^{3}He(e,e′p).

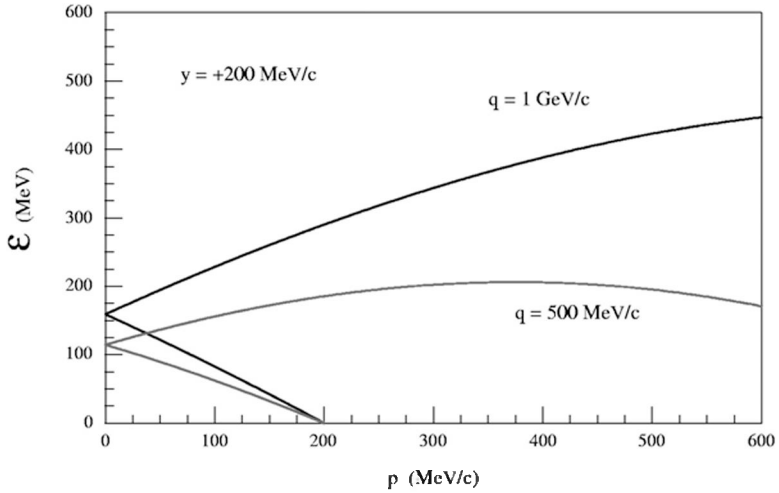

Fig. 10. As for Fig. 9, but now for $y \geq 0$.

before, except that now $p_{\min}$ is negative and so $y \equiv -p_{\min}$ is positive. Reflecting $p \to -p$ to obtain the $\cos\theta = +1$ curve from the $\cos\theta = -1$ curve as before now yields a nontrivial result: the physically allowable region must lie below the $\cos\theta = -1$ curve and above the $\cos\theta = +1$ curve, and since the latter lies in the quadrant where $\mathcal{E} \geq 0$ and $p \geq 0$, this provides a new boundary. In Fig. 10 results similar to those in Fig. 9 are shown, except now for $y \geq 0$. The physically accessible region in each case lies *above* the lines extending from $p = y$ to the $\mathcal{E}$-axis and *below* the curves extending from the $\mathcal{E}$-axis to peak at some value of p and fall again, eventually intersecting the $\mathcal{E} = 0$ line at $p_{\max} = Y$. Again we see that specific parts of the generic cross section are accessible for these kinematics.

5.4 Polarized electrons and the fifth response function

Let us now turn to a brief discussion of some specific interesting features of two-arm coincidence reactions studied with and without polarized electrons, $A(\overrightarrow{e}, e'x)$ and $A(e, e'x)$, but where the target is unpolarized. As before, the electron scattering process involves the variables q, ω and θ_e, together with the electron's helicity h, if polarized electrons are considered. The fact that particle x is detected in coincidence with the scattered electron means that we have two angles θ_x and ϕ_x to specify the direction in which particle x is going, as well as its energy E_x. Recall that above ((69,70)) we found that there are two major classes of response (again, separated using the electron helicity sum and difference),

$$\begin{aligned} \Sigma &\sim v_L W^L_{(x)} + v_T W^T_{(x)} + v_{TL} \cos\phi_x W^{TL}_{(x)} + v_{TT} \cos 2\phi_x W^{TT}_{(x)} \\ \Delta &\sim v_{TL'} \sin\phi_x W^{TL'}_{(x)} . \end{aligned} \tag{94}$$

As above, the responses here depend, for instance, on $\{q, \omega, E_x, \theta_x\}$, but not on ϕ_x; all of the ϕ_x-dependence is explicit in (94) (as is the θ_e-dependence through the v's). Thus, by varying the azimuthal angles ϕ_x and using the electron kinematical factors it is possible to isolate five responses, four when the electron beam is unpolarized plus a fifth when polarized electrons are available. Note that, in contrast to single-arm scattering with polarized electrons but unpolarized targets, this fifth response function is nonzero in general even when parity is conserved.

Also note that the fifth response can only be observed when particle x is detected out of the electron scattering plane. Perhaps not so obvious is the fact that, as well, the L and TT contributions can only be separated using out-of-plane measurements: the factor $\cos 2\phi_x$ is $+1$ in the electron scattering plane (for $\phi_x = 0°$ or $180°$); furthermore, the factors v_L and v_T are the only ones which contain no dependence on $\tan\frac{\theta_e}{2}$ (see Secs. 2 and 4) and so are fixed when q and ω are fixed. Therefore, the only way to make relative changes in the factors multiplying the L and TT responses in attempting to separate them is to perform at least one measurement with $\phi_x \neq 0°$ or $180°$.

To get some feeling for how these various response functions reflect different aspects of the dynamics underlying a specific reaction, let us briefly examine the general behavior of the fifth response. The TL' fifth response function and the usual TL response have similar structures:

$$\begin{aligned} W_{(x)}^{TL} &\sim \Re(T^*L) \\ W_{(x)}^{TL'} &\sim \Im(T^*L), \end{aligned} \tag{95}$$

where T^*L represents the appropriate (*i.e.*, determined by the dynamics of the specific problem of interest) bilinear combination of (transverse)* $\times$ (longitudinal) matrix elements. The *same* combinations occur in the two responses; the only difference is that one has the real part and the other the imaginary part. Now, if the reaction proceeds through a channel in which a single phase dominates for all projections of the current ($T \sim |T|e^{i\delta}$, $L \sim |L|e^{i\delta}$, with the same δ), then T^*L is real and, while $W_{(x)}^{TL}$ is nonzero in general, $W_{(x)}^{TL'}$ vanishes. Moreover, it happens that $W_{(x)}^{TL'}$ also vanishes in the absence of final-state interactions; specifically, in PWIA $W_{(x)}^{TL'}$ is zero. On the other hand, if $W_{(x)}^{TL'} \neq 0$, then interesting effects must be coming into play.

For example, in the Δ-region coincidence electron scattering will be driven to a large degree by the 33-amplitude with a single phase, δ_{33}, and, while $W_{(x)}^{L,T,TL,TT}$ may all be nonzero, $W_{(x)}^{TL'}$ may be expected to vanish. To the extent that it does not vanish, we will be able to access information concerning interferences of the 33-amplitude with amplitudes for other channels which are usually too weak to be studied directly. Similar considerations apply in the giant resonance region at lower excitation energies. Using the special nature of the various responses — importantly, this ability to emphasize resonant versus non-resonant behavior — should provide us with valuable new insight into nuclear dynamics.

More generally it may be shown that the L, T, TL and TT (unpolarized) responses on the one hand and the TL' (polarized electrons, but otherwise unpolarized) response on the other may be characterized by their time-reversal properties, even and odd, respectively. Time-reversal even (TRE) responses are always real parts of bilinear products involving the currents, while time-reversal odd (TRO) responses involve imaginary parts (as for TL and TL' above, respectively). As we shall see in the next section, this characterization can be generalized to include situations when target and/or final-state polarizations are specified and where wider classes of response becomes accessible.

5.5 Polarized electrons and polarized targets

The kinematics for this class of reactions, $\overrightarrow{A}(\overrightarrow{e},e'x)$, are indicated in Fig. 8. Now, as in the discussions in Sec. 4, polarization angles (θ^*,ϕ^*) are needed together with angles (θ_x,ϕ_x) which specify the direction in which particle x is detected (as in the previous subsection). The helicity sum and difference cross sections can be written in the forms [12]

$$\begin{aligned}\Sigma \sim\ & v_L W^L_{(x)}(\theta^*,\phi^*) + v_T W^T_{(x)}(\theta^*,\phi^*) \\ & + v_{TL}\left(\cos\phi_x W^{TL}_{(x)}(\theta^*,\phi^*) + \sin\phi_x \tilde{W}^{TL}_{(x)}(\theta^*,\phi^*)\right) \\ & + v_{TT}\left(\cos 2\phi_x W^{TT}_{(x)}(\theta^*,\phi^*) + \sin 2\phi_x \tilde{W}^{TT}_{(x)}(\theta^*,\phi^*)\right) \qquad (96)\\ \Delta \sim\ & v_{T'}\tilde{W}^{T'}_{(x)}(\theta^*,\phi^*) \\ & + v_{TL'}\left(\sin\phi_x W^{TL'}_{(x)}(\theta^*,\phi^*) + \cos\phi_x \tilde{W}^{TL'}_{(x)}(\theta^*,\phi^*)\right), \qquad (97)\end{aligned}$$

where each response depends on q, ω, E_x and θ_x as before, together with new dependences on the target polarization (for emphasis, the dependences on θ^* and ϕ^* are displayed here). Note that all six of the general classes of response (with the full ϕ_x-dependence involving both sines and cosines) occur already at the exclusive-1 level when the target is polarized, in contrast to the unpolarized reactions where the fullest form is only reached at the exclusive-2 level [5,12]. For an unpolarized situation, the responses with tildes vanish and the ones without revert to the form of the responses discussed above (see (94)):

$$\tilde{W}^K_{(x)}(\theta^*,\phi^*) \to 0 \qquad (98)$$

$$W^K_{(x)}(\theta^*,\phi^*) \to W^K_{(x)}. \qquad (99)$$

The target polarization information may be organized into spherical tensors characterized by rank I, where I may be even or odd, with $I=0$ corresponding to the unpolarized cross sections in Sec. 5.4. When target polarizations are considered, this is the same type of tensor decomposition encountered earlier for single-arm scattering in Sec. 4. The general break-down into time-reversal even

and odd responses is as follows:

		I = even	I = odd
$\left\{\begin{array}{c}\Sigma\\ \text{electron}\\ \text{unpolarized}\end{array}\right\}$	L	TRE	TRO
	T	TRE	TRO
	TL	TRE	TRO
	TT	TRE	TRO
$\left\{\begin{array}{c}\Delta\\ \text{electron}\\ \text{polarized}\end{array}\right\}$	T'	TRO	TRE
	TL'	TRO	TRE

As in the more limited situation without target polarizations discussed above in the previous subsection, the responses in time-reversal even or odd sectors can have rather different sensitivities to the nature of the final state. In particular, as noted above, in the absence of final-state interactions all TRO responses vanish.

In passing, it should also be noted that a very similar organization into time-reversal even and odd responses also occurs [12] for coincidence reactions $A(\vec{e},e'\vec{x})$ where the target is unpolarized but where the polarization of the outgoing particle x is measured.

To help clarify these ideas a little, let us consider a specific spinology: we take the simplest non-trivial case of a spin-1/2 target which may be unpolarized ($I=0$) or vector polarized ($I=1$). Let us characterize the polarizations by projections along three orthogonal directions: (ℓ) along $\mathbf{q}$, (n) in the direction $\mathbf{q}\times\mathbf{p}_x$, and ($s$) in the direction $\mathbf{u}_n\times\mathbf{u}_\ell$. The ϕ_x dependences of the complete set of 18 responses are the following:

		Target Unpolarized	Target Polarized ℓ	s	n
	L	1	0	0	1
Electron	T	1	0	0	1
Unpolarized	TL	$\cos\phi_x$	$\sin\phi_x$	$\sin\phi_x$	$\cos\phi_x$
	TT	$\cos 2\phi_x$	$\sin 2\phi_x$	$\sin 2\phi_x$	$\cos 2\phi_x$
Electron	T'	0	1	1	0
Polarized	TL'	$\sin\phi_x$	$\cos\phi_x$	$\cos\phi_x$	$\sin\phi_x$

With electron and target either unpolarized or both polarized, the responses are TRE; with only one or the other polarized, they are TRO. Note that even in the absence of polarized electrons there are new responses for polarized spin-1/2 targets when coincidence reactions are being considered.

6 Summary

Let us conclude with a summary of several of the issues discussed in the lectures and use one region of nuclear excitation to make the ideas more concrete. Electron scattering always begins with the same basic ingredients: an electron beam

of energy ϵ is prepared, impinges on a target and is scattered through angle θ_e to be detected at energy ϵ'. From these variables it is straightforward to construct the 3-momentum transfer q, the energy transfer ω and secondary variables such as the 4-momentum transfer Q, the variable x used in high-energy physics or the variable y used in scaling analyses. Let us suppose that for some given value of q we examine the excitation spectrum (*i.e.,* the ω dependence of the inclusive cross section) sketched in Fig. 11. At essentially zero energy loss we have the elastic scattering cross section; at somewhat higher energies generally we see a spectrum of discrete states; then at still higher energies, in the neighborhood of particle emission threshold, the giant resonances and high-spin stretched particle-hole states appear; at still higher energy loss the quasielastic peak, the peaks due to the Δ and other baryon resonances plus meson production all occur; finally at very high energies one proceeds to deep inelastic scattering. If we select some discrete state or a small region in the continuum and focus on the q dependence,

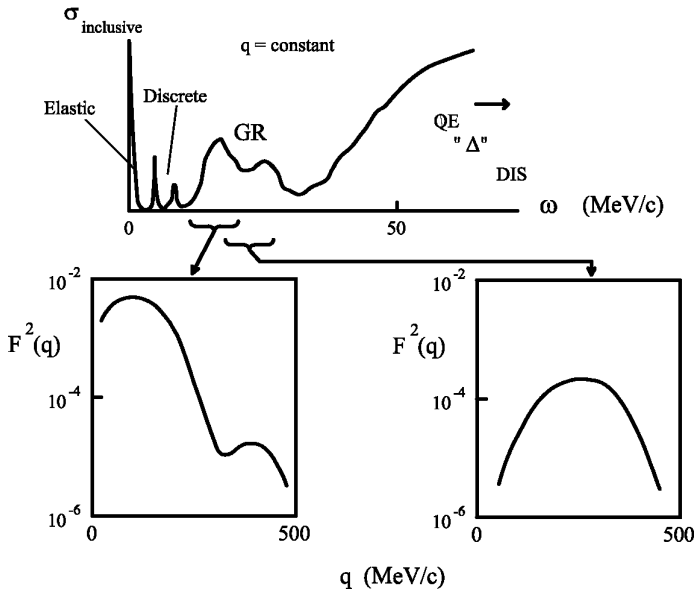

Fig. 11. Sketch showing a typical nuclear inclusive cross section at constant q as a function of ω. Characteristic features are identified: elastic scattering, excitation of discrete states, the giant resonance region (GR), and, at higher energy loss, the quasielastic (QE), baryon resonance (Δ's, N^*'s, ...) and meson production regions and finally the regime where deep inelastic scattering (DIS) dominates. Sketches of the q-dependence in the GR region of excitation are broken out in the lower two panels: the lefthand panel illustrates the typical dependence found for the familiar giant dipole resonance, while the righthand panel illustrates that for excitation of a typical high-spin stretched particle-hole state.

that is, if we consider the form factor

$$\int_{\Delta\omega} \sigma_{inclusive}\, d\omega \to F^2(q)$$

then much more information becomes available. The q dependence when Fourier-transformed gives us information on the spatial nature of the excitations involved. The L/T Rosenbluth aspect of the problem tells us (typically) how charges, currents and magnetizations are involved. And the ability to probe at both low-q (long wavelengths) and high-q (short wavelengths) while keeping ω fixed (an extremely important feature of virtual photons compared with real photons where $q = \omega$) yields critical insight into the nature of the nuclear excitations. For example, as sketched in Fig. 11 at low-q the usual, familiar giant dipole resonance is dominant, but become rather weak at high-q; in contrast, the stretched particle-hole excitations such as the $0^+ \to 14^-$ M14 in lead are negigible at low-q, but stand out once the momentum transfer becomes large enough, typically beyond 1 fm$^{-1} \sim 200$ MeV/c.

So far all we have been discussing is inclusive, unpolarized scattering. Clearly, as discussed in the lectures, having polarized targets possibly with polarized electron beams will bring with it the ability to separate the various form factors when studying elastic scattering and discrete states in general. However, when in the continuum many channels may be open:

$$\begin{aligned} A(e,e') \Leftrightarrow\ & A(e,e'p)B_0,\ B_1,\ B_2,\cdots \\ & A(e,e'n)C_0,\ C_1,\ C_2,\cdots \\ & A(e,e'\alpha)D_0,\ D_1,\ D_2,\cdots \\ & \vdots \end{aligned} \tag{101}$$

where possibly $B_2 = B_2 + n$, *etc.* The power of coincidence reactions, $(e,e'p)$, $(e,e'n)$, $(e,e'\alpha),\cdots$, becomes apparent when one now realizes that each of these channels may in principle be isolated from all others. The inclusive cross section, by contrast, sums over all of the open channels. As we have seen in the lectures, the missing energy E_m (or the quantity $\mathcal{E}$ advocated in the lectures) permits us to select a region of daughter excitation for each channel and the missing momentum p_m (or p in the discussions) yields information on the momentum flow to the daughter system and hence the wavelength scale being probed. Putting coincidence reaction studies together with spin physics provides even more, for example, via the 5^{th} response or the other TRO observables introduced above where special sensitivities to resonant versus non-resonant structure can be probed.

In summary, it is a very exciting time for the field and we all look forward to an interesting continuing program of study of the atomic nucleus via electromagnetic interactions.

Acknowledgments

This work is supported in part by funds provided by the U. S. Department of Energy (D.O.E.) under cooperative agreement #DE-FC02-94ER40818.

References

1. T. deForest, Jr. and J. D. Walecka: Adv. in Phys. **15**, 1 (1966)
2. T. W. Donnelly and J. D. Walecka: Ann. Rev. Nucl. Sci. **25**, 329 (1975)
3. J. D. Bjorken and S. D. Drell: Relativistic Quantum Mechanics (McGraw-Hill, N.Y., 1964)
4. T. W. Donnelly and A. S. Raskin: Ann. Phys. **169**, 247 (1986)
5. T. W. Donnelly: Prog. in Particle and Nuclear Physics **13**, 183 (1985)
6. R. von Gehlen: Phys. Rev. **118**, 1445 (1960); M. Gourdin: Nuovo Cim. **21**, 1094 (1961); J. D. Bjorken: (unpublished, 1960)
7. M. J. Musolf, T. W. Donnelly, J. Dubach, S. J. Pollock, S. Kowalski and E. J. Beise: Phys. Rep. **239**, 1 (1994)
8. J. E. Amaro et al.: Nucl. Phys. **A602**, 263 (1996)
9. S. Jeschonnek and T. W. Donnelly: Phys. Rev. **C57**, 2438 (1998)
10. T. W. Donnelly and I. Sick: Phys. Rev. Lett. **82**, 3212 (1999)
11. T. W. Donnelly and I. Sick: Phys. Rev. **C60**, 065502 (1999)
12. A. S. Raskin and T. W. Donnelly: Ann. Phys. **191**, 78 (1989)

The nuclear shell model

Alfredo Poves[1] and Frederic Nowacki[2]

[1] Departamento de Física Teórica. Universidad Autónoma de Madrid, E-28049, Madrid, Spain
[2] Laboratoire de Physique Theorique, Universite Louis Pasteur, F-67084, Strasbourg, France

Abstract. In this series of lectures we discuss the basic notions of the spherical shell model. Starting from a regularized nucleon-nucleon interaction, we define the model as an approximation to the exact solution of the full secular problem. We introduce the notions of valence space, effective interaction and effective operator. We analyse the structure of the realistic effective interactions, identifying their monopole part with the spherical mean field. The multipole hamiltonian is shown to have a simple and universal form that includes pairing (isovector and isoscalar), quadrupole, octupole, hexadecapole and $(\sigma \cdot \tau)$ $(\sigma \cdot \tau)$. We describe the methods of resolution of the secular problem, in particular the Lanczos method. Finally, we present some results on two different open problems in nuclear structure; the quenching of the strength of the spin operators in the nuclear medium and the spherical shell model description of deformation and superdeformation.

1 Introduction

The nuclear shell model in its most simple version, the independent particle model of Mayer and Jensen, was introduced already fifty years ago. In addition to its capacity to explain the nuclear regularities (magic numbers) and other properties as the spins and magnetic moments of nuclei in the vecinity of magic closures, it provides the natural framework to incorporate the nucleon-nucleon correlations, even if approximately. In this sense it has been a key element in the development of the theory of the nuclear structure during the intervening years. In parallel to the increase of our knowledge of the in-medium nuclear interaction and to the improvements of the many body formalism, the field of applicability of the nuclear shell model has grown considerably. From now on we will use the term "shell model" as a shorthand for symmetry conserving, configuration mixing calculations in large multiparticle basis. The shell model has been often considered to be of application only to those nuclear manifestations in which the single particle degrees of freedom are dominant. That in spite of the work of Elliott [1], that demonstrated the possibility of explaining deformation in light nuclei using the SU3 properties of the quadrupole nuclear force in an harmonic oscillator basis. In recent times, the advent of new computers and shell model codes has given access to new mass regions where collectivity shows up in a more conspicuous way, and the spherical shell model approach has proven to be able of coping with the new challenges, either close or far from the valley of stability, giving a unified description of the single particle and collective degrees

J.M. Arias and M. Lozano (Eds.): LNP 581, pp. 70–101, 2001.
© Springer-Verlag Berlin Heidelberg 2001

of freedom of the nucleus. In this lectures we plan to guide the reader from the very basic starting points of the shell model description of nuclei to some of the latest applications. Our aim is to keep, while possible, the contact with the underlying free nucleon-nucleon interaction and when the link has to be broken to try to understand why. Many books exist that can serve as introduction to the subject, but we shall quote only the more recent or those that fully develop the mathematical formalism of the theory [2]. The last complete review of the shell model approach to nuclei is due to B. A. Brown and B. H. Wildenthal [3]

The original aspects of this presentation come from a long lasting collaboration with Etienne Caurier and Andrés Zuker (IRES, Strasbourg), Joaquin Retamosa (UCM, Madrid) and Gabriel Martinez-Pinedo (University of Aarhus). These notes have a large overlap with those of a similar course given by one of us (A. P.) at the Ecole "Joliot-Curie" 1997.

The plan of this notes is as follows; in section 2 we introduce the basic notions of the spherical shell model, in section 3 we deal with the problem of the effective interactions, in section 4 we discuss the ways to solve the secular problem and the Lanczos method, finally, in section 5 we present the results of some recent large scale shell model calculations in two domains; Gamow-Teller and M1 strength in nuclei and spherical shell model and deformation.

2 Basic notions of the spherical shell model

We shall consider the nucleus as composed of Z protons and N neutrons, that interact via two-body forces and obey a non-relativistic (Schrödinger) equation. Therefore we will not consider explicitely meson or quark degrees of freedom nor shall we use relativistic kinematics. Recent advances in the relativistic mean field description of nuclei based on meson exchanges have shown that the main advantages of such an approach are that it accomodates the spin orbit interaction in a natural way, suggesting –perhaps– that its isospin dependence is different from what is assumed in the non-relativistic effective forces and that it provides a saturation mechanism for nuclear matter. Many relativistic aspects are actually incorporated in the non relativistic approach via the nucleon-nucleon interaction in the vacuum that contains many terms of relativistic origin (spin-orbit, tensor etc). The problem of saturation can be solved in the non-relativistic approach by introducing three-body forces. In mean field effective interactions, density dependent terms take care of saturation. In the shell model approach the size of the underlying mean field potential is adapted to the size of the nucleus, although some problems originating in the regularization of the nucleon-nucleon interaction may show up in the spectroscopic calculations too.

The starting point is the nucleon-nucleon interaction V_{NN}. As it corresponds to a derived interaction it is not simple. It contains many kinds of terms, central, spin-orbit, tensor, spin-spin etc. At long distances it has a Yukawa form, while at short distances it shows an extremely repulsive core. The short range repulsion is at the origin of most of the theoretical and technical problems that the nuclear many-body theories have to solve. Actually, the very idea of a shell model for the

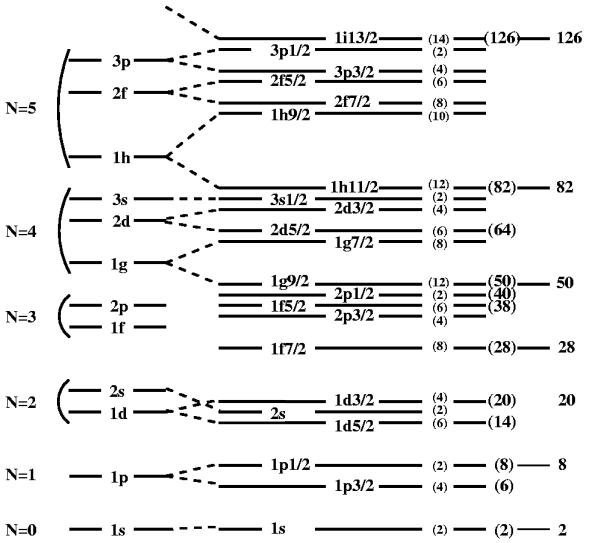

Fig. 1. The structure of the spherical mean field

nucleus may seem contradictory with this strong correlation because it rudely breaks the independent particle picture. However, very early, experimental evidence of a shell model like behaviour became available in the form of magic numbers, single particle energies, magnetic moments etc.

These experimental hints led M. Goeppert-Mayer and H. Jensen [4] to the empirical construction of the nuclear mean field, a surface corrected harmonic oscillator, whose main novelty was the very strong spin-orbit splitting needed to explain the experimental magic numbers.

$$\begin{aligned} U(r) &= \frac{1}{2}m\omega^2 r^2 + D\boldsymbol{l}^2 - C\boldsymbol{l}.\boldsymbol{s} \\ -C\boldsymbol{l}.\boldsymbol{s} &= -\frac{1}{2}(\boldsymbol{j}^2 - \boldsymbol{l}^2 - \boldsymbol{s}^2) = -\frac{1}{2}(j(j+1) - l(l+1) - \frac{3}{4}) \\ &= l+1 \quad \text{for } j = l - \frac{1}{2} \\ &= -l \quad \text{for } j = l + \frac{1}{2} \end{aligned} \tag{1}$$

The single particle levels of the nuclear mean field are represented in Fig. 1. Starting from the left hand side, we find the shell structure of the isotopic harmonic oscillator, then the splitting due to the $\mathbf{l^2}$ term and finally the actual single particle levels taking into account the spin-orbit splitting. To the right, the predicted magic numbers.

The success of the independent particle model strongly suggest that the very singular free NN interaction can be regularized in the nuclear medium. Starting with a regularized interaction, the exact solution of the secular problem, in the

(infinite) Hilbert space built on the mean field orbits, is approximated in the large scale shell model calculations by the solution of the Schrödinger equation in the valence space, using an effective interaction such that:

$$H\Psi = E\Psi \longrightarrow \mathcal{H}_{eff.}\Psi_{eff.} = E\Psi_{eff.}$$

In general, effective operators have to be introduced to account for the restrictions of the Hilbert space

$$\langle\Psi|\mathcal{O}|\Psi\rangle = \langle\Psi_{eff.}|\mathcal{O}_{eff.}|\Psi_{eff.}\rangle$$

This effective interaction can be aimed to be used in mean field calculations along the periodic table and then it has to incorporate density dependent terms or for configuration mixing calculations, in this case its comes under the name of G-matrix . The main problem of the regularization procedures based on Brueckner theory is that they fail to reproduce the saturation point of nuclear matter (the Coester line problem). This is something to be recalled when using realistic G-matrices in large scale shell model calculations.

The use of a regularized interaction implies that what we are dealing with in a shell model description are quasiparticles in Landau's sense. This will show up in observables such as spectroscopic factors in (d, p) or $(e, e' p)$ reactions, Gamow-Teller strengths or partial shell occupancies as measured by electron scattering (the best know being the 3s1/2 orbit in lead isotopes). For a fully updated and accesible discussion of these points see ref. [5].

Once we adopt a regularized interaction that is compatible with the experimental mean field (magic numbers) we can proceed using the spherical mean field orbits as the basis for the occupation number space (Fock space). We have states i, j, k, ... with energies ϵ_i, ϵ_j, ϵ_k, ... that bunch in shells and give rise to magic numbers when the energy difference between them is large enough. The relevant operators create or annhilate a particle in a generic state "i" and second quantization formalism appears as the natural one.

A "formal" solution to the A-body problem can be sketched as follows:

- We start by choosing a single particle basis, $a_i^+ \ |0>$,
- then, we build the A-particle wavefunctions,
  $a_{i1}^+ \ldots a_{iA}^+ \ |0> = \mid \phi_\alpha >$
- in terms of which, the physical states are expressed as:
  $\mid \Phi > = \sum_\alpha \mathrm{C}_\alpha \mid \phi_\alpha >$
- The solution of the secular problem:
  $\mathrm{H} \mid \Phi > = \mathrm{E} \mid \Phi >$
- is then given by the eigenvalues and eigenvectors of the matrix:
  $< \phi_\alpha \mid \mathrm{H}_{eff} \mid \phi_{\alpha'} >$

What is called spherical shell model description is an approximation to this formal solution, using a finite number of many-particle states and requiring that the many-particle wavefunctions have the quantum numbers associated to the symmetries of the Hamiltonian

$$\Psi(J,T)^\pi(N,Z)$$

As an example, starting at a doubly magic nucleus, if we limit our Hilbert space to the particle hole excitations, the formal solution above corresponds to the Tamm-Damcoff approximation .

The spherical mean field provides a basis and a zeroth order view of the nuclear dynamics. The regularized two-body interaction governs the detailed behaviour of nuclei. For the mean field picture to have a sense, we expect that it will survive to the incorporation of the full interaction, at least in most of the cases, in other words, the separation between a block of orbits and the rest has to be valid even when the interaction is switched on. These constraints define the natural valence space (set of orbits) for a given class of nuclear properties. Let's be more precise on this point. For a given nucleus (N,Z) the mean field dictates which states are occupied (those below the Fermi level) and which are empty (those above). But other states can be close enough in energy or have a structure such that the residual two-body interaction can mix all of them and produce correlated states; deformed, superfluid or whatever. Therefore, the infinite set of mean field orbits will be divided in three parts:

Inert core ; the orbits that are forced to be always full. Imagine that the core consists of N_c neutrons and Z_c protons, thus if we are studying a nucleus (N,Z) there will remain n_v=N–N_c valence neutrons and z_v=Z–Z_c valence protons.
Valence space ; the orbits available to the valence particles, that will partially occupy them according to the dictates of the effective interaction.
External space ; the remaining orbits that are always empty.

It is the task of the theory to find the valence spaces that contain the relevant degrees of freedom for a given problem as demanded by the effective interaction. The safer valence spaces for shell model calculation are those comprised between magic closures. We shall examine several typical ones to see which properties they can accomodate and which not.

p-shell, [1p3/2,1p1/2]. Calculations in this valence space can describe the behaviour of nuclei with 2<N,Z<8 (only positive/negative parity states in even/odd nuclei).
sd-shell, [1d5/2,2s1/2,1d3/2]. Positive parity states of nuclei 8<N,Z<20.
pf-shell, [1f7/2,2p3/2,2p1/2,1f5/2]. Although this valence space would naturaly cover nuclei with 20<N,Z<40, the strong spin orbit term of the spherical mean field breaks the harmonic oscillator ordering and beyond N,Z=32 the orbit 1g9/2 has to be explicitely included.

It is evident that doubly magic nuclei and their neighbours play a central role in this description. At the same time, in these valence spaces, they are represented by a single Slater determinant and if we were aiming to a description of their excited sates, another valence space containing orbits from two major shells had to be chosen. As an example, the first and second excited states of ^{16}O, a 3^- (octupole vibration) and a 0^+ (head of a deformed rotational band) at around 6 MeV excitation energy can be described in the valence space [1p1/2,1d5/2,2s1/2]

[6]. When the valence space allows for excitations into different major oscillator shells, one has to pay attention to the appearance of spurious states of the center of mass, kind of very disturbing guests that may destroy the calculation if not under full control.

Far from stability or for heavy nuclei, the proton and neutron valence spaces may have no common orbits. For instance for the very neutron rich (N>20) Al, Si, P, S, Cl, and Ar isotopes, a reasonable valence space comprises the sd-shell for the protons and the pf-shell for the neutrons.

The rapid increase in the size of the basis limits the number of orbits that can be active. Notice that for a number of valence particles n_v, z_v the number of different Slater determinants that can be built in a given valence space goes as the product of the combinatorial numbers made with the degeneracy of the space and the number of active particles. This gives

$$\binom{6}{n_v}\cdot\binom{6}{z_v};\ \binom{12}{n_v}\cdot\binom{12}{z_v};\ \binom{20}{n_v}\cdot\binom{20}{z_v}$$

for the p, sd and pf shells respectively. Therefore there will always be properties excluded from the description, as for instance negative parity states in an sd-shell calculation. Giant resonances would demand at least two contiguous major shells in the valence space, which is usually out of reach. Only spin-like giant resonances –magnetic dipole and Gamow-Teller– are naturally contained in $0\hbar\omega$ valence spaces. Clustering phenomena can be tagged in simple shell model calculations but again the full spatial correlation will demand huge valence spaces.

A valence space can be adequate to describe some properties and completely wrong for others. In table 1 we exemplify this for the case of ^{48}Cr

Notice that for the quadrupole properties $1f_{\frac{7}{2}}2p_{\frac{3}{2}}$ is a rather good space whereas for magnetic and Gamow-Teller processes the inclusion of the spin orbit partners is needed in order to get reasonable results. In the tin isotopes the natural valence space consists in a ^{100}Sn core and valence orbits:

$$(\mathrm{d}_{\frac{5}{2}}\mathrm{g}_{\frac{7}{2}}s_{\frac{1}{2}}\mathrm{d}_{\frac{3}{2}}\mathrm{h}_{\frac{11}{2}})^{\nu}$$

However, numerous E1 transitions have been measured, that are forbidden in this space because of the absence of the $1g_{9/2}$ orbit, the only one that can

Table 1. Properties of ^{48}Cr in different valence spaces

^{48}Cr	$(f_{\frac{7}{2}})^8$	$(f_{\frac{7}{2}}p_{\frac{3}{2}})^8$	$(fp)^8$
Q(2^+) (e.fm^2)	0.0	-23.3	-23.8
E(2^+) (MeV)	0.63	0.44	0.80
E(4^+)/E(2^+)	1.94	2.52	2.26
BE2($2^+ \rightarrow 0^+$) (e^2.fm^4)	77	150	216
$\sum$B(GT)	0.90	0.95	3.88

produce an electric dipole vertex with the $1h_{11/2}$ orbit.

$$(a^{\dagger}_{11/2} \cdot \tilde{a}_{9/2})^{J=1}$$

Let's work out a simple example. We want to study the low energy spectrum of ^{12}C. We limit ourselves to positive parity states. The natural valence space is therefore the p-shell and we have an "alpha particle" core. The number of valence particles is four protons and four neutrons. The two orbits of the p-shell are 1p3/2 and 1p1/2. The interaction is defined by the single particle energies of these two orbits in A=5, that we can extract from experiment, and 15 two body matrix elements $< ij(JT)|V_{eff}|kl(JT) >$, where $ijkl$ may be any of the two orbits above. For instance if $i = j = k = l =$ 1p3/2, JT can take the values 01,10,21 and 30.

Let's focuss now in the 0^+ T=0 states of ^{12}C (these are the experimental quantum numbers of the ground state, but the same procedure holds for any other values of the total angular momentum and isospin). We can build such an state in five different ways corresponding to different particle distributions among the shells and different intermediate angular momentum and isospin couplings.

$(1p3/2)^8$ (J=0,T=0) $(1p1/2)^0$ (J=0,T=0)
$(1p3/2)^6$ (J=0,T=1) $(1p1/2)^2$ (J=0,T=1)
$(1p3/2)^6$ (J=1,T=0) $(1p1/2)^2$ (J=1,T=0)
$(1p3/2)^5$ (J=1/2,T=1/2) $(1p1/2)^3$ (J=1/2,T=1/2)
$(1p3/2)^4$ (J=0,T=0) $(1p1/2)^4$ (J=0,T=0)

After that we compute the matrix of the Hamiltonian in this basis (better if you have a code to do all the angular momentum algebra cfp's etc), diagonalize and obtain eigenvalues and eigenvectors. Once this done for all the JT pairs you can draw the theoretical level scheme. With the wave functions you can compute the diagonal matrix elements of one body operators that give magnetic moments and quadrupole moments or the off diagonals whose squares represent the electromagnetic (or weak) reduced transition probabilities. Occupation numbers, spectroscopic factors and many other observables can also be obtained.

We could have chosen to work in the uncoupled or m-scheme, in this case the symmetries of the hamiltonian are not explicit in the basis, that is composed of all the Slater determinants made from all the possible partitions of the valence particles among the valence orbits: $a^{\dagger}_i|0\rangle$

$$|\Phi_\alpha\rangle = \prod_{i=nljm\tau} a^{\dagger}_i|0\rangle = a^{\dagger}_{i1}...a^{\dagger}_{iA}|0\rangle$$

The physical states come out of the diagonalization of the Hamiltonian matrix:

$$\langle\Phi_\alpha|H_{eff.}|\Phi_{\alpha'}\rangle$$

The drawback of this scheme is that the size of the matrices is maximal: $\sim\binom{d_\pi}{p} \cdot \binom{d_\nu}{n}$ but the advantage is that the Hamiltonian matrix is sparse and its

elements are very easy to compute, mainly because we can represent a Slater determinant by a machine word, where each state is a bit (0 empty 1 occupied). For instance, in our ^{12}C example one of these Slater determinants could be the following:

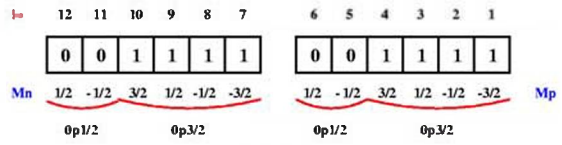

Fig. 2.

corresponding to: $a^\dagger_{10}a^\dagger_9a^\dagger_8a^\dagger_7\ b^\dagger_4b^\dagger_3b^\dagger_2b^\dagger_1\ |0\rangle$ (a and b refer to protons and neutrons).

In this example the Slater determinant is a 12 bits word, 12 being the total single particle degeneracy of the valence space. The action of the Hamiltonian on such an object is very simple, because the creation and annihilation operators are mapped into elementary bit operations.

As another example, the 0^+ states of ^{18}O, can be easily obtained using the USD interaction (which is described and listed in sec. 3.3). The basis is composed of the states $(d_{\frac{5}{2}})^2$, $(d_{\frac{3}{2}})^2$ and $(s_{\frac{1}{2}})^2$. Using the single particle energies and the two body matrix elements we can build the 3×3 secular matrix:

$$\begin{array}{ccc} (d_{\frac{5}{2}})^2 & (d_{\frac{3}{2}})^2 & (s_{\frac{1}{2}})^2 \\ \begin{pmatrix} -3.9478\times 2 & -3.1856 & -.13247 \\ +(-2.8197) & & \\ -3.1856 & 1.64658\times 2 & -1.0835 \\ & +(-2.1845) & \\ -1.3247 & -1.0835 & -3.1654\times 2 \\ & & +(-2.1246) \end{pmatrix} & \end{array}$$

Upon diagonalization, the eigenvalues, and the eigenvectors that give us the structure of the physical states in the coupled, uncorrelated basis, are obtained. The actual level scheme is: 0^+_1 (0.0 MeV), 0^+_2 (4.3 MeV), 0^+_3 (14.1MeV).

3 The interaction

We have said nothing yet about the precise effective interaction to be used in the calculation. One way to proceed, that has been frequently used, is to determine empiricaly the two body matrix elements from a fit to selected energy levels (and in some, rare, cases also to transitions). Another is to try to keep as close as possible to realistic G-matrices. However, in this approach, the empirical evidence is that some averages of matrix elements, actually those that are associated to extensive operators like the particle number or the isospin, are not well predicted by any G-matrix and have to be phenomenologically corrected. This kind of approach is dicussed in detail in [9] and will be the subject of subsection 3.3.

3.1 The interaction in second quantization

The hamiltonian can be written as:

$$\mathcal{H} = \sum_{k=1}^{A} T(k) + \sum_{k<l}^{A} W(k,l)$$

and in second quantization:

$$\mathcal{H} = \sum_{ij}^{A} \langle i|T|j\rangle a_i^\dagger a_j + \frac{1}{4}\sum_{ijkl}^{A} \langle ij|W|kl\rangle a_i^\dagger a_j^\dagger a_l a_k$$

If we define a core, the hamiltonian takes the form:

$$\mathcal{H} = \sum_{i}^{A} \epsilon_i a_i^\dagger a_j + \frac{1}{4}\sum_{ijkl}^{A} \langle ij|V|kl\rangle a_i^\dagger a_j^\dagger a_l a_k$$

where the ϵ_i's are the single particle energies relative to the core.

From this expresion we can transform to the JT-coupled scheme writing the two-body part as:

$$V = \frac{1}{4}\sum_{j_1 j_2 j_3 j_4}\sum_{m_1 m_2 m_3 m_4} \langle j_1 m_1 j_2 m_2|V|j_3 m_3 j_4 m_4\rangle \times a^\dagger_{j_1 m_1} a^\dagger_{j_2 m_2} a_{j_4 m_4} a_{j_3 m_3}$$

Introducing the operator: $\tilde{a}_{jm} = (-1)^{j+m}\ a_{j-m}$ and defining the coupling of tensors as:

$$[a^\dagger_{j_1} a^\dagger_{j_2}]^J_M = \sum_{m1m2} \langle j_1 m_1 j_2 m_2|JM\rangle a^\dagger_{j_1 m_1} a^\dagger_{j_2 m_2}$$

we obtain:

$$V = -\tfrac{1}{4}\sum_{j_1 j_2 j_3 j_4 JT} \langle j_1 j_2|V|j_3 j_4\rangle^{JT} \times \sqrt{(2J+1)(2T+1)(1+\delta_{j_1 j_2})(1+\delta_{j_3 j_4})} \times \left[[a^\dagger_{j_1} a^\dagger_{j_2}]^{JT} \times [\tilde{a}_{j_3}\tilde{a}_{j_4}]^{JT}\right]^{00}$$

3.2 Which effective interaction?

As we mentioned before, different approaches are possible to determine the effective interaction, or equivalently the set of matrix elements:

$$\langle (j_1 j_2)_{JT}|V|(j_3 j_4)_{JT}\rangle$$

Historically the first was the empirical one in which the matrix elements are fitted to a set of experimental data. The eigenenergies of the problem can be

expressed as linear combinations of the two body matrix elements and single particle energies (that we note generically by v_k).

$$E^i_{calc.} = \sum_{k=1}^{p} c^{(i)}_k v_k,$$

Thus the problem is that of minimizing the function

$$Q^2 = \sum_{i=1}^{N} (E^i_{calc.} - E^i_{exp.})^2$$

$$\frac{\partial Q^2}{\partial v_r} = 0 = \frac{\partial}{\partial v_r} \left(\sum_{i=1}^{N} ((\sum_{k=1}^{p} c^{(i)}_k v_k) - E^i_{exp.})^2 \right), \quad \text{for } r = 1, ..., p$$

$$\sum_{i=1}^{N} ((\sum_{k=1}^{p} c^{(i)}_k v_k) - E^i_{exp.})) c^{(i)}_r = 0, \quad \text{from there we get}$$

$$\sum_{i=1}^{N} ((\sum_{k=1}^{p} c^{(i)}_k v_k) - E^i_{exp.}) = \sum_{i=1}^{N} c^{(i)}_r E^i_{exp.}$$

i.e. a set of p linear equations with p parameters which is solved under the assumption that the wave functions do not change ($c^{(i)}_k$ fixed). An iterative procedure is then carried on until convergency. Examples of this approach are the interactions of Cohen and Kurath for the *p*-shell [7] and the interaction USD of Wildenthal for the *sd*-shell, that we list below [8].

The other option is to deduce the effective nucleon-nucleon interaction from the bare NN interaction. This is the aim of the theory of effective interactions. Unfortunately such a project has many difficulties. Not the least is the impossibility of getting the good saturation properties of nuclear matter without recurring to three body forces. In nuclear spectroscopy we detect also the defects of the G-matrices, but as we will see in what follows, we are now able to confine them to some combinations of matrix elements whose physical interpretation is clear as well as its relationship with the saturation issues.

An example of this is gathered in table 2, where we can observe that all the G-matrices available, fail in producing the expected shell closures at N=28. (We have listed those from Kuo and Brown [11], Kahana, Lee and Scott [12] and a set of calculations by the Oslo group using different Bonn potentials [13]. Why, will be explained in the next subsection.

3.3 The structure of the hamiltonian

From the work of M. Dufour and A. Zuker, [10] we know that any effective interaction can be split in two parts: $\mathcal{H} = \mathcal{H}_m(\text{monopole}) + \mathcal{H}_M(\text{multipole})$. $\mathcal{H}_m$ contains all the terms that are affected by a spherical Hartree-Fock variation, hence responsible of the global saturation properties and of the evolution of the spherical single particle field. This important property can be written as:

$$\langle CS \pm 1 | \mathcal{H} | CS \pm 1 \rangle = \langle CS \pm 1 | \mathcal{H}_m | CS \pm 1 \rangle$$

```
  USD INT. (SD SHELL)
   3
203 205 1001
1.64658     -3.9478        -3.16354    *** DEP. DENSITE EN (A/18)**(-0.3)


   0  203  203  203  203    0    3
     .0000   -1.4151     .0000   -2.8842
   -2.1845     .0000    -.0665     .0000
   0  205  203  203  203    1    3
     .5647     .0000    2.0337
     .0000    -.6149     .0000
   0  205  203  205  203    1    4
   -6.5058   -3.8253    -.5377   -4.5062
    1.0334    -.3248     .5894   -1.4497
   0  205  203 1001  203    1    2
   -1.7080     .2832
     .1874    -.5247
   0  205  203 1001 1001    1    1
    2.1042
     .0000
   0  205  205  203  203    0    3
     .0000     .7221     .0000    1.8949
   -3.1856     .0000   -1.6221     .0000
   0  205  205  205  203    1    4
    2.5435     .0000    2.2216     .0000
     .0000    -.2828     .0000   -1.2363
   0  205  205  205  205    0    5
     .0000   -1.6321     .0000   -1.5012     .0000   -4.2256
   -2.8197     .0000   -1.0020     .0000    -.1641     .0000
   0  205  205 1001  203    1    2
   -1.1026     .0000
     .0000    -.6198
   0  205  205 1001  205    2    3
     .0000   -1.2420
    -.8616     .0000
   0  205  205 1001 1001    0    1
     .0000   -1.1756
   -1.3247     .0000
   0 1001  203  203  203    1    2
     .3983     .0000
     .0000    -.5154
   0 1001  203 1001  203    1    2
   -4.2930   -1.8194
     .6066    -.4064
   0 1001  205  203  203    2    3
     .0000     .1887
    -.4041     .0000
   0 1001  205  205  203    2    3
     .0968    1.2032
    -.4770     .6741
   0 1001  205 1001  203    2    2
    2.0664
   -1.9410
   0 1001  205 1001  205    2    3
   -1.4474   -3.8598
    -.8183     .7626
   0 1001 1001  203  203    0    1
     .0000     .0275
   -1.0835     .0000
   0 1001 1001 1001  203    1    1
    1.2501
     .0000
   0 1001 1001 1001 1001    0    1
     .0000   -3.2628
   -2.1246     .0000
```

Table 2. Excitation energy of the 2_1^+ in doubly magic ^{48}Ca and ^{56}Ni

	Expt.	KB	KLS	Bonn A	Bonn B	Bonn C
^{48}Ca	3.83	1.80	1.60	1.23	1.30	1.41
$\langle((f_{7/2})^8\|\Psi_{GS}\rangle$		0.468	0.381	0.214	0.345	0.437
^{56}Ni	2.70	0.39	0.31	0.43	0.42	0.42
$\langle((f_{7/2})^{16}\|\Psi_{GS}\rangle$		0.04	0.015	0.018	0.011	0.019
$\langle n_{3/2}\rangle$		4.5	5.2	5.7	5.2	5.0

where CS means closed shell. For all the realistic G-matrices, $\mathcal{H}_M$ is close to right whereas $\mathcal{H}_m$ is definitely wrong. Hence, the monopole part of the G-matrices has to be empirically corrected to reproduce the structure of the "simple" nuclei CS and CS plus or minus one nucleon.

3.4 The monopole hamiltonian

The explicit form of $\mathcal{H}_m$ is :

$$H_m = H_{sp} + \sum \left[\frac{1}{(1+\delta_{ij})} a_{ij}\, n_i (n_j - \delta_{ij}) + \frac{1}{2} b_{ij} \left(T_i \cdot T_j - \frac{3n_i}{4} \delta_{ij} \right) \right].$$

H_{sp} is the term containing the single particle energies. The coefficients a and b are defined in terms of the centroids:

$$V_{ij}^{T} = \frac{\sum_J V_{ijij}^{JT}[J]}{\sum_J [J]}$$

as: $a_{ij} = \frac{1}{4}(3V_{ij}^{1} + V_{ij}^{0})$, $b_{ij} = V_{ij}^{1} - V_{ij}^{0}$, the sums run over Pauli allowed values.

We have discussed in the preceding section the bad behaviour of the monopole part of the G-matrices in the ^{56}Ni case. Let's now explain the reasons. The monopole energy of the closed shell is given by:

$$\mathrm{E}_{CS} = 16\epsilon_f + \frac{16 * 15}{2}.\mathrm{V}_{ff}$$

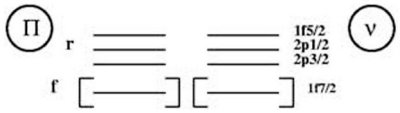

Whereas the monopole energy of the 4p-4h configuration reads:

$$\mathrm{E}_{4p4h} = 12\epsilon_f + 4\epsilon_r + 66\mathrm{V}_{ff} + 48\mathrm{V}_{fr} + 6\mathrm{V}_{rr}$$

The difference between both is given by:

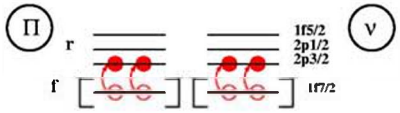

$$\Delta\mathrm{E} = 4(\epsilon_f - \epsilon_r) + 48(\mathrm{V}_{ff} - \mathrm{V}_{fr}) + 6(\mathrm{V}_{ff} - V_{rr})$$

Therefore, even small defects in the centroids can produce large changes in the relative position of these configurations due to the appearance of quadratic terms

involving the number of particles in the different orbits. This is what actually happens in the cases shown in table 2. The average interaction between the 1f7/2 orbit and the rest of the shell, as given by the G-matrices is systematically too attractive, locating the p-h configurations too low. This, combined with the larger correlation energy of the open shell configurations, compared with the closed shells, can destroy the shell closures as spectacularly as to make ^{56}Ni a perfect rotor.

3.5 The multipole hamiltonian

$\mathcal{H}_M$ can be written in two representations , particle-particle and particle-hole:

$$\mathcal{H}_M = \sum_{r\leq s,t\leq u,\Gamma} W^{\Gamma}_{rstu} Z^{+}_{rs\Gamma} \cdot Z_{tu\Gamma},$$

$$\mathcal{H}_M = \sum_{rstu\Gamma} [\gamma]^{1/2} \frac{(1+\delta_{rs})^{1/2}(1+\delta_{tu})^{1/2}}{4} \omega^{\gamma}_{rtsu} (S^{\gamma}_{rt} S^{\gamma}_{su})^0,$$

where Z^{+}_{Γ} (Z_{Γ}) is the coupled product of two creation (annihilation) operators and S^{γ} is the coupled product of one creation and one annihilation operator. The W and ω matrix elements are related by a Racah transformation:

$$\omega^{\gamma}_{rtsu} = \sum_{\Gamma} (-)^{s+t-\gamma-\Gamma} \begin{Bmatrix} r & s & \Gamma \\ u & t & \gamma \end{Bmatrix} W^{\Gamma}_{rstu} [\Gamma],$$

$$W^{\Gamma}_{rstu} = \sum_{\gamma} (-)^{s+t-\gamma-\Gamma} \begin{Bmatrix} r & s & \Gamma \\ u & t & \gamma \end{Bmatrix} \omega^{\gamma}_{rtsu} [\gamma].$$

In the preceding expressions we can replace pairs of indeces by a single one $rs \equiv x$, $tu \equiv y$, $rt \equiv a$ et $su \equiv b$, and diagonalise the matrices W^{Γ}_{xy} and $f^{\gamma}_{ab} = \omega^{\gamma}_{ab} \sqrt{(1+\delta_{rs})(1+\delta_{tu})}/4$, by unitary transformations $U^{\Gamma}_{xk}, u^{\gamma}_{ak}$:

$$U^{-1} W U = E \Longrightarrow W^{\Gamma}_{xy} = \sum_k U^{\Gamma}_{xk} U^{\Gamma}_{yk} E^{\Gamma}_k$$

$$u^{-1} f u = e \Longrightarrow f^{\gamma}_{ab} = \sum_k u^{\gamma}_{ak} u^{\gamma}_{bk} e^{\gamma}_k,$$

then

$$\mathcal{H}_M = \sum_{k,\Gamma} E^{\Gamma}_k \sum_x U^{\Gamma}_{xk} Z^{+}_{x\Gamma} \cdot \sum_y U^{\Gamma}_{yk} Z_{y\Gamma},$$

$$\mathcal{H}_M = \sum_{k,\gamma} e^{\gamma}_k \left(\sum_a u^{\gamma}_{ak} S^{\gamma}_a \sum_b u^{\gamma}_{bk} S^{\gamma}_b\right)^0 [\gamma]^{1/2},$$

that are called representations E and e.

In figure 3, we show the eigenvalue distribution of the particle-hole channel for two shells; pf and sdg. There are only a few coherent terms, and they have the expected quantum numbers; isoscalar quadrupole, octupole and hexadecapole, and isoscalar and isovector dipole (plus the center of mass term). Besides, if one analyze the structure of these terms, it turns out that they have very simple forms like $r^{\lambda} Y_{\lambda}$ or σ and $\sigma \cdot \tau$.

What is even more important is what happens if we remove these coherent states from the multipole hamiltonian and go back to the particle particle

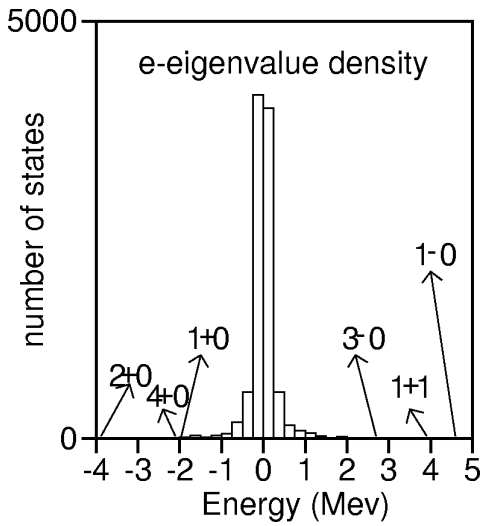

Fig. 3. e-eigenvalue density for the KLS interaction in the pf+sdg major shells. The largest ones are shown by arrows.

representation. This is presented in fig. 4. What remains is a symmetric distribution of eigenstates centered at zero which corresponds to the random part of the hamiltonian, plus three particle-particle coherent terms that are readily identified with the isoscalar and isovector monopole pairing plus the isoscalar quadrupole pairing. The rewarding aspect of this decomposition is that, not only the multipole hamiltonian can be reduced to a few terms, besides, these terms are simple and universal in a double sense; they are nearly equal for all different effective interactions and their mass dependence is well understood. In table 3, the comparison is made between the coherent terms and several schematic interactions that show the extent of the agreement between them.

Finally, we have gathered in table 4 the coherent terms of the two most popular effective interactions used in the pf-shell. The first, KB3 is just the G-matrix calculated by Kuo and Brown, the second, fpd6, [15] was obtained by a potential fit to the experimental excitation energies of a set of nuclei, the third is a newcomer, because we have naively taken the density dependent force of Gogny [16] and computed its two body matrix elements, using the wave functions obtained in a spherical Hartree-Fock calculation with the same force. The agreement is surprising, in view of the very different origins of the three interactions. This analysis makes it possible to detect the differences between them, in particular fpd6 turns out to be about ten percent stronger than KB3 at the begining of the shell. Notice also that the pairing content of the Gogny force, isovector and isoscalar, is fairly close to that of the other two, more specifically shell model, interactions. Therefore, its proton neutron pairing properties are bound to be close to correct.

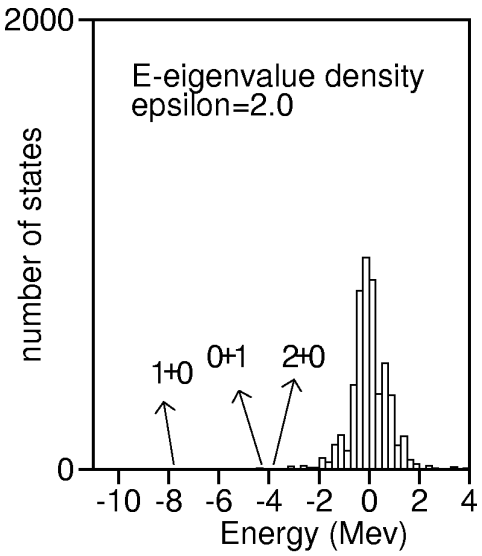

Fig. 4. E-eigenvalue density for the KLS interaction in the pf+sdg major shells $\hbar\omega = 9$, after removal of the five largest contributions in the particle-hole channel. The largest ones are shown by arrows.

Table 3. The structure of he coherent terms of the multipole hamiltonian

γ	e_1^γ	e_2^γ	e_{1+2}^γ	M	$\langle u_1 \vert M\rangle$	$\langle u_2 \vert M\rangle$	$\langle u_1 \vert u_1'\rangle$	$\langle u_2 \vert u_2'\rangle$	α^2
11	1.77	2.01	3.90	$\sigma\tau$	.992	.994	.999	1.000	.94
20	-1.97	-2.14	-3.88	r^2Y_2	.996	.997	1.000	1.000	.95
10	-1.02	-0.97	-1.96	σ	.880	.863	.997	.994	1.04
21	-0.75	-0.85	-1.60	$r^2Y_2\tau$	.991	.998	.999	.997	.94
40	-1.12	-1.24	-2.11	r^4Y_4					

Γ	E_1^Γ	E_2^Γ	E_{1+2}^Γ	P	$\langle U_1 \vert P\rangle$	$\langle U_2 \vert P\rangle$	$\langle U_1 \vert U_1'\rangle$	$\langle U_2 \vert U_2'\rangle$	α^2
01	-2.95	-2.65	-5.51	P_{01}	.992	.998	1.000	.994	1.048
10	-4.59	-4.78	-10.12	P_{10}	.928	.910	.998	.997	.991

4 The solution of the secular problem

In large scale shell model calculations the strategy to build and diagonalize the secular matrix is a major issue. First one has to decide in which coupling scheme to work. The simplest one is the so called $m-scheme$, whose basis is formed by all the Slater determinants contained in the valence space. It has the advantage of eliminating all Racah algebra, cfps, etc. The inconvenient is that the full dimension of the basis has to be carried on. The other choice is to implement "a priori" the symmetries of the Hamiltonian in the construction of the many

Table 4. Leading terms of the multipole hamiltonian

Interaction	particle-particle		particle-hole		
	JT=01	JT=10	$\lambda\tau$=20	$\lambda\tau$=40	$\lambda\tau$=11
KB3	-4.75	-4.46	-2.79	-1.39	+2.46
FPD6	-5.06	-5.08	-3.11	-1.67	+3.17
GOGNY	-4.07	-5.74	-3.23	-1.77	+2.46

particle basis. The full matrix is then divided in blocks and for each ensemble of values of the pertinent quantum numbers the dimensions are smaller. This approach is called "coupled scheme" . Its drawback is that it lacks the computational simplicity of the m-scheme. Usually only the exact quantum numbers JT are explicitely taken into account, however, approximate symmetries can be implemented as well, for instance seniority, that make truncation procedures much more efficient.

In order to obtain the relevant eigenvalues and eigenvectors two routes are available, either to build the full matrix and proceed by direct diagonalization or to use other methods as Lanczos' to obtain a part of the spectrum. For very large matrices the direct diagonalization approach is excluded due to computer size limitations, so we will concentrate in the Lanczos method . Let's mention however one of the first modern shell model codes, the Rochester Oak-Rigde MULTISHELL, a coupled, direct diagonalization code, based on the formalism of J. B. French [17]. Most of the present expertise in m-scheme Lanczos shell model codes has its roots in the Glasgow code made by Whitehead and collaborators [18]. New codes are at present available as the DUPSM (coupled), the Tokyo VECSSE (m-scheme) and the Strasbourg codes ANTOINE and NATHAN [19] that have, for the time being, the lead in dimensions and speed.

The Lanczos algorithm consist in the construction of an orthonormal basis by orthogonalization of the states $\mathcal{H}^n|\mathbf{1}\rangle$, obtained by the repeated action of the hamiltonian $\mathcal{H}$, on a basis state $|\mathbf{1}\rangle$ called pivot. From this procedure results a tridiagonal matrix. In the first step we write:

$$\mathcal{H}|\mathbf{1}\rangle = E_{11}|\mathbf{1}\rangle + E_{12}|\mathbf{2}\rangle$$

where E_{11} is just $\langle\mathbf{1}|\mathcal{H}|\mathbf{1}\rangle = \langle\mathcal{H}\rangle$, the mean value of $\mathcal{H}$. E_{12} is obtained by normalization :

$$E_{12}|\mathbf{2}\rangle = \mathcal{H}|\mathbf{1}\rangle - E_{11}|\mathbf{1}\rangle = (\mathcal{H} - E_{11})|\mathbf{1}\rangle$$

In the second step:

$$\mathcal{H}|\mathbf{2}\rangle = E_{21}|\mathbf{1}\rangle + E_{22}|\mathbf{2}\rangle + E_{23}|\mathbf{3}\rangle$$

The hermiticity of $\mathcal{H}$ implies $E_{21} = E_{12}$. E_{22} is just $\langle\mathbf{2}|\mathcal{H}|\mathbf{2}\rangle$ and E_{23} is obtained by normalization :

$$E_{23}|\mathbf{3}\rangle = (\mathcal{H} - E_{22})|\mathbf{2}\rangle - E_{21}|\mathbf{1}\rangle$$

In the row N, the following relations hold:

$$\mathcal{H}|\mathbf{N}\rangle = E_{NN-1}|\mathbf{N}-\mathbf{1}\rangle + E_{NN}|\mathbf{N}\rangle + E_{NN+1}|\mathbf{N}+\mathbf{1}\rangle$$

with $E_{NN-1} = E_{N-1N}$, $E_{NN} = \langle \mathbf{N}|\mathcal{H}|\mathbf{N}\rangle$ and $E_{NN+1}|\mathbf{N}+\mathbf{1}\rangle = (\mathcal{H} - E_{NN})|\mathbf{N}\rangle$ - $E_{NN-1}|\mathbf{N}-\mathbf{1}\rangle$

Using this procedure a tridiagonal matrix is explicitely built:

$$\langle I|\mathcal{H}|J\rangle = \langle J|\mathcal{H}|I\rangle = 0 \quad \text{if } |I-J| > 1$$

$$\begin{pmatrix} E_{11} & E_{12} & 0 & 0 & 0 & 0 \\ E_{12} & E_{22} & E_{23} & 0 & 0 & 0 \\ 0 & E_{32} & E_{33} & E_{34} & 0 & 0 \\ 0 & 0 & E_{43} & E_{44} & E_{45} & 0 \\ & & & & & \\ & & & & & \end{pmatrix}$$

The Lanczos iteration process has variational properties and the convergence for the lowest (and highest) eigenvalues is very efficient.

4.1 Lanczos strength functions

Furthermore, the Lanczos method can be used to compute global properties of the spectra, even if approximate, via the calculation of strength distributions. The idea, due to Whitehead [20] is very simple. Suppose the ground state $|G>$ of a given nucleus has been obtained by the conventional Lanczos method. Let Ω^λ denote the multipole operator we are interested in. Acting with Ω^λ on $|G>$ we obtain the sum rule state (or the doorway). It is not a physical state if H do not commute with the multipole operator, but its norm is the sum rule or equivalently the total strength of the multipole operator in the ground state of the nucleus. Lets call its normalized version $|\Lambda>$ and develop it in energy eigenstates as:

$$|\Lambda> = \frac{1}{N}\sum_E S(E)|E>$$

where

$$N^2 = \sum_E S^2(E)$$

and $S^2(E)$ is the strength function . The equality

$$<\Lambda|\mathrm{H^n}|\Lambda> = \frac{1}{\mathrm{N^2}}\sum_{\mathbf{E}} \mathrm{S^2(E)E^n}$$

shows that, taking $|\Lambda>$ as the pivot, each Lanzos iteration brings in the expectation value of two new powers of H on $|\Lambda>$, therefore after N iterations we have 2N moments of the strength function $S^2(E)$. Diagonalizing the Lanczos matrix after N iterations, the overlaps of the eigenvectors with $|\Lambda>$ give an approximation to $S^2(E)$ which has the same lowest 2N moments. In other words, one starts with a single peak that contains all the strength located at the centroid. Iteration after iteration it goes on fragmenting until the number

of iterations equals the dimension of the basis. However, for a relatively small number of iterations we should have already a very good understanding of the global behaviour of the strength.

Figs. 5 and 6 are a very clear, cartoon-like, example of how the fragmentation of a doorway state takes place as a result of the interaction. This process, as we have shown, do not modify the moments already fixed by the preceding iterations. Actually, if we smooth the spikes with gaussians having the experimental width, the shape of the resonance can be already obtained with a limited number of iterations, as it is seen in fig. 7.

4.2 Other approaches

The problem of the size of the shell model spaces has motivated other –approximate– ways of solving the secular problem. The first one is the Shell Model Monte Carlo method , (see ref. [21] for a complete review) that treats the problem statistically introducing a partition function $e^{\beta H}$ where β is the inverse of the temperature. The problem involving two body propagation is amenable to a superposition of one body propagations by using the Hubbard-Stratonovich transformation. The multidimensional integrals are then evaluated by Monte Carlo sampling. The advantage of the method is that, as the problem remains

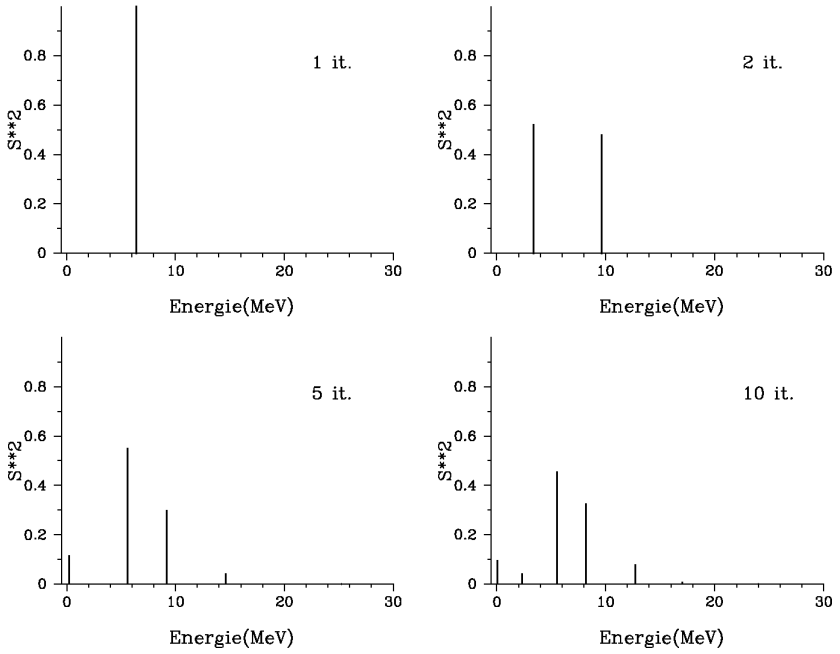

Fig. 5. Evolution of the Strength function with the number of iterations

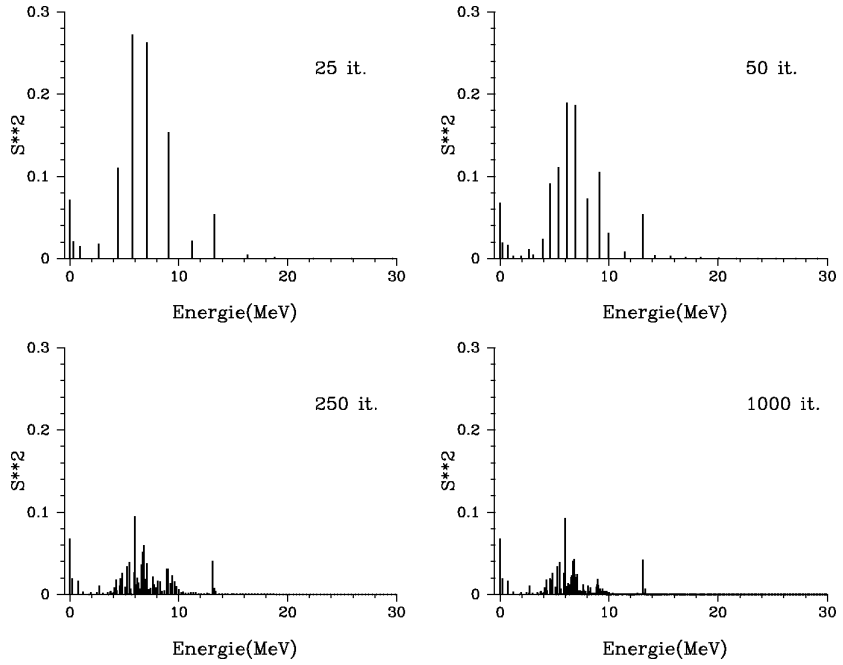

Fig. 6. Evolution of the Strength function with the number of iterations

essentially that of one body dynamics, the dimensions of the basis are tractable. However the method demands many different extrapolations; first in temperature (T→0), and then in some parameters added to the interaction in order to overcome the sign problem of the realistic interactions. It suffers also of limitations in the treatment of excited states because the cooling selects naturally the ground state. One final remark is that the method is very well suited to study finite temperature properties with the caveat, common to every shell model approach, that beyond some excitation energy the valence space will run out of states and the description will be unphysical.

Recently the same type of approach using the partition functions and the Monte Carlo evaluation of the multidimensional integrals, has been applied in a quite different way in ref. [22]. These techniques are now used to sample the Hilbert space searching for an optimal, hopefully small, basis in which to diagonalize the full hamiltonian (Quantum Monte Carlo Diagonalization Method) . The starting basis vectors are mean field solutions that break the symmetries, therefore projections have to be enforced and the method ressembles to the GCM used since long in other contexts. On the other side, the fact that only states giving a certain energy gain upon inclusion are retained, results in an energy based truncation, that can be dangerous, if not dealt with care, in cases where there is no well defined intrinsic states to start with.

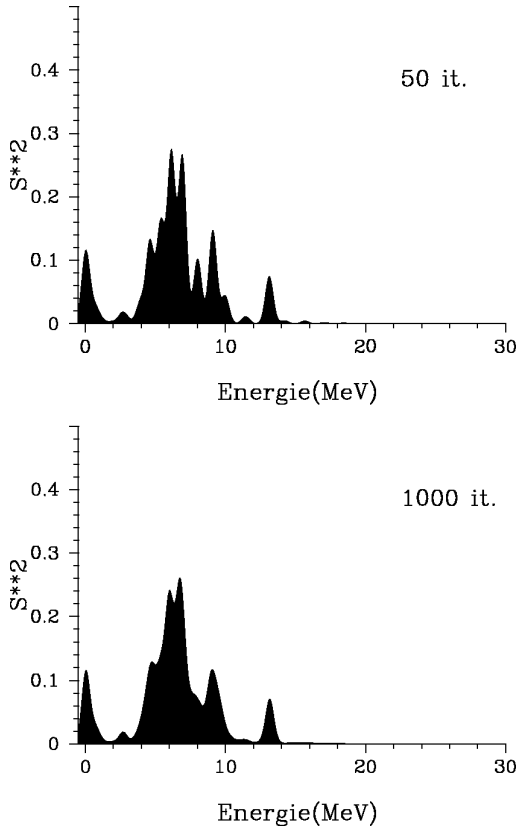

Fig. 7. Strength function convoluted with the experimental width

5 Miscellaneous applications

In the last years it has been possible to tackle the shell model description of nuclei in large valence spaces as for instance the full pf shell, using the m-scheme code ANTOINE written by E. Caurier and a realistic effective interaction (KB3) obtained from the Kuo-Brown G-matrix [11] with the necessary monopole corrections [23] in line with what we have already discussed. There is a large amount of results that explain beautifully the experimental data (and in some case predict or even correct others), these can be found in refs. [24–28]. Far from stability, we have used a valence space consisting of the pf shell for neutrons and the sd shell for protons [29]. Here we shall only address a couple of problems relevant to the modern shell model descriptions.

5.1 Quenching of spin operators in the nucleus

This is a long lasting topic, that has been extensively studied for many years. The fact that both beta decay studies and charge exchange reactions in the appropriate kinematics, give experimental Gamow Teller strengths that are systematically smaller than the theoretical predictions, has generated a lot of debate on the role of non-nucleonic degrees of freedom versus short range nuclear correlations in the renormalization of spin operators in nuclei. Full *sd*-shell calculations [30] had already established the constancy of the quenching factor, with a value q=0.77. With the advent of full pf shell calculations and using the Lanczos strength function technique we have been able to extend these calculations to higher masses.

In figure 8 we have collected the Gamow-Teller matrix elements of many individual β decays for A=41 to 52. Comparing with experiment an effective value for the weak axial constant g_A(eff)=0.74 g_A(bare) is found. This result is consistent with the value extracted from similar comparisons in the p and sd shells and point to an asymptotic value of the renormalization of 0.7 [26].

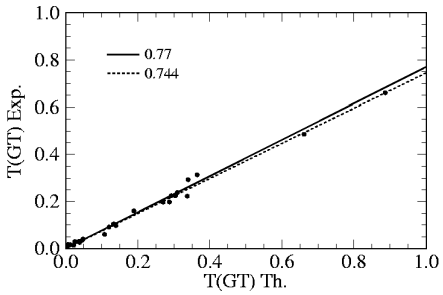

Fig. 8. Quenching of GT strength in the pf-shell

In figure 9 we have applied the Lanczos strength function method to the case of the Gamow Teller strength function of ^{48}Ca. We went to 700 iterations (the number of 1^+ T=3 states in ^{48}Sc being 8590) and smoothed the peaks with gaussians of the experimental width to compare with the results of (p, n) experiments. In first place, this illustrates the ability of the shell model approach to describe resonances in large valence spaces. The quantitative agreement is obtained using the same quenching factor that we had extracted from the comparison of individual decays. The spreading of the experimental strength compared with the calculated one in the high energy region, is due to the mixing with configurations outside the space. In ref. [28] we submit that the quenching is of nuclear origin and related to the similar one found in the spectroscopic factors.

We have extended this comparison to the M1 strength obtained in (e, e') experiments. In order to make a meaninful comparison, the calculation must be able to reproduce correctly the strength function in the energy span of the experiment as well as to indicate the relative importance of the spin and orbital

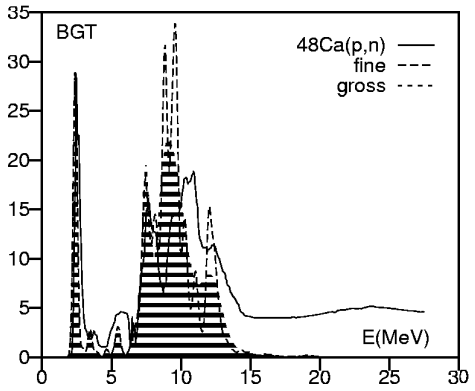

Fig. 9. ^{48}Ca (p,n) ^{48}Sc cross section compared with the calculated Gamow Teller strength function using the Lanczos method

strengths. In fig. 10 we make the comparison for the case of ^{52}Cr. Notice the very detailed agreement between experiment and theory. Based on this and similar comparisons for the remaining N=28 isotones, a quenching factor of 0.75(2) for the spin strength could be extracted, fully consistent with the Gamow-Teller results and supportive of the nuclear origin of the effect [31].

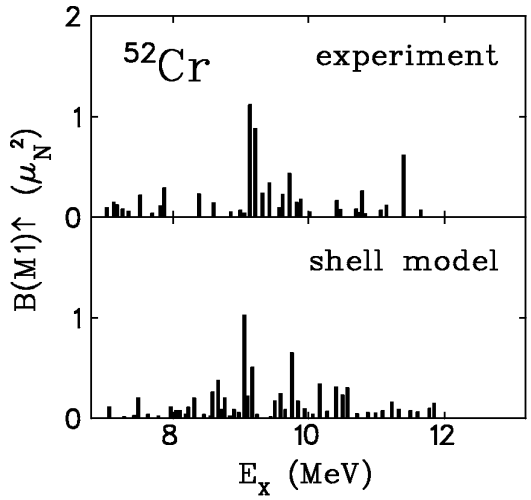

Fig. 10. M1 strength in ^{52}Cr, experiments vs. full pf-shell results

5.2 Shell model description of deformation and superdeformation

The shell model description of nuclei gives results of extreme spectroscopic quality, provided a good valence space and a good effective interaction are used. We are therefore in solid grounds to address the topic of the collective behaviour in nuclei. We shall proceed to examine the following key questions: How can we describe rotational motion within the spherical shell model, beyond the *sd*-cases to which Elliott's SU3 is applicable? How do we to get information about the intrinsic state from the shell model wavefunctions? How compares the (spherical) shell model description with the (deformed) mean field ones?

Some of these questions may sound rhetorical, but nonetheless their proper answers do not belong yet to the nuclear physics "common knowledge".

The *pf*-shell mass region is a very good place to study these aspects because full $0\hbar\omega$ calculations are still feasible and the mass and the number of active particles in the valence space make the link with heavy deformed nuclei much easier than in the very light cases. That, provided deformation shows up. But this is actually the case, as it is seen in figure 11 where the experimental level scheme of ^{48}Cr [32] is compared with the shell model calculation [33].

Notice the rotor-like spectrum up to J=10 and the backbending at J=12, reminiscent of the behaviour of heavier rotors. The E2 transition probabilities are fully collective and follow the Bohr-Mottelson prescription for a rotor in the strong coupling limit with a deformation β=0.3 (see table 5 for the experimental data [34]). Therefore, considering the nearly perfect agreement between experiment and theory in fig. 11 and in table 5, we consider that ^{48}Cr is good candidate for a rotor amenable to a spherical shell model description. We want to be more precise in our definition of a rotor and for that we shall rely in three indicators; i) the yrast band follows approximately a J(J+1) law, ii) the intrinsic quadrupole moment extracted from the B(E2) transition probabilities is constant for the different yrast states, ii) the intrinsic quadrupole moment extracted from the spectroscopic quadrupole moment is also constant for the yrast states and equal to the one extracted from the B(E2). The connexion between intrinsic and laboratory frame is made by the formulae [35]:

$$Q_0 = \frac{(J+1)\,(2J+3)}{3K^2-J(J+1)}\,Q_{spec}(J), \quad \text{for } K \neq 1$$
$$B(E2, J \;\rightarrow\; J-2) = \frac{5}{16\pi}\,e^2|\langle JK20|J-2,K\rangle|^2\,Q_0^2.$$

(for $K \neq \frac{1}{2}, 1$)

For even-even nuclei this is about as far as we can go in deciding whether we are faced with a good rotor or not. When a particle is added or removed, the collective model description of its coupling to the rotor leads to some very precise predictions that make the comparison with microscopic calculations more stringent in particular in what concerns magnetic properties. This analysis has been carried out in ref. [25] and we will not discuss it here.

Table 5 contains the information we were after, as given by the calculations (we use effective charges 1.5 for protons and 0.5 for neutrons). We have listed the B(E2) values, and the intrinsic quadrupole moments extracted from those,

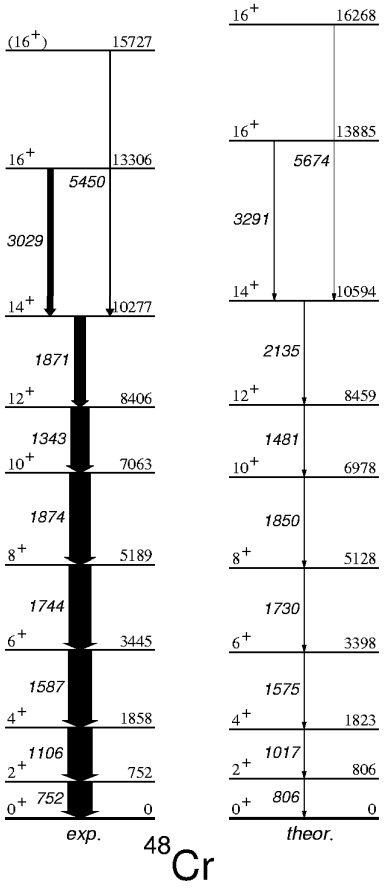

Fig. 11. ^{48}Cr level scheme; experiment *vs.* theory

Q_0(B(E2)), or from the spectroscopic quadrupole moments, $Q_0(Q_{spec})$. The requirements stated above are fulfilled up to the backbending , therefore we can conclude that ^{48}Cr is a good rotor up to J=10 where the backbending takes place. The intrinsic quadrupole moment that we obtain corresponds to a deformation β=0.3 as we had anticipated. Notice that all the quadrupole properties of the full pf-shell calculation are reproduced (and even enhanced) if we reduce the valence space to the lowest two orbits, 1f7/2 and 2p3/2 (fp space). These results are shown in the last column of the table and give us the first hint on the minimal valence spaces that can accomodate deformed nuclei. The yrast band

Table 5. ^{48}Cr; quadrupole properties of the yrast band

J	$B(E2)_{exp}$	$B(E2)_{th}$	$Q_0(B(E2))$	$Q_0(Q_{spec})$	Q_0[1f7/2, 2p3/2]
2	321(41)	228	107	103	104
4	330(100)	312	105	108	104
6	300(80)	311	100	99	103
8	220(60)	285	93	93	102
10	185(40)	201	77	52	98
12	170(25)	146	65	12	80
14	100(16)	115	55	13	50
16	37(6)	60	40	15	40

in the reduced space follows also the J(J+1) law although with a moment of inertia much larger than the experimental one. This behaviour propted us to study the origin of the rotations in cases when the spin orbit splitting is large. We found out that there is an approximate symmetry, that we call Quasi-SU3, operating in the subset of aligned orbits of a major harmonic oscillator shell, which is responsible for the onset of deformation [36].

Once the existence of a well behaved rotor is established, we can examine what happens if particles or holes are added to it. It has been shown in [25] that the mirror pairs ^{47}V-^{47}Cr and ^{49}Cr-^{49}Mn closely follow the semiclassical picture of a particle/hole strongly coupled to a rotor. When more particles or holes are added, the collective behaviour starts disappearing, nevertheles even for ^{52}Fe (the largest detailed spectroscopic calculation ever made) a rotor like band appears at low spin and an yrast trap at $J=12^+$, both are accounted for in the shell model calculation [37]. Another exemple is ^{50}Cr that was predicted to be a double backbender in [38], prediction confirmed in a subsequent experiment [39] (see figure 12).

Very recently a higly deformed excited band has been discovered in ^{56}Ni [40] having a four particle four holes structure. The band head is located at about 5 MeV excitation energy and its deformation is close to β=0.4. All these features are reproduced by an –almost– full pf-shell calculation. It turns out that the 4p-4h structure that dominates this band is the one that causes the breakdown of the N=28 shell closure in the calculations using uncorrected G-matrices.

We had also the oportunity to compare the spherical shell model results with the deformed mean field ones, more precisely with the Cranked Hartree Fock Bogolyuvov calculations using the Gogny force [33]. The results for the yrast band are presented in figure 13 .

At first glance one could conclude that the CHFB model is doing a rather poor job in view of the discrepancies. However a closer look tell us that in fact most experimental trends are there, except for a too large moment of inertia. Due to that the CHFB E_γ's are systematically smaller than the experimental ones. But, from our discussion of the results in the reduced fp space, we are aware of the fact that the quadrupole properties may be right and the moment

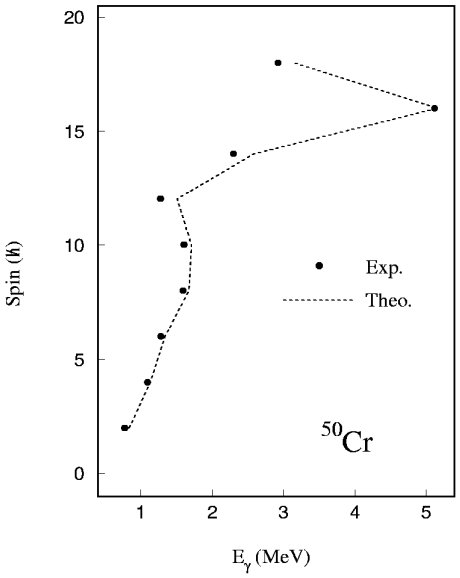

Fig. 12. Backbending in ^{50}Cr

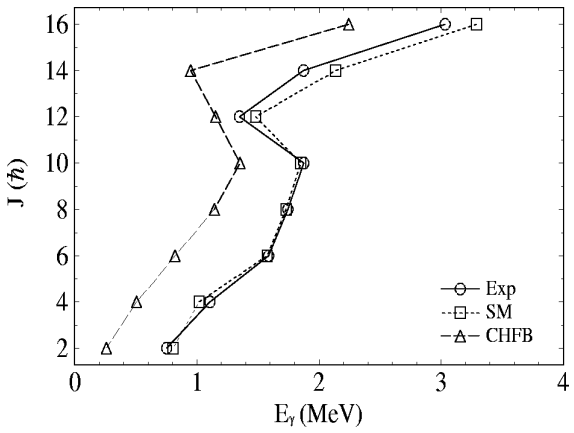

Fig. 13. ^{48}Cr, spin vs. rotational frecuency (E$_\gamma$). Experiment compared with the CHFB and the SM results.

of inertia wrong. We know also that the decoupling of the quadrupole moment and the moment of inertia is a characteristic feature of the SU3 model of Elliott . Hence, we go on with the comparison and in figure 14 we show the CHFB results for the intrinsic deformation parameters β and γ. We see that up to the backbending the nucleus is axially deformed with a deformation close to 0.3 that decreases slowly with J (0.2 at J=10) in full agreement with the shell model results. Beyond the backbending the deformation continues to decrease and there are some excursions into triaxiallity that are difficult to recast in collective terms. A very nice feature of the CHFB calculation is that it makes it possible to separate the contributions to the quadrupole moment coming from the core and from the valence orbits. The result, independent of J, is that both blocks contribute evenly, which is consistent with the effective charges we use in the shell model calculation.

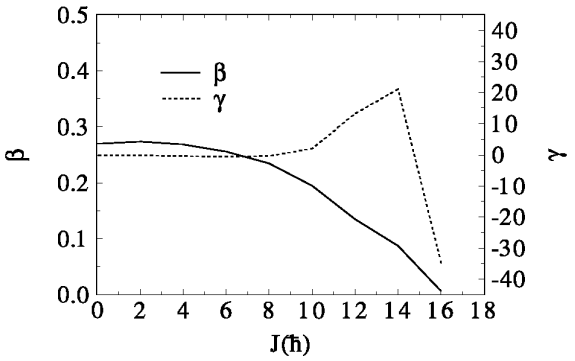

Fig. 14. Deformation parameters β and γ as a function of J in the CHFB calculation

Pairing *vs* quadrupole has been one of the classical themes in nuclear physics since the beginning of nuclear structure studies. The advent of high spin physics and improven spectroscopic data in heavy N≈Z nuclei has brought up again an old question; how does pairing evolve with angular momentum? and then a new one; which is the role of proton neutron pairing close to N=Z? We shall examine these issues in what follows. To start with, we take as the pairing T=0 and T=1 hamiltonians those extracted in ref. [10] from the realistic G-matrices (in this reference the analytical expressions –eq. 2.6– and the numeric values of the two body matrix elements –table I– can be found). We keep their notation and call P^{01} and P^{10} the isovector and isoscalar L=0 pairing hamiltonians. In order to evaluate the effect of pairing, we substract each pairing hamiltonian from the full interaction, given by KB3, we repeat the calculations and extract the pairing contributions by comparison of both sets of results.

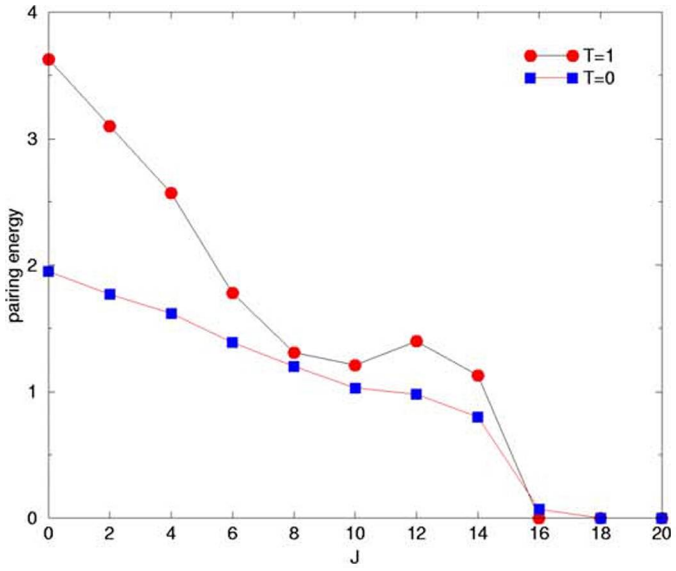

Cr48 Yrast band

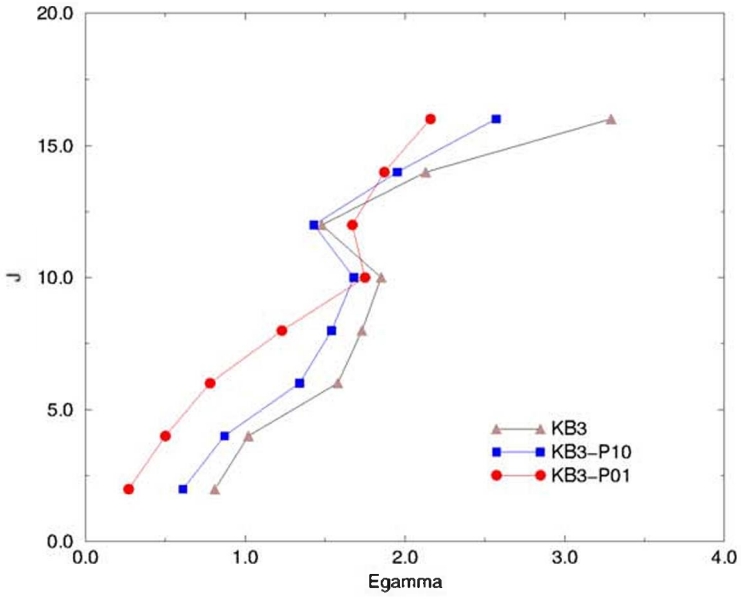

Fig. 15. The effect of T=1 and T=0 pairing in the yrast band of ^{48}Cr

We shall present results only for yrast band of ^{48}Cr. In figure 15 the pairing energy is plotted against the spin. Up to the backbending , both the T=1 and T=0 contributons decrease with J. The T=1 contribution is larger but has a much steeper slope. A plateau appears at around J=12 and then pairing goes to zero. When these results are plotted as spin versus rotational frecuency (see fig. 15) it is clearly seen that the effect is basically a change in the static moment of inertia. Therefore we can safely conclude that the defaults of the CHFB calculation are associated to the absence of proton neutron pairing in the HFB approach.

In order to settle this point, we have used the matrix element of the Gogny force, discussed in section 3.5 in a full pf-shell calculation. The results are plotted in fig. 16. It is clearly seen that the shell model calculation with the Gogny force now gives a much better moment of inertia than the CHFB with the same force. The backbending is located at the right place as well. Hence, it is demonstrated that the limitations of the HFB method in dealing with the proton-neutron pairing, that are more acute in N=Z nuclei, are the true responsible for the failures of the mean field description and not the effective interaction.

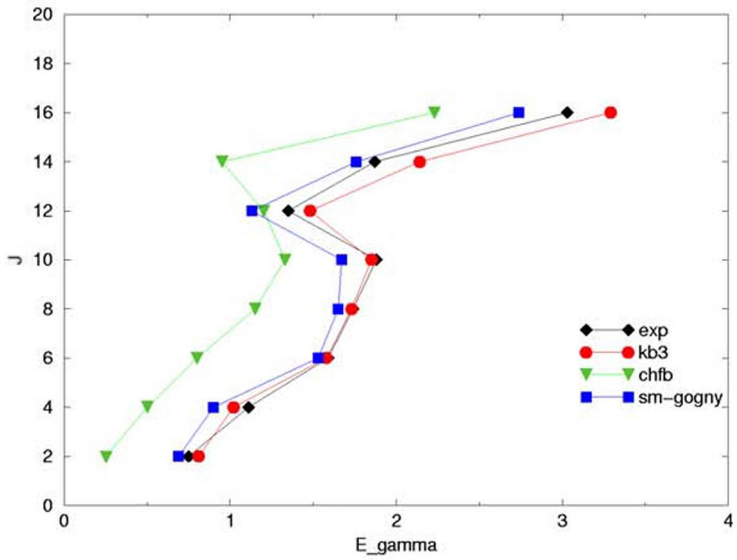

Fig. 16. The yrast band of ^{48}Cr; SM with the Gogny force

Another interesting result is that for the states below the backbending –i.e. for those that can be viewed as proceeding of the same intrinsic, well deformed state– the wave functions with or without pairing have the same quadrupole behaviour. To be more precise, their B(E2)'s and quadrupole moments are equal within a few percent and their overlaps are always better than 95%. This

means that pairing does not affect the quadrupole properties that have somehow reached saturation in the deformed regime [41].

While we have shown abundantly the capacity of large scale shell model calculations to describe well deformed nuclei, the possibility of encompassing also superdeformation seemed remote. We had advanced qualitative arguments on which should be the valence spaces necessary to produce superdeformation in ref [36]. The argument was that in favorable situations, n-particle n-hole excitations on a spherical or normally deformed stated could take advantage of a mean field geometry that enhances the quadrupole correlations. In heavy nuclei the normal deformed structures were associated to 8p-8h configurations when the particles occupy a set of Quasi-SU3 orbits while the holes sit in a Pseudo-SU3 set. However, this situation can also happen in light nuclei at the end of the *sd*-shell, where the particles excited to the pf shell follow Quasi-SU3 and the holes in the *sd*-shell, Pseudo-SU3. And, indeed, in a very recent experiment, such a superdeformed band has been found in ^{36}Ar. A shell model calculation in the combined $sd-pf$ valence space, that reproduces nicely the experimental results (see fig. 17), suggest a deformation β=0.55 and a dominant 4p-4h structure on the top of the ground state of ^{36}Ar.

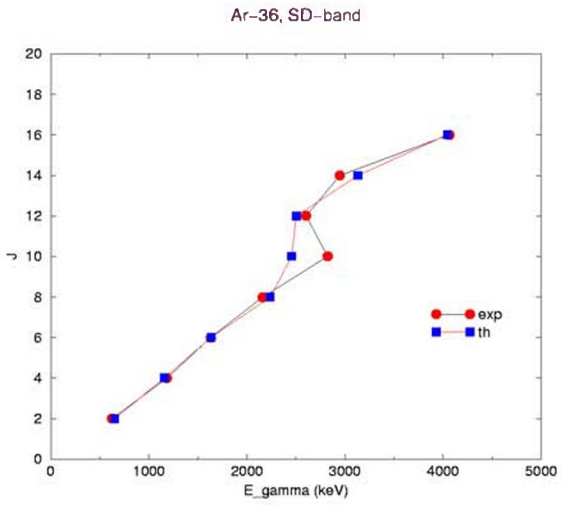

Fig. 17. The superdeformed band of ^{36}Ar, experiment vs. SM

6 Conclusions

The spherical shell model provides a description of the nuclear dynamics that makes it possible to keep a connexion with the basic initial ingredients of the problem, i.e. nucleons selfbound in vacuum by its mutual –non relativistic, two

body– interaction. In the route from the bare nucleon-nucleon to the prediction of the level scheme or decay properties of a particular nucleus, we have to pay many tolls; first, the bare interaction has to be regularized, and then, due to saturation problems, its monopole part fitted to the properties of the closed shells and closed shells +/− one nucleon. However, the separation of the effective interaction in monopole and multipole parts, and the realization that the multipole part of the realistic interactions is correct, paves the way to obtain an universal interaction for the shell model. Secondly, the valence spaces that contain the necessary degrees of freedom for a satisfactory description of the nuclear properties become exceedingly large for medium-heavy nucleus. Nevertheless, complete diagonalizations in the pf-shell, that have become recently available thanks to the impressive algorithmic advances of E. Caurier's codes, provide a realistic microcosmos in which many of the features of the heavier nuclei show up. In particular, collective deformed nuclei can be perfectly accounted for by the spherical shell model. Furthermore, sound indications on the symmetries or coupling schemes that will underlie the description of heavier nuclei are obtained, in the form of Elliott's SU3 variants. This approach has also proven to be able to encompass in the same framework the behaviour of nuclei far from stability, in spite of the increase of difficulty due to the lesser available experimental information on the effective spherical mean field in very neutron (or proton) rich nuclei.

Acknowledgments

We thank our colleagues E. Caurier, G. Martinez-Pinedo and A. Zuker for the free use we have made of their results in these notes. A.P. thanks the DGICyT for financial support (grant PB96-053).

References

1. J. P. Elliott: Proc. Royal Soc. London **A245**, 128 and 562 (1958)
2. P. J. Brussaard and P. W. M. Glaudemans: "Shell Model Applications in Nuclear Spectroscopy" North Holland 1997
   K. Heyde: "The Nuclear Shell Model" Springer 1994
   J.B. French: in *International school of physics Enrico Fermi*, Course XXXVI, C. Bloch ed. (Academic Press, New York, 1966)
   I. Talmi: "Simple models of complex nuclei", Harwood Academic publishers 1993
   A. P. Zuker: in "Contemporary Nuclear Shell Models" Lecture Notes in Physics, vol 482, p. 93. X. W. Pan *et al.* eds. Springer 1997
   A. Poves: "Le modèle en couches, Ecole Internationale Joliot-Curie" 1997
3. B.A. Brown and B.H. Wildenthal: Annu. Rev. Nucl. Part. Sci. **38**, 29 (1988)
4. M. G. Mayer: Phys. Rev. **75**, 1969 (1949), O. Haxel et al. Phys. Rev. **75**, 1766 (1949)
5. V. R. Pandharipande, I. Sick and P. K. A. deWitt Huberts: Rev. Mod. Phys. **69**, 981 (1997)
6. A. P. Zuker, B. Buck and J. B. McGrory: Phys. Rev. Lett. **21**, 39 (1968)
7. S. Cohen and D. Kurath: Nucl. Phys. **73**, 1 (1965)
8. B.H. Wildenthal: Prog. Part. Nucl. Phys. **11**, 5 (1984)

9. A. Abzouzi, E. Caurier and A. P. Zuker: Phys. Rev. Lett. **66**, 1134 (1991)
10. M. Dufour and A.P. Zuker: Phys. Rev. **C54**, 1641 (1996)
11. T. T. S. Kuo and G. E. Brown: Nucl. Phys. **A114**, 235 (1968)
12. S. Kahana, H.C. Lee and C.K. Scott: Phys. Rev. **180**, 956 (1969); Phys. Rev. **185**, 1378 (1969)
13. M. Hjort-Jensen, T. T. Kuo and E. Osnes: Phys. Rep. **261**, 125 (1995)
14. K.K. Mon and J.B. French: Ann. Phys. (NY) **95**, 90 (1975)
15. W. A. Richter, M. G. van der Merwe, R. E. Julies and B. A. Brown: Nucl. Phys. **A527** 325 (1990)
16. D. Gogny: Nucl. Phys. **A237** 399 (1975)
17. J. B. French et al.: Adv. Nucl. Phys. **3**, 193 (1969)
18. R. R. Whitehead: et al.: Adv. Nucl. Phys. **9**, 123 (1977)
19. E. Caurier: code ANTOINE, Strasbourg 1989; E. Caurier and F. Nowacki: code NATHAN, Strasbourg 1995; T. Sebe and T. Otsuka: code VECSSE, Tokyo 1994; A. Novoselsky and M. Valieres: code DUPSM, Drexel 1997
20. R. R. Whitehead: in "Moment methods in many fermion systems", edited by B. J. Dalton et al. (Plenum, New York, 1980)
21. S. E. Koonin, D. J. Dean and K. Langanke: Phys. Reports **278**, 2 (1997)
22. M. Honma, T. Mizusaki and T. Otsuka: Phys. Rev. Lett. **77**, 3315 (1996)
23. A. Poves and A. P. Zuker: Phys. Rep. **70**, 235 (1981)
24. E. Caurier, A. P. Zuker, A. Poves, and G. Martínez-Pinedo: Phys. Rev. **C50**, 225 (1994)
25. G. Martínez-Pinedo, A. P. Zuker, A. Poves and E. Caurier: Phys. Rev. **C55**, 187 (1997)
26. G. Martínez-Pinedo, A. Poves, E. Caurier and A. P. Zuker: Phys. Rev. **C53**, R2602 (1996)
27. E. Caurier, G. Martínez-Pinedo, A. Poves and A. P. Zuker: Phys. Rev. **C52**, R1736 (1995)
28. E. Caurier, A. Poves and A. P. Zuker: Phys. Rev. Lett. **74**, 1517 (1995)
29. J. Retamosa et al.: Phys. Rev. **C55**, 1266 (1997); E. Caurier et al.: Phys. Rev. **C58**, 2033 (1998)
30. B. A. Brown and B. H. Wildenthal: Nucl. Phys. **A474**, 290 (1987)
31. P. von Neumann-Cosel, A. Poves, J. Retamosa and A. Richter: Phys. Lett. **B443**, 1 (1998)
32. S. Lenzi et al.: Z. Phys. **A354**, 117 (1996)
33. E. Caurier, J. L. Egido, G. Martínez-Pinedo, A. Poves, J. Retamosa, L. M. Robledo and A. P. Zuker: Phys. Rev. Lett. **75**, 2466 (1995)
34. F. Brandolini et al: Heavy Ion Physics **5** (1997)
35. A. Bohr and B. Mottelson: "Nuclear Structure" vol I (Benjamin, Reading, 1964)
36. A. Zuker, J. Retamosa, A. Poves and E. Caurier: Phys. Rev. **C52**, R1742 (1995)
37. C. A. Ur et al: Phys. Rev. **C58**, 3163 (1998)
38. G. Martínez-Pinedo, A. Poves, L. M. Robledo, E. Caurier, F. Nowacki, and A. P. Zuker: Phys. Rev. **C54**, R2150 (1996)
39. S. Lenzi et al. Phys. Rev. **C56**, 1313 (1997)
40. D. Rudolf et al.: Phys. Rev. Lett. **82** 3763 (1999)
41. A. Poves and G. Martínez-Pinedo: Phys. Lett. **B420**, 203 (1998)
42. C. Svensson et al.: Phys. Rev. Lett. (in press)

The nuclear collective motion

Witold Nazarewicz

[1] Department of Physics, University of Tennessee, Knoxville, Tennessee 37996
[2] Physics Division, Oak Ridge National Laboratory, Oak Ridge, Tennessee 37831
[3] Institute of Theoretical Physics, University of Warsaw,
ul. Hoża 69, PL-00-681 Warsaw, Poland

Abstract. Current developments in nuclear structure are discussed from a theoretical perspective. First, the progress in theoretical modeling of nuclei is reviewed. This is followed by the discussion of nuclear time scales, nuclear collective modes, and nuclear deformations. Some perspectives on nuclear structure research far from stability are given. Finally, interdisciplinary aspects of the nuclear many-body problem are outlined.

1 Introduction

The atomic nucleus is a fascinating many-body system bound by strong interaction. The building blocks of a nucleus – protons and neutrons – are themselves composite aggregations of quarks and gluons governed by quantum chromodynamics (QCD) – the fundamental theory of strong interaction. Nuclei are exceedingly difficult to describe; they contain too many nucleons to allow for an exact treatment and far too few to disregard finite-size effects. Figure 1 shows the main challenges in our quest for understanding the nucleus. Studies at relativistic energies probe the domain of QCD; they reveal the nature of quark and gluon dynamics. Studies at lower energies probe the structure and dynamics of nuclei. The bridges illustrate major physics questions pertaining to the nucleus: the nature of hadrons, the understanding of the bare nucleon-nucleon interaction in terms of the quark-gluon dynamics, and the understanding of the effective interactions in heavy nuclei in terms of the bare force.

In this talk, I intend to review – rather briefly – a number of issues relevant to the nuclear many-body problem. Firstly, Sec. 3 covers the enormous progress that has happened in theoretical nuclear structure during recent years. (For a general overview of nuclear science, the reader is encouraged to study the recent report [2].) Some spectacular examples of the nuclear collective motion are presented in Sec. 4. The concept of nuclear deformation, i.e., anisotropic nuclear mean field, is one of the most useful and important building blocks of the unified model. In Sec. 5, several different views on the microscopic origin of nuclear deformation are presented. The common denominator is the interplay between the symmetry-breaking particle-vibration interaction and the symmetry-restoring pairing force.

One of the frontiers of today's nuclear science is the "journey to the limits" of atomic charge and nuclear mass, of neutron-to-proton ratio (see Sec. 7). The tour to the limits is not only a quest for new, exciting phenomena, but the new data are expected, as well, to bring qualitatively new information about the

J.M. Arias and M. Lozano (Eds.): LNP 581, pp. 102–140, 2001.
© Springer-Verlag Berlin Heidelberg 2001

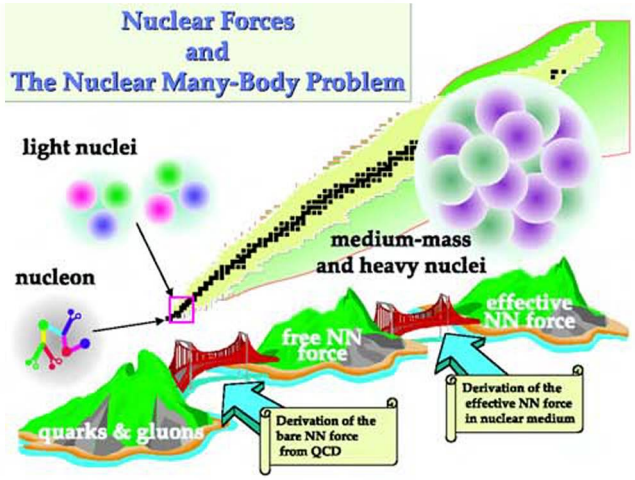

Fig. 1. From the QCD vacuum to heavy nuclei: the intellectual connection between the hadronic many-body problem (quark-gluon description of a nucleon) and the nucleonic many-body problem (nucleus as a system of Z protons and N neutrons). From Ref. [1].

fundamental properties of the nucleonic many-body system, the nature of the nuclear interaction, and nucleonic correlations at various energy-distance scales.

Section 8 discusses interdisciplinary aspects of the nuclear many-body problem, and Sec. 9 contains conclusions of these lectures.

2 The territory

The nuclear landscape, the territory of nuclear structure, is shown in the top portion of Fig. 2. Moving away from the valley stable nuclei by adding either protons or neutrons, one enters nuclear "terra incognita" which is bordered by the particle drip lines where the nuclear binding ends. The nuclei beyond the drip lines are unbound to nucleon emission. Examples of such systems are proton emitters – narrow resonances beyond the proton drip line which exist due to the confining effect of the Coulomb barrier [3]. An exciting question is whether there can possibly exist *islands* of stability beyond the neutron drip line. One such island is, of course, a neutron star which exists due to gravitation. So far, calculations for light neutron drops have not produced permanent binding [4,5]. However, it has been suggested recently [6] that areas of stability can appear in heavier nuclei as a result of shape coexistence/isomerism.

The vast territory of nucleonic matter is shown in Figure 3 which illustrates various domains of nuclear matter. The range of neutron excess, $(N-Z)/A$, in finite nuclei is from about –0.2 (proton drip line) to 0.5 (neutron drip line). The new-generation radioactive beam facilities will provide a unique capability for

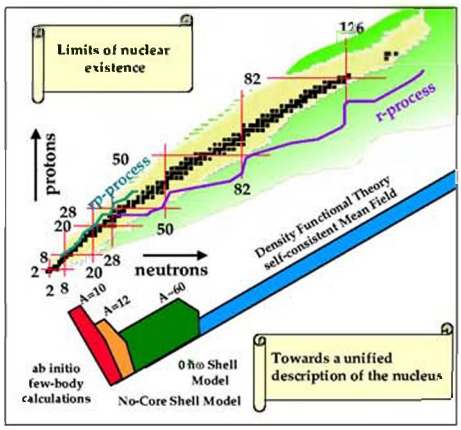

Fig. 2. Top: Nuclear landscape. Bottom: Various theoretical approaches to the nuclear many-body problem.

accessing the very asymmetric nuclear matter and for compressing neutron-rich matter approaching density regimes important for supernova and neutron star physics.

3 The nuclear many-body problem: towards the unified description of the nucleus

The common theme for the field of nuclear structure is that of the nucleon-nucleon (NN) interaction which clusters nucleons together into one composite system. Figures 1 and 2 illustrate, schematically, our main strategy in the quest for understanding the nucleus in the context of the hadronic and nucleonic many-body problem.

The free NN force can be viewed as a residual interaction of the underlying quark-gluon dynamics of QCD, similar to the intermolecular forces that stem from QED. The low-energy interaction between nucleons has a complicated spin-isospin dependence dictated by the hadron's substructure. One of the main challenges of nuclear science, indicated by the first bridge in Fig. 1, is the derivation of a nucleon-nucleon (NN) interaction from the underlying quark-gluon dynamics of QCD. Experimentally, the NN force can be studied by means of NN scattering experiments. Examples of phenomenological parameterizations based on the NN scattering data are the Bonn [8,9], Nijmegen, Reid [10], Paris [11], and Argonne [12] potentials. While the long-range part of these free (but still effective!) NN forces is well described by one-pion exchange, their short-range behavior is purely phenomenological. Here the quark-gluon degrees of freedom must be considered explicitly. (It is believed that the short-range

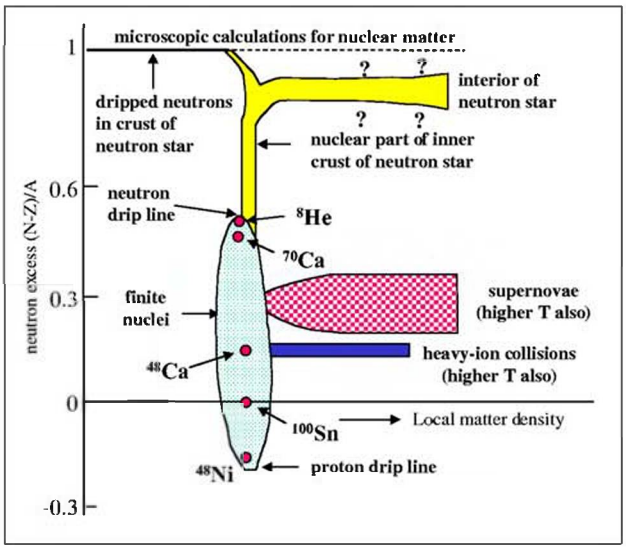

Fig. 3. Diagram illustrating the range of densities and neutron excess of importance in various contexts. (Based on Ref. [7].)

part can be well accounted for by a simple one-gluon exchange potential and the Pauli principle [13,14].)

How to tackle the problem of A strongly interacting nucleons? The general theoretical strategy is illustrated in Fig. 4. The starting point is, of course, the exact solution of the A-body Schrödinger equation (or relativistic field equations) with the bare NN force. Today, such *ab initio* calculations can be performed for very light nuclei, but still it is a very difficult task. Firstly, the corresponding dimensions are huge. Secondly, the bare NN force is very complicated (e.g., it contains tensor terms and, often, non-local terms) and the form of higher-order interactions, such as a three-body force (NNN), is not well known.

The state of the art is marked by the ab initio Green's Function Monte Carlo (GFMC) calculations [15] which have recently reached A=10. Figure 5 shows the results of GFMC calculations by the Argonne-Los Alamos-Urbana collaboration of the excitation spectrum of A=4-9 nuclei using the GFMC method. The variational Monte Carlo calculations with a free NN force have been carried out for relatively heavy systems such as ^{16}O [17]. Another ab initio method, which is currently undergoing a renaissance is the coupled-cluster [or "exp(S)"] method [18–20] (see Refs. [21–23] for recent applications). In the parallel development [24,25], ab initio calculations describing the scattering of few-body systems have brought new insights into the nature of the three-nucleon force.

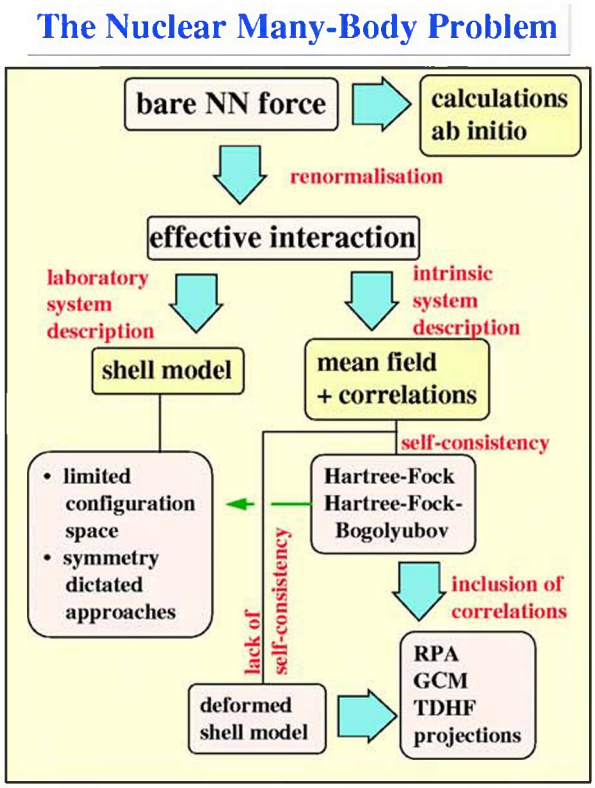

Fig. 4. The nuclear many body problem – various theoretical strategies.

While the very light nuclei can nowadays be described as A-body systems bound by a free NN force augmented by a NNN force, the conceptual framework of larger nuclei is still that of the independent particle model . Here, the basic assumption is that the nucleons are moving almost independently in a mean potential obtained by averaging out the interactions between a single nucleon and all remaining A–1 protons and neutrons. This picture is only a first approximation; it is modified by the presence of the residual interaction between the nucleons. The "effective" NN interaction in the heavy nucleus, used to determine the mean potential, differs considerably from the free NN force. In principle, it should be obtained by means of the complicated Brückner renormalization procedure which corrects the free NN interaction for the effects due to the nuclear medium [26–28]. (In practice, however, effective forces are often determined by a fit to experimental data, or by extracting interaction matrix elements from the data.) This challenging task is represented by the second bridge in Fig. 1. Many features of the effective interaction such as short range; strong dependence

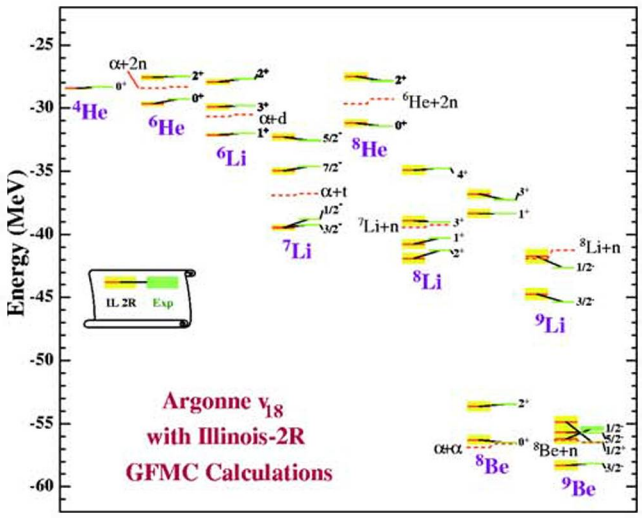

Fig. 5. GFMC calculations of excitation spectra of A=4-9 nuclei using Argonne v_{18} NN force and Illinois-2R NNN force. (From Ref. [16].)

on spins, isospins, and relative momenta of interacting nucleons; and the reduction of mass in the nuclear interior have been extracted from experimental data. Having determined the effective force, the two most commonly used strategies, represented by a forking in Fig. 4, are (i) that of the nuclear shell model and (ii) the mean-field strategy.

In the nuclear shell model , the effective two-body Hamiltonian is diagonalized in the limited configuration space. Here, the practical limitation is the size of the Hilbert space considered. Often, the realistic shell-model Hamiltonian can be further approximated by replacing it with a Hamiltonian which can be diagonalized exactly using group theoretical techniques [29–33]. The wave function of the nuclear shell model is an eigenstate of fundamental symmetry operators; it has good parity, angular momentum, and isospin. From this point of view, it is a *laboratory system* wave function.

The recently developed no-core shell model , employing the effective interaction calculated (in the large configuration space) from the NN force, has reached ^{12}C. Figure 6 shows the result of the no-core shell-model calculations [34] for positive and negative-parity states of ^{12}C. In a parallel development, Bloch-Horowitz equations have been solved for very light systems [35], and an effort has been under way [36] to marry the numerical methods of the shell model with the tools of effective theory [37] to generate effective interactions and effective operators. (In this approach the hard-core contribution is summed to all orders analytically.)

There has been substantial progress in the area of the traditional shell model [38]. In 1971, Whitehead and Watt [39] succeeded in performing shell-model cal-

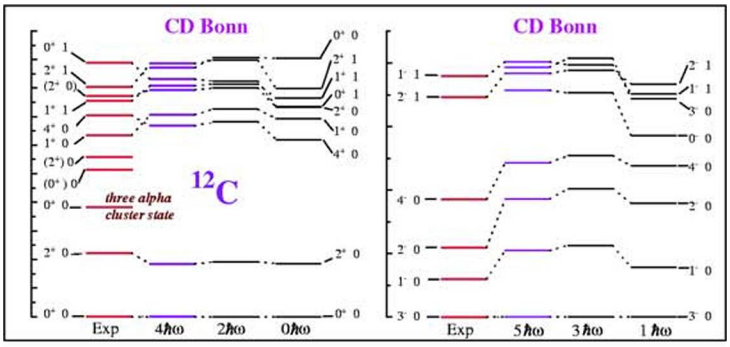

Fig. 6. No-core shell-model calculations of the excitation spectrum of ^{12}C using the CD Bonn NN interaction. (From Ref. [34].)

culations for ^{24}Mg in the full *sd* shell (with the dimension of the model space approaching 30,000). Today, this can be done in a few seconds on a modern workstation. Traditional shell-model techniques make it possible to approach the collective nuclei from the *pf* shell; the calculations involve model spaces with dimensions of several millions. However, progress in this area is going to be very slow due to exploding dimensions when increasing the number of valence nucleons [40,41] (see Fig. 7). In spite of this, the conventional shell-model calcu-

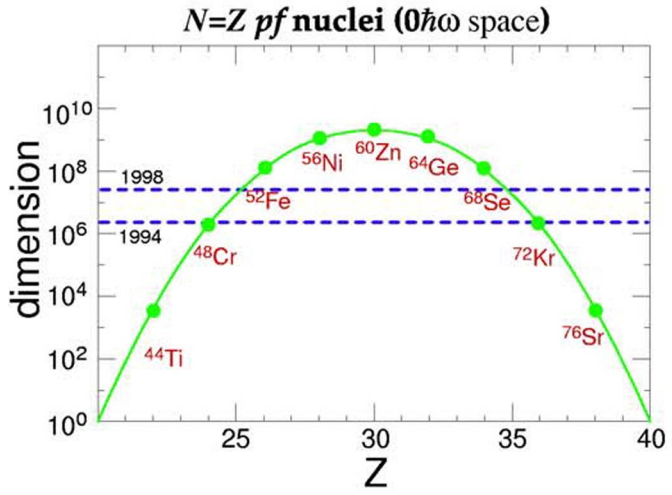

Fig. 7. Dimension of the shell-model configuration space for even-even N=Z ($20 \leq Z \leq 40$) nuclei. It is assumed that the shell-model calculations are performed in the full *pf* shell in the M scheme (here M=0) (courtesy of T. Otsuka).

lations employing realistic NN interactions [42,43] are becoming more and more efficient in handling large configuration spaces. The state-of-the-art shell-model studies of Gamow-Teller distributions of A=45-65 nuclei [44], electron capture and beta-decay rates in the pf nuclei [45], spectroscopic studies of A=50-52 isobaric chains [46], and of quadrupole and magnetic moments of the Fe isotopes [47] set the new standard in this area, although future progress is strongly limited by present-day computer resources.

One actively pursued alternative is to truncate the configuration space by applying the projected self-consistent quasiparticle basis [48,49]. Another family of novel shell-model techniques is based on the Monte Carlo method [50]. Applications of the Monte Carlo shell model have been remarkably successful in describing many structural properties of medium-mass and heavy nuclei [51–54] where the dimensions of the model space reach 10^{20}. The approach adopted by the Tokyo group [53,54] is a mixture of the projected shell model and the Monte Carlo shell model. It was applied to studies of deformed structures in the doubly-magic nucleus ^{56}Ni.

That the conventional shell model fails at short distances, due to the presence of short-range correlations, has been known for quite some time. Recently, ^{16}O(e,e′pp)^{14}C two-proton knock-out data [55,56] offered an opportunity to study one- and two-body currents and to discriminate between long-range and short-range correlations [57]. Such studies are extremely important for understanding in-medium effects in nuclear matter. Another complementary piece of data, coming from the decay studies, that is relevant to the question of two-nucleon correlations, was the recent observation [58] of the simultaneous emission of two protons from a resonance of ^{18}Ne. This new mode of nuclear decay was predicted in the 1960s, but it is only very recently that experimental efforts have found sequential emission of single protons though an intermediate state. A key remaining question is whether the two protons, as they leave the nucleus, are closely coupled together to form ^{2}He, or are emitted almost independently in a direct three-body breakup ("democratic" decay). Further studies of this phenomenon will shed new light on the nature of nucleonic superconductivity. (See Ref. [59] for recent theoretical developments.)

Despite the exciting progress in shell-model approaches, their applications to very heavy systems are still beyond our reach. Besides, for nuclei with many valence particles, the concept of valence nucleons is less useful, and the valence and inner-shell nucleons have to be treated on an equal footing. To carry out the microscopic, consistent in-medium renormalization for heavy nuclei is a difficult task. Consequently, theories and methods have been developed which use effective interactions or effective Lagrangians. Among them are the self-consistent methods based on the density-dependent effective interactions, which by now have achieved a mature state of development, as well as those based on relativistic meson-nucleon Lagrangians which have reached the state where detailed studies of results and readjustment of basic parameters are now possible.

In the strategy of the mean-field theory , the main assumption is that the many-body wave function can be – to zero order – approximated by that of inde-

pendently moving quasiparticles. Together with the variational principle applied to the effective density-dependent Hamiltonian, this leads to the Hartree-Fock (HF) or Hartree-Fock-Bogolyubov (HFB) equations [28]. In spite of the very simple form, the independent-quasiparticle wave function is a highly correlated state. In the mean-field theory, self-consistency is automatically guaranteed by the equations of motion. That is, the same wave function which generates the mean field is an eigenstate of the mean-field Hamiltonian. Since the mean-field Hamiltonian often breaks symmetries present in the laboratory system, the HFB state is an *intrinsic* wave function, which – in general – is not an eigenstate of angular momentum, parity, and particle number operators. (The microscopic mechanism responsible for the symmetry-breaking is discussed below in Sec. 5.) By restoring the intrinsically broken symmetries, one takes into account correlations going beyond the mean-field description. This can be done by various theoretical techniques such as the Random Phase Approximation (RPA), the Generator Coordinate Method (GCM), or various projection methods.

The mean-field approaches have achieved a level of sophistication and precision which allows analyses of experimental data for a wide range of properties and for arbitrarily heavy nuclei [60–63]. For instance, a self-consistent mass table has been recently developed [64] based on the Skyrme energy functional. The resulting rms error on binding energies of 1700 nuclei is around 700 keV, i.e., is comparable with the agreement obtained in the microscopic-macroscopic approaches. Figure 8 displays two-neutron separation energies for the Sn isotopes calculated in several state-of-the-art self-consistent mean-field models based on different effective interactions and, in the inset, those obtained with phenomenological mass formulae. All these models nicely describe the existing experimental data; some interesting deviations are seen when approaching the proton drip line. This figure nicely illustrates difficulties with making theoretical extrapolations into neutron-rich territory. Clearly, the differences between forces and mass formulae are greater in the region of "terra incognita" than in the region where masses are known. As seen in Fig. 8, the position of the neutron drip line for the Sn isotopes depends on the model used. Therefore, the uncertainty due to the largely unknown isospin dependence of the effective force gives an appreciable theoretical "error bar" for the position of the drip line. Unfortunately, the results presented in Fig. 8 do not tell us much about which of the forces discussed should be preferred since one is dealing with dramatic extrapolations far beyond the region known experimentally. However, a detailed analysis of the force dependence of results may give us valuable information on the relative importance of various force parameters.

Among other recent developments in theoretical nuclear structure, particularly important is the elegant explanation of the pseudo-spin symmetry of the nuclear single-particle spectra proposed thirty years ago [67,68]. Surprisingly, as demonstrated by Ginocchio [69], the roots of the pseudo-spin can be traced back to the symmetry of the Dirac equation (see also Refs. [70,71]). Consequently, the relativistic approach explains, at the same time, the depth of the average potential (around 50 MeV), the magnitude of the spin-orbit term, and the small

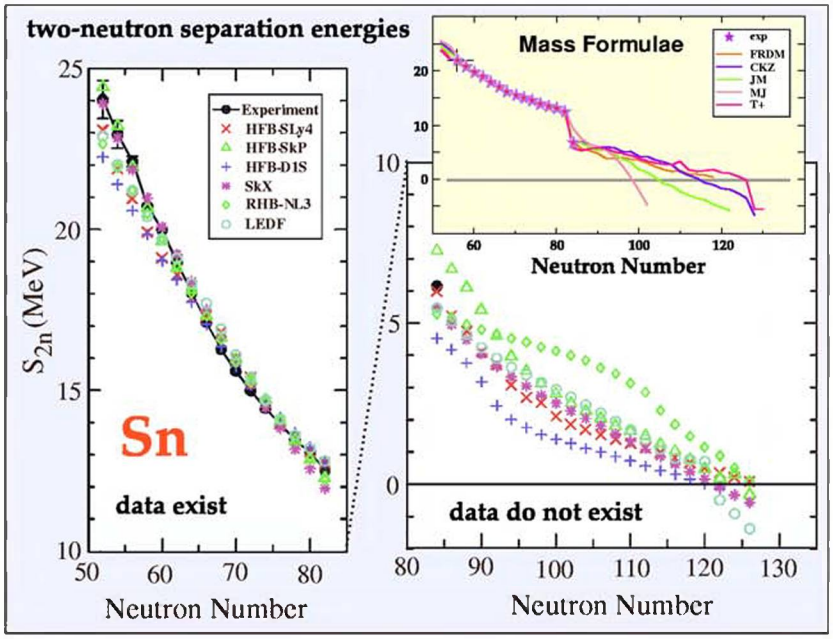

Fig. 8. Predicted two-neutron separation energies for the even-even Sn isotopes using several microscopic models [Hartree-Fock-Bogolyubov (HFB); local energy-density functional model (LEDF); relativistic Hartree-Bogolyubov (RHB)] based on effective nucleon-nucleon interactions and obtained with phenomenological mass formulas (shown in the inset at top right). Taken from Refs. [65,66] and references quoted therein.

pseudo-spin-orbit splitting. In this context, it should be noted that the traditional picture of nuclear shells and magic gaps proposed fifty years ago [72,73] should not be taken for granted. As discussed in Sec. 7 below, modifications of shell structure are expected in the limit of a large N/Z ratio.

We have learned a great deal about modes of nuclear excitations using phenomenological models, often based on ingenious intuition and symmetry considerations. These models, approaches, and approximations have been extremely successful in interpreting nuclear states and classifying nuclear states and decays. Based on this experience, and thanks to developments in theoretical modeling and computer technology, we are now on the edge of the *microscopic description*. By taking advantage of modern many-body algorithms, one can now shorten the cycle theory↔experiment↔theory. Most many-body methods of theoretical nuclear structure were introduced a long time ago (in the fifties and sixties). However, thanks to incredible progress in hardware and numerical techniques, it is only now that we can use these methods in their full glory.

Figure 2, bottom, includes a schematic illustration of the hierarchy of theoretical models spanning the chart of the nuclides. By exploring connections between these models, nuclear theory aims to develop a unified description of

the nucleus. It probably would be very naive to think of the behavior of a heavy nucleus directly in terms of the underlying quark-gluon dynamics, but undoubtedly the understanding of the bridges in Fig. 1 will make this goal qualitatively possible.

4 Nuclear modes and their time scales

Considering that the atomic nucleus is, in a good approximation, a cluster of strongly interacting nucleons (or pairs of nucleons) wandering solo in all directions, the very existence of nuclear *collective* motions such as rotations or vibrations, with all particles moving in unison, is rather astonishing.

When discussing nuclear collective motion, such as rotations and vibrations, one is often making analogies to molecules and their collective modes. As a matter of fact, many elements of the unified model have been directly transferred to nuclear physics from molecular physics [74]. But there is a fundamental difference between the nuclear and molecular world: in molecules, the fast electronic motion is strongly coupled to the equilibrium position of slowly moving ions.

This point is nicely illustrated in Fig. 9, which shows the measured spectrum of a diatomic molecule N_2. Each electronic excitation represents a bandhead upon which vibrational and rotational states are built. Vibrational states are indicated by a vibrational quantum number ν (ν=0 representing the zero-phonon state, ν=1 is a one-phonon state, and so on). Rotational levels are not plotted – there are far too many to be displayed. The time scale of molecular modes is governed by the hierarchy of excitation energies. The electronic excitations are of the order of $10^5\,\mathrm{cm}^{-1}$ (which in "nuclear" units corresponds to an eV), vibrational frequencies are $\sim 10^3\,\mathrm{cm}^{-1}$, and rotational energies are $\sim 10^{-1}\,\mathrm{cm}^{-1}$. This means that the single-particle electronic motion is from two to six orders of magnitude *faster* than molecular collective modes. Consequently, the adiabatic assumption, based on the separation of all molecular degrees of freedom into fast and slow ones, is justified due to different time scales.

Unfortunately, the total A-body wave function of the nucleus cannot, in general, be expressed in terms of slow and fast components. This is because (i) the collective nuclear coordinates are auxiliary variables which depend, in a complex way, on fast nucleonic degrees of freedom, and (ii) the nuclear residual interactions are not small. How good is the time separation between single-particle and collective nuclear motion? The typical single-particle period (i.e., the average time it takes a neutron or a proton to go across the nucleus), $T_{\mathrm{s.p.}}=4R/v_{\mathrm{F}}$ [where R is the nuclear radius and v_{F} is the Fermi velocity ($\sim 0.29\,c$)], is approximately $3{\cdot}10^{-22}$ sec. (The unit 10^{-22} sec is sometimes referred to as babysecond. The single-particle time scale is of the order of several babysec.) The typical period of nuclear rotation ($T_{\mathrm{rot}}{\approx}10^{-21}$ sec) is only $\sim$30 times greater than $T_{\mathrm{s.p.}}$, and for nuclear vibrations the period of oscillations is only slightly greater than the single-particle period. It is truly amazing that these relatively small differences in time scales seem to be sufficient to create rotating or vibrating potentials, common for all nucleons!

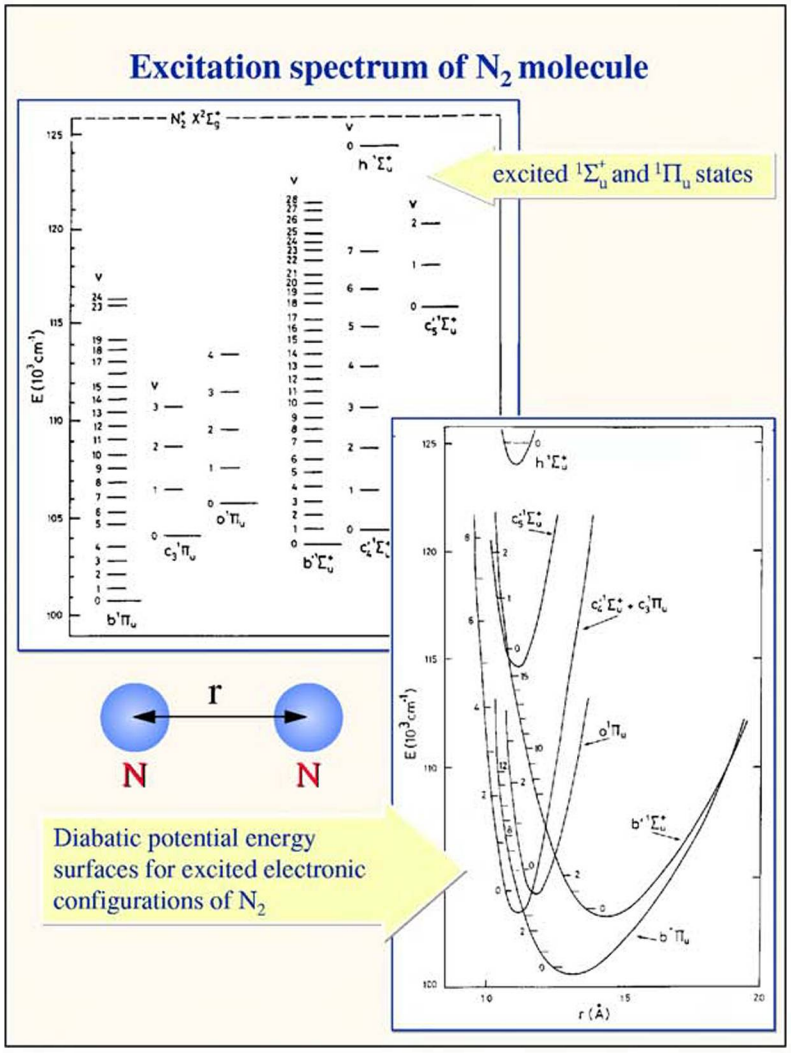

Fig. 9. Top: vibrational spectrum of N_2 molecule. Bottom: collective potentials, corresponding to different electronic configurations, as functions of the internuclear radius r (from Ref. [75]).

How "good" are the actual nuclear rotations and vibrations? Let us consider some representative experimental examples. Probably the most spectacular "molecular" rotational-vibrational nuclear spectrum is that of ^{240}Pu in its superdeformed minimum [76] (Fig. 10). This beautiful and rich structure, observed in a ^{238}U(α,2n) reaction, shows one- and two-phonon deformed quadrupole and octupole vibrational states, as well as the rotational bands built upon them. Its

spectrum shows some similarity with the molecular pattern; several low-lying excitations can be associated with one-phonon states, and some of its levels are believed to have a two-phonon nature. At first sight, the collective structures seen in ^{240}Pu are fairly regular. However, after closer inspection, many deviations from the perfect rotational and vibrational pattern can be seen. For example, the moments of inertia of rotational bands are by no means constant but show local variations as a function of angular momentum. Also, the positions of vibrational bandheads differ from the harmonic limit. Such deviations indicate that the nuclear motion is not completely collective, i.e., that the collective modes result from coherent superpositions of single-particle nucleonic excitations.

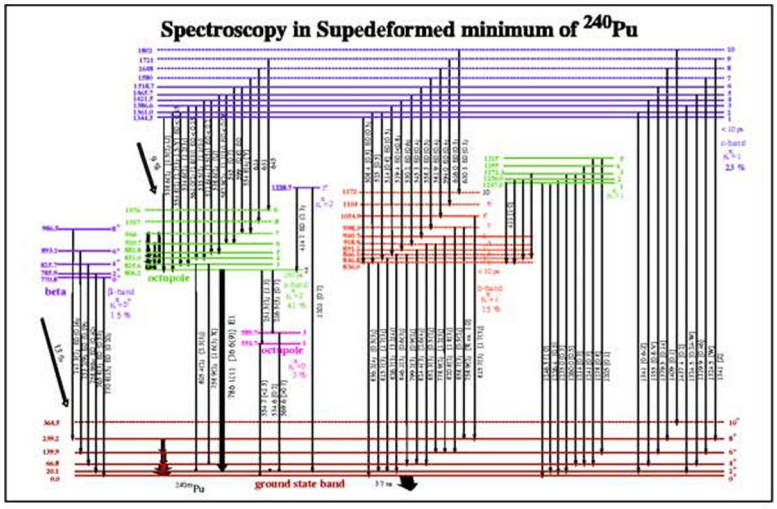

Fig. 10. Excitation spectrum of ^{240}Pu in the superdeformed minimum. Low-lying states have characteristic rotational-vibrational structure. (From Ref. [76].)

Another extreme case is shown in Fig. 11, which displays the excitation spectrum of ^{148}Gd. This spectrum looks very irregular; it is characteristic of many-particle many-hole excitations in an almost spherical nucleus. There are many states of different angular momentum and parity connected via relatively weak electromagnetic transitions. In spite of the fact that the excitation pattern looks "chaotic", most of the noncollective states of ^{148}Gd can be beautifully described in terms of well-defined quantum numbers of the nuclear shell model [78]. The collective spectrum of ^{240}Pu discussed above was not perfectly collective. Likewise, in the "mess" of noncollective levels in ^{148}Gd one can find some elements of collectivity. For instance, the energies of the four lowest states 0^+, 2^+, 4^+, 6^+, when plotted as functions of angular momentum, exhibit a characteristic parabolic pattern. As was realized around forty years ago [79], such a sequence of states indicates the presence of pairing – a collective phenomenon.

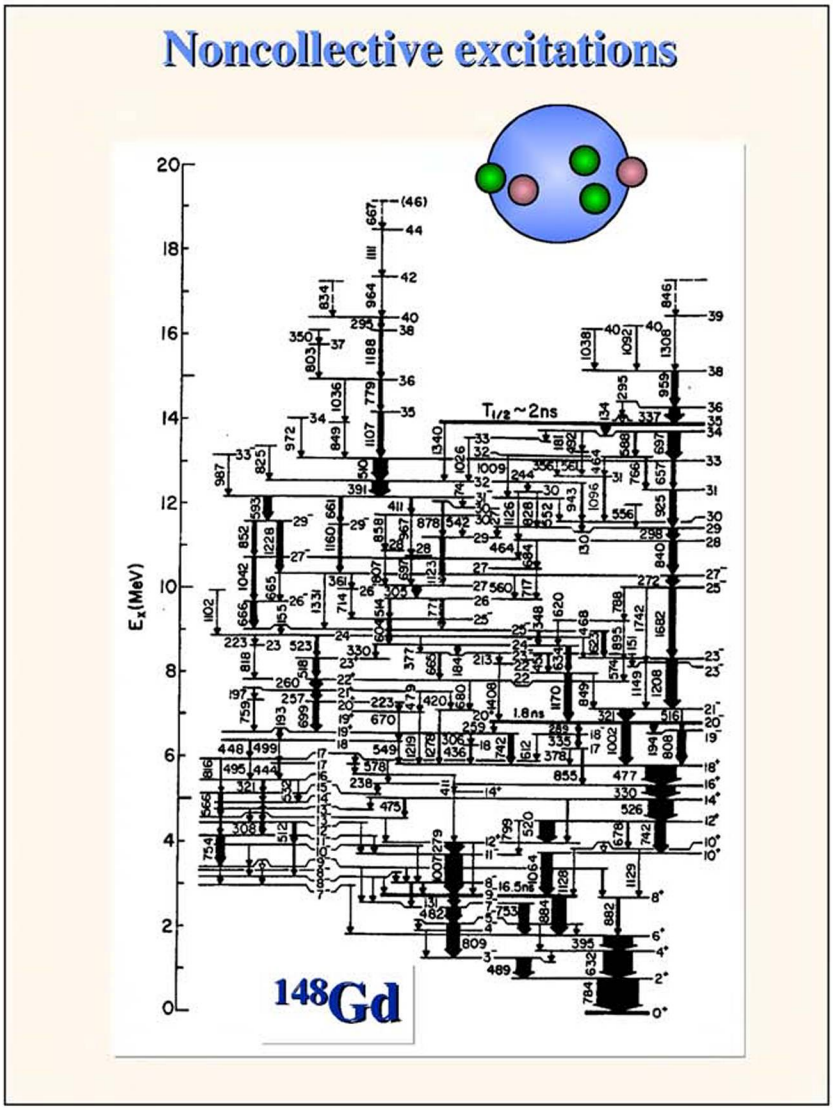

Fig. 11. Excitation spectrum of ^{148}Gd. It is a beautiful example of noncollecive nucleonic motion (from Ref. [77]).

The next example illustrates the coexistence effect. It is a particular case of the large amplitude collective motion where several nuclear configurations, characterized by different intrinsic properties, compete [82]. In the spectrum of ^{152}Dy, shown in Fig. 12, one can recognize the noncollective structure resembling that in ^{148}Gd, a collective rotational band (interpreted in terms of a deformed

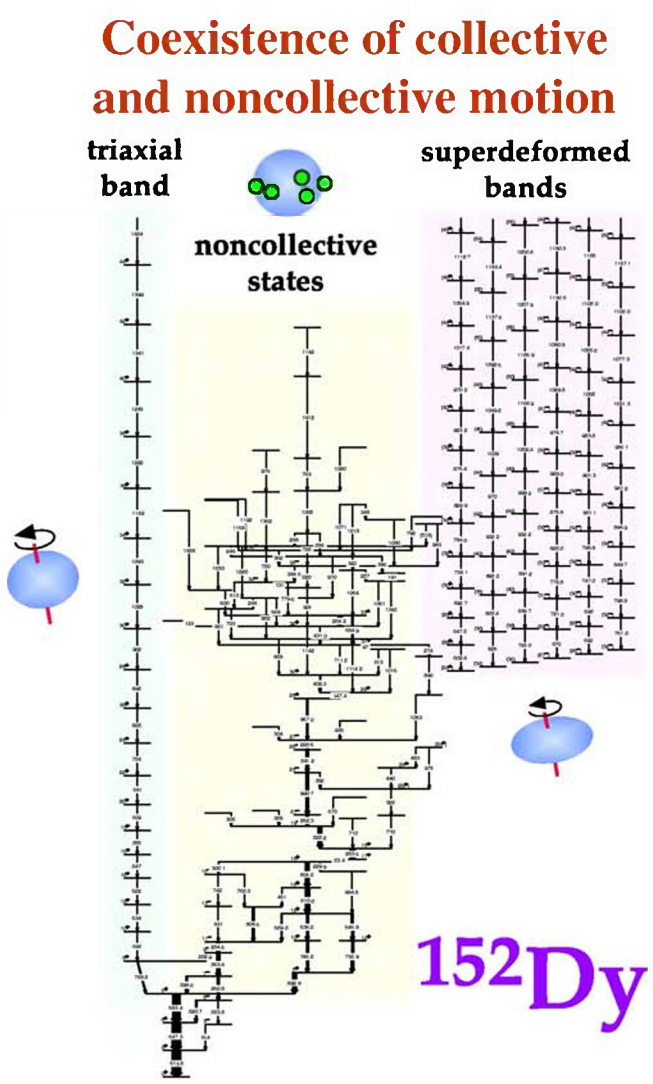

Fig. 12. Excitation spectrum of ^{152}Dy. It is a spectacular example of the coexistence of collective and noncollecive nucleonic modes. (Experimental data were taken from Refs. [80,81].)

triaxial configuration), and super-collective superdeformed bands corresponding to very large shape-elongations which are structurally isolated from the rest of the spectrum.

The last experimental example shows yet another case of nuclear collectivity – high-frequency nuclear vibrations. Figure 13 displays the cross section for the

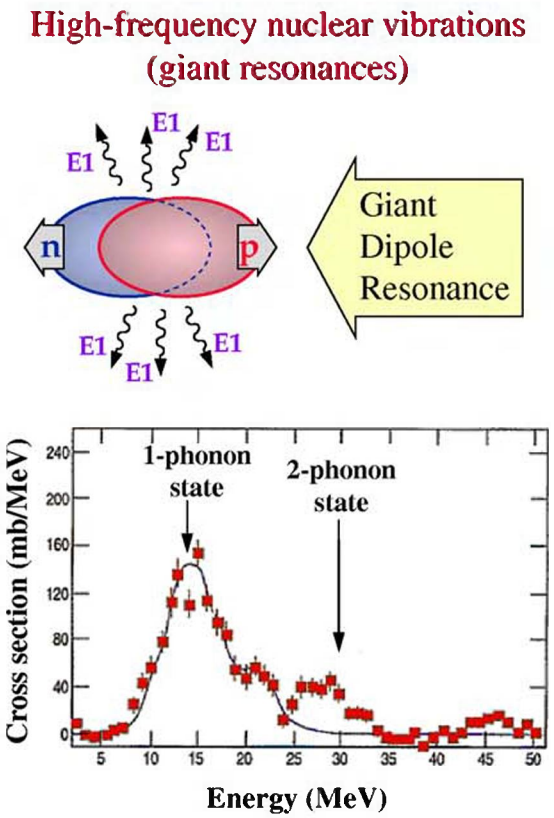

Fig. 13. One-phonon and two-phonon giant resonances in ^{208}Pb. (Experimental data were taken from Ref. [83].)

scattering of the relativistic ^{208}Pb on a xenon nucleus. The first maximum in the cross section, which appears at ~14 MeV, can be associated with the one-phonon giant dipole resonance (i.e., very fast vibration of protons against neutrons). It has been suggested [83] that the local maximum at an energy of ~28 MeV is a two-phonon giant dipole vibration. In the data shown in Fig. 13 one can also find isoscalar and isovector giant quadrupole resonances. The giant nuclear excitations are always strongly fragmented; their widths are usually more than 5 MeV. It is worth noting that the time scale corresponding to giant two-phonon vibrations is shorter than 1 babysec! The unusual harmonicity of this mode is not understood well.

One of the outstanding challenges in nuclear structure is to understand the mechanism governing the nature of nuclear collective excitations. By studying nuclear rotations and vibrations, one is probing the details of the nuclear force in a strongly interacting medium.

5 Nuclear deformations

The phenomenon of nuclear deformation has a long and interesting history. As early as 1924 it was suggested by Pauli [84] that the hyperfine structure of atomic and molecular energy levels resulted from the electromagnetic interaction with *nonspherical* atomic nuclei. (The experimental evidence was given ten years later by Schüler and Schmidt [85].) The fact that nuclei need not be spherical was then emphasized by N. Bohr in his classic paper on the nuclear liquid-drop model [86] in which he introduced the concept of nuclear *shape vibrations*. If a quantum-mechanical system is deformed, its spatial density is anisotropic. For a deformed system it is possible to define its orientation as a whole and this naturally leads to the presence of collective rotational modes. This possibility was realized as early as 1937 by N. Bohr and Kalckar [87] who had estimated for the first time the energies of lowest rotational excitations and introduced the notion of the *nuclear moment of inertia* (see also work by Teller and Wheeler [88]). In 1939, Meitner and Frisch [89] and N. Bohr and Wheeler [90] stressed the role of shape degrees of freedom during the fission process.

In 1950, Rainwater [91] observed that the experimentally measured large quadrupole moments of nuclei could be explained in terms of the *deformed shell model*; i.e., the extension of the spherical shell model to the case of the deformed average potential. In this picture, the deformed field was a direct consequence of single-particle motion in anisotropic orbits. In a following paper [92], A. Bohr formulated the basis of the particle-rotor model, introduced the concept of the intrinsic (body-fixed) nuclear system defined by means of shape deformations, and regarded nuclear shape and orientation as dynamical variables (in this connection, see also Refs. [93–97]).

The basic microscopic mechanism leading to the existence of nuclear deformations was proposed by A. Bohr in his paper on "The Coupling of Nuclear Surface Oscillations to the Motion of Individual Nucleons" [98]. As a matter of fact, this title is probably the most precise (and shortest) answer to the question: Why are nuclei deformed? The interaction between the single-particle motion of valence nucleons and the collective excitations (multipole vibrations) of the core was represented by Bohr by the particle-vibration coupling Hamiltonian,

$$H_{\rm PV} = -\sum_{\lambda\mu} \kappa_{\lambda\mu}\alpha_{\lambda\mu} \sum_i f(r_i)Y_{\lambda\mu}(\Omega_i), \tag{1}$$

where $\alpha_{\lambda\mu}$ is the amplitude of the nuclear deformation of the core, $f(r_i)Y_{\lambda\mu}(\Omega_i)$ is the multipole moment of the i-th valence nucleon, and $\kappa_{\lambda\mu}$ stands for the particle-vibration coupling strength. The coupling (1) is a central element in the analysis of nuclear collective modes and nuclear deformations.

It was forty years ago when the theory of the coupling between nuclear single-particle and collective degrees of freedom was presented by A. Bohr and Mottelson [99] and Hill and Wheeler [100]. These two works form the intellectual and conceptual basis of the nuclear unified model that turned out to be one of the most powerful tools of nuclear structure. Since the main objective of this section is to discuss the microscopic aspects of nuclear deformation rather than to

talk about the past, I should stop these brief historical remarks here. But before doing so, let me mention that already in 1935, in London, Jahn and Teller demonstrated that the electronic degeneracy in molecules could destroy the symmetry on which it was based [101]. As discussed below (see also Refs. [102,103]), a similar mechanism is responsible for the presence of deformed nuclear shapes.

5.1 Nuclear Jahn-Teller effect

The Jahn-Teller effect, or the phenomenon of *spontaneous symmetry-breaking*, first proposed for molecules, turned out to appear in many fields of physics. Deformation is a common phenomenon that appears in mesoscopic systems with many degrees of freedom (atomic nuclei, atomic clusters). It also appears in field theory (Higgs mechanism), in physics of superconductors (Meissner effect), in condensed matter physics (numerous phenomena related to spin resonance and relaxation), and other fields of physics. Since the microscopic origin of the JT effect is not well known in the nuclear structure community, this section contains a slightly higher level of detail as compared to other sections.

The adiabatic approximation by Born and Oppenheimer [104] is the natural starting point in the discussion of spontaneous symmetry-breaking. It is based on the assumption that system coordinates can be separated into *slow* (collective, relevant) coordinates, $\{\boldsymbol{Q}\}=\{Q_j\}$, and *fast* (noncollective, irrelevant) coordinates, $\{\boldsymbol{x}\}=\{x_i\}$. The separation obviously depends on the actual physical problem.

The Hamiltonian for the whole system can be written as

$$\hat{H} = T_{\boldsymbol{Q}} + T_{\boldsymbol{x}} + V(\boldsymbol{Q}, \boldsymbol{x}), \tag{2}$$

where $T_{\boldsymbol{Q}}$ and $T_{\boldsymbol{x}}$ are kinetic energies associated with slow and fast coordinates, respectively. At this point the slow and fast coordinates are treated on the same footing. The equations of motion for the Hamiltonian (2) can be written in a canonical form and the motion of the system can be described in the full phase space of collective and non-collective coordinates and associated momenta.

The stationary Schrödinger equation with Hamiltonian (2) is solved in two steps. First, at a given point in the collective phase space one solves the eigenproblem for the non-collective Hamiltonian $h=T_{\boldsymbol{x}}+V(\boldsymbol{Q}, \boldsymbol{x})$:

$$[T_{\boldsymbol{x}} + V(\boldsymbol{Q}, \boldsymbol{x})]\, \Psi_n(\boldsymbol{x}; \boldsymbol{Q}) = E_n(\boldsymbol{Q}) \Psi_n(\boldsymbol{x}; \boldsymbol{Q}), \tag{3}$$

where $\Psi_n(\boldsymbol{x}; \boldsymbol{Q})$ is the fast (single-particle) wave function which contains the slow coordinates $\{\boldsymbol{Q}\}$s parametrically, and $E_n(\boldsymbol{Q})$s are the single-particle energies at the point $\{\boldsymbol{Q}\}$. Consequently, the $E_n(\boldsymbol{Q})$s are the static potential energy surfaces in the collective space.

In the second step, the total wave function of the system is written as a product

$$\Psi = \sum_n \Psi_n(\boldsymbol{x}; \boldsymbol{Q}) \chi_n(\boldsymbol{Q}). \tag{4}$$

The collective wave functions $\chi_n(\boldsymbol{Q})$ arise from the effective potential appropriate to each single-particle state. By combining Eqs. (2-4), one obtains the coupled-channel Schrödinger equation for $\chi_n(\boldsymbol{Q})$:

$$\sum_m \left[\delta_{mn} T_{\boldsymbol{Q}} + V_{mn}(\boldsymbol{Q})\right] \chi_m(\boldsymbol{Q}) = E\chi_n(\boldsymbol{Q}). \tag{5}$$

The effective collective potential $V_{mn}(\boldsymbol{Q})$ takes into account the collective response of the single-particle energy on collective coordinates $\{\boldsymbol{Q}\}$. It contains the coupling term between different single-particle states n and m, defined through

$$\sum_m \langle n|T_{\boldsymbol{Q}}\left\{|m\rangle \chi_m(\boldsymbol{Q})\right\}. \tag{6}$$

If the coupling term is weak, the eigenfunctions of the total system are just products of collective and single-particle wave functions.

In molecular physics, the electronic states (described by means of *fast* coordinates) are strongly coupled to the equilibrium position of the ions (described by means of *slow* coordinates). The adiabatic assumption is justified due to different time scales of nuclear and electronic motions (see Fig. 9 and related discussion). In nuclear physics, the $\{\boldsymbol{Q}\}$s are fields characterizing various collective modes and $\{\boldsymbol{x}\}$s are remaining coordinates. This separation is by no means simple; the choice of proper nuclear collective coordinates is a long-standing problem [28,105]. Indeed, as discussed early in Ref. [92]: "In contrast with the molecular case, there are here no heavy particles to provide the necessary rigidity of the structure. However, nuclear matter appears to have some of the properties of coherent matter which makes it capable of types of motion for which the effective mass is large as compared with the mass of a single nucleon." The variety and richness of nuclear collective modes, appearing even in very light nuclei, suggest that the adiabatic approximation is, very often, a powerful concept.

5.2 Level crossing

In many cases the off-diagonal matrix element in Eq. (6) does not vanish and non-collective modes are strongly coupled through the collective field. An extreme coupling occurs when there are two or more non-collective states which are degenerate (or almost degenerate) at some point $\{\boldsymbol{Q}\}=\{\boldsymbol{Q}_c\}$, i.e.,

$$E_k(\boldsymbol{Q}_c) \approx E_l(\boldsymbol{Q}_c) \quad (k \neq l). \tag{7}$$

The matrix of the collective momentum $\partial/\partial\boldsymbol{Q}$, a Berry vector

$$(\boldsymbol{A})_{lk} = i\langle l|\frac{\partial}{\partial \boldsymbol{Q}}|k\rangle, \tag{8}$$

is the single most important quantity to determine the validity of the adiabatic approximation. For small collective velocities and $\boldsymbol{A}$ slowly changing in time, the motion of the system is adiabatic and can be well described by means of the

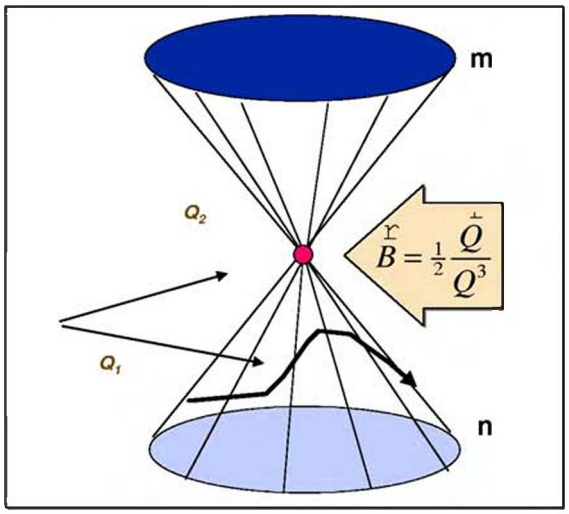

Fig. 14. Conical intersection between two potential energy surfaces m and n in a collective $\{\boldsymbol{Q}\}$-space. The crossing point contains a generalized monopole potential that tries to repel the system from the point of degeneracy. (Based on Ref. [106].)

perturbation theory. Sometimes, off-diagonal matrix elements of $(\boldsymbol{A})_{lk}$ disappear (e.g., for symmetry reasons), and Eq. (6) contains only diagonal matrix elements $(\boldsymbol{A})_{ll}$ which can be eliminated by means of a simple gauge transformation.

A wealth of very interesting physics appears at the point of degeneracy, $\{\boldsymbol{Q}\}=\{\boldsymbol{Q}_c\}$. Unlike in the static situation, it is now impossible to eliminate (8) through the gauge transformation. In particular, the Berry phase on a closed path in $\{\boldsymbol{Q}\}$-space does not vanish if the path encloses the point of degeneracy. Geometrically, the crossing point can be viewed as a *diabolical point* containing a generalized vector potential [106–108] singular at $\boldsymbol{Q}_c$, see Fig. 14. Consequently, during its collective motion the system will always try to go as far as possible from the point of degeneracy, analogously to the motion of a charged particle in the magnetic field of a monopole [107,109]. In the vicinity of Q_c, the actual eigenstates of $\hat{H}$ are mixtures of diabatic states. Consequently, around the crossing point (i) the original (fast) quantum numbers are gone and the description in terms of intrinsic Hamiltonian breaks down, (ii) the motion of the system cannot be separated into the collective and non-collective parts, and (iii) the notion of the collective adiabatic potential loses its meaning [110].

5.3 Vibronic coupling

Let us assume that collective normal modes (e.g., nuclear vibrational modes) transform according to the irreducible representations $\mathcal{T}(\lambda)$ of the symmetry group $\mathcal{T}$. Therefore, they can be written as $\{Q_{\lambda\mu}\}$, where μ labels the component of the representation λ. The single-particle states belong to a certain

group representation $\mathcal{T}(J)$ of dimension $[J]$, i.e., $|n,\boldsymbol{x}\rangle = |JM,\boldsymbol{x}\rangle$ (M labels the component of the representation J). In order to analyze the particle-vibration coupling, it is convenient to expand the *vibronic potential* V_{mn} defined in Eq. (5) with respect to collective coordinates around the point of degeneracy, $\{\boldsymbol{Q}_c\}$=$\{0\}$:

$$V_{JM,JM'}(\boldsymbol{Q}) = V_{JM,JM'}(0) + \sum_{\lambda\mu} Q_{\lambda\mu} \left(\frac{\partial V_{JM,JM'}}{\partial Q_{\lambda\mu}}\right)_{(0)} + \cdots \tag{9}$$

Then by the Hellmann-Feynman theorem and the Wigner-Eckart theorem, the linear vibronic coupling term (often referred to as the JT matrix element) can be written as

$$\left(H_{\rm JT}\right)_{MM'} = [J]^{-\frac{1}{2}} \sum_{\lambda\mu} Q_{\lambda\mu} \langle J\| \left(\frac{\partial H}{\partial Q_\lambda}\right)_{(0)} \|J\rangle \langle JM'\lambda\mu|JM\rangle, \tag{10}$$

where $\langle J\|...\|J\rangle$ is the reduced matrix element, and $\langle JM'\lambda\mu|JM\rangle$ is the corresponding Clebsch-Gordan coefficient for representations λ and J.

It is seen immediately from Eq. (10) that the JT matrix element is zero if the representation $\mathcal{T}(\lambda)$ is not contained in the product $\mathcal{T}(J) \otimes \mathcal{T}(J)$. This would mean that in such a situation the collective mode $\lambda\mu$ does not couple degenerate single-particle states. The diagonal constant of the linear coupling has the sense of the force with which the single-particle part of the system in state $|JM,\boldsymbol{x}\rangle$ affects the collective part in the direction of the collective coordinate Q_λ.

The vibronic coupling between single-particle nucleonic motion and collective modes can be estimated by means of a weak coupling model [98,111]. Here the collective subspace refers to the vibrational modes of the core, while the fast subspace is associated with the single-particle coordinates of valence particles. The particle-core interaction , which can be directly derived from the multipole-multipole force, is given by Eq. (1), i.e.,

$$V(\boldsymbol{Q},\boldsymbol{x}) = -\sum_{\lambda\mu} \kappa_{\lambda\mu} Q_{\lambda\mu} q^{val}_{\lambda\mu}. \tag{11}$$

The symmetry group of interest is the group of rotations characterized by representations (J,M). Consequently, the JT matrix element becomes

$$\left(H_{\rm JT}\right)_{M'M''} = -(2J+1)^{-\frac{1}{2}} \sum_{\lambda\mu} \kappa_{\lambda\mu} Q_{\lambda\mu} \langle J\|q^{val}_\lambda\|J\rangle \langle JM''\lambda\mu|JM'\rangle. \tag{12}$$

It is seen from Eq. (12) that the high-j states contribute the most to the JT matrix element. Indeed, for those states the value of $\langle J\|q^{val}_\lambda\|J\rangle$ is largest.

A "$Q \cdot q$" coupling (11), where Q represents the collective (bosonic) field and q describes the single-particle (fermionic) subsystem, is well known in many fields of physics (see, e.g., Ref. [112]). Examples of (Q, q) are: (photons, charged particles), (mesons, nuclei), (phonons, electrons), and (phonons, nuclei). In all of these cases, the potential energy $V(\boldsymbol{Q},\boldsymbol{x})$ in (2) can be approximated by

$$V(\boldsymbol{Q},\boldsymbol{x}) = V(\boldsymbol{Q}) + \kappa \boldsymbol{Q} \cdot \boldsymbol{q}(\boldsymbol{x}) + h(\boldsymbol{x}). \tag{13}$$

Consequently, the physics of the particle-vibration (fermion-boson) coupling is rather similar for all the systems mentioned above.

5.4 Static nuclear deformations

Let us illustrate the nuclear JT effect using simple arguments based on the Random Phase Approximation . A simple separable spherical nuclear Hamiltonian representing vibrations associated with the operator $\hat{Q}$ can be written as:

$$H = \sum_i e_i c_i^+ c_i - \frac{1}{2}\kappa \hat{Q}^+ \cdot \hat{Q}. \tag{14}$$

This Hamiltonian contains two basic ingredients of nuclear shape-collectivity, namely (i) the single-particle term representing the individual motion of nucleons around the Fermi surface, and (ii) the multipole vibrational field Q that generates the collective motion.

Within the formalism of RPA [28], the excitations of the system, $\omega_{\rm RPA}$, are solutions of the so-called dispersion equation:

$$R(\omega_{\rm RPA}) = \sum_{ph} \frac{2|\langle ph|Q|0\rangle|^2 \epsilon_{ph}}{\epsilon_{ph}^2 - \omega_{\rm RPA}^2} = \frac{1}{\kappa}, \tag{15}$$

where $R(\omega_{\rm RPA})$ is the dispersion function and ϵ_{ph} stands for the energy of a particle-hole excitation, $\epsilon_{ph} = e_p - e_h$. The lowest root of Eq. (15) usually represents the low-frequency collective vibrational state.

The total HF energy is shown as a function of average self-consistent deformation (collective coordinate) $q{=}\kappa\langle\hat{Q}\rangle_{HF}$ in the top portion of Fig. 15. Let us discuss some properties of the RPA solutions corresponding to different values of coupling constant κ. These three cases are represented in Fig. 15, top portion. If the coupling constant κ is small (weak coupling or vibrational limit), the lowest-energy solution is depressed with respect to the lowest non-collective excitation, and the wave function of the collective state becomes a coherent superposition of many particle-hole configurations. In this situation, characteristic of harmonic vibrations, the potential energy curve is quadratic around the equilibrium point, $q{=}0$, and the stiffness

$$C = (d^2E/dq^2)_{q=0} \tag{16}$$

is greater than zero. In this case, $\omega_{\rm RPA}$ represents the energy of the vibrational one-phonon excitation.

If the value of κ is increased, the energy surface softens, the low-energy vibration becomes more collective, and the vibrational frequency decreases. At the critical point (transition from spherical to deformed) when κ becomes equal to $\kappa_{\rm crit}{=}1/R(0)$, the lowest RPA solution appears at zero energy, i.e., the collective state becomes *degenerate* with the ground state. (This is precisely the famous Goldstone boson!) At this point of a boson condensation, the stiffness C vanishes and the harmonic approximation breaks down. Since the system cannot have two ground states, it becomes unstable against vibration induced by the multipole-multipole force [113].

A further increase of the coupling constant leads to *permanent shape deformation.* At this limit (strong coupling), the lowest solution of Eq. (15) has *imaginary*

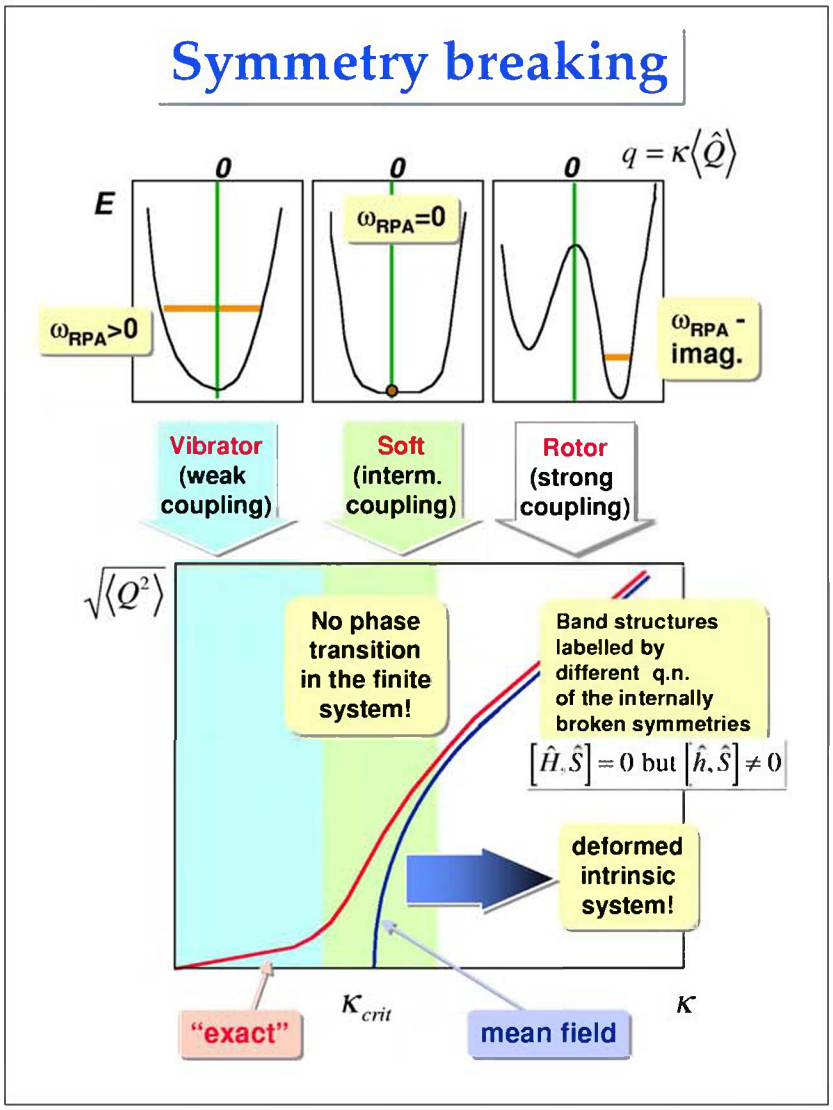

Fig. 15. Schematic diagram illustrating the mechanism of static nuclear deformation in the the mean-field picture. See text for details.

energy. Here, the stiffness at a spherical shape becomes negative and the energy becomes minimal at some non-zero value of $q{=}q_o{\neq}0$. The energy of the lowest collective vibrational state built upon the *deformed* solution is schematically indicated in Fig. 15. It can be computed by means of RPA equations analogous to those of Eq. (15), but pertaining to the deformed minimum. However, the low-

est excitations of the nucleus in this limit are not vibrations but *rotations*. The presence of stable deformations makes it possible to distinguish between various orientations of the nucleus in space; hence rotational bands (i.e.,collective excitations connected by enhanced transition matrix elements) appear.

The lower portion of Fig. 15 presents schematically the q-vs.-κ "phase diagram". Within the static mean-field theory, which becomes exact at *infinite particle number*, the self-consistent deformation is zero below the critical point, at which *the first order phase transition* takes place. For $\kappa > \kappa_{\rm crit}$ the system has static deformation (shape deformation, pair deformation, etc.). In this context, it should be emphasized that the deformed picture is valid for rather large values of coupling strength, or for very large particle numbers (for instance, in solid state physics, where N$\sim 10^{23}$). Atomic nuclei are relatively small systems and the finite size effects, which manifest through dynamical correlations (fluctuations), are extremely important. The fluctuations wash out the transition from the "spherical" to "deformed" phase, and result in a smooth and continuous pattern of q, as indicated schematically in Fig. 15.

In the rotational limit, one can define the intrinsic system of the nucleus. Although the nuclear (laboratory-system) Hamiltonian does commute with the symmetry broken by the operator $\hat{Q}$, the intrinsic-system one-body Hamiltonian (mean-field Hamiltonian, HF Hamiltonian) does not. This is precisely the essence of the symmetry-breaking: rotational bands are a manifestation of internally broken symmetries. Nuclear states forming a collective band are labeled by quantum numbers of these broken symmetries. Examples are rotational bands in nuclei having quadrupole deformations (here the collective operator is the quadrupole moment, the broken symmetry is rotational invariance, and rotational bands are labeled by angular momentum quantum numbers), octupole deformations (here the collective operator is the octupole moment, the broken symmetry is space inversion, and rotational bands are parity doublets), and pairing correlations (here the collective operator is the pair operator, the broken symmetry is particle number, and rotational bands are the ground states of neighboring even-even nuclei). See Sec. 6.1 for more examples.

Based on the above discussion, one can make an interesting observation: if the lowest particle-hole energy approaches zero, the lowest pole of the dispersion function (Eq. (15)) becomes so small that the lowest solution is always degenerate with the ground state, independent of the magnitude of the coupling strength. Consequently, if the Fermi level lies just between two or more (almost) degenerate states, the system should be unstable with respect to the mode that couples these states. This is precisely the JT mechanism.

If pairing correlations are present, the dispersion relation given by Eq. (15) is slightly modified and, in the BCS approximation, it becomes:

$$\sum_{\alpha,\alpha'} \frac{2|\langle\alpha'|Q|\alpha\rangle|^2(u_\alpha v_{\alpha'} + u_{\alpha'} v_\alpha)^2(E_\alpha + E_{\alpha'})}{(E_\alpha + E_{\alpha'})^2 - \omega^2_{\rm RPA}} = \frac{1}{\kappa}, \tag{17}$$

where $E_\alpha = \sqrt{(e_\alpha - e_F)^2 + \Delta^2}$ are the quasiparticle energies, and u_α and v_α are the usual BCS occupation coefficients. The main effect of pairing correlations

is the change in the energy denominator in Eq. (17), which now is much larger than the particle-hole energies in Eq. (15). Indeed, the energy of the lowest pole becomes $2\Delta \simeq 2$ MeV. Together with the reduction of the numerator of Eq. (17) through the uv factor, pairing correlations tend to increase the critical value of κ. One can thus say that pairing has a tendency to make the system more spherical. The extreme JT effect, with very weak residual interaction, can take place in excited nuclear states. For instance, at high angular momentum the number of broken nucleonic pairs becomes so large that pairing correlations are expected to play a minor role. At this regime the collective motion of a system should be strongly influenced by diabatic effects (level crossings) giving rise to large deformation changes [105].

6 Shell structure

It was early realized that the symmetry-breaking mechanism is ultimately related to the behavior of the single-particle level density $g(e)$ of the intrinsic Hamiltonian:

$$g(e) = \frac{dN}{de}. \tag{18}$$

($g(e)$ is simply the number of states per unit of energy.) The atomic nucleus is expected to be more bound if the level density near the Fermi level is low. In particular, the nuclear ground state should correspond to the lowest possible degeneracy. Exceptionally stable systems (magic nuclei) are those with the least degenerate single-particle level density around the Fermi level, see Fig. 16.

The nuclear shell model describes well all nuclear properties that depend on the individual nucleonic motion in the vicinity of the Fermi surface. It is not possible, however, to apply the shell model alone to calculate bulk nuclear properties like binding energies, fission barriers, etc. It is because the single-particle shell-model energy differs from the full HF energy by the residual-interaction term. On the other hand, the shell-model energy contains the two main elements of the symmetry-breaking mechanism, i.e., the single-particle level density and the perturbation due to the particle-vibration interaction. The deformation-driving force of the single-particle model can thus be estimated by means of the shell-correction method developed by Swiatecki [114] and Strutinsky and collaborators [115–118]. The main assumption of the shell-correction approach is that the total energy of a nucleus can be composed of two parts,

$$E = E^{macr} + E^{shell}, \tag{19}$$

where E^{macr} is the macroscopic energy (smoothly depending on the number of nucleons and thus associated with the "uniform" distribution of single-particle orbitals) and E^{shell} is the microscopic shell-correction term fluctuating with particle number and reflecting the non-uniformities of the single-particle level distribution.

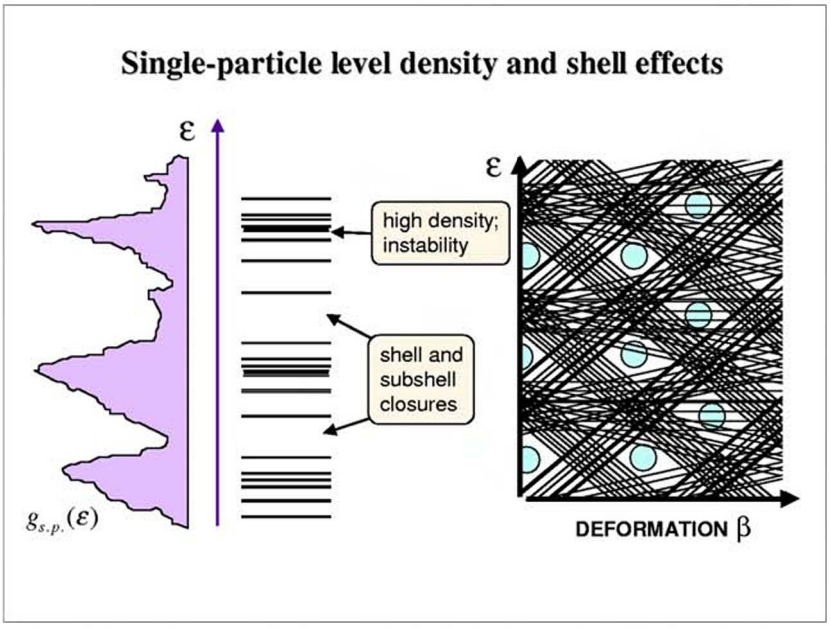

Fig. 16. Relation between single-particle level density and shell effects. Left: single-particle levels and the corresponding level density. The regions of shell and subshell closures correspond to reduced $g(e)$. Right: schematic Nilsson diagram illustrating the appearance of spherical and deformed gaps in the single-particle spectrum.

For nuclei in which the surface energy dominates, the macroscopic energy tends to favor spherical shapes. The deformation-driving force is, therefore, contained in the shell-correction term, which can be approximated by

$$E^{shell} = \sum_{i=1}^{A} e_i - \sum_{i=1}^{\infty} n_i e_i, \tag{20}$$

where the average single-particle occupation numbers n_i vary smoothly from 0 to 1 in the energy interval of the order of the energy difference between major shells. The approximation of the total energy by means of Eqs. (19) and (20) has a simple and elegant justification by means of the energy theorem formulated by Strutinsky [115,116,118].

The behavior of E^{shell} can be easily understood for any many-body system of fermions that generates average field. Indeed, if the level density around the Fermi level is large (level bunching, see Fig. 16), then the second term in Eq. (20) representing the smooth distribution of levels dominates (on the average it contains more occupied bound states) and E^{shell} is large and positive. The opposite is expected in the case of the low single-particle level density: for magic nuclei E^{shell} is large in magnitude and negative, thus leading to a strong stabilization of the total energy.

In order to understand the global features of shell-induced shape-polarization forces, it is instructive to plot the shell correction versus the number of particles and selected deformation parameters. A representative example is shown in Fig. 17 which displays the neutron shell-correction landscape of the modified harmonic oscillator potential (Nilsson potential) as a function of neutron number and quadrupole deformation ε. The topology of E^{shell} changes periodically with particle number. The lowest shell energy is expected in the regions of low single-particle level density, e.g., at spherical shapes for the magic numbers 20, 50, 82, and 126. However, when going away from these magic numbers, the spherical-shape level density becomes large [$(2j+1)$-fold spherical degeneracy] and shell correction induces the strong quadrupole polarization towards deformed shapes.

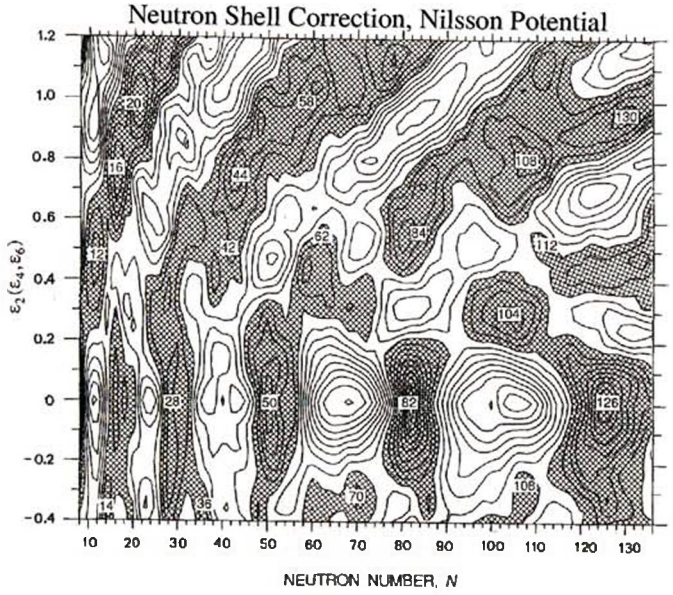

Fig. 17. Shell energy diagram in the (ε_2, N) plane. The figure is taken from Ref. [119].

The variation in the single-particle level density with shell filling, the level bunching, and the very existence of spherical and deformed magic numbers has a beautiful interpretation in terms of periodic orbits [74,120–122] in the corresponding classical problem. Indeed, the single-particle level density $g(\epsilon)=\sum_i \delta(\epsilon-\epsilon_i)$ can be represented by means of the trace formula [120,123]

$$g(\epsilon) = \tilde{g}(\epsilon) + \sum_L \sum_{k=1}^{\infty} a_{Lk}(\epsilon) \cos\left[k\left(S_L(\epsilon)/\hbar - \frac{\pi}{2}\mu_L\right)\right], \qquad (21)$$

where $\tilde{g}$ is the average level density associated with E^{macr}, while the second term in Eq. (21) is the fluctuating part of g responsible for shell effects. The shell energy can then be expressed as a sum over periodic orbits L. (S_L is the action integral associated with the orbit L, μ_L is the Maslov index, and a_{Lk} is the amplitude related to the density of classical trajectories in the neighborhood of the orbit.) Consequently, the shell structure of the many-body system (hence the presence or absence of deformation) has its deep roots in the non-linear dynamics of the corresponding classical Hamiltonian and the geometry of classical orbits [122]. The microscopic analysis of the link between the phenomenon of spontaneous symmetry-breaking and the non-linear dynamics (and chaos) is one of the most vigorously pursued recent avenues in theoretical nuclear physics. Among many examples of such analyses are: explanation of supershell effects in superdeformed nuclei [74,122] and discussion of shell structure in nuclei with permanent octupole deformations [124].

In the deformed shell model the important building block is the short-range pairing interaction. This is often approximated by means of the state-independent seniority force with the strength G. The macroscopic part of the total energy already contains the average pairing energy, which accounts for the main part of the even-odd mass difference. Therefore, it is the fluctuating part of the pairing energy, δE^{pair}, that gives an additional contribution to the total shell energy. The pairing field depends on the level density around the Fermi level, $g(e_F)$, as [125]

$$\Delta \propto \exp\Big[-\frac{1}{Gg(e_F)}\Big]. \tag{22}$$

In the case of a large single-particle level density, E^{shell} is positive but δE^{pair} is large and negative (large Δ). The opposite is true for systems with small $g(e_F)$, i.e., around large shell gaps. The cancellation between the shell energy and the pairing energy is yet another manifestation of the fact that pairing is the *symmetry-restoring* interaction. Indeed, equilibrium deformations calculated with the presence of pairing correlations are always reduced as compared to the situation without pairing.

6.1 Examples of nuclear deformations

It has been early recognized that various nuclear collective modes and deformations could be attributed to specific symmetries of the single-particle Hamiltonian and residual interaction. Indeed, as noted in Ref. [126]: "The recognition of the deformation and its degree of symmetry-breaking as the central element in defining rotational degrees of freedom opens new perspectives for generalized rotational spectra associated with deformations in many different dimensions including spin, isospin, and gauge spaces, in addition to the geometrical space of our classical world. The resulting rotational band structure may involve comprehensive families of states labeled by the different quantum numbers of the internally broken symmetries."

There are many examples of nuclear deformations [127]. The most common are the isoscalar shape deformations. Most nuclei have shapes well described

by the even-parity multipole moments (quadrupole, hexadecapole,...). Extreme quadrupole deformations have been observed in superdeformed configurations such as those shown in Figs. 10 and 12. The dramatic elongations of superdeformed states, having a very different intrinsic structure than ground-states, are excellent examples of the Jahn-Teller effect in excited (many-particle, many-hole) configurations.

It has become clear during the last few years that certain nuclei can be described in terms of intrinsic shapes with parity-breaking (odd-λ) static moments. Stable reflection-asymmetric deformation in the body-fixed frame can be attributed to octupole interaction which couples intrinsic states of oppo-

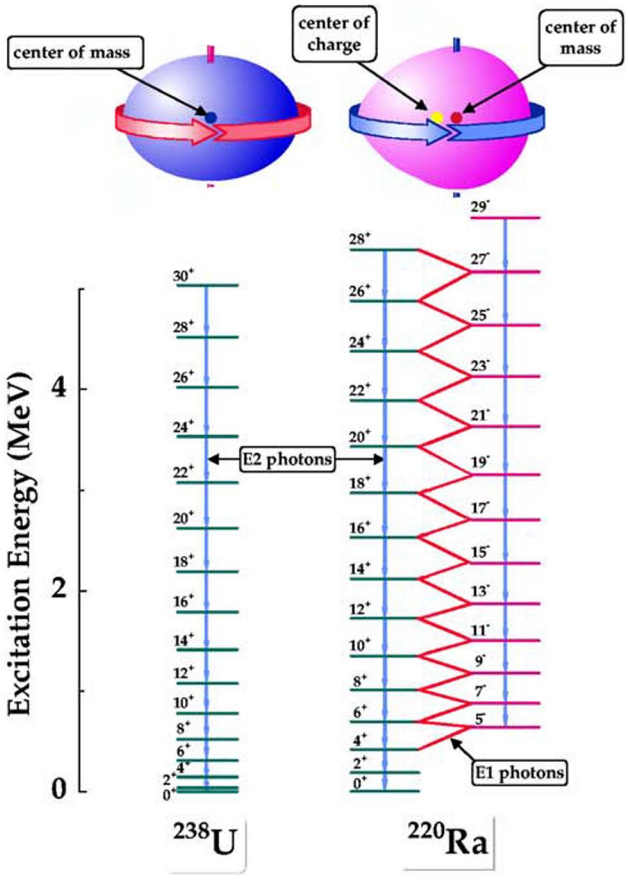

Fig. 18. Examples of nuclear collective bands. Left: ground-state band of quadrupole-deformed nucleus ^{238}U. Right: alternating-parity ground-state band of octupole-deformed nucleus ^{220}Ra.

site parity. The regions of nuclei with strong octupole correlations correspond to particle numbers around 34, 56, 88, and 134, i.e. where the maximum ΔN=3 octupole coupling occurs between the unique-parity subshell (ℓ, j) and the normal-parity subshell (ℓ-3, j-3). Experimentally, for the Ra-Th (Z∼88, N∼134) and Ba-Sm (Z∼56, N∼88) nuclei, low-lying negative-parity states, parity doublets, and alternating parity bands with enhanced E1 transitions have been established (see Ref. [128]). Figure 18 shows examples of rotational bands corresponding to quadrupole and octupole-deformed nuclear rotors.

Deformations can show up in the context of interactions other than the multipole forces. For example, for strong pairing forces, there appear deformations that can be associated with static pairing gaps defining the orientation of a nucleus in the gauge space. Here, the broken symmetry is particle number; the intrinsic wave function is not an eigenstate of the particle number operator. Interesting pairing deformations are expected in N∼Z nuclei. Strong n-p correlations are likely to produce a static moment that will lead to spontaneous breaking of isospin. The elementary excitations of such systems are represented by quasi-particles which are mixtures of protons and neutrons [129].

Interesting new deformations can appear at high-spin states. The cranking Hamiltonian, $-\boldsymbol{\omega j}$, breaks the time-reversal symmetry in the rotating reference frame. In this context, one can talk about tilted rotation (rotation around an axis which is not a principal axis of a nucleus; the reorientation angles can be considered as collective parameters) or spontaneous breaking of signature quantum number [130–133].

7 Far from stability

The uncharted regions of the (N,Z) plane contain information that can answer many questions of fundamental importance for nuclear physics: How many protons and neutrons can be clustered together by the strong interaction to form a bound nucleus? What are the proton and neutron magic numbers in the neutron-rich environment? What is the effective nucleon-nucleon interaction in a weakly bound nucleus? What are the phases of nucleonic matter? There are also related questions in the field of nuclear astrophysics. Since radioactive nuclei are produced in many astrophysical sites, knowledge of their properties is crucial to the understanding of the underlying processes. Today, the physics associated with radioactive nuclear beams (RNB) is one of the major thrusts of nuclear science worldwide.

From a theoretical point of view, exotic nuclei far from stability offer a unique test of those components of effective interactions that depend on the isospin degrees of freedom. Since the effective interaction in heavy nuclei has been adjusted to stable nuclei and to selected properties of infinite nuclear matter, it is by no means obvious that the isotopic trends far from stability, predicted by commonly used effective interactions, are correct. In models aiming at such an extrapolation, the important questions asked are: What is the density dependence of the two-body central force? What is the N/Z dependence of the one-body spin-orbit

force? What is the form of pairing interaction in weakly bound nuclei? What is the role of the medium effects and of the core polarization in the nuclear exterior (halo or skin region) where the nucleonic density is small? Similar questions are asked in connection with properties of nuclear matter, neutron droplets, and the physics of the neutron-star crust.

In many respects, weakly bound nuclei are much more difficult to treat theoretically than well-bound systems [134]. Hence, before tackling the problem of force parametrization at the extremes, one should be sure that the applied theoretical tools of the nuclear many-body problem are appropriate. The main theoretical challenge is the correct treatment of the particle continuum. For weakly bound nuclei, the Fermi energy lies very close to zero, and the decay channels must be taken into account explicitly. As a result, many cherished approaches of nuclear theory such as the conventional shell model, the pairing theory, or the macroscopic-microscopic approach must be modified. But there is also a splendid opportunity: the explicit coupling between bound states and continuum, and the presence of low-lying scattering states invite strong interplay and cross-fertilization between nuclear structure and reaction theory. Many methods developed by reaction theory can now be applied to structure aspects of loosely bound systems. Here, the representative example is the recent continuum shell-model description of the ^{16}O(p,γ)^{17}F capture reaction [135].

A significant new theme concerns shell structure near the particle drip lines. Since the isospin dependence of the effective NN interaction is largely unknown, the structure of single-particle states, collective modes, and the behavior of global nuclear properties is very uncertain in nuclei with extreme N/Z ratios. For instance, some calculations predict [134] that the shell structure of neutron drip-line nuclei is different from what is known around the beta-stability valley. According to other calculations [136], a reduction of the spin-orbit splitting in neutron-rich nuclei is expected.

Correlations due to pairing, core polarization, and clustering are crucial in weakly bound nuclei. In a drip-line system, the pairing interaction and the presence of skin excitations (soft modes) could invalidate the picture of a nucleon moving in a single-particle orbit [137,138,54,139,140]. It is expected that the low-l spectroscopic strength is dramatically broadened when approaching the neutron drip line [141,142]. In addition, since the energy of the pigmy resonance in neutron-rich nuclei is close to the neutron separation energy, the presence of soft vibrational modes is also important in the context of the astrophysical r-process [143].

A fascinating aspect of halos and skins is the presence of clustering at the nuclear ground state. It is worth noting that all known neutron halo nuclei can be described in terms of cluster structures consisting of alpha particles surrounded by neutrons. The nuclear matter calculations indicate (see, e.g., Refs. [144,145]) the presence of deuteron and alpha condensates at low densities. This suggests that the transition from a mean-field regime (corresponding to the two-fluid proton-neutron system) to the limit of weak binding (characteristic of drip-line nuclei) does not have to be smooth. Most likely, one will encounter an intermedi-

ate phase corresponding to the presence of granularities (i.e., cluster structures) in the skin region.

On the proton-rich side, recent highlights are the discovery [146] of the two-proton unbound doubly magic nucleus ^{48}Ni, the first (indirect) data on the core-breaking excitations in ^{100}Sn through the high-spin studies of ^{99}Cd (Ref. [147]), and studies of deformed proton emitters [148,149]. For a comprehensive review of challenges and opportunities in nuclear structure far from stability, I would like to refer the reader to the recent RIA White Paper [65] where many delightful examples can be found.

8 Nucleus as a finite many-body system

The atomic nucleus is a complex, finite many-fermion system of particles interacting via a complicated effective force which is strongly influenced by in-medium effects. As such, it shows many similarities to other many-body systems involving many degrees of freedom, such as molecules, clusters, grains, mesoscopic rings, quantum dots, atom condensates, and others. There are many topics that are common to all these aggregations: existence of shell structure and collective modes (e.g., vibrations in nuclei, molecules, and clusters; superconductivity in nuclei and grains), various manifestations of the large-amplitude collective motion (such as multidimensional tunneling, coexistence, and phase transitions), nonlinear phenomena (many-fermion systems are wonderful laboratories to study chaos), and the presence of dynamical symmetries.

Historically, many concepts and tools of nuclear structure theory were brought to nuclear physics from other fields. Today, thanks to the wide arsenal of methods, many ideas from nuclear physics have been applied to studies of other complex systems. There are many splendid examples of such interdisciplinary research: studies of the multidimensional tunneling and of the large-amplitude collective motion and symmetry-breaking in many-body systems, applications of the nuclear mean-field theory and its extensions to studies of static and dynamical properties of metal clusters [150,151], use of symmetry-dictated approaches to describe collective excitations of complex molecules [152], studies of supersymmetries in many-body systems [153–155], applications of the nuclear random matrix theory to various phenomena in mesoscopic systems [156–158], studies of Bose condensates [159–161], and the description of correlations in many-fermion systems [162].

A beautiful example of physics on the borderline is the treatment of finite-size effects in the description of superconductivity of ultrasmall grains [163]. As in nuclei, superconducting grains exhibit the presence of the energy gap in the spectrum, and they show the odd-even staggering of binding energies due to a blocking effect caused by the presence of an odd electron [164–167]. As seen in Fig. 19, in the presence of an external magnetic field, quasi-particle spectra of grains strongly resemble those of rotating nuclei.

A topic of great interest is the signature of classical chaos in the associated quantum system, a sub-field known as quantum chaos. A nuclear physics theory

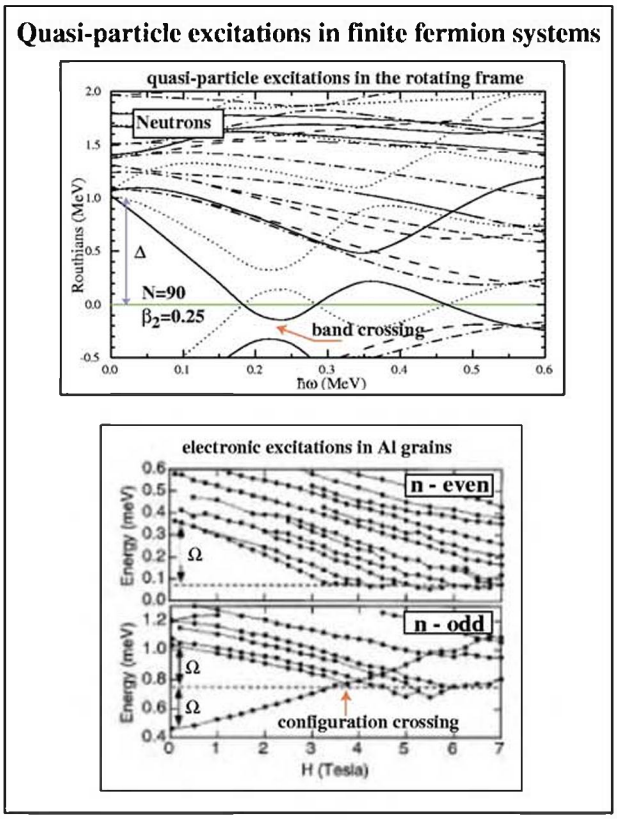

Fig. 19. Top: Quasi-particle neutron spectrum of rotating ^{160}Yb as a function of rotational frequency ω calculated within the Woods-Saxon cranking model assuming constant pairing gap Δ=1 MeV and quadrupole deformation β_2=0.25. Bottom: Measured electronic excitations in Al grains as functions of the external magnetic field H (from Ref. [163]).

(random matrix theory), developed in the 1950s and 60s to explain the statistical properties of the compound nucleus in the regime of neutron resonances [168], is now used to describe the universality of quantum chaos. Today, the random matrix theory is the basic tool of the interdisciplinary field of quantum chaos, and the atomic nucleus is still a wonderful laboratory of chaotic phenomena. Other excellent examples of interplay between chaotic and ordered motion in nuclei are parity-violation effects amplified by the chaotic environment [169], the appearance of very excited nuclear states (symmetry scars) well characterized by quantum numbers [170], and the appearance of collectivity in the many-body system governed by random two-body interactions [171–173].

The study of collective behavior, of its regular and chaotic aspects, is the domain where the unity and universality of all finite many-body systems is beautifully manifested.

9 Summary

In years to come, we shall see substantial progress in our understanding of nuclear structure – a rich and many-faceted field. An important element in this task will be to extend the study of nuclei into new domains.

There are many frontiers of today's nuclear structure. For very light nuclei, one such frontier is physics at subfemtometer distances where the internal quark-gluon structures of nucleons overlap. For heavier nuclei, the frontiers are defined by the extremes of the N/Z ratio, atomic charge and nuclear mass, and angular momentum. The journey to "the limits" is a quest for new and unexpected phenomena which await us in the uncharted territory. However, the new data are also expected to bring qualitatively new information about the effective NN interaction and hence about the fundamental properties of the nucleonic many-body system. By exploring exotic nuclei, one can magnify certain terms of the Hamiltonian which are small in "normal" nuclei, thus difficult to test. The hope is that after probing nuclear properties at the extremes, we can later improve the description of normal nuclei (at ground states, close to the valley of beta stability, etc.).

There are many experimental and theoretical suggestions pointing to the fact that the structure of exotic nuclei is different from what has been found in normal systems. New RNB facilities, together with advanced multi-detector arrays and mass/charge separators, will be essential in probing nuclei in new domains. The field is extremely rich and has a truly multidisciplinary character. Experiments with radioactive beams will make it possible to look closely into many exciting aspects of the nuclear many-body problem. A broad international community is enthusiastically using existing RNB facilities and hoping and planning for future-generation tools.

Advances in computer technology and theoretical modeling will make it possible to (i) better understand the bare NN interaction in terms of quarks and gluons, and effective interactions in complex nuclei in terms of bare forces, and to (ii) answer fundamental questions concerning nuclear dynamics. These questions on the microscopic mechanism behind the small- and large-amplitude collective motion, on the impact of the Pauli principle on nuclear collectivity, and on the origin of short-range correlations have interdisciplinary character. Particularly strong are overlaps between nuclear structure and condensed matter physics (many-body methods, superconductivity, cluster physics, physics of mesoscopic systems), atomic and molecular physics (treatment of correlations, physics of particle continuum, dynamical symmetries), nonlinear dynamics (chaotic phenomena, large-amplitude collective motion), astrophysics (nucleosynthesis, neutron stars, supernovae), fundamental symmetries physics, and, of course, computational physics. The nuclear many-body system has it all!

Acknowledgments

This research was supported by the U.S. Department of Energy under Contract Nos. DE-FG02-96ER40963 (University of Tennessee) and DE-AC05-00OR22725 with UT-Battelle, LLC (Oak Ridge National Laboratory).

References

1. W. Nazarewicz: Nucl. Phys. **A630**, 239c (1998)
2. *Nuclear Physics, the Core of Matter, the Fuel of Stars* (National Academy Press, Washington, D.C. 1999); http://www.nas.edu/bpa/reports/reports.html
3. P.J. Woods and C.N. Davids: Ann. Rev. Nucl. Part. Sci. **47**, 541 (1997)
4. B.S. Pudliner, A. Smerzi, J. Carlson, V.R. Pandharipande, S.C. Pieper, and D.G. Ravenhall: Phys. Rev. Lett. **76**, 2416 (1996).
5. A. Smerzi, D.G. Ravenhall, and V.R. Pandharipande: Phys. Rev. **C56**, 2549 (1997)
6. M.V. Stoitsov, J. Dobaczewski, P. Ring, and S. Pittel: Phys. Rev. **C61**, 034311 (2000)
7. C.J. Pethick and D.G. Ravenhall: Annu. Rev. Nucl. Part. Sci. **45**, 429 (1995)
8. R. Machleidt, F. Sammarruca, and Y. Song: Phys. Rev. **C53**, 1483 (1996)
9. R. Machleidt: Proc. Int. Conf. "Nuclear Structure'98", Gatlinburg 1998; nucl-th/9809069
10. V.G.J. Stoks, R.A.M. Klomp, C.P.F. Terheggen, and J.J. de Swart: Phys. Rev. **C49**, 2950 (1994)
11. R. Vinh Mau: this volume
12. R.B. Wiringa, V.G.J. Stoks, and R. Schiavilla: Phys. Rev. **C51**, 38 (1995)
13. K. Maltman and N. Isgur: Phys. Rev. **D29**, 952 (1984)
14. T. Barnes, S. Capstick, M.D. Kovarik, and E.S. Svanson: Phys. Rev. **C48**, 539 (1993)
15. R.B. Wiringa, S.C. Pieper, J. Carlson, and V.R. Pandharipande: Phys. Rev. **C62**, 014001 (2000)
16. S.C. Pieper: private communication 2000
17. S.C. Pieper, R.B. Wiringa, and V.R. Pandharipande: Phys. Rev. **C46**, 1741 (1992)
18. J.G. Zabolitzky: Nucl. Phys. **A228**, 272 (1974)
19. J.G. Zabolitzky: Phys. Lett. **100B**, 5 (1981)
20. K. Emrich and J.G. Zabolitzky: Nucl. Phys. **A351**, 439 (1981)
21. R.F. Bishop, E. Buendia, M.F. Flynn, and R.Guardiola: J. Phys. **G17**, 857 (1991)
22. J.H. Heisenberg and B. Mihaila: Phys. Rev. **C59**, 1440 (1999)
23. B. Mihaila and J.H. Heisenberg: Phys. Rev. Lett. **84**, 1403 (2000)
24. R. Bieber, W. Glockle, J. Golak, M.N. Harakeh, D. Huber, H. Huisman, N. Kalantar-Nayestanaki, H. Kamada, J.G. Messchendorp, A. Nogga, H. Sakai, N. Sakamoto, M. Seip, M. Volkerts, S.Y. van der Werf, and H. Witała: Phys. Rev. Lett. **84**, 606 (2000)
25. H. Witała, H. Kamada, A. Nogga, W. Glockle, Ch. Elster, and D. Huber: Phys. Rev. **C59**, 3035 (1999)
26. K.A. Brückner: in "The Many Body Problem" ed. by C. DeWitt (Wiley, New York, 1959), p. 47
27. A.L. Fetter and J.D. Walecka: "Quantum Theory of Many-Particle Systems" (McGraw-Hill, Boston, 1971)

28. P. Ring and P. Schuck: "The Nuclear Many-Body Problem" (Springer-Verlag, Berlin, 1980)
29. J.P. Elliott: Proc. Roy. Soc. (London) **A245**, 128, 562 (1958)
30. A. Arima, F. Iachello: Phys. Lett. **57B**, 39 (1975); Phys. Rev. Lett. **35**, 1069 (1975)
31. F. Iachello and I. Talmi: Rev. Mod. Phys. **59**, 339 (1987)
32. R.F. Casten and D.D. Warner: Rev. Mod. Phys. **60**, 389 (1988)
33. Contemporary Concepts in Physics, vol. 6, *Algebraic Approaches to Nuclear Structure*, R.F. Casten, P.O. Lipas, D.D. Warner, T. Otsuka, K. Heyde, and J.P. Draayer (Harwood Academic Publ., New York, 1993)
34. P. Navratil, J.P. Vary, and B.R. Barrett: Phys. Rev. Lett. **84**, 5728 (2000)
35. W.C. Haxton and C.-L. Song: Phys. Rev. Lett. **84**, 5484 (2000)
36. W.C. Haxton and T. Luu: nucl-th/0101022
37. M.J. Savage and B.R. Holstein: nucl-th/0012060
38. K. Langanke and A. Poves: Nucl. Phys. News **10**, 3 (2000)
39. R.R. Whitehead and A. Watt: Phys. Lett. **35B**, 189 (1971)
40. G. Martinez-Pinedo, A.P. Zuker, A. Poves, and E. Caurier: Phys. Rev. **C55**, 187 (1997)
41. A. Novoselsky and M. Vallieres: Phys. Rev. **C57**, R19 (1998)
42. P. Navratil and B.R. Barrett: Phys. Rev. **C57**, 562 (1998); Phys. Rev. **C57**, 3119 (1998)
43. A. Holt, T. Engeland, M. Hjorth-Jensen, and E. Osnes: Phys. Rev. **C61**, 064318 (2000)
44. E. Caurier, K. Langanke, G. Martinez-Pinedo, and F. Nowacki: Nucl. Phys. **A653**, 439 (1999)
45. G. Martinez-Pinedo, K. Langanke, and D.J. Dean: Astrophys. J. Suppl. Ser. **126**, 493 (2000)
46. A. Poves, J. Sanchez-Solano, E. Caurier, and F. Nowacki: nucl-th/0012077
47. G. Martinez-Pinedo, P. Schwerdtfeger, E. Caurier, K. Langanke, W. Nazarewicz, and T. Sohnel: nucl-th/0101026
48. A. Petrovici K.W. Schmidt, and A. Faessler: Z. Phys. **A359**, 19 (1997)
49. E. Hammaren, K.W. Schmid, and A. Faessler: Eur. Phys. J. **A2**, 371 (1998)
50. S.E. Koonin, D.J. Dean, and K. Langanke: Phys. Rep. **278**, 1 (1997); Ann. Rev. Nucl. Part. Sci. **47**, 463 (1997)
51. D.J. Dean, S.E. Koonin, G.H. Lang, W.E. Ormand, and P.B. Radha: Phys. Lett. **317B**, 275 (1993)
52. Y. Alhassid, G.F. Bertsch, D.J. Dean, and S.E. Koonin: Phys. Rev. Lett. **77**, 1444 (1996)
53. M. Honma, T. Mizusaki, and T. Otsuka: Phys. Rev. Lett. **77**, 3315 (1996)
54. T. Mizusaki, T. Otsuka, Y. Utsuno, M. Honma, and T. Sebe: Phys. Rev. **C59**, R1846 (1999)
55. C.J.G. Onderwater et al.: Phys. Rev. Lett. **81**, 2213 (1998)
56. R. Starink et al.: Phys. Lett. **474B**, 33 (2000)
57. C. Giusti, F.D. Pacati, K. Allaart, W.J.W. Geurts, W.H. Dickhoff, and H. Müther: Phys. Rev. **C57**, 1691 (1998)
58. J. Gomez del Campo, A. Galindo-Uribarri, J.R. Beene, C.J. Gross, J. F. Liang, M.L. Halbert, D.W. Stracener, D. Shapira, R.L. Varner, E. Chavez-Lomeli, and M. E. Ortiz: Phys. Rev. Lett. **86**, 43 (2001)
59. L.V. Grigorenko, R.C. Johnson, I.G. Mukha, I.J. Thompson, and M.V. Zhukov: Phys. Rev. Lett. **85**, 22 (2000)

60. J. Dobaczewski, W. Nazarewicz, and T.R. Werner: Z. Phys. **A354**, 27 (1996)
61. N. Tajima, S. Takahara, and N. Onishi: Nucl. Phys. **A603**, 23 (1996)
62. D. Hirata, K. Sumiyoshi, I. Tanihata, Y. Sugahara, T. Tachibana, and H. Toki: Nucl. Phys. **A616**, 438c (1997)
63. S.A. Fayans, S.V. Tolokonnikov, E.L. Trykov, and D. Zawischa: Nucl. Phys. **A676**, 49 (2000)
64. F. Tondeur, S. Goriely, J.M. Pearson, and M. Onsi: Phys. Rev. **C62**, 024308 (2000)
65. http://www.nscl.msu.edu/conferences/riaws00/ria-whitepaper-2000.pdf
66. *Scientific Opportunities with Fast Fragmentation Beams from RIA*, NSCL Report, March 2000. http://www.nscl.msu.edu/research/ria/whitepaper.pdf
67. A. Arima, M. Harvey, and K. Shimizu: Phys. Lett. **30B**, 517 (1969)
68. K.T. Hecht and A. Adler: Nucl. Phys. **A137**, 129 (1969)
69. J.N. Ginocchio: Phys. Rev. Lett. **78**, 436 (1997)
70. J.N. Ginocchio and D.G. Madland: Phys. Rev. **C57**, 1167 (1998)
71. J. Meng, K. Sugawara-Tanabe, S. Yamaji, P. Ring, and A. Arima: Phys. Rev. **C58**, R628 (1998)
72. M. Göppert-Mayer: Phys. Rev. **75**, 1969 (1949)
73. O. Haxel, J.H.D. Jensen, and H.E. Süss: Phys. Rev. **75**, 1766 (1949)
74. A. Bohr and B.R. Mottelson: "Nuclear Structure" (Benjamin, New York, 1975), Vol. II
75. P.K. Carroll and Kh. I. Hagim: Phys. Scr. **37**, 682 (1988)
76. D. Pansegrau, P. Reiter, D. Schwalm, H. Bauer, J. Eberth, D. Gassmann, D. Habs, T. Hartlein, F. Kock, and H.G. Thomas: Phys. Lett. **484B**, 1 (2000)
77. M.W. Drigert et al.: Nucl. Phys. **A515**, 466 (1990)
78. M. Piiparinen, P. Kleinheinz, S. Lunardi, M. Ogawa, G. de Angelis, F. Soramel, W. Meczyński, and J.Blomqvist: Z. Phys. **A337**, 387 (1990)
79. G. Racah and I. Talmi: Physica **18**, 1097 (1952)
80. M.A. Bentley et al.: J. Phys. **G17**, 481 (1991)
81. P.J. Dagnall et al.: Phys. Lett. **335B**, 313 (1994)
82. J.L. Wood, K. Heyde, W. Nazarewicz, M. Huyse, and P. van Duppen: Phys. Rep. **215**, 101 (1992)
83. K. Boretzky et al.: Phys. Lett. **384B**, 30 (1996)
84. W. Pauli: Naturwiss. **12** (1924) 741
85. H. Schüler and Th. Schmidt: Z. Phys. **94**, 457 (1935)
86. N. Bohr: Nature **137** (1936) 344
87. N. Bohr and F. Kalckar: Mat. Fys. Medd. Dan. Vid. Selsk. 14, No. 10 (1937)
88. E. Teller and J.A. Wheeler: Phys. Rev. **53**, 778 (1938)
89. L. Meitner and O.R. Frisch: Nature **143**, 239 (1939)
90. N. Bohr and J.A. Wheeler: Phys. Rev. **56**, 426 (1939)
91. J. Rainwater: Phys. Rev. **79**, 432 (1950)
92. A. Bohr: Phys. Rev. **81**, 134 (1951)
93. L.L. Foldy and F.J. Milford: Phys. Rev. **80**, 751 (1950)
94. S. Gallone and C. Salvetti: Phys. Rev. **84**, 1064 (1951)
95. S.G. Nilsson: Mat. Fys. Medd. Dan. Vid. Selsk. **29**, No. 16 (1955)
96. S.A. Moszkowski: Phys. Rev. **99**, 803 (1955)
97. K. Gottfried: Phys. Rev. **103**, 1017 (1956)
98. A. Bohr: Mat. Fys. Medd. Dan. Vid. Selsk. 26, No. 14 (1952)
99. A. Bohr and B.R. Mottelson: Kg. Danske Videnskab. Selskab, Mat.–Fys. Medd. **27**, No. 16 (1953)

100. D.L. Hill and J.A. Wheeler: Phys. Rev. **89**, 1102 (1953)
101. H.A. Jahn and E. Teller: Proc. R. Soc. London, Ser. **A161**, 220 (1937)
102. W. Nazarewicz: Int. J. Mod. Phys. **E2**, 51 (Supp. 1993)
103. W. Nazarewicz: Nucl. Phys. **A574**, 27c (1994)
104. M. Born and R.J. Oppenheimer: Ann. Physik (Leipzig) **89**, 457 (1927)
105. W. Nazarewicz: Nucl. Phys. **A557**, 489c (1993)
106. P. Ring: Proc. Workshop on *Microscopic Models in Nuclear Structure Physics*, Oak Ridge 1988, ed. by M.W. Guidry et al., (World Scientific, 1988) p. 298
107. A. Bulgac: Phys. Rev. **C41**, 2333 (1990)
108. A. Klein and N.R. Walet: Phys. Rev. **C48**, 178 (1993)
109. A. Bulgac: Phys. Rev. Lett. **67**, 965 (1991)
110. V.M. Strutinsky: Z. Phys. **A280**, 99 (1977)
111. P.-G. Reinhard and E.W. Otten: Nucl. Phys. **A420**, 173 (1984)
112. D. Schütte and J. Da Providencia: Nucl. Phys. **A282**, 518 (1977)
113. D.J. Thouless: Nucl. Phys. **22**, 78 (1961)
114. W.J. Swiatecki: in: "Proc. 2nd Int. Conf. on Nuclidic Masses", Vienna, 1963, ed. by W.H. Johnson, Jr. (Springer-Verlag, Vienna 1964), p. 58
115. V.M. Strutinsky: Nucl. Phys. **A95**, 420 (1967)
116. V.M. Strutinsky: Nucl. Phys. **A122**, 1 (1968)
117. G.G. Bunatian, V.M. Kolomietz and V.V. Strutinsky: Nucl. Phys. **A188**, 225 (1972)
118. M. Brack, J. Damgård, A.S. Jensen, H.C. Pauli, V.M. Strutinsky and C. Y. Wong: Rev. Mod. Phys. **44**, 320 (1972)
119. I. Ragnarsson and R.K. Sheline: Phys. Scr. **29**, 385 (1984)
120. R. Balian and C. Bloch: Ann. Phys. (NY) **69**, 76 (1971)
121. V.M. Strutinsky and A.G. Magner: Sov. J. Part. Nucl. **7**, 138 (1976)
122. V.M. Strutinsky, A.G. Magner, S.R. Ofengenden and T. Døssing: Z. Phys. **A283**, 269 (1977)
123. M.C. Gutzwiller: J. Math. Phys. **8** (1967) 1979; *ibid* **12**, 343 (1971)
124. K. Arita and K. Matsuyanagi: Prog. Theor. Phys. **89**, 389 (1993)
125. S.T. Belyaev: Mat. Fys. Medd. Dan. Vid. Selsk. **31** (No. 11) (1959)
126. A. Bohr: Rev. Mod. Phys. **48**, 365 (1976)
127. W. Nazarewicz and I. Ragnarsson: in: "CRC Handbook on Nuclear Decay Modes", 1993
128. P. Butler and W. Nazarewicz: Rev. Mod. Phys. **68**, 349 (1996)
129. S. Åberg, H. Flocard, and W. Nazarewicz: Ann. Rev. Nucl. Part. Sci. **40**, 439 (1990)
130. S. Frauendorf: Nucl. Phys. **A557**, 259c (1993)
131. S. Frauendorf: Rev. Mod. Phys. (to be published)
132. S. Frauendorf: Nucl. Phys. **A677**, 115 (2000)
133. V.I. Dimitrov, S. Frauendorf, and F. Dönau: Phys. Rev. Lett. **84**, 5732 (2000)
134. J. Dobaczewski and W. Nazarewicz: Phil. Trans. R. Soc. Lond. **A356**, 2007 (1998)
135. K. Bennaceur, N. Michel, F. Nowacki, J. Okołowicz, and M.Płoszajczak: Phys. Lett. **488B**, 75 (2000)
136. G.A. Lalazissis, D. Vretanar, W. Poschl, and P. Ring: Phys. Lett. **418B**, 7 (1998)
137. J. Dobaczewski, W. Nazarewicz, T.R. Werner, J.-F. Berger, C.R. Chinn, and J. Dechargé: Phys. Rev. **C53**, 2809 (1996)
138. W. Pöschl, D. Vretenar, G.A. Lalazissis, and P. Ring: Phys. Rev. Lett. **79**, 3841 (1997)
139. M. Bender: Phys. Rev. **C61**, 031302 (2000)

140. F. Barranco, R.A. Broglia, G. Colo, and E. Vigezzi: nucl-th/0005073
141. S.A. Fayans, S.V. Tolokonnikov, and D. Zawischa: Phys. Lett. **491B**, 245 (2000)
142. H. Lenske, F. Hofmann, and C. Klein: these proceedings
143. S. Goriely: Phys. Lett. **436B**, 10 (1998)
144. G. Röpke, A. Schnell, P. Schuck, and P. Nozières: Phys. Rev. Lett. **80**, 3177 (1998)
145. M. Beyer, S.A. Sofianos, C. Kuhrts, G. Röpke, and P. Schuck: Phys. Lett. **488B**, 247 (2000)
146. B. Blank et al.: Phys. Rev. Lett. **84**, 1116 (2000)
147. M. Lipoglavsek et al.: to be published
148. A.A. Sonzogni, C.N. Davids, P.J. Woods, D. Seweryniak, M.P. Carpenter, J.J. Ressler, J. Schwartz, J. Uusitalo, and W.B. Walters: Phys. Rev. Lett. **83**, 1116 (1999)
149. A.T. Kruppa, B. Barmore, W. Nazarewicz, and T. Vertse: Phys. Rev. Lett. **84** 4549 (2000)
150. W. Satuła, J. Dobaczewski, and W. Nazarewicz: Phys. Rev. Lett. **81**, 3599 (1998)
151. G.F. Bertsch and K. Yabana: Nucl. Phys. **A649**, 423c (1999)
152. F. Iachello: Nucl. Phys. **A560**, 23 (1993)
153. A. Metz, J. Jolie, G. Graw, R. Hertenberger, J. Groger, C. Gunther, N. Warr, and Y. Eisermann: Phys. Rev. Lett. **83**, 1542 (1999)
154. J. Groger, J. Jolie, R. Krucken, C.W. Beausang, M. Caprio, R.F. Casten, J. Cederkall, J.R. Cooper, F. Corminboeuf, L. Genilloud, G. Graw, C. Gunther, M. de Huu, A.I. Levon, A. Metz, J.R. Novak, N. Warr, and T. Wendel: Phys. Rev. C **62**, 064304 (2000)
155. F. Iachello: these proceedings
156. Y. Alhassid and H. Attias: Phys. Rev. Lett. **76**, 1711 (1996)
157. Y. Alhassid, M. Gökcedag, and A.D. Stone. Phys. Rev. B **58**, 7524 (1998)
158. T. Rupp, H.A. Weidenmüller, and J. Richert: Phys. Lett. **483B**, 331 (2000); Erratum Phys. Lett. **484B**, 376 (2000)
159. R. Balian, H. Flocard, and M. Véneroni: cond-mat/9802006
160. B. Mottelson: Phys. Rev. Lett. **83**, 2695 (1999)
161. G.F. Bertsch and T. Papenbrock: Phys. Rev. Lett. **83**, 5412 (1999)
162. J.N. Ginocchio and W.C. Haxton: Phys. Rev. Lett. **77**, 1568 (1996)
163. D.C. Ralph, C.T. Black, and M. Tinkham: Phys. Rev. Lett. **78**, 4087 (1997)
164. R. Rossignoli, N. Canosa, and P. Ring: Phys. Rev. Lett. **80**, 1853 (1998)
165. J. Dukelsky and G.G. Dussel: Phys. Rev. **C59**, R3005 (1999)
166. R. Balian, H. Flocard, and M. Véneroni: Phys. Rep. **317**, 251 (1999)
167. G. Sierra, J. Dukelsky, G.G. Dussel, J. von Delft, and F. Braun: Phys. Rev. B **61**, R11890 (2000)
168. F.J. Dyson and M.L. Mehta: J. Math. Phys. **4**, 701 (1963)
169. H.A. Weidenmüller: Nucl. Phys. **A574**, 75c (1994)
170. H.A. Weidenmüller: Nucl. Phys. **A520**, 509c (1990)
171. C.W. Johnson, G.F. Bertsch, D.J. Dean, and I. Talmi: Phys. Rev. Lett. **80**, 2749 (1998)
172. C.W. Johnson, G.F. Bertsch, D.J. Dean, and I. Talmi: Phys. Rev. **C61**, 014311 (2000)
173. D. Mulhall, A. Volya, V. Zelevinsky: Phys. Rev. Lett. **85**, 4016 (2000)

The interacting boson model

Francesco Iachello

Center for Theoretical Physics, Sloane Laboratory, Yale University,
New Haven, CT 06520-8120

Abstract. The Interacting Boson Model is briefly reviewed and placed in the context of existing Nuclear Structure Models.

1 Introduction

The atomic nucleus is a collection of strongly interacting particles (protons and neutrons). The number of particles ranges from $A = 1$ (the nucleon) to $A \sim 300$. *Ab initio* calculations of nuclei with $A = 2, 3$ have been feasible for some time. With recent advances in computing capabilities, *ab initio* calculations of light nuclei up to $A = 8$ have been done. The problem, however, remains how to compute properties of heavy nuclei. Beyond $A = 8$, the computing time increases tremendously and it may be difficult, in the foreseable future, to go beyond $A = 16$. A possible scheme to calculate properties of nuclei is the exploitation of the average field produced by the nucleons themselves. In 1949, the Independent Particle Model [1], [2] was introduced. In this model, each nucleon moves in the field due to all other particles. The Independent Particle Model is not sufficient to describe nuclear spectra, except in some very special cases (one particle outside a major closed shell). One needs to introduce correlations (two-body, three-body,...). This leads to the *Nuclear Shell Model.* The Shell Model, of which in 1999 the 50th anniversary was celebrated, describes properties of nuclei in terms of a Hamiltonian (in second quantized from)

$$H = E_0 + \sum_i \eta_i a_i^\dagger a_i + \frac{1}{2} \sum_{ii'kk'} v_{ii'kk'} a_i^\dagger a_k^\dagger a_{i'} a_{k'}. \tag{1}$$

This is the Hamiltonian of an assembly of interacting fermions with two-body interactions. The η_i's represent the single particle energies in the average field and the $v_{ii'kk'}$'s represent two-body interactions. The field is assumed to be central and often approximated with a harmonic oscillator. A better approximation is to use a Woods-Saxon well

$$V(r) = \frac{V_0}{1 + \exp\left(\frac{r - r_0}{a}\right)}. \tag{2}$$

Both in the harmonic oscillator and in more realistic potentials, the single particle levels cluster into shells (hence the name). A nomenclature often used to describe the correlations is to call particle-particle correlations the interactions

J.M. Arias and M. Lozano (Eds.): LNP 581, pp. 141–154, 2001.
© Springer-Verlag Berlin Heidelberg 2001

between particles in the same major shell, and particle-hole correlations the interactions between particles occupying different major shells. Out of these correlations, there emerge a variety of collective modes, which can be roughly divided into two main categories: (i) High-lying modes and (ii) Low-lying modes. The high-lying modes arise from particle-hole correlations ($1-2\ \hbar\omega$ excitations in the harmonic oscillator approximation) and are usually called giant resonances. The low-lying modes appear to be of two types:

(a) Shape modes. These are mostly due to particle-particle correlations. A phenomenogical description of these modes was put forward in 1952 [3]. In this description, usually referred to as the *Collective Model*, the nucleus is described as a liquid drop with a shape. The shape variables are the dynamical variables and all operators are written in terms of those. The Hamiltonian, for example, is written as

$$H = -\frac{\hbar^2}{2B}\left[\frac{1}{\beta^4}\frac{\partial}{\partial\beta}\beta^4\frac{\partial}{\partial\beta} + \frac{1}{\beta^2\sin 3\gamma}\frac{\partial}{\partial\gamma}\sin 3\gamma\frac{\partial}{\partial\gamma} - \frac{1}{4\beta^2}\sum_{\kappa}\frac{Q_\kappa^2}{\sin^2(\gamma-\frac{2}{3}\pi\kappa)}\right] + V(\beta,\gamma). \tag{3}$$

Here β,γ are the shape variables and the Q_κ's are the components of the angular momentum written in terms of Euler angles.

(b) Cluster modes. These are mostly due to particle-hole correlations but with many $\hbar\omega$ quanta of excitations. A phenomenological model for these modes had been introduced in the 1930's [4]. It was re-introduced in 1958 [5]. In this description, usually referred to as the *Cluster Model*, the nucleus is described as an assembly of clusters, the most notable cluster being the α-particle. The Hamiltonian is

$$H = \sum_i \frac{p_i^2}{2m_i} + \sum_{ik} V\left(\boldsymbol{r}_i - \boldsymbol{r}_k\right) \tag{4}$$

where the sum goes over all clusters.

An important problem in nuclear structure physics in the last 30 years has been how to derive collective modes from the Shell Model. A possible approach is to find the eigenvalues and eigenstates of the Shell Model Hamitonian by numerical methods. Inputs into these calculations are: (i) The single-particle energies, η_i. These can be either taken as empirical quantities to be fitted from experiment or from some theoretical estimate such as mean field theories. (ii) The two-body matrix elements, $v_{ii'kk'}$. Again these can be taken either as empirical quantities or from a theory, such as G-matrix. There are two types of numerical solutions that one can attempt: (a) Exact diagonalization. Several computer programs have been written thoughout the years (OXBASH,ANTOINE,...). These calculations are limited by the size of matrices to diagonalize. The present limit is $A \sim 50$, size $\sim 20\times 10^6$. (b) Montecarlo methods (QMC,...). There is no limitation here in the size of matrices. The only limitation is given by the size of computers and by computing time. For both methods there is a problem of interpretation. How to understand a wave function with $> 10^6$ components or a random wave function?

An analysis of nuclear spectra has revealed that the majority of nuclei have low-lying spectra of collective quadrupole type, some nuclei have low-lying spectra of cluster type and few nuclei have spectra of single particle type. Although it is difficult to quantify this statement, roughly speaking, $\sim 90\%$ of nuclei have collective quadrupole type, $\sim 5\%$ have cluster type and $\sim 5\%$ have single particle type. An understanding of nuclear structure requires foremost an understanding of collective quadrupole features. A scheme for this understanding was put forward in 1977 [6] and is based on the special nature of the particle-particle correlations in nuclei. The residual interaction between two identical particles is large ($\sim 1.5MeV$) and attractive when the two particles couple to angular momentum $J = 0$, is moderate and attractive ($\sim 0.5MeV$) when the two particles couple to angular momentum $J = 2$, and either small or repulsive for larger values of J. Hence a good approximation is that of introducing Cooper-like pairs in nuclei, S-pairs with angular momentum $J = 0$ and D-pairs with angular momentum $J = 2$. These pairs can be written as a superposition of pairs in various single particle orbitals

$$\begin{aligned} S^\dagger &= \sum_j \alpha_j \left(a_j^\dagger \times a_j^\dagger\right)_0^{(0)}, \\ D_\mu^\dagger &= \sum_{jj'} \beta_{jj'} \left(a_j^\dagger \times a_{j'}^\dagger\right)_\mu^{(2)}. \end{aligned} \tag{5}$$

A bosonization of the pairs leads then to the *Interacting Boson Model*. In the last 25 years this model has been used extensively to discuss properties of nuclei with collective character. In these lectures a brief description of the model will be given [7].

2 The interacting boson model (IBM-1)

The Interacting Boson Model is a model of even-even nuclei in which the basic constituents are nucleon pairs (no distinction between protons and neutrons) treated as bosons [8], [9].

2.1 Building blocks

The building blocks of the model are bosons with angular momentum and parity $J^P = 0^+$ (s-boson) and $J^P = 2^+$ (d-boson). It is convenient to introduce creation and annihilation operators

$$\begin{aligned} &s^\dagger, d_\mu^\dagger \quad (\mu = 0, \pm 1, \pm 2), \\ &s, d_\mu \quad (\mu = 0, \pm 1, \pm 2). \end{aligned} \tag{6}$$

The six (one+five) operators s, d can be denoted by

$$b_\alpha^\dagger, b_\alpha \quad (\alpha = 1, ..., 6). \tag{7}$$

These operators satisfy Bose commutation relations

$$\begin{aligned} \left[b_\alpha, b^\dagger_{\alpha'}\right] &= \delta_{\alpha\alpha'}; \\ [b_\alpha, b_{\alpha'}] &= \left[b^\dagger_\alpha, b^\dagger_{\alpha'}\right] = 0. \end{aligned} \tag{8}$$

In terms of these operators, a basis can be constructed as

$$\mathcal{B}: \quad \frac{1}{\mathcal{N}} b^\dagger_\alpha b^\dagger_{\alpha'} \ldots \mid 0\rangle, \tag{9}$$

where $\mathcal{N}$ is a normalization factor. For a state with N bosons, there are N creation operators. The vacuum is denoted by $\mid 0\rangle$. The bososn number N is taken to be the number of pairs in the valence shell. For example, for ${}^{152}_{62}Sm_{90}$, the nearest closed shells are at 50 (proton) and 82 (neutron). There are thus 12 valence protons and 8 valence neutrons for a total of $N = 10$ pairs. Beyond the middle of the shell, one makes use of particle-hole conjugation and counts the number of hole pairs. For example, for ${}^{134}_{56}Ba_{78}$, the nearest closed shells are at 50 (proton) and 82 (neutron). There are thus 6 valence protons and 4 hole valence neutrons for a total of $N = 5$ pairs. Quite often, a bar is placed over the number of holes, $\bar{4}$, to distinguish them from particles.

2.2 Physical operators

The hamiltonian operator. The Hamiltonian operator when written in terms of creation and annihilation operators has the form

$$H = E_0 + \sum_\alpha \varepsilon_\alpha b^\dagger_\alpha b_\alpha + \sum_{\alpha\alpha'\beta\beta'} \frac{1}{2} u_{\alpha\alpha'\beta\beta'} b^\dagger_\alpha b^\dagger_{\alpha'} b_\beta b_{\beta'}. \tag{10}$$

This Hamiltonian contains single boson energies and two-body boson-boson interactions. In recent years, three and four body interactions have been added.

Transition operators. Transition operators can be written in a similar fashion

$$T = t_0 + \sum_{\alpha\beta} t_{\alpha\beta} b^\dagger_\alpha b_\beta. \tag{11}$$

These operators contain only one-body terms. In recent years, two-body terms have also been added. Both operators, Hamiltonian and transition, are number conserving, in view of the interpretation of bosons as pairs of particles.

2.3 Lie algebra

Although not necessary, it has been found convenient to rewrite the problem in group theoretic language by introducing the elements of a Lie algebra

$$\mathcal{G}: \qquad G_{\alpha\beta} = b^\dagger_\alpha b_\beta \tag{12}$$

satisfying commutation relations

$$[G_{\alpha\beta}, G_{\gamma\delta}] = G_{\alpha\delta}\delta_{\beta\gamma} - G_{\gamma\beta}\delta_{\delta\alpha}. \tag{13}$$

Any set of elements $X_a \in \mathcal{G}$ is said to form a Lie algebra if it satisfies

$$[X_a, X_b] = \sum_c c_{ab}^c X_c \tag{14}$$

together with the Jacobi identity

$$[X_a, [X_b, X_c]] + [X_b, [X_c, X_a]] + [X_c, [X_a, X_b]] = 0. \tag{15}$$

The coefficients c_{ab}^c are called Lie structure constants. In this case, the Lie algebra is $U(6)$. Any operator can be written in terms of elements of $U(6)$

$$\begin{aligned} H &= E_0 + \sum_{\alpha\beta} \varepsilon'_{\alpha\beta} G_{\alpha\beta} + \sum_{\alpha\alpha'\beta\beta'} \frac{1}{2} u_{\alpha\alpha'\beta\beta'} G_{\alpha\beta} G_{\alpha'\beta'}, \\ T &= t_0 + \sum_{\alpha\beta} t_{\alpha\beta} G_{\alpha\beta}. \end{aligned} \tag{16}$$

2.4 Racah form

It is also convenient to introduce spherical tensors. For creation and annihilation operators one first introduces the operators

$$b^\dagger_{\ell,m}, \quad b_{\ell,m} \quad (\ell = 0, 2; -\ell \leq m \leq +\ell) \tag{17}$$

satisfying commutation relations

$$\begin{aligned} \left[b_{\ell,m}, b^\dagger_{\ell',m'}\right] &= \delta_{\ell\ell'}\delta_{mm'}, \\ [b_{\ell,m}, b_{\ell',m'}] &= \left[b^\dagger_{\ell,m}, b^\dagger_{\ell',m'}\right] = 0. \end{aligned} \tag{18}$$

Operators that transform as spherical tensors are

$$\begin{aligned} b^\dagger_{\ell,m} \\ \tilde{b}_{\ell,m} = (-)^{\ell+m} b_{\ell,-m}. \end{aligned} \tag{19}$$

Note the phase and the change of sign of the magnetic component. The elements of the Lie algebra of $U(6)$ can be written in terms of spherical tensors as

$$G^{(k)}_\kappa(\ell, \ell') = \left[b^\dagger_\ell \times \tilde{b}_{\ell'}\right]^{(k)}_\kappa; \quad (\ell, \ell' = 0, 2). \tag{20}$$

This form is called Racah form.

2.5 Physical operators in Racah form

Having introduced spherical tensors, one can exploit the rotational invariance of the problem to write the Hamiltonian in the form

$$
\begin{aligned}
H = & E_0 + \varepsilon_s \left(s^\dagger \cdot \tilde{s}\right) + \varepsilon_d \left(d^\dagger \cdot \tilde{d}\right) \\
& + \sum_{L=0,2,4} \frac{1}{2} (2L+1)^{1/2} c_L \left[\left[d^\dagger \times d^\dagger\right]^{(L)} \times \left[\tilde{d} \times \tilde{d}\right]^{(L)}\right]_0^{(0)} \\
& + \frac{1}{\sqrt{2}} v_2 \left[\left[d^\dagger \times d^\dagger\right]^{(2)} \times \left[\tilde{d} \times \tilde{s}\right]^{(2)} + \left[d^\dagger \times s^\dagger\right]^{(2)} \times \left[\tilde{d} \times \tilde{d}\right]^{(2)}\right]_0^{(0)} \\
& + \frac{1}{2} v_0 \left[\left[d^\dagger \times d^\dagger\right]^{(0)} \times \left[\tilde{s} \times \tilde{s}\right]^{(0)} + \left[s^\dagger \times s^\dagger\right]^{(0)} \times \left[\tilde{d} \times \tilde{d}\right]^{(0)}\right]_0^{(0)} \\
& + u_2 \left[\left[d^\dagger \times s^\dagger\right]^{(2)} \times \left[\tilde{d} \times \tilde{s}\right]^{(2)}\right]_0^{(0)} + \frac{1}{2} u_0 \left[\left[s^\dagger \times s^\dagger\right]^{(0)} \times \left[\tilde{s} \times \tilde{s}\right]^{(0)}\right]_0^{(0)} \quad (21)
\end{aligned}
$$

Furthermore, one can exploit number conservation, $N = n_s + n_d$, to eliminate n_s from H,

$$
\begin{aligned}
H = & E_0' + \varepsilon \left(d^\dagger \cdot \tilde{d}\right) \\
& + \sum_{L=0,2,4} \frac{1}{2} (2L+1)^{1/2} c_L' \left[\left[d^\dagger \times d^\dagger\right]^{(L)} \times \left[\tilde{d} \times \tilde{d}\right]^{(L)}\right]_0^{(0)} \\
& + \frac{1}{\sqrt{2}} v_2 \left[\left[d^\dagger \times d^\dagger\right]^{(2)} \times \left[\tilde{d} \times \tilde{s}\right]^{(2)} + \left[d^\dagger \times s^\dagger\right]^{(2)} \times \left[\tilde{d} \times \tilde{d}\right]^{(2)}\right]_0^{(0)} \\
& + \frac{1}{2} v_0 \left[\left[d^\dagger \times d^\dagger\right]^{(0)} \times \left[\tilde{s} \times \tilde{s}\right]^{(0)} + \left[s^\dagger \times s^\dagger\right]^{(0)} \times \left[\tilde{d} \times \tilde{d}\right]^{(0)}\right]_0^{(0)} . \quad (22)
\end{aligned}
$$

This Hamiltonian contains *six* independent parameters: ε, c_L' (L=0,2,4), v_L (L=0,2).

2.6 Analytic solutions

In some cases, the eigenvalue problem for H can be solved in closed analytic form. These special cases are called dynamic symmetries. These situations occur when H does not contain all the elements of the algebra $\mathcal{G}$ but only certain operators called invariant (or Casimir) operators of $\mathcal{G}$ and its subalgebra chains $\mathcal{G} \supset \mathcal{G}' \supset \mathcal{G}'' \supset \ldots$

$$H = f(C_i). \quad (23)$$

A Casimir operator is an operator that commutes with all the elements of the algebra

$$[C, X_a] = 0 \quad \text{for} \quad X_a \in \mathcal{G}. \quad (24)$$

These cases are important because they provide benchmarks for comparison with data. In the Interacting Boson Model, there are three (and only three) such situations corresponding to the group chains

$$\begin{aligned} &U(6) \supset U(5) \supset SO(5) \supset SO(3) \supset SO(2), \quad (I) \\ &U(6) \supset SU(3) \supset SO(3) \supset SO(2), \qquad (II) \\ &U(6) \supset SO(6) \supset SO(5) \supset SO(3) \supset SO(2). \quad (III) \end{aligned} \tag{25}$$

Chain I. U(5). The energy eigenvalues for this chain can be written as

$$E^{(I)}(N, n_d, v, n_\Delta, L, M_L) = E_0 + \varepsilon n_d + \alpha n_d(n_d+4) + \beta v(v+3) + \gamma L(L+1). \tag{26}$$

This energy eigenvalue describes the levels of a five-dimensional anharmonic vibrator. An experimental example of a nucleus described by this formula is ${}^{110}_{48}Cd_{62}$.

Chain II. SU(3). The energy eigenvalues for this chain can be written as

$$E^{(II)}(N, \lambda, \mu, K, L, M_L) = E_0 + \kappa(\lambda^2 + \mu^2 + \lambda\mu + 3\lambda + 3\mu) + \kappa' L(L+1). \tag{27}$$

This formula describes the spectrum of an axial rotor. An experimental example of a nucleus described by this formula is ${}^{156}_{64}Gd_{92}$.

Chain III. SO(6). The energy eigenvalues for this chain can be written as

$$E^{(III)}(N, \sigma, \tau, \nu_\Delta, L, M_L) = E_0 + A\sigma(\sigma+4) + B\tau(\tau+3) + CL(L+1). \tag{28}$$

This formula describes a so-called γ-unstable rotor. An experimental example of a nucleus described by this formula is ${}^{196}_{78}Pt_{118}$.

2.7 Numerical solutions

In the majority of cases, the Hamiltonian H must be diagonalized numerically. A computer program, called PHINT , has been written for this purpose. This program is available from zamfir@galileo.physics.yale.edu. A Hamiltonian often used, called consistent-Q Hamiltonian [10] , is

$$\begin{aligned} H &= E_0 + \varepsilon \hat{n}_d + c_1 \hat{L} \cdot \hat{L} + c_2 \hat{Q}^\chi \cdot \hat{Q}^\chi \\ \hat{Q}^\chi &= \left[d^\dagger \times \tilde{s} + s^\dagger \times \tilde{d} \right] + \chi \left[d^\dagger \times \tilde{d} \right]^{(2)}. \end{aligned} \tag{29}$$

This Hamiltonian contains four parameters. However, the parameter c_1 does not affect the wave functions since the operator $\hat{L} \cdot \hat{L}$ is diagonal. The structure of nuclei described by this Hamiltonian is thus determined only by the three parameters ε, c_2 and χ. Furthermore, it is possible to scale energies and consider as parameters only the ratio $\xi = \varepsilon/c_2$ and χ. The situation can then be conveniently represented in a two-dimensional plot, called a symmetry triangle. Each point in the triangle is characterized by a value of ξ and χ. This triangle represents then a phase diagram of nuclei. A relatively simple global classsification of nuclei is then possible.

2.8 Geometrical aspects

An alternative description of collective quadrupole states in nuclei is in terms of shape variables (Collective Model). A connection between the Collective Model and the Interacting Boson Model can be obtained by associating to the Interacting Boson Model a geometry. This association is done by introducing intrinsic or coherent states. The ground intrinsic or coherent state is

$$| N;\alpha_\mu\rangle = \left(s^\dagger + \sum_\mu \alpha_\mu d^\dagger_\mu\right)^N | 0\rangle \tag{30}$$

where the α_μ ($\mu = 0, \pm 1, \pm 2$) are five complex variables (coordinates and momenta). Instead of α_μ one can use three Euler angles $\theta_1, \theta_2, \theta_3$ and two intrinsic variables β, γ (Bohr variables). The intrinsic state can then be written as

$$| N;\beta,\gamma\rangle = \{s + \beta\left[\cos\gamma d^\dagger_0 + \frac{1}{\sqrt{2}}\sin\gamma\left(d^\dagger_{+2} + d^\dagger_{-2}\right)\right]\}^N | 0\rangle. \tag{31}$$

The space of the Interacting Boson Model can then be connected with that of the Collective Model, by plotting a surface

$$R = R_0\left[1 + \sum_\mu \alpha_\mu Y_{2\mu}(\theta,\varphi)\right]. \tag{32}$$

The Interacting Boson Model Hamiltonian can be viewed as a quantization of the Bohr Hamiltonian of Eq.(3). Its three dynamic symmetries correspond to the potentials

$$\begin{aligned} &V(\beta,\gamma) \simeq k\beta^2 \qquad (I) \\ &V(\beta,\gamma) \simeq k\left(\beta - \beta_0\right)^2 + k'(\cos 3\gamma - 1) \qquad (II) \\ &V(\beta,\gamma) \simeq k(\beta - \beta_0)^2 \qquad (III). \end{aligned} \tag{33}$$

2.9 Summary

In summary, the Interacting Boson Model:

(i) provides a classification of nuclear spectra with collective quadrupole character. The classification consists in three symmetries (I),(II),(III) and four transitional classes (A),(B),(C),(D).

(ii) provides an interpretation of nuclear spectra in terms of shape variables.

3 The proton-neutron interacting boson model (IBM-2)

A better description of even-even nuclei can be obtained by introducting explicitly proton and neutron degrees of freedom. This is because the two-body correlations in the $T = 0$ channel have different behavior than those in the $T = 1$ channel. In the proton-neutron Interacting Boson Model the basic constituents are proton pairs and neutron pairs treated as bosons.

3.1 Building blocks

It is convenient also here to introduce boson creation and annihilation operators

$$\begin{aligned} &s_\pi^\dagger, d_{\pi,\mu}^\dagger \quad ; s_\pi, d_{\pi,\mu} \\ &s_\nu^\dagger, d_{\nu,\mu}^\dagger \quad ; s_\nu, d_{\nu,\mu}. \end{aligned} \tag{34}$$

The six+six operators can be denoted by

$$b_{\rho,\alpha}^\dagger \quad ; b_{\rho,\alpha} \quad ; \rho = \pi, \nu; \alpha = 1, ..., 6 \tag{35}$$

and satisfy commutation relations

$$\begin{aligned} \left[b_{\rho,\alpha}, b_{\rho',\alpha'}^\dagger\right] &= \delta_{\rho\rho'}\delta_{\alpha\alpha'} \\ [b_{\rho,\alpha}, b_{\rho',\alpha'}] &= \left[b_{\rho,\alpha}^\dagger, b_{\rho',\alpha'}^\dagger\right] = 0. \end{aligned} \tag{36}$$

The basis $\mathcal{B}$ is now constructed with proton and neutron bosons

$$\mathcal{B}: \quad \frac{1}{\mathcal{N}} b_{\pi,\alpha}^\dagger b_{\pi,\alpha'}^\dagger ... b_{\nu,\alpha}^\dagger b_{\nu,\alpha'}^\dagger ... \mid 0\rangle. \tag{37}$$

The number of proton and neutron bosons, N_π and N_ν, is the number of valence proton and neutron pairs. Thus , for ${}^{152}_{62}Sm_{90}$, $N_\pi = \frac{1}{2}(62 - 50) = 6, N_\nu = \frac{1}{2}(90 - 82) = 4$.

3.2 Physical operators

Hamiltonian operator. The Hamiltonian operator is

$$H = H_\pi + H_\nu + V_{\pi\nu} \tag{38}$$

where

$$\begin{aligned} H_\rho &= E_0^\rho + \sum_\alpha \varepsilon_\alpha^\rho b_{\rho,\alpha}^\dagger b_{\rho,\alpha} + \sum_{\alpha\alpha'\beta\beta'} \frac{1}{2} u_{\alpha\alpha'\beta\beta'}^\rho b_{\rho,\alpha}^\dagger b_{\rho,\alpha'}^\dagger b_{\rho,\beta} b_{\rho,\beta'}; \qquad \rho = \pi, \nu \\ V_{\pi\nu} &= \sum_{\alpha\alpha'\beta\beta'} w_{\alpha\alpha'\beta\beta'} b_{\pi,\alpha}^\dagger b_{\pi,\beta}^\dagger b_{\nu,\alpha'} b_{\nu,\beta'}. \end{aligned} \tag{39}$$

Transition operators. Similarly, the transition operators are

$$T = T_\pi + T_\nu \tag{40}$$

with

$$T_\rho = t_0^\rho + \sum_{\alpha\beta} t_{\alpha\beta}^\rho b_{\rho,\alpha}^\dagger b_{\rho,\beta} + ...; \qquad \rho = \pi, \nu. \tag{41}$$

3.3 Coupled Lie algebras

The Interacting Boson Model-2 can also be written in terms of Lie algebras by introducing the bilinear products of creation and annihilation operators

$$\begin{aligned} \mathcal{G}_\pi: \quad & G^\pi_{\alpha\beta} = b^\dagger_{\pi,\alpha} b_{\pi,\beta} \qquad (\alpha,\beta = 1,...,6)\,, \\ \mathcal{G}_\nu: \quad & G^\nu_{\alpha\beta} = b^\dagger_{\nu,\alpha} b_{\nu,\beta} \qquad (\alpha,\beta = 1,...,6). \end{aligned} \tag{42}$$

Since proton and neutron operators commute, the total Lie algebra is the direct sum of the Lie algebras

$$\mathcal{G} = \mathcal{G}_\pi \oplus \mathcal{G}_\nu = U_\pi(6) \oplus U_\nu(6). \tag{43}$$

If one wishes, one may introduce a formalism similar to isospin but for bosons, called F-spin ,

$$\begin{aligned} |\,\pi\rangle &= |\,\frac{1}{2}, +\frac{1}{2}\rangle \\ |\,\nu\rangle &= |\,\frac{1}{2}, -\frac{1}{2}\rangle. \end{aligned} \tag{44}$$

In this formalism, $U(6) \otimes U_F(2)$, wave functions are denoted by

$$|\,\psi\rangle = |\,L, M_L; F, M_F\rangle. \tag{45}$$

3.4 Analytic solutions

Coupled systems have a wealth of dynamic symmetries and hence of analytic solutions. Some of these are the same as before

$$\begin{array}{lll} U_\pi(6) \supset U_\pi(5) & \searrow & \\ & & U_{\pi+\nu}(5) \supset SO_{\pi+\nu}(5) \supset SO_{\pi+\nu}(3) \supset SO_{\pi+\nu}(2) \\ U_\nu(6) \supset U_\nu(5) & \nearrow & \end{array}$$

$$\begin{array}{lll} U_\pi(6) \supset SU_\pi(3) & \searrow & \\ & & SU_{\pi+\nu}(3) \supset SO_{\pi+\nu}(3) \supset SO_{\pi+\nu}(2) \\ U_\nu(6) \supset SU_\nu(3) & \nearrow & \end{array}$$

$$\begin{array}{lll} U_\pi(6) \supset SO_\pi(6) & \searrow & \\ & & SO_{\pi+\nu}(6) \supset SO_{\pi+\nu}(5) \supset SO_{\pi+\nu}(3) \supset SO_{\pi+\nu}(2) \\ U_\nu(6) \supset SO_\nu(6) & \nearrow & \end{array}$$

but new cases also occur

$$\begin{array}{ccc} U_\pi(6) \supset SU_\pi(3) & & \\ & \searrow & \\ & & SU^*_{\pi+\nu}(3) \supset SO_{\pi+\nu}(3) \supset SO_{\pi+\nu}(2) \\ & \nearrow & \\ U_\nu(6) \supset SU_\nu(3) & & \end{array}$$

The last situation describes triaxial rotors and is not encountered in IBM-1.

3.5 Numerical solutions

A computer program, called NPBOS , has been written to diagonalize the IBM-2 Hamiltonian. This program is available from otsuka@phys.s.u-tokyo.ac.jp.

A Hamiltonian often used, called Talmi Hamiltonian , is

$$H = E_0 + \varepsilon\,(\hat{n}_{d_\pi} + \hat{n}_{d_\nu}) + \kappa \hat{Q}^{\chi_\pi}_\pi \cdot \hat{Q}^{\chi_\nu}_\nu + \lambda \hat{M}_{\pi\nu}. \tag{46}$$

This Hamiltonian is characterized by 5 parameters, $\varepsilon, \kappa, \chi_\pi, \chi_\nu, \lambda$. The parameter λ sets the scale of the mixed symmetry states to be discussed in the subsection below. The structure of the totally symmetric states is determined by 4 parameters. Apart from a scale there are thus only three independent parameters $\varepsilon/\kappa, \chi_\pi, \chi_\nu$. A phase diagram of IBM-2 can then be constructed by means of a tetrahedron. At the vertices of this tetrahedron are the four symmetries of IBM-2, denoted by the first combined subalgebra in the chain, $U(5), SU(3), SO(6)$ and $SU^*(3)$. Other cases are points inside the tetrahedron. A complete classification of nuclei is then possible within the framework of IBM-2.

3.6 Mixed symmetry states

The explicit introduction of proton and neutron degrees of freedom gives rise to a new class of states, called mixed symmetry states. The occurrence of this class can be seen by taking the tensor product

$$[N_\pi] \otimes [N_\nu] = \sum_{k=1}^{N_\nu} \oplus\, [N_\pi + N_\nu - k, k]\,, \qquad \text{if } \; N_\pi \geq N_\nu. \tag{47}$$

For example,

$$[1] \otimes [1] = [2] \oplus [11]\,. \tag{48}$$

The states of two non-identical bosons, are either totally symmetric, [2], or antisymmetric [11]. The symmetric states are the same as before (IBM-1), while the antisymmeric states are a new feature.

Mixed symmery states have now been discovered in several nuclei.

(i) Deformed nuclei. In these nuclei mixed symmetry states appear as rotational bands. The lowest band is built upon a state with $J^P = 1^+$. They were discovered in 1984, soon after their suggestion [11].

(ii) Spherical or weakly deformed nuclei. In these nuclei, mixed symmetry states appear as vibrational bands built upon a 2^+ state. Unambiguous evidence for these states has been obtained recently [12].

3.7 Geometrical aspects

There are in this case 5+5 complex vaiables, $\alpha_{\pi,\mu}, \alpha_{\nu,\mu}$. The coherent states can be written as

$$| N_\pi, N_\nu; \alpha_{\pi,\mu}, \alpha_{\nu,\mu}\rangle = \left(s^\dagger + \sum_\mu \alpha_{\pi,\mu} d^\dagger_{\pi,\mu}\right)^{N_\pi} \left(s^\dagger_\nu + \sum_\mu \alpha_{\nu,\mu} d^\dagger_{\nu,\mu}\right)^{N_\nu} | 0\rangle. \tag{49}$$

Instead of $\alpha_{\pi,\mu}, \alpha_{\pi,\nu}$, one can use three Euler angles $\theta_1, \theta_2, \theta_3$ characterizing the mass distribution, three Euler angles ϕ_1, ϕ_2, ϕ_3 characterizing the relative orientation of protons and neutrons, and four intrinsic variables (Bohr variables) $\beta_\pi, \gamma_\pi, \beta_\nu, \gamma_\nu$ characterizing the intrinsic deformations of protons and neutrons. The Interacting Boson Model-2 can then be viewed as a quantization of a two-fluid Bohr Hamiltonian.

3.8 Summary

The Interacting Boson Model-2:

(i) Provides a direct connection between the shell-model and the collective model.

(ii) Suggests an entire new class of collective states experimentally found.

Further generalizations of the Interacting Boson Model are:

(a) The Interacting Boson Model-3 [13]. In this model, $pp - nn - pn$ pairs with $T = 1, S = 0$ are introduced. The corresponding algebraic structure is $U(6) \otimes U_T(3)$.

(b) The Interacting Boson Model-4 [14]. In this model, in addition to $pp - nn - pn$ pairs with $T = 1, S = 0$, there are also pn pairs with $T = 0, S = 1$. The algebraic structure is $U(6) \otimes U_{ST}(6)$.

4 The interacting boson-fermion model

The Interacting Boson Model describes in its various versions, even-even nuclei. However, one needs to describe also even-odd, odd-even and odd-odd nuclei. In these case at least one particle is unpaired, and one must consider a more complete model of nuclei in which there are at the same time, collective (pair) degrees of freedom and single particle degrees of freedom. A model of this type was introduced in 1979 [15] and is called Interacting Boson-Fermion Model. The Interacting Boson-Fermion Model, in its two versions IBFM-1 and IBFM-2, will not be described here for lack of space and time. A detailed description can be found in [16].

The treatment of odd-even nuclei is one of the most important subjects in Nuclear Structure Physics. While the treatment of even-even nuclei can be considered to a large extent complete, that of odd-even nuclei still needs improvements.

5 Nuclear structure beyond 2000

In the last 50 years, an understanding of nuclear structure has been developed through the use of Nuclear Models. The basic model is the *Nuclear Shell Model.* From it, The *Interacting Boson Model* arises. This model, which can also be viewed as a quantization of the *Collective Model*, can be used to study collective quadrupole spectra of nuclei.

In the same 50 years, the experimental study of nuclear spectra has developed substantially. The last 20 years have been characterized by the exploration of nuclear spectra at high angular momenta. In the next decade, a major part of the research program of several laboratories will be devoted to the study of nuclei far from stability through the use of Radioactive Beam Facilities. One of the crucial questions that one needs to answer is the extent to which nuclear models can describe spectra of nuclei far from stability. In order to use the shell-model to this end, one needs to extrapolate single-particle energies and two-body matrix elements. This extrapolation is difficult, since there are in heavy nuclei many parameters. The extrapolation requires some theoretical input. This input can be provided by mean field theories for single-particle levels and G-matrix theories for two-body matrix elements. An alternative scheme is to use the Interacting Boson Model. Here the extrapolation is more manageable (there are fewer parameters than in the shell-model). Calculations of nuclei far from stability in the Interacting Boson Model already exist (See, for example, p.180 of Ref.[7]). The extent to which data will deviate from predictions may point out to new physics beyond standard models.

In the determination of new effects an important role is played by odd-even nuclei, since the main modification expected when going far from stability is a change in single particle energies. These single particle energies play a crucial role in odd-even nuclei. Calculations in odd-even nuclei far from stability exist in the Interacting Boson-Fermion Model (See, for example, p.248 of Ref.[16]). Again deviations from these calculations may indicate new effects.

A special problem is presented by light nuclei. In these nuclei, clustering correlations play an important role. The treatment of cluster configurations in the shell model is extremely complicated. Montecarlo shell-model calculations can help understanding this problem, but a simpler descriptions may be needed. At the present time, a simpler description of clustering in nuclei, called *Algebraic Cluster Model* is being developed [17]. This description can be viewed as a quantization of the *Cluster Model.* An example of this simpler description is provided by the spectrum of three particles at a vertices of an equilateral triangle. This spectrum can be simply obtained in the algebraic description. It can be applied to the study of ^{12}C, viewed as three α-particles at the vertices of an equilateral triangle. For nuclei far from stability, one needs an IBFM-like approach in which there are collective (in this case, cluster degrees of freedom) and single-particle (nucleon) degrees of freedom. For example, in ^{14}C, there are two neutrons in addition to 3α clusters.

6 Conclusions

The atomic nucleus is a complex system which shows a large amount of self-organization. The low-lying spectra appear to be dominated by collective modes:

(i) Shape modes,

(ii) Cluster modes.

In the last 50 years, nuclear structure theory has gone a long way towards understanding nuclear phenomena. The remaining problem is to explore experimentally the limits of nuclear structure, and theoretically to see whether or not new phenomena occur that cannot be explained by standard models.

Aknowledgments

This work was supported in part by U.S. DOE Grant No. DE-FG02-91ER40608.

References

1. J.H.D. Jensen, H. Suess and O. Haxel: Die Naturwissenschaften **36**, 155 (1949)
2. M. Goeppert-Mayer: Phys. Rev. **75**, 1969 (1949)
3. A. Bohr: Mat. Fys. Medd. Dan. Vid. Selsk. **26**, No.14 (1952); A. Bohr and B.R. Mottelson: Mat. Fys. Medd. Dan. Vid. Selsk. **27**, No.16 (1953)
4. J.A. Wheeler: Phys. Rev. **52**, 1083 (1937)
5. K. Wildermuth and T. Kanellopoulos: Nucl. Phys. **7**, 150 (1958)
6. A. Arima, T. Otsuka, F. Iachello and I. Talmi: Phys. Lett. **66B**, 205 (1977)
7. For an extensive review see, F. Iachello and A. Arima: "The Interacting Boson Model", Cambridge University Press, Cambridge (1987)
8. F. Iachello: Proc. Int. Conf. on "Nuclear Structure and Spectroscopy", H.P. Blok and A.E.L. Dieperink, eds., Scholar's Press, Amsterdam (1974), p.163
9. A. Arima and F. Iachello: Phys. Rev. Lett. **35**, 1039 (1975)
10. D.D. Warner and R.F. Casten: Phys. Rev. **C28**, 1798 (1983)
11. D. Bohle, A. Richter, W. Steffen, W. Steffen, A.E.L. Dieperink, N. LoIudice, F. Palumbo and O. Scholten: Phys. Lett. 137B, 27 (1984)
12. N. Pietralla, C. Fransen, P. von Brentano, A. Dewald, A. Fitzler, C. Friessner, and J. Gableske: Phys. Rev. Lett. **84**, 3775 (2000)
13. J.P. Elliott and A.P. White: Phys. Lett. **97B**, 169 (1981)
14. J.P. Elliott and J.A. Evans: Phys. Lett. **101B**, 216 (1981)
15. F. Iachello and O. Scholten: Phys. Rev. Lett. **43**, 679 (1979)
16. F. Iachello and P. van Isacker: "The Interacting Boson-Fermion Model", Cambridge University Press, Cambridge (1991)
17. R. Bijker and F. Iachello: *Phys. Rev.* **C61**, 067305 (2000)

The limits of the mean field

Elvira Moya de Guerra

Instituto de Estructura de la Materia, Consejo Superior de Investigaciones Científicas, Serrano-123, 28006-Madrid, Spain

Abstract. In these talks, we review non relativistic selfconsistent mean field theories, their scope and limitations. We first discuss static and time dependent mean field approaches for particles and quasiparticles, together with applications. We then discuss extensions that go beyond the non-relativistic independent particle limit.

On the one hand, we consider extensions concerned with restoration of symmetries and with the treatment of collective modes, particularly by means of quantized ATDHF. On the other hand, we consider extensions concerned with the relativistic dynamics of bound nucleons. We present data on nucleon momentum distributions that show the need for relativistic mean field approach and probe the limits of the mean field concept.

Illustrative applications of various methods are presented stressing the role that selfconsistency plays in providing a unifying reliable framework to study all sorts of properties and phenomena. From global properties such as size, mass, lifetime, ..., to detailed structure in excitation spectra (high spin, RPA modes, ...), as well as charge, magnetization and velocity distributions.

1 Introduction. The n-body problem

In 1960, Harry Lipkin wrote [1]: *"We can begin by looking at the fundamental paradox of the many-body problem; namely that people who do not know how to solve the three-body problem are trying to solve the n-body problem. Our choice of wave functions is very limited; we only know how to use independent particle wave functions. The degree to which this limitation has invaded our thinking is marked by our constant use of concepts which have meaning only in terms of independent particle wave functions: shell structure, the occupation number, the Fermi sea and the Fermi surface, the representation of perturbation theory by Feynman diagrams. All of these concepts are based upon the assumption that it is reasonable to talk about a particular state being occupied or unoccupied by a particle independently of what the other particles are doing. This assumption is generally not valid, because there are correlations between particles. However, independent particle wave functions are the only wave functions which we know how to use. We must therefore find some method to treat correlations using these very bad independent particle wave functions"*. Nuclear theory has come a long way since those times. Yet, these words still convey a useful message, as their essence remains valid.

The mean field theory is widely used, in various modifications, as a base for practically all microscopic calculations in many-body quantum systems. In Nuclear Physics, it is essentially an approximation scheme to reduce our problem

J.M. Arias and M. Lozano (Eds.): LNP 581, pp. 155–194, 2001.
© Springer-Verlag Berlin Heidelberg 2001

of many strongly interacting nucleons to one of non-interacting particles (or quasiparticles) in an average nuclear field. The generation of this average field from the nucleon–nucleon interaction in a selfconsistent way is achieved by the Hartree–Fock (HF) or the Hartree–Fock–Bogoliubov (HFB) methods.

The solution of the many body stationary and time dependent problems amounts to the solution of the static or time dependent Schrödinger equations:

$$H\Psi_\alpha = E_\alpha \Psi_\alpha \quad (SSE) \tag{1}$$

$$H\Psi = \mathrm{i}\frac{\partial}{\partial t}\Psi \qquad (TDSE) \tag{2}$$

It is well known from basic quantum mechanics that if the solutions of (1) are known, the evolution with time from an initial configuration of the system $\Psi(0)$ is known ($\Psi(t) = \mathrm{e}^{-\mathrm{i}Ht}\Psi(0)$) and vice versa. Knowing the evolution in time, we may determine the energy eigenvalues by Fourier transformation. In this respect, the nuclear system is as any other quantum system. In standard nuclear structure theory, we consider a nucleus as a system of A fermions interacting via (strong) two-body, or at most three-body, forces,

$$H = \sum_{k=1}^{A} K_k + \frac{1}{2}\sum_{k\neq l} V_{kl}^{(2)} + \frac{1}{6}\sum_{k\neq l\neq m} V_{klm}^{(3)}\,, \tag{3}$$

where the internal degrees of freedom of the nucleons are frozen. The two-body forces are derived from realistic nucleon–nucleon interactions in free space, involving meson exchange potentials and a repulsive short range core. Since these forces are discussed at length in the talks of R. Vinh Mau, we do not give here any details. We only mention here that the existence of a repulsive core [2] was a restraint to the implementation of Hartree–Fock approximations till Brueckner's methods and Bethe's ideas were implemented by Negele in finite nuclei, defining a density dependent Hartree–Fock method where the dependence of the G-matrix on the density matrix is replaced by dependence on the local density [3]. Even with this approximation, the solution of Brueckner–Hartree–Fock equations in finite nuclei is difficult, but in essence what it means is that the bare nucleon–nucleon force in free space is renormalized by the presence of other nucleons. This results in an effective interaction that depends on the local density and justifies the use of phenomenological density dependent effective interactions [4].

As in any Q.M. problem, saying that S is a symmetry of the system amounts to say that $[H, S] = 0$. Internal symmetries are conserved in time and can be used to classify and label the wave functions Ψ. About the many body wave function $\Psi = \Psi(1, 2, \ldots, A)$ all we know for sure has to do with symmetries and invariance principles. For instance, rotational invariance implies that J is a good quantum number of the exact states Ψ_α, and, in particular, since nucleons obey Fermi statistics, Ψ is antisymmetric with respect to interchange of any pair of nucleons. The rest we know from responses of nuclei to electroweak and hadronic probes. In principle, the state Ψ can be expanded in a complete orthonormalized basis of antisymmetric states of A-particles. Such a basis can be formed by the

set of Slater determinants :

$$\Phi_{\{n_i\}}(1,\ldots,A) = \frac{1}{\sqrt{A}} \begin{vmatrix} \varphi_{\alpha_1}^{(1)} & \cdots & \varphi_{\alpha_A}^{(1)} \\ \vdots & \ddots & \vdots \\ \varphi_{\alpha_1}^{(A)} & \cdots & \varphi_{\alpha_A}^{(A)} \end{vmatrix} \equiv \|\varphi_{\alpha_i}(i)\|, \tag{4}$$

or in second quantized notation:

$$\Phi_{\{n_i\}} = \prod_{i=1}^{N} (a_{\alpha_i}^{+})^{n_i} |0> , \tag{5}$$

where $\{n_i\} = \{n_1,\ldots,n_N\}$ represents any set of occupation numbers (with $n_i = 0,1$; $\sum n_i = A$) of the states α_i in a complete basis of single particle states $\{\alpha_i\} = \{\alpha_i,\ldots,\alpha_N\}$. Here and in what follows, coordinates $(\boldsymbol{r}_i,\sigma_i,\tau_i)$ are represented by (i), while α_i will represent the set of quantum numbers characterizing a single particle basis state, or more generally, the order number given to the basis states.

Alternatively to (1) and (2), one may use variational principles . The time dependent Schrödinger equation may be established from the action integral with fixed end points:

$$I_{12} = \int_{t_1}^{t_2} \mathcal{L}(\Psi,\Psi^*) = \int_{t_1}^{t_2} \mathrm{d}t < \Psi|\mathrm{i}\frac{\partial}{\partial t} - H|\Psi > \tag{6}$$

by means of the variational principle:

$$\frac{\delta I_{12}}{\delta\Psi(t)} = 0 = \frac{\delta I_{12}}{\delta\Psi^*(t)} . \tag{7}$$

This allows to discuss (2) in a classical context with the integrand in (6) representing the time dependent Lagrangian of the system. In the static case, one has the variational principle

$$\frac{\delta\mathcal{H}}{\delta\Psi} = \frac{\delta\mathcal{H}}{\delta\Psi^*} = 0 , \tag{8}$$

with

$$\mathcal{H} = \frac{<\Psi|H|\Psi>}{<\Psi|\Psi>} , \tag{9}$$

which is equivalent to (1).

Obviously, solving the full many body problem is equally difficult starting from (7), (8) or from (1), (2). Yet, the variational schemes are more appealing as they are amenable to more intuitive ways of thinking. The main point here is that we do not have access at once to all the information contained in the whole many-body wave function Ψ and that, for practical purposes, we can restrict the search to reduced sets of *ansatz* and degrees of freedom. Most observables we know of are represented by one-body or two-body operators and thus depend explicitly at most on one-body and two-body density matrices.

The n-body density matrix in coordinate space is defined as:

$$\rho^{(n)}(1,\ldots,n;1',\ldots,n') =< \Psi|\hat{\rho}^{(n)}(1,\ldots,n;1',\ldots,n')|\Psi >= \tag{10}$$
$$= \binom{A}{n} \int \left(\prod_{i=n+1}^{A} \mathrm{d}i \right) \Psi^*(1',\ldots,n',n+1,\ldots,A)\Psi(1,\ldots,n,n+1,\ldots,A) \, ,$$

with

$$\hat{\rho}^{(n)}(1,\ldots,n;1',\ldots,n') = a^+(1')\cdots a^+(n')a(n)\cdots a(1) \, , \tag{11}$$

where $\int \mathrm{d}i$ stands for $\int \mathrm{d}\boldsymbol{r}_i \sum_{\sigma_i} \sum_{\tau_i}$. In the single particle basis state representation, the n-body density matrix is defined as:

$$\rho^{(n)}_{\alpha_1\cdots\alpha_n,\alpha'_1\cdots\alpha'_n} =< \Psi|a^+_{\alpha'_1}\cdots a^+_{\alpha'_n}a_{\alpha_n}\cdots a_{\alpha_1}|\Psi >=< \Psi|\hat{\rho}^{(n)}_{\alpha_1\cdots\alpha_n,\alpha'_1\cdots\alpha'_n}|\Psi > \, . \tag{12}$$

Using fermion field creation and destruction operators:

$$a^+(1) = \textstyle\sum_\alpha \varphi^*_\alpha(1)a^+_\alpha \, , \quad a(1) = (a^+(1))^+ \, , \tag{13}$$

satisfying the usual anticommutation rules [5], we can relate the n-body density operator in coordinate space to that in configuration space:

$$\hat{\rho}^{(n)}(1,\ldots,n;1',\ldots,n') =$$
$$= \sum_{\substack{\alpha_1\cdots\alpha_n \\ \alpha'_1\cdots\alpha'_n}} \varphi^*_{\alpha'_1}(1')\cdots\varphi^*_{\alpha'_n}(n')\varphi_{\alpha_1}(1)\cdots\varphi_{\alpha_n}(n)\hat{\rho}^{(n)}_{\alpha_1\cdots\alpha_n\alpha'_1\cdots\alpha'_n} \, . \tag{14}$$

With these operators, it is easy to show that any one-body ($\Theta^{(1)} = \sum_i \Theta^{(1)}_i$) and two-body ($\Theta^{(2)} = (1/2)\sum_{i\neq j}\Theta^{(2)}_{ij}$) operators can be written in second quantized notation as:

$$\Theta^{(1)} = \sum_{\alpha,\alpha'} < \alpha'|\Theta^{(1)}|\alpha > \hat{\rho}^{(1)}_{\alpha,\alpha'} \, , \tag{15}$$

$$\Theta^{(2)} = \frac{1}{4}\sum_{\alpha\beta\alpha'\beta'} < \alpha'\beta'|\bar{\Theta}^{(2)}|\alpha\beta > \hat{\rho}^{(2)}_{\alpha\beta,\alpha'\beta'} \, , \tag{16}$$

with

$$< \alpha'|\Theta^{(1)}|\alpha >= \int \mathrm{d}1\varphi^*_{\alpha'}(1)\Theta^{(1)}_1\varphi_\alpha(1) = \Theta^{(1)}_{\alpha'\alpha} \, , \tag{17}$$

$$< \alpha'\beta'|\bar{\Theta}^{(2)}|\alpha\beta > = \int \mathrm{d}1\mathrm{d}2\varphi^*_{\alpha'}(1)\varphi^*_{\beta'}(2)\Theta^{(2)}_{12}\left(\varphi_\alpha(1)\varphi_\beta(2) - \varphi_\beta(1)\varphi_\alpha(2)\right) =$$
$$= \bar{\Theta}^{(2)}_{\alpha'\beta',\alpha\beta} \, . \tag{18}$$

Their expectation values in the state Ψ are then:

$$< \Psi|\Theta^{(1)}|\Psi > = Tr(\Theta^{(1)}\rho^{(1)}) \, , \tag{19a}$$
$$< \Psi|\Theta^{(2)}|\Psi > = Tr(\Theta^{(2)}\rho^{(2)}) \, . \tag{19b}$$

In particular, the expectation value of the hamiltonian in the state Ψ for $V = V^{(2)}$ depends only on the one- and two-body density matrices:

$$< \Psi|H|\Psi > = \sum_{\alpha\beta} K_{\alpha\beta}\rho^{(1)}_{\beta\alpha} + \frac{1}{4}\sum_{\alpha\beta\alpha'\beta'} \bar{V}_{\alpha\beta\alpha'\beta'}\rho^{(2)}_{\alpha'\beta'\alpha\beta} =$$
$$= Tr(K\rho^{(1)}) + \frac{1}{4}Tr(\bar{V}\rho^{(2)}) = \mathcal{H}(\rho^{(1)}, \rho^{(2)}) \,, \tag{20}$$

Let us now see how the TDSE, or equivalently the variational principle (7), is written in terms of density matrices. In general, the time derivative of the n-body density matrix can be obtained from the definition of $\rho^{(n)}$ and the time evolution of $\Psi(t)$ as follows. To shorten the notation, we write the n-body density operator and matrix elements as:

$$\hat{\rho}^{(n)}_{\alpha'_i,\alpha_i} \equiv a^+_{\alpha_1} \cdots a^+_{\alpha_n} a_{\alpha'_n} \cdots a_{\alpha'_1} \,, \tag{21}$$

$$\rho^{(n)}_{\alpha'_i,\alpha_i}(t) = < \Psi(t)|\hat{\rho}^{(n)}_{\alpha'_i,\alpha_i}|\Psi(t) >=$$
$$= < \Psi(0)|\mathrm{e}^{\mathrm{i}Ht}\hat{\rho}^{(n)}_{\alpha'_i,\alpha_i}\mathrm{e}^{-\mathrm{i}Ht}|\Psi(0) > \;. \tag{22}$$

Taking the derivative in time we get:

$$\mathrm{i}\frac{\partial}{\partial t}\rho^{(n)}_{\alpha'_i,\alpha_i} = - < \Psi(0)|\mathrm{e}^{\mathrm{i}Ht}[H, \hat{\rho}^{(n)}_{\alpha'_i,\alpha_i}]\mathrm{e}^{-\mathrm{i}Ht}|\Psi(0) >=$$
$$= - < \Psi(t)|[H, \hat{\rho}^{(n)}_{\alpha'_i,\alpha_i}]|\Psi(t) > \,, \tag{23}$$

which can be written in terms of density matrices as:

$$\mathrm{i}\frac{\partial}{\partial t}\rho^{(n)}_{\alpha'_i,\alpha_i}(t) = [K, \rho^{(n)}]_{\alpha'_i,\alpha_i} + [V^{(2)}, \rho^{(n+1)}]_{\alpha'_i,\alpha_i} + [V^{(3)}, \rho^{(n+2)}]_{\alpha'_i\alpha_i} \,. \tag{24}$$

In the static case, $\rho^{(n)}(t) = \rho^{(n)}(0)$, we have for any n, $\frac{\partial}{\partial t}\rho^{(n)} = 0$ and the SSE, or equivalently (8), reads:

$$[K, \rho^{(n)}] + [V^{(2)}, \rho^{(n+1)}] + [V^{(3)}, \rho^{(n+2)}] = 0 \,. \tag{25}$$

Therefore, with a two-body interaction, the equation for $\rho^{(n)}$ involves always $\rho^{(n+1)}$ as well. If a three-body interaction is included, there will be an additional term ($[V^{(3)}, \rho^{(n+2)}]$) involving $\rho^{(n+2)}$ as well. Non-local three-body interactions have been included by Pandharipande et al. [6] in *ab initio* calculations of few-body systems. These interactions were supposed to be necessary to explain spin-orbit in few-body systems and compressibility in nuclear matter. Nowadays, these forces are being questioned [7]. On the other hand, the use of local three-body forces (like the 3-body Skyrme force) for the spin saturated static case works well because it is equivalent to using a density dependent force [4,8]. However, using the same local three-body forces for spin non-saturated or time

dependent cases leads to unreasonable instabilities of the system [8,9]. Thus, we focus here on two-body forces ($V = V^{(2)}$ in what follows).

What is important for our purpose here is to notice that the time dependent evolution equation (24) and the static equation (25) set in a more concrete context the task of solving the TDSE or SSE many-body problem. If all we need to know about the system has to do with expectation values of one-body and two-body operators, we may restrict our search to the one-body and two-body density matrices. In absolute terms, this is not a real simplification because we know that the equation we need to solve for $\rho^{(2)}$ will also involve $\rho^{(3)}$ and so on. But the n-body correlations with $n \geq 3$ will not affect in a direct manner those expectation values. They will only affect them indirectly, mainly as a redefinition or rescaling of normalizations. Likewise, for expectation values of one-body operators, we do not need explicit knowledge of $\rho^{(2)}$, only of the effect that it may have on the solution for $\rho^{(1)}$. An example that is particularly interesting in this regard is the one-body momentum distribution, that we discuss in the last lecture.

Equation (24) is a *master equation*, equivalent to TDSE, that can be used for any *ansatz* of our variational wave function. In particular, it allows to derive HFB equations (as well as HF) in a most elegant manner. Since such a derivation is not found in text books, we do that in the next section.

2 Self-consistent mean field theory for particles and quasiparticles

2.1 Hartree–Fock approach

The Hartree–Fock theory (both static and time dependent (TDHF)) is concerned with finding the best Slater determinantal wave functions. To this end, the trial wave functions Ψ in (8) and (9) are restricted to be Slater determinantal wave functions Φ. It is easy to show that the n-body density matrix in this case becomes a determinant of 1-body density matrix elements, i.e., for

$$\Psi \;\Rightarrow\; \Phi = \prod_{i=1}^{A} a_i^+ |0> \,, \tag{26}$$

one has

$$\rho^{(n)}_{\alpha',\alpha} = \begin{vmatrix} \rho_{\alpha'_1\alpha_1} & \cdots & \rho_{\alpha'_1\alpha_n} \\ \vdots & \ddots & \vdots \\ \rho_{\alpha'_n\alpha_1} & \cdots & \rho_{\alpha'_n\alpha_n} \end{vmatrix} \,, \tag{27}$$

where $\rho_{\alpha'_1\alpha_1}$ is the one-body density matrix corresponding to the Slater determinant wave function

$$\rho_{\alpha\alpha'} = < \Phi | \hat{\rho}^{(1)}_{\alpha,\alpha'} | \Phi > = \sum_{i=1}^{A} < \alpha | i >< \alpha' | i >^* \,, \tag{28}$$

that satisfies

$$\rho^2 = \rho \,, \quad Tr\rho = A \,, \tag{29}$$

and therefore has eigenvalues 1 or 0.

The overlaps $< \alpha|i >$ define the unitary transformation between the Hartree–Fock basis i and the generic basis α:

$$|i >= \sum_{\alpha} D_{i\alpha}|\alpha >= \sum_{\alpha} < \alpha|i > |\alpha > \ . \tag{30}$$

Replacing (27) into (24), one gets immediately the well known time dependent and static Hartree–Fock equations for the one-body density matrix:

$$\mathrm{i}\frac{\partial \rho}{\partial t} = [h, \rho] \quad \text{TDHF} \tag{31}$$

$$[h, \rho] = 0 \qquad \text{SHF} \ . \tag{32}$$

h is the single particle Hartree–Fock hamiltonian that depends on the one-body density matrix:

$$h_{\alpha\alpha'} = K_{\alpha\alpha'} + \Gamma_{\alpha\alpha'}(\rho) \ , \tag{33}$$

with a kinetic energy term

$$K_{\alpha\alpha'} = \frac{1}{2M} \int \mathrm{d}\boldsymbol{r} \sum_{\sigma\tau} \left(\nabla\varphi_{\alpha}(\boldsymbol{r}\sigma\tau)\right)^{*} \left(\nabla\varphi_{\alpha'}(\boldsymbol{r}\sigma\tau)\right) \tag{34}$$

and a density dependent mean field

$$\Gamma_{\alpha\alpha'} = \sum_{\beta\beta'} < \alpha\beta|\bar{V}|\alpha'\beta' > \rho_{\beta'\beta} \ , \tag{35}$$

that has to be determined selfconsistently with ρ.

The static Hartree–Fock equation implies that h and ρ are diagonalizable in the same basis. In what follows, we call this basis the Hartree–Fock basis and denote by i the single particle states and by ϵ_i the eigenvalues of h ($h_{ij} = \epsilon_i \delta_{ij}$). The ground state Φ_0 in this basis consists of nucleons occupying the A states of lowest energy ($\epsilon_i < \lambda$, with λ the Fermi level). We label these states by h (hole states) and the empty states by p (particle states) . One therefore defines also the ground state as the Hartree–Fock vacuum satisfying $a_{\mathrm{h}}^{+}|\Phi_0 >= a_{\mathrm{p}}|\Phi_0 >= 0$. In this basis, the density matrix is $\rho_{ij} = \delta_{ij}\delta_{i\,\mathrm{h}}$ and the HF energy is:

$$< \Phi_0|H|\Phi_0 >= E_{HF} = \sum_{\mathrm{h}} K_{\mathrm{h}} + \frac{1}{2}\sum_{\mathrm{hh'}} < \mathrm{hh'}|\bar{V}|\mathrm{hh'} >= \tag{36a}$$

$$= \sum_{\mathrm{h}} \epsilon_{\mathrm{h}} - \frac{1}{2}\sum_{\mathrm{hh'}} < \mathrm{hh'}|\bar{V}|\mathrm{hh'} > \ . \tag{36b}$$

Since this basis is defined by condition (32), it is clear that, in this basis, (31) is an equation for the off-diagonal matrix elements of ρ between particles and holes (ρ_{ph}):

$$\mathrm{i}\frac{\partial \rho_{\mathrm{ph}}}{\partial t} = [h, \rho]_{\mathrm{ph}} = \sum_{i} (h_{\mathrm{p}i}\rho_{i\,\mathrm{h}} - \rho_{\mathrm{p}i}h_{i\,\mathrm{h}}) = \tag{37}$$

$$= (h_{\mathrm{pp}} - h_{\mathrm{hh}})\rho_{\mathrm{ph}} - (\rho_{\mathrm{pp}} - \rho_{\mathrm{hh}})h_{\mathrm{ph}} \ , \tag{38}$$

where now h and ρ depend on time. Thus, at variance with the static case, in TDHF the time dependent mean field $h(\rho(t))$ cannot be diagonalized simultaneously with $\rho(t)$. Intuitively this is clear since a variation in time of the Slater determinant, hence of ρ, will amount to change of configuration unless the basis is changed. In either case, the Hartree–Fock equations are non-linear equations that have to be solved by iteration.

So far, we have assumed that V_{12} is independent of the density. However, as already mentioned, in the nuclear medium, the two-body nucleon–nucleon interaction is modified to an effective density dependent interaction. In this case, the Hartree–Fock equations are slightly modified because the Hartree–Fock mean field contains also the rearrangement or saturation potential involving $\partial V_{12}/\partial\rho$ (see, for instance, [5] and references therein). In any case, the Hartree–Fock equations, even with simple local interactions of Skyrme type [4,10], are highly non-linear and have to be solved by iteration. Usually one starts with an *ansatz* for the one-body density, constructs the potential Γ, solves for the new density and so on till convergence is achieved. In this process, it is important to keep in mind that the symmetries of the total hamiltonian H are preserved on average by the TDHF equations. What this means is that for any operator Θ that commutes with H, the mean value of Θ in $\Phi(t)$ is conserved. Moreover, in the static case, if one starts with an *ansatz* $\rho^{(0)}$ for the density with certain symmetries, the final solution $\rho^{(final)}$ of the static Hartree–Fock equation will still have the same symmetry. It is important to stress this point because we know that for many nuclei the best Slater determinant to represent the ground state has no spherical symmetry, and we can never get a non-spherical solution if we start with a spherical *ansatz*. As a general rule, the more symmetries ρ is permitted to break (i.e., the more general the *ansatz* is), the more sure we can be to generate the Slater determinant that approximates best the many-body wave function.

It may sound paradoxical that when ρ breaks the symmetries of H, hence of the exact solutions, one gets a better description, however it is not. The fact is that we cannot give up explicit account of the correlations in the wave function and simultaneously preserve the symmetries. We can either use a modest single particle basis and then solve the n-body problem of (25) for the correlated n-body density preserving the symmetries of H (as in the shell model described in Poves's lectures), or search for the optimal Slater determinant and single particle basis as in the Hartree–Fock method. That this is so can be easily understood considering a simple quadrupole–quadrupole interaction:

$$V_{12} = -\chi Q_1 \cdot Q_2 \,, \qquad\qquad Q_\mu \propto r^2 Y^2_\mu(\Omega) \,. \tag{39}$$

The n-body eigenstates for this two-body interaction in a major oscillator shell can be obtained analytically by algebraic methods [11]. In this method, the n-body wave functions have the symmetries of H and, in particular, have good angular momentum quantum numbers. Each n-body state contains many product wave functions of harmonic oscillator single particle states. There is no interaction between the inert core and the n-valence particles.

On the contrary, in the Hartree–Fock method, there is no need to differentiate between valence and core nucleons, which are all interacting to construct a mean

field,

$$\Gamma_\mu = -\chi \sum_\mu Tr(Q_\mu \rho) \cdot Q_\mu + (\text{exchange term}) \,, \tag{40}$$

that has no spherical symmetry. Actually, $Tr(Q_\mu \rho) \neq 0$ only if the local density $\rho(\boldsymbol{r})$ has quadrupole deformation. For an odd-A system this may not require non-conservation of angular momentum, but for an even–even system it does. If one considers a generic basis with spherical symmetry ($\alpha = n\,l\,j\,m$), the Hartree–Fock basis will be of the form:

$$|i> = \sum_{nljm} C_i^{nljm} |nljm> \,, \tag{41}$$

as in the phenomenological Nilsson model [12], that manifestly breaks rotational invariance. Neither the single particle nor the Slater determinant representing the ground state will be an eigenstate of angular momentum. In addition, of course, translational invariance is broken by any localized Slater determinantal wave function.

In spite of their so different appearance, similar structures and rotational bands can be generated with both methods. Indeed, the violation of conservation laws by the static Hartree–Fock solutions is connected with the presence of collective modes. In the example of a deformed HF solution that we are considering here, we see that Φ_0 is not an eigenstate of angular momentum and therefore can be written as a linear combination of eigenstates of J,

$$\Phi_0 = \sum_{JM} \phi^{JM} a_{JM} \,. \tag{42}$$

J-eigenstates can then be obtained from Φ_0 using angular momentum projection techniques. The HF vacuum can be viewed as a wave packet of wave functions with different angular momentum [1,18]. Of course, the J-eigenstates in (42) are no longer single Slater determinants. We shall discuss projection techniques in the next sections, but first we introduce briefly the mean field theory of quasiparticles, i.e., the Hartree–Fock–Bogoliubov approximation.

In summary, the Hartree–Fock equations allow to get the optimal representation of the many-body problem in the space of independent particle solutions. The nucleon–nucleon interactions are in fact generating the optimal mean field for the given number of particles. Thus, in this case, correlations are taken into account indirectly through the (symmetry breaking) selfconsistent mean field.

There are other methods, particularly that of Kohn–Sham, that search for the optimal one-body density. Actually, the Kohn-Sham [13] theory has some similarity with density dependent Hartree–Fock, except that it makes no reference to a particular type of many-body wave function and ρ does not necessarily correspond to a Slater determinant (i.e., $\rho^2 \neq \rho$).

Although the static HF method was well known in Atomic Physics, convincing applications to Nuclear Physics were not achieved till early 70's. The density dependent Hartree–Fock (DDHF) method of Negele [3] was a major breakthrough that, together with the pioneering works of Vautherin and Brink [4],

opened the gate to many successful applications and allowed to understand that the strongly bound many-body system can be described in mean-field approximation using local density dependent effective interactions. Some applications of TDHF theory to heavy-ion collisions were also carried out [14].

2.2 Hartree–Fock–Bogoliubov approach

In HFB approach, one looks for the best possible "Slater determinant of quasiparticles". Quasiparticle operators q^+_β, q_β are defined in terms of particle operators a^+_α, a_α by the generalized Bogoliubov transformation :

$$q^+_\beta = \sum_\alpha U_{\beta\alpha} a^+_\alpha + V_{\beta\alpha} a_\alpha \; . \tag{43}$$

Each quasiparticle is a linear combination of *all* particle creation and *all* destruction operators. In matrix notation [15]:

$$b^+ = M^* d^+ \; , \tag{44}$$

with

$$b^+ = \begin{pmatrix} q^+ \\ q \end{pmatrix} \; , \quad d^+ = \begin{pmatrix} a^+ \\ a \end{pmatrix} \; , \tag{45}$$

$$M = \begin{pmatrix} U^* & V^* \\ V & U \end{pmatrix} \; , \quad MM^+ = M^+M = \mathbf{1} \; . \tag{46}$$

The transformation is unitary and preserves anticommutation rules, i.e., quasiparticle operators obey also Fermi statistics. Then, the U and V matrices satisfy:

$$\begin{aligned} UU^+ + VV^+ &= U^+U + V^TV^* = \mathbf{1} \\ UV^T + VU^T &= U^+V + V^TU^* = \mathbf{0} \; . \end{aligned} \tag{47}$$

The *ansatz* for the variational function is the vacuum for quasiparticle operators, i.e., is the wave function $|\varphi>$ such that:

$$q_\beta|\varphi>= 0 \qquad \forall\beta \; , \;\; \text{or} \qquad |\varphi>= \mathcal{N} \prod_\beta q_\beta|0> \; . \tag{48}$$

The product extends to all β in the basis. The aim is to take into account correlations (both of short and long range) describing the system by an independent quasiparticle approximation. By analogy to HF, the quasiparticles move independently in a selfconsistent mean field generated by the nucleon–nucleon interactions. The meaning of this *ansatz* is better understood in the limit of a pure monopole pairing force that we consider later on. For the moment, we just notice that this *ansatz* breaks an important symmetry of the system since it is not an eigenstate of the particle number operator $\hat{N} = \sum_\alpha a^+_\alpha a_\alpha$. Here we derive

the time dependent Hartree–Fock–Bogoliubov (TDHFB) equations in analogy to the TDHF equations. Since the TDHFB equations are quite general, one can then apply them to particular cases where the general transformation (43) takes simpler (more restricted) forms.

Since the *ansatz* in (47) contains many Slater determinants with different particle numbers, a constrained variational principle is used where H is replaced by $H' = H - \lambda\hat{N}$ to constrain the wave function to give the correct number of particles on average, inducing correlations. In the HF case, we saw that instead of working with the Slater determinant Φ, we could work with the one-body density matrix ρ, because the mean value of any operator Θ was given in terms of ρ. Similarly to it, one can show that *in HFB approach, the n-body density matrix depends at most on two "densities"*:

- The *normal density* ρ, which is defined as in HF case and is determined by the V matrix, its trace being constrained to give the proper particle number:

$$\rho_{\alpha\alpha'} =< \varphi|a^+_{\alpha'}a_\alpha|\varphi >= (V^+V)_{\alpha\alpha'} \ . \tag{49}$$

- The *abnormal density* κ, or pairing tensor , which is defined as:

$$\kappa_{\alpha\alpha'} =< \varphi|a_{\alpha'}a_\alpha|\varphi >= (V^+U)_{\alpha\alpha'} \ . \tag{50}$$

From (47), one can see that κ is antisymmetric and ρ is hermitian. It is easy to check that in HFB *ansatz*, ρ represents the one-body density matrix of the system (see the general eq. (12)), and $\kappa\kappa^*$ is the correlation function of the two-body density matrix:

$$\begin{aligned}\rho^{(2)}_{\alpha_1\alpha_2,\alpha'_1\alpha'_2} &= < \varphi|a^+_{\alpha'_1}a^+_{\alpha'_2}a_{\alpha_2}a_{\alpha_1}|\varphi >= \\ &= \kappa_{\alpha_1\alpha_2}\kappa^*_{\alpha'_1\alpha'_2} + \rho_{\alpha_1\alpha'_1}\rho_{\alpha_2\alpha'_2} - \rho_{\alpha_1\alpha'_2}\rho_{\alpha_2\alpha'_1} \ ,\end{aligned} \tag{51}$$

where we have used the inverse transformation of (44): $d^+ = M^T b^+$, and the fact that $|\varphi >$ is the quasiparticle vacuum.

The time evolution of the normal density can be easily obtained from the general eq. (24). For $n = 1$, and with the help of (51), we get:

$$\mathrm{i}\frac{\partial\rho}{\partial t} = [h_\lambda, \rho] - \Delta\kappa^* + \kappa\Delta^* \ , \tag{52}$$

where h_λ is a constrained Hartree–Fock hamiltonian:

$$h_\lambda = h - \lambda \ , \tag{53}$$

with h the Hartree–Fock hamiltonian ($h = K - \Gamma(\rho)$); λ, the chemical potential that can be considered time dependent; and Δ, the pairing potential:

$$\Delta_{\alpha\alpha'} = \sum_{\alpha_1\alpha_2} < \alpha\alpha'|\bar{V}|\alpha_1\alpha_2 > \kappa_{\alpha_1\alpha_2} \ . \tag{54}$$

Note that Γ is hermitian and Δ is antisymmetric, like the densities ρ and κ, respectively. Using (24) for $n = 2$, one gets the time evolution for κ. A simpler method is described below.

The variational principles in Sect. 1 were derived assuming *ansatz* with good particle number. For any such *ansatz*, κ is zero. However, one may formally derive an equation for the time evolution of κ following the same procedure as in Sect. 1 with a constrained hamiltonian $H' = H - \lambda$. In this fashion, we find:

$$\mathrm{i}\frac{\partial \kappa}{\partial t} = - < \varphi | [H', \hat{\kappa}] | \varphi > = \tag{55}$$

$$= (h_\lambda \kappa + \kappa h_\lambda^*) - \Delta\rho + \Delta(1 - \rho^*) \; . \tag{56}$$

Again the static eqs. are obtained for $\frac{\partial \rho}{\partial t} = \frac{\partial \kappa}{\partial t} = 0$.

The time dependent Hartree–Fock–Bogoliubov (TDHFB) equations can be written in a more compact form defining a generalized density matrix $\mathcal{R}$,

$$\mathcal{R}_{\alpha\beta} = < \varphi | d_\beta^+ \cdot d_\alpha | \varphi > = \begin{pmatrix} \rho & \kappa \\ -\kappa^* & (1 - \rho^*) \end{pmatrix} \; , \tag{57}$$

which is related to the quasiparticle density Q ($Q_{\alpha\beta} = < \varphi | b_\beta^+ b_\alpha | \varphi >$) by $\mathcal{R} = M^+ Q M$. We also define a HFB hamiltonian $\mathcal{H}$:

$$\mathcal{H} = \begin{pmatrix} h_\lambda & \Delta \\ -\Delta^* & -h_\lambda^* \end{pmatrix} \; . \tag{58}$$

In terms of these double-dimension matrices, the static and time dependent HFB eqs. can be written respectively as:

$$[\mathcal{H}, \mathcal{R}] = 0 \; , \tag{59}$$

$$\mathrm{i}\frac{\partial \mathcal{R}}{\partial t} = [\mathcal{H}, \mathcal{R}] \; , \tag{60}$$

with $\mathcal{H}$ depending on ρ through the Hartree–Fock potential Γ, and depending on κ through the pairing potential Δ. As in the HF case, additional rearrangement terms appear when density dependent effective interactions are used.

It is easy to see that the generalized HFB density $\mathcal{R}$ satisfies properties analogous to those of ρ in the HF case:

$$\mathcal{R}^2 = \mathcal{R} \; . \tag{61}$$

To see this, we note that the generalized quasiparticle density matrix:

$$Q_{\beta\beta'} = < \varphi | b_{\beta'}^+ b_\beta | \varphi > = \begin{pmatrix} 0 & 0 \\ 0 & 1 \end{pmatrix} \tag{62}$$

is diagonal, satisfies $Q^2 = Q$ and it is related to $\mathcal{R}$ by $Q = M \mathcal{R} M^+$. Since M is also a unitary matrix, we have:

$$\mathcal{R}^2 = (M^+ Q M)^2 = M^+ Q^2 M = M^+ Q M = \mathcal{R} \; . \tag{63}$$

The constraint $< \varphi|\hat{N}|\varphi >= A$ reads: $Tr\rho = Tr(V^+V) = A$. One therefore has that $\rho^2 - \rho = \kappa\kappa^*$ and $\kappa\rho^* = \rho\kappa$. The Hartree–Fock–Bogoliubov energy is:

$$< \varphi|H'|\varphi >= Tr\left[\left(K - \lambda + \frac{1}{2}\Gamma\right)\rho - \frac{1}{2}\Delta\kappa^*\right] . \tag{64}$$

The formal analogy between HF and HFB approaches allows to extend to HFB scheme all the methods developed in the HF scheme that are considered in the next sections. Thus, it should be clear from now on that projection methods, ATDHF, RPA equations, etc., apply equally to HFB replacing the HF vacuum Φ by the HFB vacuum φ and "one particle–hole excitations" by "two quasiparticle excitations".

2.3 BCS approximation

The BCS approximation takes into account the dominant pairing correlations that involve nucleon pairs coupled to zero angular momentum. If one solves the static HF problem ($h(\rho)\varphi_i = \epsilon_i\varphi_i$) and considers that the dominant residual interaction left out by the selfconsistent mean field approximation is a pairing interaction of the form[1]:

$$V_p = \sum_{i,j>0} G_{ij} a_i^+ a_{\bar{i}}^+ a_{\bar{j}} a_j , \tag{65}$$

where $\bar{i}$ represents the time reverse of i. One can use a simpler version of the Bogoliubov transformation (43) that involves only creation of the state i, destruction of the state $\bar{i}$, or vice versa, i.e., the quasiparticles now are defined as:

$$\begin{aligned} \alpha_i^+ &= u_i a_i^+ - v_i a_{\bar{i}} \\ \alpha_{\bar{i}}^+ &= u_i a_{\bar{i}}^+ + v_i a_i , \end{aligned} \tag{66}$$

with u and v real positive numbers satisfying: $u_i^2 + v_i^2 = 1$.

The ground state is now represented by the BCS vacuum , i.e., the vacuum to the quasiparticle operators defined in (66):

$$|\varphi_{\rm BCS} >= \prod_{i>0}(u_i + v_i a_i^+ a_{\bar{i}}^+|0> , \tag{67}$$

which clearly satisfies $\alpha_i|\varphi_{\rm BCS} >= 0$ for any i. The BCS wave function is manifestly time reversal invariant and represents even–even systems for which states $(i, \bar{i})$ are degenerate in the HF approximation. The odd-A systems in this scheme

[1] $|\bar{i} >= C e^{i\pi J_y}|i >$. Here, to simplify, we are considering only identical particles. To include also isovector $J = 0$, $\pi - \nu$ pairing, we may add a term $P_{\pi\nu}P_{\pi\nu}^+$, with $P_{\pi\nu} = (a_{\pi_i}^+ a_{\nu_{\bar{i}}}^+ + a_{\nu_i}^+ a_{\pi_{\bar{i}}}^+)/\sqrt{2}$.

are represented as one quasiparticle states (here and in what follows, i will denote states with $m > 0$; $\bar{i}$, its time reverse):

$$|\varphi_{\text{odd}} >= \alpha_k^+ |\varphi_{\text{BCS}} >= \prod_{i \neq k} (u_i + v_i a_i^+ a_{\bar{i}}^+) a_k^+ |0> , \tag{68}$$

while excitations of the even–even system are represented by two-quasiparticle states.

From (67), the meaning of u and v is apparent: v_i^2 is the probability that a pair $i\bar{i}$ be filled; u_i^2 is the complementary probability that the pair be empty. The static HFB eqs. take in this case a simple form as one replaces the U and V matrices by their corresponding expression in the BCS transformation (66):

$$\begin{array}{ll} U_{ij} = \delta_{ji} u_i & V_{ij} = -\delta_{j\bar{i}} v_i \\ U_{\bar{i}j} = \delta j\bar{i} u_i & V_{\bar{i}j} = \delta_{ji} v_i \ , \end{array} \tag{69}$$

or:

$$\rho_{\bar{i}\bar{j}} = \rho_{ij} = (V^+ V)_{ij} = v_i^2 \delta_{ij} \equiv \rho_i \delta_{ij} \ , \tag{70}$$

$$\kappa_{i\bar{j}} = -\kappa_{\bar{j}i} = (V^+ U)_{i\bar{j}} = u_i v_i \delta_{ij} \equiv \kappa_i \delta ij \ . \tag{71}$$

Then, the HFB eqs. can be written in the static case (59) as the following eigenvalue problem:

$$\begin{pmatrix} \tilde{\epsilon}_i & \Delta_i \\ \Delta_i & -\tilde{\epsilon}_i \end{pmatrix} \begin{pmatrix} u_i \\ -v_i \end{pmatrix} = E_i \begin{pmatrix} u_i \\ -v_i \end{pmatrix} \ , \tag{72}$$

where we have replaced the Hartree–Fock hamiltonian h by:

$$(h_\lambda)_{ij} = (K_i - \lambda + \Gamma_i(\rho))\, \delta_{ij} = \tilde{\epsilon}_i \delta_{ij} \ , \tag{73}$$

with

$$\Gamma_i(\rho) = \sum_j < ij|\bar{V}|ij > v_j^2 \ , \tag{74}$$

which in particular may include $G_{ii} v_i^2$ for $j = \bar{i}$. Δ_i is the pairing potential:

$$\Delta_{ik} = \delta_{k\bar{i}} \left(\sum_{j>0} G_{ij} \kappa_{j\bar{j}} \right) = -\delta_{k\bar{i}} \left(\sum_{j>0} G_{ij} v_j u_j \right) \equiv -\Delta_i \delta_{k\bar{i}} \ . \tag{75}$$

The eigenvectors have the solution:

$$v_i^2 = \tfrac{1}{2} \left(1 - \tilde{\epsilon}_i / E_i\right) \ , \ u_i^2 = 1 - v_i^2 \ , \tag{76}$$

with eigenvalues $E_i = \pm \sqrt{\tilde{\epsilon}_i^2 + \Delta_i^2}$.

The condition that, in the limit $\Delta_i = 0$, $v_i^2 = 1$ for $\epsilon_i < \lambda$ and $v_i^2 = 0$ for $\epsilon_i > \lambda$, selects the plus sign for the eigenvalues E_i, which represent the quasiparticle energies:

$$E_i = \sqrt{\tilde{\epsilon}_i^2 + \Delta_i^2} \ . \tag{77}$$

Equations (76) and (77) define the BCS equations with the constraining condition on the particle number:

$$N^{\rho}/2 = \sum_i v_i^2 \,, \quad \rho = \pi, \nu \tag{78}$$

These equations are solved selfconsistently for protons and neutrons separately, unless proton–neutron pairing interaction is included.

Usually, the Hartree–Fock equations are first solved with $v_{\mathrm{h}} = 1$, $v_{\mathrm{p}} = 0$. This defines the chemical potential λ, single particle wave functions and energies. Then, with this λ and ϵ_i's, one solves the BCS equation with a phenomenological value of Δ, to find new occupation numbers v_i. The new occupation numbers v_i are inserted in the selfconsistent potentials to get new sets of single particle solutions and so on until convergence is achieved. These procedure is called HF+BCS and has been shown to be very successful in most applications.

For applications to high spin states, the richness of the full HFB *ansatz* is necessary to deal appropriately with the time reversal non-invariant mean field (introduced by the constraint $\boldsymbol{\omega} \cdot \boldsymbol{J}$ of the cranking approximation). Most applications to ground and low-spin states give similar results in HF + BCS with fixed pairing gap or in HFB. The connection between both approaches is made by the Bloch–Messiah [16] theorem that we only mention here. Strictly speaking, the Bloch–Messiah theorem puts very restrictive conditions for the equivalence of both approaches; nevertheless, in practice, similar results are obtained for ground state properties when using effective interactions.

Since the 80's, many successful HFB calculations have been made (mainly with Gogny force [17])of yrast bands, high spin states, etc. (a topic that is discussed in the lectures of P. Ring). On the other hand, HF+BCS with Skyrme forces describes fairly well ground state properties as binding energies, r.m.s. radii, spatial and momentum density distributions, ..., of nuclei with $A \geq 16$. Both HFB and HF+BCS are the building blocks of most reliable microscopic calculations of heavy nuclei carried out nowadays.

3 Static HF or HFB solutions and restoration of symmetries

We have mentioned already that in HF approach the ground state system is represented by an independent particle wave function (Slater determinant) that breaks in general several symmetries of the total hamiltonian H. To begin with, it violates translational invariance . In the bound system, the particles must be localized in space relative to each other. In the independent particle picture, we do that by localizing them in space, i.e., breaking translational invariance. Any representation of the bound system that is eigenstate of the total linear momentum $\boldsymbol{P}$, must involve a correlated motion of the particles and thus it cannot be described by an independent particle wave function. We thus may consider that the independent particle wave function Φ describes a wave packet with various eigenstates Ψ_k of the linear momentum operator $\boldsymbol{P}$. To project a

given component Ψ_k, we can therefore use the projection operator:

$$P^{\boldsymbol{k}} = \int \mathrm{d}\boldsymbol{R} \mathrm{e}^{\mathrm{i}\boldsymbol{R}\cdot\boldsymbol{k}} \mathrm{e}^{-\mathrm{i}\boldsymbol{R}\cdot\hat{\boldsymbol{P}}} \,, \tag{79}$$

with $\hat{\boldsymbol{P}} = \sum_i \hat{\boldsymbol{P}}_i = -\mathrm{i}\sum_i \boldsymbol{\nabla}_i$, the total linear momentum operator. Then:

$$\Psi_k = \frac{1}{\mathcal{N}_k} P^{\boldsymbol{k}} \Phi = \frac{1}{\mathcal{N}_k} \int \frac{\mathrm{d}\boldsymbol{R}}{(2\pi)^3} \mathrm{e}^{\mathrm{i}\boldsymbol{R}\boldsymbol{k}} \Phi(\boldsymbol{r}_1 - \boldsymbol{R}, \ldots, \boldsymbol{r}_A - \boldsymbol{R}) \,, \tag{80}$$

where we have used the fact that if $\phi(\boldsymbol{r}_1, \ldots, \boldsymbol{r}_A)$ is a Slater determinant (see (4)) of single particle wave functions $\varphi_{\alpha_i}(\boldsymbol{r}_i)$:

$$\Phi(\boldsymbol{r}_1, \ldots, \boldsymbol{r}_A) = \|\varphi_{\alpha_i}(\boldsymbol{r}_i)\| \,, \tag{81}$$

when we act with the operator $\mathrm{e}^{-\mathrm{i}\boldsymbol{R}\cdot\boldsymbol{P}}$, we get the same Slater determinant with the coordinates displaced by an amount $\boldsymbol{R}$:

$$\mathrm{e}^{-\mathrm{i}\boldsymbol{R}\hat{\boldsymbol{P}}} \|\varphi_{\alpha_i}(\boldsymbol{r}_i)\| = \|\mathrm{e}^{-\boldsymbol{R}\boldsymbol{\nabla}_i} \varphi_{\alpha_i}(\boldsymbol{r}_i)\| = \|\varphi_{\alpha_i}(\boldsymbol{r}_i - \boldsymbol{R})\| \tag{82}$$

Since H commutes with $\hat{\boldsymbol{P}}$, it is easy to show that all the states $\Phi_{\boldsymbol{R}}$ (any $\boldsymbol{R}$) have the same energy as Φ:

$$< \Phi_{\boldsymbol{R}} | H | \Phi_{\boldsymbol{R}} > = < \Phi | H | \Phi > \,, \quad \text{for any } \boldsymbol{R} \,. \tag{83}$$

This degeneracy is a characteristic feature of any symmetry breaking by approximate solutions of the variational eqs. (8). One can take advantage of this to construct variational *ansatz* that are linear superpositions of the $\phi_{\boldsymbol{R}}$ states like in (80). This is the basis of two methods: the Generator Coordinate Method and the Method of Variation after Projection , that have been proved to give the exact inertial mass for the translational mode (see, for instance, [18]). What we want to emphasize here is that (80) describes an eigenstate of the total linear momentum and that this state is no longer a single Slater determinant. After projection the energy of the system is then obtained as:

$$< \Psi_k | H | \Psi_k > = \int \frac{\mathrm{d}\boldsymbol{r}}{\mathcal{N}_k^2 (2\pi)^3} \mathrm{e}^{\mathrm{i}\boldsymbol{r}\cdot\boldsymbol{k}} < \Phi | H \mathrm{e}^{-\sum_i \boldsymbol{r}\cdot\boldsymbol{\nabla}_i} | \Phi > \,, \tag{84}$$

with

$$\mathcal{N}_{\boldsymbol{k}}^2 = \int \frac{\mathrm{d}\boldsymbol{r}}{(2\pi)^3} \mathrm{e}^{\mathrm{i}\boldsymbol{r}\cdot\boldsymbol{k}} < \Phi | \prod_i \mathrm{e}^{-\boldsymbol{r}\cdot\boldsymbol{\nabla}_i} | \Phi > \,. \tag{85}$$

The integrand in (85) can be put in the form of a Slater determinant of the following form:

$$\mathcal{N}(\boldsymbol{r}) = < \Phi | \prod_i \mathrm{e}^{-\boldsymbol{r}\cdot\boldsymbol{\nabla}_i} | \Phi > = \|M_{\alpha\beta}(\boldsymbol{r})\| \,, \tag{86}$$

where the matrix elements $M_{\alpha\beta}(\boldsymbol{r})$ are given by:

$$M_{\alpha\beta}(\boldsymbol{r}) = \delta_{\alpha\beta} - \boldsymbol{r}\cdot < \varphi_\alpha | \boldsymbol{\nabla} | \varphi_\beta > - \frac{\boldsymbol{r}^2}{2} < \varphi_\alpha | \boldsymbol{\nabla}^2 | \varphi_\beta > + \cdots = \mathbf{1} + D(\boldsymbol{r}) \,. \tag{87}$$

Hence, the determinant in (86) can be written as:

$$\|M(\boldsymbol{r})\| = \mathrm{e}^{Tr(\ln M)} = \mathrm{e}^{Tr(D(\boldsymbol{r})-\frac{1}{2}D^2(\boldsymbol{r})+\cdots)} , \tag{88}$$

but, from parity considerations, it can easily be seen that:

$$Tr(\ln M) = -\frac{r^2}{2} < \hat{P}^2 > +O(r^4) , \tag{89}$$

with

$$< \hat{P}^2 > = < \Phi | \left(\sum_i \boldsymbol{\nabla}_i \right)^2 | \Phi > \ . \tag{90}$$

Similarly, we may expand $< \Phi | H \mathrm{e}^{\mathrm{i}\boldsymbol{r}\cdot\hat{\boldsymbol{P}}} | \Phi >$ in powers of $\boldsymbol{r}$ to give:

$$< \Phi | H \mathrm{e}^{-\mathrm{i}\boldsymbol{r}\cdot\hat{\boldsymbol{P}}} | \Phi > = \left(< \Phi | H | \Phi > -\frac{r^2}{2} \sum < \Phi | H \hat{P}^2 | \Phi >_L + O(r^4) \right) \mathcal{N} , \tag{91}$$

with

$$< \Phi | H \hat{P}^2 | \Phi >_L = \sum_{\Phi' \neq \Phi} < \Phi | H | \Phi' > < \Phi' | \hat{P}^2 | \Phi > , \tag{92}$$

and Φ' any 2-particle–2-hole excitation with respect to Φ. Keeping terms to order r^2 and integrating over r, one gets for $k = 0$:

$$E_{k=0} = \left. \frac{< \Psi_k | H | \Psi_k >}{< \Psi_k | \Psi_k >} \right|_{k=0} = E_{\mathrm{HF}} - \frac{< \hat{P}^2 >}{2\mathcal{M}} , \tag{93}$$

with

$$2\mathcal{M} = \frac{< \hat{P}^2 >^2}{< \phi | H \hat{P}^2 | \phi >_L} , \tag{94}$$

which gives an estimate of zero point motion correction to the Hartree–Fock energy, and of the inertial mass. This expression (94) for the inertial mass is obviously not right and, as already mentioned, the variation after projection method has to be used to get the right mass AM. A double projection method, where one projects on both $\boldsymbol{k}$ and $\boldsymbol{R}$ gives the translational energy for $k \neq 0$ and the right mass. We have nevertheless worked out the method in some detail for the translational mode to serve as a guide for the more complicated case of angular momentum projection that we consider in what follows.

When the HF (or HFB) solution is not an eigenstate of angular momentum, which is the general case for open shell nuclei, the states of the ground state rotational band can be approximated by projecting out of the wave function Φ the eigenfunctions of $\boldsymbol{J}^2$, J_z with eigenvalues J, M as follows:

$$\Psi^J_M = \frac{1}{\mathcal{N}^J} \sum_K \int \mathrm{d}\Omega \mathcal{D}^{+J}_{KM}(\Omega) \mathcal{R}(\Omega) \Phi(1, \ldots, A) , \tag{95}$$

The rotation operator is

$$\mathcal{R}(\Omega) = \mathrm{e}^{-\mathrm{i}\alpha J_z}\mathrm{e}^{-\mathrm{i}\beta J_y}\mathrm{e}^{-\mathrm{i}\gamma J_z} \ , \tag{96}$$

where $\int \mathrm{d}\Omega$ defines the integral over the three Euler angles α, β and γ [19]: $\int_0^{2\pi} \mathrm{d}\alpha \int_{-1}^{+1} \mathrm{d}(\cos\beta) \int_0^{2\pi} \mathrm{d}\gamma$.

The analogy between the projector in (95) and that in (79) is clear. The unitary operator for translation is replaced by the unitary operator for rotations, and the eigenstates of linear momentum are replaced by the eigenstates $\mathcal{D}^{+J}_{KM}$ of $\boldsymbol{J}$, J_z and J_3 (the z-axis in the body-fixed system).

The method explained before for the generator of the translational motion can be repeated for the generators of the rotational motion. In particular, when the Slater determinantal wave function has axial symmetry and is time reversal invariant, K is a good quantum number and takes the value 0 ($J_z|\Phi >= 0$). Then, only the integration over the angle β between 0 and $\pi/2$ has to be done numerically and one can use a similar procedure to the one discussed before to compute the norm and the expectation values of operators. In this case, the integrands are expanded in powers of $\frac{\beta}{<J_y^2>}$, instead of $\frac{r}{<P^2>}$, and the expression of the energy takes the form

$$< \Psi^{J'}_{M'}|H|\Psi^{J}_{M} >= \delta_{JJ'}\delta_{MM'}\{E_{HF} - \frac{< J_y^2 >}{2\mathcal{I}} + \frac{J(J+1)}{2\mathcal{I}}\} \ , \tag{97}$$

where the moment of inertia is given by the Yoccoz formula :

$$2\mathcal{I} = \frac{< J_y^2 >^2}{< \Phi|HJ_y^2|\Phi >_L} \ . \tag{98}$$

This approximation clearly gives an expression for the energy of projected states that follows the sequence $J(J+1)$ of the rotational band. Again the expression for the moment of inertia can be considered as an approximation to the cranking type expressions obtained when one uses variation after projection. However, at variance with the translational case, there is no exact expression for the moment of inertia with which we may compare, nor is it possible a separation like that of "intrinsic" and "centre of mass" coordinates.

Besides, for well deformed nuclei, $< J_y^2 >$ is a large quantity (typically $< J_y^2 > \geq 100$ in the rare earth region) and the expansion used in powers of $\frac{1}{<J_y^2>}$ is rapidly converging.

Isospin projection methods follow similar considerations as those for angular momentum, and are not repeated here.

To finish with this section, we recall that HFB solutions break in addition particle number . In this case, the independent quasiparticle HFB or BCS wave functions, $|\varphi >$, exhibit clearly their condition of "wave packets" containing many components of eigenfunctions of the particle number operator $\hat{N}$ with different eigenvalues. Wave functions that are eigenstates of $\hat{N}_\pi$ and $\hat{N}_\nu$ (proton and neutron particle number operators) can be constructed from $|\varphi >$ using the

projectors P_π, P_ν as follows:

$$\Psi_{N_\pi N_\nu} = \int \frac{\mathrm{d}\alpha \mathrm{d}\beta}{\mathcal{N}_{N_\pi N_\nu}} \mathrm{e}^{\mathrm{i}\alpha(N_\pi - \hat{N}_\pi)} \mathrm{e}^{\mathrm{i}\beta(N_\nu - \hat{N}_\nu)} |\varphi> \ . \tag{99}$$

A recent application of particle number and isospin projection can be found in [20] for the HFB *ansatz* corresponding to a monopole pairing hamiltonian that contains proton–proton, neutron–neutron and proton–neutron interaction. A major success of PHF(actually, angular momentum projected HF+BCS) approach were the predictions on longitudinal and transverse form factors of deformed nuclei (see [19] and refs. therein). Here we just may add two important final general comments:

1. The projected HF (or HFB) energies are lower than those of the unprojected HF (or HFB) minimum, reflecting the fact that the projected wave function contains more correlations, i.e., goes beyond mean field approximation.
2. The projected HF (or HFB) wave functions can be used as *ansatz* in the general variational principles (eqs. (7), (8)) to go beyond the mean field approximation in a fully selfconsistent way. This method is called variation after projection (VAP), which is clearly superior, but much harder to solve. What variation after projection does with respect to the mean field *ansatz* is to enlarge the space of trial wave functions that have the proper symmetries, eliminating components with different quantum numbers than the chosen ones. This induces correlations that are selfconsistently determined. The ground state energy becomes even lower.

4 Collective modes and the adiabatic time dependent Hartree–Fock approach

Nuclei present a rich variety of excitation modes. In the pure HF picture only single particle excitations can be described when a nucleon jumps from a level below Fermi level to one above. We refer to these excitations as bare particle–hole (1 ph) excitations . The presence of pairing correlations in the HFB of BCS schemes transforms the bare 1 ph excitations into two-quasiparticle excitations (2 qp); bare 2 qp excitations are the elementary modes of excitation of a BCS-like ground state.Yet, many of the known nuclear excitations demand a cooperative contribution of several nucleons in the nucleus. Such modes of excitation are called collective modes and are typically classified into rotations and vibrations in a wide sense, as well as fusion and fission modes, which are large amplitude modes and are of higher collectivity. As we saw in Sect. 2, many nuclei choose as equilibrium shape a non-spherical shape, but rather an ellipsoidal, preferably prolate shape. Such nuclei present a characteristic low line spectrum that follows the sequence $I(I+1)/2\mathcal{I}$, characteristic of a quantum mechanical rotor with collective hamiltonian

$$H_{\mathrm{rot}} = \frac{\boldsymbol{I}^2}{2\mathcal{I}} \ . \tag{100}$$

All known nuclei (except for the lighter ones) present vibrational excitations governed by collective hamiltonians of the form:

$$H_{\text{vibr}} = \sum_{\mu} \left(\frac{\Pi^{+}_{\lambda\mu}\Pi_{\lambda\mu}}{2M_{\lambda}} + \frac{K_{\lambda}}{2} X^{+}_{\lambda\mu} X_{\lambda\mu} \right) \equiv \sum_{\mu} \omega_{\lambda} F^{+}_{\lambda\mu} F_{\lambda\mu} \ . \tag{101}$$

The phonon operator F or the collective coordinate X may correspond to a variety of small amplitude oscillations of the system around equilibrium (oscillations of shape, volume, charge, ...) and may also involve spin and isospin degrees of freedom. Well deformed nuclei may also undergo fission when the Coulomb repulsion wins over surface tension, in the collective hamiltonian

$$H_{\text{fis}} = \frac{P^{2}_{\epsilon}}{2M(\epsilon)} + V(\epsilon) \ , \tag{102}$$

where ϵ denotes elongation and where we make explicit reference to the dependence on ϵ of the inertial mass and potential energy, though other additional macroscopic or collective parameters are also needed to describe the process.

4.1 ATDHF

The purpose of ATDHF (adiabatic time dependent Hartree–Fock approximation) is to describe such collective processes within the framework of the selfconsistent mean field concept. More specifically, the theory aims at deriving microscopically (from the basic nucleon–nucleon interaction) the inertial parameters of the system assigned to various collective modes, and particularly to large amplitude collective modes where the adiabaticity concept may apply.

ATDHF was originally formulated in two different ways by Villars [21,22] and by Baranger and Veneroni [23]. The latter formulation follows from the TDHF eq. (31) assuming that $\rho(t)$ can be decomposed into a time even part $\rho_0(t)$, and a time odd part $\chi(t)$ (that keeps small at any time and that can be regarded as the canonical conjugate momentum to ρ_0). I will discuss here a state vector formulation of Villars [21] and Villars and myself [22], which is somewhat more intuitive and better suited to further extensions of the theory like quantization, or the study of friction or damping along the fission path.

A common feature to all collective hamiltonians ((100)–(102)) is that they are quadratic in the collective velocities. Except for translational motion that completely decouples from the intrinsic variables of the system, the actual nuclear collective modes present anharmonicities and are not completely decoupled from one another. Yet the phenomenological hamiltonians (100)–(102) describe in a first approximation our experimental information on collective modes. Then, to begin with, the adiabaticity assumption can be made of a slow collective motion with negligible coupling to other modes, whose amplitude can be large (like in the case of elongation in the path to fission).

We restrict attention to a particular mode, that we assume for simplicity to be characterized by a single coordinate q and velocity $v = p/M(q)$. We may then

parametrize the time dependence of the wave function $\Psi(t)$ in the variational principle, (6)–(7), in terms of the time dependence of these canonical conjugate coordinates $\Psi(t) = \Psi(q(t), p(t))$. Hence the Lagrangian in (6) reads:

$$\begin{aligned}\mathcal{L} &= <\Psi(q,p)|\mathrm{i}\frac{\partial}{\partial t} - H|\Psi(q,p)>= \\ &= <\Psi(q,p)|\left(\mathrm{i}\dot{q}\frac{\partial}{\partial q} + \dot{p}\frac{\partial}{\partial p}\right)|\Psi(q,p)> - \mathcal{H}(q,p)\ . \end{aligned} \tag{103}$$

Equation (103) reflects the fact that we are assuming that any other degrees of freedom of the system are frozen or evolve through the evolution of q and p. We shall see later on how this constraint can be released [22]. Now if, as in TDHF, we assume that $\Psi(t)$ is a Slater determinant at any time and that the motion is slow, we can write

$$\Psi(t) \simeq \Phi(q,p) = \Phi(q) + \mathrm{i}pQ\Phi(q) + \cdots = \mathrm{e}^{\mathrm{i}pQ}\Phi(q)\ , \tag{104}$$

with $\Phi(q)$ a Slater determinant and Q a hermitian one-body operator, to be determined by the variational principle. For simplicity, we shall assume that the nucleus is even–even, so that $\Phi(q)$ is time-even and so is Q. By virtue of Thouless theorem [24], Q can be chosen to be a 1 ph operator. We can therefore expand the Lagrangian in powers of p to write the least action principle in (7) as

$$\delta I_{12} = \delta\int_{t_1}^{t_2} \mathrm{d}t\,(p\dot{q} < \Phi(q)|[P, \mathrm{i}Q]|\Phi(q) > -\mathcal{H}(q,p)) = 0\ , \tag{105}$$

We have introduced a new operator (time-odd), defined by the relation

$$P|\Phi(q)>= \mathrm{i}\frac{\partial}{\partial q}|\Phi(q)> \tag{106}$$

and a classical hamiltonian

$$\mathcal{H}(q,p) =< \Phi(q)|\mathrm{e}^{-\mathrm{i}pQ}H\mathrm{e}^{\mathrm{i}pQ}|\Phi(q)>= \frac{P^2}{2M(q)} + V(q)\ , \tag{107}$$

where we have used the fact that from time reversal invariance

$$< \Phi(q)|[H,Q]|\Phi(q)>= 0\ , \tag{108}$$

and the slow velocity assumption allows to truncate the expansion to second order in p. The inertial parameters are thus to be determined from $\Phi(q)$ and Q as follows:

$$V(q) =< \Phi(q)|H|\Phi(q)>\ , \qquad \tfrac{1}{M(q)} =< \Phi(q)|[[H,\mathrm{i}Q],\mathrm{i}Q]|\Phi(q)>\ . \tag{109}$$

Then, if we impose the condition that at any time (i.e., at any q value)

$$< \Phi(q)|[P,\mathrm{i}Q]|\Phi(q)>= 1\ , \tag{110}$$

we see that the Lagrangian in (105) acquires the form of a standard classical Lagrangian, and that, taking variations with respect to q and p, we get Hamilton's equations of motion

$$\dot{p} = -\frac{\partial \mathcal{H}}{\partial q} , \quad \dot{q} = \frac{\partial \mathcal{H}}{\partial p} , \tag{111}$$

which ensure that p is the canonical conjugate momentum of q.We then call condition (110) the canonical condition.

Hence, to know how the system evolves, all we need is to find out what are $V(q)$ and $M(q)$, and hence how we can determine $\Phi(q)$ and Q. The equations for Q and $\Phi(q)$ are obtained again from the minimum action principle (7) with $\Psi(t)$ replaced by (104); using the p-expansion and the definitions (106) and (109), we get

$$< \delta\Phi(q)| \left(H - \frac{\partial V}{\partial q} Q \right) + p \left([H, \mathrm{i}Q] - \frac{P}{M} \right) + O(p^2) |\Phi(q) >= 0 , \tag{112}$$

where $\delta\Phi(q)$ is any Slater determinant orthogonal to $\Phi(q)$ (i.e., any 1 ph excitation). Since (112) has to be satisfied independently of the p value, we end up with two conditions:

1. $< \delta\Phi(q)|H - \frac{\partial V}{\partial q} Q|\Phi(q) >= 0$ and h.c.
2. $< \delta\Phi(q)|[H, \mathrm{i}Q] - \frac{P}{M}|\Phi(q) >= 0$ and h.c.

These conditions express the fact that the action must be stationary with respect to small changes in $\Phi(q)$ at any fixed (q, p) point and, together with condition (110), form a set of selfconsistency conditions to determine optimal Slater determinantal wave functions along the collective (adiabatic) path. These three conditions are static equations that are to be satisfied at any point q. The consistency of these equations with the equations of motion and definitions (109), that determine the classical collective path according to Hamilton's equations, can be shown. The actual consistency of these equations can be easily shown by taking in particular $\delta\Phi = Q\Phi$ or $\delta\Phi = P\Phi$ in the static variational equations.

Condition 1 is a static constrained Hartree–Fock equation with Lagrange multiplier $\lambda = \frac{\partial V}{\partial q} =< \Phi(q)|[H, -\mathrm{i}P]|\Phi(q) >$. These conditions imply that the energy surface has a minimum with respect to variations perpendicular to the collective path at any point q along the path, the constraining operator determined selfconsistently by the system.

In realistic applications, it is not an easy task to solve this set of selfconsistent conditions at arbitrary points of the collective path. The clearest case is when we start at the ground state, i.e., at the point q_0 where the potential has its absolute minimum. At this point, we must have

$$< \Phi_0|[H, -\mathrm{i}P_0]|\Phi_0 >= \left. \frac{\partial V}{\partial q} \right|_{q=q_0} = 0 \tag{113}$$

and

$$< \Phi_0|[[H, -\mathrm{i}P_0], -\mathrm{i}P_0]|\Phi_0 >= \left. \frac{\partial^2 V}{\partial q^2} \right|_{q=q_0} = K > 0 . \tag{114}$$

Therefore, at this point conditions 1 and 2 read

$$< \delta\Phi_0|H|\Phi_0 >= 0 \,, \tag{115}$$

$$< \delta\Phi_0|[H, -\mathrm{i}P_0] - KQ_0|\Phi_0 >= 0 \,, \tag{116}$$

$$< \delta\Phi_0|[H, \mathrm{i}Q_0] - P_0/M|\Phi_0 >= 0 \,, \tag{117}$$

where the subscript 0 means that wave functions and operators are at $q = q_0$. Condition (116) is obtained from condition 1 by taking the derivative with respect to q and then the limit $q = q_0$. Equation (115) is nothing else than the static unconstrained HF equation for the ground state, while (116) (117) are the RPA (Random Phase Approximation) equations for the oscillations of the system around equilibrium, subject to the canonical condition (110), that ensures normalization. These eqs. can be written down in the standard form [25] as follows. Since Q_0 (P_0) are hermitian time-even (time-odd) 1 ph operators acting on Φ_0, we may write

$$Q_0 = \sum_{ph} \left(\alpha_{ph} a_p^+ a_h + \alpha_{ph}^* a_h^+ a_p\right) \equiv \frac{1}{\sqrt{2M\omega}} \left(A^+ + A\right) \,, \tag{118}$$

$$P_0 = \mathrm{i} \sum_{ph} \left(\beta_{ph} a_p^+ a_h - \beta_{ph}^* a_h^+ a_p\right) \equiv \mathrm{i}\sqrt{\frac{M\omega}{2}} \left(A^+ - A\right) \,. \tag{119}$$

Using the standard notation for the operators A^+, A:

$$A^+ = \sum_{ph} \left(X^{ph} a_p^+ a_h - Y^{ph} a_h^+ a_p\right) \,, \tag{120}$$

with

$$X^{ph} = \sqrt{\frac{1}{2M\omega}} \left(\beta_{ph} + (M\omega)\alpha_{ph}\right) \tag{121}$$

$$Y^{ph} = \sqrt{\frac{1}{2M\omega}} \left(\beta_{ph}^* - (M\omega)\alpha_{ph}^*\right) \,, \tag{122}$$

it is a simple matter to show that (116), (117) take the standard form

$$< \delta\Phi_0|[H, A^+]|\Phi_0 >= \omega < \delta\Phi_0|A^+|\Phi_0 > \tag{123}$$

$$< \delta\Phi_0|[H, A]|\Phi_0 >= -\omega < \delta\Phi_0|A|\Phi_0 > \,, \tag{124}$$

which are the well known RPA equations

$$\begin{pmatrix} \mathcal{A} & \mathcal{B} \\ \mathcal{B}^* & \mathcal{A}^* \end{pmatrix} \begin{pmatrix} X \\ Y \end{pmatrix} = \omega \begin{pmatrix} X \\ -Y \end{pmatrix} \,, \tag{125}$$

for the normal modes of the system when ω is real and positive.

$\omega = \sqrt{K/M}$ is the phonon energy and X, Y the forward and backward phonon amplitudes subject to the normalization condition

$$\sum_k \left(X_k^2 - Y_k^2\right) = 1 \,, \tag{126}$$

that follows from the canonical condition (110).

We denote by k the 1 particle–hole state element $\mathrm{p}_k\mathrm{h}_k$ (i.e., $\mathrm{p}_k\mathrm{h}_k \equiv k$). In this notation, the $\mathcal{A}$ and $\mathcal{B}$ matrices are

$$\mathcal{A}_{kk'} = \delta_{kk'}(\epsilon_{\mathrm{p}_k} - \epsilon_{\mathrm{h}_k}) - < \mathrm{p}_k\mathrm{h}_{k'}|\bar{V}|\mathrm{p}_{k'}\mathrm{h}_k > \tag{127}$$

$$\mathcal{B}_{kk'} = < \mathrm{p}_k\mathrm{p}_{k'}|\bar{V}|\mathrm{h}_k\mathrm{h}_{k'} > \ . \tag{128}$$

Thus, we see that RPA equations are correlated 1ph-excitations.

In this approximation, the excitation energies ω on the ground state are described not just by single 1 ph excitations, but rather by sets of correlated ph excitations, the correlations being determined by the same two-body interaction that is used to generate the mean field single particle basis. Thus, one goes beyond mean field approximation without losing selfconsistency. The consistency between the mean field (HF or HFB) basis and the residual interaction, is a crucial point (often overlooked in practical applications) to ensure that RPA solutions exist and are meaningful.

The RPA equations can be derived in many ways, yet the above derivation is particularly simple and intuitive. The main point is that the RPA equations appear clearly linked to the condition of minimum for the Hartree–Fock energy. An equivalent formulation in terms of the one-body density matrix and the energy density functional $\mathcal{E}(\rho)$ is

$$\frac{\partial \mathcal{E}}{\partial \rho_k} = 0 \,, \qquad \frac{\partial^2 \mathcal{E}}{\partial \rho_k \partial \rho_{k'}} > 0 \ . \tag{129}$$

The generalization to the HFB scheme is straightforward. In that case, of course, one has that Φ_0 in (115)–(117) represents the HFB vacuum and $\delta\Phi_0$, any two-quasiparticle excitation. Similarly, the operators Q_0, P_0 (and hence A, A^+) are two-quasiparticle operators. Likewise, in (129), $\mathcal{E}$ is replaced by the HFB energy functional that depends on ρ and κ ($\mathcal{E} = \mathcal{E}(\rho, \kappa)$), and (129) is extended to take also variations with respect to the pairing tensor κ. The RPA equations become QRPA equations and their solutions correspond to correlated two-quasiparticle excitations.

It is also instructive to consider the **rotational mode** in this scheme. Let Φ_0 be the unconstrained HF minimum of an axially symmetric even–even nucleus, i.e., Φ_0 satisfies

$$< \delta\Phi_0|H|\Phi_0 >= 0 \tag{130}$$

and has a certain deformation ($d_0 =< \Phi_0|Q_{20}|\Phi_0 >$). If $\Phi(q)$ represents the static solution rotated by an angle q around the axis x (perpendicular to the symmetry axis), we can write

$$|\Phi(q) >= \mathrm{e}^{-\mathrm{i}qJ_x}|\Phi_0 > \,, \qquad P|\Phi(q) >= J_x\Phi(q) \ . \tag{131}$$

If q is time dependent, changing at a rate $\dot{q}$, we write the time dependent wave function $\Phi(t)$ as

$$\Phi(t) = \mathrm{e}^{\mathrm{i}\dot{q}G}\mathrm{e}^{-\mathrm{i}qJ_x}|\Phi_0 >= \mathrm{e}^{-\mathrm{i}qJ_x}\mathrm{e}^{\mathrm{i}\dot{q}G_0}|\Phi_0 >= \mathrm{e}^{-\mathrm{i}qJ_x}\mathrm{e}^{\mathrm{i}pQ_0}|\Phi_0 > , \tag{132}$$

with G_0 a time-even 1 ph operator to be determined, $p = \dot{q}/\mathcal{I}$, $Q_0 = \mathcal{I}G_0$ and $\mathcal{I}$ the moment of inertia. In this case, the condition 1 is simply (130), as the potential energy $V =< \Phi(q)|H|\Phi(q) >$ does not depend on angle q (i.e., $[H, J_x] = 0$), and condition 2 reads

$$< \delta\Phi(q)|[H, \mathrm{i}Q] - \frac{P}{\mathcal{I}(q)}|\Phi(q) >=< \delta\Phi_0|[H, \mathrm{i}Q_0] - \frac{J_x}{\mathcal{I}}|\Phi_0 >= 0 . \tag{133}$$

This is an equation for Q_0, or rather for $Q_0\mathcal{I} = G_0$, which together with the canonical condition, $< \Phi_0|[Q_0, -\mathrm{i}J_x]|\Phi_0 >= 1$, gives for the moment of inertia:

$$\mathcal{I} =< \Phi_0|[G_0, -\mathrm{i}J_x]|\Phi_0 >=< \Phi_0|[[H, \mathrm{i}G_0], \mathrm{i}G_0]|\Phi_0 > , \tag{134}$$

which represents the selfconsistent cranking result. In the simplest approximation, (134) leads to the Inglis moment of inertia , or to

$$\mathcal{I} = \sum_{\alpha\beta}(u_\alpha v_\beta - v_\alpha u_\beta)^2 \frac{| < \alpha|j_x|\beta > |^2}{E_\alpha + E_\beta} \tag{135}$$

in the HFB scheme. However, (134) is more general than (135), it can be used as a variational principle for $\mathcal{I}$ if we write

$$\mathcal{I} = \frac{[< \Phi_0|[G_0, -\mathrm{i}J_x]|\Phi_0 >]^2}{< \Phi_0|[[H, \mathrm{i}G_0], \mathrm{i}G_0]|\Phi_0 >} , \tag{136}$$

involving the total 2-body interaction.

4.2 Quantization

RPA can be considered as the small amplitude limit of ATDHF because the set of selfconsistency conditions (115)–(117) can be obtained using an expansion in powers of q of the ATDHF *ansatz* in (104):

$$\Phi(t) = (1 + \mathrm{i}(pQ - qP) + \cdots)\,|\Phi_0 >= \mathrm{e}^{\mathrm{i}T(q,p)}|\Phi_0 > , \tag{137}$$

with

$$T = T(q, p) = pQ - qP \tag{138}$$

a hermitian operator depending on the variables q and p.

Here and in what follows, to simplify the notation, we assume (without loss of generality) $q_0 = 0$. It is clear that in this limit, ATDHF provides a way to determine the inertial mass and restoring force parameters (M, K) of the collective vibrational mode. These parameters are obtained quantum mechanically, i.e., as expectation values of operators in the HF (or HFB) state Φ_0. Yet, the collective

motion is described classically by Hamilton's eqs. (111) for the classical coordinate and conjugate momentum. To describe the actual (115) collective nuclear mode, we need to quantize the classical variables and hamiltonian. This implies that (q, p) are to be considered as coordinate and linear momentum operators satisfying Heisenberg uncertainty principle $[\hat{q}, \hat{p}] = \mathrm{i}\hbar$.

Since the quantal states we are representing are phonon states of frequency ω, we define phonon creation and destruction operators

$$F^+ = \sqrt{\tfrac{M\omega}{2}}\,(\hat{q} - \mathrm{i}\hat{p}/M\omega)\ , \qquad F = (F^+)^+\ , \tag{139}$$

satisfying boson commutation rules, and quantal states $|f_0>, |f_1>, \ldots, |f_n>$ in the phonon space representing the phonon vacuum, one-phonon state, ..., n-phonon state, respectively, i.e.,

$$F|f_0> = 0 \tag{140}$$

$$|f_n> = \frac{(F^+)^n}{\sqrt{n!}}|f_0>\ . \tag{141}$$

Since these states represent the quantal collective ground state and excitations, we can write expectation values of any operator Θ between the actual nuclear states Ψ_n, Ψ_m as [26]

$$<\Psi_n|\Theta|\Psi_m> = \int \mathrm{d}q f_n^*(q)\hat{\theta}\left(q, \hat{p} = -\mathrm{i}\frac{\partial}{\partial q}\right) f_m = <f_n|\hat{\theta}(\hat{q}, \hat{p})|f_m>\ , \tag{142}$$

where $\hat{\theta}(\hat{q}, \hat{p})$ is the representation of the operator Θ in collective space. Then we may consider that

$$\theta(q,p) = <\Phi(q,p)|\Theta|\Phi(q,p)> = <\Phi_0|\mathrm{e}^{-\mathrm{i}T(q,p)}\Theta\mathrm{e}^{\mathrm{i}T(q,p)}|\Phi_0> = \tag{143}$$

$$= <\Phi_0|\Theta + [\Theta, \mathrm{i}T(q,p)] + \frac{1}{2}[[\Theta, \mathrm{i}T], \mathrm{i}T] + \cdots|\Phi_0> \tag{144}$$

is the classical representation of the operator $\hat{\theta}(\hat{q}, \hat{p})$, and that the latter can be obtained by an expansion like that in (144), in which the classical variables (q, p) in the exponent T are replaced by their quantal analogs ($\hat{q}$, $\hat{p}$). Thus, the particle–hole operator T in (138) is transformed into [26]

$$\hat{T} \equiv \hat{T}(\hat{q}, \hat{p}) = -\mathrm{i}(A^+F - AF^+)\ , \tag{145}$$

which is a two-fold operator acting as a microscopic (ph-operator) on the HF vacuum and as a phonon operator in collective space. The quantal representation in (144) then gives for the operator $\hat{\theta}(\hat{q}, \hat{p})$ an expansion in powers of F, F^+ operators:

$$\hat{\theta}(\hat{q}, \hat{p}) = \Theta_{0,0} + (\Theta_{0,1}F + \Theta_{1,0}F^+) + \Theta_{1,1}F^+F + (\Theta_{0,2}F^2 + \Theta_{2,0}(F^+)^2)\ , \tag{146}$$

with coefficients:

$$\begin{aligned}
\Theta_{0,0} &= <\Phi_0|\Theta|\Phi_0> -\frac{1}{2} <\Phi_0|[[\Theta, A^+], A] - [\Theta, A]A^+ + [\Theta, A^+]A|\Phi_0> \\
\Theta_{0,1} &= <\Phi_0|[\Theta, A^+]|\Phi_0> \\
\Theta_{1,0} &= - <\Phi_0|[\Theta, A]|\Phi_0> \\
\Theta_{1,1} &= -\frac{1}{2} <\Phi_0|[[\Theta, A^+], A] + [[\Theta, A], A^+]|\Phi_0>
\end{aligned} \tag{147}$$

The two-phonon term must be taken with caution as it is most sensitive to anharmonicities.

Substitution of (146) into (142) gives the following meaning to these coefficients: $\Theta_{0,0}$ is the expectation value of the operator Θ in the ground state phonon vacuum; $\Theta_{0,1}$ and $\Theta_{1,0}$ are the matrix elements of the operator Θ between the phonon vacuum and the one-phonon state; $\Theta_{1,1}$ is the expectation value of Θ between 1-phonon states and so on. This gives in particular for the ground state energy

$$<\Psi_0|H|\Psi_0> = <f_0|\hat{\mathcal{H}}|f_0> = H_{0,0} = E_{\mathrm{HF}} - \omega \sum_{\mathrm{ph}} |Y_{\mathrm{ph}}|^2 \,, \tag{148}$$

which gives a quantal (zero point) energy correction to the Hartree–Fock energy analogous to that obtained in the generator coordinate method. This energy is called the RPA correlated ground state energy.

Similar arguments can be used to obtain zero point energy corrections and quantal collective hamiltonians for large amplitude collective modes. For applications to the description of fission or fusion path, it is more convenient to use the formulation of [22,26], where several collective degrees of freedom are allowed to develop along the path. This permits in particular to study the coupling between small and large amplitude modes, and to establish a framework for a microscopic description of friction or damping. The actual power of this fully selfconsistent scheme has not been fully exploited in realistic calculations, but the elements introduced in this section, like constrained HF (or HFB), RPA (or QRPA), as well as zero point energy corrections are currently taken into account in many microscopic calculations of energy spectra [27], fission barriers [28], electromagnetic response functions [29] and β-decay half-lives [30]. Some of these recent results are illustrated in Figs.1, 2, and 3.

4.3 Generator coordinate method

To finish with this section, we point out that the quantized ATDHF approach has a parallelism with the generator coordinate method (GCM). In GCM, one looks for solutions of variational problems starting with the *ansatz*

$$\Psi = \int (\mathrm{d}\bar{q}) f(\bar{q}) \Phi(\bar{q}) \,, \tag{149}$$

where $\bar{q} = (q_1, \ldots, q_n)$ are the generator coordinates, that may or may not be interpreted as collective coordinates. The weight functions $f(\bar{q})$ are determined by the variational condition

$$\frac{\delta \mathcal{E}}{\delta f(\bar{q})} = 0 \ , \quad \mathcal{E} = \frac{<\Psi|H|\Psi>}{<\Psi|\Psi>} \ , \tag{150}$$

leading to the Hill–Wheeler equation

$$\int (\mathrm{d}\bar{q}') < \Phi(\bar{q})|H - E|\Phi(\bar{q}') > f(\bar{q}') = 0 \ . \tag{151}$$

We also note that GCM and variation after projection methods may be treated in parallel, although GCM is not necessarily related to broken symmetries. Here we just apply the method to the vibrational modes around equilibrium shape (Φ_0), to show the analogy with quantized ATDHF. We then may represent $\Phi(\bar{q})$ as

$$|\Phi(\bar{q}) >= \exp(\sum_{\mathrm{ph}} q_{\mathrm{ph}} a_{\mathrm{p}}^{+} a_{\mathrm{h}})|\Phi_0 > \ , \tag{152}$$

where q_{ph} are complex parameters. The scalar product is given by

$$< \Phi(\bar{q})|\Phi(\bar{q}') >= \exp\left(Tr \ln(1 + A)\right) = \exp\left(Tr(A - \frac{1}{2}A^2 + \cdots)\right) \ , \tag{153}$$

where the non zero matrix elements of A are

$$A_{\mathrm{hh}'} = \sum_{\mathrm{p}} q^*_{\mathrm{ph}} q'_{\mathrm{ph}'} \ . \tag{154}$$

The integrand of the Hill–Wheeler eq. (151) can then be expanded in terms of $\bar{q}$, $\bar{q}'$ to give:

$$\frac{< \Phi(\bar{q})|H - E|\Phi(\bar{q}') >}{< \Phi(\bar{q})|\Phi(\bar{q}') >} = E_{\mathrm{HF}} - E + \sum_{k,k'} \mathcal{A}_{kk'} q^*_k q'_{k'} + \frac{1}{2}\mathcal{B}^*_{kk'} q'_k q'_{k'} + \frac{1}{2}\mathcal{B}_{kk'} q^*_k q^*_{k'} \ , \tag{155}$$

with $\mathcal{A}$ and $\mathcal{B}$ the matrices defined in (127), (128). Substitution of this equation into Hill–Wheeler equations leads to the RPA equations if we approximate the overlap function by

$$< \Phi(\bar{q})|\Phi(\bar{q}') > \cong \mathrm{e}^{TrA} = \mathrm{e}^{\bar{q}^* \cdot \bar{q}'} \ . \tag{156}$$

This is known as the quasiboson approximation because the overlap function has the form of a scalar product of coherent states

$$< \bar{q}|\bar{q}' >=< 0|\mathrm{e}^{\bar{q}^* \cdot \bar{b}} \mathrm{e}^{\bar{q}' \cdot \bar{b}^+}|0 >= \mathrm{e}^{\bar{q}^* \cdot \bar{q}'} \ , \tag{157}$$

with $\bar{b}^+ = (b_1^+, \ldots, b_n^+)$ boson creation operators and $|0>$ the boson vacuum. We now consider $f(\bar{q})$ in (151) as the Bargmann representation of a state $|f>$ (i.e., $f(\bar{q}) =< \bar{q}|f >$) and make use of the properties of coherent states

$$b_k|\bar{q} >= q_k|\bar{q} > , \quad b_k^+|\bar{q} >= \frac{\partial}{\partial q_k}|\bar{q} > \tag{158}$$

and of the completeness relation

$$\int \mathrm{d}\bar{q}|\bar{q}><\bar{q}| = 1 \,, \tag{159}$$

as well as of (157), to write the Hill–Wheeler equation as

$$\mathcal{H}_C|f>=(E-E_0)|f> \,, \tag{160}$$

with

$$\mathcal{H}_C = \sum_{kk'}(\mathcal{A}_{kk'}b_k^+b_{k'} + \frac{1}{2}\mathcal{B}_{kk'}b_k^+b_{k'}^+ + \frac{1}{2}\mathcal{B}_{kk'}^*b_kb_{k'}) \,. \tag{161}$$

The transformation that diagonalizes this hamiltonian leads to the RPA equations (125).

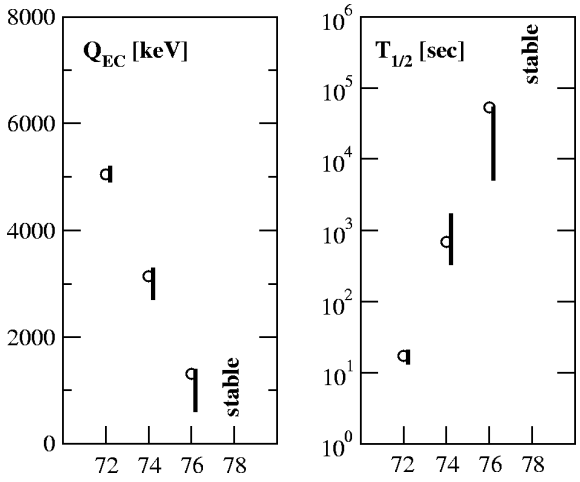

Fig. 1. Q_{EC} values and β-decay half-lives of even-even Kr isotopes

Recent applications of the methods discussed in the previous sections are illustrated in Figs. 1, 2, and 3.

Fig.1 shows results of beta decay half-lives of several Kr even-even isotopes (from stable $A = 78$ to proton rich $N = Z$), obtained in a consistent HF+BCS+QRPA scheme that has no free parameters.The experimental values are indicated by open circles in the top panels. Vertical segments represent "theoretical error bars", to indicate that different values are obtained depending on the effective 2-body Skyrme type interaction (Sk3 or SG2) used in the calculations.

These "error bars" include also results corresponding to beta-decay from different HF+BCS minima,which as seen in Fig.2 in most cases are very close

in energy. The occurrece of shape coexistence in these isotopes is seen in Fig.2, where we plot the energy as a function of qudrupole deformation. As a general rule (see also [29,30]) prolate shapes with Sk3 force give the largest half-lives.It is remarkable that half-lives ranging from few seconds to several hours are well accounted for by the QRPA calculations.

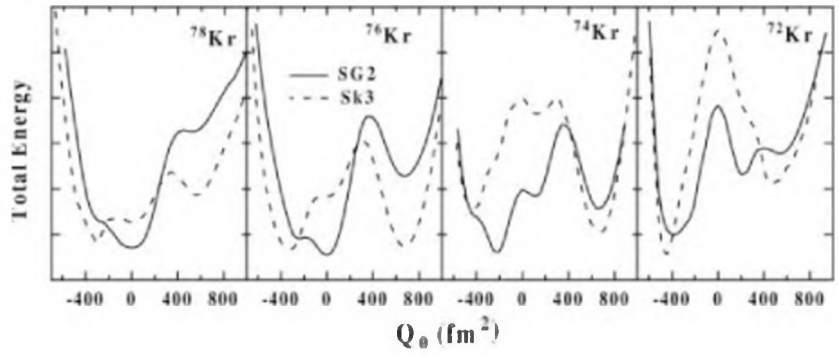

Fig. 2. Energy profiles from HF+BCS calculations with two different Skyrme type forces of even-even Kr isotopes

In Fig.3 we show recent HFB calculations of the fission path of ^{254}No by Egido and Robledo [28],where quadrupole and octupole deformations are active degrees of freedom.Zero point energy corrections discussed in sections 3 and 4 are also taken into account in the curve labled HFB+ZPE.

5 Relativistic bound nucleon dynamics probed by quasielastic electron scattering

In previous lectures, we discussed microscopic methods and approaches to go beyond mean field approximation using as support an optimal single particle basis provided by non-relativistic selfconsistent mean field theory. In this section, we look at the boundaries of non-relativistic mean field from other point of view, that of relativistic mean field theory. Although most of nuclear structure can be understood treating bound nucleons non-relativistically, it pays to study what are the implications of Dirac equation for bound particles. The subject of relativistic mean field (RMF) theory will be discussed by P. Ring. I will concentrate here on the implications that relativistic bound nuclear dynamics has for observational features in quasielastic electron scattering.

Mean field based theories may not compete with shell model oriented approaches in their spectroscopic achievements in medium mass nuclei. Yet, except for the very light systems, selfconsistent mean field theories have no substitute in

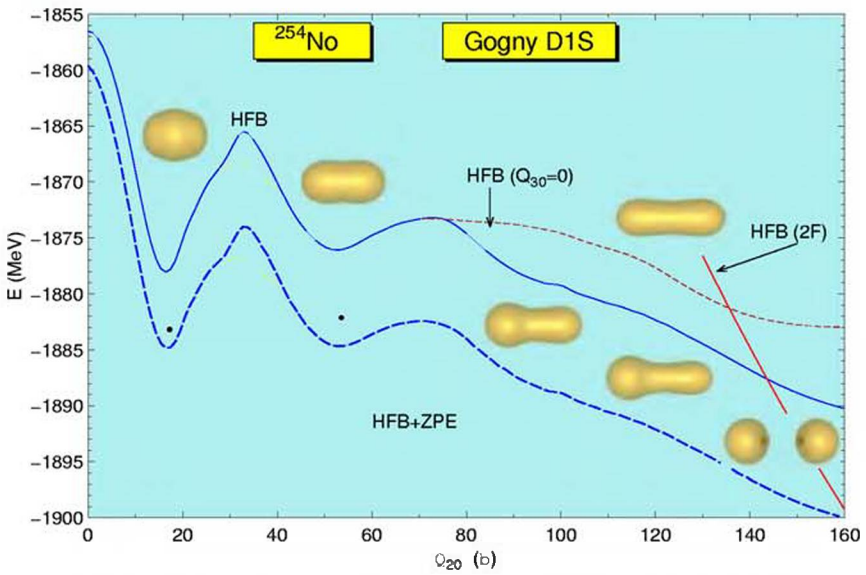

Fig. 3. Fission path calculations for ^{254}No by Egido and Robledo [28]

describing spatial and momentum distributions on nucleons in nuclei. It has been already mentioned that DDHF approach describes well charge and magnetization density distributions of spherical nuclei and that even the electric and magnetic form factors of deformed nuclei are well understood with angular momentum projected DDHF wave functions. As explained in the talks of T.W. Donnelly, these properties are measured experimentally by elastic and inelastic electron scattering to discrete nuclear states.

Elastic electron scattering maps out the charge and magnetic form factors of nuclei. Similarly, quasielastic electron scattering maps out the momentum distributions. When an electron interacts with a bound proton and knocks it out of the nucleus, the outgoing proton can be measured in coincidence with the electron and the bound nucleon wave function in momentum space can be mapped out. This process dominates the electron–nucleus cross section when the energy transfer $\omega \simeq |Q^2|/2M$ (i.e., when the scaling variable $y \simeq 0$ or the Bjorken $x \simeq 1$). Relativistic effects of bound nucleon dynamics are expected to be seen preferentially in their momentum distributions, and thus (e,e'p) coincidence measurements at quasielastic kinematics can be thought of as the main source of information of the role of relativity in the nuclear interior. Actually, very little is known phenomenologically because:

- In high energy physics, particles are always treated as plane waves and their internal structure is oversimplified.
- In atoms and nuclei, electrons and nucleons can mainly be treated non-relativistically. However, it is well known that spin-orbit interaction origi-

nates from Dirac equation and that,in particular, the different central potentials (Coulomb and Woods-Saxon type potentials) in atoms and nuclei explain the fact that spin-orbit is much stronger in nuclei.

Except for spin-orbit interaction, there is very little knowledge about characteristic features of relativity for bound particles. An issue that may be crucial to understand quark dynamics in the hadron interior.

In a series of papers [31], we have investigated this issue comparing predictions on momentum distributions obtained with relativistic and non-relativistic nucleon wave functions. To make a long story short, we may summarize it as follows:

1. Relativistic (RDWIA) and non-relativistic (DWIA) approximations were used to analize existing data on hole states close to Fermi level in ^{208}Pb and ^{40}Ca, with the conclusion that the spectroscopic factors S_α obtained in RDWIA were larger than those obtained in DWIA. For $3s_{1/2}$ shell in ^{208}Pb, S_α(RDWIA) $\simeq 0.7$ and S_α(DWIA) $\simeq 0.5$. A reduction from the HF value $S_\alpha = 1$ to $S_\alpha = 0.7$ at most is what can be expected from short range correlation effects [32], while long range correlations are expected to cause less than a 10% effect, except in soft nuclei [26]. Thus, on theoretical grounds, a spectroscopic factor of 0.7 for the $3s_{1/2}$ shell in ^{208}Pb is better justified than one of 0.5.
2. For high missing momentum P_m (i.e., for high bound nucleon momentum), RDWIA calculations agree with experiment much better than DWIA. The latter give too small cross sections when using wave functions and spectroscopic factors fitted to the lower P_m-sector.
3. The longitudinal-transverse response (R_{TL}) reaches much larger absolute values in RDWIA than in DWIA. In addition, for spin–orbit partner orbitals ($l_{j=l-1/2}$, $l_{j=l+1/2}$), RPWIA predicts a larger effect on $|R_{TL}|$ for the jackknifed ($l_{j=l-1/2}$) than for the stretched state [33], a prediction that has been confirmed experimentally [34].

In what follows, I will describe why this is so. But first we explain what the terms RDWIA and DWIA mean: DWIA stands for distorted wave impulse approximation, the prefix R is used to denote relativistic approach. To avoid confusion, we have to make it clear that relativistic or non-relativistic refers only to the treatment of the nucleon wave functions and current operator. At the energies involved in (e,e'p) experiments, electrons are ultrarelativistic, and the expressions for differential cross sections are obtained from a relativistic invariant amplitude

$$\mathcal{M} = l^\mu J_\mu / |Q^2| \,, \tag{162}$$

with l^μ the leptonic current and J_μ the hadronic current. When final state interactions are taken into account and nucleon distorted waves are used for the outgoing nucleon, the four-vector hadronic current J_μ is written as

$$J_\mu(\omega, q) = \int \mathrm{d}\boldsymbol{p} \bar{\Psi}_F(\boldsymbol{p}+\boldsymbol{q}) \hat{J}_\mu(\omega, q) \Psi_B(\boldsymbol{p}) \,. \tag{163}$$

In RDWIA, Ψ_B and $\bar{\Psi}_F$ are relativistic bound [35] and scattering [36] wave functions, respectively and $\hat{J}_\mu$ is the relativistic free nucleon current operator. In DWIA, the nucleon wave functions are obtained from Schrödinger equations with phenomenological (Woods–Saxon type) potentials and the 4×4 matrices $\hat{J}_\mu$ are replaced by non-relativistic 2×2 matrices $\hat{J}^{nr}_\mu$ for free bispinors, which are usually truncated to order $(P/M)^2$. Thus, there are three types of relativistic effects of different nature to be examined:

- Effects due to above mentioned truncations of the current operator which are kinematical, i.e., come from relativistic kinematics compared to the non-relativistic one.
- Effects due to the $S-V$ potentials, which are dynamical. Among the latter, we have to distinguish between complex $S-V$ optical potentials [36] used for the scattering nucleon wave and real $S-V$ potentials [35] used for the bound nuclear states.

The effects of the $S-V$ potentials are best discussed transforming Dirac equations for Ψ

$$[\gamma_0 \bar{E} - \boldsymbol{\gamma} \cdot \boldsymbol{p} - \bar{M}]\Psi = 0 \,, \tag{164}$$

with

$$\bar{E} = E - V \,, \quad \bar{M} = M - S \,, \tag{165}$$

into Schrödinger like equations for the upper (Ψ_{up}) and lower (Ψ_{down}) components

$$\Psi^\kappa = \begin{pmatrix} \Psi^\kappa_{up} \\ \Psi^\kappa_{down} \end{pmatrix} \,. \tag{166}$$

From Dirac eq. (164), we get

$$\Psi^\kappa_{up} = \frac{\boldsymbol{\sigma} \cdot \boldsymbol{p}}{\bar{E} - \bar{M}} \Psi^\kappa_{down} \tag{167}$$

$$\Psi^\kappa_{down} = \frac{\boldsymbol{\sigma} \cdot \boldsymbol{p}}{\bar{E} + \bar{M}} \Psi^\kappa_{up} \,. \tag{168}$$

We recall that the label κ in four-spinors Ψ stands for j- and π-quantum numbers. The relativistic parity operator

$$\Pi = \gamma^0 P \quad (\text{with } P(\Phi(\boldsymbol{r})) = \Phi(-\boldsymbol{r})) \,, \tag{169}$$

has eigenvalue $\pi = (-1)^\kappa \kappa/|\kappa|$, and the total angular momentum eigenvalue is $j = |\kappa| - 1/2$. Thus, j^+ corresponds to $\kappa = \text{even} > 0$ ($j = \kappa - 1/2$) or to $\kappa = \text{odd} < 0$ ($j = -\kappa - 1/2$), and j^- corresponds to $\kappa = \text{odd} > 0$ ($j = \kappa - 1/2$) or to $\kappa = \text{even} < 0$ ($j = -\kappa - 1/2$). From (167), (168), it is clear that Ψ^κ_{up} and Ψ^κ_{down} have opposite parity, and their eigenvalues of orbital angular momentum differ by one unit. Since in the non-relativistic limit only Ψ^κ_{up} prevails, we may use the l-label of this components to characterize the κ states and the label $\bar{l}$

to characterize the l-eigenvalue of Ψ^{κ}_{down}. From the above arguments, it is clear that j^{π} states are characterized using the following correspondence:

$$
\begin{aligned}
j^{+} \rightarrow & \begin{cases} \kappa > 0\,, \ l = \kappa = \text{even}\,, & \bar{l} = \kappa - 1 = \text{odd}\,, \ j = \kappa - 1/2 \\ \kappa < 0\,, \ l = |\kappa| - 1 = \text{even}\,, & \bar{l} = |\kappa| = \text{odd}\,, \quad j = |\kappa| - 1/2 \end{cases} \\
j^{-} \rightarrow & \begin{cases} \kappa > 0\,, \ l = \kappa = \text{odd}\,, & \bar{l} = \kappa - 1 = \text{even}\,, \ j = \kappa - 1/2 \\ \kappa < 0\,, \ l = |\kappa| - 1 = \text{odd}\,, & \bar{l} = |\kappa| = \text{even}\,, \quad j = |\kappa| - 1/2 \end{cases}
\end{aligned}
\tag{170}
$$

As we shall see, these relations are important to understand the third point above mentioned. They are also at the origin of pseudospin symmetry invoked by Ginochio [37]. After separation of angular and spin dependence in (167), (168), one gets the standard coupled linear differential equations for $g_{\kappa} = g_{l}$ and $f_{\kappa} = f_{\bar{l}}$, whose solutions are used in RDWIA calculations [31,33]. However, to understand dynamical relativistic effects, it is better to rewrite (164) (or (167), (168)) as:

$$
\left(\boldsymbol{\nabla}^2 + \frac{1}{A_+} \frac{\partial A_+}{\partial r} \left(\frac{\boldsymbol{\sigma} \cdot \boldsymbol{l}}{r} - \frac{\partial}{\partial r} \right) + A_+ A_- \right) \Psi^{\kappa}_{up} = 0 \tag{171}
$$

$$
\left(\boldsymbol{\nabla}^2 + \frac{1}{A_-} \frac{\partial A_-}{\partial r} \left(\frac{\boldsymbol{\sigma} \cdot \boldsymbol{l}}{r} - \frac{\partial}{\partial r} \right) + A_+ A_- \right) \Psi^{\kappa}_{down} = 0\,, \tag{172}
$$

with

$$
A_{\pm} = \bar{E} \pm \bar{M}\,, \tag{173}
$$

which are Schrödinger like equations, with non-local potentials, equivalent to Dirac eq. (164). Note that V includes Coulomb potential, and S is defined with opposite sign to the usual convention for convenience of notation (thus, in nuclear matter, $V_0 \simeq 330$MeV and $S_0 \simeq 430$MeV). Equations (171) and (172) show that Ψ_{up} and Ψ_{down} are subject to the same central energy dependent potential

$$
U_C \equiv \frac{(\bar{E}^2 - \bar{M}^2) - (E^2 - M^2)}{2M} = \frac{V^2 - S^2 - 2(VE - MS)}{2M}\,, \tag{174}
$$

but to different spin–orbit and non-local potentials (or different effective masses). Furthermore, one can remove the non-local terms in (171), (172) to make the equations look like standard Schrödinger equations with central potentials. It is a simple matter to show that the function

$$
K(r) = \sqrt{A}\,, \quad A = \tfrac{A_+}{E+M} = 1 - \tfrac{V+S}{E+M} \tag{175}
$$

does this for us. If we define a bispinor

$$
\Phi^{l}_{j}(\boldsymbol{r}) = K(r) \Psi^{\kappa}_{up}(\boldsymbol{r})\,, \tag{176}
$$

(171) takes the form

$$
\left(-\frac{\nabla^2}{2M} - U_{\mathrm{DEB}} \right) \Phi^{l}_{j}(\boldsymbol{r}) = 0 \tag{177}
$$

$U_{\rm DEB}$ is called the Dirac equivalent Schrödinger potential. It contains a new central potential ($V_C = U_C + V_D$) and the spin–orbit potential

$$U_{\rm DEB} = U_C + V_D + V_{SO}\boldsymbol{\sigma}\cdot\boldsymbol{l}\,, \tag{178}$$

with the well known spin–orbit term

$$V_{SO} = \frac{1}{2Mr}\frac{1}{A_+}\frac{\partial A_+}{\partial r} \tag{179}$$

and the Darwin term

$$V_D = \frac{1}{2M}\left[\frac{(\nabla^2 K(r))}{K(r)} - 2\left(\frac{1}{K}\frac{\partial K}{\partial r}\right)^2\right]\,. \tag{180}$$

We are now in a position where we may compare standard non-relativistic optical potentials to DEB ones. In Figs.4 and 5, we show by solid lines the various terms of the potentials and the function $K(r)$ for kinematical conditions that match those of(e,e'p) experiments used to extract above mentioned spectroscopic factors in ^{208}Pb (where protons of 100 MeV were detected). $U_{\rm DEB}$ relativistic terms in Fig.4 are obtained from the $S-V$ global potentials of [36]. The standard non-relativistic terms are those used in the non-relativistic analyses obtained from fits to elastic scattering from ^{208}Pb of 100 MeV protons.

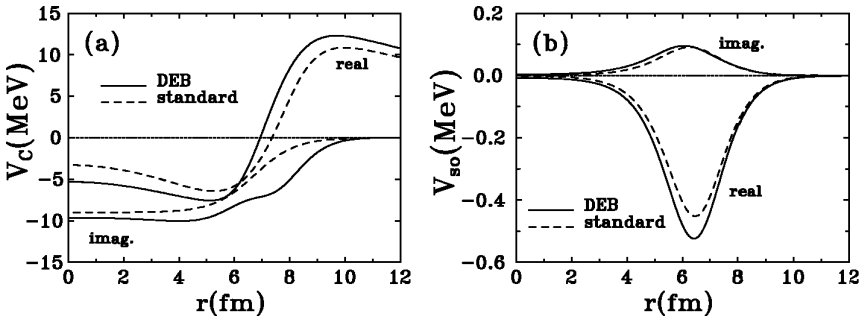

Fig. 4. Real and imaginary parts of Central and spin-orbit standard and DEB optical potentials for 100 MeV protons on ^{208}Pb

Let us then study point 1. The comparison of the spectroscopic factors (S_α(RDWIA) $\simeq$ (7/5)S_α(DWIA)) indicates that RDWIA produces more absorption than DWIA. However, as seen in Figs.4(a) and 4(b), neither real nor imaginary parts of standard and DEB potentials differ in a way that explains such a big effect. Why is then an increased absorption?

The answer to this question is in (176) and in Fig.5, which show that the relativistic component Ψ_{up} has an important depletion in the nuclear interior compared to $\Phi(r)$. This important effect of "increased absorption in the nuclear

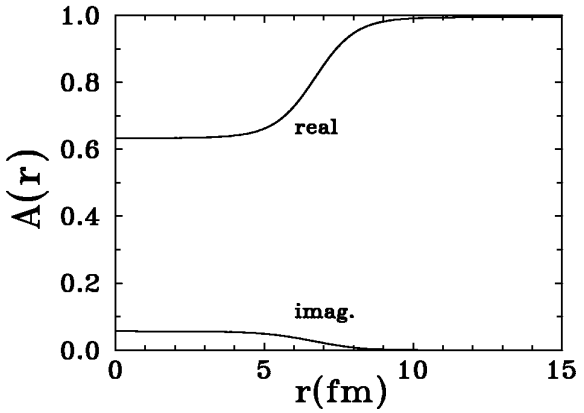

Fig. 5. Real and imaginary parts of $A(r)$

interior" is due to the Darwin or non-local potential $\left(V_{\rm non-loc} = \frac{1}{2M}\frac{{\rm d}\ln A_+}{{\rm d}r}\frac{\rm d}{{\rm d}r}\right)$, which similarly to spin–orbit potential (V_{SO}), comes out automatically from Dirac equations with $S-V$ potentials. Such an effect can also be incorporated in phenomenological non-relativistic potentials. The advantage of using Dirac phenomenology is that both V_{SO} and $V_{\rm non-loc}$ come from the same $S-V$ relativistic potentials. The increased suppression of the scattering wave function in the nuclear interior produced by $K(r)$ (non-locality factor) can also be interpreted as due to the reduced effective mass in the nuclear interior (for $E \simeq M$, $K^2(r) \simeq M^*(r)/M \simeq 0.6$ in nuclear matter). *In this sense, we may consider that (e,e'p) experiments are a probe of the effective mass* . We stress here that this effect is less and less important as the kinetic energy of the detected outgoing proton becomes larger and larger.

The answer to remaining questions 2 ,3 (why in RDWIA we have larger high momentum components? and why increased asymmetry or R_{TL} response?), can be understood as due mainly to the role of the down (Ψ^κ_{down}) components of the bound nucleon wave function. More precisely, these effects are mainly due to the dynamical enhancement of down components of Ψ^κ_B. This in turn is also related to the effective mass because as seen from (168)

$$\Psi^\kappa_{down} - \frac{\boldsymbol{\sigma}\cdot\boldsymbol{p}}{E+M}\Psi^\kappa_{up} = \left(\frac{1}{\bar{E}+\bar{M}} - \frac{1}{E+M}\right)\boldsymbol{\sigma}\cdot\boldsymbol{p}\Psi^\kappa_{up}\,. \tag{181}$$

Thus, the dynamical enhancement of Ψ^κ_{down} is proportional to $(M^*/M)^{-1}$ for $E \simeq M$. Note that the dynamical enhancement of down components increases with increasing binding energy.

In non-relativistic approaches, the current operator $\hat{J}_\mu$ is expanded in a basis of free nucleon plane waves. This amounts to a truncation of the nucleon propagator that ignores negative energy solutions of the free Dirac equation, and thus negative energy projections of the bound nucleon wave functions. In RDWIA,

this truncation is not made.Thus, non-zero overlaps of bound nucleon wave functions with Dirac sea (which are proportional to the dynamical enhancement of the down components) contribute to the cross section. This contributions enhance the high momentum components and the TL asymmetry of the reduced cross section [33] in a way that makes theory compatible with experimental observations.

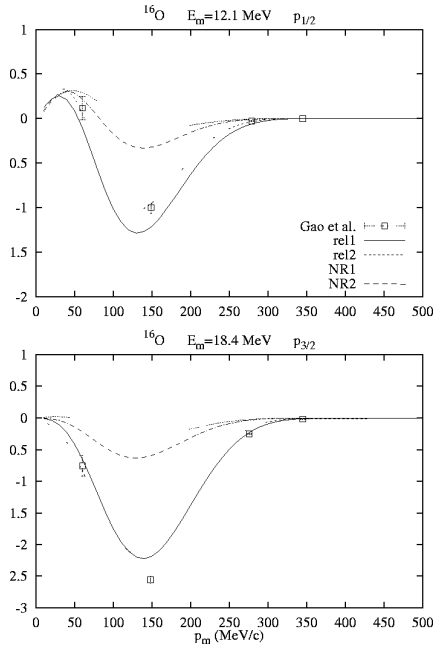

Fig. 6. R_{TL} response for proton knockout from $p_{1/2}$ and $p_{3/2}$ orbitals in ^{16}O. Relativistic calculations with cc1 and cc2 current operators are labelled as rel1, rel2 , respectively. NR1 and NR2 stand for nonrelativistic calculations

This is illustrated in Fig. 6, where we show the TL response (R_{TL}) calculated in relativistic and non-relativistic approaches [33]. The RDWIA results seem to be confirmed by recent experimental data also shown in the figure [34]. Not only the enhancement of the asymmetry and $|R_{TL}|$, but also the fact that the latter reaches larger values for $p_{3/2}$ than for $p_{1/2}$ bound states seems to be confirmed by data and can be understood by inspection of the cross section in RPWIA (i.e., omitting the effect of final state interactions and using plane waves for the outgoing nucleon,within relativistic scheme).

If we expand the bound nucleon wave function in momentum space $\Psi^{\kappa}(\boldsymbol{p})$ in the complete basis of positive (u) and negative (v) energy free Dirac spinors, we

have

$$\Psi_m^\kappa(\boldsymbol{p}) = \sum_s \left\{ u(\boldsymbol{p},s)\mathcal{N}_{\kappa m}^{(+)s}(\boldsymbol{p}) + v(\boldsymbol{p},s)\mathcal{N}_{\kappa m}^{(-)s}(\boldsymbol{p}) \right\} , \tag{182}$$

with $\mathcal{N}^{(+)}$, $\mathcal{N}^{(-)}$ the positive and negative energy projections:

$$\mathcal{N}_{\kappa m}^{(+)s}(\boldsymbol{p}) = \bar{u}(\boldsymbol{p},s)\Psi_m^\kappa(\boldsymbol{p}) = \sqrt{\frac{E_p+M}{2M}} < s|\Psi_{up}^{\kappa m} - \frac{\boldsymbol{\sigma}\cdot\boldsymbol{p}}{E_p+M}\Psi_{down}^{\kappa m} > \equiv$$
$$\equiv \tilde{\alpha}_\kappa(p) < s|\mathrm{i}^l \Phi_m^\kappa(\Omega_p) > \tag{183}$$

$$\mathcal{N}_{\kappa m}^{(-)s}(\boldsymbol{p}) = -\bar{v}(\boldsymbol{p},s)\Psi_m^\kappa(\boldsymbol{p}) = \sqrt{\frac{E_p+M}{2M}} < s|\Psi_{down}^{\kappa m} - \frac{\boldsymbol{\sigma}\cdot\boldsymbol{p}}{E_p+M}\Psi_{up}^{\kappa m} > \equiv$$
$$\equiv \tilde{\beta}_\kappa(p) < s|\mathrm{i}^l \Phi_m^{-\kappa}(\Omega_p) > \ . \tag{184}$$

Note that $\mathcal{N}_\kappa^{(-)}(\boldsymbol{p})$ is zero in the limit of plane waves as well as in the non-relativistic limit, and is proportional to the dynamical enhancement of Ψ_{down}^κ. Using plane waves for the outgoing nucleon wave function and the expression in (182) for the bound nucleon wave function, it is easy to show that the differential cross section takes the form

$$\left(\frac{\mathrm{d}\sigma}{\mathrm{d}\boldsymbol{k}_e \mathrm{d}\boldsymbol{p}_N}\right)_{\mathrm{RPWIA}} \propto \left[\sigma_{uu}^{ep} N_{uu}(p) + \sigma_{vv}^{ep} N_{vv}(p) + \sigma_{uv}^{ep} N_{uv}(p)\right] , \tag{185}$$

where the two last terms come from the negative energy component $\mathcal{N}_s^{(-)}(\boldsymbol{p})$ and are not present in the non-relativistic (PWIA) approach. In the latter approach, one has the factorized expression:

$$(\mathrm{d}\sigma)_{\mathrm{PWIA}} \propto \sigma_{uu}^{ep} N_{uu}(p) \ . \tag{186}$$

In DWIA, factorization is lost also in non-relativistic approach, but the asymmetry caused by the two additional terms in (185) produces an enhanced RDWIA asymmetry.

Finally, the fact that as seen from (170), the down component of $p_{1/2}$ is an s-wave while that of the $p_{3/2}$ is a d-wave, explains the different effect on the TL response for the $p_{1/2}$ state . This is a genuine relativistic effect that cannot be accounted for in non-relativistic approaches.

Acknowledgments

The assistance of A. Escuderos and Dr. P. Sarriguren in the preparation of the TeX files is warmly acknowledged. I am also indebted to Dr. P.- H. Heenen, Dr. J.L. Egido and Dr. L.M. Robledo for permission to use their results in this series of lectures. This work has been supported in part by M.E.C. and by M.C.Y T. (Spain) under contract PB98/0676.

References

1. H.J. Lipkin: Ann. Phys. **9**, 272 (1960)
2. A repulsive core that goes to infinity as $r \to 0$ has recently been derived from QCD, see F. Fernández, A. Valcarce, U. Straub, A. Faessler: J. Phys. G **19**, 2013 (1993); A. Valcarce, P. González, F. Fernández, V. Vento: Phys. Lett. B **367**, 35 (1996)
3. J.W. Negele: Phys. Rev. **C1**, 1260 (1970)
4. D. Vautherin, D.M. Brink: Phys. Rev. **C5**, 626 (1972); J.W. Negele, D. Vautherin: Phys. Rev. **C5**, 1472 (1972); J.W. Negele, D. Vautherin: Phys. Rev. **C11**, 1031 (1975)
5. P. Ring, P. Schuck: *The Nuclear Many-Body Problem* (Springer-Verlag, New York Inc. 1980); I.Zh. Petkov, M.V. Stoitsov: *Nuclear Density Functional Theory* (Clarendon Press, Oxford 1991)
6. V.R. Pandharipande: Nucl. Phys. **A655**, 157c (1999)
7. L. Zamick, H. Geesman ,private communication
8. P. Sarriguren, E. Moya de Guerra, R. Nojarov: Z. Phys. **A357**, 143 (1997) and refs. therein
9. M. Coloma, M. Di Toro, G. Fabbri, S. Maccarone: Phys. Rev. **C57**, 1410 (1998); M. Di Toro in: *Structure and Stability of Nucleon and Nuclear Systems, International Summer School at Predeal, Rumania, 1998*, ed. by A.A. Raduta, S. Stoica, I.I. Ursu (World Scientific, Singapore 1999)
10. T.H.R. Skyrme: Phil. Mag. **1**, 1043 (1956)
11. J.P. Elliott: Proc. Roy. Soc. London **A245**, 128 (1958); ibid. **A245**, 562 (1958)
12. S.G. Nilsson: Mat. Fys. Medd. Dan. Vid. Selsk. **29** no. 16 (1955)
13. W. Kohn, L.J. Sham: Phys. Rev. **140**, A1133 (1965); P. Hohenberg, W. Kohn: Phys. Rev. **136**, B864 (1964)
14. P. Bonche, S.E. Koonin, J.W. Negele: Phys. Rev. **C13**, 1226 (1976); R.Y. Cusson, J.A. Maruhn, H.W. Meldner: Phys. Rev. **C18**, 2589 (1978); J.W. Negele: Rev. Mod. Phys. **54**, 913 (1982)
15. Here the notation and conventions follow closely those of A.L. Goodman: Adv. Nucl. Phys. **11**, 263 (1979)
16. C. Bloch, A. Messiah: Nucl. Phys. **39**, 95 (1962); see also [12]
17. D. Gogny: Nucl. Phys. **A237**, 399 (1975); J. Dechargé, D. Gogny: Phys. Rev. **C21**, 1568 (1980)
18. F. Villars: Varenna Lectures **36**, 1 (1966); F. Villars in *Proceedings of the International Conference on Nuclear Selfconsistent Fields*, ed. by G. Ripka and M. Porneuf (North Holland, Amsterdam 1975)
19. E. Moya de Guerra: Phys. Rep. **138**(6), 293 (1986); E. Moya de Guerra, S. Kowalsky: Phys. Rev. **C22**, 1308 (1980); A.E.L. Dieperink, E. Moya de Guerra: Phys. Lett. **B189**, 267 (1987)
20. A.A. Raduta, E. Moya de Guerra: Ann. Phys. (N.Y.) (2000), in press
21. F. Villars: Nucl. Phys. **A285**, 269 (1977)
22. E. Moya de Guerra, F. Villars: Nucl. Phys. **A285**, 297 (1977)
23. M. Baranger, M. Veneroni: Ann. Phys. (N.Y.) **114**, 123 (1978)
24. D.J. Thouless: Nucl. Phys. **21**, 225 (1960)
25. For more details on RPA equations and their schematic solutions, see: D.J. Rowe: *Nuclear Collective Motion* (Methuen, London 1970); A. de Shalit, H. Feshbach: *Theoretical Nuclear Physics V.I: Nuclear Structure* (John Wiley & Sons, N.Y. 1974)
26. E. Moya de Guerra: Phys. Rev. Lett. **48**, 922 (1982); E. Moya de Guerra in: *Mathematical and Computational Methods in Nuclear Physics*, ed. by J.S. Dehesa, J.M.G. Gocula, A. Polls (Springer–Verlag, Amsterdam 1084)

27. A. Valor, P.-H. Heenen, P. Bonche: Nucl. Phys. **A671**, 145 (2000), and to be published; R. Rodríguez-Guerra, J.L. Egido, L.M. Robledo: Phys. Lett. **B474**, 15 (2000)
28. L.M. Robledo, L. Egido: Phys. Rev. Lett. (2000), to be published
29. P. Sarriguren, E. Moya de Guerra, R. Nojarov: Phys. Rev. **C54**, 690 (1996); E. Moya de Guerra, L. Zamick: Phys. Rev. **C47**, 2604 (1993)
30. P. Sarriguren, E. Moya de Guerra, A. Escuderos: Nucl. Phys. **A658**, 13 (1999); ibid. **A635**, 55 (1998); A. Raduta et al.: Nucl. Phys. (2000), in press
31. J.M. Udías et al.: Phys. Rev. **C48**, 273 (1993); ibid. **C51**, 3246 (1995); ibid. **C51**, R1488 (1996)
32. V.R. Pandharipande, C.N. Papanicoles, J.Wambach: Phys. Rev. Lett. **53**, 1133 (1984); C. Mahaux, R. Sartor: Adv. Nucl. Phys. **20**, 1 (1991)
33. J.M. Udías et al.: Phys. Rev. Lett. **83**, 5451 (1999); J.A. Caballero et al.: Nucl. Phys. **A632**, 323 (1998); ibid. **A643**, 189 (1998)
34. J. Gao et al.: Phys. Rev. Lett. **84**, 3265 (2000)
35. B.D. Serot, J.D. Walecka: Adv. Nucl. Phys. **16**, 1 (1986)
36. E.D. Cooper, S. Hama, B.C. Clark, R.L. Mercer: Phys. Rev. **C47**, 297 (1993), and refs. therein
37. J.N. Ginocchio: Phys. Rev. Lett. **78**, 436 (1997); K. Sugawara-Tanabe, A. Arima: Phys. Rev. **C58**, R3065 (1998)

The microscopic treatment of the nuclear system

Peter Ring

Physikdepartment der Technischen Universität München,
D-85747 Garching, Federal Republic of Germany

Abstract. Modern microscopic theories treat the nuclear structure in the framework of relativistic field theories. We discuss recent applications of Relativistic Mean Field (RMF) and Relativistic Hartree-Bogoliubov (RHB) theory for structure phenomena at the limits of stability, such as the quenching of the spin-orbit splitting far from the valley of stability, halo phenomena at the neutron drip-line, proton-radioactivity, rotational bands at superdeformed shapes and collective vibrations with low-lying dipole strength for nuclei with large neutron excess.

1 Introduction

New experimental facilities in planing will allow in future years the investigation of new regions of the periodic table, nuclei far from the valley of stability and super-heavy nuclei bound only by shell effects. It is therefore a challenge for theoretical investigations to provide models with a high predictive power. In the region of very light nuclei, essential progress has been made in solving the many-body problem ab initio using forces derived from the nucleon-nucleon scattering data. For the large majority of nuclei, however, in particular those interesting for astrophysical processes, the most successful theoretical techniques are still microscopic models models based on the mean field approximation. These models are in principle density functional theories, where the density functional is parameterized by a phenomenological ansatz. They are very successful, because being effective theories they include in a global way a large number of important effects going beyond the mean field, such as Brueckner correlations, ground state correlations, vacuum polarization, exchange terms etc. Of course the form of the density functionals should contain basic physical phenomena. Arguments of simplicity and the proper treatment of the underlying symmetries play an essential role.

After thirty years of considerable progress with non-relativistic models connected with the names of Skyrme [1] or Gogny [2], relativistic models gain in recent years more and more interest. Since the early days of nuclear physics one has known that the spin plays an important role in our understanding of nuclear spectra, and that, in principle, one should use a relativistic theory for a complete description of the nuclear system even in the low energy domain, where relativistic kinematics plays no role. Early attempts in this direction of Teller et al [3], however, have been forgotten and it was much later – in the seventies – that Walecka [4,5] pointed out the power, the simplicity and the elegance of a

J.M. Arias and M. Lozano (Eds.): LNP 581, pp. 195–232, 2001.
© Springer-Verlag Berlin Heidelberg 2001

phenomenological relativistic description of the nuclear system. Walecka and collaborators proposed a linear model, which includes only very few degrees of freedom, besides the Coulomb field essentially only a scalar attraction (parametrized by the σ-meson) a vector repulsion (the ω-meson) and the isospin dependence in the form of a vector meson (ρ-meson). Lorentz-symmetry and relativistic invariance lead then, without any further parameters to nuclear saturation, a large spin-orbit interaction, time-reversal breaking mean fields, properties which had to be adjusted in the non-relativistic models separately.

In fact it turned out that the Walecka model with all its beauty and elegance, is far from being able to describe nuclear properties in a satisfying way. Finite nuclei are determined to a large extent by surface properties and these cannot be described properly in the simple Walecka model. The break through came with the inclusion of an effective density dependence in the model by Boguta and Bodmer [6] in the form of non-linear coupling terms between the mesons. This non-linear model is know today under the name Relativistic Mean Field (RMF) theory. It became very popular in the last ten years and it has been applied nearly all over the periodic table.

RMF theory is a phenomenological theory. It is conceptually similar to density dependent Hartree-Fock theory with Skyrme forces, which is nowadays standard for the microscopic description of nuclear properties over the entire periodic table. It shares with this theory, that it contains only a few parameters which are adjusted to data of nuclear matter and a few closed shell nuclei. All the other nuclei are described with one parameter set.

In this series of lectures a overview is given of a number of recent investigations of problems of low energy nuclear structure within the framework of RMF theory. In section 2 we give a short summary of the basic facts of relativistic mean field theory. In section 3 we discuss the problem of pairing and the extension of relativistic mean field theory to relativistic Hartree-Bogoliubov theory. The other sections are devoted to recent applications, such as the quenching of the spin-orbit splitting in section 4, the formation of halo's at the neutron drip-line in section 5, investigations of the proton drip-line and proton radioactivity in section 6, the description of superdeformed rotational states in section 7, and recent applications of time-dependent relativistic mean field theory within the framework of relativistic RPA in section 8. In section 9 we give a short summary and an outlook.

2 Relativistic mean field theory

Relativistic Mean Field (RMF) theory is a classical relativistic field theory similar to classical electrodynamics. Only the nucleons are treated as quantum mechanical Dirac-particles with the four component wave functions ψ_i moving with relativistic dynamics in several classical meson fields. As in any mean field theory, these fields describe in an average way the interaction produced by the exchange of the corresponding mesons. The theory is phenomenological similar as the density dependent Hartree-Fock theories with Skyrme or Gogny forces. Therefore

the number of mesons entering this theory is limited and the corresponding parameters, the meson masses and the coupling constants between mesons and nucleons are neither derived from a more fundamental theory, nor taken from the properties of these mesons in the vacuum, rather they are adjusted to data of the correlated nuclear many-body system.

The mean field produced by the exchange of single pions is neglected. It breaks parity, a fact not observed in nature. Pions are, however, taken into account indirectly by the mean field of the so-called σ-meson . This particle has not been observed experimentally so far as a resonance, but it has been interpreted as a complicated bound state of two pions in the medium. On the phenomenological level we cannot decide whether this interpretation is the proper one. Many experimental observations, however indicate the importance of a large scalar field in the nucleus. This scalar field is taken into account by the phenomenological σ-meson in RMF-theory. Since relativistic covariance leads to attractive fields for scalar particles and to repulsive fields for vector particles, we need in addition a vector meson, the ω-meson. This particle has been observed in nature as a resonance at $m_\omega = 783$ MeV. σ- and ω-meson carry both isospin 0. For nuclei with large neutron excess we need in addition a meson carrying isospin 1, the ρ-meson, which is also observed in nature as a resonance at $m_\rho = 763$ MeV. Finally we need the Coulomb-force, i.e. the photon.

Apart from the Dirac wave functions $\psi_i(x)$ $(i = 1 \ldots A)$ for the nucleons we therefore have one field for the scalar σ-meson $\sigma(x)$ and 4 fields for each Lorentz-vector particle, i.e. for the ω-meson: $\omega^\mu(x)$, for the three iso-vector ρ-mesons $\boldsymbol{\rho}^\mu(x)$ and for the photon $A^\mu(x)$.

In order to keep the number of adjustable parameters small, we use the experimental values for the masses of the nucleons m_N and the masses of the ω- and the ρ-meson. In this most primitive version of the theory we have only four parameters, the mass of the σ-meson m_σ and the three coupling constants g_σ, g_ω and g_ρ. The rest is more or less given by Lorentz invariance and the principle of simplicity (minimal coupling). It leads to the following Lagrangian density:

$$\begin{aligned}\mathcal{L} = {} & \bar{\psi}\left(\not{p} - g_\omega \not{\omega} - g_\sigma \sigma - m_N\right)\psi \\ & + \frac{1}{2}\partial_\mu\sigma\partial^\mu\sigma - \frac{1}{2}m_\sigma^2\sigma^2 - \frac{1}{4}\Omega_{\mu\nu}\Omega^{\mu\nu} + \frac{1}{2}m_\omega^2\omega_\mu\omega^\mu, \end{aligned} \tag{1}$$

where $\Omega_{\mu\nu} = \partial_\mu\omega_\nu - \partial_\nu\omega_\mu$ is the field tensor for the vector mesons. For simplicity we neglect in this and in the following equations the other vector mesons, the ρ-mesons $\boldsymbol{\rho}^\mu$ and the photons A^μ, because they are treated in a similar way as the ω. In all the calculations, however, these fields are fully taken into account.

Although this simple version of the Walecka-model is able to give a qualitative description of saturation and many nuclear properties [4,5], it fails to describe properly the experimental surface properties. Boguta and Bodmer [6] therefore extended the model by including a nonlinear self-coupling of the scalar mesons, i.e. the mass term $\frac{1}{2}m_\sigma^2\sigma^2$ in the Lagrangian (1) is replaced by a polynomial of forth order $U(\sigma) = \frac{1}{2}m_\sigma^2\sigma^2 + \frac{1}{3}g_2\sigma^3 + \frac{1}{4}g_3\sigma^4$ containing two additional parameters g_2 and g_3. Conceptually this is equivalent to the modification of the

original Skyrme force with its linear density dependence by a modified density dependence of the type ρ^α. All the great quantitative achievements of RMF-theory in recent years were only possible in non-linear versions of the theory. Most of them use the non-linear coupling of the σ-mesons, but there are also more recent versions containing non-linear ω-couplings [7], where the mass term $\frac{1}{2}m_\omega^2\omega_\mu\omega^\mu$ is replaced by $\frac{1}{2}m_\omega^2\omega_\mu\omega^\mu+\frac{1}{4}c_3(\omega_\mu\omega^\mu)^2$. Nowadays standard and rather uniform parameter sets have been adjusted in the literature. Some of them are given in Table. 1.

Using the fields ψ_i, σ and ω as dynamical variables Hamiltons variational principle allows to derive the Euler-equations as equations of motion: the Dirac equation for the nucleon spinors and Klein-Gordon equations for the meson fields:

$$\{\gamma_\mu(i\partial^\mu + g_\omega\omega^\mu) + (m_N + g_\sigma\sigma)\}\,\psi_i = 0, \tag{2}$$

$$\{-\Delta + \partial_t^2\}\sigma \;+\; U'(\sigma) \qquad = -g_\sigma\rho_s \tag{3}$$

$$\{-\Delta + \partial_t^2 \;+\; m_\omega^2\}\,\omega^\mu \qquad = g_\omega j^\mu \tag{4}$$

The scalar density $\rho_s = \langle\bar\psi\psi\rangle$ and the baryonic current $j^\mu = \langle\bar\psi\gamma^\mu\psi\rangle$ are calculated from the solution of the Dirac equations by summing over all particle states with the appropriate BCS occupation probabilities v_i^2:

$$\rho_s = \sum_i v_i^2\,\bar\psi_i\psi_i, \qquad j^\mu = \sum_i v_i^2\,\bar\psi_i\gamma^\mu\psi_i. \tag{5}$$

In principle we should – in a relativistic theory – include into these sums also negative energy solutions of the Dirac equations, the anti-particle states in the Dirac sea, i.e. to allow for a polarization of the vacuum. In principle this can be done [8] using a suitable renormalization procedure. In such a case, however, the parameters of the Lagrangian have to be readjusted and so far no essential differences have been found for such a readjusted renormalized theory compared to a theory summing only over the positive energy solutions. Since one is dealing with a phenomenological theory where the parameters are adjusted to experimental data, one therefore usually uses the *no sea approximation* and restricts the sums in Eqs. 5 over positive energy solutions only. However this does not mean that vacuum polarization is neglected completely. It is just taken care of in a global way by the phenomenologically adjusted parameters.

The quantities ρ_s and j^μ serve as sources in the Klein-Gordon equations (3) and (4), which determine the mesons fields. These meson fields, finally, enter the Dirac equation (2) and determine the motion of the nucleons in a self-consistent way. The whole system of equations is solved by iteration.

For the ground state properties of even-even nuclei we have the static limit with meson fields constant in time and in addition time reversal invariance, i.e. the currents vanish. In this case the theory becomes extremely simple:

$$\{\boldsymbol{\alpha p} + V + \beta(M - S)\}\,\psi_i = \epsilon_i\psi_i, \tag{6}$$

$$-\Delta\,\sigma \;+\; U'(\sigma) \qquad = -g_\sigma\rho_s, \tag{7}$$

$$\{-\Delta + \; m_\omega^2\}\,\omega^0 \qquad = g_\omega\rho_v. \tag{8}$$

where the attractive scalar field $S(\mathbf{r})$ and the repulsive vector field $V(\mathbf{r})$ in the Dirac equation are determined by the corresponding meson fields

$$S(\mathbf{r}) = -g_\sigma \sigma(\mathbf{r}) \tag{9}$$

and

$$V(\mathbf{r}) = g_\omega \omega_0(\mathbf{r}). \tag{10}$$

In a relativistic theory we have to distinguish two types of densities, the scalar density $\rho_s = \langle \bar{\psi}\psi \rangle$, and the vector density $\rho_v = \langle \psi^+ \psi \rangle$, the time-like component of the current. The vector density is the usual baryon density. It contains the sum of the squares of large and small components, which are normalized to unity. The scalar density contains the difference of the square of large and small components and is not normalized. This purely relativistic effect prevents the theory from an attractive collapse: in the case of a very strong attractive σ-field the gap in the Dirac equations becomes relatively small. However, the theory remains stable, because in such a case the small components become relatively large too and the scalar density is quenched. Since this quantity is the source of the scalar field, the latter is quenched too in a self-consistent way and the collapse, which one would find in an equivalent non-relativistic system, is prevented.

The six parameters m_σ, g_σ, g_ω m_ρ, g_2, and g_3 have been obtained by careful fitting of experimental data of nuclear matter and a few finite spherical nuclei. Pairing properties are taken into account in the constant gap approximation. In Table 1 we show standard parameter sets (the masses are given in MeV, the parameter g_2 in fm^{-1} and the other coupling constants are dimensionless) and some results for symmetric nuclear matter: the baryon density ρ_0 (in units of fm^{-3}), the binding energy per particle E/A, the incompressibility K, the asymmetry parameter J (all given in units of MeV), and the effective mass m^*/m.

The standard set was for a long time NL1 [9]. Since it produced a too large value for the asymmetry parameter J, two new sets NL-SH [10] and NL3 [11] have been more carefully adjusted to the isospin properties of nuclei in the nineties. They are thus particularly suitable for calculations in the region of exotic nuclei far from the line of β-stability. All these sets (apart from NL2 [9]) share the problem of having a negative value for the non-linear parameter g_3 proportional to σ^4. The classical solutions of the field equations move only in a local minimum. For very large σ-values the theory becomes unstable even in the classical limit. We have to keep in mind, however, that we are dealing with a phenomenological theory adjusted to the classical limit for not too high densities, where everything is stable. Already by this reason the theory is by no means a fully fledged quantum theory. We also give in Table 1 the parameter set NL2, which has a positive value g_3. It is successful for the description of light nuclei. It fails, however, completely for heavy nuclei. In addition we give the parameter set of Horowitz and Serot [12], which contains only linear coupling terms. It produces a much to high value for the incompressibility K_{nm} of nuclear matter. The parameter set TM1 [13] finally contains also a non-linear ω-coupling.

Table 1. Various sets of meson parameters and results for symmetric nuclear matter. Details are given in the text.

	HS	NL1	NL2	NL3	NL-SH	TM1
m_N	939.0	938.0	938.0	939.0	939.0	938.0
m_σ	520.0	492.25	504.89	508.194	526.059	511.198
m_ω	783.0	795.359	780.00	782.501	783.0	783.0
m_ρ	770.0	763.0	763.0	763.0	763.0	770.0
g_σ	10.47	10.1377	9.1112	10.217	10.444	10.0289
g_ω	13.80	13.2846	11.4928	12.868	12.945	12.6139
g_ρ	4.035	4.9755	5.3866	4.474	4.3830	4.6322
g_2	0.0	−12.1724	−2.304	−10.431	−6.9099	−7.2325
g_3	0.0	−36.2646	13.7844	−28.885	−15.8337	0.6183
c_3	0.0	0.0	0.0	0.0	0.0	71.3075
ρ_0	0.148	0.152	0.146	0.148	0.146	0.145
E/A	−15.731	−16.423	−17.029	−16.240	−16.328	-16.3
K_{nm}	545.0	211.7	399.2	271.8	355.0	281.0
m^*/m	0.54	0.57	0.67	0.59	0.60	0.634
J	34.9	43.5	43.9	37.4	36.1	36.9

Using various parameter sets (as for instance NL1 and NL3 given in Table 1) one has calculated the ground state properties of many nuclei in the periodic table in recent years [14], in particular binding energies, nuclear radii, charge distributions and nuclear deformation parameters. One- and multi-dimensional energy surfaces have been produced by constraint Hartree calculations [15,16]. Apart from the region of transitional nuclei, where the whole concept of a mean field theory breaks down, the agreement with experimental data is excellent. It is of the same quality as standard Skyrme and Gogny results.

3 Relativistic Hartree-Bogoliubov theory

The inclusions of pairing correlations is essential for the correct description of structure phenomena in open-shell nuclei and in deformed nuclei. The relativistic mean field theory, as described in the previous section, does not include pairing correlations. The Lagrangian contains only single-particle field operators with the structure $\psi^\dagger\psi$. In a generalized single-particle theory pairing correlations can only be described by field operators $\psi^\dagger\psi^\dagger$ and $\psi\psi$, which do not conserve the particle number. Therefore pairing correlations are often included only in a phenomenological way within the simple BCS approximation [14] using occupations factors

$$v_k^2 = \frac{1}{2}\left[1 - \frac{\epsilon_k - \lambda}{\sqrt{(\epsilon_k - \lambda)^2 + \Delta^2}}\right]$$

in the sums for the calculation of the densities and the currents in Eqs. (5). The pairing gap Δ is usually determined from experimental binding energies. However, the BCS model presents only a poor approximation for exotic nuclei far from the valley of β-stability, because (i) it requires the knowledge of the binding energies, which is often not available in this region and (ii) close to the drip-lines one has to occupy partially levels in the continuum, which leads to an unbound system of a nucleus surrounded by evaporating neutrons. In the non-relativistic approach this problem is solved in the framework of Continuum Hartree-Fock-Bogoliubov (CHFB) theory [17–19].

The relativistic extension of Hartree-Fock-Bogoliubov (HFB) theory was introduced in Refs. [20,21]. The starting point is again the Lagrangian (1). By performing the quantization of the meson fields and using similar Greens function techniques as they have been used in the non-relativistic case by Gorkov [22] relativistic Dirac-Hartree-Bogoliubov equations are derived.

As in non-relativistic HFB theory [23], the ground state of a nucleus $|\Phi\rangle$ is described as the vacuum with respect to independent quasiparticle operators, which are defined by a unitary Bogoliubov transformation of the single-nucleon creation and annihilation operators. The generalized single-particle Hamiltonian contains two average potentials, the self-consistent Hartree-Fock field Γ which includes all the long range *ph*-correlations and the pairing file Δ which sums up the *pp*-correlations. In the relativistic extension the exchange terms are usually neglected in Γ, and the resulting Relativistic Hartree-Bogoliubov (RHB) equations read

$$\begin{pmatrix} h_D - m_N - \lambda & \hat{\Delta} \\ -\hat{\Delta}^* & -h_D^* + m_N + \lambda \end{pmatrix} \begin{pmatrix} U_k(\mathbf{r}) \\ V_k(\mathbf{r}) \end{pmatrix} = \begin{pmatrix} U_k(\mathbf{r}) \\ V_k(\mathbf{r}) \end{pmatrix} E_k. \tag{11}$$

where h_D is the single-nucleon Dirac Hamiltonian

$$h_D = \boldsymbol{\alpha}(\boldsymbol{p} - g_\omega \boldsymbol{\omega}) + g_\omega \omega_0 + \beta(m_N + g_\sigma \sigma) \tag{12}$$

and m_N is the nucleon mass. The chemical potential λ has to guarantee the conservation of particle number on the average. The pairing field Δ is in general an integral operator

$$\hat{\Delta} U_k(\mathbf{r}) = \int d^3r' \Delta(\mathbf{r}, \mathbf{r}') U_k(\mathbf{r}') \tag{13}$$

with the kernel

$$\Delta_{\alpha\alpha'}(\mathbf{r}, \mathbf{r}') = \frac{1}{2} \sum_{\beta\beta'} V_{\alpha\alpha'\beta\beta'}(\mathbf{r}, \mathbf{r}') \kappa_{\beta\beta'}(\mathbf{r}, \mathbf{r}'). \tag{14}$$

α, β are the Dirac-indices of the spinors and

$$\kappa_{\beta\beta'}(\mathbf{r}, \mathbf{r}') = \langle \Phi | \psi_{\alpha'}(\mathbf{r}') \psi_\alpha(\mathbf{r}) | \Phi \rangle = \sum_{E_k > 0} U^*_{\alpha k}(\mathbf{r}) V_{\alpha' k}(\mathbf{r}') \tag{15}$$

is the pairing tensor. $V_{\alpha\alpha'\beta\beta'}(\mathbf{r},\mathbf{r}')$ is the relativistic two-body interaction in the pairing channel. If one derives it from the Lagrangian using Gorkov-factorization one obtains the one-boson-exchange interaction of the mesons in the Lagrangian.

In Ref. [20] these forces have been used to investigate the pairing properties of symmetric nuclear matter and it has been shown that the usual RMF parameters of the Lagrangian as for instance NL1 are not able to produce realistic pairing properties of nuclear matter as one knows them form non-relativistic calculations using Gogny forces [24]. The reason it that the behavior of these forces at large relative momenta or short distances is not adjusted properly in relativistic mean field calculations, where only momenta up to the Fermi surfaces are important. Because of the large meson masses the relativistic exchange forces have too short a range as compared to non-relativistic Gogny-forces, i.e. they reach to very large momenta and produce a pairing gap at the Fermi surface, which is roughly 3 times larger as that obtained with Gogny forces.

More recent calculations [25] with relativistic one-meson exchange forces of the Bonn-group [26] which are adjusted to the nucleon scattering data give satisfying agreement with phenomenological Gogny forces, because they have a proper cut-off at large relative momenta describing the $^1S_0$-phase shifts properly. Of course, it is still an open question, why one should use bare nucleon-nucleon interactions in the pairing channel. In the Hartree-channel one knows since the early days of nuclear physics [27] that one cannot use bare nucleon-nucleon interactions for Hartree- or Hartree-Fock calculations. This seems to be no longer true in the $^1S_0$-channel of the pairing force. On the other hand the use of one-meson exchange forces in the *pp*-channel is technically rather complicated. Therefore, so far in none of the applications of RHB-theory for finite nuclei relativistic meson exchange forces have been used. In most of the successful applications of the theory in recent years one therefore used non-relativistic Gogny-forces in the pairing channel [28–37,39]. The justification for this approximation is that pairing correlations play an essential role only in a small energy interval around the Fermi surface, where relativistic effects can be neglected. Gogny forces provide a fully self-consistent parameter-free description of pairing correlations all over the periodic table. They are carefully adjusted in the literature [2,40]. Having a realistic finite range they do not need any energy- or momentum-cut-off. There exist also fully relativistic RHB-calculations using a relativistic δ-force [41] in a finite oscillator space. They depend crucially on a strength parameter, which is adjusted for this configuration space to the Gogny calculations of Ref. [32]. Therefore their predictive power is rather limited.

As an example of RHB calculations with Gogny forces we show in Fig. 1 one- and two-neutron separation energies for the chain of Ni-isotopes obtained with the parameter set NL3 in the Hartree- and for the Gogny force D1S in the pairing-channel .

In the following we discuss several applications of Relativistic Hartree-Bogoliubov Theory with Gogny forces for nuclei far from the line of β-stability and for nuclei at high spins.

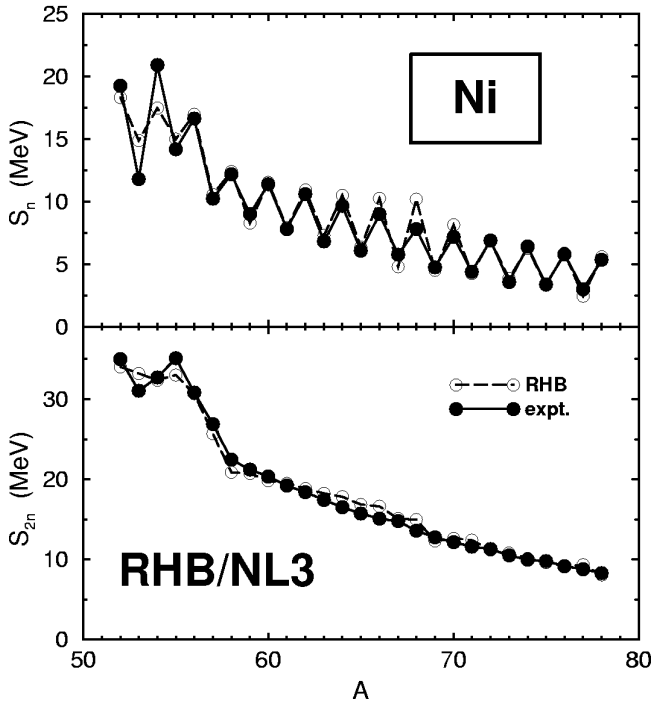

Fig. 1. One- and two-neutron separation energies in Ni Isotopes (from Ref. [32]).

4 Quenching of the spin-orbit splitting

The spin-orbit interaction plays a central role in the physics of nuclear structure. It is rooted in the basis of the nuclear shell model, where its inclusion is essential in order to reproduce the experimentally established magic numbers. In non-relativistic models based on the mean field approximation, the spin-orbit potential is included in a phenomenological way. Of course such an ansatz introduces an additional parameter, the strength of the spin-orbit interaction. The value of this parameter is usually adjusted to the experimental spin-orbit splittings in spherical nuclei, for example ^{16}O. On the other hand, in the relativistic framework the nucleons are described as Dirac spinors. This means that in the relativistic description of the nuclear many-body problem, the spin-orbit interaction arises naturally from the Dirac-Lorenz structure of the effective Lagrangian. No additional strength parameter is necessary, and relativistic models reproduce the empirical spin-orbit splittings.

Experiments with radioactive nuclear beams provide the opportunity to study nuclei with large neutron excess. Neutron drip lines of relatively light nuclei have become accessible, and the investigation of properties of such exotic objects is becoming one of the most exciting challenges in the physics of nuclear structure. Because of their relevance to the r-process in nucleosynthesis, nuclei

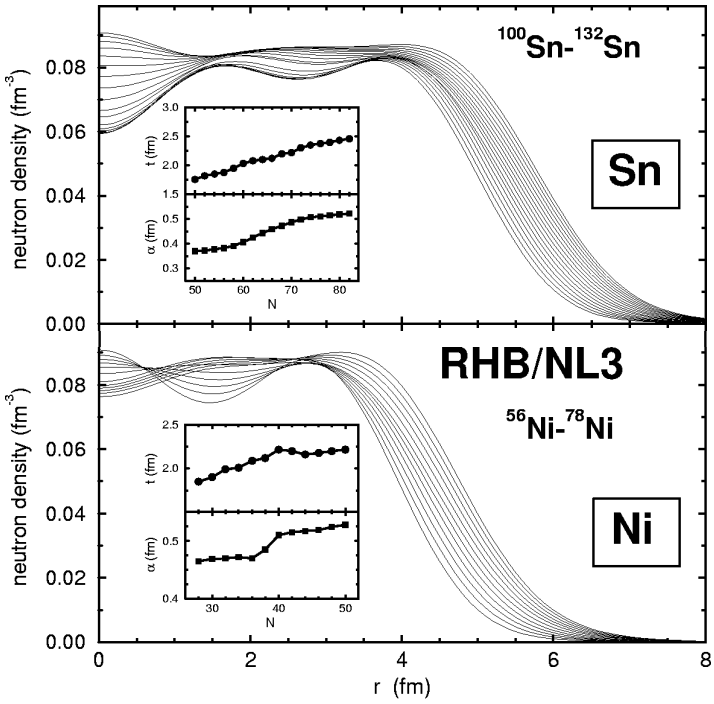

Fig. 2. Density distributions in Sn and Ni isotopes calculated within RHB theory using the parameter set NL3 in the Hartree channel and the Gogny force D1S in the pairing channel. (from Ref. [32]).

close to the neutron drip line are also very important in nuclear astrophysics. Knowledge of their structure and properties would help the determination of astrophysical conditions for the formation of neutron rich stable isotopes [42]. For drip line isotopes, nuclear shell effects become very important and the spin-orbit term plays an essential role. Very different scenarios for the isospin dependence of the spin-orbit interaction have been suggested in the Skyrme model [43], and in the relativistic mean-field theory [44]. In the following present work we investigate the behavior of the spin-orbit potential in light and medium heavy neutron rich nuclei using the Relativistic Hartree-Bogoliubov (RHB) theory.

In the relativistic mean-field approximation, the spin-orbit potential originates from the addition of two large fields: the field of the vector mesons (short range repulsion), and the scalar field of the sigma meson (intermediate attraction). In the first order approximation, and assuming spherical symmetry, the spin orbit term can be written as

$$V_{s.o.} = \frac{1}{r}\frac{\partial}{\partial r} V_{ls}(r), \tag{16}$$

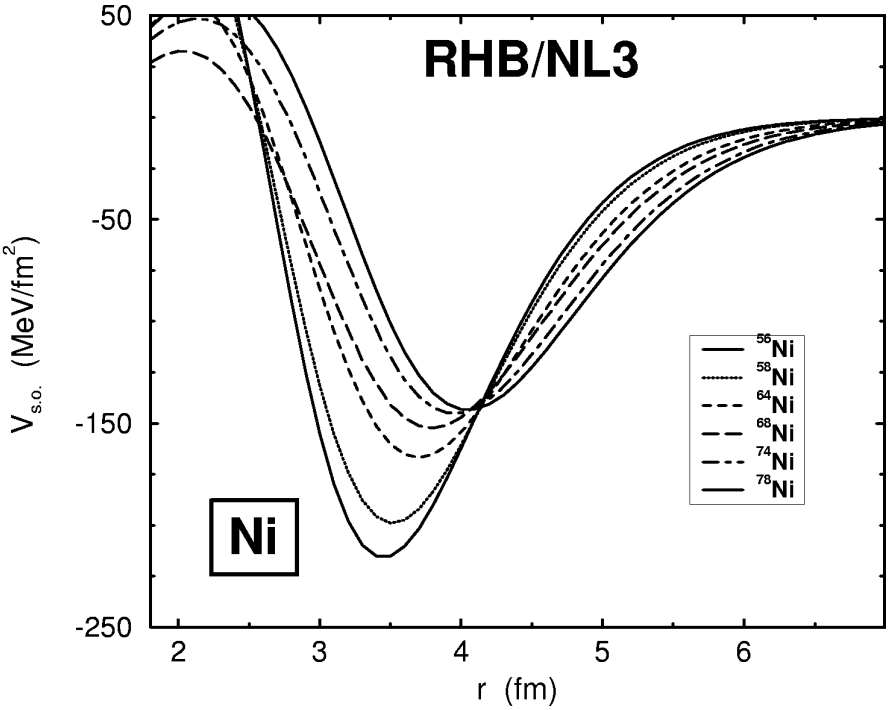

Fig. 3. Spin-orbit potentials defined in Eq. (16) for Ni isotopes (from Ref. [32]).

where V_{ls} is the spin-orbit potential [21,45]

$$V_{ls} = \frac{m}{m_{eff}}(V + S). \tag{17}$$

V and S denote the repulsive vector and the attractive scalar potentials, respectively. m_{eff} is the effective mass

$$m_{eff} = m - \frac{1}{2}(V + S). \tag{18}$$

In Fig. 2 we show the density distributions for two chains of Ni- and Sn-isotopes. The inserts show that the surface thickness t and the diffuseness parameter α grows steadily, if one leaves the valley of β-stability. The surface thickness is defined to be the change in radius required to reduce $\rho(r)/\rho_0$ from 0.9 to 0.1 (ρ_0 is the maximal value of the neutron density). The diffuseness parameter α is determined by fitting the neutron density profiles to the Fermi distribution

$$\rho(r) = \rho_0 \left(1 + \exp(\frac{r - R_0}{\alpha})\right)^{-1} \tag{19}$$

where R_0 is the half-density radius. With the increase of the number of neutrons the effective spin orbit potential $V_{s.o.}$ in Eq. (16) decreases, because it is pro-

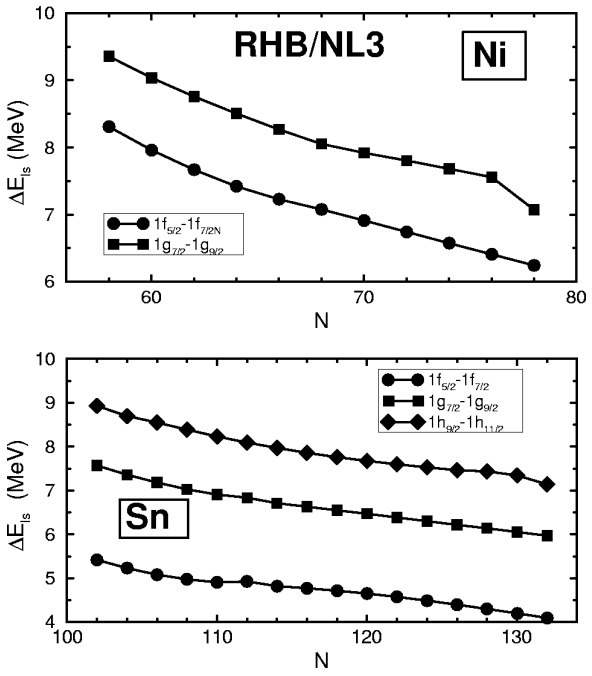

Fig. 4. Spin-orbit splittings in Ni and Sn isotopes as a function of the neutron number (from Ref. [32]).

portional to the slope of $V + S$. This is shown clearly in Fig. 3 for the chain of Ni-isotopes. This implies a weakening of the spin-orbit splitting of the neutron levels in the canonical basis

$$\Delta E_{ls} = \epsilon_{n,l,j=l-1/2} - \epsilon_{n,l,j=l+1/2} \tag{20}$$

as it is shown in Fig. 4 for several spin-orbit partners in the Ni- and Sn-chains. Obviously this effect is more pronounced for lighter nuclei and it becomes dramatic in the Ne region as shown in Fig. 5. These results are at variance with those calculated within the non-relativistic Skyrme model, which has a different isospin dependence of the spin-orbit term [46].

5 The neutron drip-line and halo phenomena

Since the experimental discovery of neutron halo phenomena in ^{11}Li [47], the study of exotic nuclei has become a very challenging topic in nuclear physics. Experimentally a sudden rise in the interaction cross-sections has been observed for light neutron-rich nuclei, specifically while going from ^{9}Li to ^{11}Li, ^{12}Be to ^{14}Be and ^{15}B to ^{17}B. This sudden increase in the interaction cross-sections has

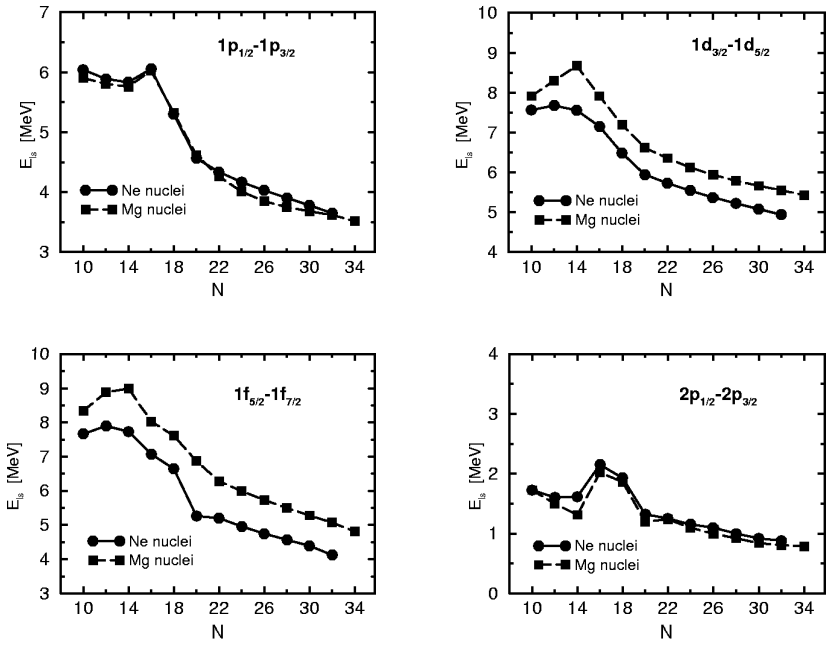

Fig. 5. Spin-orbit splittings in Ne and Mg isotopes as a function of the neutron number (from Ref. [46]).

been attributed to a relatively large *rms* matter radius as compared to that expected from the conventional mass dependence $1.2A^{1/3}$. This large radius has been interpreted by the fact that filling in more and more neutrons in the nuclear well, the Fermi surface for the neutrons comes close to the continuum limit in the nucleus ^{11}Li. Due to the small single-neutron separation energy, the tails of the two wave functions of the last filled orbital ($1p_{1/2}$) reach very far outside of the nuclear well and a neutron halo is formed.

Although this simple interpretation is based on the mean field picture, several microscopic theoretical investigations within self-consistent mean field models have failed [48–51]. In fact, it would be a strange accident if the last occupied neutron level in ^{11}Li would so close to the continuum limit that the tail of the last two uncorrelated neutron wave functions reaches so far out as would be necessary to reproduce the large experimental radius observed. Therefore, in the non-relativistic scheme Bertsch et al [48] and Sagawa [50] introduced an artificial modification to the potential in order to reproduce the small separation energy in their mean field calculations using Skyrme interactions. In this way the authors were able to reproduce qualitatively the observed trends, although some discrepancies still remained.

Koepf et al [49] were the first to investigate the neutron halo in relativistic mean field (RMF) theory both for spherical symmetrical and axially deformed cases. They found large deformations for the lighter Li isotopes, but a spherical shape for ^{11}Li. As in the non-relativistic investigations the binding energy of the $1p_{1/2}$ was too large so as to reproduce a neutron halo. Zhu et al [51] improved the result of the RMF calculations by applying a similar modification to the potential as in Ref. [50] in order to adjust the proper size of the halo.

Bertsch and Esbensen [52] recognized that pairing correlations play an essential role. Performing a quasiparticle continuum RPA calculation using a core of ^{9}Li and a density dependent interaction of zero range in the pairing channel, they found a large neutron halo for the nucleus ^{11}Li and could reproduce the proper size of the experimental matter radius.

We discuss here an investigation based on Relativistic Hartree-Bogoliubov theory [53] where pairing correlations and the scattering of Cooper pairs into the continuum were taken into account in a fully self-consistent way using the continuum Hartree-Bogoliubov formalism in the framework of relativistic mean field theory. In this calculations a density dependent δ-force was used in the pairing channel. For a fixed cut-off energy of 120 MeV the strength was adjusted to corresponding calculations in ^{7}Li with a Gogny force.

In Fig. 6 we show the calculated density distributions for the neutrons in the isotopes ^{9}Li and ^{11}Li. It is clearly seen that the increase of the matter radius is caused by a large neutron halo in the nucleus ^{11}Li. Its density distribution is in very good agreement with the experimental density of this isotope indicated with its error bars by the shaded area.

Fig. 7 we show the average potential $V - S$ together with the single-particle levels in the canonical basis (for details of the definition of the canonical basis see Ref. [23]). The microscopic structure of this halo can be understood by the fact that the Fermi level for the neutrons is very close to the continuum limit in close vicinity to the $\nu 1p_{1/2}$ level below the continuum and the $\nu 2s_{1/2}$ level in the continuum. Pairing correlations cause a partial occupation (given by the length of the lines for the levels) of both the $\nu 1p_{1/2}$ and the $\nu 2s_{1/2}$ level, i.e. a scattering of Cooper pairs in the continuum. This is in contrast to earlier Skyrme and RMF calculations without pairing, where the last occupied $\nu 1p_{1/2}$ level had to be shifted artificially very close to the continuum limit by an adjustment of the potential. In the RHB-calculations the halo is not formed by two neutrons sitting in occupying the $\nu 1p_{1/2}$ level very close to the continuum limit, but it is formed by Cooper-pairs scattered mainly into two levels $\nu 1p_{1/2}$ and $\nu 2s_{1/2}$. This is made possible by the fact that the $\nu 2s_{1/2}$ level comes down close to the Fermi level in this nucleus and by the pairing interaction coupling the levels below the Fermi surface to the continuum.

In contrast to the earlier explanations with use the accidental coincidence that one single-particle level is so close to the continuum threshold that the tail of its wave function forms a halo, this is a much more general mechanism, which could possibly be observed in other halo nuclei also. One needs only a bunching of single particle levels with small orbital angular momenta and correspondingly

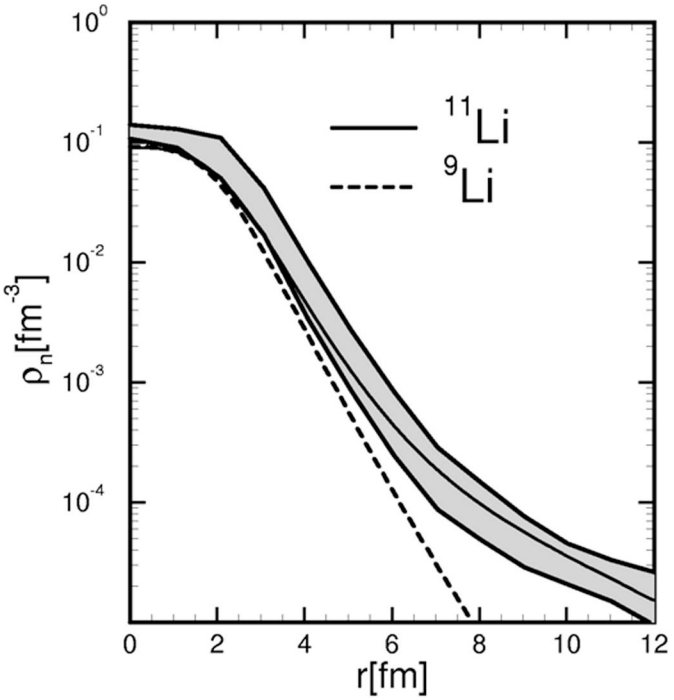

Fig. 6. Neutron density in the nuclei ^{9}Li and ^{11}Li (from Ref. [53]).

small centrifugal barriers close, but not directly, at the continuum limit. In fact, going along the neutron drip-line there are several such regions, in particular the region where the $2p$ and the $3p$ levels come close to the continuum limit. In the first case a multi-particle halo in the region of heavy Ne-isotopes has been predicted in Ref. [30] and in the latter case a giant halo has been predicted for the region of very neutron rich Zr-isotopes in Ref. [54].

6 The proton drip-line

So far we discussed applications of Relativistic Hartree-Bogoliubov theory on the neutron rich side up to the neutron drip-line. This area is in particular interesting because of its large neutron excess and the phenomena connected with the coupling to the continuum such as neutron halo's. On the other hand the neutron drip-line has so far been reached in experiments only for rather light nuclei. For medium heavy and heavy nuclei there is no comparison with experiments and the theoretical predictions are therefore connected with large uncertainties.

This is different for the proton drip-line. It has been reached or can be reached in near future up to rather heavy nuclei. Because of the Coulomb wall the coupl-

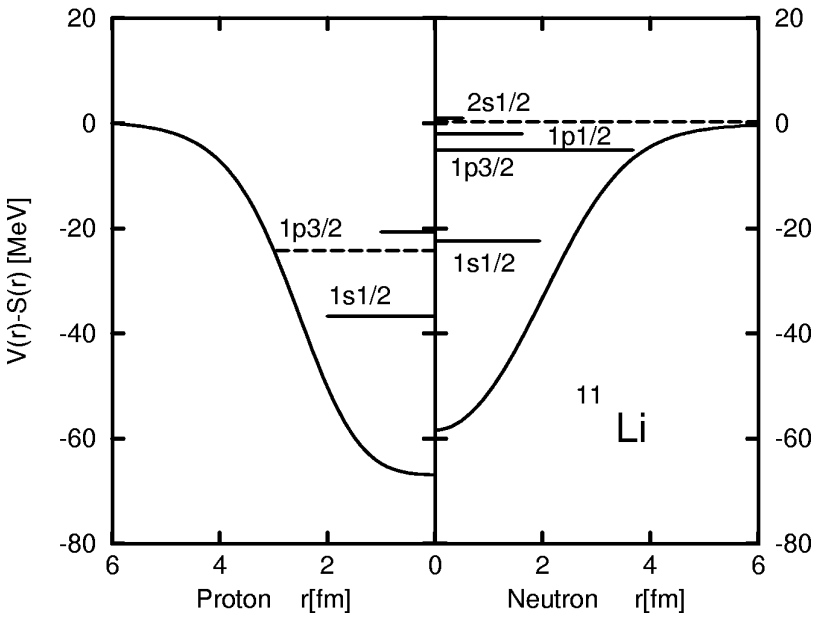

Fig. 7. Average Potentials $V - S$ for protons and neutrons in the nucleus ^{11}Li. Details are given in the text (from Ref. [53]).

ing to the continuum does not play such an important role and the standard methods of nuclear structure physics can be applied more easily here. On the other side, there are also very interesting experimental phenomena seen or predicted in this region, such as proton-emission or pn-pairing in the vicinity of the N=Z line. The precise knowledge of the nuclear structure along the proton drip-line in the region $30 < Z < 50$ (see Fig. 8) is also of great interest for astrophysical investigations, because the path of rapid proton process leads through this region.

The structure and decays modes of nuclei at and beyond the proton drip-line represent therefore one of the most active areas of experimental and theoretical studies of exotic nuclei with extreme isospin values today. In the last few years many new data on ground-state and isomeric proton radioactivity have been reported. In particular, detailed studies of odd-Z ground-state proton emitters in the regions $51 \leq Z \leq 55$ and $69 \leq Z \leq 83$, have shown that the systematics of spectroscopic factors is consistent with half-lives calculated in the spherical WKB or distorted-wave Born (DWBA) approximations [55,56].

In the theoretical description of ground-state and isomeric proton radioactivity, two essentially complementary approaches have been reported. One possibility is to start from a spherical or deformed phenomenological single-particle potential, a Woods-Saxon potential for instance, and to adjust the parameters of the potential well in order to reproduce the experimental one-proton separation

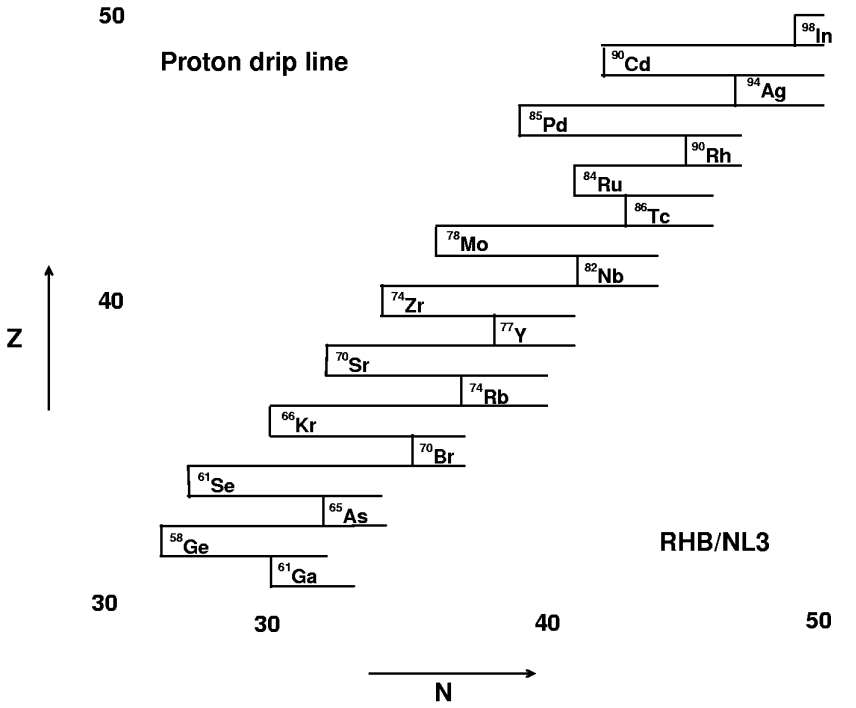

Fig. 8. The proton drip-line between Z = 30 and Z = 50 (from Ref. [38]).

energy. The width of the single-particle resonance is then determined by the probability of tunneling through the Coulomb and centrifugal barriers. Since the probability strongly depends on the valence proton energy and on its angular momentum, the calculated half-lives provide direct information about the spherical or deformed orbital occupied by the odd proton. For a spherical proton emitter it is relatively simple to calculate half-lives in the WKB or DWBA approximations [56]. On the other hand, it is much more difficult to quantitatively describe the process of three-dimensional quantum mechanical tunneling for deformed proton emitters. Modern reliable models for calculating proton emission rates from deformed nuclei have been developed only recently [57,58]. A shortcoming of this approach is that it does not predict proton separation energies, i.e. the models do not predict which nuclei are likely to be proton emitters. In fact, if they are used to calculate decay rates for proton emission from excited states, the depth of the central potential has to to be adjusted for each proton orbital separately. In addition, the models of Refs. [56–58] do not provide any information about the spectroscopic factors of the proton orbitals. Instead, experimental spectroscopic factors are defined as ratios of calculated and measured half-lives, and the deviation from unity is attributed to nuclear structure effects.

In Refs. [33–35] relativistic Hartree Bogoliubov (RHB) theory has been used to calculate properties of proton-rich spherical even-even nuclei with $14 \leq Z \leq 28$,

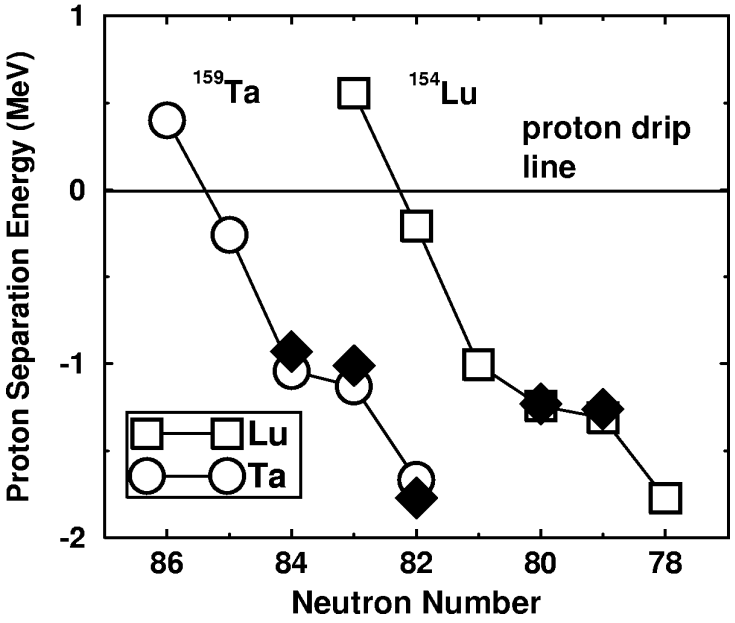

Fig. 9. Proton separation energies in Ta and Lu isotopes. Empty symbols are calculations within RHB theory and full symbols are experiments (from Ref. [37]).

and to describe odd-Z deformed ground-state proton emitters in the region $53 \leq Z \leq 69$. The RHB framework has been also used to study the location of the proton drip-line, the ground-state quadrupole deformations and one-proton separation energies at and beyond the drip line, the deformed single particle orbitals occupied by the odd valence proton, and the corresponding spectroscopic factors, i.e. the BCS-occupation factors u_μ^2 in the canonical basis. The results of fully self-consistent calculations have been compared with experimental data on ground-state proton emitters. However, since it is very difficult to use the self-consistent ground-state wave functions in the calculation of proton emission rates, the RHB model provides informations which are complementary to those obtained with the models of Refs. [56–58].

As an example (for details see Ref. [37]) we show in Fig. 9 the one-proton separation energies

$$S_p(Z,N) = B(Z,N) - B(Z-1,N) \tag{21}$$

for the Lu and Ta isotopes as function of the number of neutrons. The predicted drip-line nuclei are ^{154}Lu and ^{159}Ta. In the process of proton emission the valence particle tunnels through the Coulomb and centrifugal barriers, and the decay probability depends strongly on the energy of the proton and on its angular momentum. In rare-earth nuclei the decay of the ground-state by direct proton emission competes with β^+ decay; for heavy nuclei also fission or α decay

Table 2. Lu ground-state proton emitters. Results of the RHB calculation for the one-proton separation energies S_p, quadrupole deformations β_2, and the deformed single-particle orbitals occupied by the odd valence proton, are compared with predictions of the macroscopic-microscopic mass model, and with the experimental transition energies. All energies are in units of MeV; the RHB spectroscopic factors are displayed in the sixth column.

	N	S_p	β_2	p-orbital	u^2	Ω_p^π	S_p	β_2	E_p exp.
^{149}Lu	78	-1.77	-0.158	$7/2^-[523]$	0.60	$5/2^-$	-1.51	-0.175	
^{150}Lu	79	-1.31	-0.153	$7/2^-[523]$	0.61	$5/2^-$	-1.00	-0.158	1.261(4)
^{151}Lu	80	-1.24	-0.151	$7/2^-[523]$	0.58	$7/2^-$	-0.99	-0.150	1.233(3)

can be favored. In general, ground-state proton emission is not observed immediately after the drip-line. For small values of the proton separation energies, the width is dominated by the β^+ decay. On the other hand, large separation energies result in extremely short proton-emission half-lives, which are difficult to observe experimentally. For a typical rare-earth nucleus the separation energy window in which ground-state proton decay can be directly observed is about 0.8 – 1.7 MeV [56]. In Fig. 9 the calculated separation energies (empty symbols) are compared with experimental transition energies (full symbols) for ground-state proton emission in ^{150}Lu, ^{151}Lu, ^{155}Ta , ^{156}Ta, and ^{157}Ta. In all five cases an excellent agreement is observed between model predictions and experimental data. In addition to ^{151}Lu, which was the first ground-state proton emitter to be discovered [59], and ^{150}Lu, the self-consistent RHB calculation predicts ground-state proton decay in ^{149}Lu. The calculated one-proton separation energy -1.77 MeV corresponds to a half-life of a few μs, if one assumes that the nucleus is spherical. Direct proton emission with a half-life of the order of few μs is just above the lower limit of observation of current experimental facilities. For the Lu ground-state proton emitters, in Table 2 the results of the RHB model calculation are compared with the predictions of the finite-range droplet (FRDM) mass model [60] : the projection of the odd-proton angular momentum on the symmetry axis and the parity of the odd-proton state Ω_p^π, the one-proton separation energy, and the ground-state quadrupole deformation. Included are also the RHB spectroscopic factors. The separation energies are compared with the experimental transition energies in ^{150}Lu and ^{151}Lu. Both theoretical models predict oblate shapes for the Lu proton emitters, and similar values for the ground-state quadrupole deformations. On the other hand, while the FRDM assigns spin and parity $5/2^-$ to the deformed single-particle orbitals occupied by the odd valence proton in all three proton emitters, the RHB model predicts the $7/2^-[523]$ Nilsson orbital to be occupied by the odd proton. We also notice that the RHB separation energies are much closer to the experimental values. The spectroscopic factors of the $7/2^-[523]$ orbital are displayed in the sixth column of Table 2. The spectroscopic factor of the deformed odd-proton orbital k is defined as the probability that this state is found empty in the daughter nucleus with even number of protons.

7 Relativistic mean field theory in the rotating frame

In non-relativistic nuclear physics the cranking model plays an important role in the description of rotating nuclei. It has been introduced with phenomenological arguments already in the fifties by Inglis [61]. Later-on it has been shown, that it can be derived from a microscopic many-body theory as an approximate variation after angular momentum projection [62]. Therefore it is the symmetry breaking mean field version of a variational theory with fixed angular momentum. In the self-consistent version [63] it allows to include alignment effects [64] as well as polarization effects induced by the rotation, such as Coriolis-anti-Pairing or changes of the deformation. But already in the simplified version of the *Rotating Shell Model* with fixed mean fields [65] it is able to describe successfully an extremely large amount of data in the high spin region of deformed nuclei.

The cranking idea can be used for a relativistic description too [68,69]: one simply transforms the coordinate system to a frame rotating with constant angular velocity $\boldsymbol{\Omega}$ around a fixed axis is space assuming – as in non-relativistic nuclear physics – that this axis is perpendicular to the symmetry axis of the nucleus in its ground state. According to the cranking prescription the absolute value of the angular velocity $|\Omega|$ will be determined after the self-consistent solution of the equations of motion in the rotating frame by the Inglis condition [61]:

$$J = \frac{1}{|\Omega|}\langle \boldsymbol{\Omega}\boldsymbol{J}\rangle_\Omega \;=\; \sqrt{I(I+1)} \tag{22}$$

In this way we obtain for the classical field equations in the rotating frame:

$$\{\boldsymbol{\alpha}(\boldsymbol{p} - g_\omega\boldsymbol{\omega}) + g_\omega\omega_0 + \beta(m_N + g_\sigma\sigma) - \boldsymbol{\Omega}\boldsymbol{J}\}\psi_i = \epsilon_i\psi_i \tag{23}$$

$$\left\{-\Delta + (\boldsymbol{\Omega}\boldsymbol{L})^2\right\}\sigma \;+\; U'(\sigma) \qquad = -g_\sigma\rho_s \tag{24}$$

$$\left\{-\Delta + (\boldsymbol{\Omega}\boldsymbol{L})^2 \;+\; m_\omega^2\right\}\omega^0 \qquad = g_\omega\rho_v \tag{25}$$

$$\left\{-\Delta + (\boldsymbol{\Omega}\boldsymbol{J})^2 \;+\; m_\omega^2\right\}\boldsymbol{\omega} \qquad = g_\omega\boldsymbol{j} \tag{26}$$

These equations are very similar to the RMF equations in the non-rotating frame. There are only three essential differences:

1. The Dirac equation (23) contains a Coriolis term $\boldsymbol{\Omega}\boldsymbol{J}$ in full analogy to non-relativistic cranking.
2. The Klein-Gordon equations for the mesons contain terms proportional to the square of the corresponding Coriolis terms. It turns out, however, that they can be neglected completely for all realistic cranking frequencies, because (i) they are quadratic in Ω and (ii) mesons being bosons are to a large extend in the lowest s-states with only small d-admixtures
3. The Coriolis operator in the Dirac equation breaks time-reversal invariance. Currents $\boldsymbol{j}$ are induced, which form the source of magnetic potentials in the Dirac equation (*nuclear magnetism*). In this way the charge current $\boldsymbol{j}_c$ is the source of the normal magnetic potential $\boldsymbol{A}$, the iso-scalar baryon

current $\boldsymbol{j}_B$ is the source of the spatial components $\boldsymbol{\omega}$ of the ω-mesons and the iso-vector baryon current $\boldsymbol{j}_3$ is the source of the spatial component $\boldsymbol{\rho}_3$ of the ρ-mesons. In contrast to the Maxwellian magnetic field $\boldsymbol{A}$ having a small electro-magnetic coupling, the large coupling constants of the strong interaction causes the fields $\boldsymbol{\omega}$ and $\boldsymbol{\rho}$ to be important in all cases, where they are not forbidden by symmetries, such as time reversal. They have a strong influence on the magnetic moments [66] in odd mass nuclei, where time reversal is broken by the odd particle, as well as on the moment of inertia in rotating nuclei, where time reversal is broken by the Coriolis field [67].

7.1 Superdeformed rotational bands in the Hg region

The investigation of superdeformation in different mass regions still remains in the focus of low-energy nuclear physics. Experimental data on superdeformed rotational (SD) bands are now available in different parts of the periodic table, namely, in the mass regions $A \sim 60$, 80, 130, 150 and 190. This richness of data provides the necessary input for a test CRMF theory at superdeformation. It has been applied in a systematic way for the description of SD bands observed in the $A \sim 60$ and the $A \sim 150$ mass regions. The pairing correlations in these bands are considerably quenched in these mass regions and at high rotational frequencies a very good description of experimental data is obtained in the unpaired formalism in most of the cases as shown in Refs. [70–72].

On the contrary, pairing correlations have a considerable impact on the properties of SD bands observed in the $A \sim 190$ mass region and more generally on rotational bands at low spin. Different theoretical mean field methods have been applied for the study of SD bands in this mass region. These are the cranked Nilsson-Strutinsky approach based on a Woods-Saxon potential [73], self-consistent cranked Hartree-Fock-Bogoliubov approaches based either on Skyrme [74] or Gogny forces [75,76]. It was shown in different theoretical models that in order to describe the experimental data on moments of inertia one should go beyond the mean field approximation and deal with fluctuations in the pairing correlations using particle number projection. This is typically done in an approximate way by the Lipkin-Nogami method [77–79]. With exception of approaches based on Gogny forces, special care should also be taken to the form of the pairing interaction. For example, quadrupole pairing has been used in addition to monopole pairing in the cranked Nilsson-Strutinsky approach. Density dependent pairing has been used in connection to Skyrme forces. These require, however, the adjustment of additional parameters to the experimental data.

Yrast SD bands in ^{194}Pb and ^{194}Hg are linked by experimental observation of the transitions to the low-spin level scheme. In addition, there is a tentative linking of SD band in ^{192}Pb. These data provide an opportunity to compare with experiment in a direct way not only calculated dynamic moments of inertia

$$J^{(2)} = \frac{dJ}{d\omega}, \tag{27}$$

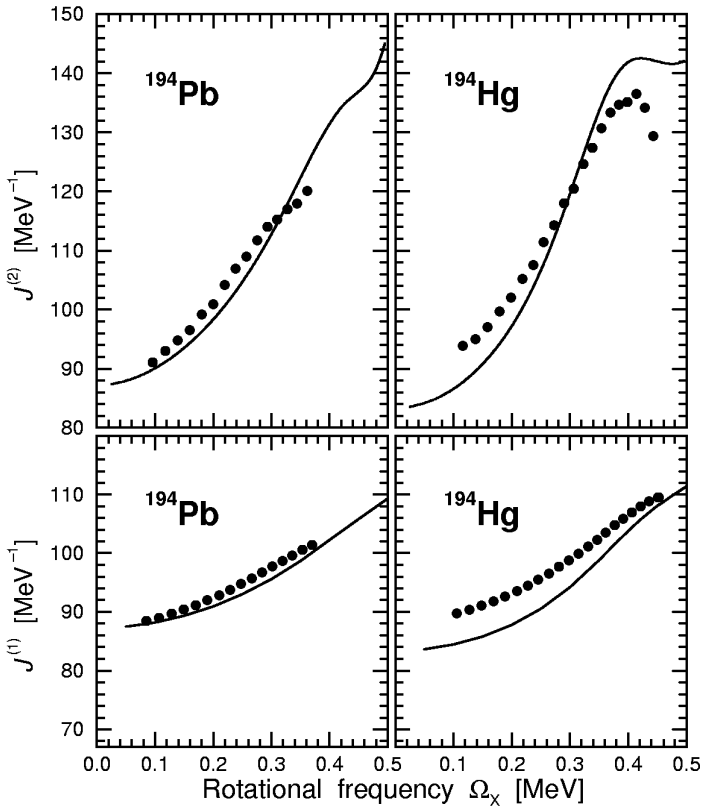

Fig. 10. Dynamic ($J^{(2)}$) (upper panels) and kinematic ($J^{(1)}$) (bottom panels) moments of inertia. The experimental values (full circles) are compared with CRHB calculations (solid lines) (from Ref. [39]).

but also kinematic moments of inertia

$$J^{(1)} = \frac{J}{\omega}. \tag{28}$$

On the contrary, at present the yrast SD bands in ^{190,192}Hg and ^{196}Pb are not linked to the low-spin level scheme yet. Thus some spin values consistent with the signature of the calculated yrast SD configuration should be assumed for the experimental bands when a comparison is made with respect of the kinematic moment of inertia $J^{(1)}$.

In Figs. 10 and 11 we show theoretical results obtained within the Cranked Relativistic Hartree-Bogoliubov approach. The parameter set NL1 is used in the *ph*-channel and the Gogny force D1S in the pairing channel. The theoretical $J^{(1)}$ values agree well with the experimental ones in the cases of linked SD bands in ^{194}Pb and ^{194}Hg. The comparison of theoretical and experimental $J^{(1)}$ values

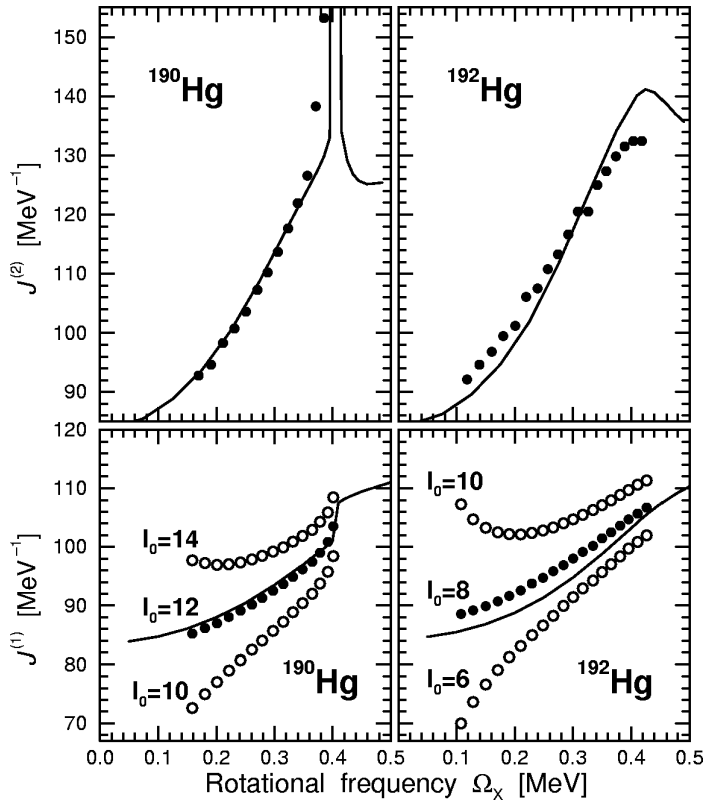

Fig. 11. The same as in Fig. 10 but for yrast SD bands in ^{190,192}Hg (from Ref. [39]).

indicates that the lowest transitions in the yrast SD bands of ^{190}Hg and ^{192}Hg with energies 316.9 and 214.4 keV, respectively, most likely correspond to the spin changes of $14^+ \rightarrow 12^+$ and $10^+ \rightarrow 8^+$. If these spin values are assumed, good agreement between theory and experiment is observed. Calculated and experimental values of the dynamic moment of inertia $J^{(2)}$ agree also well.

The increase of kinematic and dynamic moments of inertia in this mass region can be understood in the framework of CRHB theory as emerging from a combination of three effects: the gradual alignment of a pair of $j_{15/2}$ neutrons, the alignment of a pair of $i_{13/2}$ protons at a somewhat higher frequency, and decreasing pairing correlations with increasing rotational frequency. With increasing rotational frequency, the $J^{(2)}$ values determined by the alignment in the neutron subsystem decrease but this process is compensated by the increase of $J^{(2)}$ due to the alignment of the $i_{13/2}$ proton pair. This leads to the increase of the total $J^{(2)}$-value at $\Omega_x \geq 0.45$ MeV. The shape of the peak (plateau) in $J^{(2)}$ depends on a delicate balance between alignments in the proton and neutron subsystems which depends on deformation, rotational frequency and Fermi

energy. For example, no increase in the total moment of inertia $J^{(2)}$ has been found in the calculations after the peak up to $\Omega_x = 0.5$ MeV in ^{192,194}Hg (see Figs. 10 and 11). It is also of interest to mention that the sharp increase in $J^{(2)}$ of the yrast SD band in ^{190}Hg is also reproduced in the present calculations. One should note that the calculations slightly overestimate the magnitude of $J^{(2)}$ at the highest observed frequencies. The possible reasons could be the deficiencies either of the Lipkin-Nogami method or the cranking model in the band crossing region or both of them. Calculated values of transition quadrupole moments Q_t are close to the measured ones, however, more accurate and consistent experimental data on Q_t is needed in order to make detailed comparisons between experiment and theory.

7.2 Moments of inertia at the ground state

One of the oldest problems in our understanding of collective motion of nuclei is the moments of inertia of ground state rotational bands in well deformed nuclei. They depend in a very sensitive way on the collective properties such as deformations and on pairing correlations of these many-body systems. Since rotational bands have been detected in nuclei nearly fifty years ago and since the first microscopic calculations of the moments of inertia by Inglis [61], these quantities have been used as a testing ground for nearly all microscopic theories of collective motion. They describe the response of the strongly interacting nuclear many-body system to an external Coriolis field breaking time reversal symmetry. They are, therefore, in some sense comparable to the static magnetic susceptibility in condensed matter physics.

The earliest microscopic calculations were based on a mean field of a deformed harmonic oscillator. In these calculations, residual interactions were neglected. In this way one found the values of the moments of inertia identical to those of a rigid body with the same shape, in strong disagreement with the experimentally observed values, which where considerably smaller. It has been pointed out already very early [80,81] that residual two-body interactions would lower the values of the moment of inertia obtained in the Inglis model. The most important correlations causing such a reduction are pairing correlations [82]. In fact, Belyaev [83] showed that a simple extension of the Inglis formula in the framework of the BCS theory is able to reduce the theoretical moments of inertia dramatically because of the large energy gap in the spectrum of quasiparticle excitations occurring in the denominator of the Belyaev formula. Therefore, the small moments of inertia of the rotational bands provided one of the most important experimental hints for a superfluid behavior of these heavy open shell nuclei. Extended calculations using the theory of Belyaev have been carried out by Nilsson and Prior [84] using the BCS model based on the single particle spectrum of the Nilsson potential.

Apart from the fact that the results of these calculations were relatively successful, there are, as we know today, a number of open problems, namely:

i) Belyaev's formula is based on generalized mean field theory violating essential symmetries. It was pointed out already by Migdal [85,86] that Galileian

invariance is broken. He therefore modified the Belyaev formula by taking into account more complicated correlations to correct the violation of this symmetry.

ii) Since Belyaev's formula describes only quasi-particles moving independently, higher order correlations have to be taken into account. This has been done by Thouless and Valatin [87] who considered all orders of the interaction in a theory describing the linear response of the system to the external Coriolis field. Marshalek and Weneser [88] showed that the method of Thouless and Valatin preserves all the symmetries violated in the mean field approximation in linear order. In that sense Migdal's formula was just a special case to deal with Galilean invariance. Marshalek showed in a series of papers (see for example Ref. [89]) that this is just the linear approximation of a more general theory based on Boson expansion techniques treating the symmetries appropriately in all orders.

iii) Much more elaborated versions of the cranked Nilsson model [90,91] showed that the $\boldsymbol{l}^2$-term in this model, which corrects in an elegant way the fact that realistic potentials for heavy nuclei are much flatter than an oscillator in the nuclear interior, introduces a strong spurious momentum dependence. This leads to the values for the moments of inertia deviating considerably from the experimental values. However, this problem is to large extent cured by Strutinsky renormalization of the moments of inertia.

Realistic applications of the Thouless-Valatin theory are by no means trivial. They should be based on self-consistent solutions of the mean field equations, because only for those solutions the RPA theory preserves the symmetries [23]. In addition, they require the inversion of the RPA-matrix. Meyer-ter-Vehn et al. [92] have carried out such calculations in a restricted configuration space replacing the self-consistent mean field in an approximate way by the Woods-Saxon potential. As residual interaction they used density dependent Migdal forces F^{ω} in the *ph*-channel and F^{ξ} in the *pp*-channel. These interactions have been carefully adjusted to experimental data for the underlying configuration space. The results of these calculations showed, that there are indeed effects originating from both channels, each of them modifying the Belyaev values, but cancelling themselves to a large extent. Therefore one could understand why older calculations [84] based on the generalized mean field model gave reasonable results as compared to the experiment.

Nowadays there are theories available where the Hartree-(Fock)-Bogoliubov equations can be solved in a fully self-consistent way in the rotating frame for finite angular velocity $\boldsymbol{\Omega}$. Using the resulting wave functions $|\Phi_\Omega\rangle$ the Thouless-Valatin moment of inertia can be found as

$$J = \frac{d}{d\Omega}\langle\Phi_\Omega|J_x|\Phi_\Omega\rangle\Big|_{\Omega=0}. \tag{29}$$

In this way one avoids the inversion of the full RPA-matrix, a task which is so far technically impossible for realistic forces in a full configuration space.

Calculated moments of inertia are given in Fig. 12. Cranked Relativistic Hartree-Bogoliubov (CRHB) calculations are compared with Cranked Hartree-Fock-Bogoliubov (CHFB) calculations with Gogny forces. Comparing results without particle number projection and those with particle number projections

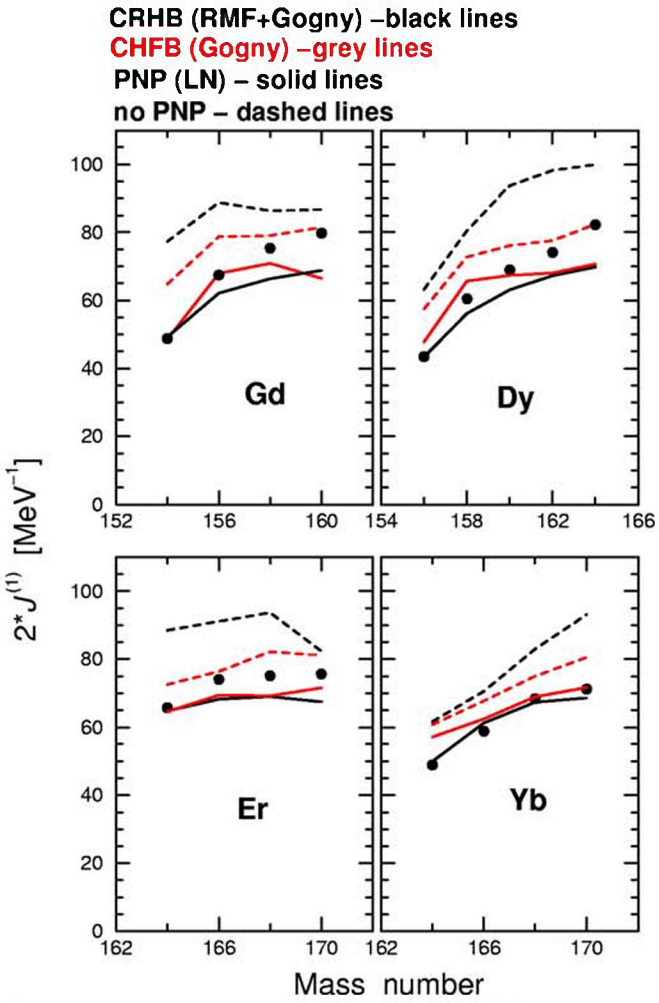

Fig. 12. Moments of inertia at the ground state in several chains of rare earth isotopes (from Ref. [93]).

in the Lipkin-Nogami approximation PNP(LN), it is clear that the moments of inertia are systematically larger in the relativistic case. Although one cannot completely exclude that this feature is to some extent connected with a different angular momentum content of single-particle orbitals in relativistic and non-relativistic calculations, a detailed analysis of pairing energies and moments of inertia suggests that this fact can be explained in a more realistic way by the different effective masses of the two theories: $m^*/m \sim 0.6$ in RMF theory and ~ 0.7 in the non-relativistic theory. Thus the corresponding level density in the vicinity of the Fermi level is smaller in the relativistic theory which in

general leads to weaker pairing correlations as compared with non-relativistic calculations and as a result to larger moments of inertia. PNP(LN) restores to a large extent the correct size of pairing correlations and thus its effect is larger in relativistic calculations. The average decrease of the moments of inertia due to PNP(LN) over the considered set of nuclei is 1.35 and 1.15 in relativistic and non-relativistic calculations, respectively. It is also clearly seen that PNP(LN) improves in average and especially in relativistic case the agreement between experimental and calculated moments of inertia. The level of agreement between calculations with PNP(LN) and experiment is similar in both theories, however, some discrepancies still remain.

8 Time dependent RMF theory

So far most of these investigations have been concentrated on ground states of nuclei all over the periodic table, but in several cases one has used such theories very successfully also for the description of excited states very. An example we have seen in the last section, where Cranked Relativistic Mean Field (CRMF) theory was used to determines the lowest state in a rotating frame. This has turned out to be very successful in describing a large variety of phenomena in rotational bands of superdeformed nuclei in a fully microscopic way.

In a further attempt Time Dependent RMF (TDRMF) theory has been used to describe giant resonances in nuclei [96–98]. The time-dependent classical equations of motion

$$i\partial_t \psi_i = \hat{h}(t)\psi_i = \{\alpha[\nabla - \mathbf{V}(\mathbf{r},t)] + V(\mathbf{r},t) + \beta m - S(\mathbf{r},t)\}\,\psi_i \tag{30}$$

are solved for time-dependent mean fields

$$S(\mathbf{r},t) = -g_\sigma \sigma(\mathbf{r},t), \tag{31}$$

$$V_\mu(\mathbf{r},t) = g_\omega \omega_\mu(\mathbf{r},t) + g_\rho \boldsymbol{\tau}\boldsymbol{\rho}_\mu(\mathbf{r},t) + eA_\mu(\mathbf{r},t), \tag{32}$$

Neglecting retardation these fields are given at each time t by the solution of the Klein-Gordon Equations:

$$\left[-\Delta + m_\sigma^2\right]\,\sigma(\mathbf{r},t) = -g_\sigma\,\rho_s(\mathbf{r},t) - g_2\,\sigma^2(\mathbf{r},t) - g_3\,\sigma^3(\mathbf{r},t) \tag{33}$$

$$\left[-\Delta + m_\omega^2\right]\,\omega_\mu(\mathbf{r},t) = g_\omega\,j_\mu(\mathbf{r},t) \tag{34}$$

where the densities and the currents are given by

$$\rho_s(\mathbf{r},t) = \sum_{i=1}^{A} \bar{\psi}_i(\mathbf{r},t)\psi_i(\mathbf{r},t), \tag{35}$$

$$j_\mu(\mathbf{r},t) = \sum_{i=1}^{A} \bar{\psi}_i(\mathbf{r},t)\gamma_\mu\psi_i(\mathbf{r},t) \tag{36}$$

With these densities one calculates time dependent expectation values $R(t)$, $D(t)$, or $Q(t)$ for the root mean square radii, the isovector dipole moments or the quadrupole moments which show in the case of small amplitude excitations pronounced oscillations. A Fourier analysis of these results allows to determine the resonance energies. Using the non-linear parameter sets NL1 or NL3 it was in is possible is this way to describe rather successfully the energies of the giant monopole resonances (GMR) as well as those of the giant dipole (GDR) and the giant quadrupole (GQR) resonances [96–98]. No new adjustment of the parameters of the Lagrangian was necessary. The disadvantage of these time dependent RMF calculations is that they require on one side a very large computational effort and on the other side they are – apart from the monopole case – based on deformed mean fields. Therefore they break rotational symmetries and mix quantum numbers. Such calculations cannot be used to describe low-lying collective excitations.

The standard tool for the description of excited states in non-relativistic descriptions [99,100], the Random Phase Approximation (RPA) has so far been applied successfully for the relativistic models only very recently and so far only in a few very specific cases [101,102]. This slow development has two essential reasons. Of course, Relativistic Random Phase Approximation (RRPA) codes are around since more than fifteen years [103–107], but those where based on the linear version of the Walecka model, which is not able to describe realistic nuclei, and therefore the results obtained with these codes were not in agreement with experiments.

Even the consideration of current conservation [108], which requires to include ah-configurations, i.e. configurations where a particle is removed from the Fermi sea and put into the empty Dirac sea (sometimes called *Pauli blocking terms*), does not change this situation dramatically. It is certainly important for the proper treatment of the spurious states and for low-lying excitations with the same quantum numbers, but it has an essential influence on the giant resonances only for isoscalar excitations [109] .

The break through came only after the development of new techniques to include the non-linear terms in RRPA [110]. Only with these techniques was it possible to realize the large effects of the ah -configurations on the isoscalar giant resonances and to include them in the calculations for relativistic linear response [101] or for the diagonalization of the RRPA-matrix [102]. These large effects where completely unexpected, because they occur in particular for quantum numbers ($T = 0, J^\pi = 0^+$ or 2^+) orthogonal to the spurious mode ($T = 0, J^\pi = 1^-$). They have no non-relativistic analogon: they are caused by the fact that the matrix elements coupling the ah-configurations to the normal ph-configurations through the exchange of scalar mesons are essentially suppressed because of orthogonality between negative energy and positive energy spinors. This quenching of the scalar part of the interaction disturbs the detailed balance between scalar attraction and vector repulsion and one is left with unexpected large matrix elements corresponding to the exchange of the vector particles. By this effects the coupling matrix elements between ah-configurations and the nor-

mal ph-configurations are extremely large. Therefore they can have an influence on the physical ph-configurations, even if distance in energy is more than 1200 MeV and because of the no-crossing role of Wigner this leads always to a repulsive effect: the inclusion of the ah-configurations shifts the resonances to higher energies.

The time-dependent calculations include automatically both effects: they are, of course, based on the non-linear version of the model and they automatically include ah-configurations, because they are an immediate consequence of the *no-sea* approximation in the relativistic mean field. A rigorous derivation of the RRPA-equations in the small amplitude limit of TDRPA [109] shows that the small variation of the density matrix $\delta\rho$ has not only the usual ph-components with a particle orbit p above the Fermi sea and a hole orbit h in the Fermi sea, but also components with a particle a in the Dirac sea and a hole h' in the Fermi sea. The *no-sea* approximation is imposed automatically at each time in TDRMF calculations because only particles in the Fermi sea are propagated in time explicitly [96]- [98]. An analogous propagation of the negative energy spinors would leave them automatically at each step in time orthogonal to the particles in the Fermi sea. This does not mean, however that by expanding the time-dependent Dirac spinors in terms of the static basis, one does not have to include anti-particles with respect to the stationary basis. Just by reasons of completeness such configurations show up.

There are two practical ways to obtain in RRPA the physical quantities relevant to nuclear excitations. The first method is to calculate directly the linear response function of the nucleus whereas the second method consists in solving the RPA equations in matrix form. In both cases one starts with a self-consistent solution for the ground state and obtains in this way the static mean field. Technically this is achieved by diagonalizing the Dirac equation in a spherical harmonic oscillator basis including 20 oscillator shells [14]. Among the solutions a set of particle-hole (ph) and anti-particle-hole(ah) pairs with the appropriate quantum numbers is chosen. Their number is restricted by a maximal ph-energy ($\epsilon_p - \epsilon_h \leq E_{max}$) and a minimal ah-energy ($\epsilon_a - \epsilon_h \geq E_{min}$). The corresponding 4-component spinors are then used to build the unperturbed polarization operator II^0 or the RPA matrix.

The linear response of the nucleus with respect to an external operator is given by the imaginary part of the retarded polarization operator

$$R(F,F;\mathbf{k},\omega) = \frac{1}{\pi} Im II^R(F,F;\mathbf{k},\mathbf{k};\omega) \ , \tag{37}$$

where F is a one-body operator represented by a 4×4 matrix. The polarization operator is calculated as a solution of the linearized Bethe-Salpeter equation in momentum space (for details see Ref. [110]).

For linear models, the meson propagators are of the well known Yukawa form. In general, i.e. with non-linear meson couplings, the meson propagators can no longer be given in analytical form, but they can be obtained numerically by

solving a Klein-Gordon equation,

$$(\partial^\mu \partial_\mu + \frac{\partial^2 U_\phi(\phi)}{\partial \phi^2}|_{\phi_0}) D_\phi(x,y) \;=\; -\delta(x-y), \tag{38}$$

where $U_\phi(\phi)$ is the generalized mass term in the effective Lagrangians with meson self-interactions. For non-linear σ models it is parametrized as [9,11]:

$$U_\sigma(\sigma) \;=\; \frac{1}{2} m_\sigma^2 \sigma^2 + \frac{1}{3} g_2 \sigma^3 + \frac{1}{4} g_3 \sigma^4. \tag{39}$$

In some versions of effective Lagrangians self-interactions of the ω -field self-interactions are also considered [13]:

$$U_\omega(\omega) \;=\; \frac{1}{2} m_\omega^2 \omega^\mu \omega_\mu + \frac{1}{4} c_3 (\omega^\mu \omega_\mu)^2. \tag{40}$$

We obtain after a Fourier transformation the propagators in momentum space,

$$(\omega^2 - \mathbf{k}^2) D_\phi(\mathbf{k},\mathbf{k}',\omega) - \frac{1}{(2\pi)^3} \int S_\phi(\mathbf{k}-\mathbf{k}_1) D_\phi(\mathbf{k}_1,\mathbf{k}',\omega) d^3k_1 \;=\; (2\pi)^3 \delta(\mathbf{k}-\mathbf{k}'), \tag{41}$$

where $S_\phi(\mathbf{k}-\mathbf{k}_1)$ is the Fourier transform of $\frac{\partial^2 U_\phi(\phi)}{\partial \phi^2}|_{\phi_0}$,

$$S_\phi(\mathbf{k}-\mathbf{k}_1) \;=\; \int e^{-i(\mathbf{k}-\mathbf{k}')\mathbf{r}} \frac{\partial^2 U_\phi(\phi)}{\partial \phi^2}|_{\phi_0} d^3r \;. \tag{42}$$

In the absence of meson self-interaction terms the propagators are diagonal in momentum space, $D_\phi(\mathbf{k}_1,\mathbf{k}_2,\omega)=\delta(\mathbf{k}_1-\mathbf{k}_2) D_\phi(\mathbf{k}_1)$ and we have simply,

$$D_\phi(\mathbf{k},\omega) \;= \pm \frac{1}{(2\pi)^3} \frac{1}{\omega^2 - \mathbf{k}^2 - m_\phi^2 + i\eta} \;, \tag{43}$$

where the plus (minus) sign corresponds to vector (scalar) mesons. In the linear response formalism retardation (the frequency dependence of the propagator) can be easily taken into account, which is not the case in the time-dependent formulation [111] nor in cases where the RPA equations are solved by matrix diagonalization in configuration space. However, because of the fact that the meson masses are very large compared to nuclear excitation energies retardation effects play only a negligible role in calculations of collective modes.

In the matrix diagonalization method [109] one must build in configuration space the RPA matrices:

$$A = \begin{pmatrix} (\epsilon_p - \epsilon_h)\delta_{pp'}\delta_{hh'} & 0 \\ 0 & (\epsilon_a - \epsilon_h)\delta_{aa'}\delta_{hh'} \end{pmatrix} + \begin{pmatrix} V_{ph'hp'} & V_{ph'ha'} \\ V_{ah'hp'} & V_{ah'ha'} \end{pmatrix} \tag{44}$$

$$B = \begin{pmatrix} V_{pp'hh'} & V_{pa'hh'} \\ V_{ap'hh'} & V_{aa'hh'} \end{pmatrix} \tag{45}$$

where the residual interaction V has the form:

$$V(\mathbf{r}_1,\mathbf{r}_2) = D_\sigma(\mathbf{r}_1,\mathbf{r}_2)\, \beta^{(1)}\beta^{(2)} + D_\omega(\mathbf{r}_1,\mathbf{r}_2) \left(1 - \boldsymbol{\alpha}^{(1)}\boldsymbol{\alpha}^{(2)}\right) \;. \tag{46}$$

Here, $\alpha^{(i)}$ and $\beta^{(i)}$ are the Dirac matrices acting in the space of particle i, and we have omitted for simplicity to write the contributions of the ρ-meson and the photon.

The eigenmodes of the system are determined by the usual RPA equations in configuration space (matrix-RPA):

$$\begin{pmatrix} A & B \\ -B^* & -A^* \end{pmatrix} \begin{pmatrix} X \\ Y \end{pmatrix}_\nu = \begin{pmatrix} X \\ Y \end{pmatrix}_\nu \Omega_\nu \ . \tag{47}$$

One can then express transition densities and transition amplitudes in terms of the RPA amplitudes (X_ν, Y_ν) [23]. The RPA-matrix has a dimension of twice the number of ph-pairs and it is obviously non Hermitian. However, in non-relativistic investigations with real matrix elements and with positive definite matrices $(A \pm B)$ one can reduce the number by a factor 2 and end up with a symmetric eigenvalue problem of half this dimension (for details see Ref. [23]). This is no longer the case for relativistic RPA, because the matrix A has large negative diagonal elements and eigenvalues connected with the ah-excitations $(\epsilon_a - \epsilon_h) < -1200$ MeV. This enhances the computational effort of the matrix diagonalization method for relativistic RPA calculations considerably as compared to the that of the non-relativistic case.

As an application we study in the following the distribution of the isovector dipole strength in nuclei at and far from the valley of stability within the framework of fully self-consistent RRPA, including configurations spaces with negative-energy Dirac states. Two basic dipole modes have been observed. In Fig. 13 we display the isovector dipole strength distribution in ^{208}Pb (left panel), and the corresponding transition densities to the two states at 7.29 MeV and at 12.95 MeV (right panel). The discrete spectrum of RRPA has been folded with a Lorentzian distribution with a width of 0.5 MeV. The calculated energy E=12.95 MeV of the main peak in Fig. 13 has to be compared with the experimental value of the excitation energy of the isovector giant dipole resonance: 13.3±0.1 MeV. In the energy region between 5 and 11 MeV two prominent peaks are found: 7.29 MeV and 10.10 MeV. The lower peak can be identified as the pygmy dipole resonance by the following reasons:

The transition densities to the states 7.29 MeV and 12.95 MeV are displayed in the right panel of Fig. 13. The proton and neutron contributions are shown separately; the dotted line denotes the isovector transition density and the solid line has been used for the isoscalar transition density. Although the isoscalar B(E1)-value to all states must identically vanish, the corresponding isoscalar transition densities to different states need not to be identically zero. The transition density for the main peak at 12.95 MeV display a radial dependence characteristic for the isovector giant dipole resonance: the protons and neutron densities oscillate with opposite phases. The total isovector transition density is much larger than the isoscalar component. At large radii both have a similar radial dependence. A very different behavior is observed for the transition densities to the states at 7.29 MeV: the proton and neutron densities in the interior region are not out of phase. There is almost no contribution of the protons in the surface region.

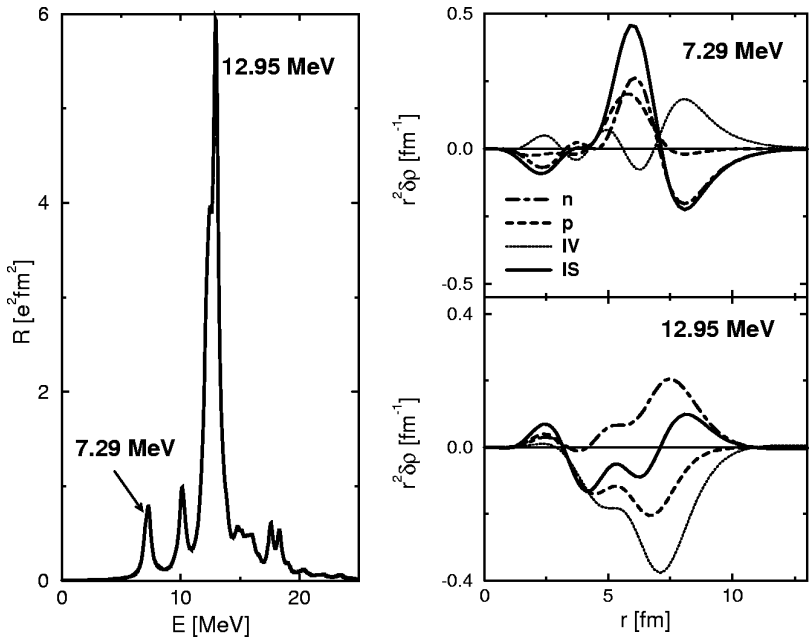

Fig. 13. Isovector dipole strength distribution in ^{208}Pb (left panel) and transition densities for the two peaks at 7.29 MeV and 12.95 MeV (right panel). All transition densities are multiplied with the factor r^2 (from Ref. [94]).

In the interior the isoscalar transition density dominates over the isovector one. The large neutron component in the surface region contributes to the formation of a node in the isoscalar transition density.

The phenomenon of low-lying isovector strength was already studied almost thirty years ago in the framework of the three-fluid hydrodynamical model [112]: the protons, the neutrons in the same orbitals as the protons, and the excess neutrons. Two normal modes of dipole vibrations were identified: (i) vibrations of protons against the two types of neutrons, and (ii) the vibrations of the excess neutrons against the proton-neutron core. In the case of neutron rich nuclei, the later mode corresponds to pygmy resonances.

The same effect of an increasing low-lying dipole strength is found even more pronounced in neutron rich nuclei far from the valley of stability. In Fig. 14 we plot the distribution of the isovector dipole strength for neutron rich Ca-isotopes. As the neutron excess increases, the spectra become more fragmented, and starting with ^{54}Ca, the onset of low-lying dipole strength is observed below 10 MeV. This result is in agreement with non-relativistic RPA-calculations [113]. No dipole strength is found below 10 MeV for ^{48}Ca. In the RRPA strength

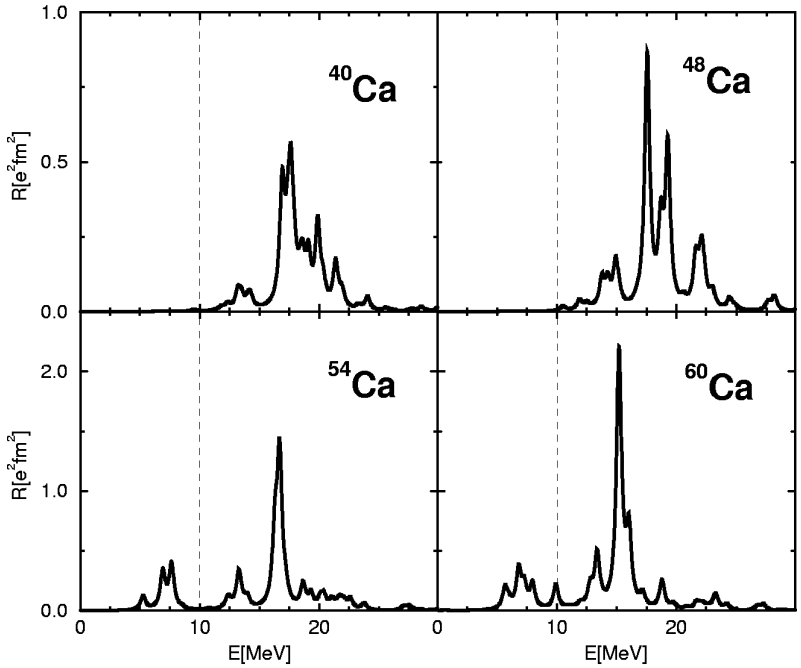

Fig. 14. RRPA isovector dipole strength distributions in Ca isotopes. The thin dashed line separates the region of giant resonances from the low energy region below 10 MeV (from Ref. [95]).

function of the extremely neutron rich nucleus ^{60}Ca, the low-energy region is strongly fragmented, with many peaks of similar intensity. Together they exhaust 10 % of the EWSR, compared with 40 % of the EWSR exhausted by the main IVGDR peak at 15.2 MeV.

The RRPA transition densities for the state at 7.3 MeV (illustrative for the low-energy region) and for the GDR state at 15.2 MeV are compared in Fig. 15. The transition densities for the state at 15.2 MeV display the characteristic behavior of the giant dipole resonance, the protons and neutrons oscillate with opposite phases. For the low-lying state we observe again a large neutron-component in the surface region, characteristic for a pygmy resonance. In particular we notice the long tail of the neutron transition density for the state at 7.3 MeV.

In Fig. 16 we compare the RRPA results for the centroid energies of the GDR in the Ni isotopes with the empirical relation 78 $A^{-1/3}$ MeV. The centroids in the low-energy region below 10 MeV are compared with the hydrodynamical prediction (SIS) for the excitation of the pygmy resonances in the two-fluid model of Suzuki, Ikeda and Sato [114] in the lower panel. We notice that the RRPA

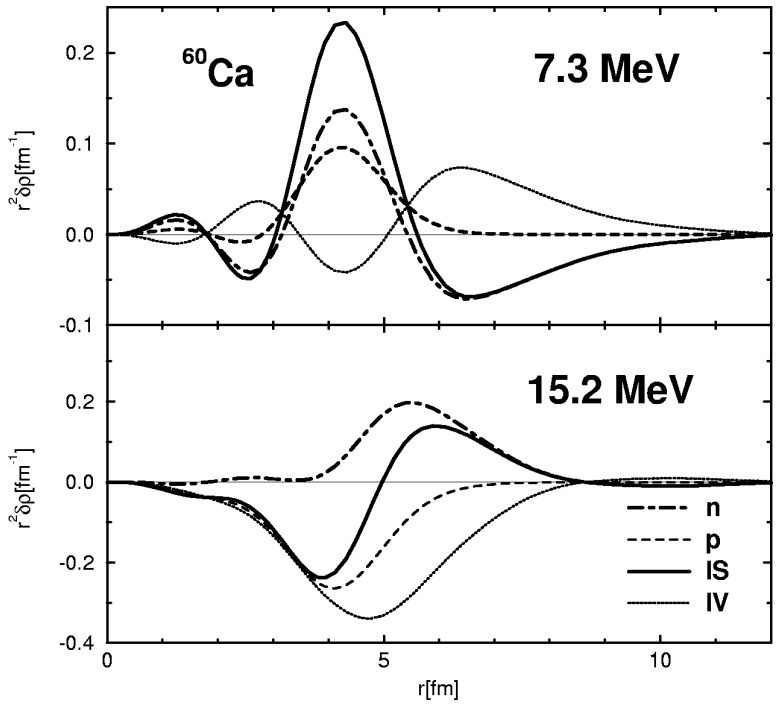

Fig. 15. Transition densities for the peaks at 7.3 MeV and 15.2 MeV in ^{60}Ca. Both isoscalar and isovector transition densities are displayed, as well as the separate proton and neutron contributions. All transition densities are multiplied by r^2. (from Ref. [95]).

energies are in fair agreement with the empirical mass dependence of the GDR. The SIS model predicts the pygmy dipole resonance to increase with neutron excess, in contrast to the RRPA results which display the opposite behavior.

9 Conclusion and outlook

Within recent years a large number of problems in nuclear structure physics have been tackled by relativistic mean field theory. It has turned out, that this theory is very successful in describing nuclear properties over the entire periodic table with a minimal set or parameters in a fully microscopic way. It is a phenomenological theory as all the other competing non-relativistic density dependent Hartree-Fock theories, but is goes beyond these theories in several respects: (a) it incorporates relativistic phenomena such as the large scalar attraction and the large vector repulsion in a consistent way, (b) it deals properly with the spin-orbit term in the nuclear medium, which has a great influence on many details in nuclear structure, (c) it uses the field-theoretical techniques

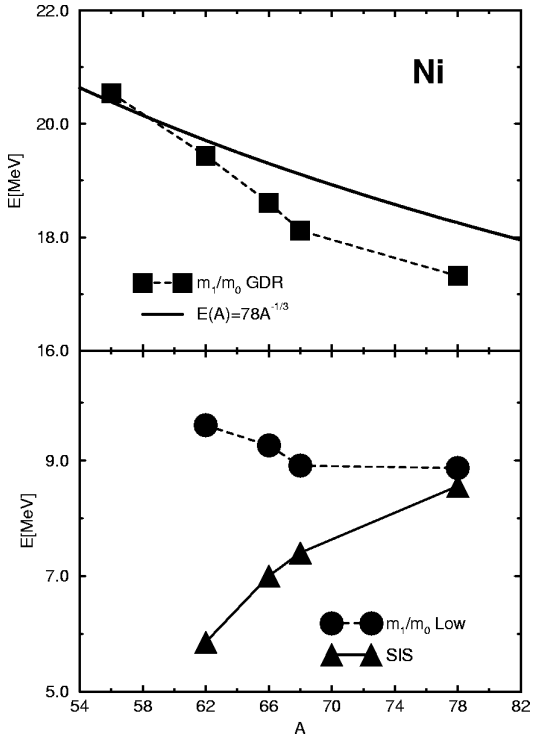

Fig. 16. Centroid energies of the isovector dipole strength distribution in the region of the giant resonances (upper panel), and in the low-energy region below 10 MeV (lower panel), as a function of the mass number of the Ni isotopes. More details are given in the text (from Ref. [95]).

and the language of nucleons and mesons. It is therefore much better suited to provide a connection to more fundamental theories derived from QCD, and (d) it is in many ways technically simpler, requiring less manpower, than Skyrme or Gogny theories, which are either non-local or have to take into account non-local effects by complicated momentum dependencies.

There is certainly a lot to be done: A microscopic theory based on fully relativistic meson-exchange potentials has so far been developed only in nuclear matter. Applications to finite nuclei are missing. It is still not clear, whether the isospin dependence is included properly in the present RMF-models, where all the isospin dependence has its origin in the vector-meson ρ. Looking into relativistic Brueckner calculations there should be also a scalar field carrying isospin (δ-meson). So far the available experimental data do not allow to disentangle the isospin-dependence of the scalar and the vector channel properly enough. A better knowledge of the experimental isospin dependence of the spin-orbit splitting would certainly be helpful in this direction. The isospin carrying π-meson is

not included in most of the present high precision fits. It enters only via the exchange term, which complicates the numerical effort considerably. However, there are indications that the tensor force connected with the pion exchange has an essential influence on the spin-orbit splitting. Increasing computer power will certainly allow in the next future to address those questions and to obtain in this way a more reliable predictive power for extrapolating our present models in the unknown regions far from stability and in the region of super-heavy nuclei.

Acknowledgments

I would like to express my deep gratitude to all my collaborators, in particular to A.V. Afanasjev, H. Berghammer, G.A. Lalazissis, J. König, N. Paar, M. Serra, D. Vretenar, and A. Wandelt. Without their great enthusiasm and without their efforts these investigations would not have been possible. This work was supported by the Bundesministerium für Forschung und Bildung under the project 06 TM 979

References

1. D. Vautherin, D.M. Brink: Phys. Rev. **C5**, 626 (1972)
2. J. Dechargé, D. Gogny: Phys. Rev. **C21**, 1568 (1980)
3. M.H. Johnson, E. Teller: Phys. Rev. **98**, 783 (1955)
4. J.D. Walecka: Ann. Phys. (N.Y.) **83,** 491 (1974)
5. B.D. Serot, J.D. Walecka: Adv. Nucl. Phys. **16,** 1 (1986)
6. J. Boguta, A.R. Bodmer: Nucl. Phys. **A292**, 413 (1977)
7. A.R. Bodmer: Nucl. Phys. **A526**, 397 (1991)
8. Z.Y. Zhu, H.J. Mang, P. Ring: Phys. Lett. **254B**, 325 (1991)
9. P.G. Reinhard, M. Rufa, J. Maruhn, W. Greiner, J. Friedrich: Z. Phys. **A323**, 13 (1986)
10. M.M. Sharma, M.A. Nagarajan, P. Ring: Phys. Lett. **B312**, 377 (1993)
11. G.A. Lalazissis, J. König, P. Ring: Phys. Rev. **C55**, 540 (1997)
12. C.J. Horowitz, B.D. Serot: Phys. Lett. **140B**, 181 (1984)
13. Y. Sugahara, H. Toki: Nucl. Pys. **A579,** 557 (1994)
14. Y.K. Gambhir, P. Ring, A. Thimet: Ann. Phys. (N.Y.) **198**, 132 (1990)
15. W. Koepf, P. Ring: Phys. Lett. **212B**, 397 (1988)
16. D. Hirata, H. Toki, I. Tanihata, P. Ring: Phys. Lett. **B314**, 168 (1993)
17. Bulgac: preprint (1980) unpublished
18. J. Dobaczewski, H. Flocard, J. Treiner: Nucl. Phys. **A422, 103** (1984)
19. J. Dobaczewski, W. Nazarewicz, T.R. Werner, J.F. Berger, C.R. Chinn, J. Dechargé: Phys. Rev. **C53,** 2809 (1996)
20. H. Kucharek, P. Ring: Z. Phys. **A339,** 23 (1991)
21. P. Ring: Prog. Part. Nucl. Phys. **37**, 193 (1996)
22. L.P. Gorkov: Sov. Phys. JETP **7**, 505 (1958)
23. P. Ring, P. Schuck: *The Nuclear Many-body Problem*, Springer Verlag, Heidelberg (1980)
24. H. Kucharek, P. Ring, P. Schuck, R. Bengtsson, M. Girod: Phys. Lett. **216B,** 249(1989)
25. M. Serra, A. Rummel, P. Ring: to be published

26. R. Machleidt: Adv. Nucl. Phys. **19**, 189 (1989)
27. K.A. Brueckner, J.L. Gammel, H. Weitzner: Phys. Rev. **110**, 431 (1958)
28. T. Gonzalez-Llarena, J.L. Egido, G.A. Lalazissis, P. Ring: Phys. Lett. **B379**, 13 (1996)
29. J. Meng, W. Pöschl, P. Ring: Z. Phys. **A358**, 123 (1997)
30. W. Pöschl, D. Vretenar, G.A. Lalazissis, P. Ring: Phys. Rev. Lett. **79**, 3851 (1998)
31. G.A. Lalazissis, D. Vretenar, W. Pöschl, P. Ring: Nucl. Phys. **A632**, 363 (1998)
32. G.A. Lalazissis, D. Vretenar, P. Ring: Phys. Rev. **C57**, 2294 (1998)
33. D. Vretenar, G.A. Lalazissis, P. Ring: Phys. Rev. **C57**, 3071 (1998)
34. G.A. Lalazissis, D. Vretenar, P. Ring: Nucl. Phys. **A650**, 133 (1999)
35. D. Vretenar, G.A. Lalazissis, P. Ring: Phys. Rev. Lett. **82**, 4595 (1999)
36. G.A. Lalazissis, D. Vretenar, P. Ring, M. Stoitsov, L. Robledo: Phys. Rev. **C60**, 014310 (1999)
37. G.A. Lalazissis, D. Vretenar, P. Ring: Phys. Rev. **C60**, 051302 (1999)
38. G.A. Lalazissis, D. Vretenar, P. Ring: Nucl. Phys. **A679**, 481 (2001)
39. A.V. Afanasjev, J. König, P. Ring: Phys. Rev. **C60**, 051303 (1999)
40. J.F. Berger, M. Girod, D. Gogny: Nucl. Phys. **A428**, 32 (1984)
41. F.B. Guimaraes, B.V. Carlson, T. Frederico: Phys. Rev. **C54**, 2385 (1996)
42. K.L. Kratz: Rev. Mod. Astron. **1**, 184 (1988)
43. J. Dobaczewski, I. Hamamoto, W. Nazarewicz, J.A. Sheikh: Phys. Rev. Lett. **72,** 981 (1994)
44. M.M. Sharma, G.A. Lalazissis, W. Hillebrandt, P. Ring: Phys. Rev. Lett. **72**, 1431 (1994)
45. W. Koepf, P. Ring: Z. Phys. **A339,** 81 (1991)
46. G.A. Lalazissis, D. Vretenar, W. Pöschl, P. Ring: Phys. Lett. **B418**, 7 (1998)
47. I. Tanihata *et al*: Phys. Rev. Lett. **55**, 2676 (1985)
48. G.F. Bertsch, B.A. Brown, H. Sagawa: Phys. Rev. **C39**, 1154 (1989)
49. W. Koepf, Y.K. Gambhir, P. Ring, M.M. Sharma: Z. Phys. **A340**, 119 (1991)
50. H. Sagawa: Phys. Rev. **B286**, 7 (1992)
51. Z.Y. Zhu *et al*: Phys. Lett. **B328**, 1 (1994)
52. G.F. Bertsch, H. Esbensen: Ann. Phys. (N.Y.) **209**, 327 (1991)
53. J. Meng, P. Ring: Phys. Rev. Lett. **77**, 3963 (1996)
54. J. Meng, P. Ring: Phys. Rev. Lett. **80**, 460 (1998)
55. P.J. Woods, C.N. Davids: Annu. Rev. Nucl. Part. Sci. **47**, 541 (1997)
56. S. Aberg, P.B. Semmes, W. Nazarewicz: Phys. Rev. **C56**, 1762 (1997)
57. K. Rykaczewski *et al*: Phys. Rev. **C60**, 011301 (1999)
58. E. Maglione, L.S. Ferreira, R.J. Liotta: Phys. Rev. Lett. **81**, 538 (1998): Phys. Rev. **C59**, R589 (1999)
59. S. Hofmann, W. Reisdorf, G. Münzenberg, F.P. Hessberger, J.R.H. Schneider, P. Armbruster: Z. Phys **A305**, 125 (1982)
60. P. Möller, J.R. Nix, K.-L. Kratz: At. Data Nucl. Data Tables **66**, 131 (1997)
61. D.R. Inglis: Phys. Rev. **96,** 1050 (1954)
62. R. Beck, H.J. Mang, P. Ring: Z. Phys. **231**, 26 (1970)
63. P. Ring, R. Beck, H.J. Mang: Z. Phys. **231**, 10 (1970)
64. B. Banerjee, H.J. Mang, P. Ring: Nucl. Phys. **A215**, 366 (1973)
65. P. Ring, H.J. Mang: Phys. Rev. Lett. **33**, 1174 (1974)
66. Ulrich Hofmann, P. Ring: Phys. Lett. **214B**, 307 (1988)
67. J. König, P. Ring; Phys. Rev. Lett. **71**, 3079 (1993)
68. W. Koepf, P. Ring; Nucl. Phys. **A493**, 61 (1989)
69. K. Kaneko, M. Nakano, M. Matsuzaki: Phys. Lett. **B317**, 261 (1993)

70. A.V. Afanasjev, J. König, P. Ring: Nucl. Phys. **A608**, 107 (1996)
71. A.V. Afanasjev, G.A. Lalazissis, P. Ring: Nucl. Phys. **A634**, 395 (1998)
72. A.V. Afanasjev, I. Ragnarsson, P. Ring: Phys. Rev. **C59**, 3166 (1999)
73. W. Satula, R. Wyss: Phys. Rev. **C50**, 2888 (1994)
74. J. Terasaki, P.-H. Heenen, P. Bonche, J. Dobaczewski, H. Flocard: Nucl. Phys. **A593**, 1 (1995)
75. M. Girod, J.P. Delaroche, J.F. Berger, J. Libert: Phys. Lett. **B325**, 1 (1994)
76. A. Valor, J.L. Egido, L.M. Robledo: Phys. Lett. **B392**, 249 (1997)
77. H.J. Lipkin: Ann. Phys. **31**, 525 (1960)
78. Y. Nogami: Phys. Rev. **134**, B313 (1964)
79. H.X. Pradhan, Y. Nogami, J. Law: Nucl. Phys. **A512**, 61 (1990)
80. A. Bohr, B.R. Mottelson: Mat. Fys. Medd. Dan. Vid. Selsk. **30**, No. 1 (1955)
81. S. A. Moszkowski: Phys. Rev. **103,** 1328 (1956)
82. A. Bohr, B.R. Mottelson, D. Pines: Phys. Rev. **110** 936 (1958)
83. S.T. Belyaev: Nucl. Phys. **24**, 322 (1961)
84. S.G. Nilsson, O. Prior: Mat. Fys. Medd. Dan. Vid. Selsk. **32**, No. 16 (1961)
85. A.B. Migdal: Nucl. Phys. **13**, 655 (1959)
86. A.B. Migdal: Sov. Phys. JETP **10**, 176 (1960)
87. D.J. Thouless, J.G. Valatin: Nucl. Phys. **31**, 211 (1962)
88. E.R. Marshalek and J. Weneser: Phys. Rev. **C2**, 1682 (1970)
89. E.R. Marshalek: Phys. Rev. **C35**, 1900 (1987)
90. G. Andersson *et al*: Nucl. Phys. **A268**, 205 (1976)
91. K. Neergård, V.V. Pashkevich, S. Frauendorf: Nucl. Phys. **A262**, 61 (1976)
92. J. Meyer, J. Speth, J.H. Vogeler: Nucl. Phys. **A193**, 60 (1972)
93. J. König, P. Ring, L.M. Robledo, J.L. Egido: Phys. Rev. **C62**, 054306 (2000)
94. D. Vretenar, N. Paar, P. Ring, G.A. Lalazissis: Phys. Rev. **C63**, in print (2001)
95. D. Vretenar, N. Paar, P. Ring, G.A. Lalazissis: Nucl. Phys. **A235**, in print (2001)
96. D. Vretenar, H. Berghammer, P. Ring: Nucl. Phys. **A581**, 679 (1995)
97. B. Podobnik, D. Vretenar, P. Ring: Z. Phys. **A354**, 375 (1996)
98. D. Vretenar, G.A. Lalazissis, R. Behnsch, W. Pöschl, P. Ring: Nucl. Phys. **A621**, 853 (1997)
99. V. Gillet, N. Vinh Mau: Nucl. Phys. **54**, 321 (1964)
100. P. Ring, J. Speth: Nucl. Phys. **A235**, 315 (1974)
101. Zhong-yu Ma, Nguyen Van Giai, A. Wandelt, D. Vretenar, P. Ring: Nucl. Phys. **A685**, in print (2001)
102. D. Vretenar, A. Wandelt, P. Ring: Phys. Lett. **B487**, 334 (2000)
103. R.J. Furnstrahl: Phys. Lett. **152B**, 313 (1985)
104. S. Nishizaki, H. Kurasawa, T. Suzuki: Phys. Lett. **B171**, 1 (1986)
105. K. Wehrberger, F. Beck: Phys. Rev. **C37**, 1184 (1988)
106. M. L'Huiller, N. Van Giai: Phys. Rev. **C39**, 2022 (1989)
107. C.J. Horowitz, J. Piekarewicz: Phys. Rev. Lett. **62**, 391 (1989)
108. J.F. Dawson, R.J. Furnstahl: Phys. Rev. **C42**, 2009 (1990)
109. P. Ring, Zhong-yu Ma, Nguyen Van Giai, D. Vretenar, A. Wandelt, L.-I. Cao: Nucl. Phys. in print, (2001)
110. Z.Y. Ma, N. Van Giai, H. Toki, M.L. L'Huillier: Phys. Rev. **C42**, 2385 (1997)
111. D. Vretenar, P. Ring, G.A. Lalazissis, N. Paar: Nucl.Phys. **A649**, 29c (1999)
112. Radhe Mohan, M. Danos, L.C. Biedenharn: Phys. Rev. **C3**, 1740 (1971)
113. F. Catara, E.G. Lanza, M.A. Nagarajan, A. Vitturi: Nucl. Phys. **A624**, 449 (1997)
114. Y. Suzuki, K. Ikeda, H. Sato: Prog. Theor. Phys. **83**, 180 (1990)

Semi-classical methods in nuclear physics

David M. Brink

Theoretical Physics, 1 Keble Road, Oxford OX1 3NP, UK

Abstract. These lecture notes present an introduction to some semi-classical techniques which have applications in nuclear physics. Topics discussed include the WKB method, approaches based on the Feynman path integral, the Gutzwiller trace formula for level density fluctuations and the Thomas-Fermi approximation and the Vlasov equation for many-body problems. There are applications to heavy ion fusion reactions, bremsstrahlung emission in alpha decay and nuclear response functions.

1 Introduction

Semi-classical mechanics is an approximation to quantum mechanics which is valid in the limit of large quantum numbers, or more generally, where de Broglie wavelengths are small compared with characteristic dimensions of a quantum problem. Semi-classical mechanics is valid in the limit of large quantum numbers or, more generally, where $\hbar$ is small compared with a classical action which is characteristic of a particular problem. The idea can be introduced by examples which have been used by other lecturers during this course.

Deformed nuclei have rotational spectra which can be approximated by the energy states of a rigid rotor

$$E_I = \frac{\hbar^2}{2\Im} I(I+1) \tag{1}$$

where $\Im$ is the moment of inertia and the angular momentum I is even. For large angular momenta the angular velocity ω is related to I by the classical relation $\hbar I = \Im\omega$. The γ-ray transition energies in the spectrum are related to the angular velocity by

$$E_I - E_{I-2} = 2\hbar\omega. \tag{2}$$

Equation (2) is used to measure the angular velocity of a rotating nucleus even when the spectrum deviates from that of a rigid rotor.

In some situations quantum mechanics is mixed with classical mechanics. An example is Time Dependent Hartree-Fock theory (TDHF). The time dependence of the mean field is classical while the motion of the nucleons in the mean field is quantal. In the Strutinsky shell correction method the total energy of a nucleus E_{TOT} is a combination of a classical liquid drop term E_{LD} and a quantal shell correction term E_{SHELL}

$$E_{TOT} = E_{LD} + E_{SHELL}. \tag{3}$$

J.M. Arias and M. Lozano (Eds.): LNP 581, pp. 233–258, 2001.
© Springer-Verlag Berlin Heidelberg 2001

This is another example of applying classical ideas to one aspect of a system and quantum ideas to another part.

In the next section we discuss two different approaches to semi-classical mechanics. The idea of the WKB (Wentzel, Kramers and Brillouin) method is to look for approximate solutions of the Schrödinger equation which are valid in the semi-classical limit. The Feynman path integral approach uses a stationary phase approximation for the path integral. Later in the lecture notes there are discussions of barrier penetration based on the path integral method, heavy ion fusion reactions, bremsstrahlung emission in alpha decay, level density fluctuations and the Strutinsky shell-correction method, the Thomas-Fermi approximation and the Vlasov equation.

2 The WKB method in one dimension

The Schrödinger equation is

$$-\frac{\hbar^2}{2m}\frac{d^2\psi}{dx^2}+V(x)\psi=E\psi \tag{4}$$

Looking for an approximate solution of the form $\psi=\varphi e^{iS/\hbar}$ and neglecting φ'' we get the usual WKB expressions for φ and S. In a classically allowed region where $E>V(x)$ and $p(x)=\hbar k(x)=\sqrt{2m(E-V(x))}$ is the local momentum

$$\varphi=\frac{1}{\sqrt{k(x)}} \qquad \text{and} \qquad S=\pm\int k(x)dx \tag{5}$$

and $k(x)$ is the local wave number. In a classically forbidden region ($V(x)>E$)

$$\varphi=\frac{1}{\sqrt{\gamma(x)}} \qquad \text{and} \qquad S=\mp i\int \gamma(x)dx \tag{6}$$

where $\hbar\gamma(x)=\sqrt{2m(V(x)-E)}$. The WKB approximation is not valid near a classical turning point where the local momentum $p(x)$ is zero. A more accurate connecting formula must be used to determine the boundary condition at a turning point . For example if there is a turning point at $x=a$ and if the region $x<a$ is classically forbidden and the region $x>a$ is allowed then there is a solution which decays exponentially in the forbidden region

$$\psi(x)\simeq\frac{C}{2\sqrt{\gamma(x)}}\exp\left[-\int_x^a\gamma(x)dx\right] \qquad \text{when} \quad x<a \tag{7}$$

and oscillates in the allowed region

$$\psi(x)\simeq\frac{C}{\sqrt{k(x)}}\sin\left(\int_a^x k(x)dx+\frac{\pi}{4}\right) \qquad \text{when} \quad x<a. \tag{8}$$

The matching condition (8) can be derived by approximating the potential $V(x)\simeq A(x-a)$ by a linear function of x near the turning point [13, Sect. 47]. It

can also be derived by analytical continuation [6],[12],[5, Sect. 3.3]. If $V(x)$ is an analytical function near a turning point at $x = a$ then the exact solution of the Schrödinger equation $\psi(x)$ is also analytic at and near the turning point. The WKB approximation is an analytic function near the turning point but has a branch point at $x = a$. The two functions are different in the complex plane, but a WKB solution can be a good approximation to an exact solution in certain regions of the comlex plane sufficiently far from the turning point. Thus making an analytic continuation of eq.(7) of the decaying solution for $x < a$ along a contour in the upper half of the complex x-plane to the real axis for $x > a$ gives the incoming wave component of (8) while making an analytic continuation along a contour in the lower half plane gives the outgoing wave component.

3 Feynman path integral

3.1 The time dependent propagator

Another approach to semi-classical quantum mechanics is to start with the Feynman propagator [8], [2],[5]. The propagator $K(x_1, x_0; T)$ from an initial point x_0 to a final point x_1 after a time T can be defined either as a matrix element between initial or final states in the coordinate representation

$$K(x_1, x_0; T) = \left\langle x_1 \left| \exp\left(-\frac{iHT}{\hbar}\right) \right| x_0 \right\rangle \tag{9}$$

or as a Feynman path integral

$$K(x_1, x_0; T) = \int D[x(t)] \exp\left(\frac{i}{\hbar} S[x(t)]\right) \tag{10}$$

where

$$S[x(t)] = \int_0^T \mathcal{L}(x, \dot{x}) dt = \int_0^T \left(\frac{1}{2} m\dot{x}^2 - V(x(t))\right) dt \tag{11}$$

is the classical action calculated for a path $x(t)$ which satisfies boundary conditions

$$x(0) = x_0 \qquad \text{and} \qquad x(T) = x_1. \tag{12}$$

The integral in eq.(10) implies a sum over all paths satisfying these boundary conditions.

Let $S(x_0, x_1; T)$ be the action calculated along a path which satisfies the classical equations of motion

$$\frac{d}{dt}\left(\frac{\partial \mathcal{L}}{\partial \dot{x}}\right) - \left(\frac{\partial \mathcal{L}}{\partial x}\right) = 0 \tag{13}$$

with boundary conditions $x(0) = x_0$ and $x(T) = x_1$. This action function satisfies three relations which are needed later

$$\frac{\partial S}{\partial x_1} = p_1, \qquad \frac{\partial S}{\partial x_0} = -p_0, \qquad \frac{\partial S}{\partial T} = -E. \tag{14}$$

Here p_0 and p_1 are the momenta at the ends of the classical path (at $t = 0$ and $t = T$) and E is the total energy which is constant along the path. A path $x_c(t)$ satisfying the classical equation of motion is a path which makes the action stationary, $\delta S[x_c(t)] = 0$.

3.2 The stationary phase approximation

The method of stationary phase gives an approximate formula for the integral

$$I = \int_a^b g(z) \exp\left(\frac{i}{\hbar}\psi(z)\right) dz \tag{15}$$

where $g(z)$ and $\psi(z)$ are real functions of a real variable z. The idea is that in the limit where $\hbar$ is small the exponential in eq.(15) is a rapidly oscillating function of z except near points z_α where $\psi(z)$ is stationary

$$\left(\frac{d\psi}{dz}\right)_{z_\alpha} = \psi'(z_\alpha) = 0. \tag{16}$$

Then one can assume that the main contribution to the integral comes from near these stationary points because the contributions of nearby points will be in phase and will add constructively. In other regions the contributions will cancel because of the rapidly varying phase. If the stationary points are isolated from one another the contributions I_α of each z_α can be obtained by approximating the integrand by a gaussian function and replacing the limits (a, b) by $(-\infty, \infty)$. The integral can be evaluated to give

$$I_\alpha \simeq g(z_\alpha) \left|\frac{2\pi\hbar}{\psi''(z_\alpha)}\right|^{1/2} \exp\left(\frac{i}{\hbar}\psi(z_\alpha) + i\mu_\alpha\frac{\pi}{4}\right) \tag{17}$$

The index μ_α depends on the sign of $\psi''(z_\alpha)$

$$\mu_\alpha = \pm 1 \qquad \text{if} \qquad \psi''(z_\alpha) \gtrless 0. \tag{18}$$

The semi-classical limit of the Feynman propagator K is obtained by evaluating the path integral by the method of stationary phase. The basic assumption is that the most important contributions to the path integral come from the neighbourhoods of classical paths $x_c(t)$ for which the action integral is stationary

$$\delta S[x_c(t)] = 0. \tag{19}$$

These paths satisfy the classical equations and the boundary conditions (12). If there is just one classical path satisfying the boundary conditions, the application of the stationary phase method gives an expression analogous to eq.(16)

$$K(x_1, x_0; T) \simeq \left|\frac{1}{2\pi\hbar}\frac{\partial^2 S}{\partial x_0 \partial x_1}\right|^{1/2} \exp\left(\frac{i}{\hbar}S(x_1, x_2; T) - i\frac{\nu\pi}{2}\right). \tag{20}$$

The index ν is an integer depending on the number of turning points on the path $x_c(t)$.

The semi-classical propagator (20) is exact for some simple potentials; for free particle motion and for linear and quadratic potentials. For a harmonic oscillator potential $V(x) = \frac{1}{2}m\omega^2 x^2$

$$S(x_1, x_2; T) = \frac{m\omega}{2\sin\omega T}\left[(x_1^2 + x_2^2)\cos\omega T - 2x_1x_2\right], \tag{21}$$

$$\frac{\partial^2 S}{\partial x_0 \partial x_1} = \frac{m\omega}{\sin\omega T} \tag{22}$$

while for a parabolic barrier $V(x) = -\frac{1}{2}m\omega^2 x^2$

$$S(x_1, x_2; T) = \frac{m\omega}{2\sinh\omega T}\left[(x_1^2 + x_2^2)\cosh\omega T - 2x_1x_2\right], \tag{23}$$

$$\frac{\partial^2 S}{\partial x_0 \partial x_1} = \frac{m\omega}{\sinh\omega T} \quad . \tag{24}$$

3.3 Historical notes on the stationary phase method

Stokes (1856) [20] was the first to use the stationary phase argument to find an approximate expression for the Airy integral. Kelvin formulated the general procedure in 1887 and used it to study "Waves produced by a single impulse in water of any depth" [11]. He writes a general wave as a superposition of harmonic waves, which corresponds to an impulse at $x = 0$ when $t = 0$. In his notation the expression is

$$u = \int_0^\infty dm \cos m[x - tf(m)]. \tag{25}$$

Here m is the wave number and $f(m)$ is the phase velocity. He then makes the stationary phase argument as follows:

When $x - tf(m)$ is very large, the parts of the integral which lie on the two sides of a small range, $\mu - \alpha$ to $\mu + \alpha$, vanish by annulling interference; μ being a value, or the value, of m which makes

$$\frac{d}{dm}\{m[x - tf(m)]\} = 0. \tag{26}$$

Kelvin finds the stationary point, expands about it to second order and evaluates the resulting Fresnel integral. He then discusses several examples. The dispersion relation for deep sea waves is $f(m) = \sqrt{g/m}$. The stationary point μ is given by

$$x = \frac{1}{2}t\sqrt{\frac{g}{\mu}} \qquad \text{or} \qquad \mu = \frac{gt^2}{4x^2}. \tag{27}$$

Expanding the argument of the cosine in eq.(25) about the stationary point and evaluating the resulting Fresnel integral gives

$$u(x) \simeq \frac{t}{gx^{3/2}}\cos\left(\frac{gt^2}{4x} - \frac{\pi}{4}\right).$$

It is a good approximation if t is not too small.

4 The energy representation

The propagator or Green's function in the energy representation is defined by

$$G(x_1, x_0; E) = \frac{1}{i\hbar} \int_0^\infty K(x_1, x_0; T) \exp\left(\frac{iET}{\hbar}\right) dT. \tag{28}$$

Using the definition (9) this is equivalent to .

$$G(x_1, x_0; E) = \left\langle x_1 \left| \frac{1}{E + i\epsilon - H} \right| x_0 \right\rangle = \sum_n \frac{\phi_n(x_1)\phi_n^*(x_0)}{E + i\epsilon - E_n}. \tag{29}$$

The wave-functions $\phi_n(x)$ represent a complete set of eigenstates of the Hamiltonian H with energy E_n and the small imaginary factor $i\epsilon$ ensures that $G(x_1, x_0; E)$ is the propagator from x_0 to x_1. Substituting the semi-classical expression (20) for the time dependent propagator into the integral (28) and evaluating it by the method of stationary phase gives a semi-classical expression for the propagator in the energy representation

$$G(x_1, x_0; E) = \sum_\alpha \frac{1}{i\hbar} \frac{1}{|\dot{x}_0 \dot{x}_1|^{1/2}} \exp\left(\frac{i}{\hbar} \int_{x_0}^{x_1} p_\alpha(x) dx - i\chi_\alpha\right). \tag{30}$$

Here $\dot{x}_0$ and $\dot{x}_1$ are the particle velocities at x_0 and x_1 respectively. The sum is taken over all classical paths α with energy E which start at x_0 and end at x_1; and $p_\alpha(x)$ is the local momentum at x on the path α. The phase χ_α is determined by the sign of the second derivative of S_α with respect to T. Penetration through a potential barrier is an example of a one-dimensional problem where one classical path gives the dominant contribution to the Green's function. We will discuss this application later in the present section. The semi-classical classical propagator $G(x_1, x_0; E)$ for a bound state problem has contributions from many paths and will be analyzed in section 4 of these lecture notes.

Consider the propagator $G(x_1, x_0; E)$ from a point x_0 to a point x_1 on opposite sides of a barrier representated by a potential $V(x)$ with a maximum between x_0 and x_1. If the energy E is above the top of the barrier there is a unique stationary point in the integral (28) associated with the real classical path from the initial to the final point at the given energy. The semi-classical propagator, given by eq.(30), has a magnitude depending on the velocities at the initial and final points and a phase depending on the integral of the local momentum. When the energy E is below the top of the barrier there is no real classical path linking the initial and final points and no stationary point in the integral (28). There is, however, a dominant saddle point at $T = T_a + T_b - i\tau$ in the complex T-plane and the saddle point evaluation of the integral (28) leads to a semi-classical propagator which is still given by eq.(30) but now the argument of the exponent is a sum of three parts

$$\frac{i}{\hbar} \int_{x_0}^{x_1} p(x) dx = \frac{i}{\hbar} \int_{x_0}^{a} p(x) dx - K(a, b; E) + \frac{i}{\hbar} \int_b^{x_1} p(x) dx. \tag{31}$$

There are real contributions to the phase from the initial point x_0 to the classical turning point a to the left of the barrier and from the right-hand turning point b to the final point x_1 and a sub-barrier contribution

$$K(a,b,E) = -\frac{i}{\hbar}\int_a^b p(x)dx = \frac{1}{\hbar}\int_a^b \sqrt{2m(V(x)-E)}dx > 0. \tag{32}$$

Because $E < V(x)$ under the barrier the velocity and momentum are both imaginary

$$p(x) = mv(x) = i\sqrt{2m(V(x)-E)}. \tag{33}$$

The time for the motion in the classically forbidden region from a to b is imaginary and is given by

$$i\tau = \int_a^b \frac{dx}{v(x)} = i\int_a^b dx\sqrt{\frac{m}{2(V(x)-E)}}. \tag{34}$$

As a consequence of eq.(31) the square of the magnitude of the propagator at a sub-barrier energy E is decreased by a factor

$$P(a,b,E) = \exp(-2K(a,b,E)) \tag{35}$$

in going from a to b. This is just the semi-classical barrier penetration factor which can also be derived using the WKB method.

4.1 The parabolic potential barrier

The parabolic barrier

$$V(x) = V_0 - \frac{1}{2}m\omega^2 x^2 \tag{36}$$

has a height V_0 and characteristic frequency constant ω. When the incident energy is below the barrier top integrals for $\tau(a,b,E)$ and $K(a,b;E)$ can be calculated analytically with the results

$$\tau(a,b,E) = \frac{1}{\omega} \qquad \text{and} \qquad K(a,b;E) = \pi\frac{V_0 - E}{\hbar\omega} \tag{37}$$

both are independent of V_0 provided $E < V_0$. The barrier penetration constant is given by (34)

$$P(a,b,E) = \exp\left(-2\pi(V_0 - E)/\hbar\omega\right) \tag{38}$$

provided the incident energy is sufficiently far below the barrier top, $2\pi(V_0 - E) \gtrsim \hbar\omega$. There is a generalization which is valid over the whole energy range

$$P(a,b,E) = \frac{1}{1+\exp\left(2\pi(V_0 - E)/\hbar\omega\right)} \quad . \tag{39}$$

Sufficiently far below the top of the barrier ($V_0 - E \gg \hbar\omega$) this goes over to the simpler relation in eq.(38). If the incident energy is far enough above the barrier top ($E - V_0 \gg \hbar\omega$) then the penetrability goes to unity.

The Schrödinger equation with the potential (36) has exact solutions which can be expressed in terms of parabolic cylinder functions [1] and the penetration factor (39) can be derived from the asymptotic forms of the solutions. It can also be obtained either by the propagator method or by analytic continuation of WKB wave functions. The analytic continuation argument is given in Landau and Lifschitz [13] section 50. The derivation form the propagator $G(x_1, x_0; E)$ starts with eq.(28) and uses the exact form of $K(x_1, x_0; T)$ for the parabolic barrier from eqs.(20) and (23). When the points x_0 and x_1 are far from the barrier on opposite sides the integral (28) can be evaluated by a change of variables [18], [5] to give

$$G(x_1, x_0; E) \propto I_0(\beta) = \int_{-\infty}^{\infty} \exp\left[ie^{-y} - (\frac{1}{2} + i\beta)y\right] dy$$

$$= \exp\left[\frac{i\pi}{4} + \frac{\pi\beta}{2}\right] \Gamma\left(\frac{1}{2} + i\beta\right) \tag{40}$$

where $\beta = (V_0 - E)/\hbar\omega$ and $\Gamma(1/2 + i\beta)$ is a gamma function. The penetration factor is

$$P(a, b, E) = |I_0(\beta)|^2 = \frac{1}{2\pi} \exp(\pi\beta) \left|\Gamma\left(\frac{1}{2} + i\beta\right)\right|^2 = \frac{1}{1 + \exp(2\pi\beta)} \quad . \tag{41}$$

The modulus of the gamma function is given in Abramowitz and Stegun [1, 6.1.30].

4.2 Fusion excitation functions

The results of the previous section have been used by C.Y. Wong to obtain a very simple formula for heavy ion fusion cross sections for energies near and below the Coulomb barrier. The true heavy ion Coulomb plus centrifugal barrier is approximated by a parabolic barrier with height depending on the angular momentum in each partial wave l

$$E_l = B_0 + \frac{\hbar^2}{2\mu R^2} l(l+1) \tag{42}$$

Here B_0 is the height of the Coulomb barrier and R is the radial position. The second term in eq.(42) is the modification due to the centrifugal energy. The fusion cross section is proportional to a sum over partial waves of barrier penetration factors for each l with a degeneracy factor $(2l + 1)$

$$\sigma(E) = \frac{\pi}{k^2} \sum_l \frac{2l+1}{1 + \exp\left(2\pi\left(E_l - E\right)/\hbar\omega\right)} \tag{43}$$

The sum can be approximated by an integral and evaluated to give a total fusion cross section at each center of mass energy E

$$\sigma_W(E, B_0) = \frac{R_0^2 \hbar\omega}{2E} \ln\left(1 + \exp\left(\frac{2\pi}{\hbar\omega}(E - B_0)\right)\right) \tag{44}$$

The Wong fusion cross section formula (44) depends on E and the Coulomb barrier height B_0. This cross section decreases exponentially for energies well below the barrier and has the classical form

$$\sigma(E) = \pi R_0^2 \left(1 - \frac{B_0}{E}\right) \tag{45}$$

well above the barrier top.

When compared with experiment the cross section in eq.(44) decreases much too rapidly for energies below the barrier. Many authors have argued that there are important physical effects which are not taken into account by the simple barrier penetration model. In particular there is a coupling between the radial degree of freedom and various internal collective degrees of freedom of the target and projectile which should be taken into account. If the collective degrees of freedom have a period T_{coll} which is sufficiently small ($T_{coll}\omega \lessapprox 1$) one can make a sudden approximation and assume that the collective degree of freedom does not change during the fusion process. Each value of the collective degree of freedom has a particular value of the barrier height which leads to a probability distribution of barrier heights $D(B)$ and a total fusion cross section

$$\sigma(E) = \int \sigma_W(E, B) D(B) dB \tag{46}$$

Lindsay, Nagarajan and Rowley [15], [14] developed an eigen-channel theory for the barrier height distribution. Each eigen-channel has a probability w_α and a barrier height B_α so that

$$D(B) = \sum_\alpha w_\alpha \delta(B - B_\alpha) \tag{47}$$

This theory has led to a very fruitful way of analyzing experimental fusion data [17] which involves the second derivative of $E\sigma$. For a classical barrier with a height B

$$\frac{1}{\pi R^2} \frac{d^2 E\sigma}{dE^2} = \delta\left(E - B\right) \tag{48}$$

If there is a distribution of classical barriers with a distribution function $D(E)$

$$\frac{1}{\pi R^2} \frac{d^2 E\sigma}{dE^2} = D(E) \tag{49}$$

For a single Wong barrier

$$\frac{1}{\pi R^2} \frac{d^2 E\sigma_W}{dE^2} = G(x) = \frac{2\pi}{\hbar\omega} \frac{e^x}{(1 + e^x)^2} \tag{50}$$

where

$$x = \frac{2\pi}{\hbar\omega}(E - B) \tag{51}$$

In the case where there is a distribution of eigenchannels

$$\frac{1}{\pi R^2}\frac{d^2E\sigma}{dE^2} = \bar{D}(E) = \int D(B)G(x)dB = \sum_\alpha w_\alpha G(x_\alpha) \tag{52}$$

It turns out that $\bar{D}(E)$ can be extracted from the experimental data by a numerical evaluation of the second derivative on the left hand side of eq.(52). The values of w_α and B_α extracted by fitting the data are sensitive to details of the collective motion. For example, measurements of the energy dependence of the fusion cross- section can yield detailed information on the nuclear shape [16].

5 Bremsstrahlung in alpha-decay

In α-decay the α-particle appears on the surface of the emitting nucleus, it penetrates the Coulomb barrier and is accelerated by the Coulomb field outside the barrier. Bremsstrahlung (photon) emission can take place during the acceleration phase outside the barrier. This contribution should be described well by classical electromagnetic theory. The photon emission amplitude can also have a contribution from the sub-barrier region and might also be influenced by the α-formation process. Both of these are essentially quantal processes. The experiment of Kasagi et al.[10] on bremsstrahlung emission in the α-decay of ^{210}Po was motivated by a desire to understand the relative importance of the three contributions. Their results were in disagreement with the predictions of classical theory and were also not in agreement with a simple semi-classical theory. This was surprising because the Sommerfeld parameter $\eta = Z_{eff}e^2/\hbar v \simeq 22 \gg 1$ and, under these conditions, a semi-classical theory would be expected to give reasonably accurate predictions. Bertsch and Papenbrock [3] made a quantum mechanical calculation using the Fermi golden rule for the photon emission with modified Coulomb wave functions for the initial and final state of the α-particle. Their theory was in agreement with the data within the experimental errors. Subsequently Dyakonov [7] obtained satisfactory results with a semi-classical theory. In this section we discuss the relation between these different theoretical approaches and try to understand why the classical and simple semi-classical approaches fail. It turns out that the sub-barrier contributions to the photon emission amplitude are important for a consistent theoretical description, but that it is unlikely that there is a strong dependence on the α-formation process.

According to classical electromagnetic theory the energy spectrum of the photons emitted during the acceleration outside the Coulomb barrier is

$$\frac{dP}{dE_\gamma} = \frac{2\alpha Z_{eff}^2}{3\pi E_\gamma c^2}\left|I(\omega)\right|^2 \tag{53}$$

where $I(\omega)$ is the Fourier transform of the alpha particle acceleration $a(t)$,

$$I(\omega) = \int_0^\infty a(t)e^{i\omega t}dt \tag{54}$$

Here $E_\gamma = \hbar\omega$ is the photon energy. The alpha velocity is zero at time $t = 0$ when it emerges from the barrier. For high frequency photons the Fourier transform $I(\omega)$ has an asymptotic expansion in inverse powers of ω which can be obtained from eq.(53) by repeated integration by parts. The leading term is

$$I(\omega) \sim \frac{1}{\omega} ia(0) \tag{55}$$

The relation (55) predicts a high γ-energy spectrum $dP/dE_\gamma \sim E_\gamma^{-3}$. The experiment shows a much faster decrease with energy. There is a classical low frequency theorem which is in agreement with the experimental bremsstrahlung results

$$I(\omega) \to v_\infty \qquad \text{as} \qquad \omega \to 0, \tag{56}$$

where v_∞ is the asymptotic alpha velocity at a large distance from the parent nucleus.

The quantum calculation of Bertsch and Papenbrock was based on a specific model for the alpha decay. The alpha particle was assumed to move in a potential which is a constant inside the parent nucleus and is a Coulomb potential outside,

$$V(r) = -V_0, \quad r < r_0 \quad \text{and} \quad V(r) = Zze^2/r, \quad r > r_0. \tag{57}$$

The depth V_0 and radius r_0 were adjusted to give the experimental binding energy of the alpha particle in ^{210}Po. Bertsch and Papenbrock calculated the photon emission using Fermi's golden rule for the transition rate

$$w_{i->f} = \frac{2\pi}{\hbar} \left| \left\langle f \left| \frac{e}{mc} \mathbf{A}_0 \cdot \mathbf{p} \right| i \right\rangle \right|^2 \rho_f \tag{58}$$

and made the dipole approximation, $\mathbf{A}_0 =$ constant. The identity

$$\left[\left(\frac{\mathbf{p}^2}{2m} + V(r) \right), \mathbf{A}_0 \cdot \mathbf{p} \right] = -i\hbar \mathbf{A}_0 \cdot \nabla V(r) \tag{59}$$

allows the matrix element of the alpha momentum $\mathbf{p}$ in eq.(58) to be replaced by a matrix element of the gradient of the potential $\nabla V(r)$;

$$\hbar\omega \left\langle f \left| \frac{e}{mc} \mathbf{A}_0 \cdot \mathbf{p} \right| i \right\rangle = -i\hbar \left\langle f \left| \mathbf{A}_0 \cdot \nabla V(r) \right| i \right\rangle . \tag{60}$$

This lead to the following expression for the photon emission spectrum

$$\frac{dP}{dE_\gamma} = \frac{4Z_{eff}^2 e^2}{3m^2c^2} \frac{1}{E_\gamma} \left| \left\langle \Phi_f \left| \frac{dV}{dr} \right| \Phi_i \right\rangle \right|^2 \tag{61}$$

Here $\Phi_i(r)$ is the radial wave function of the initial state with $l = 0$ and $\Phi_f(r)$ is the wave function of the final state with $l = 1$. The initial state $\Phi_i(r)$ was chosen to be a Gamow state with an outgoing boundary condition. In the case of the decay of ^{210}Po the life time is so long that the wave number k_i can be

taken to be real. The final state $\Phi_f(r)$ is a scattering state in the potential $V(r)$ with wave-number k_f.

Both the initial and final states are combinations of regular and irregular Coulomb wave functions for $r > r_0$. Bertsch and Papenbrock calculated the radial matrix element $\langle \Phi_f \, | dV/dr | \, \Phi_i \rangle$ by a combination of analytical and numerical methods and obtained a photon emission spectrum which was in agreement with the data of Kasagi et al. to within the experimental error bars. The dominant contribution came from the imaginary part of the radial matrix element. This part could be calculated analytically and was insensitive to the sub-barrier part of the wavefunction. The real part of the radial matrix element was calculated numerically and was found to be much smaller. It contributed only a few percent to the final result. With the potential (57) the derivative dV/dr has a delta-function at $r = r_0$. There is a strong cancellation between the contribution of this delta-function to the real part of the radial matrix element of dV/dr and the contribution coming from $r > r_0$. It is this cancellation which makes $\mathrm{Re} \, \langle \Phi_f \, | dV/dr | \, \Phi_i \rangle << \mathrm{Im} \, \langle \Phi_f \, | dV/dr | \, \Phi_i \rangle$.

Bertsch and Papenbrock calculated the low frequency limit of the radial matrix element and found

$$|\langle \Phi_f \, | dV/dr | \, \Phi_i \rangle| = \sqrt{mE_\alpha/\pi\hbar} = \frac{v_\infty}{\sqrt{2\pi\hbar}} \qquad \text{as} \qquad \omega \to 0. \tag{62}$$

in agreement with the classical low frequency limit in eq.(56). This low-frequency behaviour (62)of the photon emission matrix element is very general. It can also be derived from the matrix element on the left hand side of eq.(60). Then it depends only on the long-range behaviour of the initial and final wave functions and is quite independent of the exact form of the α-nucleus potential.

Takigawa et. al. [21] repeated the calculation of Bertsch and Papenbrock and studied the role of the tunnelling region in more detail. They performed a quantum mechanical analysis in a way which has a close relation to semi-classical theory. They also studied the effect of different choices of the potential parameters V_0 and r_0 which gave a different number of nodes in the internal wave function but always the same resonance energy. The final results were not very sensitive to the number of nodes. They stressed that a proper treatment of the delta-function in dV/dr at r_0 is essential.

There is a simple semi-classical extension of (53) which is inspired by the argument in sect. 4 that the alpha-particle propagates in imaginary time underneath the Coulomb barrier . This suggests replacing the Fourier transform in eq.(53) by

$$I_1(\omega) = \int_{i\tau}^{\infty} a(t) e^{i\omega t} dt \tag{63}$$

where $i\tau$ ($\tau > 0$) is a suitable imaginary time related to a real starting radius r_τ under the barrier by a formula similar to eq.(). The integral in (63) is taken along a contour C in the complex t-plane running from $t{=}i\tau$ to $t = 0$ along the imaginary t-axis and from $t = 0$ to $t = \infty$ along the real axis. The large-ω behaviour is improved by this substitution but the low frequency relation (56)

is changed to

$$I_1(\omega) \to v_\infty + iv_0 \qquad \text{as} \qquad \omega \to 0, \tag{64}$$

where iv_0 is the imaginary velocity at r_0. The resulting γ-spectrum is very dependent on the choice of r_τ. Now we discuss a resolution of this difficulty which is related to the work of Dyakonov.

The analysis of Bertsch and Papenbrock and of Takigawa et al have shown that it is important to treat the photon emission under the barrier in a consistent way. The potential (57) has a discontinuity at r_0 which has been shown to be very important [21] but is not easy to treat by semiclassical methods. In order to avoid this difficulty we replace the potential (57) which has a discontinuity at r_0 by a smooth potential where depth inside the barrier is adjusted to give a bound state at the experimental energy. With this new potential there is an internal turning point at r_0 and an external turning point at r_e. We suppose that it is smooth enough for the semi-classical connection formula to be used at both of these turning points. We use eq.(63) with $\tau = \tau_0$ corresponding to the internal turning point. The alpha particle velocity is zero at both the internal and external turning points so that $v_0 = 0$ in eq.(64) and we recover the correct low energy behaviour. Integrating eq.(63) by parts we get

$$I_1(\omega) = \int_{i\tau_0}^{\infty} a(t)e^{i\omega t}dt = (v(0) - v(\tau_0)e^{i\omega\tau_0} - i\omega \int_{i\tau_0}^{\infty} v(t)e^{i\omega t}dt \tag{65}$$

The boundary term is zero because the alpha-velocity is zero at both the internal and external turning points and eq.(65) reduces to

$$I_1(\omega) = -i\omega v(\omega) = -i\omega \int_{i\tau_0}^{\infty} v(t)e^{i\omega t}dt \tag{66}$$

Eq.(66) is the semi-classical analogue of the quantum mechanical relation between the matrix elements in eq.(60). The conclusion of this discussion is that the Fourier transform of the acceleration, $I(\omega)$, in the formula for the photon spectrum (53) should be replaced by $I_1(\omega)$ from eq.(66).

Now we can make a connection with the semi-classical calculation of Dyakonov [7]. He replaced $I_1(\omega)$ by $-i\omega v(\omega)$ in the expression eq.(53) for the energy spectrum of the bremsstrahlung, then he used a pure Coulomb potential to calculate the Fourier transform $v(\omega)$. He argued that, because of the exponential damping of the integral in eq.(66) under the barrier, the contribution from small values of r is not very important and assumed that the alpha particle starts at $r_0 = 0$. The dominant contribution to the bremsstrahlung spectrum comes from the real part of $I_1(\omega)$. The imaginary part of $I_1(\omega)$ has a contributions from outside the barrier and from under the barrier. These have opposite signs and there is a significant cancellation so that the imaginary part accounts for less than 20% of the total photon emission probability for the highest photon energies studied in the experiment of Kasagi et al, and a smaller percentage for lower photon energies. If the sub-barrier contribution is emitted one gets the

classical spectrum which is larger than the quantum result at the highest energies by a factor of 50. This is in agreement with the conclusions of Bertsch and Papenbrock and Takigawa et al.

We conclude this discussion by making a connection with the semi-classical analysis in ref.[21]. The aim is to show how eq.(66) follows from making a semi-classical approximation to the wave functions in the matrix element in eq.(61). Before starting we note that the classical bremsstrahlung formula (53, 54) and the semi-classical formulae (65, 66) assume that the motion of the alpha particle in the final state is in the radial direction so that its orbital angular momentum l is zero. In the quantum calculation the initial state is an s-state and the final state is a p-state with $l = 1$. This angular momentum is small compared with the Sommerfeld parameter $\eta \approx 22$ and its contribution is not very important. It is included in the semi-classical analysis in ref.[21] but it will be neglected here in order to simplify the discussion. With this simplification the radial wave functions of the initial and final states are

$$\Phi_i^{sc}(r) \sim \frac{1}{\sqrt{k_i(r)}} \exp\left(i \int_{ri}^{r} k_i(r)dr\right), \tag{67}$$

$$\Phi_f^{sc}(r) \sim \frac{1}{\sqrt{k_f(r)}} \sin\left(\int_{r_{ef}}^{r} k_f(r)dr + \frac{\pi}{4}\right), \tag{68}$$

Here $k_i(r)$ and $k_f(r)$ are the local wave numbers of the initial and final states corresponding to energies E_i and $E_f = E_i - \Delta E$, where $\Delta E = \hbar\omega$ is the energy of the omited radiation. The product of the semi-classical wave functions in the matrix element of dV/dr is the sum of two terms. One with a rapidly oscillating phase will be neglected. The other term with a slowly varying phase gives a contribution to the matrix element from the external region

$$\left\langle \Phi_f \left| \frac{dV}{dr} \right| \Phi_i \right\rangle_{ext} \sim \int_{r_e}^{\infty} \frac{dV}{dr} \frac{dr}{\hbar\sqrt{k_f(r)k_i(r)}} \exp\left(i \int_{r_{ei}}^{r} k_i(r)dr - i \int_{r_{ef}}^{r} k_f(r)dr\right) \tag{69}$$

$$\approx \int_{r_e}^{\infty} \frac{dV}{dr} \frac{dr}{\hbar k(r)} \exp\left(i \int_{r_e}^{r} \frac{\Delta E}{\hbar v(r)} dr\right) \approx \int_0^{\infty} a(t) e^{i\omega t} dt \tag{70}$$

This is just the amplitude (54) for bremsstrahlung emission in the classical region outside the barrier. In making the step from eq.(69) to eq.(70) we have assumed that $\Delta E = \hbar\omega$ is small enough to be able to neglect the difference between the external turning points in the initial and final states. In the pre-exponential term $k_f \approx k_i \approx k$, while in the exponent $k_i(r) - k_f(r) \approx \Delta E/\hbar v(r)$ where $v(r)$ is the particle velocity outside the barrier.

The semi-classical sub-barrier contribution can be evaluated in a similar way. The initial and final wave functions under the barrier are

$$\Phi_i^{sc}(r) \sim \frac{1}{\sqrt{\gamma_i(r)}} \exp\left(\int_{r}^{r_{ei}} \gamma_i(r)dr\right), \tag{71}$$

$$\Phi_f^{sc}(r) \sim \frac{1}{\sqrt{\gamma_f(r)}} \exp\left(-\int_r^{r_{ef}} \gamma_f(r)dr\right), \tag{72}$$

and the sub-barrier contribution to the transition matrix element is

$$\left\langle \Phi_f \left| \frac{dV}{dr} \right| \Phi_i \right\rangle_{sub} \approx \int_{r_0}^{r_e} \frac{dV}{dr} \frac{dr}{\hbar\gamma(r)} \exp\left(-\int_r^{r_e} \frac{\Delta E}{\hbar v(r)} dr\right) \approx \int_{i\tau_0}^{0} a(t) e^{i\omega t} dt \tag{73}$$

Combining eqs.(70) and (73) leads to the amplitude I_1 in eq.(65, 66). There are several points which have not been addressed in the above discussion. One is to check that the amplitudes in front of the semi-classical wave functions combine correctly. Another is to study the effect of the non-zero angular momentum in the final state. A third is to study the contribution of the internal region $0 < r < r_0$. A fourth is to try to extend the semi-classical argument to include the case of a discontinuous potential like the one used by Bertsch and Papenbrock.

We conclude this discussion with a remark about the external turning point in eq.(69) and also in the derivation of eq.(73). In fact there are two different turning points r_{ei} and r_{ef} for the initial and final states [21]. They are approximated by an average value r_e in going from eq.(69) to (70). There is a similar approximation in the derivation of eq.(73). Also the WKB wave functions are not accurate approximations to the true wave functions near the turning point. However this difficulty can be avoided by using the analytical continuation argument at the end of section 2.

6 The Gutzwiller trace formula

The simple WKB approximation is only useful for one dimensional problems, or separable problems which can be reduced to the one dimensional case. The path integral method and semi-classical methods based on it can be extended to apply to non-separable problems. Some of these extensions are based on the Gutzwiller trace formula which is the topic of this section. The section begins with an introduction to the WKB quantization condition in one dimension. This is followed by a derivation of the same quantization rule starting from the semi-classical propagator and Gutzwiller's trace formula. Then we discuss extensions to multi-dimensional problems. Our treatment is very schematic. Systematic discussions are given in Gutzwiller's book [9] and in the book of Brack and Bhaduri [2].

The energies of bound states in a one-dimensional potential $V(x)$ can be easily estimated using the WKB method. The trajectory of a particle with energy E has classical turning points at $x = a$ and $x = b$ with $a < b$. The WKB wave function satisfying the matching condition at the left-hand turning point at $x = a$ is

$$\psi(x) \simeq \frac{C}{\sqrt{p(x)}} \sin\left(\int_a^x \frac{p(x)}{\hbar} dx + \frac{\pi}{4}\right) \tag{74}$$

where $p(x)$ is the local momentum. The wave function with the WKB matching condition at the right-hand turning point is

$$\psi(x) \simeq \frac{C'}{\sqrt{p(x)}} \sin\left(\int_x^b \frac{p(x)}{\hbar} dx + \frac{\pi}{4}\right) \tag{75}$$

For a bound state these two wave functions must be consistent and one obtains the WKB quantization condition

$$\int_a^b p(x)dx = (n + \frac{1}{2})\pi\hbar \tag{76}$$

There is a simple extension of the WKB method to several dimensions in the case of separable systems. For example for a particle moving three dimensions in a spherically symmetrical potential, the Schrödinger equation is separable in spherical coordinates. The wave functions in the (θ, ϕ) variables have a simple analytical form and the radial wave function can be approximated by the WKB method. Other examples of separable systems are the deformed harmonic oscillator which can be separated in rectangular coordinates, a spheroidal potential, separable in spheroidal coordinates and the Coulomb potential, separable in parabolic coordinates. There is no simple method for finding the approximate energy states for a non-separable potential. One has to resort to numerical solutions of the Schrödinger equation.

A characteristic of the nuclear systems is the existence of shell structure. In the shell model single particle levels are grouped together. This property is most pronounced in the harmonic oscillator shell model. There are high degeneracies and a unique spacing $\hbar\omega$. Levels are clustered together with a characteristic pattern for other potentials like the Woods-Saxon and when a suitable spin-orbit interaction is added one obtains the shell structure which gives rise to the magic numbers. One approach to the study of shell structure is to find the individual energy levels and to look for groupings. Another is to study fluctuations in the single particle density of states. With this approach it is possible to go beyond separable systems by using the Gutzwiller trace formula or related methods. The idea is to divide the single particle level density $g(E)$ into a smooth part and a fluctuating part.

$$g(E) = g_{smooth}(E) + \delta g_{fluct}(E) \tag{77}$$

The smooth part might be approximated by the Thomas-Fermi or extended TF level density. The problem is to understand the fluctuating part.

The actual level density $g(E)$ of a bound system with a discrete spectrum is a sum over δ-function spikes, one for each eigenstate with energy E_n

$$g(E) = \sum_n \delta(E - E_n) \tag{78}$$

A smoothed level density $\bar{g}(E)$ can be obtained from this by averaging with some suitable normalized weight function $\Delta(E)$ with $\int \Delta(E)dE = 1$

$$\bar{g}(E) = \sum_n \Delta(E - E_n) \tag{79}$$

The generalization of the Green's function (28) to three dimensions is

$$\tilde{G}(\mathbf{r},\mathbf{r}_0;E+i\varepsilon)=\sum_n \frac{\phi_n(\mathbf{r})\phi_n^*(\mathbf{r}_0)}{E+i\varepsilon-E_n} \tag{80}$$

where the $\phi_n(\mathbf{r})$ are a complete set of eigenstates of the Hamiltonian with energies E_n. To get the level density we can use the trace of the Green's function which can be calculated by putting $\mathbf{r}_0=\mathbf{r}$ and integrating over $\mathbf{r}$.

$$\mathrm{Tr}G=\int G(\mathbf{r},\mathbf{r};E+i\varepsilon)d^3\mathbf{r}=\sum \frac{1}{E+i\varepsilon-E_n} \tag{81}$$

The smoothed level density can be obtained from $\mathrm{Im}(\mathrm{Tr}G)$ by using the relation

$$g(E)=-\frac{1}{\pi}\mathrm{Im}\int G(\mathbf{r},\mathbf{r};E+i\epsilon)d^3\mathbf{r}=\frac{1}{\pi}\sum_n \frac{\varepsilon}{(E-E_n)^2+\varepsilon^2} \tag{82}$$

where the averaging function Δ is a Lorenzian with a width of 2ε. This is Gutzwiller's trace formula [9],[2]. Using a semi-classical expression for the Green's function yields an approximate level density.

One can obtain some insight by applying the method to a one-dimensional problem. The semiclassical Green's function (30) evaluated at $x_0=x_1=x$ is

$$G(x,x;E)=\frac{1}{i\hbar\dot{x}}\sum_n \exp\left(\frac{i}{\hbar}\int_x^x p_n(x)dx-i\chi_n\right) \tag{83}$$

where the sum is taken over all orbits n with energy E starting at x and ending at x. There are two classes of such orbits;

1. Periodic orbits: In all of these cases the integral over momentum is independent of x
$$\frac{1}{\hbar}\int_x^x p_n(x)dx=n\frac{1}{\hbar}\oint p(x)dx=nI_0 \tag{84}$$
The integral $\oint p(x)dx=\hbar I_0>0$ is the integral of the momentum around a simple closed path and n is the number of repetitions. The sign of the integral is always positive no matter whether the particle starts moving to the left or the right. The orbits with $n=1$ are singly periodic and those with $n>1$ are multiply periodic. All of these orbits are doubly degenerate. For the case with $n=0$ the path is of zero length. It can be shown that $\chi_n=n\pi$ for these all these orbits.
2. Orbits with an odd number of turning points. In all of these cases the integral over momentum depends on x. The phase is rapidly oscillating, the integral over x in $\mathrm{Tr}G$ is small in the semi-classical limit and the contribution of these orbits can be neglected.

Taking the degeneracy of the different orbits into account the trace of the Green's function is

$$\mathrm{Tr}G(E)=\frac{T}{i2\hbar}\left[1+2\sum_{n\geqq 1}\exp\left(ni(I_0-\pi)\right)\right]=\frac{iT}{2\hbar}\cot\left(\frac{I_0-\pi}{2}\right) \tag{85}$$

where T is the period of the closed orbits. The trace of the Green's function has poles corresponding to energy eigenvalues E_m when $I_0 - \pi = 2m\pi$ where m is an integer. In other words

$$\oint p(x)dx = (2m+1)\pi\hbar \tag{86}$$

This is just the semi-classical quantization condition (76). Finally a comment about the contribution of the paths of zero length to the density of states. From eq.(85) it is $g_0(E) = T/2\pi\hbar = (\hbar\omega)^{-1}$ which is just the Thomas-Fermi density of states for motion in one dimension.

The semi-classical propagator from $\mathbf{r}$ to $\mathbf{r}_0$ at an energy E in several dimensions is

$$G(\mathbf{r},\mathbf{r}_0,E) = \sum_{class\,orb} 2\pi\,(2\pi i\hbar)^{-(D+1)/2}\sqrt{|\mathcal{D}|}\exp\left[\frac{i}{\hbar}S(\mathbf{r},\mathbf{r}_0,E) - i\mu\pi/2\right] \tag{87}$$

Here D is the dimension of the space and $\mathcal{D}$ is the determinant

$$\mathcal{D}(\mathbf{r},\mathbf{r}_0;E) = \begin{vmatrix} \frac{\partial^2 S}{\partial\mathbf{r}\partial\mathbf{r}_0} & \frac{\partial^2 S}{\partial\mathbf{r}_0\partial E} \\ \frac{\partial^2 S}{\partial\mathbf{r}\partial E} & \frac{\partial^2 S}{\partial E^2} \end{vmatrix} \tag{88}$$

and $S(\mathbf{r},\mathbf{r}_0;E) = \int p(\mathbf{r})d\mathbf{r}$ is the action calculated along the classical path with end points $\mathbf{r}_0$ and $\mathbf{r}$. The integral over $\mathbf{r}$ in the expressions (81) and (82) are calculated by the stationary phase method . The stationary point $\mathbf{r}$ in the integral for TrG is given by the condition

$$\left[\frac{\partial S}{\partial\mathbf{r}}\right] = \left[\frac{\partial S(\mathbf{r}_1,\mathbf{r}_0;E)}{\partial\mathbf{r}_0} + \frac{\partial S(\mathbf{r}_1,\mathbf{r}_0;E)}{\partial\mathbf{r}_1}\right]_{\mathbf{r}_0=\mathbf{r}_1=\mathbf{r}} = \mathbf{p}_0 - \mathbf{p}_1 = 0 \tag{89}$$

At the stationary point both the coordinates and momenta at the initial and final points are equal. Thus only the *periodic closed orbits* from the sum over classical trajectories contribute to the level density. As in the case of one dimension there are simply periodic orbits, multiply periodic orbits and orbits of zero length. The orbits of zero length give the smooth Thomas- Fermi contribution $g_{TF}(E)$ to the density of states. The true periodic orbits give the fluctuating contribution $\delta g_{fluct}(E)$.

There is a wide class of problems for which the periodic orbits give the dominant contribution to the integral over $\mathbf{r}$ in the expressions for TrG and $g(E)$ in eqs.(81) and (82) but there are important differences depending on the degeneracies of the orbits. If the classical system corresponding to the quantum problem is chaotic then most classical trajectories are ergodic and not periodic. But there are usually some isolated periodic orbits, some stable and some unstable. In the semiclassical limit these orbits contribute to the fluctuating term $\delta g_{fluct}(E)$ in the density of states. For integrable systems where there are continuous symmetries, for example for a particle moving in a central potential, there are continuous classes of periodic orbits. The periodic orbits still contribute to

$\delta g_{fluct}(E)$ but the techniques for calculating their contribution is different from the case where there are isolated periodic orbits.

The upshot of it all is that the semi-classical level density $g_{scl}(E) = g_{TF} + \delta g_{fluct}(E)$ is the sum of two parts, a smooth part $g_{TF}(E)$ Thomas-Fermi part from the trajectories of zero length in the Gutzwiller method, and a fluctuating part $\delta g_{fluct}(E)$ which comes from the sum over periodic orbits. The method of calculating the fluctuating part is different for chaotic or integrable systems but its contribution can always be written in the condensed form [2, eq. (5.48)]

$$\delta g_{fluct}(E) = \sum_{po} \delta_{po}(E) \qquad \text{where} \qquad \delta_{po}(E) = \mathrm{Im}\mathcal{A}_{po}(E) \exp i(S_{po}(E) + \phi) \tag{90}$$

In this equation ϕ is a phase which is some combination of Maslov indices, $S_{po}(E)$ is the semi-classical action and $\mathcal{A}_{po}(E)$ is a coefficient which depends on the stability properties of the periodic orbit. The sum over periodic orbits should give a density of states which is a sum of delta functions eq.(78).In fact the sum converges slowly and sometimes diverges. It is useful to introduce an energy averaged state density. In eq.(82) the delta-functions are averaged with a Lorenzian distribution, but sometimes a Gaussian average is more useful. For a Gaussian of width γ

$$g_\gamma(E) = \frac{1}{\pi\sqrt{\gamma}} \sum_i \exp[-(E - E_i)^2/\gamma^2] \tag{91}$$

the semiclassical contribution of different orbits can be evaluated approximately to give [2, Sect. 5.5]

$$\delta g_{fluct}(E) = \sum_{po} e^{-(\gamma T_{po}/2\hbar)^2} \delta g_{po}(E) \tag{92}$$

Thus each orbit is damped exponentially and orbits with longer periods are damped more strongly than the short ones. Note that the period $T_{po} = nT_{ppo}$ where n is the number of repetitions and T_{ppo} is the period of a primitive periodic orbit. In many applications the first repetitions are sufficient to give a well converged course grained level density. There are analogous relations to the shell corrections for the particle number and total energy for a system of Fermions filled up to a Fermi level μ.

Strutinsky [19], [2, Sect. 4.6.2] has proposed a semi-empirical approach to the study of the fluctuating part of the single particle level density which is less fundamental then Gutzwiller's method but much simpler to use especially for the lower part of the energy spectrum. Let $V(r)$ and $V_0(r)$ be two potentials which are similar so that one might assume that the fluctuating parts of the level density are similar for the two potentials. If the Schrödinger equation can be solved exactly for $V_0(r)$ then $\delta g_{fluct}(E)$ can be calculated exactly for V_0 with any appropriate averaging method. This can be used as an estimate for the fluctuating part of the level density of V. We will come back to this in the next section and discuss the Strutinsky averaging approach applied to nuclear structure problems.

7 The Thomas-Fermi and Hartree-Fock approximations

The Fermi gas model of nuclear matter assumes that nucleons move in plane wave states and that, in the ground state, the single particle states are filled up to a Fermi energy $\varepsilon_f = \hbar^2 k_f^2/2m$ where k_f is the Fermi wave number. The nucleon density is related to the Fermi momentum and Fermi energy by

$$\rho_0 = 4\frac{1}{(2\pi)^3}\frac{4\pi}{3}k_f^3 = \frac{2}{3\pi^2}k_f^3 = \frac{2}{3\pi^2}\left(\frac{2m}{\hbar^2}\right)^{3/2}\varepsilon_f^{3/2} \tag{93}$$

for a system with an equal number of neutrons and protons. The factor 4 reflects the fact that for each eigenvalue $\mathbf{k}$ there are four spin-isospin states. Typical values are

$$\rho_0 = 0.17 \quad \text{fm}^{-3}, \qquad k_f = 1.36 \quad \text{fm}^{-1}, \qquad \varepsilon_f = 37 \quad \text{MeV} \tag{94}$$

The average energy density is $(\hbar^2/2m)\tau_0$ where

$$\tau_0 = \langle k^2 \rangle \rho_0 = \kappa(\rho_0)^{5/3}, \qquad \kappa = \frac{3}{5}\left(\frac{3\pi^2}{2}\right)^{2/3}. \tag{95}$$

The Thomas-Fermi model is a simple semi-classical extension of the Fermi gas model. The nucleons are assumed to move in a potential $V(\mathbf{r})$ which is a slowly varying function of position. At each point the nuclear material is like a piece of nuclear matter with a local density $\rho(r)$ and a local Fermi wave number k_f related by

$$\rho_{\rm TF}(r) = \frac{2}{3\pi^2}k_f(r)^3 \qquad \text{where} \quad k_f(r) = \left[\frac{2m}{\hbar^2}(\lambda - V(r))\right]^{1/2}. \tag{96}$$

The Fermi energy λ is determined by the condition

$$A = \int \rho_{\rm TF}(r) d^3r. \tag{97}$$

The kinetic energy density is $(\hbar^2/2m)\tau_{\rm TF}(r)$ where $\tau_{\rm TF}(r) = \kappa(\rho_{\rm TF}(r))^{5/3}$ as in eq.(95).

Skyrme-Hartree-Fock (SHF) theory writes the ground state energy of a nucleus as an integral of a Hamiltonian density $H(\mathbf{r})$ as

$$E_0 = \int H(\mathbf{r}) d^3\mathbf{r} \tag{98}$$

where the energy density is a function of a particle density $\rho(\mathbf{r})$ a kinetic energy density $(\hbar^2/2m)\tau(\mathbf{r})$ and a spin-orbit density $\mathbf{J}(\mathbf{r})$. A simplified form of the Hamiltonian density is

$$H(\mathbf{r}) = \frac{\hbar^2}{2m}\tau + \frac{3}{8}t_0\rho^2 + \frac{1}{16}t_3\rho^3 + t_a\tau\rho + t_b\left(\nabla\rho\right)^2 - \frac{3}{4}W_0\rho\left(\nabla\cdot\mathbf{J}\right). \tag{99}$$

The densities are expressed in terms of the single particle wave functions ϕ_i of occupied states as

$$\rho(\mathbf{r}) = \sum_i^A |\phi_i(\mathbf{r})|^2 , \qquad \tau(\mathbf{r}) = \sum_i^A |\nabla\phi_i(\mathbf{r})|^2 , \tag{100}$$

$$\mathbf{J}(\mathbf{r}) = \frac{1}{2i} \left[(\nabla - \nabla') \times \mathbf{s}(\mathbf{r}, \mathbf{r}')\right]_{\mathbf{r}=\mathbf{r}'} .$$

In this equation $\mathbf{s}(\mathbf{r}, \mathbf{r}')$ is a spin density. The term containing $\mathbf{J}(\mathbf{r})$ gives rise to the spin-orbit interaction in the Skyrme model, the $\rho\tau$ term leads to nucleon effective mass and the $(\nabla\rho)^2$ contributes to the nuclear surface energy. Minimizing E_0 with respect to the single particle wave functions leads to the Hartree-Fock self-consistent equations for the ground-state energy, particle density, and single particle energies. Shell effects have their origin in the kinetic energy density and the spin-orbit term. The Hartree-Fock method gives a good description of nuclear shell effects and a good account of the surface properties, provided one has a good parametrization of the density functional (99). Is it possible to achieve good results in a simpler way? There are two simplified approaches which go a long way to achieving this goal. One is the Thomas-Fermi approximation and the other is the Strutinsky averaging procedure. Both can be regarded as semi-classical approximations.

Omitting the spin-orbit term from the energy functional (99) and replacing $\tau(\mathbf{r})$ by the Thomas-Fermi approximation $\tau_{\mathrm{TF}}(\mathbf{r})$ gives an approximate expression for E_0 in (98). Minimizing with respect to the nucleon density $\rho(\mathbf{r})$ gives the Thomas-Fermi approximation for the ground state energy and the nucleon density distribution. The results obtained are reasonably accurate, but two effects are missing. One is the shell structure which is contained in $\tau(\mathbf{r})$ and the spin-orbit term. The other is that the proper treatment of $\tau(\mathbf{r})$ influences the surface properties and this contribution is neglected. The extended Thomas-Fermi (ETF) method gives an improved approximation to the kinetic energy density which improves the calculated surface properties of nuclei, but it does not introduce shell effects.

Strutinsky invented the shell correction method (cf. [2] section 4.6.2) as an approximate way of taking into account shell effects which are not included in the Thomas-Fermi or ETF approaches.. The idea is to write the total energy of a nucleus as a sum of two parts

$$E_{tot} = E_{smooth} + \delta E \tag{101}$$

The smooth part is calculated by the ETF method or alternatively by using a phenomenological liquid drop formula. The shell correction δE is obtained from the eigenvalue spectrum of the mean field in which the nucleons move. The smooth part of the energy depends on some parameters a_k specifying the size and shape of the nucleus. The mean field and hence the shell correction δE also depends on these parameters. The total energy is minimized with respect to the a_k and there is a balance between the smooth term and the shell correction

which eventually determines the nuclear shape and the single particle energies. The shell correction is calculated from

$$\delta E(A) = \sum_{E_n<\mu} E_n - \int_0^{\bar{\mu}} E\bar{g}(E)dE \tag{102}$$

where the averaged level density

$$\bar{g}(E) = \sum_n \Delta(E - E_n) \tag{103}$$

Here $\Delta(E-E_n)$ is some suitable averaging function like the Gaussian in eq.(91). The occupation numbers for the single particle states are $\nu_n = 1$ if $E_n < \mu$ and $\nu_n = 0$ if $E_n \geqslant \mu$. The energies μ and $\bar{\mu}$ are chosen so that the total particle number is

$$A = \sum_{E_n<\mu} \nu_n = \int_0^{\bar{\mu}} \bar{g}(E)dE.$$

The Strutinsky averaging method is underpinned by the Strutinsky energy theorem (for a derivation see Bhaduri and Brack, Appendix 3 [2]). The Strutinsky method can be looked on as an approximation to Hartree-Fock theory. It has a number of advantages. For example it can be used in models with varying degrees of sophistication depending on the forms chosen for the parametrization of E_{smooth} and for the mean field which determines the single particle energies. It has been used very extensively in the theoretical study of deformed rotating nuclei.

8 Time dependent theory

There is no dynamics in the Thomas-Fermi theory or in the density functional method. Dynamics can be introduced in a classical or semi-classical approach through the phase space density $f(\mathbf{r},\mathbf{p},t)$ which is the nucleon density in coordinate and momentum space at a time t. Here we always imagine a nuclear system with equal numbers of neutrons and protons where the two kinds of nucleons have the same phase space densities. This restriction can be removed easily. The phase space density is normalized so that

$$\int f(\mathbf{r},\mathbf{p},t)d^3\mathbf{r}d^3\mathbf{p} = A. \tag{104a}$$

The particle and kinetic energy densities are

$$\rho(\mathbf{r}) = \int f(\mathbf{r},\mathbf{p},t)d^3\mathbf{p}, \qquad \frac{\hbar^2}{2m}\tau(\mathbf{r}) = \frac{1}{2m}\int \mathbf{p}^2 f(\mathbf{r},\mathbf{p},t)d^3\mathbf{r}. \tag{105}$$

The Pauli principle can be incorporated into the theory by imposing the condition that the maximum phase space density is $4/(2\pi\hbar)^3$, that is 4 nucleons

(2 protons and 2 neutrons) in each quantum cell of phase space. For nucleons moving in a potential $V(r)$ the phase space distribution corresponding to the time independent Thomas-Fermi ground state is

$$f(\mathbf{r},\mathbf{p}) = \frac{4}{(2\pi\hbar)^3} \qquad \text{if} \qquad \frac{p^2}{2m} + V(r) < \varepsilon_f, \tag{106}$$

$$f(\mathbf{r},\mathbf{p}) = 0 \qquad \text{if} \qquad \frac{p^2}{2m} + V(r) \geqslant \varepsilon_f, \tag{107}$$

where ε_f is the Fermi energy. The Fermi momentum is

$$p_f(r) = \sqrt{2m(\varepsilon_f - V(r))}. \tag{108}$$

These relations lead to the Thomas-Fermi expression for $\tau(r)$. The relations (106,107) show that the phase space density depends only on the magnitude of the momentum and is therefore isotropic in momentum space.

There is a close connection between the semi-classical phase space density and the quantum single particle density matrix $\rho(\mathbf{r},\mathbf{r}')$. The Wigner distribution function is defined by the Fourier transform

$$f_W(\mathbf{r},\mathbf{p}) = \frac{1}{(2\pi\hbar)^3}\int d^3\mathbf{s}\ \rho(\mathbf{r}+\frac{\mathbf{1}}{\mathbf{2}}\mathbf{s},\mathbf{r}-\frac{\mathbf{1}}{\mathbf{2}}\mathbf{s})\exp\left(\frac{i\mathbf{p}.\mathbf{s}}{\hbar}\right). \tag{109}$$

The phase space density $f(\mathbf{r},\mathbf{p})$ can be regarded as the semi-classical limit of $f_W(\mathbf{r},\mathbf{p})$. There is also a similarity between the Time Dependent Hartree-Fock (TDHF) mean field theory and classical mean field theory. The TDHF mean field equations for the single particle density matrix can be written as

$$i\hbar\frac{\partial\rho}{\partial t} = [h,\rho] \tag{110}$$

Here h is the self consistent single particle Hamiltonian

$$h = \frac{\mathbf{p}^2}{2m} + V(\mathbf{r},t) \tag{111}$$

and $V(\mathbf{r},t)$ is the self-consistent potential. The corresponding semi-classical equation is the Vlasov or self-consistent Liouville equation

$$\frac{\partial f}{\partial t} = \{h,f\} = -\frac{\mathbf{p}}{m}\cdot\nabla_{\mathbf{r}}f + \nabla_{\mathbf{r}}V(\mathbf{r})\cdot\nabla_{\mathbf{p}}f \tag{112}$$

There is a very close connection between the solutions of the Vlasov equation and the solutions of the classical equations of motion of a particle with a Hamiltonian h moving according to the classical equations of motion

$$\frac{\partial\mathbf{r}}{\partial t} = \frac{\partial h}{\partial\mathbf{p}}, \qquad \frac{\partial\mathbf{p}}{\partial t} = -\frac{\partial h}{\partial\mathbf{r}} \tag{113}$$

The solutions of the Vlasov equation (112) can be expressed in terms of the classical equations of motion (113). Suppose that at time t a particle has position and momentum $(\mathbf{r}(t), \mathbf{p}(t))$. At $t = 0$ its position and momentum were $(\mathbf{r}_0, \mathbf{p}_0)$ where these initial values depend on $\mathbf{r}, \mathbf{p}$ and t. If the initial phase space density is f_0 then the solution of the Vlasov equation is

$$f(\mathbf{r}, \mathbf{p}, t) = f_0(\mathbf{r}_0, \mathbf{p}_0, 0) \tag{114}$$

This is just Liouville's Theorem. The proof is given in textbooks on classical mechanics. In the case of the Vlasov equation it has interesting consequences. According to eqs.(106, 107) the phase space density is either $4/(2\pi\hbar)^3$ or zero. From eq.(114) density of the occupied region of phase space is always the same. Only the boundaries are changed. In particular the density is never larger than $4/(2\pi\hbar)^3$ and the Pauli principle is preserved. The particle number and average energy are also conserved.

8.1 Response function of a Fermi fluid

Equation (114) shows that the time dependence of the phase space density is related to the classical mechanics of single particle motion in the potential $V(r)$. We carry this investigation a little further [4] by studying the response of a Fermi fluid to an external field $Q(r)\beta(t)$. The Hamiltonian is

$$h = \frac{p^2}{2m} + V(r) + Q(r)\beta(t) = h_0(\mathbf{r}, \mathbf{p}) + Q(r)\beta(t). \tag{115}$$

We assume that the potential is time independent and that the external field is weak enough so that the Vlasov equation can be solved by linear response, that is by writing $f(\mathbf{r}, \mathbf{p}, t) = f_0(\mathbf{r}, \mathbf{p}) + g(\mathbf{r}, \mathbf{p}, t)$ and working to the first order in g. Here $f_0(\mathbf{r}, \mathbf{p})$ is the equilibrium phase space density corresponding to the Thomas-Fermi distribution (107, 108). Equation (112) takes the linearized form

$$\frac{\partial g}{\partial t} = \{h, g\} + \beta(t)\{Q, f_0\}. \tag{116}$$

We also assume that $V(r)$ is a central time independent potential. The external field only disturbs the surface of the Fermi surface in phase space so that $g \propto \delta(h_0(\mathbf{r}, \mathbf{p}) - \varepsilon_f)$. The time dependence of g is determined by the natural frequencies of the classical orbits in the potential $V(r)$ with energy $E = \varepsilon_f$. The character of these orbits depends on the potential. In general they are precessing planar orbits.

The radial motion oscillates between a maximum and a minimum value and the angle of the point of maximum distance precesses uniformly. There are two important quantities; i) the period T of radial motion, ii) the precession angle Γ, ie. the angle between one point of maximum distance in an orbit and the next. In general these depend on the energy and angular momentum of the orbit. The natural frequencies of the orbits are

$$\omega_n(N) = n\omega_0 + N\omega_0/\nu \tag{117}$$

where

$$\omega_0 = 2\pi/T, \qquad \nu = 2\pi/\Gamma. \tag{118}$$

The possible values of Γ and ν depend on the shape of the potential. Here are some examples

1. An elliptic orbit in a Coulomb potential has $\Gamma = 2\pi$ and $\nu = 1$.
2. An elliptic orbit in a spherical oscillator potential has $\Gamma = \pi$ and $\nu = 2$.
3. A square well potential. There are several possibilities: i) an orbit along a diameter has $\Gamma = \pi$ and $\nu = 2$; ii)a triangular orbit has $\Gamma = 2\pi/3$ and $\nu = 3$; a square orbit has $\Gamma = \pi/2$ and $\nu = 4$; a 5-point star orbit has $\Gamma = 4\pi/5$ and $\nu = 2.5$. For a fixed energy the value of ν increases with the angular momentum of the orbit.
4. A Woods-Saxon potential: The possibilities depend on the potential parameters and on ε_f. In a typical case ν ranges from $\nu = 2$ for a zero angular momentum orbit to a maximum of $\nu = 2.9$ for a high angular momentum orbit [4].

The response function at a frequency ω has the general form

$$S_L(\omega) = \int_0^{\lambda_{\max}} \lambda d\lambda \sum_{n,N} R_L(\lambda, n, N)\delta(\omega - \omega_n(N)) \tag{119}$$

The integral is over the possible values of the angular momenta of the orbits. The weight function $R_L(\lambda, n, N)$ depends on the mulipolarity **L** of the field $Q(\mathbf{r})$ as well detailed properties of the orbits. The possible values of N are restricted by the mulipolaraity

1. Monopole: $N = 0$.
2. Quadrupole: $N = 2, 0, -2$.
3. Octupole: $N = 3, 1, -1, -3$.

The detailed form of the weight function and some numerical examples are given in ref.[4]. The calculated strength functions have a lot of structure which depend strongly on the mutipolarity of the excitation operator and which resemble the quantum mechanical particle-hole strength functions calculated with the same potential and particle number.

Acknowledgments

I would like to thank the organizers of the Oromana School for the opportunity to attend the school and to lecture there. It was a great pleasure to meet and discuss with the students at the school, with my Spanish colleagues and with the other lecturers. I would also like to thank G.F. Bertsch, K. Hagino and T. Papenbrock for interesting and helpful discussions relating to the problem of bremsstrahlung emission in alpha decay.

References

1. M.Abramowitz and I.A. Stegun: "Handbook of mathematical functions" (Dover, New York 1972)
2. M. Brack and R.K. Bhaduri: "Semiclassical Physics" (Addison-Wesley, Reading Mass. 1997)
3. T. Papenbrock and G.F. Bertsch : Phys. Rev. Lett. **80**, 4141 (1998)
4. D.M. Brink, A. Dellafiore and M. di Toro: Nucl. Phys. **A456**, 205 (1986)
5. D.M. Brink: "Semi-classical methods in nucleus-nucleus scattering" (CUP, Cambridge 1985)
6. R.B. Dingle: "Asymptotic expansions: Their derivation and interpretation" (Academic Press, London 1973)
7. M.I. Dyakonov: Phys. Rev. **C 60**, 037602-1 (1999)
8. R.P. Feynman and A.R. Hibbs: "Quantum mechanics and path integrals" (McGraw-Hill, New York 1965)
9. M.C. Gutzwiller: "Chaos in Classical and quantum systems" (Springer Verlag, New York, 1990)
10. J. Kasagi, H. Yamazaki, N. Kasajima, T. Ohtsuki and H. Yuki: Phys. Rev. Lett. **79**, 371 (1997)
11. Kelvin, Lord (W. Thomson): Philos. Mag. **23**, 252 (1887)
12. J. Knoll and R. Schaeffer: Ann. Phys. **97**, 307 (1976)
13. L. Landau and M. Lifshitz: "Quantum mechanics" (Pergamon Press, London 1958)
14. M.A. Nagarajan, N. Rowley and R. Lindsay: J. Phys. **G12**, 529 (1986)
15. R. Lindsay and N.Rowley: J. Phys. **G10**, 805 (1984)
16. N. Rowley: "Proceedings of the 4th international symposium on the foundations of quantum mechanics in the light of new technology", Japanese J. Appl. Phys., Tokyo, Japan (1993)
17. N. Rowley, G.R. Satchler and P.H. Stelson: Phys. Lett. **B254**, 25 (1991)
18. D.M. Brink and U. Smilansky: Nucl. Phys. **A405**, 301 (1983)
19. V.M. Strutinsky: Nucl. Phys. **A122**, 1 (1968)
20. G.G. Stokes: Cambridge Philos. Trans. **9**, 166 (1865)
21. N. Takigawa, Y.Nozawa, K. Hagino, A. Ono and D.M. Brink: Phys. Rev. **C59**, R593 (1999)

Scattering and reactions of halo nuclei

Ronald C. Johnson

Department of Physics, School of Physics and Chemistry, University of Surrey, Guildford, Surrey, GU2 7XH, UK

Abstract. In these lectures I describe some of the key features of halo nuclei and how these features require a re-think of theories required to adequately describe their collisions with stable nuclei. I provide the basic scattering theory needed to understand few-body models of halo cross sections. The 'frozen halo' approximation is explained in detail and applications of the theory to elastic scattering, break-up and transfer reactions are discussed.

1 Introduction

Several times in the lectures at this Summer School we have been shown a picture of the N-Z plane with the valley of stability displayed and an indication of the position of the neutron and proton drip lines. There has been some emphasis on the properties of medium mass and heavy nuclei far from the valley of stability. My lectures will be mainly concerned with the neutron dripline in the region of small N and Z where very different types of phenomena occur and theories emphasise a different set of degrees of freedom than is usual in heavy nuclei.

One of the most exciting scientific developments in recent years has been the advent of accelerated beams of radioactive nuclei with exotic combinations of neutron and proton numbers. The new techniques produce beams of nuclei which decay by the weak interaction but are stable against decay into their constituents. Nuclear reactions induced by beams incident on targets of ordinary stable nuclei are important sources of information about the structure of the exotic species. For example, experiments of this type led to the discovery of the important new class of nuclei known as halo nuclei.[1–3]

New experiments are extending our understanding of these novel systems. The mechanisms involved in reactions involving haloes and other nuclei far from the valley of stability present a special challenge to theorists. An important consideration is that exotic nuclei are often very weakly bound and easily broken up in the Coulomb and nuclear fields of the target nucleus. Halo nuclei are an extreme case with almost zero binding energy. As a consequence, theories which address the special features associated with strong coupling to excited states of the projectile which may be in the continuum are a prerequisite if reliable information on nuclear structure is to be deduced from reaction experiments. On the other hand, many of the relevant experiments, both current and planned, involve projectile energies which allow simplifying assumptions to be made which help to make the theory more transparent. I will present some of the insights obtained in this way with illustrations from recent experiments.

J.M. Arias and M. Lozano (Eds.): LNP 581, pp. 259–291, 2001.
© Springer-Verlag Berlin Heidelberg 2001

1.1 One-neutron halo nuclei

Key features of halo nuclei [4] remind us of some familiar features of the deuteron. For present purposes we can ignore the small deuteron D-state and consider the deuteron to be a $1S$ state in an attractive n-p potential of depth about 30MeV and range about 1 fm. The deuteron has a binding energy of $\varepsilon_d = 2.2$ MeV. Quantum mechanics tells us that in the classically forbidden region where the n-p separation r is bigger than 1fm the space part of the deuteron's wavefunction will have the form

$$\phi_0 = N_d \frac{\exp(-\lambda_d r)}{r}, \qquad r > 1\text{fm}, \tag{1}$$

where N_d is a normalisation constant. The constant λ_d is determined from the deuteron binding energy by $\lambda_d = \sqrt{2\mu\varepsilon_d/\hbar^2}$ where μ is the reduced mass of the n-p system. This is the functional form predicted by Yukawa for the interaction associated with the exchange of massive particles. Particle exchange also proceeds through classically forbidden regions and hence gives rise to the same functional dependence on distance.

The small deuteron binding energy results in the value $1/\lambda_d = 4.2$fm which is much larger than the range of the n-p interaction and means that in the deuteron the neutron and proton spend a significant part of the time in the classically forbidden region. Indeed, for many purposes its a good approximation to approximate the deuteron wavefunction by the form (1) for *all* values of r.

The one-neutron halo nucleus ^{11}Be can be described in a similar picture. It costs 0.503 MeV to remove a neutron from ^{11}Be and leave ^{10}Be in its ground state. The simplest version of the halo model describes the corresponding component of the ^{11}Be wavefunction as a ^{10}Be core and a neutron in an S-state. For n-core separations r bigger than the core radius the neutron wavefunction is

$$\phi_0 = N_{11} \frac{\exp(-\lambda_{11} r)}{r}, \tag{2}$$

where $1/\lambda_{11} = 6.7$ fm as detemined by the neutron separation energy.

The key point here is that $1/\lambda_{11}$ is much bigger than the size of the core so that the classically forbidden region outside the core plays a very important role, just as in the case of the deuteron.

There are however some important differences between the d and ^{11}Be cases. In the first place, unlike the deuteron, ^{11}Be has a bound excited state with a separation energy of 0.18 MeV. Secondly the Pauli principle demands that the ground state of ^{11}Be be a $2S$ state with a node in the core region in contrast with the nodeless function which simple potential models give for the deuteron. This reflects the fact that underlying this 2-body picture of ^{11}Be is a many fermion system.

The qualitative features associated with very weak binding suggests that an approach based on the 2-body picture might be a good starting point for studying the structure of ^{11}Be, in contrast with mean field models which emphasise the identity of all nucleons. It is this possibility of an alternative good starting point for models of their structure which makes halo systems interesting from

a theoretical point of view. For an excellent bibliography and a discussion of corrections to the basic few-body models see [5].

In these lectures I will concentrate on one-neutron halos. Much of what I have to say is also relevant to multi-neutron halos such as the famous two-neutron halo ^{11}Li [1,4].

2 Nuclear reaction theory

Nuclear reactions play a crucial role in the study of nuclei and halo nuclei are no exception. Well developed theories of nuclear reactions already exist [7]. The interesting questions for theory are whether these theories will work for reactions involving halo nuclei, and if not, how should they be modified.

The weak binding of halo nuclei makes a positive answer to the first question unlikely. The weak binding of the neutron to ^{11}Be, for example, means that the halo degree of freedom is easily excited by the nuclear and Coulomb fields of a target nucleus. The weak binding also means that even a small transfer of momentum from the relative motion of the 2 nuclei will excite the halo nucleus into the continuum of unbound states from which fragments may propagate to large distances. We have to learn how to treat such configurations realistically. This is especially difficult when the fragments are charged.

2.1 Few-body models

It is natural to base the reaction theory for halo systems on few-body models. Here I emphasise approaches which treat only the halo degrees of freedom explicitly, the other nuclear sub-systems being parameterised in terms of effective 2-body interactions.

As a concrete example we consider a 3-body model of reactions induced by a ^{11}Be projectile on a ^{12}C target. The 3 bodies involved are the ^{10}Be core and the halo neutron which make up our model of the projectile and the target. This system has been studied at GANIL at beam energies of 50 MeV/A.

A suitable set of co-ordinates to describe the system is shown in Figure 1. The Hamiltonian in the over-all centre of mass system is assumed to be

$$H = T_R + H_{nC} + V_{nT}(\boldsymbol{r}_{nT}) + V_{CT}(\boldsymbol{r}_{CT}), \tag{3}$$

where T_R is the total kinetic energy of the 3-bodies in the overall centre of mass system and H_{nC} is the Hamiltonian for the $n-C$ relative motion.

$$T_R = -\frac{\hbar^2}{2\mu_{PT}}\nabla_R^2, \quad H_{nC} = -\frac{\hbar^2}{2\mu_{nC}}\nabla_r^2 + V_{nC}(\boldsymbol{r}), \tag{4}$$

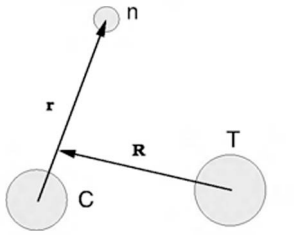

Fig. 1. Co-ordinates used in a 3-body model of a one neutron halo nucleus interacting with a target T

where μ_{PT} and μ_{nC} are reduced masses. The 2-body potentials V_{nC}, V_{CT} and V_{nT} are functions of the relative co-ordinates indicated as their arguments where

$$\boldsymbol{r}_{nT} = \boldsymbol{R} + \beta \boldsymbol{r}, \quad \beta = \frac{m_C}{m_P} \tag{5}$$

$$\boldsymbol{r}_{CT} = \boldsymbol{R} - \alpha \boldsymbol{r}, \quad \alpha = \frac{m_n}{m_P} \tag{6}$$

$$m_P = m_n + m_C. \tag{7}$$

These 2-body potentials depend only on relative co-ordinates and cannot excite the internal degrees of freedom of the core and the target nucleus. Such effects effects are taken into account implicitly by allowing V_{CT} and V_{nT} to be complex optical potentials which describe the relevant 2-body elastic scattering at the correct relative velocity. For weakly bound halo nuclei the latter can be taken to be the relative velocity of the projectile and target.

It is important to appreciate the significance of eigenfunctions of this model H. They are functions $\Psi(\boldsymbol{r}, \boldsymbol{R})$ which satisfy

$$H\Psi = E\Psi, \tag{8}$$

and describe that component of the true many-body wavefunction in which the target is in its ground state. The model eigenfunctions do have components in which the projectile is excited, but only those states which correspond to exciting the halo degrees of freedom including the continuum of break-up states. The model wavefunction can therefore only describe cross sections for elastic scattering, certain inelastic excitations of the projectile, elastic break-up of the projectile in which the target and core are left in their ground states, and the total reaction cross section.

2.2 Two-body scattering

In order to understand our approach to the 3-body system we must first remind ourselves of the formalism of 2-body scattering and learn how to express it in language which can be adapted to the many-body case.

The optical potential V_{nT} in the 3-body Hamiltonian (3) is a complex function of r_{nT} which is taken from the analysis of $n-T$ elastic scattering. It will usually have a Woods-Saxon shape, *i.e.*,

$$V_{nT}(r_{nT}) = \frac{-V_0 - iW_0}{1+\exp\left[(r_{nT}-R_0)/a\right]}, \tag{9}$$

where a typical value of the real depth parameter V_0 at low neutron energy is 40 MeV and the imaginary depth W_0 is about 0.26 V_0. The radius parameter R_0 is given by $1.2\mathrm{A}_T^{1/3}$ fm and the diffuseness $a = 0.65$ fm.

For V_{CT}, where C is ^{10}Be and T is ^{12}C, the analogous parameters would be $V_0 = 120$ MeV, $W_0 = 0.5V_0$, $R_0 = 0.75(\mathrm{A}_C^{1/3} + \mathrm{A}_T^{1/3})$ fm, $a = 0.65$ fm.

I emphasise that these values are quoted for illustration only. All the optical parameters may depend on the centre of mass energy of the interacting nuclei and may have a more sophisticated geometrical form than I have indicated above. For nuclei with spin there may be important spin dependent terms such as the familiar $\boldsymbol{L}.\boldsymbol{I}$ interaction and we should not forget that for charged particles there will be Coulomb terms which must be included. For 'ordinary' nuclei and the nucleon the systematics of the optical potential parameters are well understood. An important aspect of our approach is that we do not assume that these systematics apply to halo and other weakly bound nuclei. The few-body models allow us to input relatively well understood physics for the sub-systems which make up an exotic projectile.

To calculate the scattering of a particle from a target represented by a central potential $V(R)$ we have to solve the equation

$$(T_R + V(R))\chi(\boldsymbol{R}) = E\chi(\boldsymbol{R}), \tag{10}$$

where the kinetic energy operator T_R is as defined in (4) with an appropriate reduced mass. We require solutions which are regular at $R = 0$ and which for $R \to \infty$ in the direction $\hat{\boldsymbol{R}}$ satisfy

$$\chi(\boldsymbol{R}) \to \exp(i\boldsymbol{K}.\boldsymbol{R}) + f(\hat{\boldsymbol{R}})\exp(iKR)/R, \tag{11}$$

where $\boldsymbol{K}$ is the incident momentum. For present purposes I have ignored Coulomb forces (their long range introduces well understood technical complications in the 2-body problem), and spin dependence.

The elastic differential cross section is related to f by

$$\frac{d\sigma}{d\Omega_{\hat{\boldsymbol{R}}}} = \mid f(\hat{\boldsymbol{R}}) \mid^2 . \tag{12}$$

Calculating f for given V is a completely solvable problem. We use the fact that for a central V angular momentum is conserved just as in classical mechanics. This means that we can find solutions of (10) which are eigenfunctions of $\boldsymbol{L}^2$ and L_z where $\boldsymbol{L} = \boldsymbol{R} \wedge (i^{-1})\nabla_R$ is the angular momentum operator (in units of $\hbar$) and z is an arbitrary z-axis. Such solutions have the form

$$\chi(R,\theta,\phi) = \chi_{LM}(R)Y_{LM}(\theta,\phi), \tag{13}$$

where the angles (θ, ϕ) describe the direction of $\boldsymbol{R}$ in the chosen co-ordinate system. The spherical harmonics Y_{LM} are angular momentum eigenfunctions and satisfy

$$\boldsymbol{L}^2 Y_{LM} = L(L+1)Y_{LM}, \tag{14}$$

$$L_z Y_{LM} = M Y_{LM}. \tag{15}$$

The radial function $\chi_{LM}(R)$ satisfies the ordinary differential equation

$$-\frac{\hbar^2}{2\mu_{PT}}\frac{1}{R}\frac{d^2}{dR^2}(R\chi_{LM}(R)) + [V(R) + \frac{\hbar^2}{2\mu_{PT}}\frac{L(L+1)}{R^2}]\chi_{LM}(R) = E\chi_{LM}(R). \tag{16}$$

This equation has a unique solution within a constant of proportionality when the condition $\lim_{R\to 0} R\chi_{LM}(R) = 0$ is imposed.

For a finite range potential satisfying $V(R) = 0$, $R > R_0$ this unique solution has the form

$$\chi_{LM}(R) \stackrel{R\geq R_0}{=} \alpha(\cos\delta_L \mathrm{j}_L(KR) + \sin\delta_L \mathrm{n}_L(KR) \tag{17}$$

$$\stackrel{KR\gg L}{\to} \alpha \sin(KR - L\pi/2 + \delta_L)/KR, \tag{18}$$

where α is a constant independent of R and in the second line I have used the asymptotic forms of the regular and irregular spherical Bessel functions:

$$\mathrm{j}_L(KR) \stackrel{KR\gg L}{\to} \sin(KR - L\pi/2)/KR \tag{19}$$

$$\mathrm{n}_L(KR) \stackrel{KR\gg L}{\to} \cos(KR - L\pi/2)/KR. \tag{20}$$

In these equations the phase shifts δ_L appear. They are functions of energy and angular momentum and contain all the interesting dependence of the scattering on the potential V. The phaseshifts are complex if V is. The terminology is easily understood from eq.(18). If V is identically zero for all R the correct solution of eq.(16) is the spherical Bessel $\mathrm{j}_L(KR)$ with asymptotic form eqs.(19,20). Thus δ_L determines the phase difference at large distance between the free ($V = 0$) and the scattering wavefunction for a given L.

In order to relate the phase shifts to the scattering amplitude and hence to cross sections we must learn how to choose the c_{LM} so that the superposition

$$\chi(\boldsymbol{R}) = \sum_{LM} c_{LM}\chi_L^{(+)}(\boldsymbol{R})Y_{LM}(\hat{R}), \tag{21}$$

has the asymptotic form (11). I have added a (+) superscript to χ_L to designate that this function is normalized so that it satisfies eq. (17) with $\alpha = 1$.

It is easy to find the correct c_{LM}'s because we already know that the incident plane wave has the expansion

$$\exp i\boldsymbol{K}.\boldsymbol{R} = 4\pi \sum_{LM} i^L Y_{LM}^*(\hat{K})Y_{LM}(\hat{R})\mathrm{j}_L(KR). \tag{22}$$

A simple calculation using eqs.(18)-(22) and (11) gives

$$c_{LM} = 4\pi \exp(i\delta_L) i^L Y^*_{LM}(\boldsymbol{K}), \tag{23}$$

and hence

$$f^{(+)}(\theta,\phi) = 4\pi \sum_{LM} Y^*_{LM}(\hat{K}) Y_{LM}(\theta,\phi) \exp(i\delta_L) \sin\delta_L / K, \tag{24}$$

$$\chi^{(+)}_{\boldsymbol{K}}(\boldsymbol{R}) = 4\pi \sum_{LM} i^L Y^*_{LM}(\hat{K}) Y_{LM}(\hat{R}) \exp(i\delta_L) \chi^{(+)}_L(R), \tag{25}$$

where (θ,ϕ) are the angles defining the direction of observation with respect to a chosen co-ordinate system.

Eq.(24) shows explicitly the relation between the scattering amplitude and the set of phase shifts. The scattering amplitude is related to the elastic differential cross section by eq.(12). The phase shifts also determine the total reaction cross section, which is a measure of the flux going into all channels except the elastic channel and is given by

$$\sigma_R = \frac{\pi}{K^2} \sum_L (2L+1)(1-|S_L|^2), \tag{26}$$

where

$$S_L = \exp(2i\delta_L), \tag{27}$$

is the elastic S-matrix (a 1x1 matrix in this special case).

Eq.(25) gives the relation between the full scattering state wavefunction in 3 dimensional space and its components with definite angular momentum L. The radial wavefunctions, $\chi^{(+)}_L(R)$, have an asymptotic form which is determined by the phase shifts. At finite distances $\chi^{(+)}_L(R)$ is determined obtained by solving the radial equation (16) numerically or otherwise. The phase-shift is found by matching the numerical value of the logarithmic derivative at some $R > R_0$ to the formula (17). Knowing the phase-shift the computed numerical values of the radial wavefunction can now be re-normalized so that it satisfies eq.(17) with $\alpha = 1$, thus defining $\chi^{(+)}_L(R)$.

The function $\chi^{(+)}_{\boldsymbol{K}}(\boldsymbol{R})$ defined in this way is an example of a 'distorted wave' . The subscript tells us that it is associated with an incident plane wave with momentum $\boldsymbol{K}$. This label does *not* mean that $\chi^{(+)}_{\boldsymbol{K}}(\boldsymbol{R})$ is an eigenfunction of the momentum operator with eigenvalue $\boldsymbol{K}$! The superscript $(+)$ indicates that $\chi^{(+)}_{\boldsymbol{K}}(\boldsymbol{R})$ asymptotically has an *outgoing* spherical wave component. The complete asymptotic form is as in the RHS of eq.(11).

2.3 The mysterious $\chi^{(-)}_{\boldsymbol{K}}(\boldsymbol{R})$

In formulating theories of complex collisions we frequently come across other scattering states which asymptotically look like a plane wave plus an ingoing

spherical wave. We can construct such a state using the same radial wavefunctions by making a different choice for the c_{LM} in eq.(21) (simply change the factor $\exp i\delta_L$ in eq.(23) to $\exp -i\delta_L$.

In nuclear physics where the potentials V are frequently complex another case occurs. $\chi^{(-)}_{\boldsymbol{K}}(\boldsymbol{R})$ is defined to be a solution of eq.(10) with incoming spherical waves and with V replaced by its complex conjugate V^*:

$$(T_R + V^*(R))\chi^{(-)}_{\boldsymbol{K}}(\boldsymbol{R}) = E\chi^{(-)}_{\boldsymbol{K}}(\boldsymbol{R}). \tag{28}$$

It is easy to show that the radial part of this function must be the complex conjugate of $\chi^{(+)}_L$ within a multiplicative factor and hence does not require separate calculation and a new phase-shift. We find

$$\chi^{(-)}_{\boldsymbol{K}}(\boldsymbol{R}) \rightarrow \exp(i\boldsymbol{K}.\boldsymbol{R}) + f^{(-)}(\hat{\boldsymbol{R}})\exp(-iKR)/R, \tag{29}$$

$$f^{(-)}(\theta,\phi) = 4\pi\sum_{LM}(-1)^L Y^*_{LM}(\hat{K})Y_{LM}(\theta,\phi)\exp -i\delta^*_L \sin\delta^*_L/K, \tag{30}$$

$$\chi^{(-)}_{\boldsymbol{K}}(\boldsymbol{R}) = 4\pi\sum_{LM} i^L Y^*_{LM}(\hat{K})Y_{LM}(\hat{R})\exp -i\delta^*_L(\chi^{(+)}_L(R))^*. \tag{31}$$

With these definitions the precise relationship between $\chi^{(+)}$ and $\chi^{(-)}$ is

$$(\chi^{(-)}_{\boldsymbol{K}}(\boldsymbol{R}))^* = \chi^{(+)}_{-\boldsymbol{K}}(\boldsymbol{R}). \tag{32}$$

These 2 distorted waves and their multi-channel generalisations appear frequently in theories of nuclear reactions.

3 Formal methods

3.1 The 2-body case

We have seen that the problem of the scattering of 2 bodies interacting through a potential is completely solvable. We want to be able to recognise such solvable sub-problems when they appear in the formulation of many-body theories and to achieve this we must learn how to write the 2-body results in a more formal way.

We define the 2-body state $\mid \chi^{\varepsilon}_{\boldsymbol{K}} >$ as the solution of

$$(E + i\varepsilon - T_R - V) \mid \chi^{\varepsilon}_{\boldsymbol{K}} >= i\varepsilon \mid \boldsymbol{K} >, \tag{33}$$

where T_R is the kinetic energy operator and $\mid \boldsymbol{K} >$ is the incident plane wave state

$$< \boldsymbol{R} \mid \boldsymbol{K} >= \exp(i\boldsymbol{K}.\boldsymbol{R}) \tag{34}$$

Clearly for $\varepsilon \rightarrow 0$ the state $\mid \chi^{\varepsilon}_{\boldsymbol{K}} >$ satisfies the same equation as $\mid \chi^{(+)}_{\boldsymbol{K}} >$, eq.(10), but unlike the latter eq.(33) has the unique solution

$$\mid \chi^{\varepsilon}_{\boldsymbol{K}} >= \frac{i\varepsilon}{(E + i\varepsilon - T_R - V)} \mid \boldsymbol{K} >, \tag{35}$$

and incorporates the correct boundary conditions for $\varepsilon > 0$. To show this we re-write eq.(33) as

$$(E + i\varepsilon - T_R) \mid \chi^{\varepsilon}_{\boldsymbol{K}} >= i\varepsilon \mid \boldsymbol{K} > + V \mid \chi^{\varepsilon}_{\boldsymbol{K}} >, \tag{36}$$

and multiply both sides of this equation by the inverse of the operator $E + i\varepsilon - T_R$. We deduce

$$\begin{aligned} \mid \chi^{\varepsilon}_{\boldsymbol{K}} > &= \frac{i\varepsilon}{E + i\varepsilon - T_R} \mid \boldsymbol{K} > + \frac{1}{E + i\varepsilon - T_R} V \mid \chi^{\varepsilon}_{\boldsymbol{K}} > \\ &= \mid \boldsymbol{K} > + \frac{1}{E + i\varepsilon - T_R} V \mid \chi^{\varepsilon}_{\boldsymbol{K}} >, \end{aligned} \tag{37}$$

where we have used the result

$$(E - T_R) \mid \boldsymbol{K} >= 0. \tag{38}$$

When written out in configuration space eq.(37) is an integral equation for $\chi^{\varepsilon}_{\boldsymbol{K}}(\boldsymbol{R})$. In the same basis and for $\varepsilon \ll E$ and *positive* the matrix elements of $(E + i\varepsilon - T_R)^{-1}$ are

$$\begin{aligned} < \boldsymbol{R} \mid \frac{1}{E + i\varepsilon - T_R} \mid \boldsymbol{R}' > \quad &= \quad -\frac{2\mu}{4\pi\hbar^2} \frac{\exp{(iK|\boldsymbol{R} - \boldsymbol{R}'|)}}{|\boldsymbol{R} - \boldsymbol{R}'|} \exp{(-\frac{\varepsilon K|\boldsymbol{R} - \boldsymbol{R}'|}{2E})} \\ &\overset{R \gg R'}{\rightarrow} -\frac{2\mu}{4\pi\hbar^2} \frac{\exp{(iKR - i\boldsymbol{K}'.\boldsymbol{R}')}}{R} \exp{(-\frac{\varepsilon KR}{2E})}, \end{aligned} \tag{39}$$

where $\boldsymbol{K}'$ has the same magnitude as $\boldsymbol{K}$ but points in the direction (θ, ϕ) of $\boldsymbol{R}$. The quantity μ is the reduced mass of the 2-body system.

Using (39) in (37) we find that for R well outside the range of V but not large compared with $\frac{2E}{\varepsilon K}$

$$\chi^{\varepsilon}_{\boldsymbol{K}}(\boldsymbol{R}) \rightarrow \exp{(i\boldsymbol{K}.\boldsymbol{R})} + f^{\varepsilon}(\theta, \phi) \frac{\exp{(iK - \frac{\varepsilon K}{2E})R}}{R}, \tag{40}$$

where

$$f^{\varepsilon}(\theta, \phi) = -\frac{2\mu}{4\pi\hbar^2} < \boldsymbol{K}' \mid V \mid \chi^{\varepsilon}_{\boldsymbol{K}} > . \tag{41}$$

The scattering amplitude f introduced in (11) is given by

$$\begin{aligned} f &= \lim_{\varepsilon \rightarrow 0^+} f^{\varepsilon}, \\ &= -\frac{2\mu}{4\pi\hbar^2} < \boldsymbol{K}' \mid V \mid \chi^{(+)}_{\boldsymbol{K}} > . \end{aligned} \tag{42}$$

The amplitude f^{ε} also has a physical meaning. It can be thought of as the scattering amplitude for an incident wave packet with a spread in time of order $\hbar/\varepsilon$[8].

Eq.(42) expresses the scattering amplitude as a matrix element of the potential V between a plane wave describing the final observed state and the distorted

wave $\mid \chi_{\boldsymbol{K}}^{(+)} >$ which, of course, also depends implicitly on V. This expression does not at first sight appear very useful as a way of determining V. However this type of expression, especially when generalised to systems with many degrees of freedom, lends itself well to generating useful insights and approximations.

As a simple application, let us suppose that the potential V is very weak. Then one would expect that to first order in V the distorted wave in (42) might usefully approximated by the incident plane wave $\mid \boldsymbol{K} >$. The resulting formula is the famous Born approximation

$$\begin{aligned} f^{\mathrm{Born}} &= -\frac{2\mu}{4\pi\hbar^2} < \boldsymbol{K}' \mid V \mid \boldsymbol{K} > \\ &= -\frac{2\mu}{4\pi\hbar^2} \int d\boldsymbol{R} \exp{(i\boldsymbol{Q}\cdot\boldsymbol{R})} V(R), \end{aligned} \tag{43}$$

where $\boldsymbol{Q}$ is the momentum transfer, $\boldsymbol{Q} = \boldsymbol{K} - \boldsymbol{K}'$.

Another way of looking at the matrix element in (42) it to relate it to a matrix element of a new operator $\mathcal{T}(E + i\varepsilon)$ defined by

$$\mathcal{T}(E + i\varepsilon) = V + V \frac{1}{E + i\varepsilon - T_R - V} V. \tag{44}$$

Acting on a plane wave with momentum $\boldsymbol{K}$ related to E by

$$K = \sqrt{\frac{2\mu E}{\hbar^2}}, \tag{45}$$

we find

$$\begin{aligned} \mathcal{T}(E + i\varepsilon) \mid \boldsymbol{K} > &= V \frac{1}{E + i\varepsilon - T_R - V} [(E + i\varepsilon - T_R - V) + V] \mid \boldsymbol{K} > \\ &= V \frac{i\varepsilon}{E + i\varepsilon - T_R - V} \mid \boldsymbol{K} > \\ &= V \mid \chi_{\boldsymbol{K}}^{(+)} >, \end{aligned} \tag{46}$$

where we have used the result (35) to identify $\mid \chi_{\boldsymbol{K}}^{(+)} >$ in the 2nd line in (46). Taking the inner product of both sides of (46) with a plane wave state $\mid \boldsymbol{K'} >$, where $\boldsymbol{K}'$ has the same magnitude as $\boldsymbol{K}$ and is given by (45), we obtain

$$f^{\varepsilon}(\theta, \phi) = -\frac{2\mu}{4\pi\hbar^2} < \boldsymbol{K}' \mid \mathcal{T}(E + i\varepsilon) \mid \boldsymbol{K} > . \tag{47}$$

The operator $\mathcal{T}(E + \varepsilon)$ has matrix elements between plane wave states with arbitrary momentum. It is only when the initial and final momenta are related to E by [45] that these so-called on-shell matrix elements are related to the scattering amplitude. The half-on-shell matrix elements with $K$and E related by [45] but K' arbitrary determine the distorted wave $\mid \chi_{\boldsymbol{K}}^{(+)} >$. To see this we use the last line in (37) and the result (46) to obtain

$$\begin{aligned} \mid \chi_{\boldsymbol{K}}^{\varepsilon} > &= \mid \boldsymbol{K} > + \frac{1}{E + i\varepsilon - T_R} \mathcal{T}(E + i\varepsilon) \mid \boldsymbol{K} > \\ &= \mid \boldsymbol{K} > + \int d\boldsymbol{K}' \frac{\mid \boldsymbol{K}' >< \boldsymbol{K}' \mid \mathcal{T}(E + i\varepsilon) \mid \boldsymbol{K} >}{E + i\varepsilon - E'}, \end{aligned} \tag{48}$$

where

$$E' = \frac{\hbar^2 (K')^2}{2\mu}. \tag{49}$$

We see that all quantities of physical interest are determined by the $\mathcal{T}$-operator. Conversely, both the on-shell and half-off-shell matrix elements of $\mathcal{T}$ can be found by solving the Schrödinger equation for $\mid \chi^+_{\boldsymbol{K}} >$.

An important advantage of the formal methods we have introduced in this section is that they allow us to manipulate explicit expressions for wavefunctions and scattering amplitudes using the rules of operator algebra without having to deal with singular operators. For $\varepsilon \neq 0$ operators like $(E + i\varepsilon - H)^{-1}$ exist for any real E and for Hamiltonians H of physical interest. Boundary conditions have been taken care of once and for all by the ε prescription. The price we have to pay is that in carrying out these manipulations we have to remember thet the scattering states satisfy inhomogeneous equations such as eq.(33) rather than eigenvalue equations like eq.(10).

Of course at the end of the day we are interested in the limit $\varepsilon \to 0^+$. In the many-body case this limit has to be taken with care, but in practical nuclear reaction calculations this does not usually cause a problem. Difficulties with this limiting process can arise, for example, in the formulation of exact numerical solutions of the 3-body scattering problem. A re-formulation in terms of the Faddeev equations is then an advantage, but for the purpose of exposing the structure of many body theories this step and its generalisations to more than 3 bodies is not necessary.

3.2 Target with internal degrees of freedom

For definiteness we consider the scattering of a neutron from a target A which has a set of bound states $\phi_0(\xi), \phi_2(\xi), \ldots, \phi_N(\xi)$ where ξ denotes the set of internal co-ordinates of A. By convention 0 labels the ground state, 1 the first excited state, and so on. The generalisation of the eq.(10) is

$$(T_R + H_A + V(\boldsymbol{R}, \xi))\chi(\boldsymbol{R}, \xi) = E\chi(\boldsymbol{R}, \xi), \tag{50}$$

where H_A is the Hamiltonian which describes the internal motion of A. T_R is the total kinetic energy operator of the neutron and the target in the overall centre of mass system and is defined in eq.(4) with a reduced mass μ_{nT}. $\boldsymbol{R}$ is the relative co-ordinate of the neutron and the centre of mass of A. The potential term $V(\boldsymbol{R}, \xi)$ depends on both $\boldsymbol{R}$ and ξ. It describes the interaction between the neutron and the target and at the most basic level can be expressed as the sum of the 2-body interactions between the neutron and the target nucleons. The ξ would then denote the co-ordinates of the target nucleons relative to its centre of mass.

One approach to solving eq.(50) is to expand χ as a superposition of the set of states ϕ_i which form a complete set if all possible states of A are included. The coefficients in the expansion are functions of $\boldsymbol{R}$ which are the solution of a set of coupled differential equations.

The expansion is

$$\chi(\boldsymbol{R},\xi) = \chi_0(\boldsymbol{R})\phi_0(\xi) + \chi_1(\boldsymbol{R})\phi_1(\xi) + \ldots \tag{51}$$

Coupled equations are obtained by substituting the expansion (51) into (50), multiplying by ϕ_i and integrating over all ξ for $i = 0,\ 1\ldots, N$. The resulting equations for $i = 0,\ 1\ldots, N$ are

$$(E_i - T_R - V_{ii})\chi_i = \sum_{j\neq i} V_{ij}\chi_j, \tag{52}$$

where we have used the eigenvalue equations satisfied by the ϕ_i and their orthonormality relations

$$H_A\phi_i = \epsilon_i\phi_i, \tag{53}$$

$$\int d\xi \phi_i^*\phi_j = \delta_{ij}. \tag{54}$$

The energies E_i are defined by $E_i = E - \epsilon_i$.

The coupling potentials V_{ij} are functions of $\boldsymbol{R}$ defined by

$$V_{ij}(\boldsymbol{R}) = \int d\xi \phi_i^*(\xi)V(\boldsymbol{R},\xi)\phi_j(\xi). \tag{55}$$

The functions $\chi_i(\boldsymbol{R})$ have a definite physical meaning. They tell us the relative probability as a function of $\boldsymbol{R}$ for the target A being in state i. The different possibilities for i are frequently referred to as 'channels' and the E_i are the corresponding channel energies. If the incident channel is $i = 0$ the boundary conditions to be satisfied by the χ_i for values of R outside the range of the coupling potentials are

$$\chi_0^{(+)} \to \exp(i\boldsymbol{K}_0.\boldsymbol{R}) + f_{00}^{(+)}(\hat{\boldsymbol{R}})\exp(iK_0R)/R, \tag{56}$$

$$\chi_i^{(+)} \to f_{i0}(\hat{\boldsymbol{R}})\exp(iK_iR)/R, \quad i \neq 0 \tag{57}$$

where the channel momenta K_i are defined by

$$K_i = \sqrt{\frac{2\mu_{nT}E_i}{\hbar^2}}, \tag{58}$$

provided that $E_i > 0$. If $E_i < 0$ the channel is said to be 'closed' and the corresponding χ_i vanishes exponentially at large distances. There is therefore no outgoing flux in a closed channel and the crosssection for exciting the target into state i will vanish.

If the potentials $V_{ij} = 0$ vanish for $i \neq j$ there will be no coupling between channels. In this limit the regular solution of the coupled equations satisfying the conditions (57) is $\chi_i = 0$ for $i \neq 0$ and χ_0 satisfies

$$(E_0 - T_R - V_{00})\chi_0 = 0. \tag{59}$$

Only the cross section for the elastic scattering of the neutron by the target in its ground state is non zero.

According to (59) elastic scattering in the zero coupling case is generated by V_{00} which has the explicit expression (we assume the ground state has spin 0 for simplicity)

$$\begin{aligned} V_{00}(\boldsymbol{R}) &= \int d\xi \phi_0^*(\xi) V(\boldsymbol{R}, \xi) \phi_o(\xi). \\ &= \sum_i \int d\xi \mid \phi_0(\xi) \mid^2 v_{ni}(\boldsymbol{R} - \boldsymbol{r}_i) \end{aligned} \tag{60}$$

where the summation over i includes all the nucleons in the target and the $\boldsymbol{r}_i$ are the co-ordinates of the target nucleons relative to the target centre of mass. If the target consists of A identical nucleons (60) reduces to

$$V_{00}(\boldsymbol{R}) = A \int d\boldsymbol{r}_1 \rho(\boldsymbol{r}_1) v_{n1}(\boldsymbol{R} - \boldsymbol{r}_1), \tag{61}$$

where $\rho(\boldsymbol{r}_1)$ is the ground state one-body density of the target.

Eq.(61) is the simplest possible model for the optical potential. It relates the effective interaction between the projectile and the target to the fundamental 2-body interactions between the projectile and the target constituents and their density distribution in space. Eq(61) is often referred to as the folding model because of the way the co-ordinates appear in the integral in (61). Note that if the 2-body interaction v_{ni} is real so is V_{00}. This model cannot account for the imaginary part of the optical potential because it corresponds to a theoretical model where no flux is lost to non-elastic channels. We will see below by explicit calculation in a special case how open inelastic channels give rise to a complex effective interaction.

3.3 Formal theory of the multi-channel case

The formal approach developed in Subsection 3.1 is easily generalised to include the possibility that the target has internal degrees of freedom. Eq.(33) is replaced by

$$(E + i\varepsilon - T_R - H_A - V) \mid \chi^{\varepsilon}_{\boldsymbol{K}_0} >= i\varepsilon \mid \boldsymbol{K}_0, \phi_0 >, \tag{62}$$

where

$$< \boldsymbol{R}, \xi \mid \boldsymbol{K_0}, \phi_0 >= \exp(i\boldsymbol{K}_0.\boldsymbol{R}) \phi_0(\xi). \tag{63}$$

is the wavefunction corresponding to a plane wave incident on the target in its ground state.

The presence of the $i\varepsilon$ term on the right hand side of (62) means that the coupled equations equivalent to (52) are

$$(E_i + i\varepsilon - T_R - V_{ii}) \mid \chi^{\varepsilon}_i > = \sum_{j \neq i} V_{ij} \mid \chi^{\varepsilon}_j > + \delta_{i0} \mid \boldsymbol{K}_0 >, \tag{64}$$

where the channel components are related to $\mid \chi^{\varepsilon}_{\boldsymbol{K}_0} >$ by

$$\chi^{\varepsilon}_{\boldsymbol{K}_0}(\boldsymbol{R},\xi) = \sum_i \chi^{\varepsilon}_i(\boldsymbol{R})\phi_i(\xi). \tag{65}$$

For $N = 1$ (2 channels) these equations reduce to

$$(E_0 + i\varepsilon - T_R - V_{00}) \mid \chi^{\varepsilon}_0 > = V_{01} \mid \chi^{\varepsilon}_1 > + \mid \boldsymbol{K}_0 >, \tag{66}$$

$$(E_1 + i\varepsilon - T_R - V_{11}) \mid \chi^{\varepsilon}_1 > = V_{10} \mid \chi^{\varepsilon}_0 > . \tag{67}$$

The second equation allows us to express $\mid \chi^{\varepsilon}_1 >$ in terms of $\mid \chi^{\varepsilon}_0 >$ as

$$\mid \chi^{\varepsilon}_1 >= (E_1 + i\varepsilon - T_R - V_{11})^{-1} V_{10} \mid \chi^{\varepsilon}_0 > . \tag{68}$$

Substituting this result into the first of eqs.(67) gives an equation for $\mid \chi^{\varepsilon}_0 >$ which is

$$(E_0 + i\varepsilon - T_R - V_{00} - V_{01}(E_1 + i\varepsilon - T_R - V_{11})^{-1} V_{10} \mid \chi^{\varepsilon}_0 >= \mid \boldsymbol{K}_0 > . \tag{69}$$

We recognise this as a 2-body elastic scattering equation for $\mid \chi^{\varepsilon}_0 >$ with the effective potential

$$\mathcal{V}_{opt} = V_{00} + V_{01}(E_1 + i\varepsilon - T_R - V_{11})^{-1} V_{10} \tag{70}$$

This analysis shows how an effective potential can always be found which generates the exact elastic scattering. Note that the second term in eq.(70) has an imaginary part in the limit $\varepsilon \to 0^+$, but only if $E_1 > 0$, *i.e.*. above the threshold for exciting the state ϕ_1. Furthermore this imaginary part is negative, indicating that it is associated with a loss of probability flux from the incident channel. Our treatment of the $N = 1$ problem is a special case of a general theory due to Feshbach[6]. A discussion of effective interactions including the effect of energy averaging and additional references can be found in Section 2.9 of ref.[7].

3.4 Inelastic scattering and the DWBA

From eq.(68) we obtain an explicit expression for the amplitude for exciting the state ϕ_1. We use the operator identity

$$\frac{1}{A} - \frac{1}{B} = \frac{1}{A}(B - A)\frac{1}{B}, \tag{71}$$

to deduce

$$\frac{1}{(E_1 + i\varepsilon - T_R - V_{11})} = \frac{1}{(E_1 + i\varepsilon - T_R)}\left[1 + V_{11}\frac{1}{(E_1 + i\varepsilon - T_R - V_{11})}\right], \tag{72}$$

and therefore

$$\mid \chi^{\varepsilon}_1 >= \frac{1}{(E_1 + i\varepsilon - T_R)} \Omega_1^{(-\varepsilon)\dagger} V_{10} \mid \chi^{\varepsilon}_0 >, \tag{73}$$

where

$$\Omega_1^{(-\varepsilon)} = \left[1 + \frac{1}{(E_1 - i\varepsilon - T_R - V_{11})} V_{11}\right]. \tag{74}$$

Following similar reasoning as in the analysis surrounding eq.(40) we find that for $R \to \infty$ and $\varepsilon \to 0^+$

$$< \boldsymbol{R} \mid \chi_1^+ > \to f_{10}^{(+)} \frac{\exp(iK_1 R)}{R}, \tag{75}$$

where

$$f_{10}^{(+)} = -\frac{2\mu}{4\pi\hbar^2} < \boldsymbol{K}_1 \mid \Omega_1^{(-)\dagger} V_{10} \mid \chi_0^{(+)} >, \tag{76}$$

and the wave number $\boldsymbol{K}_1$ is in the direction of observation and has magnitude

$$K_1 = \sqrt{\frac{2\mu}{\hbar^2} E_1}. \tag{77}$$

Note that in eq.(76), $\chi_0^{(+)}$ is the exact elastic scattering distorted wave as generated by $\mathcal{V}_{opt}$, or by solving the coupled equations (67).

It can be shown that for $\varepsilon \to 0$ through positive values

$$< \boldsymbol{K}_1 \mid \Omega_1^{(-)\dagger} =< \chi_{\boldsymbol{K}_1}^{(-)} \mid, \tag{78}$$

where $\mid \chi_{\boldsymbol{K}_1}^{(-)} >$ is a distorted wave of the type defined in Sub-section 2.3 and generated by the potential V_{11}. The inelastic scattering amplitude (76) can therefore be written

$$f_{10}^{(+)} = -\frac{2\mu}{4\pi\hbar^2} < \chi_{\boldsymbol{K}_1}^{(-)} \mid V_{10} \mid \chi_{\boldsymbol{K}_0}^{(+)} >, \tag{79}$$

where we have written χ_0^{ε} as $\chi_{\boldsymbol{K}_0}^{(+)}$ to conform to our earlier notation in the limit $\varepsilon \to 0$.

The DWBA as originally formulated can be obtained from this exact expression by replacing the initial distorted wave by the distorted wave generated by the potential V_{00} instead of $\mathcal{V}_{opt}$. This approximation includes the diagonal elements V_{11} and V_{00} to all orders but the potential V_{10} responsible for coupling the 2 channels is included in first order only. The usual Born approximation of inelastic scattering corresponds to replacing the 2 distorted waves by plane waves. The DWBA attempts to do better than that by recognising that the target-projectile interaction will scatter the 2 nuclei and convert the plane waves into distorted plane waves. The DWBA is a consistent way to take this physical effect into account when the channel coupling is weak enough to be treated to 1st order.

We emphasise that in the realistic multi-channel situation we frequently meet in nuclear physics the DWBA as just defined is rarely used. An expression with a structure similar to (79) is used but with the 2 distorted waves generated by complex potentials which fit elastic scattering data. This is called the 'Distorted Wave Method' by Satchler [7]. Modern computer methods emphasise exact solutions of coupled channels models although Distorted Wave ideas often still underlie much qualitative thinking about nuclear reactions.

3.5 Practical evaluation of DW matrix elements

It is useful to have some insight into how expressions such as (79) are actually evaluated. For central distorting potentials the 2 distorted waves have expansions of the form introduced in subsection 2.2. We can write

$$\chi^{(+)}_{\boldsymbol{K}_0}(\boldsymbol{R}) \quad = 4\pi \sum_{L_0 M_0} i^{L_0} Y^*_{L_0 M_0}(\hat{K}_0) Y_{L_0 M_0}(\Omega_R) \exp(i\delta^0_{L_0}) \chi^{(+)}_{L_0}(R), \tag{80}$$

$$(\chi^{(-)}_{\boldsymbol{K}_1}(\boldsymbol{R}))^* = 4\pi \sum_{L_1 M_1} (-1)^{L_1} i^{L_1} Y_{L_1 M_1}(\hat{K}_1) Y^*_{L_1 M_1}(\Omega_R) \exp(i\delta^1_{L_1}) \chi^{(+)}_{L_1}(R) \tag{81}$$

Inserting these expressions into (79) we obtain

$$f^{(+)}_{10} = -\frac{8\pi\mu}{\hbar^2} \sum_{L_0 M_0 L_1 M_1} i^{L_0 - L_1} Y^*_{L_0 M_0}(\hat{K}_0) Y_{L_1 M_1}(\hat{K}_1) \exp i(\delta^0_{L_0} + \delta^1_{L_1}) \tag{82}$$

$$\times \int_0^\infty R^2 dR \chi^{(+)}_{L_1}(R) < L_1 M_1 \mid V_{10} \mid L_0 M_0 > \chi^{(+)}_{L_0}(R), \tag{83}$$

with summation over L_0, M_0, L_1, M_1. Integration over the direction of $\boldsymbol{R}$ and the internal co-ordinates of the target are contained in the matrix element $< L_1 M_1 \mid V_{10} \mid L_0 M_0 >$

$$< L_1 M_1 \mid V_{10} \mid L_0 M_0 >= \int d\Omega_R \, d\xi \, Y^*_{L_1 M_1}(\Omega_R) \phi^*_1(\xi) V_{10}(\boldsymbol{R}, \xi) \phi_0(\xi) Y_{L_0 M_0}(\Omega_R). \tag{84}$$

By making a multipole expansion of the interaction V_{10} this matrix element can be factorised into reduced multipole matrix elements, which contain all the dependence on the structure of the target states ϕ_0 and ϕ_1, Clebsch-Gordan coefficients which carry the implications of angular momentum conservation and form factors which depend on the radial co-ordinate R (see, *e.g.*, Section 5.6 of ref.[7]). We do not have space to expand further on these important ideas here.

Standard codes exist which evaluate DW amplitudes such as (83) and solve the coupled equations (52) exactly for given poentials and target wave functions as a routine matter [12].

We note that most of the formulae in this section have to be modified when the nuclei involved are charged. The formal expressions we have used are perfectly valid when all the Coulomb interactions are screened at large distances. The correct expressions to be used for partial wave expansions when the uninteresting dependence on the screening radius is extracted are given in many standard texts, *eg*, [7]. Recent reviews which include Coulomb and spin-dependent effects can be found in [13] and [14].

3.6 Many-body $\mathcal{T}$-operator

As in the 2-body case we introduce an operator $\mathcal{T}$ whose on-shell matrix elements are proportional to the inelastic and inelastic scattering amplitudes. The key

difference is that this operator now acts in the space of the variables ξ as well as $\boldsymbol{R}$. The definition of $\mathcal{T}$ is

$$\mathcal{T}(E+i\varepsilon) = V + V\frac{1}{E+i\varepsilon - T_R - H_A - V}V. \tag{85}$$

This expression has exactly the same formal structure as (44) in the 2-body case, but the presence of the target Hamiltonian, H_A in the denominator in (85) makes this $\mathcal{T}$ a much more complicated operator.

In terms of $\mathcal{T}$ the elastic and inelastic scattering amplitudes are given by

$$f^{\varepsilon}(\theta,\phi)_{i0} = -\frac{2\mu}{4\pi\hbar^2} < \boldsymbol{K}_i, \phi_i \mid \mathcal{T}(E+i\varepsilon) \mid \boldsymbol{K}_0, \phi_0 >, \tag{86}$$

and the scattering state is expreessed in terms of the off-shell matrix elements of $\mathcal{T}$ through

$$\mid \chi^{\varepsilon}_{\boldsymbol{K}_0} >= \mid \boldsymbol{K}_0, \phi_0 > + \sum_i \int d\boldsymbol{K}' \frac{\mid \boldsymbol{K}', \phi_i >< \boldsymbol{K}', \phi_i \mid \mathcal{T}(E+i\varepsilon) \mid \boldsymbol{K}_0, \phi_0 >}{E_0 + \epsilon_0 + i\varepsilon - E' - \epsilon_i}. \tag{87}$$

The point about these formal expressions is that they help us to recognise quantities that are calculable using standard techniques when they are buried in a complicated theory of a nuclear reaction. To calculate a matrix element of a $\mathcal{T}$ operator in practice one usually, but not always re-expresses the calculation in terms of coupled differential equations.

4 Scattering of halo nuclei

We now return to the consideration of few-body models of the scattering of halo systems introduced in Section 2.1. As in that Section I will take as a specific example a 3-body model of reactions induced by a ^{11}Be projectile on a ^{12}C target. The 3 bodies involved are the ^{10}Be core and the halo neutron, which make up our model of the projectile, and the target.

The Hamiltonian in the over-all centre of mass system is that given in eq.(3) which I repeat here for convenience.

$$H = T_R + H_{nC} + V_{nT}(\boldsymbol{r}_{nT}) + V_{CT}(\boldsymbol{r}_{CT}). \tag{88}$$

Possible states of the halo are eigenstates of H_{nC} and satisfy

$$\begin{aligned} (H_{nC} - \epsilon_i)\phi_i(\boldsymbol{r}) &= 0, \ i = 0, 1, 2 \ldots, \\ (H_{nC} - \epsilon_k)\phi_{\boldsymbol{k}}(\boldsymbol{r}) &= 0, \quad \epsilon_k = \frac{\hbar^2 k^2}{2\mu_{nC}}, \end{aligned} \tag{89}$$

where we have distinguished between discrete bound states labelled by i and the continuum states labelled by momentum $\boldsymbol{k}$. Transitions to the latter correspond to elastic break-up.

One approach to finding scattering state solutions to eq.(8) is to proceed as in Section 3.2 and look for solutions as an expansion in the complete of functions of $\boldsymbol{r}$ defined in eq.(89):

$$\Psi(\boldsymbol{R},\boldsymbol{r}) = \phi_0(\boldsymbol{r})\chi_0(\boldsymbol{R}) + \phi_1(\boldsymbol{r})\chi_1(\boldsymbol{R}) + \cdots , \\ + \int d\boldsymbol{k}\phi_{\boldsymbol{k}}(\boldsymbol{r})\chi_{\boldsymbol{k}}(\boldsymbol{R}). \tag{90}$$

The functions $\chi_i(\boldsymbol{R})$, $\chi_{\boldsymbol{k}}(\boldsymbol{R})$ in eq.(90) give the amplitudes for exciting the various halo states. All of them have the form of outgoing spherical waves at large R with amplitudes which determine the corresponding excitation cross sections. The function $\chi_0(\boldsymbol{R})$ also includes a plane wave describing the incident beam.

The χ's satisfy a set of coupled differential equations which, if we ignore the continuum terms in eq.(90), have the form

$$(E_0 - T_{\boldsymbol{R}} - V_{ii}(\boldsymbol{R}))\chi_i(\boldsymbol{R}) = \sum_{j\neq i} V_{ij}(\boldsymbol{R})\chi_j(\boldsymbol{R}) \\ i,\ j = 0,\ 1, \ldots , \tag{91}$$

where $E_i = E - \epsilon_i$ and the coupling potentials $V_{ij}(\boldsymbol{R})$ are given by

$$V_{ij} = \int d\boldsymbol{r}\phi_i^*(\boldsymbol{r})[V_{nT}(\boldsymbol{R} + \beta\boldsymbol{r}) + V_{CT}(\boldsymbol{R} - \alpha\boldsymbol{r})]\phi_j(\boldsymbol{r}). \tag{92}$$

The coupling potentials describe the way tidal forces generated by the interactions between the components C and n of the projectile and the target can cause excitations of the projectile. It is the variation of the potentials on a scale of the order of the size of the projectile which generate terms with $i \neq j$ which would otherwise vanish by the orthogonality of the $\phi_j(\boldsymbol{r})$.

When the continuum terms on the right hand side of eq.(90) are included the generalisation of eq.(91) now includes coupling terms which couple discrete and continuum terms as well as terms coupling the continuum to itself. These terms involve coupling potentials like eq.(92) but with at least one of the $\phi_i(\boldsymbol{r})$ replaced by a $\phi_{\boldsymbol{k}}(\boldsymbol{r})$. These are the couplings which induce break-up of the halo and which are expected to play a prominent role in reactions involving halo nuclei.

One way of handling these equations when continuum couplings are important is to map the continuum onto a discrete square-integrable basis which is orthogonal to the bound states ϕ_i. This CDCC method pioneered by the Kyushu Group [15,16] makes use of this idea. This approach has been successfully applied to the scattering of deuterons and other loosely bound nuclei but has difficulties when long range Coulomb couplings are included [17]. This approach will not be considered in detail here. Instead we will discuss a widely used approximation to the many-body scattering problem which is sometimes much simpler to implement than the CDCC method and provides interesting insights into the role of the continuum in the scattering of halo nuclei.

4.1 Adiabatic approximation

The adiabatic approximation is based on the observation that at sufficiently high incident energy the halo degrees of freedom may be regarded as 'frozen' over the time needed for the projectile to traverse the target. This does *not* mean that we assume that the projectile remains in the same eigenstate ϕ_0 of H_{nC}, but rather that the co-ordinate $\boldsymbol{r}$ is frozen. This approximation is at the basis of Glauber's theory of composite particle scattering [18], versions of which have been widely used in the analysis of reactions involving halo nuclei. The adiabatic approximation retains its usefulness, however, even when the other assumption of Glauber's theory, *i.e.*, the eikonal approximation, is not invoked.

We can get some insight into the validity of the adiabatic approximation and how it can be implemented by considering the time dependent version of eq.(8)

$$H\Psi(\boldsymbol{R},\ \boldsymbol{r},\ t) = i\hbar\partial\Psi(\boldsymbol{R},\ \boldsymbol{r},\ t)/\partial t. \tag{93}$$

The substitution

$$\Psi = \exp(-i(H_{nC} - \epsilon_0)t/\hbar)\Phi, \tag{94}$$

transforms eq.(93) into the equivalent form

$$(T_R + \epsilon_0 + V_{nT}(\boldsymbol{R} + \beta\boldsymbol{r}(t)) + V_{CT}(\boldsymbol{R} - \beta\boldsymbol{r}(t)))\Phi = i\hbar\partial\Phi/\partial t, \tag{95}$$

where the term in H_{nC} has been removed at the expense of a time dependent $\boldsymbol{r}(t)$ satisfying

$$\boldsymbol{r}(t) = \exp(i(H_{nC} - \epsilon_0)t/\hbar)\, r\, \exp(-i(H_{nC} - \epsilon_0)t/\hbar). \tag{96}$$

The adiabatic approximation replaces $\boldsymbol{r}(t)$ by $\boldsymbol{r}(0) = \boldsymbol{r}$ in eq.(95). A sufficient condition for this to be accurate over the collision time t_{coll} is

$$(H_{nC} - \epsilon_0)t_{coll}/\hbar \ll 1. \tag{97}$$

When this adiabatic condition is satisfied, stationary state solutions of eq.(95) satisfy

$$(T_R + V_{nT}(\boldsymbol{R} + \beta\boldsymbol{r}) + V_{CT}(\boldsymbol{R} - \beta\boldsymbol{r}))\Phi = E_K\Phi, \tag{98}$$

where $E_K = E - \epsilon_0$ is the incident kinetic energy and we have assumed a time dependent factor $\exp(-iEt/\hbar)$ for times satisfying eq.(97).

In eq.(98) $\boldsymbol{r}$ is no longer a dynamical variable but a parameter. The 3-body problem we started with has been reduced to a set of 2-body problems, one for each value of $\boldsymbol{r}$. The resulting solution $\phi^{\mathrm{Adia}}(\boldsymbol{R}, \boldsymbol{r})$ is a superposition of all the projectile states $(\phi_i(\boldsymbol{r}), \phi_{\boldsymbol{k}}(\boldsymbol{r}))$.

The adiabatic approximation to the transition amplitude to a particular projectile state is calculated by projecting onto that state and examining the coefficient of the outgoing wave for R asymptotically large. If $f(\theta, \phi, \boldsymbol{r})$ is the scattering amplitude in the direction θ, ϕ calculated from eq.(98) for a fixed value of $\boldsymbol{r}$, then the scattering amplitude for exciting state i is

$$f_{i0} = \int d\boldsymbol{r}\phi_i^*(\boldsymbol{r})f(\theta, \phi, \boldsymbol{r})\phi_0(\boldsymbol{r}). \tag{99}$$

Examples of the application of this method to composite particle scattering including several frozen degrees of freedom can be found in refs. [19–23]. When the 2-body scattering problem eq.(98) is solved using the additional assumption of straight line trajectories in $\boldsymbol{R}$-space the results are equivalent to Glauber's [18] theory. Calculations along these lines [1,2,39,24,25,42] have been of great importance in the interpretation of reaction cross sections for halo nuclei in terms of nuclear sizes. Some of the earlier calculations used a further approximation to Glauber's many body theory theory known variously as the 'optical limit', the 'static limit', or the 'folding model'. It has been proved recently [27] that for a given halo wave function the 'folding model' always overestimates the total reaction cross section for strongly absorbed particles. Published complete Glauber calculations [24,25,42] are consistent with this theorem.

It is clearly desirable to convert the adiabatic condition eq.(97) into a quantitative estimate expressed in terms of the parameters of the collision process of interest and to devise methods of calculating the leading corrections to the adiabatic scattering amplitudes. It is clear that eq.(97) requires small projectile excitation energies (slow halo degrees of freedom) and high incident energies (short collision times). Qualitative estimates along these lines can be found in refs. [18,32,33], and some progress has been made in deriving correction terms for transfer reactions [28] and elastic scattering [34]. Here we shall assume that the adiabatic approximation is adequate and confine ourselves to the scattering of halo nuclei at energies for which a simple estimate indicates there is a good case for this to be a valid starting point.

The adiabatic approximation can also be regarded as an approximate solution of the coupled equations eq.(91) when all the channel energies E_i are assumed to be degenerate and equal to E_0. Multiplying the ith equation by $\phi_i(\boldsymbol{r})$, summing up all the equations over i using the completeness of the $\phi_i(\boldsymbol{r})$, one obtains an equation equivalent to eq.(98) with ϕ identified as $\sum \phi_i \chi_i$. This derivation does not give an immediate indication of the conditions for the validity of the approximation.

A recent review of many applications of the adiabatic approximation to few-body models of the scattering of halo nuclei can be found in [29].

4.2 Special cases

Implementation of the adiabatic approximation requires the calculation of scattering solutions $\phi^{\mathrm{Adia}}(\boldsymbol{R}, \boldsymbol{r})$ of eq.(98). Eq.(98) for fixed $\boldsymbol{r}$ is equivalent to a 2-body problem in a potential which is non-central, even if V_{nt} and V_{CT} are themselves central, and an exact solution requires the solution of coupled equations [19,20,23]. There are 2 cases when an enormous simplification occurs:

1. *When $\phi^{\mathrm{Adia}}(\boldsymbol{R}, \boldsymbol{r})$ is required at the point $r = 0$ only.*
   Eq.(98) then reduces to a 2-body central force problem in the potential $V_{nT}(R) + V_{CT}(R)$. This insight has been exploited [19,30,28] to give a theory of deuteron stripping and pick-up which includes deuteron break-up effects in a simple way.

2. *When one of the interactions, V_{nT} say, between the constituents of the projectile and the target is zero [31].*
   We shall refer to this special case as 'the recoil model' because the only way the projectile can be excited or broken up is through recoil of the core following scattering by the target. Note that the other 2 interactions V_{nC} and V_{CT} can be of arbitrary strength or range and may include Coulomb terms.

In case 2 the exact solution of eq.(98) corresponding to a projectile in its ground state ϕ_0 incident with momentum $\boldsymbol{K}$ on a target T is [31,33,32]

$$\phi_{\boldsymbol{K}}^{(+)\mathrm{Adia}}(\boldsymbol{r},\boldsymbol{R}) = \phi_0(\boldsymbol{r}\,)\, e^{i\alpha\boldsymbol{K}\cdot\boldsymbol{r}} \chi_{\boldsymbol{K}}^{(+)}(\boldsymbol{R}-\alpha\boldsymbol{r}), \tag{100}$$

where $\chi_{\boldsymbol{K}}^{(+)}$ is a distorted wave which describes the scattering of a particle of mass μ_{PT} (the projectile-target reduced mass) from the potential V_{CT}, *i.e.*,

$$\begin{aligned}[T_{R'} + V_{CT}(\boldsymbol{R}'))]\ \chi_{\boldsymbol{K}}^{(+)}(\boldsymbol{R}') &= E_K \chi_{\boldsymbol{K}}^{(+)}(\boldsymbol{R}'),\\ \chi_{\boldsymbol{K}}^{(+)}(\boldsymbol{R}') &\overset{R'\to\infty}{\to} \exp(i\boldsymbol{K}\cdot\boldsymbol{R}') + f_{CT}\exp(iKR')/R'\ .\end{aligned} \tag{101}$$

Note that in eq.(100) the distorted wave has the argument $(\boldsymbol{R}-\alpha\boldsymbol{r})$, which is just the $C-T$ separation. The distorted wave corresponds to a model in which all effects due to the halo neutron are ignored apart from its contribution to the mass of the projectile. In the following we will refer to this limit as the scattering of a 'no-halo' projectile.

We emphasise that the three-body wave function, eq.(100), includes components which describe break-up and excitations of the projectile. This is clear from the complicated dependence on $\boldsymbol{r}$, through the argument of $\chi_{\boldsymbol{K}}^{(+)}$ and the exponential factor $\exp(i\alpha\boldsymbol{K}\cdot\boldsymbol{r})$ which will result in a non-vanishing overlap with any of the states $(\phi_i(\boldsymbol{r}), \phi_{\boldsymbol{k}}(\boldsymbol{r}))$.

4.3 Applications of the adiabatic 'recoil model'

The exact elastic scattering transition amplitude for the projectile, from initial state $\boldsymbol{K}$ into final state $\boldsymbol{K}'$, is

$$T_{el}(\boldsymbol{K}',\boldsymbol{K}) = \int d\boldsymbol{r} \int d\boldsymbol{R}\ \phi_0^*(\boldsymbol{r}\,)\ e^{-i\boldsymbol{K}'\cdot\boldsymbol{R}}\ V_{CT}(\boldsymbol{R}-\alpha\boldsymbol{r}\,)\ \Psi_{\boldsymbol{K}}^{(+)}(\boldsymbol{r},\boldsymbol{R}), \tag{102}$$

where $\Psi_{\boldsymbol{K}}^{(+)}(\boldsymbol{r},\boldsymbol{R})$ is the exact scattering state solution of eq.(8)

Using the adiabatic approximation to $\Psi_{\boldsymbol{K}}^{(+)}$, eq.(100), and making the change of variable from $\boldsymbol{R}$ to $\boldsymbol{R}' = \boldsymbol{R}-\alpha\boldsymbol{r}$ this factorises as

$$\begin{aligned}T_{el}(\boldsymbol{K}',\boldsymbol{K}) = &\left[\int d\boldsymbol{r}\,|\phi_0(\boldsymbol{r}\,)|^2\ e^{i\alpha(\boldsymbol{K}-\boldsymbol{K}')\cdot\boldsymbol{r}}\right]\\ &\times\left[\int d\boldsymbol{R}'\ e^{-i\boldsymbol{K}'\cdot\boldsymbol{R}'}\ V_{CT}\ (\boldsymbol{R}')\ \chi_{\boldsymbol{K}}^{(+)}(\boldsymbol{R}')\right].\end{aligned} \tag{103}$$

The second integral here is just the transition amplitude $T_{no-halo}(\boldsymbol{K}', \boldsymbol{K})$ for a 'no-halo' projectile scattering by the core-target potential V_{cT}. The same result for T_{el} is obtained by examining the asymptotic form of eq.(100) in the elastic channel.

The effects of projectile excitation and structure in eq.(103) arise entirely through the first integral, the form factor

$$F(\boldsymbol{Q}) = \int d\boldsymbol{r}\, |\phi_0(\boldsymbol{r})|^2 \ \exp(i\boldsymbol{Q}\cdot\boldsymbol{r}), \tag{104}$$

where $\boldsymbol{Q} = \alpha(\boldsymbol{K} - \boldsymbol{K}')$.The corresponding elastic scattering differential cross section is therefore

$$\left(\frac{d\sigma}{d\Omega}\right)_{el} = |F(\boldsymbol{Q})|^2 \times \left(\frac{d\sigma}{d\Omega}\right)_{no-halo}, \tag{105}$$

where $(d\sigma/d\Omega)_{no-halo}$ is the cross section for a projectile, with mass μ, scattering by the core-target interaction and is therefore very closely related to the experimental core-target elastic scattering.

The importance of eq.(105) is that it clarifies the relevant scattering angles and incident energies at which a halo of a given size and structure will be manifest as a deviation from the scattering due to a projectile which does not have the spatial extension associated with a loosely bound halo particle.

Eq. (105) is reminiscent of factorisations which occur in electron scattering when Born approximation and approximate distorted wave theories are used. Note, however, that the present analysis does not involve Born approximation in any sense. Only if all intermediate states are included do the second and higher order terms in the Born series factorise in this way [33]. The same argument obtains for the factorisation of the wavefunction in eq.(100).

^{11}Be is a good example of a binary, ^{10}Be+n, single neutron halo nucleus and ^{19}C is also a single neutron halo candidate [35]. Both systems have small $\alpha = m_n/m_P$ ratios. For ^{11}Be+^{12}C, there are small angle elastic scattering data [36] for both the ^{10}Be core and the ^{11}Be composite, but at energies of 59.4 MeV/A and 49.3 MeV/A, respectively. Ideally these data are required at the same energy per nucleon to provide the necessary information on V_{CT}, which is an essential ingredient in applications of eq.(105).

According to eq.(105) the formfactor $|F(Q)|^2$, which multiplies the point particle cross section, reflects the modifications to the scattering due to the composite nature of the projectile. In Figure 2 we show calculated squared formfactors as a function of the centre-of-mass angles which are appropriate for the elastic scattering of ^{11}Be (upper part) and ^{19}C (lower part) from ^{12}C at 49.3 MeV/A and 30 MeV/A, respectively. These calculations demonstrate the sensitivity of the formfactor to the halo properties. Conversely, they demonstrate the information about the halo-core relative motion wavefunction which is available in principle from halo nucleus elastic scattering data.

The strong deviations from unity shown in Figure 2 reflect in momentum space the long exponential tails of the halo wavefunctions we discussed in Section

1.1. In the notation of that Section, a neutron wavefunction with a λ-value corresponding to a typical non-halo nucleus the formfactor would hardly deviate at all from unity over the angular range of Figure 2.

For ^{11}Be, the halo is seen to result in a reduction in the elastic differential cross section by a factor of between 2 and 4 at 20°, compared to that for 'no-halo' scattering. There is also a significant sensitivity to the assumed rms separation of the valence and core particles.

For ^{19}C, the squared formfactors which result from a pure $2s_{1/2}$ (solid curve) or $1d_{5/2}$ (dashed curve) neutron state are shown. The departures from 'no-halo'

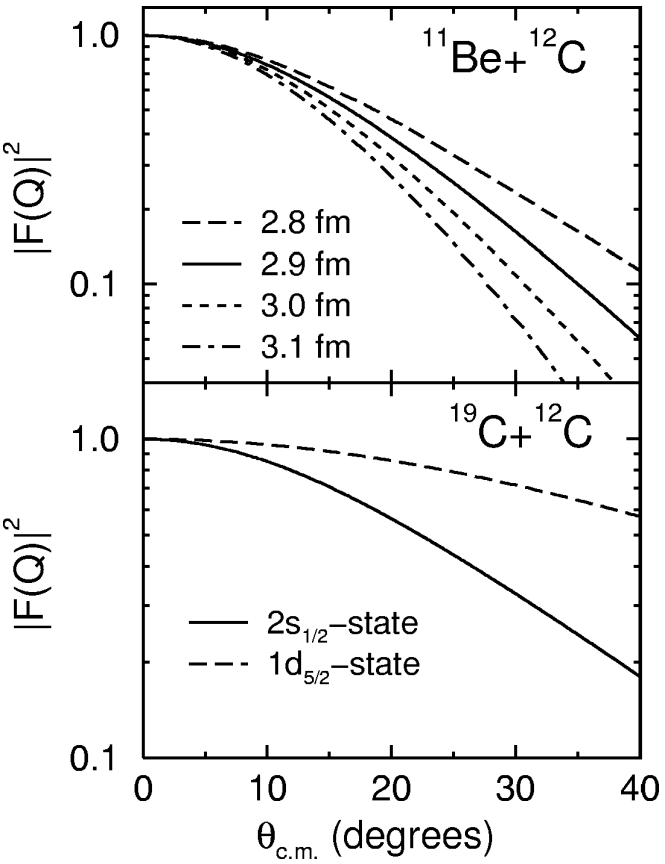

Fig. 2. Calculated $|F(Q)|^2$, as a function of centre-of-mass scattering angle for the elastic scattering of ^{11}Be (upper part) and ^{19}C (lower part) from ^{12}C at 49.3 MeV/A and 30 MeV/A, respectively.

scattering are predicted to be significantly different for a $2s_{1/2}$ and $1d_{5/2}$ valence neutron, with almost a factor of 2 difference in the cross sections at 20°. We note that, although the leading term in the expansion of the formfactor about $Q = 0$ gives a deviation from unity proportional to the mean squared separation of the core and valence particles in the projectile, the values of Q which enter in the examples above are such that this leading order term is inadequate and there is sensitivity to higher order moments except at the very smallest angles.

For ^{11}Be the wavefunctions were taken to be pure $2s_{1/2}$ neutron single particle states, with separation energy 0.503 MeV, calculated in a central Wood-Saxon potential [37]. By changing the binding potential geometry we generate ^{11}Be composites with different rms matter radii and hence $|F(Q)|^2$. For ^{19}C the ground state structure is presently uncertain with speculations of it being a pure $2s_{1/2}$ state, $1d_{5/2}$ state or a linear combination of such configurations [38]. The neutron separation energy was 0.240 MeV.

Figure 3 shows the elastic differential cross section angular distributions (ratio to Rutherford) for ^{11}Be+^{12}C scattering at 49.3 MeV/A calculated with a number of different models of the scattering mechanism.

The dashed curve shows the 'no-halo' projectile differential cross section $(d\sigma/d\Omega)_{no-halo}$ calculated using the core-target potential. It might be expected that the main effect of the extended size of the projectile could be accounted for by calculating the scattering by a potential $V_{fold}(R)$ which averages $V_{nT}(\boldsymbol{R}+\beta\boldsymbol{r}) + V_{CT}(\boldsymbol{R}-\alpha\boldsymbol{r})$ over the probability density for $\boldsymbol{r}$ predicted by the ground state halo density, *i.e.*

$$V_{fold}(R) = \int d\boldsymbol{r}[V_{nT}(\boldsymbol{R}+\beta\boldsymbol{r}) + V_{CT}(\boldsymbol{R}-\alpha\boldsymbol{r})]|\phi_0(r)|^2. \qquad (106)$$

The dot-dashed curve in Figure 3 shows the cross section calculated using the folding model interaction, eq.(106) . The similarity of the folding and 'no-halo' calculations makes clear that the effects associated simply with folding the core and valence particle interactions over the size of the halo are relatively minor compared with the effects taken into account in the solid curve. The latter is obtained using the result eq.(105) with the squared formfactor shown by the short dashed line (the 2.9 fm rms case of Fig.2).

The physical difference between the theory which produces the solid line and the 'folding' result is that the former does not assume that the projectile remains in its ground state during the scattering but correctly takes into account (insofar as the adiabatic approximation is adequate) the large projectile excitation and break up effects induced by the target. It is remarkable that such complicated multistep processes are fully accounted for by eq.(105) when the interaction between the halo and the target is ignored. Note, however, that at small angles the 'folding' diffraction pattern is shifted to smaller angles as one would expect for the more spatially extended potential of eq.(106).

We recall that the special case under discussion ignores the interaction between the valence neutron and the target. In fact this interaction is not negligible and must be taken into account in a detailed comparison with experiment. This

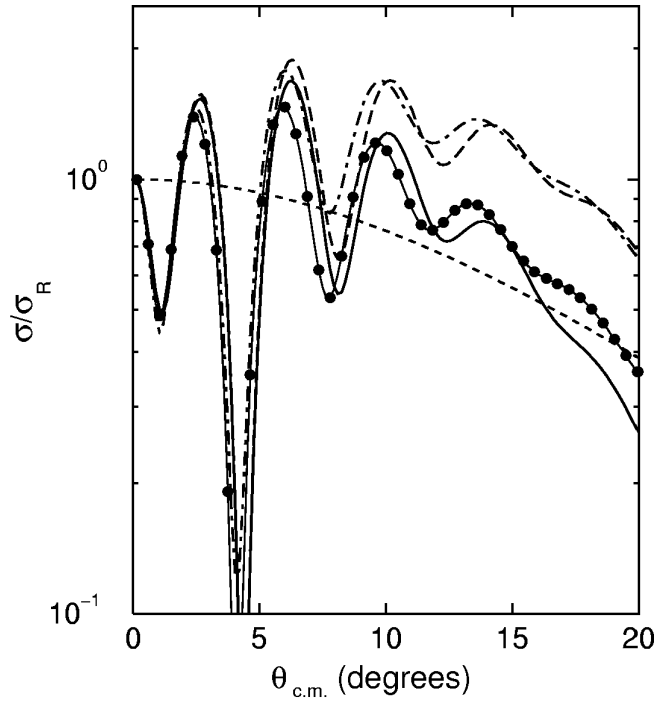

Fig. 3. Calculated elastic differential cross section angular distributions (ratio to Rutherford) for ^{11}Be+^{12}C scattering at 49.3 MeV/A. The curves are discussed in the text.

is not a difficulty since exact adiabatic calculations which include the interaction between all the halo particles and the target are possible for both two and three-body projectile systems [23,22]. Such calculations have also been carried out for 4- and 5-body projectiles within the eikonal approximation [40,41].

In Figure 4 we show the results of such adiabatic calculations for ^{11}Be+^{12}C scattering at 49.3 MeV/A. These include the neutron+^{12}C optical potential tabulated in [43], and correspond to the four ^{11}Be wavefunctions with different rms radii discussed in connection with Figure 2. The data are from [36]. We note that the behavior of the cross sections expected on the basis of the formfactors of Figure 2 and the insights the 'recoil model' provides are not effected in any major way by the neutron-target interaction. These results suggest that elastic scattering data of sufficient quality could yield independent information on halo structures.

The full circle symbols in Figure 3 are also full adiabatic model calculation including V_{nT}. They can be compared with the solid line results which are also adiabatic but do not include V_{nT}. The agreement is reasonable and suggests that

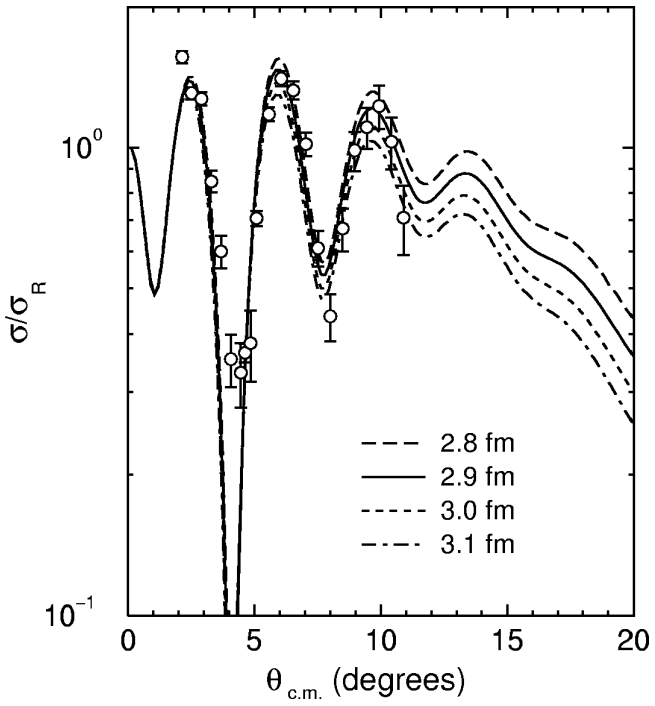

Fig. 4. Calculated elastic differential cross section angular distributions (ratio to Rutherford) for ^{11}Be+^{12}C scattering at 49.3 MeV/A calculated using the adiabatic approximation and including the neutron-target interaction.

V_{CT} dominates in this system, although the effects of the valence neutron-target interaction are not negligible.

The 'recoil model' teaches us that halo nucleus elastic scattering angular distributions are strongly affected by projectile excitation channels and the spatial size of the halo. These effects are principally manifest through a formfactor which depends only on the halo ground state wavefunction and whose square multiplies the 'no halo' cross section. The latter is defined to be the cross section for a particle with the mass of the projectile but which interacts with the target through the core-target potential with no folding in of the halo density. This potential is in principle to be obtained from core-target scattering at the same energy per nucleon as that of the halo nucleus scattering of interest. In fact to a good approximation at the energy used in Figure 2 the 'no halo' cross section can be evaluated directly from the core-target cross section at the same energy per nucleon and momentum transfer.

5 Other applications of the 'recoil model'

We have already mentioned the application of the adiabatic approximation to the calculation of reaction cross sections for halo nuclei in Sub-section 4.1. The approximation has also been widely used to treat deuteron break-up effects in stripping and pick-up reactions (see [28] and [48] and references therein). The special case of the 'recoil model' has had some other interesting recent applications.

5.1 Coulomb break-up of neutron halo nuclei

One situation when the neglect of the interaction between the halo neutron and the target can be justified is when Coulomb forces dominate. We will now explain how the 'recoil model' can be used used as the starting point of a non-perturbative quantum mechanical theory of the Coulomb break-up of neutron halo nuclei. [45–47].

Some care is required in using the adiabatic wavefunction to calculate break-up amplitudes. The explicit form of the solution eq.(100) makes it clear that at large core-neutron separations, $r \to \infty$, the presence of the factor ϕ_0 means that, independently of the details of the 3-body Hamiltonian, $\phi_{\boldsymbol{K}}^{(+)\mathrm{A}dia}(\boldsymbol{r}, \boldsymbol{R})$ vanishes exponentially. The large r region is where one would expect to look for breakup flux and therefore $\phi_{\boldsymbol{K}}^{(+)\mathrm{A}dia}(\boldsymbol{r}, \boldsymbol{R})$ can not be used to calculate break-up amplitudes by looking at its asymptotic form.

It follows that to use the three-body wave function of eq.(100) to calculate a Coulomb breakup amplitude we must restrict its use to regions of the six-dimensional $(\boldsymbol{r},\boldsymbol{R})$ space where r is finite. In particular, we do not attempt to extract the breakup amplitude from the asymptotics of our approximate adiabatic solution. Ref [45] procceeds instead as follows.

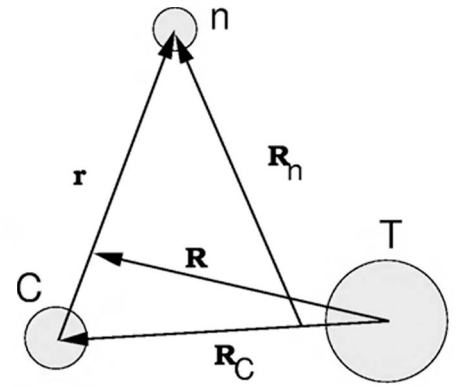

Fig. 5. Definition of the co-ordinate system adopted for the core, valence, and target three-body system.

We first rewrite the *exact* three-body Schrödinger equation of eq. (8), prior to having made any adiabatic approximation, as

$$[E - T_{\boldsymbol{R}_n} - T_{\boldsymbol{R}_C} - V_{CT}(\boldsymbol{R}_C)]\,\Psi^{(+)}_{\boldsymbol{K}}(\boldsymbol{r},\boldsymbol{R}) = V_{nC}(\boldsymbol{r})\Psi^{(+)}_{\boldsymbol{K}}(\boldsymbol{r},\boldsymbol{R}) \quad . \tag{107}$$

where $T_{\boldsymbol{R}_n}$ and $T_{\boldsymbol{R}_C}$ are the kinetic energies in the coordinates $\boldsymbol{R}_n$ and $\boldsymbol{R}_C$. These Jacobi co-ordinates are defined so that $\boldsymbol{R}_n$ connects n with the centre-of-mass of C and T, and $\boldsymbol{R}_C$ is the $C-T$ separation (see Figure 5). They are particularly suitable when $V_{nT} = 0$.

Because of the short ranged factor $V_{nC}(\boldsymbol{r})$ the right-hand-side eq.(107) requires the wqavefunction $\Psi^{(+)}_{\boldsymbol{K}}(\boldsymbol{r},\boldsymbol{R})$ only for finite separations $\boldsymbol{r}$. We can therefore justifiably evaluate it using the adiabatic wavefunction $\phi^{(+)\mathrm{A}dia}_{\boldsymbol{K}}(\boldsymbol{r},\boldsymbol{R})$ as a good approximation to $\Psi^{(+)}_{\boldsymbol{K}}$. This yields the inhomogeneous equation

$$[E - T_{\boldsymbol{R}_n} - T_{\boldsymbol{R}_C} - V_{CT}(\boldsymbol{R}_C)]\,\hat{\Psi}^{(+)}_{\boldsymbol{K}}(\boldsymbol{r},\boldsymbol{R}) = V_{nC}(\boldsymbol{r})\phi^{(+)\mathrm{A}dia}_{\boldsymbol{K}}(\boldsymbol{r},\boldsymbol{R}) \tag{108}$$

For a given adiabatic wavefunction eq.(108) can be solved using Green function techniques to give a solution which has the correct 3-body asymptotics [45] and from which an expression for the break-up amplitude into any final state can be read off. The break-up amplitude calculated in this way for a three-body final state with Jacobi momenta $\boldsymbol{q}_C$ and $\boldsymbol{q}_n$ corresponding to $\boldsymbol{R}_n$ and $\boldsymbol{R}_C$, is found to be [45]

$$\bar{T}_{\mathrm{AD}}(\boldsymbol{q}_n\boldsymbol{q}_C,\boldsymbol{K}) = \left\langle e^{i\boldsymbol{q}_n\cdot\boldsymbol{R}_n}\chi^{(-)}_{\boldsymbol{q}_C}(\boldsymbol{R}_C)\,|V_{nC}(\boldsymbol{r})|\,\bar{\Psi}^{(+)}_{\boldsymbol{K}}(\boldsymbol{r},\boldsymbol{R})\right\rangle \ , \tag{109}$$

where $\chi^{(-)}_{\boldsymbol{q}_C}$ is an Coulomb distorted wave with in-going scattered waves describing the scattering of the outgoing core by the target.

It is shown in [45] that the break-up amplitude $\bar{T}_{\mathrm{A}D}$ of eq.(109) is exactly the same as the expression obtained by using the adiabatic wavefunction directly in the exact post-form transition amplitude.

Note that although the adiabatic approximation neglects the projectile excitation energy in the calculation of the adiabatic three-body wavefunction $\bar{\Psi}^{(+)}_{\boldsymbol{K}}$, this does not mean that the break-up amplitude is calculated using the the zero adiabaticity parameter $\xi = 0$ limit, of semi-classical theories [49]. As the analysis above shows, $\bar{T}_{\mathrm{A}D}$ includes a final state wavefunction with the correct kinematics and excitation energies required by energy conservation, unlike analogous $\xi = 0$ semi-classical calculations.

5.2 Break-up transition amplitude

It is shown in [45] that the amplitude $\bar{T}_{\mathrm{AD}}$ of eq.(109) factorises exactly as

$$\begin{aligned}\bar{T}_{\mathrm{AD}}(\boldsymbol{q}_n\boldsymbol{q}_C,\boldsymbol{K}) \quad &= \quad \left[\int d\boldsymbol{r}\, e^{-i\boldsymbol{P}_n\cdot\boldsymbol{r}}V_{nC}(\boldsymbol{r})\phi_0(\boldsymbol{r})\right] \\ &\quad \times \left[\int d\boldsymbol{R}_C\, e^{-i\boldsymbol{Q}_n\cdot\boldsymbol{R}_C}\chi^{(-)*}_{\boldsymbol{q}_C}(\boldsymbol{R}_C)\chi^{(+)}_{\boldsymbol{K}}(\boldsymbol{R}_C)\right] \\ &= \quad \langle \boldsymbol{P}_n|V_{nC}|\phi_0\rangle \ \left\langle \boldsymbol{Q}_n,\chi^{(-)}_{\boldsymbol{q}_C}|\chi^{(+)}_{\boldsymbol{K}}\right\rangle \quad ,\end{aligned} \tag{110}$$

where we have defined $\boldsymbol{P}_n = \boldsymbol{q}_n - \alpha\boldsymbol{K}$ and $\boldsymbol{Q}_n = \frac{m_T}{m_T+m_C}\boldsymbol{q}_n$.

The two factors in Eq.(110) separate out the structure and dynamical parts of the calculation. The overlap of the three continuum functions, $\langle \boldsymbol{Q}_n, \chi^{(-)}_{\boldsymbol{q}_C} | \chi^{(+)}_{\boldsymbol{K}} \rangle$, can be evaluated in closed form and expressed in terms of the bremsstrahlung integral [45]. This factor now contains all the dynamics of the breakup process and is readily calculated for given incident and outgoing momenta in terms of the charges and masses of C and T.

The structure of the projectile enters through the vertex function $\langle \boldsymbol{P}_n | V_{nC} | \phi_0 \rangle$ and is also simply evaluated given any structure model for the projectile. In Coulomb dissociation, momentum can be transferred to the valence particle only by virtue of its interaction V_{nC} with the core. Since the term $\alpha \boldsymbol{K}$ in $\boldsymbol{P}_n$ is the fraction of the incident momentum of the projectile which is carried by the valence particle, this structure vertex displays explicitly this momentum transfer from the ground state via V_{nC}.

The result (110) allows a fully finite-range treatment of the core-neutron particle interaction V_{nC} without any approximation additional to the adiabatic assumption. The theory is thus applicable to projectiles with any ground state orbital angular momentum structure, and also includes breakup contributions from all contributing Coulomb multipoles and relative orbital angular momenta between the neutron and core fragments. Unlike DWBA theories it includes the initial and final state interactions V_{CT} and V_{nC} to all orders.

The theory has been successfully applied to the break-up of high energy deuterons in the forward direction [45,50], and with appropriate generalisation, to the Coulomb break-up of one- and two-neutron halo nuclei [46,47]. Here we briefly mention the case of deuteron break-up.

The (d, pn) elastic breakup data have been measured at the RIKEN Accelerator Research Facility, Saitama, at 140 and 270 MeV, and at the Research Centre for Nuclear Physics (RCNP), Osaka, at 56 MeV in a kinematical condition of $\theta_p \approx \theta_n \approx 0°$. The targets were ^{12}C, ^{28}Si, ^{40}Ca, ^{90}Zr, ^{118}Sn, ^{165}Ho and ^{208}Pb at E_d=140 and 270 MeV and ^{12}C, ^{40}Ca, ^{90}Zr, and ^{208}Pb at E_d=56 MeV.

The calculations and data at 140 MeV are compared in Figure 6 for all measured targets. The errors shown in the figure are statistical only. The solid lines show the elastic breakup cross sections, as a function of the detected (laboratory) proton energy, calculated using eq.(110). The overall agreement of the calculated magnitudes, Z_T-dependence, and the proton energy dependence, with the data is good and improves with increasing target charge. The factor of 40 increase in the magnitudes of the measured cross sections in going from ^{12}C to ^{208}Pb is seen to be well reproduced as a function of Z_T. Figure 6 does not, however, reveal the complex way that the calculated cross sections are built up in the integrations over the experimental solid angle acceptances. We refer to refs. [45,50] for these crucial considerations and for a full discussion of the results at all 3 incident energies.

We emphasise again that these calculations are non-perturbative and fully quantum mechanical. They are based on a theory which is very different from the DWBA both in principle and in terms of the numerical results obtained.

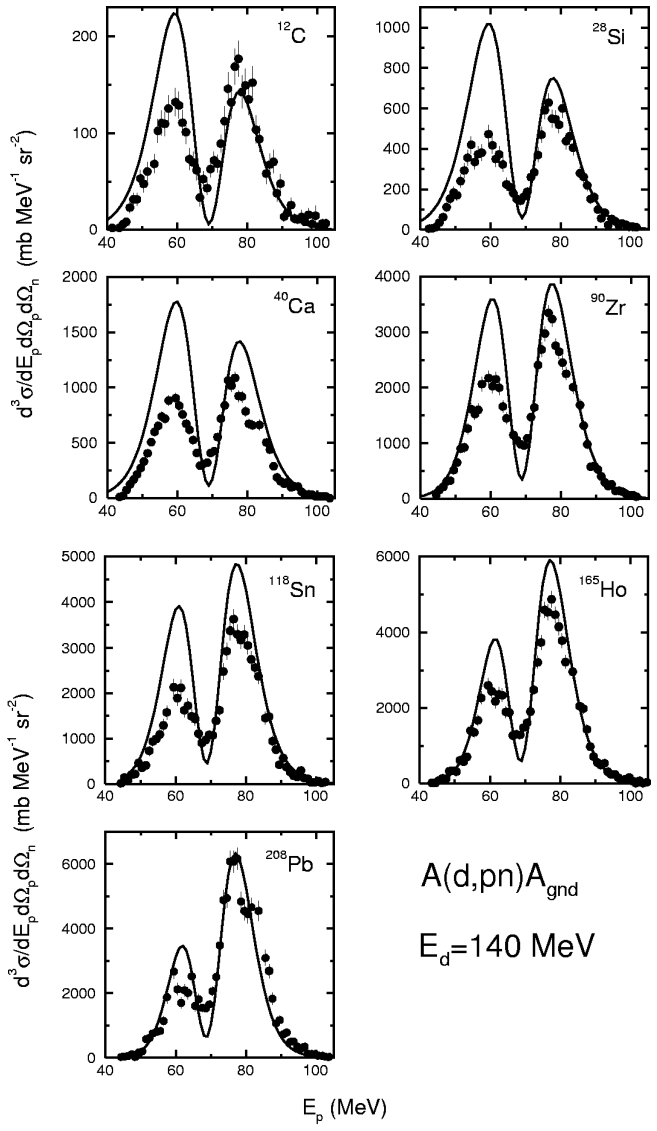

Fig. 6. Experimental and calculated adiabatic model (solid curves) triple differential cross sections for deuteron break-up near 0° in the laboratory frame at E_d =140 MeV. The calculations are averaged over the neutron and proton solid angles actually used in the experiment. The data are from ref.[50].

These differences are discussed in detail in ref. [45]. Final state interactions between the outgoing fragments are fully taken into account, apart from the nuclear interaction between the neutron and the target. The nuclear interaction between the neutron and the proton is accounted for to all orders.

The results of ref.[45,50] are consistent with an underlying physical picture in which Coulomb breakup is the dominant mechanism. There are, however, indications of a missing and interfering contribution, particularly on the lighter targets which may result from breakup by the nuclear forces between the projectile and the target which are ignored in the model of refs. [45,50].

5.3 Deuteron stripping and pick-up on halo nuclei

We have already mentioned the use of the adiabatic approximation to treat multi-step processes via deuteron break-up channels in stripping and pick-up reactions. This is special case 1. of Sub-section 4.2. A recent development has been to use the adiabatic approximation to additionally treat excitations of a halo nucleus produced as the final state in a (d,p) reaction. It is shown in ref. [48] how the simplicity of the 'recoil model' can be exploited to give a very convenient way of evaluating what would otherwise be a very complicated multi-channel calculation. See also [34] for an application to recent ^{11}Be(p,d)^{10}Be data from GANIL [51].

6 Conclusions

I hope I have conveyed to you some of the fascination of nuclear reactions with halo and other weakly bound nuclei. New experiments are giving a new challenge to theory. Groups in Surrey and elsewhere are working very hard to meet this challenge.

A particular challenge to theory is to understand and evaluate the leading corrections to the adiabatic theory and to learn how to apply them to transfer and break-up reactions. There is also a need to understand how the few-body models of reactions described here can be related to the underlying many-fermion structure of the halo nucleus.

Acknowledgements

I am grateful to J.M. Arias and M. Lozano for giving me the opportunity to come to Seville and lecture at their Summer School. I very much enjoyed meeting and discussing physics with the participants.

References

1. I. Tanihata H. Hamagaki, O. Hashimoto, S. Nagamiya, Y. Shida,N. Yoshikawa, O. Yamakawa, K. Sugimoto, T. Kobayashi, D.E. Greiner, N. Takahashi, and Y. Nojiri, Phys. Lett. **B160**, 380 (1985)

2. I. Tanihata, T. Kobayashi, O. Yamakawa, T. Shimoura, K. Ekuni, K. Sugimoto, N. Takahashi, T. Shimoda and H. Sato: Phys. Lett. **B206**, 592 (1988)
3. I. Tanihata, H. Hamagaki, O. Hashimoto, Y. Shida, N. Yoshikawa, K. Sugimoto, O. Yamakawa, T. Kobayashi, and N. Takahashi: Phys. Rev. Lett. **55**, 2676 (1985)
4. P.G. Hansen, A.S. Jensen and B. Jonson: Annual Rev. Nucl. Part. Sci. **45**, 591 (1995)
5. I.J. Thompson, B.V. Danielin, V.D. Efros, J.S. Vaagen, J.M. Bang, and M.V. Zhukov: Phys. Rev. **C61**, 024318 (2000)
6. H. Feshbach: Ann. Phys.(N.Y.) **5**, 357 (1958)
7. G. R. Satchler: "Direct Nuclear Reactions", Oxford University Press, Oxford, 1983
8. B. Lippmann and J. Schwinger: Phys. Rev. **79**, 469 (1950)
9. M.L. Goldberger and K M. Watson: "Collision Theory",Wiley, New York, 1964
10. R. Taylor: "Scattering Theory", Wiley, New York, 1972
11. D. M. Brink and G. R. Satchler: "Angular Momentum", 2nd Edition, Clarendon Press, Oxford, 1968
12. I.J. Thompson: Comp. Phys. Rep. **7**, 167 (1988)
13. I.J. Thompson: "Methods of direct reaction theory" in "Scattering" eds. R.Pike and P.Sabatier, Academic Press, Chapter 3.1.2, in the press
14. J. Gomez-Camacho and R.C. Johnson: "Polarisation in nuclear physics" in "Scattering" eds. R.Pike and P.Sabatier, Academic Press, Chapter 3.1.4, in the press
15. M. Kamimura, M. Yahiro, Y. Iseri, H. Kameyama, Y. Sakuragi and M. Kawai: Prog. Theor. Phys. Suppl. **89**, 1 (1986)
16. N. Austern, Y. Iseri, M. Kamimura, M. Kawai, G. Rawitscher and M. Yahiro: Phys. Rep. **154**, 125 (1987)
17. F.M. Nunes and I.J. Thompson: Phys. Rev. **C59**, 2652 (1999)
18. R. J. Glauber: in "Lectures in Theoretical Physics", edited by W E Brittin (Interscience, New York, 1959), Vol. 1, pp 315-414
19. R.C. Johnson and P.J.R. Soper: Phys. Rev. **C1**, 976 (1970)
20. H. Amakawa, S. Yamaji, A. Mori and K. Yazaki: Phys. Lett. **B82**, 13 (1979)
21. J.S. Al-Khalili and R.C. Johnson: Nucl. Phys. **A546**, 622 (1992)
22. J.A. Christley, J.S. Al-Khalili, J.A. Tostevin and R.C. Johnson: Nucl. Phys. **A624**, 275 (1997)
23. I.J. Thompson: Computer Programme ADIA, Daresbury Laboratory Report, 1984, unpublished
24. J.S. Al-Khalili and J.A. Tostevin: Phys. Rev. Lett. **76**, 3903 (1996)
25. J.S. Al-Khalili, I.J. Thompson and J.A. Tostevin: Phys. Rev. **C54**, 1843 (1996)
26. J.A. Tostevin, R.C. Johnson, J.S. Al-Khalili: Nucl. Phys. **A630**, 340c (1998)
27. R.C. Johnson and C.J. Goebel: Phys. Rev. **C61**, 027603 (2000)
28. A. Laid , J.A. Tostevin and R.C. Johnson: Phys. Rev. **C48**, 1307 (1993)
29. J.S. Al-Khalili and J.A. Tostevin: "Few-body models of nuclear reactions" in "Scattering" eds. R.Pike and P.Sabatier, Academic Press, Chapter 3.1.3, in the press
30. J. D. Harvey, R.C. Johnson: Phys. Rev. **C3**, 636 (1971)
31. R.C. Johnson, J.S. Al-Khalili, J.A. Tostevin: Phys. Rev. Lett. **79**, 2771 (1997)
32. R.C. Johnson: J. Phys. G: Nucl. Part. Phys. **24**, 1583 (1998)
33. R.C. Johnson: "Elastic scattering and elastic break-up of halo nuclei in a "recoil model" in Proc. Eur. Conf. On Advances in Nuclear Physics and Related Areas, Thessoloniki, Greece, July 8-12, 1997, (eds. D.M. Brink, M.E. Grypeos and S.E. Massen, Giahoudi-Giapouli, Thessaloniki, 1999) 156-162

34. R.C. Johnson, J.S. Al-Khalili, N.K.Timofeyuk and N. Summers: Nuclear reactions involving weakly bound nuclei, "Experimental Nuclear Physics in Europe", 21-26 June 1999, Seville, Spain (eds. B. Rubio, M. Lozano and W. Gelletly, AIP Conf Proc. 495 American Institute of Physics, 1999) 297-300
35. D. Bazin et al.: Phys. Rev. Lett. **74**, 3569 (1995)
36. P. Roussel-Chomaz: private communication, 1996
37. J.S. Al-Khalili, J.A. Tostevin and J.M. Brooke: Phys. Rev. **C55**, R1018 (1997)
38. D. Ridikas, M.H. Smedberg, J.S. Vaagen and M.V. Zhukov: Europhys. Lett. **37**, 385 (1997)
39. G.D. Alkhazov, M.N. Andronenko, A.V. Dobrovosky, P. Egelhof, G.E. Gavrilov, H. Geissel, H. Irnich, A.V. Khanzadeev, G.A. Korolev, A.A. Lobodenko, G. Münzenberg, M. Mutterer, S.R. Neumaier, F. Niskel, W. Schwab, D.M. Seliverstov, T. Suzuki, J.P. Theobald, N.A. Timofeev, A.A. Vorobyov and V.I. Yatsoura: Phys. Rev. Lett. **78**, 2313 (1997)
40. J.A. Tostevin, J.S. Al-Khalili, M. Zahar, M. Belbot, J. J. Kolata, K. Lamkin, D.J. Morrissey, B.M. Sherrill, M. Lewitowicz, A.H. Wuosmaa: Phys. Rev. **C56** R2929 (1997)
41. J.S. Al-Khalili and J.A. Tostevin: Phys. Rev **C57**, 1846 (1998)
42. J.A. Tostevin and J.S. Al-Khalili: Phys. Rev. **C59**, R5 (1999)
43. J.S. Al-Khalili, I.J. Thompson and J.A. Tostevin: Nucl. Phys. **A581**, 331 (1995)
44. J. A. Tostevin, R.C. Johnson and J.S Al-Khalili: Nucl. Phys. **A630**, 340c (1998)
45. J.A. Tostevin, S. Rugmai and R. C. Johnson: Phys. Rev. **C57**, 3225 (1998)
46. P. Banerjee, I. J. Thompson, and J. A. Tostevin: Phys. Rev. **C58** 1042 (1998)
47. P. Banerjee, J. A. Tostevin, and I. J. Thompson: Phys. Rev. **C58**, 1337 (1998)
48. N.K. Timofeyuk and R.C. Johnson: Phys. Rev. **C59**, 1545 (1999)
49. G. Baur, and H. Rebel: J. Phys. G: Nucl. Part. Phys. **20**, 1 (1994)
50. J.A. Tostevin, S. Rugmai, R.C. Johnson, H. Okamura , S. Ishida , N. Sakamoto, H. Otsu, T. Uesaka, T. Wakasa , H. Sakai , T. Niizeki, H. Toyokawa, Y. Tajima , H.Ohnuma, M. Yosoi, K. Hatanaka , T. Ichihara: Phys. Lett. **B424**, 219 (1998)
51. S. Fortier, S. Pita, J.S. Winfield, W.N. Catford, N.A. Orr, J. Van de Wiele, Y. Blumenfield, R. Chapman, S.P.G. Chappell, N.M. Clarke,N. Curtis, M. Freer, S. Gales, K.L. Jones, H. Langevin-Joliot, H. Laurent, I.Lhenry, J.M. Maison, P. Roussel-Chomaz, M. Shawcross, M. Smith, K. Spohr, T. Suomijarvi and A. de Vismes: Phys. Lett. **B461**, 2 (1999)

Nuclear physics away from the valley of stability

Juha Aysto

ISOLDE, CERN, Geneva, Switzerland, *and*
Department of Physics, University of Jyvaskyla, Finland

Abstract. Recent experimental developments in studies of exotic nuclei far from the valley of stability are discussed in these lectures. Discussion starts with general aspects related to the production of exotic nuclei and nuclear beams, including some selected examples. Following this technical part some recent advances in the structure studies of very neutron-rich nuclei and heavy nuclei are presented. Finally, newest progresses on low-energy ion manipulation techniques are described.

1 Introduction

Studies of nuclei far from the valley of beta stability offer new opportunities for research in the areas of nuclear structure physics, atomic physics and chemistry as well as in astrophysics, material science and biophysics. In nuclear physics there are a number of identified and exciting topics to be addressed in the coming years together with unexpected phenomena always related to the new frontiers of physics. The well-defined goals of nuclear structure physics will be (i) defining the positions of the drip-lines, especially for neutrons, (ii) probing the evolution of nuclear structure within long isospin chains, (iii) searching for the existence boundaries of the heaviest elements, (iv) understanding the neutron halo and continuum structure of nuclei at the drip lines. In addition, the microscopic nature of pairing correlations between like and unlike nucleons, exotic collective modes and shell structure as well as the spin-orbit force are still to large extent not understood on the microscopic level. These goals, each a major research field in itself, will necessarily have to be coupled with research on nuclear reaction mechanisms associated with projectiles and/or targets of abnormal neutron-to-proton ratios. In addition, certain key isotopes along the Z=N line provide an ideal laboratory for testing the validity of the standard model through precision measurements of weak decays as well as testing the atomic parity violation through studies of chains of atoms, such as radioactive Francium isotopes. In nuclear astrophysics, energy generation and element synthesis in various astrophysical sites depend on nuclear processes involving exotic nuclei far from the valley of stability.

Experimental studies of exotic nuclei employ nuclear reactions both with stable projectiles and with radioactive beams. These two approaches are complementary, although the emphasis is presently moving towards radioactive ion beam driven experiments. The following list shows what information different experimental approaches can provide us on nuclei far from stability. It also includes experiments which involve various techniques developed to manipulate

J.M. Arias and M. Lozano (Eds.): LNP 581, pp. 292–315, 2001.
© Springer-Verlag Berlin Heidelberg 2001

ions and their motion and modify ion beams over a broad energy range from meV to GeV. These techniques are having an important impact on sensitivity of handling radioactive species. Ultimately, single isotope experiments are necessary for reaching very far from stability in any direction.

- **Stable projectile beams and targets**
  - spectroscopy studies of exotic nuclei
    - excited structures: E^*, I^π, τ
    - decay properties: Q-values, lifetimes τ_i, correlations
    - ground state properties: m, μ, Q, $< r^2 >^{1/2}$
    - limits of stability: S_n, S_p, B_F
  - production of radioactive beams
- **Fast radioactive beams**
  - post-accelerated low energy beams
    - (sub) Coulomb-barrier studies
    - transfer reaction studies
    - astrophysical reactions
  - secondary high energy beams
    - identification and spectroscopy studies
    - scattering and reaction experiments
- **Manipulation of radioactive ion beams**
  - deceleration, storing and cooling of fast ions (GeV $\rightarrow$ MeV)
  - cooling, bunching and trapping of slow ions (keV $\rightarrow$ meV)

Fig. 1 shows the nuclear chart, as we know it today. As we can observe the experiments are already probing the proton-drip line well beyond Z=82 but instead the knowledge on nuclei near the neutron-drip line and in the heavy element region is only superficial, and therefore the future experiments will be addressing these important unknown regions. In these lectures general aspects related to the production of exotic nuclei and nuclear beams are discussed with some selected examples concerning the recent advances in the structure studies of very neutron-rich nuclei and heavy nuclei. Finally, newest progresses on low-energy ion manipulation techniques are described.

2 Production of exotic nuclei

2.1 Production reactions

Commonly used nuclear reactions to produce nuclei far from the valley of beta-stability or in the heavy element region are (i) complete fusion reactions induced by light or heavy ions, (ii) low-energy fission either spontaneous or induced by thermal neutrons or photons, (iii) intermediate energy fission induced by charged particles, (iv) transfer or deep-inelastic peripheral collisions near the Coulomb barrier energies or (v) high-energy collisions. In all these reactions, the process has a typical two-step mechanism. The first step involves the formation of an excited intermediate nucleus and the second step is evaporation or decay of this

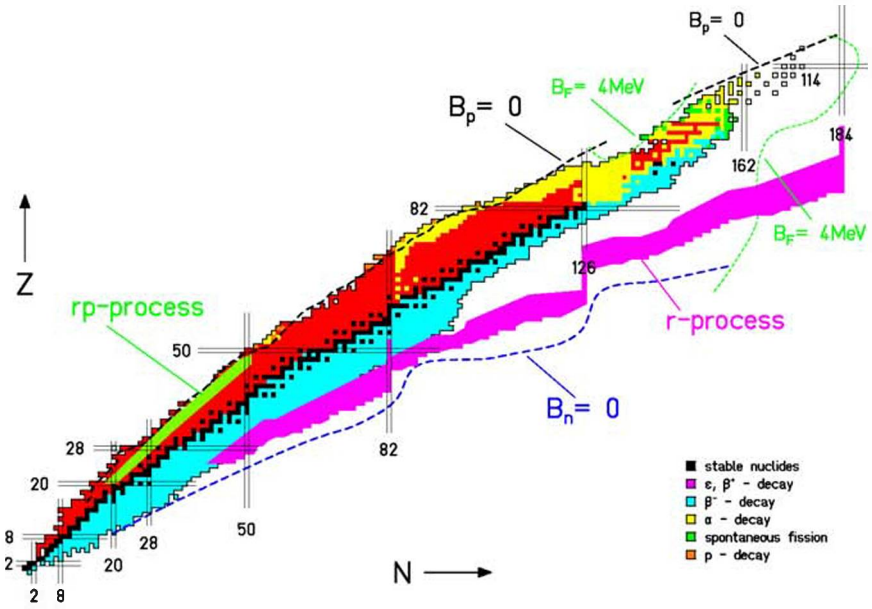

Fig. 1. The nuclear chart which includes the current knowledge of atomic nuclei as shaded areas. It also shows the estimated limits of existence of nuclei against proton and neutron emission and spontaneous fission. From ref. [1].

intermediate system. Due to the sensitivity of the second step on the binding energies of emitted particles, it is difficult to reliably calculate the cross sections close to the proton-drip line, where the binding energy of the least bound proton approaches zero.

Fusion evaporation reactions induced by light proton-rich projectiles, p or ^{3}He, have shown to be very useful for producing light proton rich nuclei below Calcium. A good example of such a reaction is p+^{24}Mg $\rightarrow$ ^{22}Al+3n, which was used in the first study of the two-proton radioactivity of ^{22}Al [2]. On the other hand, the heavy-ion induced reactions are necessary for synthezising heavier exotic isotopes in the nuclear chart above Calcium. A nice example here is the ^{40}Ca+^{58}Ni reaction which leads to a compound system ^{98}Ag, which via subsequent evaporation produces large number of neutron-deficient nuclei close to the Z=N line just below the doubly magic ^{100}Sn isotope, for example see ref. [3]. In heavy element research two different approaches are used. The cold fusion reactions utilize the doubly magic ^{208}Pb or an odd proton ^{209}Bi as targets and beams of neutron-rich stable isotopes in the Ni to Ge region as projectiles [4]. Due to the positive reaction Q-values the compound systems can be produced (as cold) at low excitation energy, just below the energy of the Coulomb barrier. This leads to a dominance of a 1n or a 2n evaporation channels. In another variant, heavier actinide targets such as ^{244}Pu, are bombarded with light heavy ion beams leading to more neutron-rich compound systems but with considerably

higher excitation energy which then results in higher neutron multiplicity in the exit channel [5]. In both cold and hot fusion the compound nucleus formation probability is suffering from the fast competing fission process so that typical total cross sections for the heaviest known elements are in the 0.1 or 1 picobarn level. A common problem in addition to small cross section is the narrowness of the excitation function which is expected to be as small as of the order of couple of MeV only.

Fission reaction is the most important reaction to produce highly neutron-rich nuclei in the mass region between A=70 and 160. Thermal-neutron induced fission reaction in combination with Isotope Separation On-Line technique has been producing beams of exotic nuclei for three decades now, see ref. [6] as an example of a reactor based facility at Studsvik, Sweden. With a well-known difficulty of low production rates for symmetric fission this reaction is well complemented by intermediate energy fission which has high cross sections for symmetric fission reactions. Typical examples of the latter fission mode are the intermediate energy fission (E^* = 20-40 MeV) produced in proton + uranium reactions [7,8], or fissioning of fast relativistic primary uranium or secondary projectiles in flight where typical excitation energies of the order of 10-20 MeV are involved. In fission by flight kinematically well focused beam of secondary fragments is obtained and high sensitivity in reaching very far from the valley of stability is reached. For example, nuclei as heavy as ^{110}Zr and ^{78}Ni [9] have been observed in these reactions. However, the intensities are yet too small for precision experiments by nuclear spectroscopy.

Fig. 2 shows a typical mass yield curve in fission as modelled by Rubchenya [10], where three different modes of fission are observed. One symmetric and three different asymmetric fission modes, of which the highly asymmetric mode, the super-asymmetric fission, was found in experiments at the IGISOL mass separator at Jyvaskyla [11]. The super-asymmetric mass division is influenced by the nuclear shells at Z =28 and N = 50 and by the tails of the second asymmetric component and the symmetric component, whose contribution is changing with excitation energy of the fissioning nucleus, as demonstrated in Fig. 3. This reaction mode can reach extreme light masses in fission, as exemplified in recent experiments on neutron-rich Co and Ni isotopes at the Leuven isotope separator facility [12].

Fragmentation reactions as a means to produce exotic nuclei far from the valley of stability were "invented" at Berkely in the late 70's. In these first experiments the energetic beams of ^{40}Ar and ^{48}Ca ions were fragmented at about 1 GeV/nucleon energies and several exotic new isotopes were discovered. Further experiments on secondary fragments lead to the discovery of the extended size of the ^{11}Li isotope [14] which soon was interpreted as a neutron halo around the ^{9}Li core nucleus [15]. Since then, fragmentation reactions at several laboratories have been utilized in probing the limits of nuclei along the proton and neutron drip-lines in a broad energy range from some 50 MeV/nucleon up to 1 GeV/nucleon [16]. Today, the proton drip-line is well characterized all the way up to Z=83 whereas the neutron-drip line is believed to have been reached

only up to oxygen. Fragmentation provides favourable conditions for kinematical focusing of the secondary particles which therefore can be easily separated by magnetic separators from the primary beam and even from each other. The main difficulty lies in the fact that reaction products are very energetic and experiments requiring slow ions are made difficult.

Inverse process to projectile fragmentation, the spallation or a fragmentation of a heavy target by energetic protons has long been used as production reactions at the so called ISOL facilities. This process is presently used at two major facilities, ISOLDE at CERN [17,18] and ISAC at TRIUMF in Canada [19].

2.2 Production of radioactive beams

There are two basic methods to produce radioactive beams. One relies on the Isotope Separator On-Line (ISOL) method and the other one is called In-Flight, see ref. [1] for extensive presentations of both techniques.

The key parameter characterising different production and separation methods is the luminosity L defined as,

$$L = N_p N_T \quad ,$$

Where N_p is the projectile beam intensity and N_T is the target thickness. For calculating the production rate, one needs the luminosity and the production cross section as well as the total efficiency of the experimental setup,

$$N_F = L\sigma\epsilon \quad ,$$

where σ is a cross section and ϵ is an efficiency of a separator or a spectrometer system. In Table 1 some typical examples of different reaction/production scenarios are presented.

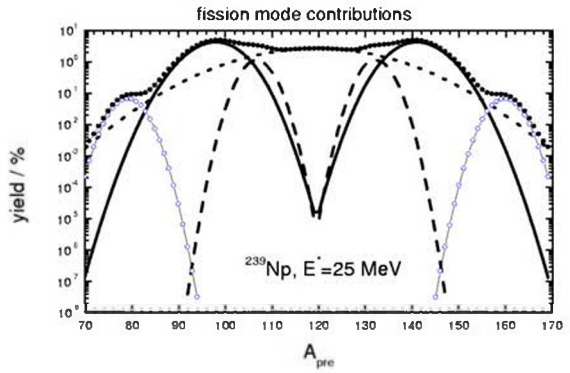

Fig. 2. Mass distribution of fission products from p+^{238}U compound fission at E*=25 MeV of the compound nucleus.

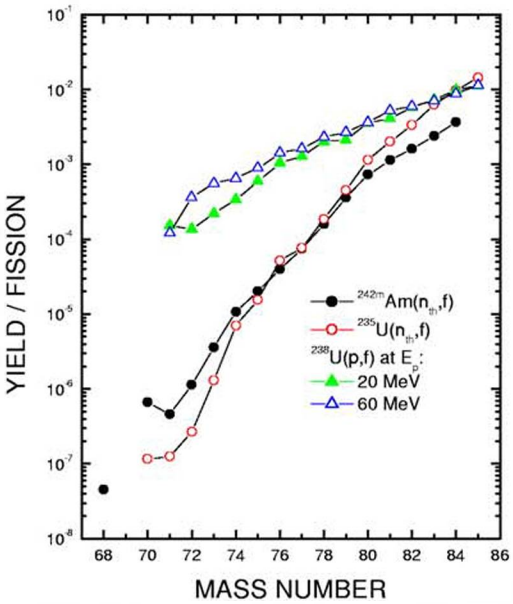

Fig. 3. Comparison of the fission fragment yields measured in proton induced fission of ^{238}U at 20 and 60 MeV to the thermal n-induced yields of ^{235}U and ^{242}Am, see ref. [13].

In summary, the decisive factors in selecting the production method for a specific experiment are the luminosity, the cross section and the efficiency. This approach does not show an important third dimensions, the time axis. For example, although the luminosity is very high for target spallation reactions, the strong dependence of the delay time on the Z of the isotope may cause large differences on the rates for different half-life nuclei.

2.3 ISOLDE facility at CERN

The idea of the Isotope Separator On-Line (ISOL) technique is to produce clean mass separated beams of rare radioactive isotopes in a continuous process. The common operating principles of all ISOL systems are stopping, acceleration and mass separation of the reaction products. The main operational differences between various ISOL techniques, however, are on the stopping of the reaction products and on the following ionisation process, required for the acceleration stage.

At ISOLDE (Fig.4), radioactive nuclides are produced in thick high-temperature targets via spallation, fission or fragmentation reactions [17]. For a review of ISOLDE physics the reader is referred to a recent special issue of Hyperfine Interactions [20]. The targets are placed in the external proton beam of the PS Booster. In the PS Booster four small synchrotrons pre-accelerate protons,

Table 1. Typical examples of different reaction/production scenarios

Thermal-n induced fission $N_p \approx 10^{12-14}\ \ s^{-1}$, $N_T \approx\ \ 1\ g/cm^2 \approx 2.5\ 10^{21}\ \ atoms/cm^2$	$L \approx 10^{9-11}\ barn^{-1}s^{-1}$
Heavy Ion fusion evaporation	$L \approx 10^{7}\ barn^{-1}s^{-1}$
Projectile fragmentation	$L \approx 10^{10}\ barn^{-1}s^{-1}$
Target spallation/fragmentation energetic protons	$L \approx 10^{13}\ barn^{-1}s^{-1}$
Storage ring experiments with fixed targets $N_p \approx 10^{11}\ \ s^{-1}$ times enhancement of $2\ 10^6$, $N_T \approx 10^{14}\ \ /cm^2$.	$L \approx 10^{7}\ barn^{-1}s^{-1}$

delivered by Linac, up to 1.0-1.4 GeV after which the protons are injected into the CERN Proton synchrotron (PS). The PSB delivers every 1.2 seconds a pulse of 3.2 10^{13} protons.

The most crucial parameters concerning the operation of ISOLDE are related to the target and the ion source. Ideally, the reaction products should leave the target fast (i.e. short release time) and the ion source should efficiently produce an ion beam, preferably containing for the most part the isotopes of the studied element. The development work is therefore closely related to chemistry and engineering of materials at extreme conditions.

The ISOLDE targets serve two different isotope separators, namely GPS (General purpose separator) and HRS (High resolution separator). With the HRS one single mass can be separated with a resolution of M/ΔM=5000, enabling even isobaric purification.

Since later on in these lectures we discuss the spectroscopic studies of very neutron-rich isotopes of Al and Na, it is of interest to remark that the $^{34-35}$Al and ^{33}Na isotopes were produced by using a Uranium Carbide target with a thickness of 46 g cm^{-2} and the reaction products were ionized in a tungsten surface-ionization source. The production rates for some Na and Al isotopes are given in Table 2 [21].

The time structure of the ISOLDE beam is built on the proton pulses, the time interval between pulses being a multiple of 1.2 s. The acceleration high voltage of 60 kV is brought to zero 35 μs before the proton beam impact and restored to its normal value after 6 ms. This pulsed power supply avoids the unnecessary load on the acceleration voltage from the intense ionisation in the air during the beam impact. Followed by the proton pulse, the beam of accelerated radioactive ions is driven through the separator for a certain time, so-called "beam gate", and then cut of until the next proton pulse.

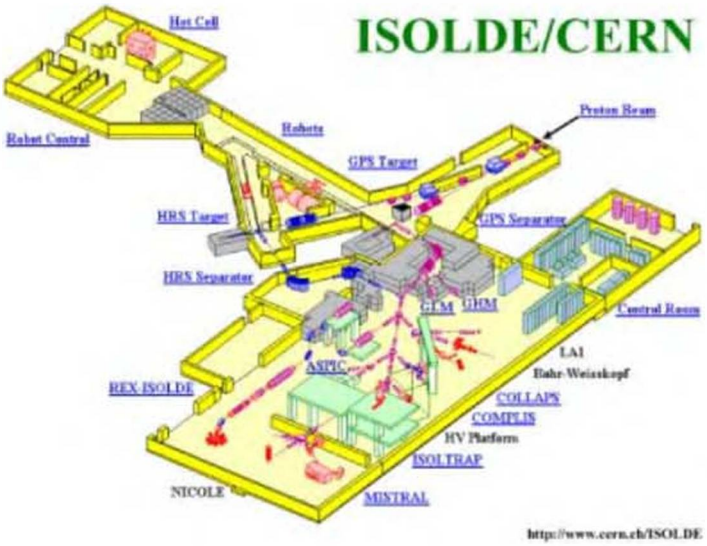

Fig. 4. The lay-out of the ISOLDE Facility at CERN. See ref. [18].

Table 2. ISOLDE production rates of some neutron-rich Na and Al isotopes

Na isotope	Production rate [at/μC]	Al isotope	Production rate [at/μC]
^{30}Na	8 10^4	^{33}Al	10^3
^{32}Na	560	^{34}Al	135
^{33}Na	50	^{35}Al	100

Until now more than 600 isotopes of more than 60 elements (Z=2 to 88) have been produced, in some cases with half-lives down to milliseconds and intensities up to 10^{11} ions/s. Neutron-rich nuclei are produced in fission or fragmentation reactions, either directly with very energetic protons or indirectly by secondary neutrons of considerably lower energy. The commonly used targets are uranium or thorium carbide targets, which provide the optimum release properties for a large number of elements. Radioactive atoms released are then diffusing through the transport line into a plasma or a surface ion source, or a hot cavity for resonant laser ionization. Presently, the laser ionization schemes developed include nearly thirty chemical elements. For example, at ISOLDE selective laser ionization has been used in a variety of experiments on Be isotopes produced in high-energy p-induced reactions. These experiments have included the production of ^{7}Be for ^{7}Be(p,γ)^{8}B cross section measurement, the measurement of the nuclear magnetic moment of ^{11}Be leading to strong indication of single neutron halo and the decay study of ^{14}Be, a candidate for a two-neutron halo. The release properties of various elements from the thorium and uranium targets are reported in ref. [22].

2.4 Fast beams of radioactive nuclei

There are two methods to produce fast radioactive beams as shown in Fig. 5. One relies on the Isotope Separator On-Line (ISOL) method and the other one is called In-Flight, see refs. [1,16] for extensive presentations of both techniques.

In the ISOL method radioactive isotopes are first produced at rest by a driver accelerator in a thick target, a catcher or an ion guide. After releasing from the target and following ionization and acceleration up to a few 10 keV energy through a mass selective device, these nuclei are accelerated in a post accelerator typically up to 2 - 50 MeV/u energy. In the In-Flight method the

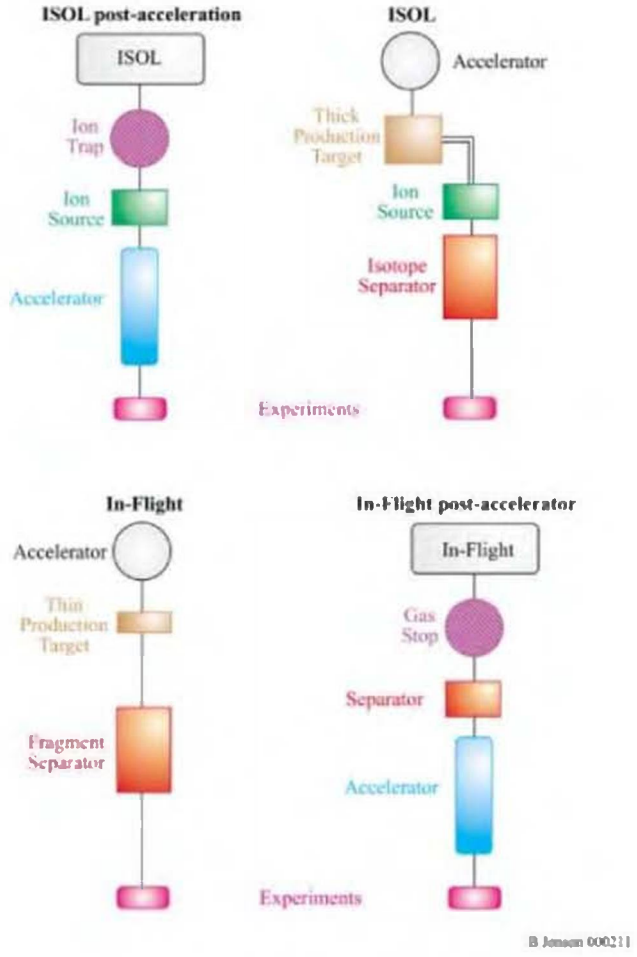

Fig. 5. Schematic presentation of the ISOL and IN-FLIGHT techniques to produce radioactive ion beams. From ref. [1].

initially energetic (50-1000 MeV/u) ions are fragmented or fissioned in flight and subsequently transported to a secondary target after their purification in mass, charge and momentum distribution. The resulting beams at the ISOL and In-Flight RNB facilities are complementary in their energy, intensity and isospin range. Therefore both types of facilities are intensively pursued world wide today.

In Europe, the first prototype ISOL facility has been in operation since 1989 at Louvain-La-Neuve, Belgium [23]. It uses a low energy driver cyclotron coupled to a K=110 MeV cyclotron as post accelerator. At the end of 1999 the first radioactive ion beam (^{19}Ne) was accelerated with the new CYCLONE44 in the 0.2 to 1.7 MeV/u energy range. This facility has mostly been used for studies of nuclear astrophysics in the region of light elements. It employs radioactive beams near stability with high intensities (up to 10^9 ions/s) and with energies from 0.2 MeV/u up to 12 MeV/u for some beams.

At CERN the ISOLDE facility is used to deliver low-energy radioactive ions to the REX-ISOLDE LINAC-type post accelerator [24]. SPIRAL at GANIL will be using the present GANIL cyclotrons as a driver [25]. This concept employs a novel charge breeding principle based on the coupled Penning trap and the EBIS charge breeder. In addition, the ISOL-based facilities providing beams of fission product ions are being launched in Europe at the new high-flux reactor in Munich, at the SPIRAL II facility at GANIL and in Dubna. In these concepts, fission products are to be produced in fission induced by high-energy protons and secondary neutrons (CERN), protons or deuterons and secondary neutrons (GANIL), or by photons (Dubna, GANIL). Furthermore, a new plan is proposed in the UK employing a 200 MeV proton driver accelerator.

In North America, ISOL-based RNB facilities or projects are planned or are operational at ORNL in Oak Ridge, at TRIUMF in Vancouver, at ANL in Argonne and at LBNL in Berkeley. At ORNL, the driver accelerator is a 100 MeV proton cyclotron and the post-accelerator is a 25 MV Tandem. The facility has recently started its physics programme and accelerated fission product ion beams are available with intensities in the 10^5 to 10^6 ions/s. The ISAC project at TRIUMF uses a 500 MeV, 100 μA proton synchrotron as a driver accelerator. The post-accelerator is linac producing RNBs up to 1.5 MeV/u, a second stage up to 7 MeV/u was recently approved.

In western Europe two In-Flight facilities are operational, one at GANIL in Caen and the other one at GSI in Darmstadt. The GANIL cyclotrons produce heavy primary ion beams up to 95 MeV/u with a beam power of 2 kW, which soon will be increased to 6 kW [26]. Fast secondary radioactive beams are produced by fragmentation in thin targets followed by a high-acceptance magnetic separation system to produce pure beams of energetic radioactive ions. At GSI the primary beams of 1 GeV/u heavy ions accelerated in the UNILAC and the SIS synchrotron are used to produce secondary beams by fragmentation or by fission in-flight [26]. These beams are purified in the fragment separator FRS and can further be injected and cooled in the Experimental Storage Ring ESR.

Similar in-flight facilities have been operational in North America at MSU and in Japan at RIKEN. At MSU the heavy ion beams have been available at energies between 100 and 200 MeV/u energy range. The facility is presently being upgraded by coupling the K500 and K1200 superconducting cyclotrons. The fragment separator is also being upgraded, leading to expected intensities of two to three orders of magnitude higher than before. At RIKEN the RNBs are produced with primary beams of 135 MeV/u and the fragment separator RIPS. In future, the energies of the primary beams will be raised up to 400 MeV/u for light and 150 MeV/u for heavy nuclei. The future plan also includes the construction of three fragment separators, as well as storage and cooler rings and an electron linac for electron-RNB collisions. In eastern Europe, the Flerov Laboratory at Dubna and in China the IMP laboratory at Lanzhou are also pursuing the fragmentation reactions as sources of secondary RNBs in the energy range below 100 MeV/u.

The future plans in Europe include a substantial upgrade of the GSI facility to produce ultimately 2 GeV/u uranium beams with intensity up to 10^{12} ins/s with fully upgraded fragment separator as well as cooler and electron rings for versatile programme on exotic nuclei. Similarly, the EURISOL study project funded by the EU-RTD programme aims at producing a preliminary design for the second generation ISOL-based RNB facility with qualifications second to none existing at the moment [27]. Major projects for the next generation ISOL RNB facilities are also proposed in the US as the RIA (Rare Isotope Accelerator) project and in Japan at the Japan hadron factory. In all these plans the instrumentation for experiments will need special developments in the fields of detector systems for gamma- and charged particle spectrometry as well as of magnetic spectrometers and ion manipulation techniques employing ion and neutral atom traps.

3 Spectroscopic investigations of neutron-rich nuclei at magic neutron numbers

3.1 Shell structure

The breakthrough in the development of the shell model was the inclusion of the strong spin-orbit interaction in the single-particle potential. It was only after this modification that the experimentally observed magic numbers could be reproduced by the model. Normally, when we talk about the experimental confirmation of the magic numbers, we refer to the data close to the valley of stability. Good examples of magic neutron-rich nuclei close to the valley of stability are doubly magic nuclei $^{48}Ca_{28}$ and $^{208}Pb_{126}$.

One of the key issues of today's nuclear spectroscopy is to learn about the evolution of the nuclear shell structure when moving out from the valley of stability close to the drip lines where exotic new structures such as neutron halos or skins are predicted to occur, see Fig. 6. In fact, such measurements have been performed already on some light nuclei below Z=20 proton number and around the N=20 and N=28 magic neutron numbers. Experiments on the

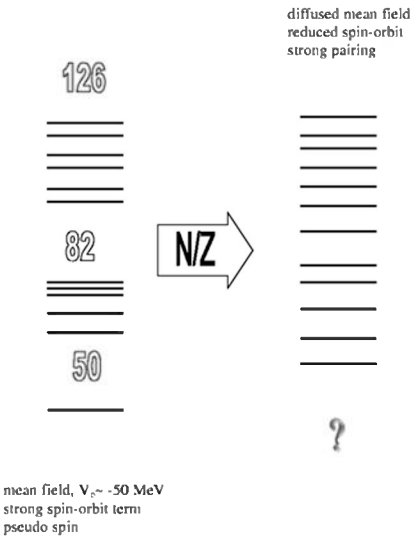

Fig. 6. Nuclear shell structure in the valley of beta-stability and far out. Due to changes with N/Z ratio in the nuclear mean field, pairing and in spin-orbit coupling effects, the shell structure is expected to be modified significantly. This may lead even to the disappearance of the standard magic nucleon numbers [30].

next heavier neutron magic numbers are still in their early stage. For example, significant new experimental developments are needed to measure the needed rare isotopes in the ^{78}Ni region, below ^{132}Sn at N=82, as well as below ^{208}Pb at N=126. So far, the spectroscopic study of ^{78}Ni has been out of experimental reach and the production rates have allowed only the mere identification of few of these nuclei. Such developments are actively being pursued in many laboratories employing multiples of techniques and production methods. Finally, one should mention that indirect evidence for the weakening of the N=82 shell gap has been obtained from the analysis of the r-process produced element abundances at the A=130 abundance peak [28]. This interpretation has gained some more support from the systematic studies of the low-lying levels in neutron-rich Cd isotopes [29].

In this context, to provide an example, we will focus on describing some recent experiments on neutron-rich nuclei near N=20 which in the valley of stability is a well known closed shell. In this region, however, unexpected deformation was observed via an irregularity in the binding energy systematics more than 20 years ago [31]. The observation could not be explained by the shell model calculation within the major sd-shell. Instead, nucleon excitations across the major shell to the fp-shell was required. These so-called "intruder configurations" are in competition with the normal states of the nucleus and in some specific cases the states may be inverted so that the ground state is dominated by an intruder

configuration. Such an inversion causes the vanishing of the N=20 shell closure in the very neutron-rich region and can be observed as deformed configurations.

The shell model interpretation of the island of inversion has progressed with new experimental results on masses, decay properties and Coulomb excitation experiments with radioactive beams. Beta decay measurements of Na isotopes [32, 33] have enabled the study of low energy level schemes of some neutron-rich Mg isotopes, such as ^{32}Mg. In addition, the beta-decay study of ^{34}Al [34] demonstrated the double-magicity of ^{34}Si (Z=14, N=20).

3.2 In-beam experiments with radioactive beams in the N=20 region

Experiments with radioactive projectiles are opening up a new frontier in learning about the excited states of exotic nuclei. The main processes that could be applied are Coulomb excitation, one-nucleon transfer and inelastic scattering experiments. Nearly all experimental data gained so far has been produced by Coulomb excitation process. Due to the availability of wanted beams only fragmentation produced neutron-rich isotopes have been applied in these experiments so far. In near future, the REX-ISOLDE facility at CERN will provide first low-energy beams of neutron-rich Na isotopes for in-beam studies. These experiments will include Coulomb excitation as well as one nucleon transfer experiments. For the latter, see the discussion in refs. [35,36].

The power of the Coulomb excitation is in the fact that the cross section is directly proportional to the B(E2) value and to the product of the Z of the projectile (P) and the target (T):

$$\sigma \approx Z_P^2 Z_T^2 B(E2) 1/E \ ,$$

where E is the energy. Moreover, when assuming that one is dealing with the rotational excitations of the axially deformed nucleus the B(E2) value can be related to the quadrupole deformation in the following way:

$$\beta_2 = (4\pi/3)\ B(E2)^{1/2}/ZeR^2 \ ,$$

where R is the mean radius of the nucleus.

Coulomb excitation at intermediate energies provides a sensitive probe in studying the B(E2) values of the low-lying states of nuclei far from the stability line. Such a study at Riken [37] employing a 50 MeV/nucleon ^{32}Mg beam and a high-Z Pb target resulted for ^{32}Mg (Z=12, N=20) a B(E2;$0_1^+ \rightarrow 2_1^+$) value of 45478 e^2fm^4, which confirms a very large deformation $\beta \approx 0.5$ for ^{32}Mg, as already suggested by the low excitation energy of the 2^+ state. Furthermore, recent investigations through in beam Coulomb excitation on a Au target at NSCL [38, 39] have provided a systematic study of B(E2; $0_1^+ \rightarrow 2_1^+$) values for even $^{32-38}$Si nuclei, revealing a vibrational quadrupole collectivity for these isotopes. These measured B(E2) values could be reproduced by the shell model calculation when assuming N=20 as a closed shell for Si isotopes. The transformation from sphericity to deformation is illustrated in Figure 7, where the 0_1^+

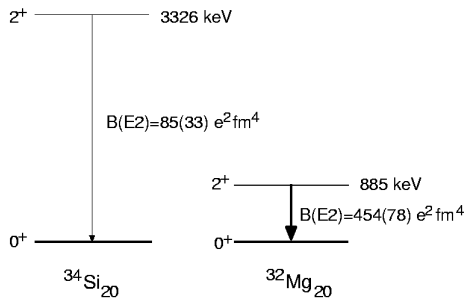

Fig. 7. The 0_1^+ ground state and 2_1^+ excited state of ^{34}Si and ^{32}Mg. The B(E2; $0_1^+ \rightarrow 2_1^+$) values of ^{34}Si and ^{32}Mg are taken from ref. [37] and [38], respectively.

ground state and 2_1^+ excited state are shown for ^{34}Si and ^{32}Mg, together with their corresponding B(E2; $0_1^+ \rightarrow 2_1^+$) values.

Subsequent Coulomb excitation studies at NSCL [40,41] have enabled the first observation of an excited state in ^{31}Na, which corresponds to a rotational excitation built on a strongly deformed ground state. They also reveal excited states in ^{33}Si and ^{34}P, which appear to have spherical shapes and thus are located along the boundary of island of deformation.

3.3 β-decay studies of ^{33}Na and ^{35}Al

Allowed beta decay is a highly selective process which for nuclei near the closed shells can provide valuable information on single particle states both for protons and neutrons. Since no direct information on single particle states existed in the N=20 region a series of experiments were conducted at ISOLDE where the beams of exotic ^{33}Na and ^{34,35}Al isotopes are available. These decays should probe the single particle excitations in the N=20 and 21 isotopes, ^{32}Mg, ^{33}Mg, ^{34}Si and ^{35}Si. In fact, it is not only the direct beta decay but also the beta-delayed neutron and two neutron decay which together provide information on the excited states of daughter nuclei. The setup used in these experiments is shown in Fig. 8 [42]. It allowed via efficient beta-trigger for a complete spectroscopy, registering neutron time-of-flight spectra from a few 10 keV up to MeV, gamma-ray spectra as well as various coincidences between different radiations. For general presentation of experimental methods of nuclear spectroscopy the readers are referred to ref. [43].

Based on the complete evaluation of the data decay schemes were constructed revealing a rich source of information on the evolution of the single neutron states in N=21 isotopes. The decay scheme of ^{35}Si is shown in Fig. 9. It reveals states both in ^{34}Si and ^{35}Si.

The study of the ^{35}Si nucleus (N=21), which can be referred as a key-nucleus, provides new information on the evolution of neutron orbits outside the N=20 closed shell. This offered a new step in N=21 systematics, starting from the well known single particle spectrum of ^{41}Ca [44]. Furthermore, the investigation of

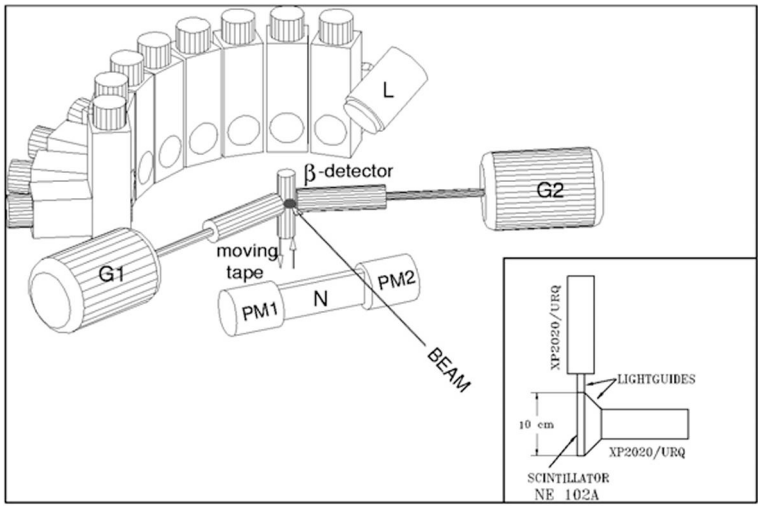

Fig. 8. The detector setup used in the experiments on ^{33}Na and ^{34,35}Al decays.

the ^{33}Mg (Z=12, N=21) level scheme was a logical next step in the N=21 series [45]. The interpretation of the results is largely based on shell model calculations by F. Nowacki and E. Caurier. They use a valence space of the full *sd*-shell for Z-8 protons and the *sd*- and *pf*-shells for the neutrons [46]. The *pf*-shell has been truncated only to the $1f_{7/2}$ and $2p_{3/2}$ sub-shells due to dimensionality arguments. The nuclear states are formed either by $0\hbar\omega$ or by $1\hbar\omega/2\hbar\omega$ neutron excitations, corresponding to excitations inside the major shell (*pf*) or from *sd*- to *pf*-shell, respectively. The protons remain in the *sd*-shell, as demonstrated in ref. [46]. As a summary, the evolution of the excited states in N=21 isotopes from ^{41}Ca down to ^{33}Na is shown in Fig. 10. It shows that at ^{33}Mg the ground state has become $3/2^+$ suggesting a leading configuration as $(\pi\ f_{7/2})^2(\nu\ d_{3/2})^{-1}$ for the ground state of ^{33}Mg, and therefore giving the direct evidence for the shell inversion phenomenon.

4 Heavy ion spectroscopy

4.1 Decay studies

Investigation of heavy neutron-deficient nuclei and their decay modes near and along the proton-drip line can be performed efficiently by using heavy-ion fusion reactions in combination with high-transmission recoil separators. These separators can be divided into two categories, those operating in vacuum and those operating with gas-filled magnetic fields. Two examples of vacuum-operating separators are the velocity filter SHIP at GSI [47] and the Fragment mass Analyzer FMA at Argonne [48]. Both of these separators employ the combination of the magnetic and electric fields and provide extremely high suppression of the

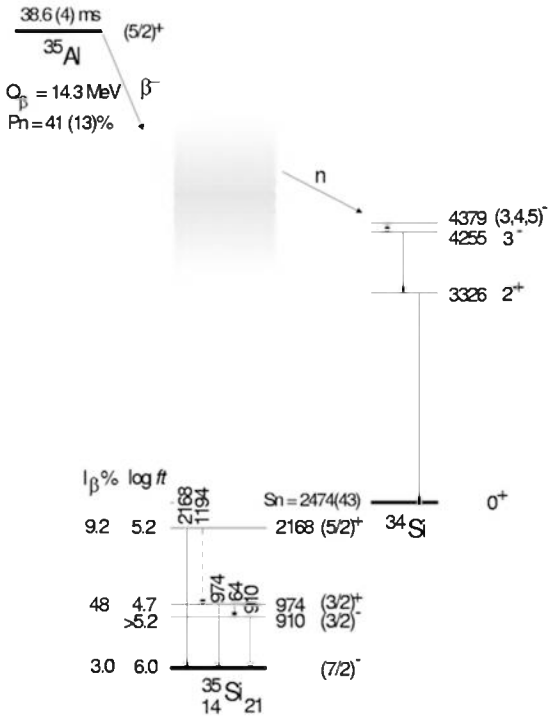

Fig. 9. The decay scheme of ^{35}Si as observed at ISOLDE experiments.

primary beam in the focal plane of the device. However, in this presentation we will discuss the gas-filled separator concept which recently has shown remarkably high sensitivities in the decay as well as in-beam spectroscopy of heavy nuclei.

The gas-filled separator principle provides simultaneous charge and velocity focusing of recoil ions emerging from the target following the fusion evaporation process. In vacuum, the charge state distribution of ions is broad and only one or two charge states can be focused into the focal point of the separator magnet simultaneously. In a gas-filled magnet the average charge of ions, which undergo constant charge exchange reactions with gas atoms, is expressed as $q \approx v/v_o\, Z^{1/3}$, which results in the magnetic rigidity for ions helium gas:

$$B_\rho = 0.0227A/Z^{1/3} \text{ (in Tesla meter).}$$

The width of the charge distribution is a function of the gas-pressure in a magnet. For example, in the case of RITU separator operating at Jyvaskyla [49] the optimum He-gas pressure is about 0.5 mbar. Due to the high transmission and charge distribution width the separator cannot provide as high mass resolving power as the vacuum operated FMA, for example. However, the high transmission, being at best nearly 50%, and the extremely good suppression of the primary beam in the case of asymmetric reactions, makes the gas-filled separators

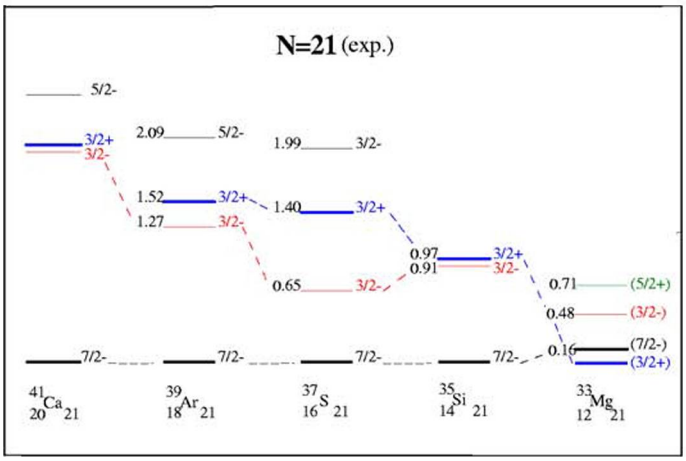

Fig. 10. Systematics of excited states of N=21 isotopes.

the most sensitive general purpose instruments in heavy element spectroscopy. The principle guiding the design of RITU has been to improve he transmission of the conventional gas-filled Dipole Quadrupole Quadrupole (QDD) separator by adding a vertically focusing dipole in front of the dispersive element. RITU has an angular acceptance of 10 msr, the maximum rigidity is 2.2 T m, the bending angle is 25 degrees, and the dispersion is 10 mm.

The research work using RITU has concentrated on decay and in-beam studies of very neutron-deficient isotopes of heavy elements ranging from tungsten to nobelium. So far, nearly 20 new isotopes of Hg, Po, At, Rn, Fr, Ra, Ac, and Th have been synthesized and their alpha decay properties have been determined. Decay studies of intruder and isomeric states in Bi, Po, and At isotopes have also been performed.

4.2 Recoil decay taggin technique

Generally, in-beam gamma-ray and electron spectroscopy methods form the backbone for the studies of exotic nuclear shapes and excitations. The first major breakthrough in in-beam studies of nuclei far from stability was achieved, when the gas-filled recoil separator RITU was used together with the DORIS array consisting of 9 TESSA-type Compton suppressed Ge-detectors. The recoil and their alpha-decay tagging provided very high sensitivity for the gamma-decay study of the level structures of the weakly produced ^{194}Po and ^{192}Po, see ref. [52].

In RDT technique prompt radiation from the excited evaporation residues is observed with a detector array placed around the target in correlation with the recoil ions detected later, with a delay of some 100 ns, in the position sensitive implantation detector on the focal plane of the separator. The nuclei are identified

by the measurement of the decay properties (alpha, proton and beta-gamma) using the silicon and other detectors. The construction of RITU target area allows the provision of close-geometry packing of BGO-suppressed Ge detectors around the target area which provide an excellent facility for gamma-spectroscopic studies of medium and heavy-mass nuclei. The high granularity, i.e. the high number of γ-detector elements allows for high efficiency detection of gamma-ray cascades with simultaneous correction for Doppler shifts in the gamma-ray spectra [43].

High selectivity for separating the fusion reaction products from other processes and primary beam makes it possible to do in-beam gamma-ray spectroscopy with cross sections as low as 100 nbarn.

A number of gamma-ray arrays have been used in conjunction with RITU in order to perform recoil-gated and recoil-decay-tagged (RDT) in-beam measurements, see Fig. 11. So far, excited states have been observed for the first time in about 30 nuclei. Highlights from the in-beam studies include determination of the octupole deformed character of ^{226}U, systematical studies of collectivity in radium isotopes ^{206,208,210}Ra and ^{207,209,211}Ra, and observation of the ground state band of ^{252}No [50] and ^{254}No [51]. The focal plane detector setups allow a variety of coincidence studies such as (α,γ), (α,e^-), and (γ,γ) to be performed either stand-alone or in conjunction with in-beam measurements.

In studies of the excited structures of ^{254}No isotope the ^{208}Pb target was bombarded with a beam of ^{48}Ca ions at energy of 216 MeV. The total irradiation time in this experiment was 350 hours. Prompt gamma-rays were observed with the SARI array which consisted of four clover-type Ge detectors positioned at 50 degrees angle with respect to the beam direction. The recoils or evaporation residues were then implanted on the focal plane into a position-sensitive 16-strip

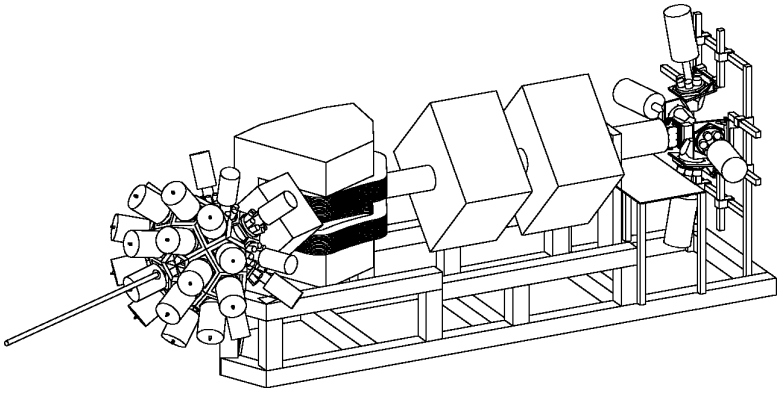

Fig. 11. JUROSPHERE frame connected to the RITU gas-filled separator. The beam enters from left on the target surrounded by a gamma-ray array. Evaporation residue ions are transported through the QDQQ gas-filled separator and implanted in the focal plane in a position sensitive Si detector surrounded by an array of beta and gamma-ray detectors detecting the decay of implanted nuclei. For more details and general discussion on the setup, see ref. [50].

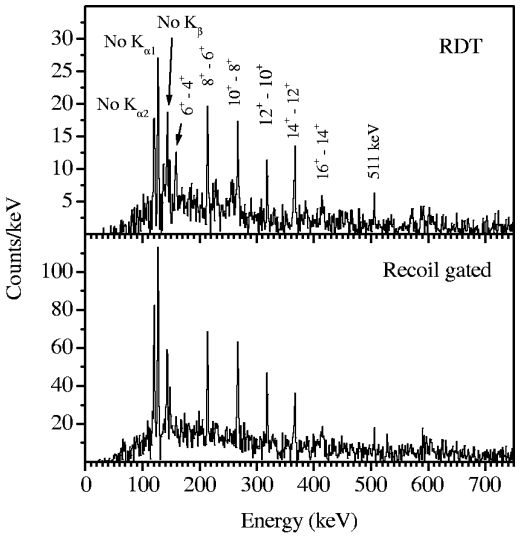

Fig. 12. (top) A singles gamma-ray spectrum from the ^{48}Ca + ^{208}Pb reactions gated with fusion-evaporation residues and tagged with the ^{254}No alpha decays. (bottom) The same gamma-ray spectrum but without alpha tagging, [51].

Si detector (PSSD) measuring 80 mm (horizontal) and 35 mm (vertical). In addition, germanium detectors were adjacent to the focal plane PSSD in order to detect isomeric or delayed gamma-rays.

The total efficiency of the separator system was measured as about 15%. Fig. 12 shows at the bottom the gamma-ray spectrum measured with the SARI array in coincidence with the ^{254}No residues observed on the focal plane detector, whereas the top part shows the same spectrum but measured in correlation with only those events where the alpha decay is observed in the Si-detector in the same position where the ion was implanted. The spectra reveal the observation of the ground state rotational band of ^{254}No up to the spin 16. This experiment has opened up a new frontier in the heavy element research where detailed structure information is now becoming available to complement the previous data on the ground state decays only.

5 Ion traps. New tools in precision measurements of exotic nuclei

5.1 General

Low-energy radioactive ions have been long used for studies of the ground state and decay properties of exotic nuclei either after their implantion in solids or by having them to interact as a beam collinearly with the laser beam. These studies have lead to enormous success in characterising properties of nuclei far

from stability. Only the atomic mass determinations have remained beyond experimental techniques. Only recently, the application of the ion trap technology has allowed for precise determination of masses of exotic nuclei in a systematic way with precisions not available before. Development of these techniques has mainly been done at ISOLDE, where several ion traps or Penning traps, have been constructed in recent years. This field has now also extended to a more general technology to manipulate ions and ion beams making them more suitable for high precision and higher sensitivity experiments.

5.2 Mass measurements by Penning traps

The basic idea behind a mass measurement by a Penning trap is to determine the exact angular cyclotron frequency ω_C of an ion moving in a homogeneous magnetic field,

$$\omega_C = q/mB \ .$$

The value of the magnetic field B required for the mass determination can be determined from the cyclotron frequency of an ion with a well-known mass. For a detailed description of Penning traps for mass measurements see the review in ref. [53]. Penning traps provide presently the highest accuracy, reaching $\delta m/m \approx 10^{-10}$, for light stable isotopes [54]. In recent years, a very successful programme at ISOLDE employing a Tandem Penning trap system has measured masses of about 200 radioactive short-lived isotopes with typical precisions of 20 keV or better, for example see ref. [55] for the results concerning rare-earth isotopes. In these measurements low energy ions were introduced into the Penning trap system by a two step process where they were first collected on a foil of a secondary ion source system. Low energy ions were then produced via surface ionization by heating the foil. In a new setup at ISOLDE these steps have been replaced by a linear radio-frequency quadrupole ion beam buncher [56]. In order to accumulate continuously delivered ions to the trap, ions have to lose enough energy during passing through the trap. This can be achieved by using buffer gas. After a sufficient number of ions have been accumulated, cooled and centered, the ion bunch will be ejected by switching the trap potential. With this new considerably faster injection system of ions into the precision trap mass measurements could be extended to isotopes with half-lives less than 1 s.

5.3 Cooling and bunching of low-energy ion beams

Two recently developed novel concepts for improving the purity and the quality of the radioactive ion beams are the buffer-gas filled RFQ for ion beam cooling and bunching [56,57, 58] and the previously mentioned Penning trap which can also be used for isobar purification. Following the pioneering work at ISOLDE several projects are underway in Europe [57,59]. In the following we concentrate on the system under construction at the IGISOL mass separator facility in Jyvaskyla for improving the experiments on neutron-rich nuclei from fission.. The trap system [60] consists of an ion beam cooler based on the gas-filled linear

RFQ and of a Penning trap with two adjacent trapping zones, one for the isobar purification and the other for performing high-accuracy mass measurements.

The cooling of an ion beam is done in three steps. First the 40 keV beam has to be decelerated with an electrostatic lens system and injected into a closed radio frequency quadrupole (RFQ) linear rod structure. In the RFQ the ions will experience an average force towards the centre of the device and hence be trapped in transverse direction (x-y -plane). The RFQ is filled with helium buffer gas. Hence the ions will lose energy in collisions with neutral He atoms and the amplitude of the oscillation of ions will be reduced. Thus the ions are driven to the centre of the rod structure. Finally the ions will reach a thermal equilibrium with the buffer gas. The cooled ions will then be guided with a miniature RFQ to a better vacuum, extracted from the cooler and accelerated back to 40 keV minus the original energy spread.

The first successful tests performed with radioactive ^{112}Rh ions showed that cooling works efficiently and ions with initial energy spread as large as >50 eV could be cooled down to 1 eV or even better. Moreover, the transmission efficiency of >60% was measured nearly independent on the emittance and energy spread of the incoming ion beam.

In some cases (e.g. when the cooled beam is injected into an ion trap or in laser spectroscopy experiment) it would be advantageous to have a bunched or instead of a dc beam. For this purpose beam bunching in the cooler was tested. It was shown that the dc IGISOL beam can be accumulated in the cooler and released in 20 's bunches. Recently, it has been demonstrated that the bunching can increase the sensitivity of collinear laser spectroscopy by at least a factor of 1000.

The task of the Penning trap, the second device of the ion manipulation system at IGISOL, is to accept cooled, continuous or bunched, beams from the RFQ cooler, perform an isobaric purification and deliver clean, mono-isotopic bunched beams for nuclear spectroscopy investigations [61]. The cylindrical Penning trap at IGISOL is a quadrupole trap which makes use of static electric and magnetic fields for three dimensional confinement of ions. The static quadrupole electric fields for axial trapping of ions are created by a set of ring electrodes at negative potential and by two end-cap electrodes at zero potential. The radial confinement is achieved with homogeneous axial magnetic field of 7 T produced by super-conducting solenoid. With combination of buffer gas cooling and an azimuthal quadrupole RF-electric field a mass dependent centering of ions can be achieved in the Penning trap. This allows for a mass selective ejection of ions in short time bunches. In order to achieve this goal, a cylindrical Penning trap placed in a B=7 T super-conducting magnet field is used. The magnet, delivered by Magnex, is a solenoid with two homogeneous magnetic field regions, each with inhomogeneity within a 1 cm^3 volume of less than 10^{-6} and 10^{-7}, respectively. Isobaric purification of the radioactive beam will be performed in the cylindrical Penning trap positioned in the first region. The second region is foreseen to contain, at a later stage, a precision Penning trap for the nuclear mass measurements. The precision trap will operate at 10^{-6} mbar pressure and mass resolving power of $\delta m/m = 10^{-7}$ can be achieved with it [62].

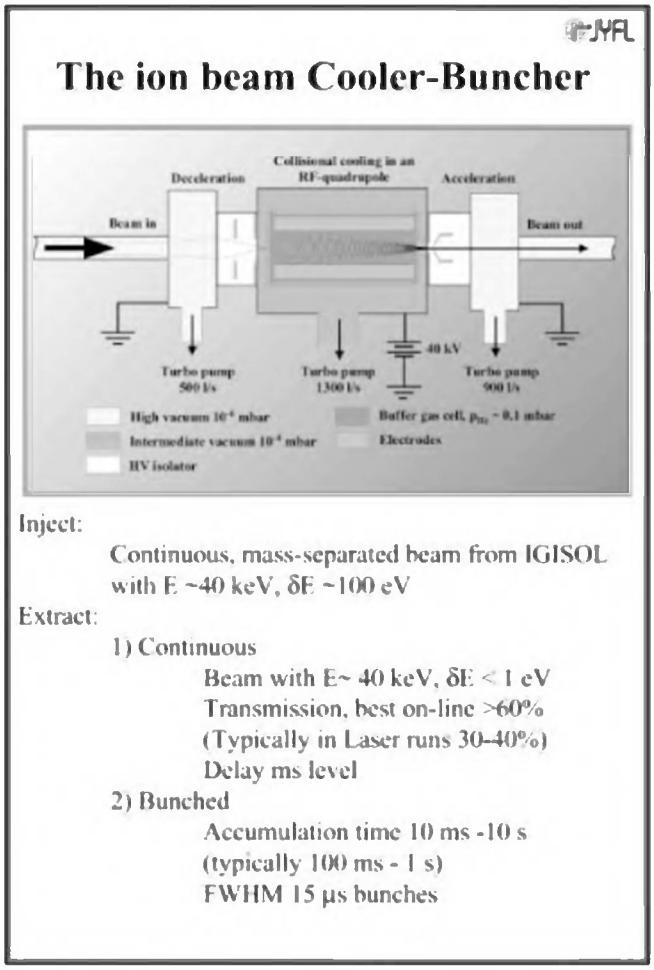

Fig. 13. The operating principle of the buffer-gas filled RFQ Cooler in use at the IGISOL Facility. A similar device is also in use at ISOLDE. (Courtesy of Arto Nieminen).

References

1. B. Jonson, et al.: Report of The NuPECC Working Group on Radioactive Nuclear Beam Facilities, March 2000
2. M. Cable et al.: Phys. Rev. Lett. **50**, 404 (1983)
3. K. Schmidt et al.: Eur. Phys. J. **A3**, 303 (2000)
4. S. Hofmann and G. Mnzenberg: Rev. Mod. Phys. **72**, 733 (2000)
5. Yu. Ts. Oganessian: Nature **400**, 303 (1999)
6. J. Galy et al.: Eur. Phys. J. **A3**, 331 (2000)

7. P. P. Jauho et al.: Phys. Rev. **C49**, 1379 (1994)
8. G. Lhersonneau et al.: Eur. Phys. J. **A9**, 385 (2000)
9. W. Schwab et al.: Eur. Phys. J. **2**, 179 (1998)
10. W. Rubchenya: private communication and to be published
11. M. Huhta et al.: Phys. Lett. **B405**, 230 (1997)
12. L. Weissman et al.: Phys. Rev. **C59**, 2004 (1999)
13. J. Aysto and V. Rubchenya: Eur. Phys. J. **A**, in print
14. I. Tanihata et al.: Phys. Lett. **B160**, 380 (1985)
15. P.G. Hansen and B. Jonson: Europhys. Lett. **4**, 409 (1987)
16. H. Geissel, G. Mnzenberg and K. Riisager: Ann. Rev. Nucl. Part. Sci. **45**, 163 (1995)
17. E. Kugler: Hyperfine Interactions **129**, 23 (2000)
18. http://www.cern.ch/isolde/
19. http://www.triumf.ca/isac/isac_home.html
20. D. Forkel-Wirth and G. Bollen (eds.): Hyperfine Interactions **129**, 1 (2000)
21. S. Nummela: Ph D thesis, to be published
22. A. Evensen et al.: Nucl. Instr. Meth. **B126**, 160 (1997)
23. J. Vervier: Nucl. Phys. **A616**, 97c (1997)
24. D. Habs et al.: Nucl. Instr. Meth. **B126**, 218 (1997)
25. M. Bourgarel et al.: Proc. int. Conf. Cyclotrons and their Applications, Caen 1998, IOP Publ., p.311
26. http://www.gsi.de/gsi.research.html and http://www.ganil.fr
27. http://www.ganil.fr/eurisol/index.html
28. M. Hannawald et al.: Phys. Rev. **C62**, 054301 (2000)
29. T. Kautzsch et al.: Eur. Phys. J. **A9**, 201 (2000)
30. W. Nazarewicz: APS 100 Years Conference 1999
31. C. Thibault et al.: Phys. Rev. **C12**, 644 (1975)
32. D. Guillemaud-Mueller et al.: Nucl. Phys. **A426**, 37 (1984)
33. G. Klotz et al.: Phys. Rev. **C47**, 2502 (1993)
34. P. Baumann, et al.: Phys. Lett. **B228**, 458 (1989)
35. K. Lenske and G. Schrieder: Eur. Phys. J. **A2**, 41 (1998)
36. C. Gund et al.: Eur. Phys. J. **A10**, 85 (2001)
37. T. Motobayashi, et al.: Phys. Lett. **B346**, 9 (1995)
38. R.W. Ibbotson et al.: Phys. Rev. Lett **80**, 2081 (1998)
39. R.W. Ibbotson et al.: Phys. Rev. **C59**, 642 (1999)
40. B.V. Pritychenko, et al.: MSUCL-1157, June-2000
41. B.V. Pritychenko, et al.: MSUCL-1157, June-2000
42. Z. Radivojevicz et al.: submitted to Nucl. Instr. Meth.
43. J. Kantele: "Handbook of Nuclear Spectrometry", Academic Press, London, 1995
44. S. Nummela, et al.: Phys. Rev. **C63**,044316 (2001)
45. S. Nummela et al.: submitted for publication
46. E. Caurier, F. Nowacki, A. Poves and J. Retamosa: Phys. Rev. **C58**, 2033 (1998)
47. http://www.gsi.de/ship/home.html
48. http://www.phy.anl.gov/fma/index.html
49. M. Leino et al.: Nucl. Instr. Meth. **B99**, 653 (1995); see also http://www.phys.jyu.fi
50. R. Julin: Nucl. Phys. **A685**, 221c (2001)
51. M. Leino et al.: Eur. Phys. J. **A6**, 63 (1999)
52. K. Helariutta, et al.: Phys. Rev. **C54**, R2799 (1996)
53. G. Bollen et al.: Nucl. Instr. Meth. **A368**, 675 (1996)

54. M. Bradley et al.: Phys. Rev. Lett. **83**, 4510 (1999)
55. D. Beck et al.: Eur. Phys. J. **A8**, 307 (2000)
56. F. Herfurth et al.: Nucl. Instr. Meth., in press
57. A. Nieminen et al.: Nucl. Instr. Meth., in press
58. M.Lunney and R. Moore: Int. J. Mass Spectr. **190/191**, 153 (1999)
59. http://www.phys.jyu.fi/research/igisol/exotraps/
60. http://www.phys.jyu.fi/research/igisol/
61. J. Szerypo, et al.: Proc. Zakopane School of Nuclear Physics, September 2000
62. G. Bollen: Physica Scripta **T59**, 165 (1995)

Structure of vacuum and elementary matter: from superheavies via hypermatter to antimatter

Walter Greiner

Institut für Theoretische Physik, J.W. Goethe-Universität,
D-60054 Frankfurt, Germany

Abstract. The extension of the periodic system into various new areas is investigated. Experiments for the synthesis of superheavy elements and the predictions of magic numbers are reviewed. Different ways of nuclear decay are discussed like cluster radioactivity, cold fission and cold multifragmentation, including the recent discovery of the tripple fission of ^{252}Cf. Furtheron, investigations on hypernuclei and the possible production of antimatter–clusters in heavy–ion collisions are reported. Various versions of the meson field theory serve as effective field theories at the basis of modern nuclear structure and suggest structure in the vacuum which might be important for the production of hyper– and antimatter. A perspective for future research is given.

1 From superheavies via hypermatter to antimatter

There are fundamental questions in science, like e. g. "how did life emerge" or "how does our brain work" and others. However, the most fundamental of those questions is "how did the world originate?". The material world has to exist before life and thinking can develop. Of particular importance are the substances themselves, i. e. the particles the elements are made of (baryons, mesons, quarks, gluons), i. e. elementary matter. The vacuum and its structure is closely related to that. On this I want to report today. I begin with the discussion of modern issues in nuclear physics.

The elements existing in nature are ordered according to their atomic (chemical) properties in the **periodic system** which was developped by Mendeleev and Lothar Meyer. The heaviest element of natural origin is Uranium. Its nucleus is composed of $Z = 92$ protons and a certain number of neutrons ($N = 128 - 150$). They are called the different Uranium isotopes. The transuranium elements reach from Neptunium ($Z = 93$) via Californium ($Z = 98$) and Fermium ($Z = 100$) up to Lawrencium ($Z = 103$). The heavier the elements are, the larger are their radii and their number of protons. Thus, the Coulomb repulsion in their interior increases, and they undergo fission. In other words: the transuranium elements become more instable as they get bigger.

In the late sixties the dream of the superheavy elements arose. Theoretical nuclear physicists around S.G. Nilsson (Lund)[1] and from the Frankfurt school[2–4] predicted that so-called closed proton and neutron shells should counteract the repelling Coulomb forces. Atomic nuclei with these special **"magic" proton and neutron numbers** and their neighbours could again be rather stable. These magic proton (Z) and neutron (N) numbers were thought to be $Z = 114$

J.M. Arias and M. Lozano (Eds.): LNP 581, pp. 316–342, 2001.
© Springer-Verlag Berlin Heidelberg 2001

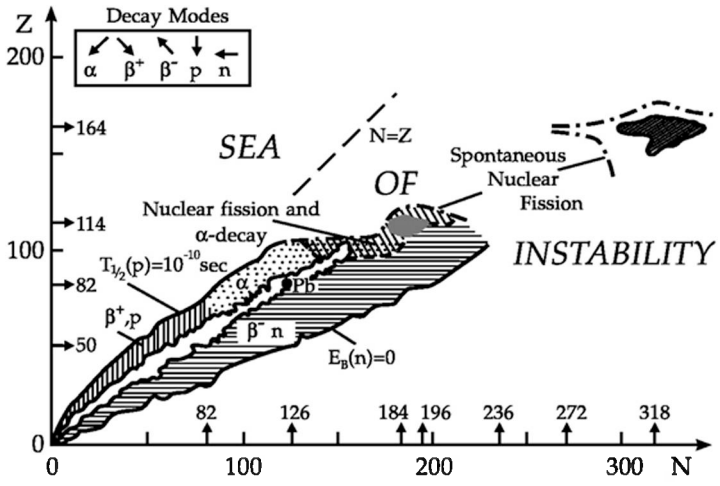

Fig. 1. The periodic system of elements as conceived by the Frankfurt school in the late sixties. The islands of superheavy elements ($Z = 114$, $N = 184$, 196 and $Z = 164$, $N = 318$) are shown as dark hatched areas.

and $N = 184$ or 196. Typical predictions of their life times varied between seconds and many thousand years. Fig.1 summarizes the expectations at the time. One can see the islands of superheavy elements around $Z = 114$, $N = 184$ and 196, respectively, and the one around $Z = 164$, $N = 318$.

The important question was how to produce these superheavy nuclei. There were many attempts, but only little progress was made. It was not until the middle of the seventies that the Frankfurt school of theoretical physics together with foreign guests (R.K. Gupta (India), A. Sandulescu (Romania))[5] theoretically understood and substantiated the concept of bombarding of double magic lead nuclei with suitable projectiles, which had been proposed intuitively by the russian nuclear physicist Y. Oganessian[6]. The two-center shell model, which is essential for the description of fission, fusion and nuclear molecules, was developed in 1969-1972 together with my then students U. Mosel and J. Maruhn[7]. It showed that the shell structure of the two final fragments was visible far beyond the barrier into the fusioning nucleus. The collective potential energy surfaces of heavy nuclei, as they were calculated in the framework of the two-center shell model , exhibit pronounced valleys, such that these valleys provide promising doorways to the fusion of superheavy nuclei for certain projectile-target combinations (Fig. 4). If projectile and target approach each other through those **"cold" valleys**, they get only minimally excited and the barrier which has to be overcome (fusion barrier) is lowest (as compared to neighbouring projectile-target combinations). In this way the correct projectile- and target-combinations for fusion were predicted. Indeed, Gottfried Münzenberg and Sigurd Hofmann and their group at GSI [8] have followed this approach. With the help of the SHIP mass-separator and the position sensitive detectors, which were especially

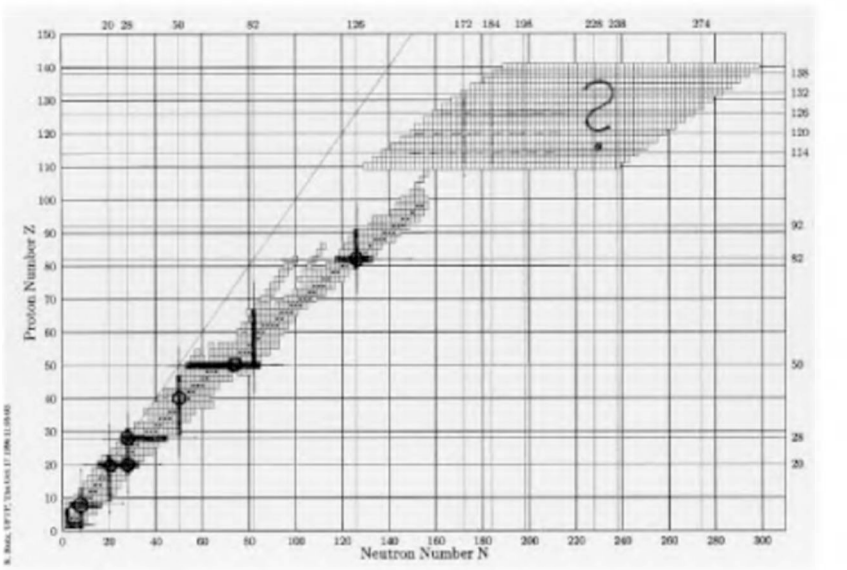

Fig. 2. The shell structure in the superheavy region around $Z = 114$ is an open question. As will be discussed later, meson field theories suggest that $Z = 120, N = 172, 184$ are the magic numbers in this region.

developped by them, they produced the pre-superheavy elements $Z = 106$, 107, ... 112, each of them with the theoretically predicted projectile-target combinations, and only with these. Everything else failed. This is an impressing success, which crowned the laborious construction work of many years. The before last example of this success, the discovery of element 112 and its long α-decay chain, is shown in Fig. 6. Very recently the Dubna–Livermore–group produced two isotopes of $Z = 114$ element by bombarding ^{244}Pu with ^{48}Ca (Fig. 3). Also this is a cold–valley reaction (in this case due to the combination of a spherical and a deformed nucleus), as predicted by Gupta, Sandulescu and Greiner [9] in 1977. There exist also cold valleys for which both fragments are deformed [10], but these have yet not been verified experimentally. The very recently reported $Z = 118$ isotope fused with the cold valley reaction [12] ^{58}Kr + ^{208}Pb by Ninov et al. [13] yields the latest support of the cold valley idea.

Studies of the shell structure of superheavy elements in the framework of the meson field theory and the Skyrme-Hartree-Fock approach have recently shown that the magic shells in the superheavy region are very isotope dependent [14] (see Fig. 7). **According to these investigations $Z = 120$ being a magic proton number seems to be as probable as $Z = 114$.** Additionally, recent investigations in a chirally symmetric mean–field theory (see also below) result also in the prediction of these two magic numbers[38,40]. The corresponding magic neutron numbers are predicted to be $N = 172$ and - as it seems to a lesser extend - $N = 184$. Thus, this region provides an open field of research.

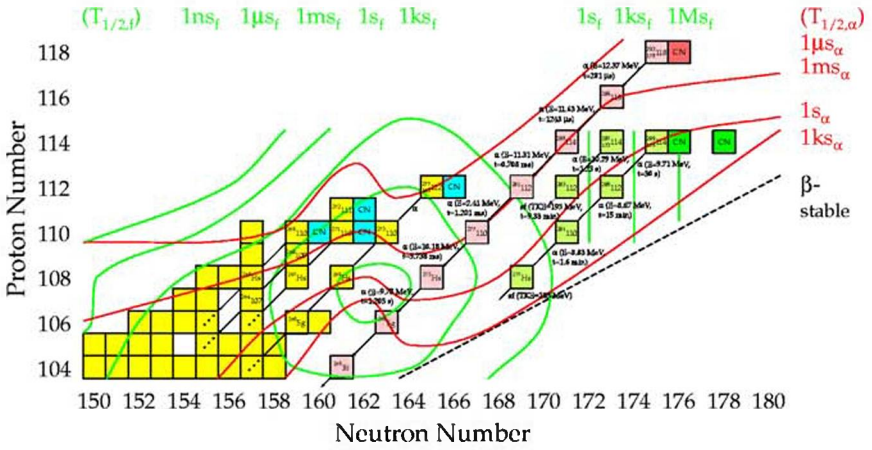

Fig. 3. The $Z = 106 - 112$ isotopes were fused by the Hofmann–Münzenberg (GSI)–group. The two $Z = 114$ isotopes were produced by the Dubna–Livermore group. It is claimed that three neutrons are evaporated. Obviously the lifetimes of the various decay products are rather long (because they are closer to the stable valley), in crude agreement with early predictions [3,4] and in excellent agreement with the recent calculations of the Sobicevsky–group [11]. The recently fused $Z = 118$ isotope by V. Ninov et al. at Berkeley is the heaviest one so far.

R.A. Gherghescu et al. have calculated the potential energy surface of the $Z = 120$ nucleus. It utilizes interesting isomeric and valley structures (Fig. 8). The charge distribution of the $Z = 120, N = 184$ nucleus indicates a hollow inside. This leads us to suggest that it might be essentially a fullerene consisting of 60 α-particles and one additional binding neutron per alpha. This is illustrated in Fig 5. The protons and neutrons of such a superheavy nucleus are distributed over 60 α particles and 60 neutrons (forgetting the last 4 neutrons).

The determination of the chemistry of superheavy elements, i. e. the calculation of the atomic structure — which is in the case of element 112 the shell structure of 112 electrons due to the Coulomb interaction of the electrons and in particular the calculation of the orbitals of the outer (valence) electrons — has been carried out as early as 1970 by B. Fricke and W. Greiner[15]. Hartree-Fock-Dirac calculations yield rather precise results.

The potential energy surfaces, which are shown prototypically for $Z = 114$ in Fig 4, contain even more remarkable information that I want to mention cursorily: if a given nucleus, e. g. Uranium, undergoes fission, it moves in its potential mountains from the interior to the outside. Of course, this happens quantum mechanically. The wave function of such a nucleus, which decays by tunneling through the barrier, has maxima where the potential is minimal and minima where it has maxima. This is depicted in Fig. 9.

The probability for finding a certain mass asymmetry $\eta = \dfrac{A_1 - A_2}{A_1 + A_2}$ of the fission is proportional to $\psi^*(\eta)\psi(\eta)\mathrm{d}\eta$. Generally, this is complemented by a

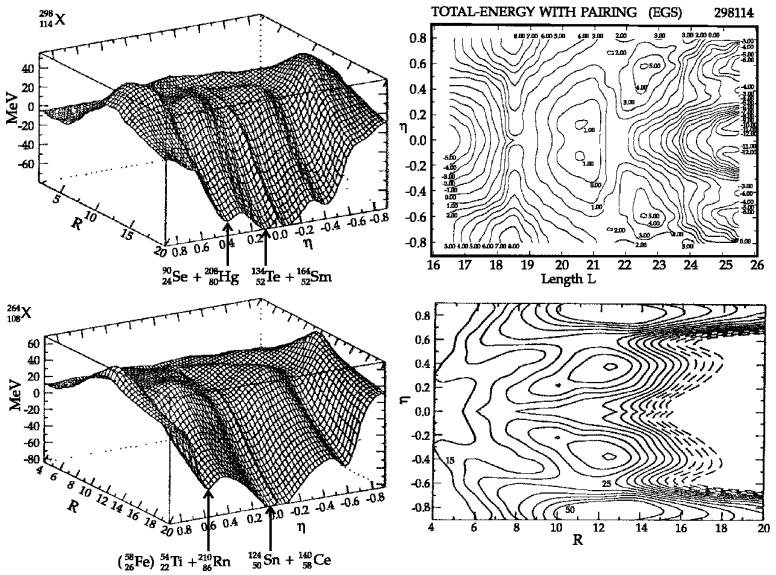

Fig. 4. The collective potential energy surface of $^{264}108$ and $^{184}114$, calculated within the two center shell model by J. Maruhn et al., shows clearly the cold valleys which reach up to the barrier and beyond. Here R is the distance between the fragments and $\eta = \dfrac{A_1 - A_2}{A_1 + A_2}$ denotes the mass asymmetry: $\eta = 0$ corresponds to a symmetric, $\eta = \pm 1$ to an extremely asymmetric division of the nucleus into projectile and target. If projectile and target approach through a cold valley, they do not "constantly slide off" as it would be the case if they approach along the slopes at the sides of the valley. Constant sliding causes heating, so that the compound nucleus heats up and gets unstable. In the cold valley, on the other hand, the created heat is minimized. The colleagues from Freiburg should be familiar with that: they approach Titisee (in the Black Forest) most elegantly through the Höllental and not by climbing its slopes along the sides.

coordinate dependent scale factor for the volume element in this (curved) space, which I omit for the sake of clarity. Now it becomes clear how the so-called **asymmetric** and **superasymmetric** fission processes come into being. They result from the enhancement of the collective wave function in the cold valleys. And that is indeed, what one observes. Fig. 10 gives an impression of it.

For a large mass asymmetry ($\eta \approx 0.8,\ 0.9$) there exist very narrow valleys. They are not as clearly visible in Fig. 4, but they have interesting consequences. Through these narrow valleys nuclei can emit spontaneously not only α-particles (Helium nuclei) but also ^{14}C, ^{20}O, ^{24}Ne, ^{28}Mg, and other nuclei. Thus, we are lead to the **cluster radioactivity** (Poenaru, Sandulescu, Greiner [16]).

By now this process has been verified experimentally by research groups in Oxford, Moscow, Berkeley, Milan and other places. Accordingly, one has to revise what is learned in school: there are not only 3 types of radioactivity (α-, β-, γ-radioactivity), but many more. Atomic nuclei can also decay through

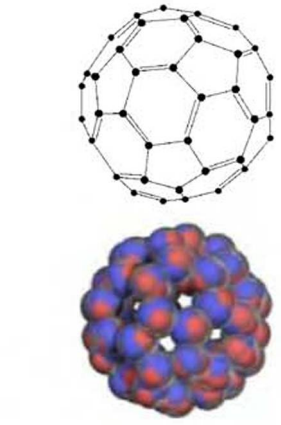

Fig. 5. Typical structure of the fullerene ^{60}C. The double bindings are illutsrated by double lines. In the nuclear case the Carbon atoms are replaced by α particles and the double bindings by the additional neutrons. Such a structure would immediately explain the semi–hollowness of that superheavy nucleus, which is revealed in the mean–field calculations within meson–field theories. (Lower picture by H. Weber.)

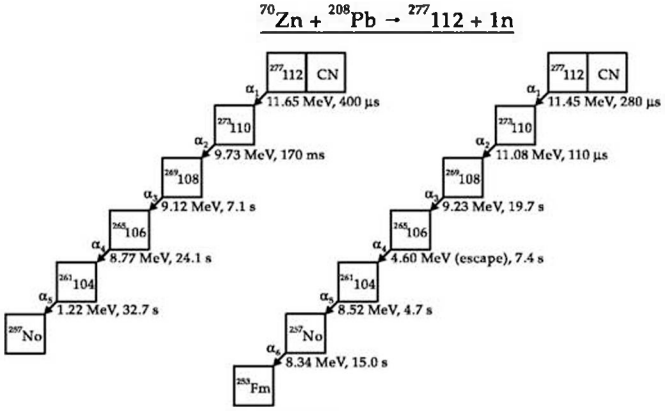

Fig. 6. The fusion of element 112 with ^{70}Zn as projectile and ^{208}Pb as target nucleus has been accomplished for the first time in 1995/96 by S. Hofmann, G. Münzenberg and their collaborators. The colliding nuclei determine an entrance to a "cold valley" as predicted as early as 1976 by Gupta, Sandulescu and Greiner. The fused nucleus 112 decays successively via α emission until finally the quasi-stable nucleus ^{253}Fm is reached. The α particles as well as the final nucleus have been observed. Combined, this renders the definite proof of the existence of a $Z = 112$ nucleus.

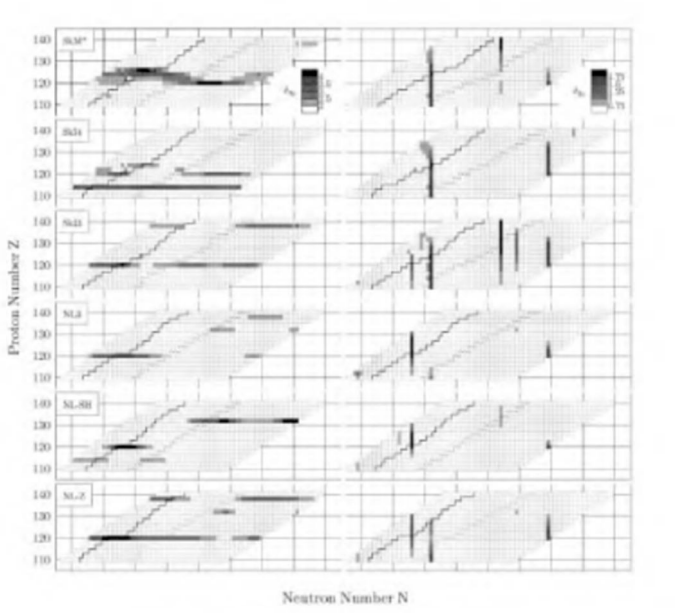

Fig. 7. Grey scale plots of proton gaps (left column) and neutron gaps (right column) in the N-Z plane for spherical calculations with the forces as indicated. The assignment of scales differs for protons and neutrons, see the uppermost boxes where the scales are indicated in units of MeV. Nuclei that are stable with respect to β decay and the two-proton dripline are emphasized. The forces with parameter sets SkI4 and NL-Z reproduce the binding energy of $^{264}_{156}108$ (Hassium) best, i.e. $|\delta E/E| < 0.0024$. Thus one might assume that these parameter sets could give the best predictions for the superheavies. Nevertheless, it is noticed that NL-Z predicts only $Z = 120$ as a magic number while SkI4 predicts both $Z = 114$ and $Z = 120$ as magic numbers. The magicity depends — sometimes quite strongly — on the neutron number. These studies are due to Bender, Rutz, Bürvenich, Maruhn, P.G. Reinhard et al. [14].

spontaneous cluster emission (that is the "spitting out" of smaller nuclei like carbon, oxygen,...). Fig. 11 depicts some nice examples of these processes.

The knowledge of the collective potential energy surface and the collective masses $B_{ij}(R,\eta)$, all calculated within the Two-Center-Shell-Model (TCSM) , allowed H. Klein, D. Schnabel and J. A. Maruhn to calculate lifetimes against fission in an "ab initio" way [17].

Utilizing a WKB-minimization for the penetrability integral

$$\mathcal{P} = e^{-\mathrm{I}}, \quad \mathrm{I} = \min_{\forall\,\mathrm{paths}} \tfrac{2}{\hbar} \int_S \sqrt{2m(V(R,\eta)-E)}\, ds$$

$$= \min_{\forall\,\mathrm{paths}} \tfrac{2}{\hbar} \int_0^1 \sqrt{\underbrace{2mg_{ij}}_{B_{ij}}(V(x_i(t)-E)\tfrac{dx_i}{dt}\tfrac{dx_j}{dt}}\, dt \qquad (1)$$

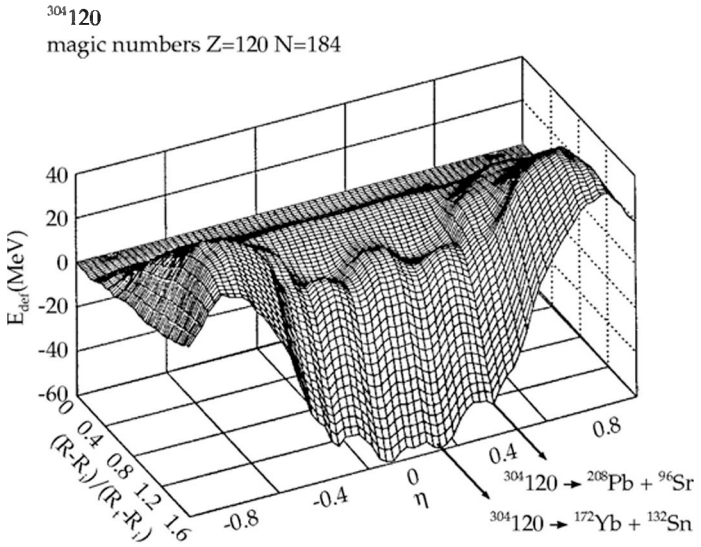

Fig. 8. Potential energy surface as a function of reduced elongation $(R-R_i)/(R_t-R_i)$ and mass asymmetry η for the double magic nucleus $^{304}120$. $^{304}120_{184}$.

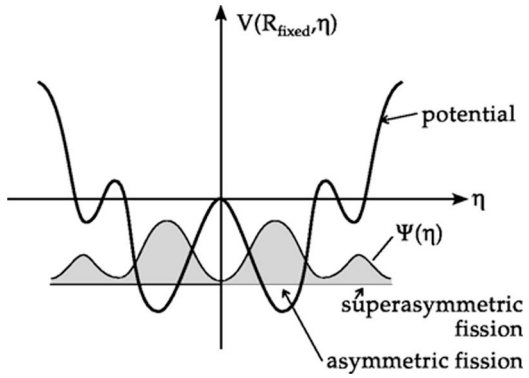

Fig. 9. The collective potential as a function of the mass asymmetry $\eta = \dfrac{A_1 - A_2}{A_1 + A_2}$. A_i denotes the nucleon number in fragment i. This qualitative potential $V(R_{\text{fixed}}, \eta)$ corresponds to a cut through the potential landscape at $R = R_{\text{fixed}}$ close to the scission configuration. The wave function is drawn schematically. It has maxima where the potential is minimal and vice versa.

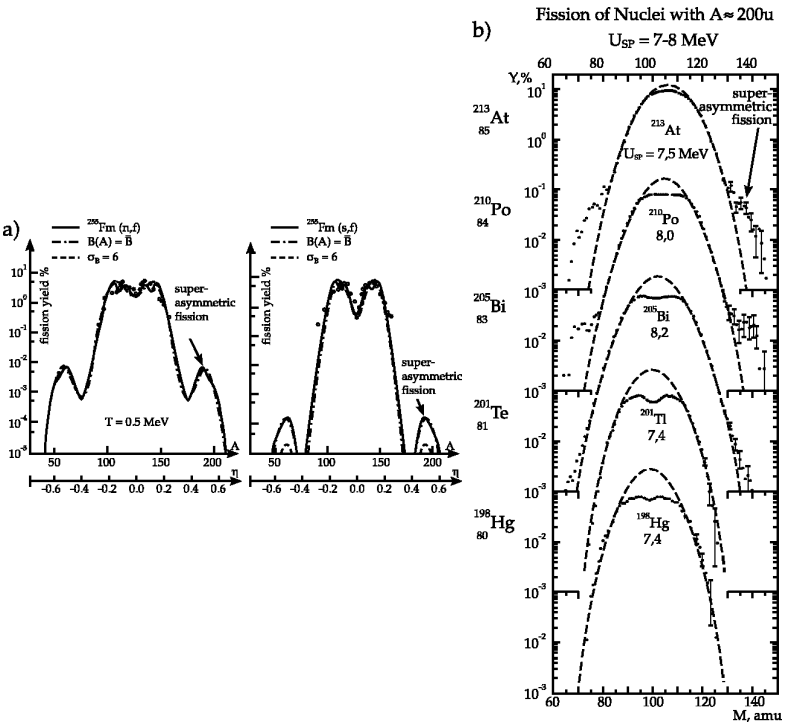

Fig. 10. Asymmetric (a) and symmetric (b) fission. For the latter, also superasymmetric fission is recognizable, as it has been observed only a few years ago by the russian physicist Itkis — just as expected theoretically.

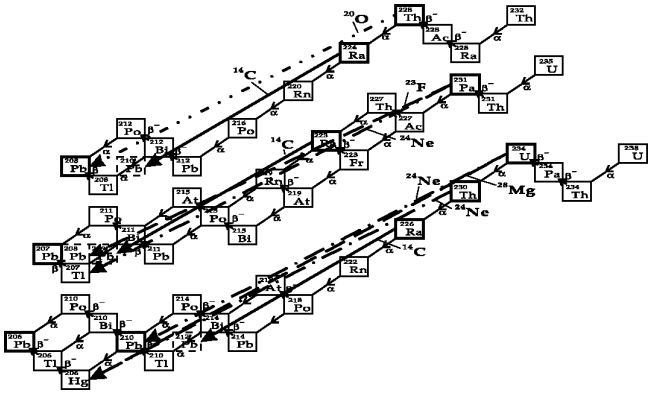

Fig. 11. Cluster radioactivity of actinide nuclei. By emission of ^{14}C, ^{20}O,... "big leaps" in the periodic system can occur, just contrary to the known α, β, γ radioactivities, which are also partly shown in the figure.

where $ds^2 = g_{ij}dx_i dx_j$ and g_{ij} – the metric tensor – is in the well-known fashion related to the collective masses $B_{ij} = 2mg_{ij}$, one explores the minimal paths from the nuclear ground state configuration through the multidimensional fission barrier (see Fig. 12).

The thus obtained fission half lives are depicted in the lower part of figure 12. Their distribution as a function of the fragment mass A_2 resembles quite well

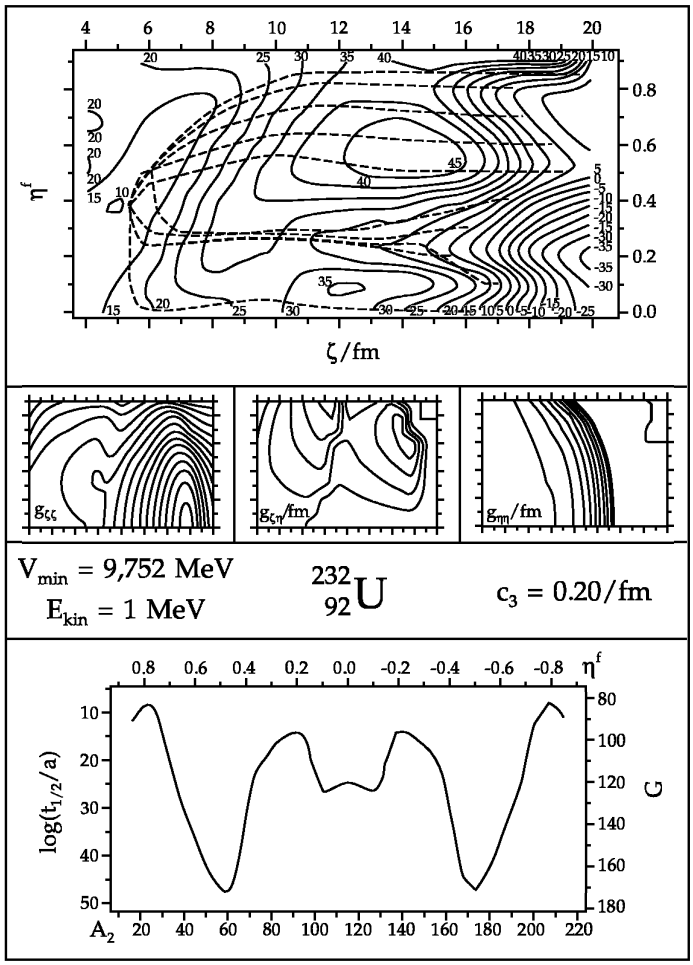

Fig. 12. The upper part of the figure shows the collective potential energy surface for $^{232}_{92}$U with the groundstate position and various fission paths through the barrier. The middle part shows various collective masses, all calculated in the TCSM. In the lower part the calculated fission half lives are depicted.

the asymmetric mass distribution. Cluster radioactive decays correspond to the broad peaks around $A_2 = 20$, 30 (200, 210). The confrontation of the calculated fission half lives with experiments is depicted in Fig. 13. One notices "nearly quantitative" agreement over 20 orders of magnitude, which is – for an ab-initio calculation – remarkable!

Finally, in Fig. 14, we compare the lifetime calculation discussed above with one based on the Preformation Cluster Model by D. Poenaru et al. [18] and recognize an amazing degree of similarity and agreement.

The systematics for the average total kinetic energy release for spontaneously fissioning isotopes of Cm and No is following the Viola trend, but ^{258}Fm and ^{259}Fm are clearly outside. The situation is similar also for ^{260}Md, where two components of fission products (one with lower and one with higher kinetic energy) were observed by Hulet et al. [19]. The explanation of these interesting observations lies in two different paths through the collective potential. One reaches the scission point in a stretched neck position (i.e. at a lower point of the Coulomb barrier - thus lower kinetic energy for the fragments) while the other one reaches the scission point practically in a touching-spheres-position (i.e. higher up on the Coulomb barrier and therefore highly energetic fragments) [20]. The latter process is cold fission ; i.e., the fission fragments are in or close to their ground state (cold fragments) and all the available energy is released as kinetic energy. Cold fission is, in fact, typically a cluster decay. The side-by-side occurence of cold and normal (hot) fission has been named bi-modal fission [20]. There has now been put forward a phantastic idea [21] in order to study

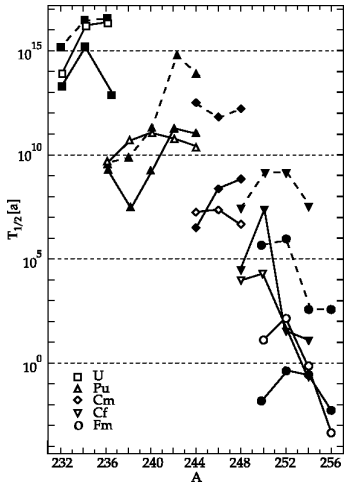

Fig. 13. Fission half lives for various isotopes of $Z = 92$ (□), $Z = 94$ (△), $Z = 96$ (◇), $Z = 98$ (▽) and $Z = 100$ (○). The black curves represent the experimental values. The dashed and dotted calculations correspond to a different choice of the barrier parameter in the Two Center Shell Model ($c_3 \approx 0.2$ and 0.1 respectively).

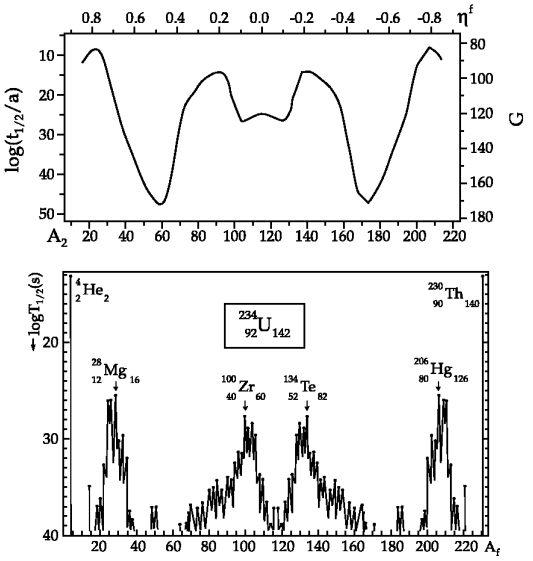

Fig. 14. Comparison of the fission half lives calculated in the fission model (upper figure – see also Fig. 12) and in the Preformation Cluster Model [18]. In both models the deformation of the fission fragments is not included completely.

cold fission (Cluster decays) and other exotic fission processes (ternary-, multiple fission in general) very elegantly: By measuring with e. g. the Gamma–sphere characteristic γ-transitions of individual fragments in coincidence, one can identify all these processes in a direct and simple way (Fig. 15). First confirmation of this method by J. Hamilton, V. Ramaya et al. worked out excellently [22]. This method has high potential for revolutionizing fission physics! With some physical intuition one can imagine that **triple** - and **quadriple** fission processes and even the process of **cold multifragmentation** will be discovered - absolutely fascinating! We have thus seen that fission physics (cold fission, cluster radioactivity, ...) and fusion physics (especially the production of superheavy elements) are intimately connected.

Indeed, very recently, tripple fission of

$$\begin{aligned} {}^{252}\mathrm{Cf} &\rightarrow {}^{146}\mathrm{Ba} + {}^{96}\mathrm{Sr} + {}^{10}\mathrm{Be} \\ &\rightarrow {}^{112}\mathrm{Ry} + {}^{130}\mathrm{Sn} + {}^{10}\mathrm{Be} \\ &\rightarrow \ldots \end{aligned}$$

has been identified by measuring the various γ–transitions of these nuclei in coincidence (see Fig. 16).

Even though the statistical evidence for the ^{10}Be line is small (≈ 50 events) the various coincidences seem to proof that spontaneous tripple fission out of the ground state of ^{252}Cf with the heavy cluster ^{10}Be as a third fragment exists. Also other tripple fragmentations can be expected. One of those is also denoted

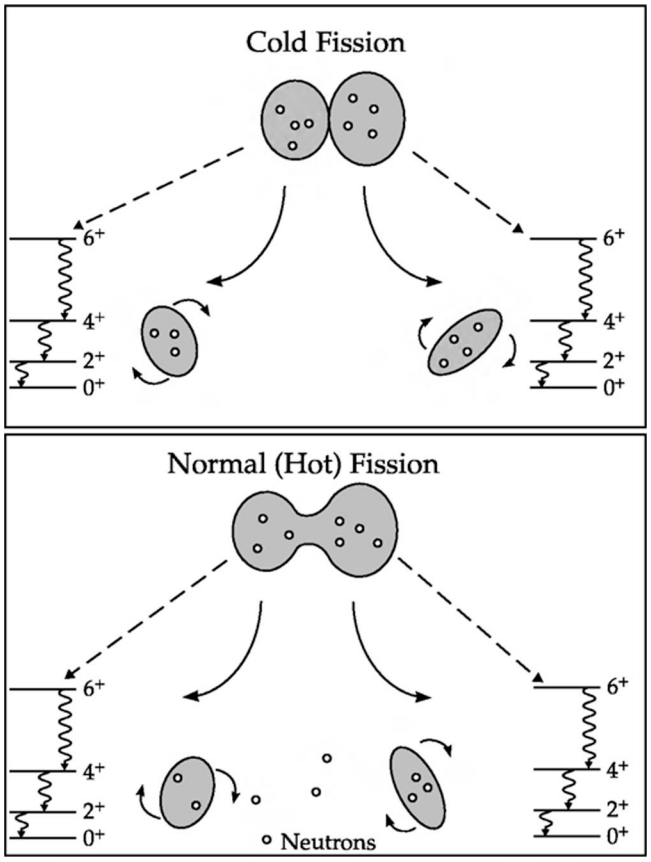

Fig. 15. Illustration of cold and hot (normal) fission identification through multiple γ-coincidencs of photons from the fragments. The photons serve to identify the fragments.

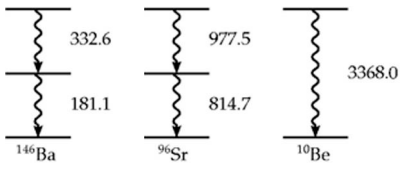

Fig. 16. The γ–transitions of the three fission products of ^{252}Cf measured in coincidence. Various combinations of the coincidences were studied. The free 3368 keV line in ^{10}Be has recently been remeasured by Burggraf et al.[23], confirming the value of the transition energy within 100 eV.

above. In fact, there are first indications, that this break–up is also observed. The most amazing observation is, however, the following: The cross coincidences seem to suggest that one deals with a simultaneous three–body breakup and not with a cascade process. For that one expects a configuration as shown in Fig. 17.

Consequently the ^{10}Be will obtain kinetic energy while running down the combined Coulomb barrier of ^{146}Ba and ^{96}Sr and, therefore, the 3368 keV line of

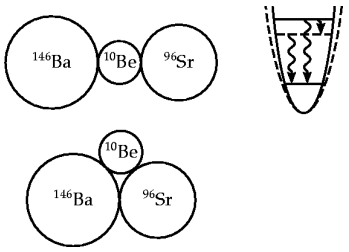

Fig. 17. Typical linear cluster configuration leading to tripple fission of ^{252}Cf. The influence of both clusters leads to a softening of the ^{10}Be potential and thus to a somewhat smaller transition energy. Some theoretical investigations indicate that the axial symmetry of this configuration might be broken (lower lefthand figure).

^{10}Be should be Doppler–broadened. Amazingly, however, it is not and, moreover, it seems to be about 6 keV smaller than the free ^{10}Be γ–transition. If this turns out to be true, the only explanation will be that the Gamma is emitted while the nuclear molecule of the type shown in Fig. 17 holds. The molecule has to live longer than about 10^{-12} sec. The nuclear forces from the ^{146}Ba and ^{96}Sn cluster to the left and right from ^{10}Be lead to a softening of its potential and therefore to a somewhat smaller transition energy. Thus, if experimental results hold, one has discovered long living ($\approx 10^{-12}$ sec) complex nuclear molecules. This is phantastic! Of course, I do immediately wonder whether such configurations do also exist in e.g. U + Cm soft encounters directly at the Coulomb barrier. This would have tremendous importance for the observation of the spontaneous vacuum decay [26], for which "sticking giant molecules" with a lifetime of the order of 10^{-19} sec are needed. The nuclear physics of such heavy ion collisions at the Coulomb barrier (giant nuclear molecules) should indeed be investigated!

As mentioned before there are other tri–molecular structures possible; some with ^{10}Be in the middle and both spherical or deformed clusters on both sides of ^{10}Be. The energy shift of the ^{10}Be–line should be smaller, if the outside clusters are deformed (smaller attraction $\Leftrightarrow$ smaller softening of the potential) and bigger, if they are spherical . Also other than ^{10}Be–clusters are expected to be in the middle. One is lead to the molecular doorway picture. Fig. 18 gives a schematic impression where within the potential landscape cluster–molecules are expected to appear, i.e. close to the scission configuration. Clearly, there will not be a single tri–molecular configuration, but a variety of three–body fragmentations leading to a spreading width of the tri–molecular state. This is schematically shown in Fig. 19.

Finally, these tri–body nuclear molecules are expected to perform themselves rotational and vibrational (butterfly, whiggler, β–, γ–type) modes. The energies were estimated by P. Hess et al [24]; for example rotational energies typically of the order of a few keV (4 keV, 9 keV, ...). A new molecular spectroscopy seems possible!

The "cold valleys" in the collective potential energy surface are basic for understanding this exciting area of nuclear physics! It is a master example for understanding the **structure of elementary matter** , which is so important for other fields, especially astrophysics, but even more so for enriching our "Weltbild", i.e. the status of our understanding of the world around us.

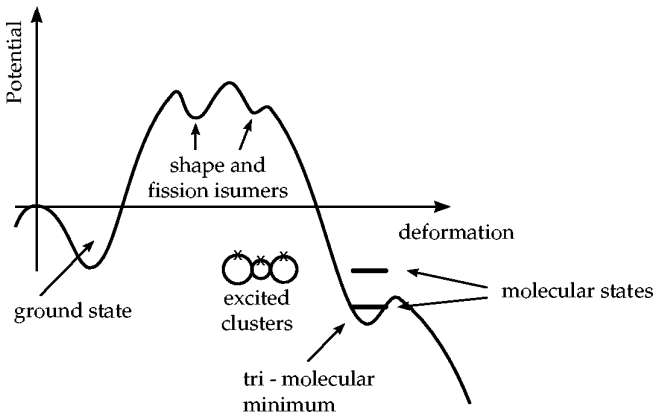

Fig. 18. Cluster molecules: Potential energy curve of a heavy nucleus showing schematically the location of groundstate, shape– and fission–isomeric states and of tri–molecular states.

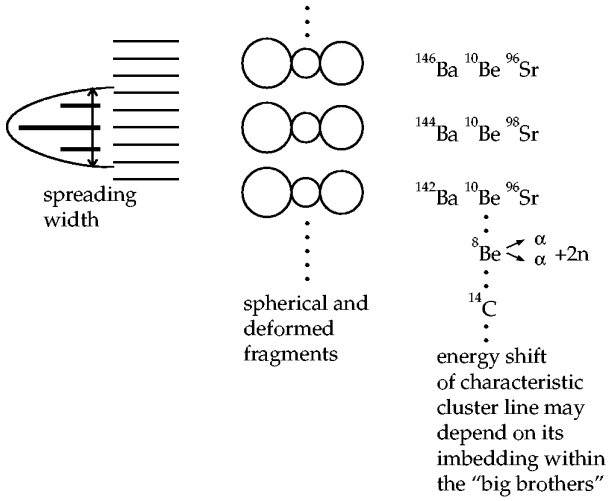

Fig. 19. Microstructure of tri–molecular states: Various tri–cluster configurations are spread out and mix with background states. Thus the tri–molecular state obtains a spreading width.

Nuclei that are found in nature consist of nucleons (protons and neutrons) which themselves are made of u (up) and d (down) quarks. However, there also exist s (strange) quarks and even heavier flavors, called charm, bottom, top. The latter has just recently been discovered. Let us stick to the s quarks. They are found in the 'strange' relatives of the nucleons, the so-called hyperons (Λ, Σ, Ξ, Ω). The Λ-particle, e. g., consists of one u, d and s quark, the Ξ-particle even of an u and two s quarks, while the Ω (sss) contains strange quarks only.

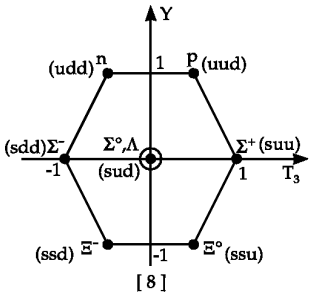

Fig. 20. Important baryons are ordered in this octet. The quark content is depicted. Protons (p) and neutrons (n), most important for our known world, contain only u and d quarks. Hyperons contain also an s quark. The number of s quarks is a measure for the strangeness.

Fig. 20 gives an overview of the baryons, which are of interest here, and their quark content.

If such a hyperon is taken up by a nucleus, a **hyper-nucleus** is created. Hyper-nuclei with one hyperon have been known for 20 years now, and were extensively studied by B. Povh (Heidelberg)[27]. Several years ago, Carsten Greiner, Jürgen Schaffner and Horst Stöcker[28] theoretically investigated nuclei with many hyperons, **hypermatter**, and found that the binding energy per baryon of strange matter is in many cases even higher than that of ordinary matter (composed only of u and d quarks). This leads to the idea of extending the periodic system of elements in the direction of strangeness.

One can also ask for the possibility of building atomic nuclei out of **antimatter**, that means searching e. g. for anti-helium, anti-carbon, anti-oxygen. Fig. 21 depicts this idea. Due to the charge conjugation symmetry antinuclei should have the same magic numbers and the same spectra as ordinary nuclei. However, as soon as they get in touch with ordinary matter, they annihilate with it and the system explodes.

Now the important question arises how these strange matter and antimatter clusters can be produced. First, one thinks of collisions of heavy nuclei, e. g. lead on lead, at high energies (energy per nucleon $\geq$ 200 GeV). Calculations with the URQMD-model of the Frankfurt school show that through **nuclear shock waves** [29–31] nuclear matter gets compressed to 5–10 times of its usual value, $\rho_0 \approx 0.17$ fm^3, and heated up to temperatures of $kT \approx 200$ MeV. As a consequence about 10000 pions, 100 Λ's, 40 Σ's and Ξ's and about as many antiprotons and many other particles are created in a single collision. It seems conceivable that it is possible in such a scenario for some Λ's to get captured by a nuclear cluster. This happens indeed rather frequently for one or two Λ-particles; however, more of them get built into nuclei with rapidly decreasing probability only. This is due to the low probability for finding the right conditions for such a capture in the phase space of the particles: the numerous particles travel with every possible momenta (velocities) in all directions. The chances for hyperons and antibaryons to meet gets rapidly worse with increasing number. In order to produce multi-Λ-nuclei and antimatter nuclei, one has to look for a different source.

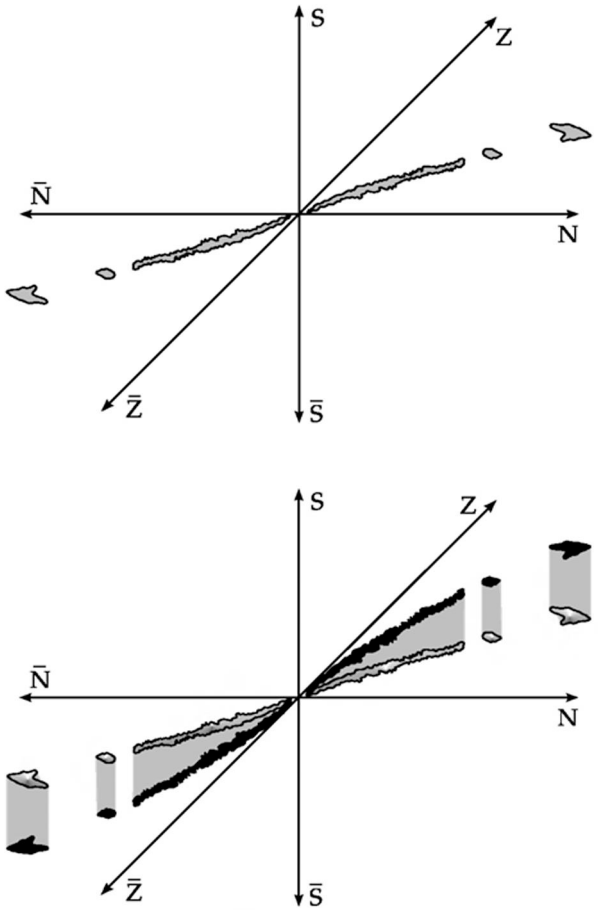

Fig. 21. The extension of the periodic system into the sectors of strangeness (S, $\bar{S}$) and antimatter ($\bar{Z}$, $\bar{N}$). The stable valley winds out of the known proton (Z) and neutron (N) plane into the S and $\bar{S}$ sector, respectively. The same can be observed for the antimatter sector. In the upper part of the figure only the stable valley in the usual proton (Z) and neutron (N) plane is plotted, however, extended into the sector of antiprotons and antineutrons. In the second part of the figure it has been indicated, how the stable valley winds out of the Z-N-plane into the strangeness sector.

In the framework of meson field theory the energy spectrum of baryons has a peculiar structure, depicted in Fig. 22. It consists of an upper and a lower continuum, as it is known from the electrons (see e. g. [26]). Of special interest in the case of the baryon spectrum is the potential well, built of the scalar and the vector potential, which rises from the lower continuum. It is known since P.A.M. Dirac (1930) that the negative energy states of the lower continuum have to be occupied by particles (electrons or, in our case, baryons). Otherwise

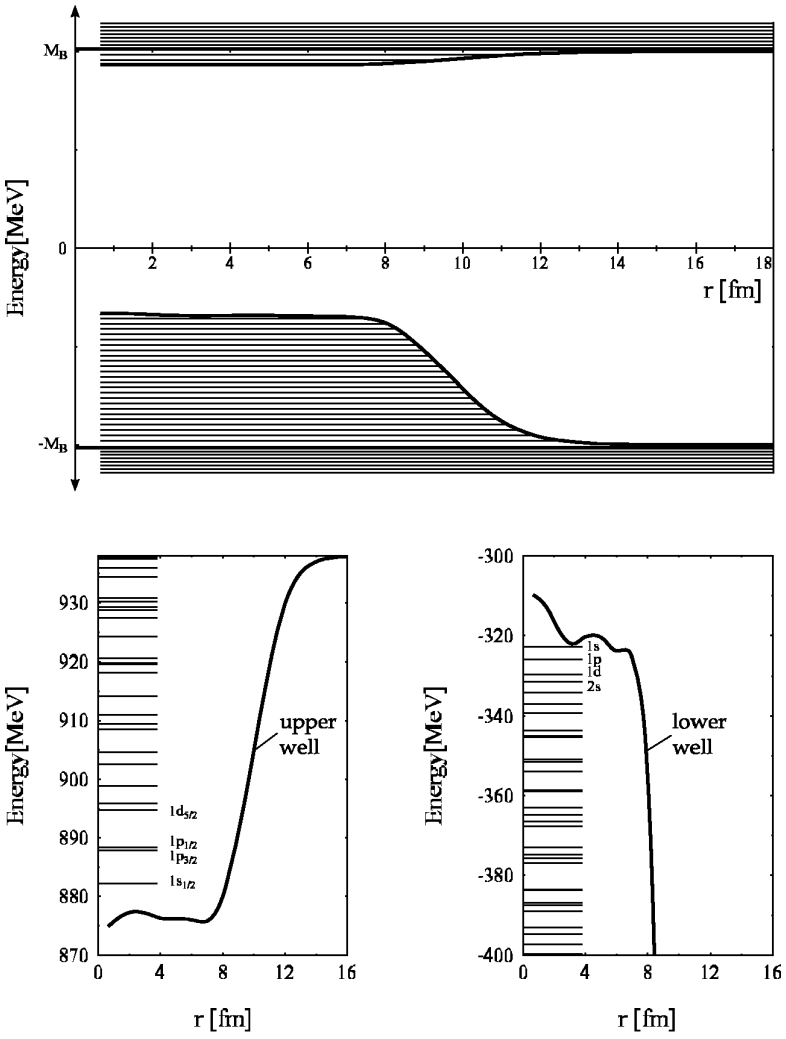

Fig. 22. Baryon spectrum in a nucleus. Below the positive energy continuum exists the potential well of real nucleons. It has a depth of 50-60 MeV and shows the correct shell structure. The shell model of nuclei is realized here. However, from the negative continuum another potential well arises, in which about 40000 bound particles are found, belonging to the vacuum. A part of the shell structure of the upper well and the lower (vacuum) well is depicted in the lower figures.

our world would be unstable, because the "ordinary" particles are found in the upper states which can decay through the emission of photons into lower lying states. However, if the "underworld" is occupied, the Pauli-principle will prevent this decay. Holes in the occupied "underworld" (Dirac sea) are antiparticles.

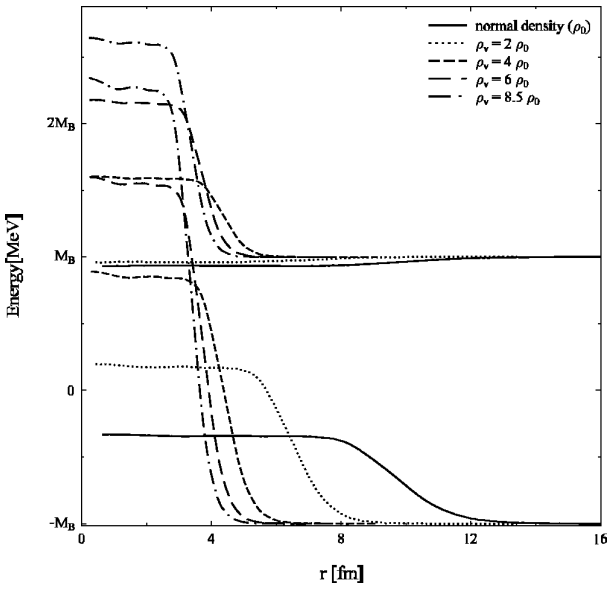

Fig. 23. The lower well rises strongly with increasing primary nucleon density, and even gets supercritical (spontaneous nucleon emission and creation of bound antinucleons). Supercriticality denotes the situation, when the lower well enters the upper continuum.

The occupied states of this underworld including up to 40000 occupied bound states of the lower potential well represent the **vacuum** . The peculiarity of this strongly correlated vacuum structure in the region of atomic nuclei is that — depending on the size of the nucleus — more than 20000 up to 40000 (occupied) bound nucleon states contribute to this polarization effect. Obviously, we are dealing here with a **highly correlated vacuum**. A pronounced shell structure can be recognized [32–34]. Holes in these states have to be interpreted as bound antinucleons (antiprotons, antineutrons). If the primary nuclear density rises due to compression, the lower well increases while the upper decreases and soon is converted into a repulsive barrier (Fig. 23). This compression of nuclear matter can only be carried out in relativistic nucleus-nucleus collision with the help of shock waves, which have been proposed by the Frankfurt school[29,30] and which have since then been confirmed extensively (for references see e. g. [35]). These **nuclear shock waves** are accompanied by heating of the nuclear matter. Indeed, density and temperature are intimately coupled in terms of the hydrodynamic Rankine-Hugoniot-equations. Heating as well as the violent dynamics cause the creation of many holes in the very deep (measured from $-M_B c^2$) vacuum well. These numerous bound holes resemble antimatter clusters which are bound in the medium; their wave functions have large overlap with antimatter clusters. When the primary matter density decreases during the expansion stage of the heavy ion collision, the potential wells, in particular the lower one, disappear.

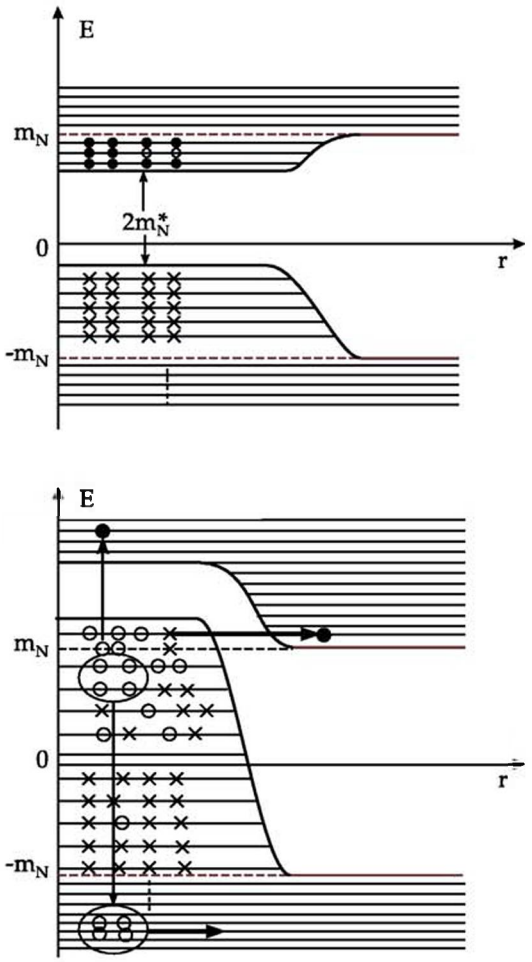

Fig. 24. Due to the high temperature and the violent dynamics, many bound holes (antinucleon clusters) are created in the highly correlated vacuum, which can be set free during the expansion stage into the lower continuum. In this way, antimatter clusters can be produced directly from the vacuum. The horizontal arrow in the lower part of the figure denotes the spontaneous creation of baryon-antibaryon pairs, while the antibaryons occupy bound states in the lower potential well. Such a situation, where the lower potential well reaches into the upper continuum, is called supercritical. Four of the bound holes states (bound antinucleons) are encircled to illustrate a "quasi-antihelium" formed. It may be set free (driven into the lower continuum) by the violent nuclear dynamics.

The bound antinucleons are then pulled down into the (lower) continuum. In this way antimatter clusters may be set free. Of course, a large part of the antimatter will annihilate on ordinary matter present in the course of the expansion.

However, it is important that this mechanism for the production of antimatter clusters out of the highly correlated vacuum does not proceed via the phase space. The required coalescence of many particles in phase space suppresses the production of clusters, while it is favoured by the direct production out of the highly correlated vacuum. In a certain sense, the highly correlated vacuum is a kind of cluster vacuum (vacuum with cluster structure). The shell structure of the vacuum levels (see Fig. 22) supports this latter suggestion. Fig. 24 illustrates this idea.

The mechanism is similar for the production of multi-hyper nuclei (Λ, Σ, Ξ, Ω). Meson field theory predicts also for the Λ energy spectrum at finite primary nucleon density the existence of upper and lower wells. The lower well belongs to the vacuum and is fully occupied by Λ's.

Dynamics and temperature then induce transitions ($\Lambda\bar{\Lambda}$ creation) and deposit many Λ's in the upper well. These numerous bound Λ's are sitting close to the primary baryons: in a certain sense a giant multi-Λ hypernucleus has been created. When the system disintegrates (expansion stage) the Λ's distribute over the nucleon clusters (which are most abundant in peripheral collisions). In this way multi-Λ hypernuclei can be formed.

Of course this vision has to be worked out and probably refined in many respects. This means much more and thorough investigation in the future. It is particularly important to gain more experimental information on the properties of the lower well by (e, e' p) or (e, e' p p') and also ($\bar{\mathrm{p}}_\mathrm{c}\mathrm{p}_\mathrm{b}$, $\mathrm{p}_\mathrm{c}\bar{\mathrm{p}}_\mathrm{b}$) reactions at high energy ($\bar{\mathrm{p}}_\mathrm{c}$ denotes an incident antiproton from the continuum, p_b is a proton in a bound state; for the reaction products the situation is just the opposite)[36]. Also the reaction (p, p' d), (p, p' ^{3}He), (p, p' ^{4}He) and others of similar type need to be investigated in this context. The systematic scattering of antiprotons on nuclei can contribute to clarify these questions. Problems of the meson field theory (e. g. Landau poles) can then be reconsidered. An effective meson field theory has to be constructed. Various effective theories, e. g. of Walecka-type on the one side and theories with chiral invariance on the other side, seem to give different strengths of the potential wells and also different dependence on the baryon density [37]. The Lagrangians of the Dürr-Teller-Walecka-type and of the chirally symmetric mean field theories look quite differently. We exhibit them — without further discussion — in the following equations:

$$\mathcal{L} = \mathcal{L}_{\mathrm{kin}} + \mathcal{L}_{\mathrm{BM}} + \mathcal{L}_{\mathrm{vec}} + \mathcal{L}_0 + \mathcal{L}_{\mathrm{SB}}$$

Non-chiral Lagrangian :

$$\begin{aligned}
\mathcal{L}_{\mathrm{kin}} &= \frac{1}{2}\partial_\mu s \partial^\mu s + \frac{1}{2}\partial_\mu z \partial^\mu z - \frac{1}{4}B_{\mu\nu}B^{\mu\nu} - \frac{1}{4}G_{\mu\nu}G^{\mu\nu} - \frac{1}{4}F_{\mu\nu}F^{\mu\nu} \\
\mathcal{L}_{\mathrm{BM}} &= \sum\nolimits_B \overline{\psi}_B \big[i\gamma_\mu \partial^\mu - g_{\omega B}\gamma_\mu \omega^\mu - g_{\phi B}\gamma_\mu \phi^\mu - g_{\rho B}\gamma_\mu \tau_B \rho^\mu \\
&\qquad - e\gamma_\mu \frac{1}{2}(1+\tau_B)A^\mu - m_B^* \big] \psi_B
\end{aligned}$$

$$\mathcal{L}_{\rm vec} = \frac{1}{2}m_\omega^2\omega_\mu\omega^\mu + \frac{1}{2}m_\rho^2\rho_\mu\rho^\mu + \frac{1}{2}m_\phi^2\phi_\mu\phi^\mu$$
$$\mathcal{L}_0 \quad = -\frac{1}{2}m_s^2 s^2 - \frac{1}{2}m_z^2 z^2 - \frac{1}{3}bs^3 - \frac{1}{4}cs^4$$

Chiral Lagrangian :

$$\mathcal{L}_{\rm kin} = \frac{1}{2}\partial_\mu\sigma\partial^\mu\sigma + \frac{1}{2}\partial_\mu\zeta\partial^\mu\zeta + \frac{1}{2}\partial_\mu\chi\partial^\mu\chi - \frac{1}{4}B_{\mu\nu}B^{\mu\nu} - \frac{1}{4}G_{\mu\nu}G^{\mu\nu} - \frac{1}{4}F_{\mu\nu}F^{\mu\nu}$$
$$\mathcal{L}_{\rm BM} = \sum_B \overline{\psi}_B\big[i\gamma_\mu\partial^\mu - g_{\omega B}\gamma_\mu\omega^\mu - g_{\phi B}\gamma_\mu\phi^\mu - g_{\rho B}\gamma_\mu\tau_B\rho^\mu$$
$$-e\gamma_\mu\frac{1}{2}(1+\tau_B)A^\mu - m_B^*\big]\psi_B$$
$$\mathcal{L}_{\rm vec} = \frac{1}{2}m_\omega^2\frac{\chi^2}{\chi_0^2}\omega_\mu\omega^\mu + \frac{1}{2}m_\rho^2\frac{\chi^2}{\chi_0^2}\rho_\mu\rho^\mu + \frac{1}{2}m_\phi^2\frac{\chi^2}{\chi_0^2}\phi_\mu\phi^\mu + g_4^4(\omega^4 + 6\omega^2\rho^2 + \rho^4)$$
$$\mathcal{L}_0 \quad = -\frac{1}{2}k_0\chi^2(\sigma^2+\zeta^2) + k_1(\sigma^2+\zeta^2)^2 + k_2(\frac{\sigma^4}{2}+\zeta^4) + k_3\chi\sigma^2\zeta - k_4\chi^4$$
$$+\frac{1}{4}\chi^4\ln\frac{\chi^4}{\chi_0^4} + \frac{\delta}{3}\ln\frac{\sigma^2\zeta}{\sigma_0^2\zeta_0^2}$$
$$\mathcal{L}_{\rm SB} = -\left(\frac{\chi}{\chi_0}\right)^2\left[m_\pi^2 f_\pi\sigma + \left(\sqrt{2}m_K^2 f_K - \frac{1}{\sqrt{2}}m_\pi^2 f_\pi\right)\zeta\right]$$

The non-chiral model contains the scalar-isoscalar field s and its strange counterpart z, the vector-isoscalar fields ω_μ and ϕ_μ, and the the ρ-meson ρ_μ as well as the photon A_μ. For more details see [37]. In contrast to the non-chiral model, the $SU(3)_L \times SU(3)_R$ Lagrangian contains the dilaton field χ introduced to mimic the trace anomaly of QCD in an effective Lagrangian at tree level (For an explanation of the chiral model see [37,38]).

The connection of the chiral Lagrangian with the Walecka-type can be established by the substitution $\sigma = \sigma_0 - s$ (and similarly for the strange condensate ζ). Then, e.g. the difference in the definition of the effective nucleon mass in both models (non-chiral:$m_N^* = m_N - g_s s$, chiral:$m_N^* = g_s\sigma$) can be removed, yielding:

$$m_N^* = g_s\sigma_0 - g_s s \equiv m_N - g_s s \tag{2}$$

for the nucleon mass in the chiral model.

Nevertheless, if the parameters in both cases are adjusted such that ordinary nuclei (binding energies, radii, shell structure,...) and properties of infinite nuclear matter (equilibrium density, compression constant K, binding energy) are well reproduced, the prediction of both effective Lagrangians for the dependence of the properties of the correlated vacuum on density and temperature is remarkably different. This is illustrated to some extend in Fig. 25. Accordingly, the chirally symmetric meson field theory predicts much higher primary densities (and temperatures) until the effects of the correlated vacuum are strong enough so that the mechanisms described here become effective. In other words, according to chirally symmetric meson field theories the antimatter-cluster-production and multi-hypermatter-cluster production out of the highly correlated vacuum

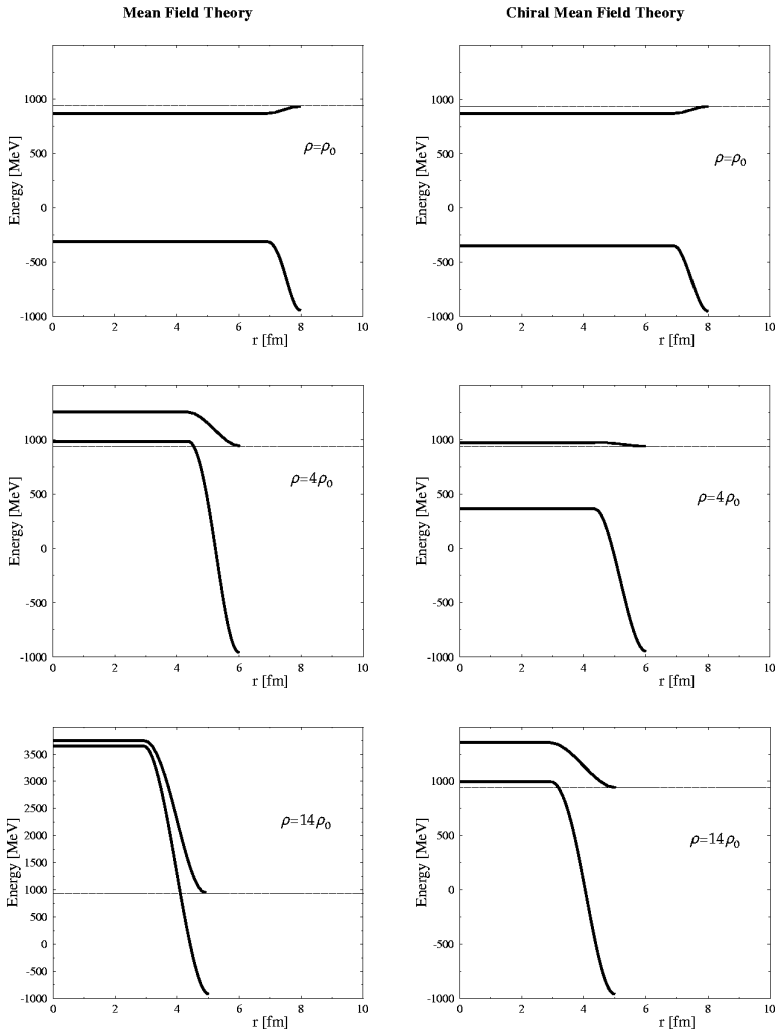

Fig. 25. The potential structure of the shell model and the vacuum for various primary densities $\rho = \rho_0$, $4\rho_0$, $14\rho_0$. At left the predictions of ordinary Dürr-Teller-Walecka-type theories are shown; at right those for a chirally symmetric meson field theory as develloped by P. Papazoglu, S. Schramm et al. [37,38]. Note however, that this particular chiral mean–field theory does contain ω^4 terms. If introduced in both effective models, they seem to predict quantitatively similar results.

takes place at considerably higher heavy ion energies as compared to the predictions of the Dürr-Teller-Walecka-type meson field theoories. This in itself is a most interesting, quasi-fundamental question to be clarified. Moreover, the question of the nucleonic substructure (form factors, quarks, gluons) and its influence

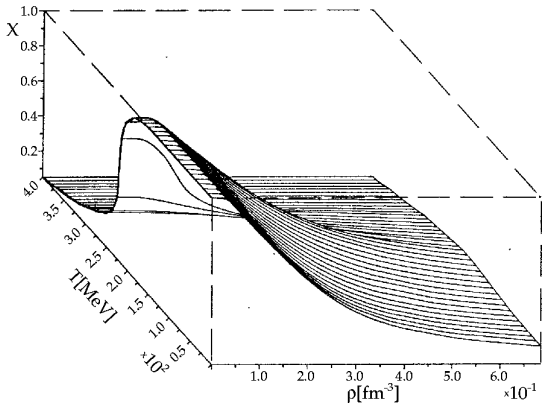

Fig. 26. The strong phase transition inherent in Dürr-Teller-Walecka-type meson field theories, as predicted by J. Theis et al. [39]. Note that there is a first order transition along the ρ-axis (i.e. with density), but a simple transition along the temperature T-axis. Note also that this is very similar to the phase transition obtained recently from the Nambu-Jona-Lasinio-approximation of QCD [41].

on the highly correlated vacuum structure has to be studied. The nucleons are possibly strongly polarized in the correlated vacuum: the Δ resonance correlations in the vacuum are probably important. Is this highly correlated vacuum state, especially during the compression, a preliminary stage to the quark-gluon cluster plasma? To which extent is it similar or perhaps even identical with it? It is well known for more than 10 years that meson field theories predict a phase transition qualitatively and quantitatively similar to that of the quark-gluon plasma [39] — see Fig. 26.

The extension of the periodic system into the sectors hypermatter (strangeness) and antimatter is of general and astrophysical importance. Indeed, microseconds after the big bang the new dimensions of the periodic system, we have touched upon, certainly have been populated in the course of the baryo- and nucleo-genesis. Of course, for the creation of the universe, even higher dimensional extensions (charm, bottom, top) come into play, which we did not pursue here. It is an open question, how the depopulation (the decay) of these sectors influences the distribution of elements of our world today. Our conception of the world will certainly gain a lot through the clarification of these questions.

For the Gesellschaft für Schwerionenforschung (GSI), which I helped initiating in the sixties, the questions raised here could point to the way ahead. Working groups have been instructed by the board of directors of GSI, to think about the future of the laboratory. On that occasion, very concrete (almost too concrete) suggestions are discussed — as far as it has been presented to the public. What is missing, as it seems, is a **vision on a long term basis**. The ideas proposed here, the verification of which will need the **commitment for 2–4 decades of research**, could be such a vision with considerable attraction

for the best young physicists. The new dimensions of the periodic system made of hyper- and antimatter cannot be examined in the "stand-by" mode at CERN (Geneva); a dedicated facility is necessary for this field of research, which can in future serve as a home for the universities. The GSI — which has unfortunately become much too self-sufficient — could be such a home for new generations of physicists, who are interested in the **structure of elementary matter**. GSI would then not develop just into a detector laboratory for CERN, and as such become obsolete. I can already see the enthusiasm in the eyes of young scientists, when I unfold these ideas to them — similarly as it was 30 years ago, when the nuclear physicists in the state of Hessen initiated the construction of GSI.

Acknowledgments

I am grateful to Dipl.-Phys. Thomas Bürvenich for helping me in the technical production of these proceedings.

References

1. S.G: Nilsson et al.: Phys. Lett. **B28**, 458 (1969); Nucl. Phys. **A131**, 1 (1969); Nucl. Phys. **A115**, 545 (1968)
2. U. Mosel, B. Fink and W. Greiner: Contribution to "Memorandum Hessischer Kernphysiker" Darmstadt, Frankfurt, Marburg (1966)
3. U. Mosel and W. Greiner: Z. Physik **217**, 256 (1968); **222**, 261 (1968)
4. a) J. Grumann, U. Mosel, B. Fink and W. Greiner: Z. Physik **228**, 371 (1969)
   b) J. Grumann, Th. Morovic, W. Greiner: Z. f. Naturforschung **26a**, 643 (1971)
5. A. Sandulescu, R.K. Gupta, W. Scheid, W. Greiner: Phys. Lett. **B60**, 225 (1976)
   R.K. Gupta, A. Sandulescu, W. Greiner: Z. f. Naturforschung **32a**, 704 (1977)
   R.K. Gupta, A.Sandulescu and W. Greiner: Phys. Lett. **B64**, 257 (1977)
   R.K. Gupta, C. Parrulescu, A. Sandulescu, W. Greiner: Z. Physik **A283**, 217 (1977)
6. G. M. Ter-Akopian et al.: Nucl. Phys. **A255**, 509 (1975)
   Yu.Ts. Oganessian et al.: Nucl. Phys. **A239**, 353 and 157 (1975)
7. D. Scharnweber, U. Mosel and W. Greiner: Phys. Rev. Lett. **24**, 601 (1970)
   U. Mosel, J. Maruhn and W. Greiner: Phys. Lett. **B34**, 587 (1971)
8. G. Münzenberg et al.: Z. Physik **A309**, 89 (1992)
   S.Hofmann et al.: Z. Phys **A350**, 277 and 288 (1995)
9. R. K. Gupta, A. Sandulescu and Walter Greiner: Z. für Naturforschung **32a**, 704 (1977)
10. A. Sandulescu and Walter Greiner: Rep. Prog. Phys **55**, 1423 (1992); A. Sandulescu, R. K. Gupta, W. Greiner, F. Carstoin and H. Horoi: Int. J. Mod. Phys. **E1**, 379 (1992)
11. A. Sobiczewski: Phys. of Part. and Nucl. **25**, 295 (1994)
12. R. K. Gupta, G. Münzenberg and W. Greiner: J. Phys. G: Nucl. Part. Phys. **23**, L13 (1997)
13. V. Ninov, K. E. Gregorich, W. Loveland, A. Ghiorso, D. C. Hoffman, D. M. Lee, H. Nitsche, W. J. Swiatecki, U. W. Kirbach, C. A. Laue, J. L. Adams, J. B. Patin, D. A. Shaughnessy, D. A. Strellis and P. A. Wilk: preprint
14. K. Rutz, M. Bender, T. Bürvenich, T. Schilling, P.-G. Reinhard, J.A. Maruhn, W. Greiner: Phys. Rev. **C56**, 238 (1997)

15. B. Fricke and W. Greiner: Phys. Lett. **B30**, 317 (1969)
B. Fricke, W. Greiner, J.T. Waber: Theor. Chim. Acta (Berlin) **21**, 235 (1971)
16. A. Sandulescu, D.N. Poenaru, W. Greiner: Sov. J. Part. Nucl. **11(6)**, 528 (1980)
17. Harold Klein: thesis, Inst. für Theoret. Physik, J.W. Goethe-Univ. Frankfurt a. M. (1992)
Dietmar Schnabel: thesis, Inst. für Theoret. Physik, J.W. Goethe-Univ. Frankfurt a.M. (1992)
18. D. Poenaru, J.A. Maruhn, W. Greiner, M. Ivascu, D. Mazilu and R. Gherghescu: Z. Physik **A328**, 3009 (1987); Z. Physik **A332**, 291 (1989)
19. E. K. Hulet, J. F. Wild, R. J. Dougan, R. W.Longheed, J. H. Landrum, A. D. Dougan, M. Schädel, R. L. Hahn, P. A. Baisden, C. M. Henderson, R. J. Dupzyk, K. Sümmerer, G. R. Bethune: Phys. Rev. Lett. **56**, 313 (1986)
20. K. Depta, W. Greiner, J. Maruhn, H.J. Wang, A. Sandulescu and R. Hermann: Intern. Journal of Modern Phys. **A5**, No. 20; 3901 (1990)
K. Depta, R. Hermann, J.A. Maruhn and W. Greiner: in "Dynamics of Collective Phenomena", ed. P. David, World Scientific, Singapore (1987) 29
S. Cwiok, P. Rozmej, A. Sobiczewski, Z. Patyk: Nucl. Phys. **A491**, 281 (1989)
21. A. Sandulescu and W. Greiner in discussions at Frankfurt with J. Hamilton (1992/1993)
22. J.H. Hamilton, A.V. Ramaya et al.: Journ. Phys. **G20**, L85 (1994)
23. B. Burggraf, K. Farzin, J. Grabis, Th. Last, E. Manthey, H. P. Trautvetter, C. Rolfs: "Energy Shift of first excited state in ^{10}Be ?", accepted for publication in Journ. of. Phys. **G**
24. P. Hess et al.: "Butterfly and Belly Dancer Modes in ^{96}Sr + ^{10}Be + ^{146}Ba", in preparation
25. E.K. Hulet et al.: Phys. Rev. **C40**, 770 (1989)
26. W. Greiner, B. Müller, J. Rafelski: "QED of Strong Fields", Springer Verlag, Heidelberg (1985). For a more recent review see W. Greiner, J. Reinhardt, "Supercritical Fields in Heavy–Ion Physics", Proceedings of the 15th Advanced ICFA Beam Dynamics Workshop on Quantum Aspects of Beam Physics, World Scientific (1998)
27. B. Povh: Rep. Progr. Phys. **39**, 823 (1976); Ann. Rev. Nucl. Part. Sci. **28**, 1 (1978); Nucl. Phys. **A335**, 233 (1980); Progr. Part. Nucl. Phys. **5**, 245 (1981); Phys. Blätter **40**, 315 (1984)
28. J. Schaffner, Carsten Greiner and H. Stöcker: Phys. Rev. **C45**, 322 (1992); Nucl. Phys. **B24**, 246 (1991); J. Schaffner, C.B. Dover, A. Gal, D.J. Millener, C. Greiner, H. Stöcker: Annals of Physics **235**, 35 (1994)
29. W. Scheid and W. Greiner: Ann. Phys. **48**, 493 (1968); Z. Phys. **226**, 364 (1969)
30. W. Scheid, H. Müller and W. Greiner: Phys. Rev. Lett. **13**, 741 (1974)
31. H. Stöcker, W. Greiner and W. Scheid: Z. Phys. **A286**, 121 (1978)
32. I. Mishustin, L.M. Satarov, J. Schaffner, H. Stöcker and W.Greiner: Journal of Physics G (Nuclear and Particle Physics) **19**, 1303 (1993)
33. P.K. Panda, S.K. Patra, J. Reinhardt, J. Maruhn, H. Stöcker, W. Greiner: Int. J. Mod. Phys. **E6**, 307 (1997)
34. N. Auerbach, A. S. Goldhaber, M. B. Johnson, L. D. Miller and A. Picklesimer: Phys. Lett. **B182**, 221 (1986)
35. H. Stöcker and W. Greiner: Phys. Rep. **137**, 279 (1986)
36. J. Reinhardt and W. Greiner: to be published.
37. P. Papazoglou, D. Zschiesche, S. Schramm, H. Stöcker, W. Greiner: J. Phys. G **23**, 2081 (1997); P. Papazoglou, S. Schramm, J. Schaffner-Bielich, H. Stöcker, W. Greiner: Phys. Rev. **C57**, 2576 (1998)

38. P. Papazoglou, D. Zschiesche, S. Schramm, J. Schaffner–Bielich, H. Stöcker, W. Greiner: nucl–th/9806087, accepted for publication in Phys. Rev. **C**
39. J. Theis, G. Graebner, G. Buchwald, J. Maruhn, W. Greiner, H. Stöcker and J. Polonyi: Phys. Rev. **D28**, 2286 (1983)
40. P. Papazoglou: PhD thesis, University of Frankfurt, 1998; C. Beckmann et al.: in preparation
41. S. Klimt, M. Lutz, W. Weise: Phys. Lett. **B249**, 386 (1990)